sensors

Special Issue Reprint

LoRa Communication Technology for IoT Applications

Edited by
Luca Leonardi

mdpi.com/journal/sensors

MDPI

LoRa Communication Technology for IoT Applications

LoRa Communication Technology for IoT Applications

Guest Editor

Luca Leonardi

MDPI

Basel • Beijing • Wuhan • Barcelona • Belgrade • Novi Sad • Cluj • Manchester

Guest Editor
Luca Leonardi
Department of Electrical,
Electronic and Computer
Engineering
University of Catania
Catania
Italy

Editorial Office
MDPI AG
Grosspeteranlage 5
4052 Basel, Switzerland

This is a reprint of the Special Issue, published open access by the journal *Sensors* (ISSN 1424-8220), freely accessible at: https://www.mdpi.com/journal/sensors/special_issues/P5ZJD7K80D.

For citation purposes, cite each article independently as indicated on the article page online and as indicated below:

Lastname, A.A.; Lastname, B.B. Article Title. *Journal Name* **Year**, *Volume Number*, Page Range.

ISBN 978-3-7258-4475-3 (Hbk)
ISBN 978-3-7258-4476-0 (PDF)
https://doi.org/10.3390/books978-3-7258-4476-0

Contents

sensors

MDPI

Review

LoRaWAN Meets ML: A Survey on Enhancing Performance with Machine Learning

Arshad Farhad and Jae-Young Pyun *

Wireless and Mobile Communication System Laboratory, Department of Information and Communication Engineering, Chosun University, Gwangju 61452, Republic of Korea; arshad@chosun.ac.kr
* Correspondence: jypyun@chosun.ac.kr

Abstract: The Internet of Things is rapidly growing with the demand for low-power, long-range wireless communication technologies. Long Range Wide Area Network (LoRaWAN) is one such technology that has gained significant attention in recent years due to its ability to provide long-range communication with low power consumption. One of the main issues in LoRaWAN is the efficient utilization of radio resources (e.g., spreading factor and transmission power) by the end devices. To solve the resource allocation issue, machine learning (ML) methods have been used to improve the LoRaWAN network performance. The primary aim of this survey paper is to study and examine the issue of resource management in LoRaWAN that has been resolved through state-of-the-art ML methods. Further, this survey presents the publicly available LoRaWAN frameworks that could be utilized for dataset collection, discusses the required features for efficient resource management with suggested ML methods, and highlights the existing publicly available datasets. The survey also explores and evaluates the Network Simulator-3-based ML frameworks that can be leveraged for efficient resource management. Finally, future recommendations regarding the applicability of the ML applications for resource management in LoRaWAN are illustrated, providing a comprehensive guide for researchers and practitioners interested in applying ML to improve the performance of the LoRaWAN network.

Keywords: LoRa; LoRaWAN; Internet of Things (IoT); machine learning (ML); resource management; spreading factor (SF); transmission power (TP); simulation; artificial intelligence; deep learning; reinforcement learning; dataset

1. Introduction

The Internet of Things (IoT) is a rapidly growing field that involves connecting a wide range of devices to the Internet to enable communication and data exchange between them. IoT enables seamless integration of the physical and digital worlds, revolutionizing various domains such as healthcare, transportation, agriculture, and industrial automation [1–4]. In IoT connectivity, several technologies have emerged to address the diverse requirements of IoT applications. These technologies comprise Long-Range Wide Area Networks (LoRaWAN), SigFox, Narrowband (NB)-IoT, Weightless, and Long Term Evolution for Machines (LTE-M) [5–8]. The key features of these IoT technologies are illustrated in Table 1. Sigfox offers a simple and low-cost deployment, while NB-IoT leverages the existing cellular infrastructure and provides higher data rates. The Weightless protocol provides flexibility and scalability, and LTE-M supports enhanced mobility and coverage. LoRaWAN [9] is among the leading low-power wide area network (LPWAN) technologies that have gained significant attention recently due to its ability to provide long-range communication with low power consumption. As a result, it has been extensively adopted by academia and industries for the IoT.

Table 1. Key features of widely adopted IoT technologies [10,11].

Feature	LoRaWAN	Sigfox	NB-IoT	Weightless	LTE-M
Spectrum	ISM band (region-specific)	868 MHz, 915 MHz	1800 MHz, 2100 MHz	915 MHz, 2400 MHz	1800 MHz, 2100 MHz
Bandwidth	125, 250, and 500 kHz	100 Hz	Narrowband, typically 200 kHz	LTE bandwidth, typically up to several MHz	Typically several MHz
Modulation	Chirped spread spectrum	Ultra Narrowband)	GMSK	various (depends on the variant (GFSK)	OFDM
Payload size	Up to 243 bytes	Up to 128 bytes	Up to 1600 bytes	Up to 255 bytes	Up to 1500 bytes
Data rate	Up to 100 kbps	Up to 100 bps	Up to 200 kbps	Up to 1 Mbps	Up to 1 Mbps
Range [km]	Urban = 5, Rural = 20	Urban = 10, Rural = 40	Urban = 1, Rural = 10	Up to 10 km	Up to 10 km
Adaptive data rate	Yes	No	Yes	Yes	Yes
Energy consumption	Very low	Very low	Low to moderate	Low	Low to moderate
Mobility support	Yes (without ADR)	No	Limited	Limited	Limited
Localization	RSSI and TDoA [12,13]	No	No	Yes	Varies
Private network	Yes	No	Yes	Yes	Yes
Bidirectional communication	Yes	No	Yes	Yes	Yes
Deployment	Public	Closed	Public	Public	Public
Simulators [public]	Yes [14–30]	Yes [31–33]	Yes [34,35]	Not publicly available	Yes [35–38]

Long Range (LoRa) is the physical layer (PHY) primarily based on chirp spread spectrum (CSS) modulation, making it capable of achieving long-range and low power consumption [39]. LoRaWAN is the medium access control layer (MAC) responsible for efficiently managing communication between LoRa end devices (ED) and gateways (GW). In addition, LoRaWAN offers features such as adaptive data rate (ADR) for efficient resource management, bi-directional communication, and strong security, making it a robust and scalable solution for IoT deployments [40]. With their long range, ultra-low power consumption, and efficient network management, LoRa and LoRaWAN are revolutionizing the IoT landscape, empowering businesses and industries with seamless connectivity and enabling innovative IoT applications across various sectors [41].

1.1. Existing Surveys on LoRa/LoRaWAN and Motivation

The specification of LoRa provides a detailed overview of the PHY and LoRaWAN features along with the ADR, retransmission procedures, and other features [42]. However, the decision-making of resource parameters configuration and optimal allocation to EDs [e.g., SF, bandwidth (BW), coding rate (CR), and transmission power (TP)] is left open to developers and academic researchers, allowing them to create and develop solutions for IoT applications.

In recent years, the LoRa/LoRaWAN has been surveyed in various aspects, such as ADR optimizations, mobility management, simulation tools, routing, security, etc., highlighting advantages, disadvantages, and future recommendations, as illustrated in Table 2. Table 2 presents the existing surveys and tutorials with the main focus and brief description of the topics covered on LoRa/LoRaWAN. In addition, the current surveys and tutorials in Table 2 are not focusing on the resource allocation issue addressed using machine learning (ML) methods for the LoRa/LoRaWAN. Therefore, this survey fills the stated gap by presenting a constructive and comprehensive review of the use of ML in LoRa/LoRaWAN.

Table 2. Overview of surveys and tutorials on LoRa and LoRaWAN from 2018 to July 2023.

Ref.	Year	Main Focus of Survey	Brief Description of Main Topics Covered
[43]	2018	Pros and Cons of LoRaWAN	Compared existing solutions along with pros and cons and highlighted challenges and solutions.
[44]	2018	Security risks of LoRaWAN	Discussed and analyzed the impact and likelihood of each security threat in LoRaWAN.
[45]	2018	LoRa and its applications	Presented a comprehensive review regarding LoRa and its applications.
[46]	2019	advantages and disadvantages	Compared NB-IoT, LoRa, and Wi-Fi HaLow in terms of their main characteristics.
[47]	2019	Comparative study	Studied LoRaWAN, NB-IoT, LTE-M, and Sigfox and their use in WSN scenarios.
[48]	2019	Edge and Fog computing	Discussed LoRa-based edge and fog computing paradigms, highlighted pros and cons.
[49]	2019	LoRa/LoRaWAN challenges	Reviewed challenges of LoRa in scalability, capacity, and signal collision.
[50]	2019	Overview of LoRaWAN, DASH7, and NB-IoT	Reviewed the architectures and addressed the mobility management issues, and presented a comparative study of LoRaWAN, DASH7, and NB-IoT.
[51]	2019	Overview LPWA technologies	Provided an overview of the existing solutions and identified key research challenges to be addressed in LPWA technologies.
[52]	2019	LoRaWAN simulators	Reviewed several existing available simulators for LoRa/LoRaWAN along with design requirements and their limitations and how to improve simulators.
[53]	2019	Security and energy	Overviewed LoRaWAN in terms of security and energy based on existing state-of-the-art.
[54]	2019	Capacity of LoRaWAN	Studied the capacity of LoRaWAN in terms of ADR, channels, SF, RF, and ED density, along with challenges and future research opportunities.
[55]	2019	LoRaWAN simulators	Provided an overview of existing simulators for LoRa/LoRaWAN with requirements and limitations.
[56,57]	2020	ADR optimization	Reviewed the existing ADR solutions, discussed the impact on the performance of LoRaWAN networks, identified challenges and future optimization techniques for improving the ADR.
[58]	2020	LoRa networking challenges	Investigated the challenges in terms of networking faced during deployment, presented recent solutions, and discussed open issues considering practical large-scale deployment of LoRa networks.
[59]	2020	Feasibility of adapting UDN	Carried the feasibility of adapting an ultra-dense network (UDN) within LoRaWAN and provided details of Mesh-LoRaWAN topology for UDN.
[60]	2020	Visual data transmission	Evaluated existing techniques regarding the image transmission over LoRa networks, presented challenges, and solutions to overcome them.
[61]	2020	LoRaWAN mesh networks	Presented a review and comparative analysis on the classification of multihop communication solutions, discussed issues and highlighted future research directions.
[62]	2020	Security in LoRaWAN	Analyzed security issues and possible network attacks in LoRaWAN and presented countermeasures preventing LoRaWAN from attacks.
[63]	2020	Routing in LoRaWAN	Discussed related approaches concerning multihop communication and routing protocols.
[64]	2020	Confirmed traffic in LoRaWAN	Highlighted use cases, examined several aspects of confirmed traffic along with existing solutions.
[65]	2020	Performance review of LoRa	Discussed the LoRa technology and reviewed performance.
[66]	2021	Use of ML in LoRa	Surveyed the general issues related to LoRaWAN, overviewed the ML solutions, and highlighted key future research directions.
[67]	2021	LoRaWAN optimizations	Presented existing solutions in five aspects: coexistence, resource allocation, MAC layer, network planning, and mobility support.
[68]	2021	UAV-Based LoRa communication	Studied deployments of UAV-based LoRa network and reviewed systematically focusing on the communication setup and its performance.
[69]	2021	ADR enhancements	Reviewed the existing ADR solutions with regard to mobility.
[70]	2021	Routing in LoRaWAN	Investigated routing approaches in multi-hop networks.
[71]	2021	Comparative analysis LoRaWAN and NB-IoT	Compared LoRaWAN and NB-IoT in terms of power consumption, security, latency, and throughput perspectives.
[72]	2021	Performance evaluation	Studied the factors affecting the capacity of the LoRa networks and its performance.
[73]	2021	Simulation tools	Presented the available simulation tools utilized for LoRaWAN performance assessment in ns-3.
[74]	2022	Resource allocation (e.g., SF)	Presented a concise overview of the traditional SF assignment methods to IoT end devices.
[75]	2022	LoRaWAN optimizations	Discussed various aspects, including bandwidth, modulation, data rate, coverage, link budget, payload, power efficiency, security, ADR optimizations, and localization concerning LoRaWAN.
[76]	2022	LoRa networking techniques	Surveyed the LoRa network techniques in LoRa (PHY layer), LoRaMAC layer (WAN), and application layers along with challenges and future trends.
[77]	2022	LoRaWAN protocols	Provided an extensive survey on the existing LoRaWAN communication protocols focusing on the energy efficiency at both LoRa (PHY layer) and LoRaMAC layer (WAN).
[78]	2022	Energy efficiency	Surveyed the existing works on energy efficiency at LoRa and LoRaWAN.
[79,80]	2022	LoRa simulators	Presented a comparative study simulation tool for the simulation of LoRa/LoRaWAN networks.
[81]	2022	LoRaWAN security	Highlighted vulnerabilities and security attacks, discussed their systematic mitigation approaches.
[82]	2022	Recent advancement in LoRa	Reviewed LoRa concerning analysis, communication, security, and applications.
[83]	2023	Scalability in LoRaWAN	Discussed scalability challenges with existing state-of-the-art solutions to assist LoRaWAN deployment in massive IoT networks.
[84]	2023	Artificial Intelligence of Medical Things (AIoMT)	Explored the current literature in the AIoMT, emphasized the powerful association between AI and IoT technologies.
Our survey		ML for resource management (e.g., SF, TP, BW)	This survey presents an in-depth review of resource management issues with state-of-the-art ML solutions, discussing the LoRaWAN frameworks for dataset collection, providing a constructive review on the ns-3-based ML frameworks, and presents future recommendations.

1.2. Methodology

We started with a systematic literature review methodology for this survey on improving LoRaWAN performance with ML, as illustrated in [85]. We first comprehensively searched the abstracts of all papers on IEEE Xplore, ACM, Elsevier, Wiley, and MDPI databases for LoRa/LoRaWAN and AI/ML/DL/RL. The search yielded approximately 148 papers, which include all aspects of LoRa/LoRaWAN resolved through ML techniques, as illustrated in Figure 1.

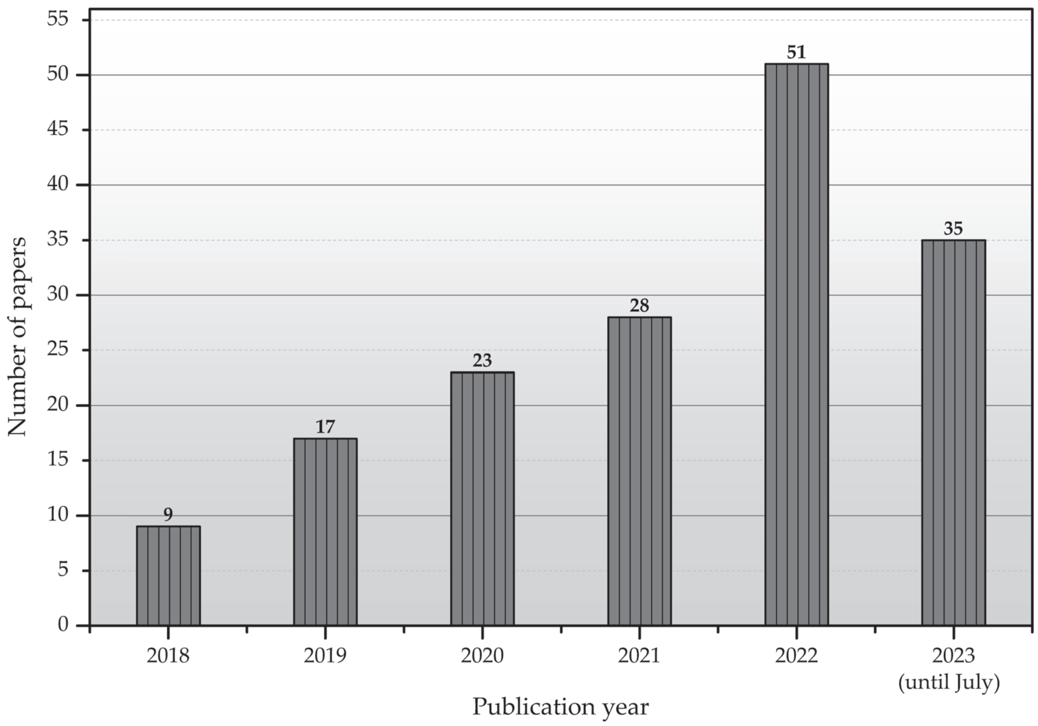

Figure 1. Number of published articles found in the existing literature for improving the performance of LoRaWAN using ML applications.

However, this survey only focuses on the performance improvement of LoRaWAN achieved using efficient resource management (e.g., channel allocation, SF, TP, and BW) through ML. Out of 148 papers, we found 36 papers dealing with resource management issues. This number also includes manually adding a small number of papers not found by our initial search, using backward reference searching and cross-citation techniques.

1.3. Scope and Contribution of the Survey

In contrast to published surveys and tutorials highlighted with a brief description of the main topics covered in Table 2, which present many characteristics or provide a comprehensive evaluation of the LoRa and LoRaWAN communication systems, where a comparison with other LWPAN technologies, potentials of both LoRa and LoRaWAN, ADR optimization/enhancement techniques, interference/collision mitigation, and available simulators for LoRa/LoRaWAN are the major topics, our survey mainly focuses on resource allocation issue addressed through ML for improving LoRaWAN performance.

The contribution of this survey, compared to the surveys and tutorials presented in Table 2, is as follows:

1. We provide a systematic overview of the different areas of LoRaWAN performance where ML/DL/RL has been applied. We discuss the core LoRaWAN issues that can be addressed with ML/DL/RL and provide examples of how ML/DL/RL has been used to address these issues;
2. We discuss the publicly available LoRaWAN frameworks, which can potentially be applied for dataset collection. A comprehensive study has been carried out to highlight the best features for efficient resource allocation and the ML/DL/RL methods for improving LoRaWAN performance;
3. We extensively provide a discussion on the Network Simulator-3-based ML/DL/RL frameworks that could be utilized for efficient resource allocation with comprehensive scenarios;

4. We identify open challenges in each area of LoRaWAN performance, discuss future research directions concerning resource allocation, and highlight potential benefits of ML for improving LoRaWAN performance.

1.4. Structure of the Survey

Section 2 highlights the core features of LoRa and LoRaWAN. Section 3 presents state-of-the-art methods for improving LoRaWAN performance using ML, DL, and RL. Section 4 elaborates on the existing LoRaWAN frameworks that could be utilized for dataset collection, discusses the required features, and highlights the best suitable ML methods for resource allocation concerning the features. Section 5 discusses the publicly available datasets utilized for various LoRaWAN deployments and IoT applications. Section 6 presents the existing publicly available ns-3-based ML frameworks and discusses how to utilize them for improving the performance of LoRaWAN. Section 7 presents a detailed discussion and highlights the potentials and limitations of the resource management ML methods applied on EDs and NS sides. Section 8 elaborates on the open research opportunities regarding efficient resource management, whereas Section 9 provides concluding remarks on this survey paper.

2. Core Features of LoRa and LoRaWAN

This section briefly presents the core features of LoRa and LoRaWAN.

2.1. LoRa-Long Range

LoRa [86] is a radio frequency (RF) modulation technology that defines the PHY layer features for long-range communications. LoRa is a proprietary PHY layer modulation based on CSS modulation to achieve long-range communication [87]. CSS is a subset of Direct-Sequence Spread Spectrum (DSSS), helping the GW to recover a weak signal and achieve high sensitivity, enabling increased coverage at a lower data rate (DR) [88,89]. In addition, LoRa utilizes five configurable resource parameters, i.e., SF, TP, CR, BW, and carrier frequency (CF), to fine-tune the link performance and energy consumption [56,74,79,90,91]. These configurable resource parameters of LoRa communication are discussed here.

2.1.1. Spreading Factor (SF)

The number of bits encoded in a symbol by LoRa is an adjustable resource parameter known as the SF. LoRa operates in six SFs (i.e., $SF_7 \sim SF_{12}$), utilized by the ED during uplink (UL) transmission. To transmit a UL packet, the EDs select a random channel using ALOHA channel access mechanism [92]. Furthermore, the choice of SF an ED utilizes during the communication plays a significant role for different reasons: a higher SF (e.g., 11, 12) complies with a high distance coverage; however, it indicates a low DR and high time-on-air (ToA) [67,93,94]. For example, the ToA for a packet size of 51B and 1% duty cycle (DC), considering the EU region (i.e., 868 MHz), is illustrated in Table 3. Table 3 is computed using The Things Network (TTN) community network platform, where the TTN has utilized the LoRaWAN regional parameters [9], consisting of the duty-cycled limited transmissions to comply with the European Telecommunications Standards Institute (ETSI) regulations. In the EU region, the ETSI imposes DC limitations, where LoRaWAN complies with a maximum DC of 1%. The TTN uses a fair access policy (FAP) [95], allowing ED to send data to GW for at most 30 s of ToA and ten downlink messages (including acknowledgments for confirmed packets) per ED per 24 h [96,97]. Based on the TTN network, SF_{11} and SF_{12} are only allowed when ADR is enabled. Increasing the SF by one step doubles the ToA (for the same BW). It also indicates that a single transmission on SF_{10} takes more time than 6 on SF_7, or may need about the same ToA as 3 on SF_7, SF_8, and SF_9 combined. As a consequence of this behavior, the use of ADR or blind ADR is suggested for SF and TP adjustment [98–100].

Table 3. Time-on-air, duty cycle, and fair access policy (FAP) conditions at 125 kHz and packet size of 51B [101,102].

Conditions	SF7	SF8	SF9	SF10	SF11	SF12
ToA [ms]	118.0	215.6	390.1	698.4	1478.7	2793.5
1% DC [s]	11.8	21.6	39.0	69.8	147.9	279.3
1% DC [msg/h]	305	167	92	51	24	12
FAP [avg · s]	339.9	620.8	1123.6	2011.3	4258.5	8045.2
FAP [avg/h]	10.6	5.8	3.2	1.8	0.8	0.4
FAP [msg/h]	254	139	76	42	20	10

2.1.2. Transmission Power (TP)

In LoRa, TP is an adjustable parameter with a step of 2, ranging from 2 to 14 dBm. TP is controlled by the ADR, implemented at the ED and NS sides to control the energy consumption of EDs [103,104].

2.1.3. Coding Rate (CR)

LoRa uses forward error correction (FEC) to improve the reliability of wireless transmissions. FEC adds redundant bits to the data, which can be used to correct errors occurring during transmission. The CR determines the redundancy added to the data. The smaller the CR, the more redundant bits are added, and the more reliable the transmission will be. However, a smaller CR will also increase the time it takes to transmit the data. The CR can be chosen among 4/5, 4/6, 4/7, and 4/8. The smallest CR, 4/8, provides the best reliability but takes the longest ToA to transmit the data. The largest CR, 4/5, provides the least reliability but sends the data the fastest. The choice of CR depends on the application that requires high reliability, such as industrial automation. A large CR should be used for applications that require fast data transmission, such as asset tracking.

2.1.4. Carrier Frequency (CF)

CF in LoRaWAN is the frequency at which a LoRa ED transmits data toward GW. It is typically selected from a range of frequencies in a particular region. The CF affects the capacity and power consumption of ED. For example, the LoRa CF can be programmed in steps of 61 Hz between 137 MHz to 1020 MHz. However, depending on the particular LoRa chip, this range may be limited to 860 MHz to 1020 MHz [103]. LoRa supports different ISM frequencies (in MHz), namely EU863-870 (Europe), US902-928 (North America), EU433 (Asia), CN470-510, CN779-787 (China), AU915-928 (Australia), KR920-923 (Korea), and IN865-867 (India) [9].

2.1.5. Bandwidth (BW)

LoRa operates in three BW: 125, 250, and 500 kHz. The BW is determined by the regional parameters, as specified in the LoRaWAN specifications [9]. A LoRa-modulated signal comprises 2^{SF} chips spread over the available BW. The SF parameter controls the spreading BW and the signal sensitivity to noise. A larger SF value results in a wider spreading of BW and lower sensitivity to noise. However, it reduces the DR.

2.2. Long Range Wide Area Network (LoRaWAN)

LoRaWAN defines MAC layer features as consisting of a star-of-stars topology comprising many EDs, GW, NS, and application servers, as shown in Figure 2. The EDs in LoRaWAN network are classified as *Class A*, *Class B*, and *Class C* [105]. *Class A* EDs are battery-powered and consume ultra-low energy. These EDs are bi-directional and receive acknowledgment (ACK) from NS with two available receive windows (*RXs*). *Class B* EDs are also battery-powered and provide bi-directional communication. These EDs support unicast and multicast transmission, though they have more *RXs* and are synchronized with a beacon frame transmitted by the GW after a certain time. Finally, *Class C* EDs use more power and listen all the time, excluding the transmission time. Among these EDs classes, *Class A* EDs deal with sensors and are implemented in IoT applications, owing to their energy efficiency and bi-directional communications [79]. Furthermore, LoRaWAN supports two communication modes: confirmed and unconfirmed.

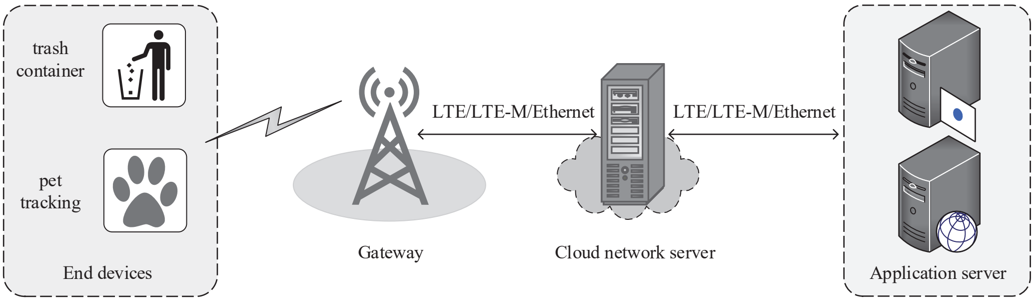

Figure 2. LoRaWAN network.

2.2.1. Confirmed Mode

In LoRaWAN, the ED initiates data transmission with an SF and TP. The SF and TP are allocated by the NS using the ADR mechanism, as defined in [99,106–113]. The ADR determines the values of SF and TP based on the highest SNR value of the last 20 packets received at the NS. The NS reduces the SF and increases or decreases the value of TP by 2 to reduce energy consumption. However, the newly adapted SF and TP might not successfully deliver the packet to the NS. Therefore, in confirmed mode, the ED utilizes a recovery ADR based on the retransmission procedure on the ED side. When the retransmission counter is a multiple of two, the ED increases its SF, and a TP of 14 dBm is adopted at the time of packet transmission [114]. It increases the chances of successfully delivering a packet to the NS with increased energy consumption costs.

2.2.2. Unconfirmed Mode

The unconfirmed mode does not require a downlink ACK from the NS. However, to determine the connectivity loss between the ED and GW, the ED enables ADR ACK bit by sending a MAC command *ADRACKReq* in the LoRa frame header (FHDR) after 64 (default) UL packets [9]. In such a case, the NS must send an ACK, but not immediately. Furthermore, LoRaWAN utilizes ADR for SF and TP management in confirmed and unconfirmed modes.

3. LoRaWAN Meets ML

This section mainly focuses on existing ML methods applied to LoRa and LoRaWAN for efficient resource management (e.g., SF, TP, BW, and CR) for improving LoRaWAN network performance and efficiency. In the remainder of this section, we present the existing ML, DL, and Reinforcement Learning (RL) methods applied to LoRaWAN.

3.1. Improving LoRaWAN Performance Using ML

Here, we identify the need for ML and present state-of-the-art methods for enhancing LoRaWAN performance through efficient resource management. These ML methods applied for improving the performance of LoRa and LoRaWAN are shown in Table 4.

3.1.1. Need for Machine Learning

ML is a rapidly growing field with many applications, including wireless communications [115–119]. ML can be utilized to improve the performance, efficiency, and security of wireless networks [120,121]. However, ML is applied in a mathematical model deficit and algorithm deficit cases in IoT scenarios [122]. In LoRaWAN, resource management decision-making is left open to developers and researchers, allowing them to develop intelligent solutions for demanding IoT applications. One approach is to utilize ML for resource management, revolutionizing the optimization of SF, TP, BW, and other important parameters. ML algorithms empower LoRaWAN networks to dynamically allocate resources, predict network traffic, mitigate interference, and optimize energy consumption, thereby enhancing network capacity, reliability, and battery life. With ML-driven insights, operators can proactively plan network expansions, ensure the quality of service (QoS), and achieve self-optimizing networks that autonomously adapt to changing conditions [123,124]. This cutting-edge technology releases the full potential of LoRaWAN, transforming it into an intelligent, adaptive, and efficient IoT infrastructure for a wide range of applications.

3.1.2. Machine Learning: The State-of-the-Art

The existing state-of-the-art ML methods can be classified into supervised and unsupervised.

Supervised Approaches

A load-balancing method for dense heterogeneous IoT networks, such as smart city scenarios, was proposed in [125]. The dataset was gathered from a TTN Mapper (mapping the coverage of TTN GWs based on user data) [126] of frequency, DR, latitude, longitude, RSSI, and SNR. These features describe the successful UL packet transmission from ED to the GW. The authors trained different ML techniques, such as Multiple Linear Regression (MLR), Gaussian Naive Bayes (GNB), Linear Discriminant Analysis (LDA), Quadratic Discriminant Analysis (QDA), Decision Tree (DT), Random Forest (RF), Extremely Randomized Trees (ET), and Voting (Ensemble Learning). The classifiers were applied to an urban IoT network, where the simulation results showed an improved packet success ratio (PSR) and reduced energy consumption of a LoRaWAN network.

In [127], an SF allocation scheme using a support vector machine (SVM) and DT to resolve the collision issue in the LoRaWAN network has been proposed. The training dataset was generated using Simulator for LoRa SimLoRaSF [128] (SF), a custom simulator designed for LoRaWAN using Python. The dataset contains the X and Y coordinates of the ED along with successful SF. The input is labeled as successful (if the packet was successfully received at the GW), interfered (when a packet was unsuccessful due to Co-SF interference), and under sensitivity (when a packet is arriving under the required sensitivity threshold at a specific SF). The SVM and DT classifiers are trained for optimal SF allocation. Their simulation results showed that the SVM and DT could efficiently classify the SF, improving the PSR and transmission energy consumption compared to the random SF allocation method. However, the SimLoRaSF does not consider the downlink communication, which is an essential part of the LoRaWAN.

The authors in [129] solve the resource classification problem (e.g., TP) for static EDs in LoRaWAN through various ML techniques, such as RF, SVM, logistic regression (LR), K-nearest neighbor (KNN), LDA, and GNB. The authors used LoRaSim [30,130,131] network simulator for dataset collection, which is designed for LoRaWAN IoT networks based on Python. The ML algorithms were trained on data from previous packet transmissions, such as SF, CR, Nakagami path loss, and the distance between the ED and GW. As a result, every combination of SF and CR pairs has one optimal TP associated with it. The dataset was split into training and testing by 70% and 30%, respectively. From classification results, it was observed that the RF method achieved the highest accuracy of 92.96% compared to other ML techniques. Their simulation results revealed that suitable TP classification leads to a higher PSR than other non-ML methods, such as ADR.

The authors in [132] proposed a combined path loss and shadowing (CPLS) technique, where ML methods such as LR, SVM, RF, and Artificial Neural Network (ANN) were trained on RSSI, ToA, SF, and SNR. The dataset was collected through a testbed utilizing four static EDs in a line-of-sight (LoS) scenario. After removing the outliers and wrong data collected from the sensors, they divided the dataset into training (80%) and testing (20%). To this end, the authors suggested an enhanced ADR for SF and TP allocation to static EDs. The ML methods were evaluated with root-mean-square error (RMSE), achieving up to 1.566 dB and R^2 up to 0.94. The enhanced ADR results revealed reduced energy consumption by 43% compared to the ADR of LoRaWAN.

The paper [133] proposed an ML approach based on a learning-automata mechanism to extend the lifetime of IoT EDs utilized for forest monitoring. Their proposed approach selects the most energy-efficient ED to act as a cluster head. The simulation results showed that the proposed learning-automata mechanism increased the lifetime of IoT EDs by up to 6.7 times. Their proposed approach has empirically proven that the learning automaton consistently converges on the most suitable ED to serve as the cluster head based on energy consumption metrics, proving their proposed approach is scalable and can easily be adapted to different IoT applications.

Unsupervised Approaches

One of the challenges of LoRaWAN is the collision occurring between the packets of EDs when transmitted at the same time with the same SF over the same channel. A K-means clustering algorithm was proposed for reducing collision probabilities [134]. Their proposed K-means are responsible for grouping EDs with similar traffic patterns. EDs belonging to different groups have different priorities, and the channel access for the UL packet transmission is determined by the given priority. Their method showed improved performance in terms of collision probability for class *A* and *B* devices. Their proposed method is simple, scalable, and efficient for reducing collision probabilities in LoRaWAN. Similarly, ED profiling using K-means was utilized in [135] to predict the behavior of LoRaWAN traffic. The authors grouped the EDs using the same SF and packet size and trained DT and Long Short-Term Memory (LSTM) using unsupervised traffic pattern classification methods. Their simulation results showed improved performance in terms of PSR by reducing the impact of interference. However, in a dynamic LoRaWAN network, ED profiling can be time-consuming because resources (e.g., SF and TP) are application-dependent. Therefore, their proposed method is applicable to static LoRaWAN network environments.

A learning-automaton-based ML approach was proposed on the NS in [136] to select between two MAC protocols: TDMA and Slotted ALOHA. The selection of each MAC protocol depends on the network traffic load. If the network traffic load is high, TDMA is chosen for packet transmission to avoid collisions. If the network traffic load is low, Slotted ALOHA is utilized for communication to reduce packet delay. The learning automaton adapts the MAC protocol selection based on the feedback received from the environment. The proposed learning automaton-based ML approach has been evaluated in simulation, showing improved performance in the presence of event traffic.

Table 4. ML methods applied for improving the performance of LoRa and LoRaWAN.

Ref.	Year	ML Model(s)	ML Approach	Features	Deployment Platform	Dataset Tool	Application(s)
[125]	2018	MLR, GNB, LDA, QDA, DT, RF, ET, Voting	Supervised	RSSI, SNR	Python tool	TTN Mapper [126]	Smart city
[127]	2019	SVM, DT	Supervised	X and Y coordinates, SF	SimLoRaSF simulator [128]	SimLoRaSF simulator [128]	✗
[129]	2023	RF, SVM, LR, KNN, LDA, GNB	Supervised	SF, CR, path loss, and distance	LoRaSim	LoRaSim	Smart parking
[132]	2023	LR, SVM, RF, ANN	Supervised	RSSI, ToA, SF, SNR	✗	Testbed	✗
[133]	2023	Learning-automata	Supervised	RSSI, ToA, SF, SNR	✗	Testbed	Forest monitoring
[134]	2019	K-means	Unsupervised	Traffic patterns and priority	✗	Simulation	✗
[135]	2020	DT, LSTM	Unsupervised	SF and packet size	✗	Tested	Water metering
[136]	2022	Learning-automata	Unsupervised	Traffic pattern	✗	Simulation	Environmental monitoring
[136]	2022	AR, TFT	Unsupervised	Time-stamp, SNR, duty cycle, number of transitions, SF, frequency, ADR, successful transmission, and failed transmission	✗	ns-3 simulator	Smart home/city

✗ = not mentioned in the referenced paper.

The authors in [137] proposed two AI methods, an autoregressor (AR) model and a temporal fusion transformer (TFT) model, for classifying and detecting LoRaWAN traffic to optimize the LoRaWAN network performance. The authors collected a dataset using the ns-3 simulator, where the EDs are placed in an 8 km circle with a centered GW. They considered all possible criteria as features for EDs, including the inter packets time, SNR, DC, number of UL transmissions, SF, frequency, ADR, successful transmission at the GW, and failed transmission. The simulation was executed for 365 days, resulting in a 100 GB database. The TFT method was utilized to forecast the behavior of the LoRaWAN network, and the AR method to detect the surge in traffic with overall classification precision between 94.50 and 99%. However, the suggested AI methods have not been utilized in the ns-3 for online testing.

3.2. Improving LoRaWAN Performance Using DL

We begin by highlighting the importance of DL in the LoRaWAN network. We then delve into the cutting-edge DL methods currently employed for solving the resource management issue to enhance the performance of LoRaWAN networks. These DL methods applied for improving the performance of LoRa and LoRaWAN are illustrated in Table 5.

3.2.1. Need for Deep Learning

DL can improve the performance of LoRaWAN networks by optimizing resource parameters, predicting network traffic, mitigating inter- and intra-interferences, and optimizing energy consumption [138–148]. Furthermore, to dynamically allocate resources to EDs, such as BW, SF, and TP, a DL method can be trained on a large dataset generated using simulation tools (e.g., ns-3 or Matlab) or testbeds. Finally, the trained DL method can be deployed on EDs or network servers (ns-3 or testbed deployments) for efficient resource allocation, improving the performance of the LoRaWAN network.

3.2.2. Deep Learning: The State-of-the-Art

An Extended Kalman Filter (EKF)-based LSTM method based on regression method for predicting collision in LoRaWAN network was proposed in [141]. They generated the dataset for a number of collisions for each 20 min interval using the *LoRaSim* simulator [131]. For training the LSTM, the dataset was split into 70% and 30% into training and testing and scaled to [0, 1]. They utilized the pre-trained LSTM along with EKF for collision analysis. Their results showed an improved RMSE of 0.9863 compared to other approaches, such as Gated Recurrent Unit (GRU) and Recurrent Neural Network (RNN). Hence, with low RMSE, the LSTM-EKF has reduced the number of collisions in online simulation and yielded better performance. The collision in the LoRa network is directly linked with the SF; hence, SF has not been considered for adaptive configuration. As a result, their proposed LSTM-EKF can lead to underperformance when utilized in a dynamic LoRaWAN network.

The study in [146] proposed DeepLoRa, an environment-aware path loss model, utilizing satellite photos to categorize a land cover using Bi-LSTM accurately. In DeepLoRa, first, each pixel of the picture map was class-labeled, which divided the land cover into two classes, non-line of sight (NLoS, buildings, trees) and LoS (no attenuation), to reflect the actual land-cover type. Second, they divided LoRa lines from an ED to GW into identically sized micro-links. Each was then embedded into a different sequence element based on a land cover map. To determine the Estimated Signal Power (ESP) received by GW, the model integrated the sequences with specific input parameters and anticipated related path loss. For all land cover categories, the accuracy of land cover classification was 97.4% (which can be regarded as a true environment reflection). Furthermore, DeepLoRa performed at least 50% better than other models.

A neural-enhanced LoRa demodulation method (NELoRa) was proposed in [143]. A Deep Neural Network (DNN) was trained on a spectrogram of amplitude and phase. The authors conducted indoor and outdoor experiments, and three metrics, i.e., Symbol

Error Rate (SER), SNR Gains, and Battery Life Gain (BLG), were used for the performance evaluation of NELoRa. The evaluations showed that NELoRa could obtain much lower SERs. As a result, the proposed NELoRa brought significant gains in the SNR thresholds compared to the dechirp process, and the highest SNR gain observed was 5.94 dB under SF_7 and 500 kHz of BW. NELoRa resulted in consistent and higher BLG of 27% compared to the baseline.

The paper proposed a DL method [149] for managing the transmission interval of IoT devices in LoRa networks by utilizing Intel Berkeley Research Lab Data [150]. Using an autoencoder, the proposed method first clusters the IoT EDs concerning their data patterns. Second, a local LSTM prediction model is trained using the Intel lab IoT dataset for each cluster to predict the next transmission interval of each ED involved in communication. The Monte Carlo simulation with the Intel lab IoT dataset showed 31% improved scalability.

The paper [147] proposed a DL method for joint collision detection and resource management (e.g., SF). The proposed work utilizes two DL methods: fully connected neural networks (FCNNs) for collision detection and CNN for SF management. The dataset used to train the DL methods was generated using the $SimLoRaSF$ simulator [127], containing the X and Y coordinates of the ED along with SF. The results showed improved prediction accuracy and energy consumption compared to traditional ML methods such as SVM, DT, and RF.

Recently, the authors in [148] proposed an AI framework for SF classification using GRU. To train the GRU model, the dataset was generated in ns-3 and labeled in two ways:

1. *Group-based SF labeling:* the 6 UL packets, represented with $UL_1, UL_2, \ldots, UL_6$ transmitted with SF_7 to SF_{12} were organized into one group (g). From each g, the lowest SF was chosen among successful ACK receptions;
2. *Input sequence labeled with SF:* once the SF labeling of each g was completed, the authors generated an input sequence of 20 groups with a corresponding labeled SF.

Their proposed AI framework is comprised of two modes: offline and online. The GRU model is trained based on one-time generated data in the offline mode. After training, a pre-trained (i.e., inference model) is utilized in the online mode, which yields the best SF during real-time simulation. The inference model was utilized on the ED side, where the new data with 20 UL sequences for determining the best SF was generated. Once the UL sequence reached a size of 20, the input was fed into the inference model to predict a suitable SF for the next UL packet transmission. Simulation results showed improved PSR compared to the typical ADR approach. However, the GRU model with two layers comprised 990.71k parameters (i.e., space complexity) and 249.67 Mega Floating-point Operations Per Second (MMac FLOPs, representing time complexity); the proposed model deployed on LoRa devices would be computationally costly. To address this issue, the authors in [114] proposed a DNN with reduced computational 13.54 MMac FLOPs and space complexity 52.9k parameters with the use of six sequences of UL packets during the online mode to lower the convergence period and energy consumption.

3.3. Improving LoRaWAN Performance Using RL

Here, we discuss the advanced RL methods utilized to address the resource management challenge and further enhance the overall performance of LoRaWAN networks. The cutting-edge RL techniques are designed to intelligently manage network resources like BW, SF, and TP to maximize efficiency and deliver optimal results. These RL methods improving the performance of LoRaWAN are highlighted in Table 6.

Table 5. DL methods applied for improving the performance of LoRa and LoRaWAN.

Ref.	Year	DL Model(s)	DL Approach	Features	Deployment Platform	Dataset Tool	Application(s)
[141]	2020	LSTM, LSTM-EKF	Regression	Collisions	LoRaSim	LoRaSim	Smart city
[146]	2021	Bi-LSTM	Supervised	Pathloss	Testbed	Testbed	Localization
[143]	2021	DNN	Supervised	RSSI and SNR	Testbed	Testbed	Smart parking
[149]	2021	Autoencoder, LSTM	Supervised	Sensory data (temperature, humidity, light, voltage)	Monte Carlo simulation	Intel Lab Data [150]	✗
[147]	2022	SVM, DT, FCNN, CNN, RF	Supervised	X and Y coordinates of the ED, SF	SimLoRaSF simulator [127,128]	SimLoRaSF simulator [127,128]	✗
[148]	2022	GRU	Supervised	ED position, SNR, received power	LoRaWAN ns-3 [151]	LoRaWAN ns-3 [151]	Metering
[114]	2023	DNN, LSTM, GRU, SVM	Supervised	ED position, SNR, received power	LoRaWAN ns-3 [151]	LoRaWAN ns-3 [151]	Pet-tracking and metering

✗ = not mentioned in the referenced paper.

3.3.1. Need for Reinforcement Learning

RL approach has several advantages over traditional methods of optimizing LoRaWAN networks [129,152–155].

1. RL is a data-driven approach, learning rules and policies from experience by interacting with the network and observing the results;
2. RL is a dynamic approach, adapting itself to environmental changes. LoRaWAN networks are constantly changing owing to ED mobility and the underlying propagation environment. As a result, RL can be used to learn how to optimize the network parameters for these changes, ensuring that the network remains reliable and efficient;
3. RL is a scalable approach; thereby, it can be used to optimize large and complex networks.

RL has been utilized in different IoT applications, such as robotics, game-playing, network policy control, and resource optimization [156–159]. For example, in LoRaWAN, RL could be used to optimize the resources (e.g., SF and TP) by training agents (i.e., EDs) for making decisions to maximize the overall network efficiency and minimize interference and energy consumption [160,161].

3.3.2. Reinforcement Learning: The State-of-the-Art

Paper [162] proposed an RL approach for optimizing and updating LoRa communication parameters. The authors mathematically modeled the average per-node throughput of LoRaWAN networks by considering the heterogeneity of IoT deployments. The authors utilized the RL method to derive optimal disseminating policies by aiming to maximize the accumulated average per-node throughput. The authors compared their approach to the LoRaWAN ADR mechanism. The authors showed that their approach achieved a remarkable increase in the accumulated average per-node throughput of 147%.

Paper [163] proposed a novel method for resource allocation in LoRaWAN networks. The method used Q-learning, an RL technique, to learn the optimal resource allocation policy for each ED in the network. In the proposed method, the GW acts as an agent of Q-learning, where the Q-reward is based on the weighted sum of the number of successfully received packets in the proposed method. The Q-learning method was evaluated using simulation, and it has improved the average PSR by about 20% compared to a random resource allocation scheme.

Table 6. RL methods for improving the performance of LoRa and LoRaWAN.

Ref.	Year	RL Model(s)	Reward Feature(s)	Platform	Application(s)
[162]	2019	Evolution strategies (ES) algorithm	Channel conditions	Simpy [164]	✗
[163]	2019	UCB	Q-learning	✗	Gas and water meters
[165]	2019	UCB	ACK	Matlab	Smart metering
[166]	2020	DQN	PDR, ToA, and power usage	✗	✗
[167]	2020	DQN	Network reliability and the power efficiency	Simulation	✗
[168]	2020	DQN	Mobility, channel conditions, traffic load	Simulation	✗
[159]	2021	Q-learning	✗	✗	✗
[169]	2021	RL	SF Sensitivity	LoRa-MAB [21,170]	Monitoring
[154]	2021	RL-ADR	ToA and energy consumption	ns-3	✗
[152]	2021	RL	DER and SNR	LoRaEnergySim [171]	Industrial monitoring
[153]	2021	DRL	Energy cost	Monte Carlo simulations	Real-time application
[172]	2022	MAB	ACK	LoRa-MAB [21,170]	Metering
[155]	2022	DRL	Number of ED, reliability, energy efficiency	Testbed	✗
[173]	2022	DRL	Collision rate and the packet loss rate of EDs	LoRaSim simulator [131]	✗
[174]	2023	Q-Learning, Boltzmann exploration algorithm	Success probability	MULANE [175]	✗
[176]	2023	Multi-arm bandit	Energy	ns-3 module [151]	✗
[177]	2023	DRL	Collision or packet lost	LoRaSim simulator [131]	✗
[178]	2023	Multi-agent regression model	Number of EDs, distribution of EDs, the traffic pattern of EDs	Simulation	✗

✗ = not mentioned in the referenced paper.

To improve the PSR, the authors in [165] proposed a retransmission method based on an Upper Confidence Bound (UCB) algorithm that is used to solve the multi-armed bandit problem. In [165], first, the ED retransmits a packet with random channel selection and learns the quality of each channel based on a positive ACK reception. Then, after learning the best channel for retransmission, the EDs can retransmit on the highest-rewarded channel. Hence, improving the PSR. Their results showed improved PSR compared to random channel selection schemes.

A deep RL (DRL) method was proposed for the dynamic adjustment of SF and TP to mitigate the collision problem in LoRaWAN [166]. The authors considered the PSR, ToA, and TP of an ED as a reward function. To mitigate the collision behavior of the LoRaWAN network, a deep Q-network (DQN) was deployed at the GW for SF and TP management. As a result, their proposed method improved the PSR by 500% under 100 EDs deployed in a 4.5 km region.

The authors in [167] proposed a multi-agent Q-learning algorithm to dynamically allocate TP and SF to EDs during UL packet transmission in a LoRa network. In a LoRa multi-agent system, each agent represents one LoRa ED, where the ED works together with the environment to determine the best TP and SF allocation policies for every UL transmission. The simulation results demonstrated that the suggested algorithm could greatly enhance the energy efficiency and reliability of LoRa networks.

The authors in [168] proposed a DRL method called LoRaDRL-based on DQN for intelligent resource allocation in dense LoRa networks. The primary aim of the proposed LoRaDRL approach is to learn the optimal policy for allocating channels to LoRa EDs. LoRaDRL assigns resources to the EDs by considering the mobility of EDs, the channel conditions, and the traffic load in the network. LoRaDRL results showed improved PDR under dense deployments and mobile EDs compared to the state-of-the-art resource allocation algorithms, such as LoRaSim [131] and LoRa-MAB [21,170].

An RL algorithm was introduced in [169] for SF and TP optimization to improve energy consumption and PSR. The SF and TP are optimized based on the required level of SF sensitivity threshold of the GW. They implemented the RL algorithm in the $LoRa$–MAB simulator [21,170], which is based on Exponential Weights for Exploration and Exploitation (EXP3). The results showed an improved PSR and energy consumption compared to the

LoRa-MAB algorithm [21]. Similarly, an RL-ADR was proposed in [154] to optimize the SF allocation. The agent is trained using the LoRaWAN ns-3 module, considering the variations in the SNR behavior. In addition, the reward function is based on the ToA and energy consumption. Both ToA and energy consumption are measured from each last received packet at the NS. The RL agent learns the efficient SF allocation policies based on the ToA and energy consumption. The proposed RL-ADR is evaluated in comparison with the traditional ADR mechanism of LoRaWAN, where it showed improved energy consumption owing to the fast response of the trained RL agent for efficient SF allocation during communication by the NS. Furthermore, [152] also proposed an RL-based optimized ADR for SF and TP allocation to EDs. The authors of [152] utilized *LoRaEnergySim* simulator [171], where the states are data extraction rate (DER) and SNR pairs. Moreover, [152] considers SF and TP pair as actions. The results of [152] showed improved DER compared to the traditional ADR mechanism. Another DRL approach has been proposed for optimal channel and SF assignment to EDs in LoRa networks [153]. Their proposed DRL approach utilizes a DQN to learn the optimal policy for channel and SF allocation. They trained the DQN on a historical data dataset to minimize the grid power consumption while satisfying the QoS requirements of the EDs. The proposed approach is evaluated in Monte Carlo and RL simulations and showed improved performance in assigning a suitable channel to EDs, thereby lowering the energy cost.

The authors of [172] proposed the MIX-MAB algorithm for suitable transmission parameters (i.e., SF) allocation to EDs. In MIX-MAB, LoRa EDs interact with the environment, including GWs, to learn the best actions based on the successful reception of ACK messages. In MIX-MAB, an ED always initiates a UL packet transmission towards GW using an SF. In return, the ED receives an ACK upon the successful reception of the packet on the NS. When the ED receives an ACK, it assigns a reward to that successful SF. As a result, this SF is used for the next UL packet transmission. The MIX-MAB was evaluated in *LoRa–MAB* simulator [21,170] with one GW located at the center of a disc-shaped cell with a radius of 4.5 km, where 100 LoRa EDs were uniformly distributed, each ED transmits 15 packets/hour. The simulation results showed improved convergence time and PSR compared to the LoRa-MAB algorithm.

The authors of [155] proposed a multi-agent DRL ADR mechanism at the NS side for efficient SF and TP allocation to EDs. The proposed multi-agent DRL ADR mechanism consists of three independent DRL algorithms, one for each slice, replacing the traditional LoRaWAN ADR mechanism for assigning TP and SF to EDs. The SF and TP are allocated to EDs based on the rewards such as the number of ED, reliability, and energy efficiency. Their proposed multi-agent DRL ADR mechanism showed improved energy consumption compared to the traditional ADR. Another approach based on DRL for optimizing the SF allocation is studied to improve the GW capacity of the LoRa network [173]. The proposed approach utilizes a DQN to learn the optimal SF assignment policy for a given network state. The reward is computed based on the collision rate and the packet loss rate of EDs. The authors of [131] performed simulation using the *LoRaSim* simulator, where the results showed a reduced collision rate by up to 30% compared to the existing Min-airtime and Min-distance based SF allocation approaches [130].

An algorithm called Low-Power LP-MAB (MAB) [179] was designed to configure the transmission parameters (e.g., SF) of ED in a centralized manner to improve energy consumption and PSR. The LP-MAB algorithm works on the NS side by interacting with the ED. The NS transmits ACK upon successful packet reception to the ED, where the ED learns the best SF for the subsequent UL packet transmission based on the received ACK for the previous successful communication on a particular SF. As a result, the simulation results of LP-MAB outperform other approaches in terms of energy consumption and PSR.

A Q-learning approach was proposed in [174], known as the score table-based evaluation and parameters surfing (STEPS) approach. STEPS is responsible for dynamically allocating the required SF for UL transmission based on the success probability of the packet and score table. The simulations were conducted using *MULANE* [175] simulator for different EDs (e.g., 50, 100, 250, 500, 600, and 750). Initially, during the deployment phase, all EDs utilize the same SF. Their results revealed that their proposed STEPS approach could reduce energy consumption by 24% to 27%. Furthermore, it was realized that this achievement was possible due to a reduction in collisions. In other experiments regarding bi-directional communication, their proposed STEPS approach enhanced the network throughput by 18% in a smaller network, while 33% in a relatively larger network compared to ADR, BADR, and LoRaMAB [170].

The paper [176] proposed a lightweight RL approach for appropriate SF allocation to EDs in a LoRaWAN network. The lightweight RL approach utilizes MAB to learn the trade-off between energy consumption and DR. To ensure feasibility, the authors have integrated explicit MAC commands into their proposed method and implemented them in the ns-3 module [151]. Their extensive simulation results showed that their lightweight RL approach outperforms the traditional ADR in single and multi-GW scenarios regarding PSR and energy consumption, owing to learning the optimal SF for each ED in a given environment.

The authors of [177] proposed an SF redistribution method under limited network resources to improve the ED capacity of the LoRa GW. Their proposed method uses a DRL technique to learn the optimal SF allocation for each node, minimizing the collision rate and energy consumption. Simulation results using *LoRaSim* [131] showed improved capacity.

Paper [178] proposed a multi-agent regression model to improve network planning in time-slotted communications for LoRaWAN. The proposed agent is based on multi-output regression responsible for predicting the network scalability for a given set of joining EDs. The dataset used for training the agent was generated using a series of simulations, considering the features such as the number of EDs, the distribution of EDs, the traffic pattern of EDs, and the channel conditions. The agent utilizes the dataset to train the multi-output regression model. Once the model is trained, the agent predicts the network scalability for a given joining EDs. The simulation results revealed a 3% reduction in the mean absolute error, indicating that the agent can make accurate predictions.

4. Simulators and Frameworks for Dataset Collection

In the existing literature, few works have surveyed the publicly available LoRaWAN network simulators [52,55,73,79,80,180]. Therefore, this section highlights a few LoRaWAN frameworks that have been utilized or can be used for dataset collection to resolve collision and resource management issues in the LoRaWAN network. Furthermore, Table 7 illustrates a comparison of dataset collection frameworks and applicable ML methods based on suggested features for resource classification.

4.1. LoRaSim: LoRa Simulator

LoRaSim is based on Python, designed to simulate LoRaWAN collision behavior, and mainly consists of four configurations: (1) it simulates a single GW, (2) supports up to 24 GWs, (3) simulates EDs and GWs with a directional antenna, (4) and comprised of multiple networks [30,130,131].

LoRaSim [131] can be used to study the performance of different LoRaWAN network configurations and to evaluate the impact of interference. The interference model in LoRaSim is comprehensive, considering both co-SF and inter-SF interference. Co-SF interference occurs when two or more packets are sent on the same SF. Inter-SF interference occurs when a packet is sent on a different SF than another packet.

On the one hand, a packet is received correctly if it satisfies three thresholds: the minimum co-SF, the minimum inter-SF, and the minimum SNR. On the other hand, a packet is lost only if the overlap of packets is in the time-critical region of the considered packet. The time-critical region is the part of the packet most important for correct reception.

Table 7. Comparison of publicly available LoRaWAN frameworks for dataset collection and applicable ML methods based on the required features for resource classification.

Features	Dataset Collection Frameworks				ML Techniques with Required Features for Learning	
	LoRaSim	**SimLoRaSF**	**LoRaWAN-Sim**	**ns-3 Module**	**Applicable ML Techniques**	**Features for Resource Classification (e.g., SF, TP)**
Simulation platform	Python	Python	Python	ns-3	✗	✗
Frequency region	EU-868	EU-868	EU-868	EU-868	✗	✗
Device type	*A*	*A*	*A*	*A*	✗	✗
ADR	✗	✗	✗	✓	RL [21,154,170]	ToA, energy consumption, ACK, PSR [21,154,170]
Propagation loss model	log-distance	log-distance	Okumura Hata	log-distance	RF, DT, SVM, DNN	RSSI, SNR, distance, frequency, LoS, NLoS, Antenna height.
Energy consumption model	✓	✓	✓	✓	SVM, DNN, Ensemble, Naive Bayes, DT	Payload Size, DR, TP, SNR, channel occupancy, distance from GW
Mobility environment	✗	✗	✗	✓	SVM, KNN, LSTM, DNN, RL, Hybrid	RSSI, speed, acceleration, location, trajectory, SNR, time-stamp
Buildings environment	✗	✗	✗	✓	ANN, SVM, GPs, DT	Height, density, material, obstructions, RSSI, NLoS conditions
Interference model	✓	✓	✓	✓	LR, DT, SVM, RF, KNN, RNN	RSSI, CIR, SINR, interference power, type of interference
Channel access method	Aloha	Aloha	Aloha	Aloha	Logistic regression, SVM, DT, KNN, Naive Bayes, DNN, Ensemble	LBT, retransmission limit, DC, channel type, no. of EDs
Confirmed mode (ACK)	✗	✗	✗	✓	Logistic regression, SVM, DT, KNN, DNN, Ensemble	Retransmission count, ACK, PSR, DR, ToA, Link margin, history of packets
Unconfirmed mode (no-ACK)	✓	✓	✓	✓	SVM, DT, KNN, DNN, Ensemble	DR, SNR, RSSI, Link margin, history of packets, PER

✗ = not mentioned in the referenced paper; ✓ = defined in the referenced paper.

LoRaSim is a valuable framework for understanding the behavior and performance of LoRaWAN. It can be used to design and optimize LoRaWAN networks to ensure reliable and efficient communication, as utilized in [29,30,70,141,173,181–196].

4.2. SimLoRaSF: Simulator for LoRa SF

SimLoRaSF is a LoRaWAN simulator that can be used to study the impact of different SFs on network performance [127,128]. It is a Python-based framework that uses a discrete-event simulation model. It works by creating a virtual LoRaWAN network and then simulating the transmission of packets between EDs in the network by keeping a track record of the packet transmission time, the SF, the transmitting source (e.g., ED), the packet size, the duration (e.g., ToA), and status of each transmission (e.g., ACK).

The packet transmission is categorized into three statuses: transmitted, interfered with, or under sensitivity. A packet is considered successful if it is received correctly by the GW. A packet transmission is considered interfered with if it is corrupted by interference from another transmission in the network. A packet transmission is considered under sensitivity if the SNR is too low for the destination node to receive it correctly.

4.3. LoRaWANSim: LoRaWAN Simulator

The LoRaWANSim [197,198] is a powerful simulator framework that can be used to study the behavior of LoRaWAN networks under PHY and MAC layer features. The framework provides a flexible simulation environment, allowing users to control PHY and MAC layer parameters. The PHY layer models the PHY transmission and reception of LoRa signals. It implements a complete LoRa transceiver, including the ability to generate modulated signals and perform demodulation tasks. It also considers factors such as interference and multiple GW scenarios. The MAC layer models the data traffic on the LoRaWAN network. It manages channel access, ensuring multiple EDs can share the same channel without interfering. Furthermore, it considers UL and downlink interference occurring over the same channel, DC limitations of 1%, and energy consumption.

4.4. ns-3: Network Simulator-3

The LoRaWAN ns-3 module [151,199] is among the most widely used simulators for utilizing ML, offering a wide range of LoRaWAN features, such as bi-directional communication, confirmed and unconfirmed modes, support for the ADR on the ED and NS-sides, buildings, DC limitations on the EU-868 MHz frequency, energy consumption module, etc. Furthermore, other promising features and modules, for instance, ADR in unconfirmed mode [7], mobility patterns [200], blind ADR [113] and ML methods [114,148] have been added by other researchers. However, they are not publicly available. Furthermore, this ns-3 module [151,199] has been extensively utilized in the literature [7,10,27,100,113,114,148,199–203].

4.5. Remarks

These dataset collection frameworks offer valuable tools for researchers and practitioners to analyze and optimize LoRaWAN networks. These frameworks enable the study of collision behavior [30], performance evaluation under different SFs, and their impact on the LoRaWAN network performance [127], investigation of PHY and MAC layer features [197], and a complete ns-3 framework for LoRaWAN analysis. The frameworks have been widely used in the literature, demonstrating their effectiveness in understanding and improving LoRaWAN network performance. Among these simulators, the state-of-the-art ns-3 module [151] has been utilized for intelligent SF allocation in the existing literature using DNN and multi-arm bandits approaches in [114,176].

5. LoRaWAN Datasets

The LoRa research community lacks a large dataset that can be used to study the resource allocation, interference, collision issues, and behavior of LoRaWAN networks in various conditions. The existing datasets are typically small and specific to a particular network or application owing to a few large-scale deployments of LoRaWAN. In addition, the data collected from LoRaWAN networks are not well-documented, making it challenging to use for research purposes. Despite these limitations, the existing datasets can be utilized to examine a variety of aspects of LoRaWAN networks. For example, the LoRaWAN dataset can be used to study the performance of LoRaWAN networks under different conditions, the impact of resource management on network performance, and the traffic patterns of LoRaWAN EDs. The rest of this section discusses the available datasets designed for different IoT applications.

5.1. Localization

A large dataset for LoRaWAN and Sigfox was collected in urban and rural areas from 17 November 2017 to 5 February 2018, which contains the RSSI at each GW, latitude and longitude of the ED, and the SF utilized during data transmission [204]. The authors utilized the dataset in [205] for indoor localization, where the results showed that the mean location estimation error for Sigfox was recorded as 214.58 m and 688.97 m in rural and urban scenarios, respectively. In addition, the mean location estimation error for the urban LoRaWAN dataset was 398.40 m. The datasets presented in [204,205] can be leveraged to evaluate the performance of LoRaWAN-based indoor positioning systems by developing new fingerprinting algorithms. The dataset has been extensively utilized for LoRaWAN-based indoor positioning systems in [206–213]. Similarly, 100 RSSI values were collected for a target node and for the 11 anchors at LoS and NLoS in indoor and outdoor environments for improving the localization through LoRa measurements [214,215].

The authors in [216,217] generated a dataset called the "LoRaWAN at the Edge Dataset (LoED)." The LoED dataset [218] was collected under an urban scenario for four months, where nine GWs were utilized in central London. Among nine GWs, five were outdoor (line-of-sight (LoS)), four GWS located indoors with limited LoS, and one had no-LoS on the ground. The data was captured for a 2–4 month period generated by smart city applications. Overall, 11,263,001 packets were collected from 8503 unique EDs, comprised of the features such as cyclic redundancy check (CRC), RSSI, SNR, SF, frequency, bandwidth, CR, packet type, device address, etc.

The LoRa RF fingerprinting dataset was collected considering indoor and outdoor scenarios comprising FFT and I/Q samples for indoor localization [219–221]. On the one hand, the dataset was collected for five consecutive days for indoor scenarios. During indoor dataset collection (e.g., room, outdoor, and office environments), 25 EDs were utilized, where every ED transmits 10 UL packets with an interval of 20 s. On the other hand, the outdoor dataset comprised four different scenarios regarding the distance: 5 m, 10 m, 15 m, and 20 m away from the GW.

The LoRaWAN performance mainly depends on several factors, including the distance between the ED and the GW, the underlying propagation environment, and the network traffic. To study the LoRaWAN network, the authors in [222] generated a dataset (publicly available, [223]) using 311 outdoor tests for 39 GW, which contains data regarding the long-term behavior of the LoRaWAN channel in Brno, Czech Republic. The dataset was collected under different environments, including urban, suburban, and rural areas, for two months, and included information about the SNR and RSSI concerning the closest GW distance.

The authors of [224] collected a fingerprinting dataset by conducting two studies on indoor and outdoor environments. The first study was conducted at the Brno University of Technology in Brno, Czech Republic, and the second was conducted at the University Politechnica of Bucharest in Bucharest, Romania. The dataset [225] comprises the RSSI information for various GWs using SF_7, SF_9, SF_{10}, and SF_{12}. The study showed reduced positioning accuracy in indoor and outdoor experiments. However, the SF dataset is limited since the authors have used only SF_7, SF_9, SF_{10}, and SF_{12}.

5.2. Weather Forecast

Owing to the long range of LoRaWAN, it can often be utilized in outdoor environments. However, the performance of LoRaWAN is greatly affected by weather conditions, such as humidity, temperature, and atmospheric pressure. Therefore, the authors in [226] generated a dataset about the correlation between RSSI and SNR conditions from 8 LoRaWAN EDs and a weather station. The dataset [215] was collected for more than 80 days in a vineyard in Italy, including more than 190,000 records of RSSI, GPS coordinates, temperature, humidity, and pressure data. Researchers can use the dataset to develop new algorithms for studying and improving the performance of LoRaWAN under different weather conditions.

5.3. Security Attacks

LoRaWAN networks can be vulnerable to security attacks. Therefore, the study in [227] investigated the use of LoRa metadata to detect the presence of security flaws within the network. The authors in [227] collected a dataset of LoRaWAN transmissions for two months with SNR and RSSI measurements. The data collected included normal, collided, and jammed metadata, where normal values are annotated as CRC_{OK} and DoS attacks were denoted as CRC_{BAD}. They utilized various ML methods (e.g., logistic regression, DT, RF, and XGBoost) to predict the presence of jamming and security attacks. Among the ML methods, XGBoost was the most accurate ML method for predicting security attacks, since it was found that SNR and RSSI can be used to pinpoint normal versus anomalous signals.

5.4. Signal Quality/Path Loss

When designing a LoRaWAN network, it is essential to consider the path loss between the EDs and the GWs. Several factors, including distance, frequency, and weather, can affect path loss. The authors in [228] presented a LoRaWAN measurement dataset collected in Medellin, Colombia. The dataset [229] was collected for about four months by considering only four EDs, which include information about path loss, the distance between ED and GW, frequency, temperature, relative humidity, barometric pressure, particulate matter, and energy consumption. Furthermore, the authors claimed that leveraging the dataset would enable the estimation of weather-induced variations in path loss for LoRaWAN deployments, leading to enhanced precision in tracking and positioning data and the development of more efficient energy reduction strategies.

The dataset in [230,231] was generated using two GW and six mobile EDs in a 6×6 km^2 urban area in Tsinghua University, Beijing, China. The dataset [232] was collected over four months comprising RSSI, PDR of the transmitted packets, locations of the ED and GW, and timestamps of each measurement.

The dataset [233,234] was collected in indoor and outdoor environments where, during the indoor data collection, the distance between the EDs and the GW varied from 5 to 50 m. The floor map illustrated the walls, doors, and windows between the EDs and the GW. In the outdoor environment, railway stations were used without considering obstacles between the EDs and the GW. The dataset includes features such as the timestamp, the SNR, and the RSSI of the received packet at the GW.

5.5. Smart City

The dataset [235,236] is divided into two parts: LoRa parameters and sensor readings. The LoRa parameters dataset contains the timestamp of packet transmission, the channel used in packet transmission, the device extended unique identifier (DevEUI), the SNR, the RSSI, and the frame counter (FCNT). In comparison, the sensor dataset includes data about the measured quantities, such as CO2, sound average, sound peak, motion, light, temperature, humidity, and battery levels. The Smart Campus dataset can be used for various applications, including time-series forecasting and number of people prediction.

5.6. Resource Allocation

Mainly, the SF allocation is dependent on the underlying propagation environment, mobility, ED position, and sensitivity. Therefore, in our previous work [114,148], we generated a dataset using the state-of-the-art ns-3 module [151], which is publicly available [237]. The dataset was generated for 10 days with a UL period of 10 min, which mainly comprises ED locations (i.e., X and Y coordinates), RSSI, SNR, the distance between ED and GW, and the ACK status of every UL packet transmitted with each SF. The dataset in [237] can be utilized for resource management (e.g., SF) for static and mobile EDs.

5.7. Remarks

In addition to existing datasets, few datasets are publicly available with limited documentation. For example, LoRaWAN traffic analysis dataset [238], outdoor experiments conducted for LoRa RSSI [239,240], LoRaWAN dataset using SF [241], and LoRa time series dataset [242]. Furthermore, apart from [237] dataset, these datasets [205,215,218,221,223,225] are not designed for resource management. However, they can be tested for resource allocation since most datasets include RSSI, SNR, and device location information, which are efficient features for resource management. In conclusion, Table 8 provides additional information regarding the datasets discussed in this section.

Table 8. Summary of existing datasets utilized for different applications of LoRaWAN.

Year	Paper Ref.	Tool Used	Dataset Variables	Size of Dataset	Purpose	ML Method
2018	[205]	Testbed	SF, RSSI, ED positions [204]	123,5229	Localization	KNN
2019	[215]	Testbed	RSSI [214]	✗	Localization	Least squares
2020	[218]	Testbed	CRC, RSSI, SNR, SF, frequency, bandwidth, coding rate, packet type [216]	11,263,001	Smart city, capacity planning	✗
2021	[221]	Testbed	IQ/FFT [220]	✗	Localization	CNN
2021	[223]	Testbed	SNR, RSSI, Frequency [222]	✗	✗	✗
2022	[225]	Testbed	RSSI [224]	Outdoor = 16,054, indoor = 7752	Localization	KNN, LR, DT, SVM

Table 8. *Cont.*

Year	Paper Ref.	Tool Used	Dataset Variables	Size of Dataset	Purpose	ML Method
2022	[215]	Testbed	RSSI, GPS coordinates, along with weather data [226]	190,000	Weather forecast	✗
2022	[227]	Testbed	RSSI, SNR, CRC	✗	Security analysis	Logistic regression, DT, RF, and XGBoost
2022	[229]	Testbed	Timestamp, ED id, energy consumption, SF, SNR, distance, frequency, and other sensory data [228]	930,753	Positioning, energy behavior of LoRa	Linear regression
2022	[232]	Testbed	Timestamp, RSSI, PDR, locations of ED and GW [230,231]	✗	Tracking	✗
2023	[234]	Testbed	Timestamp, SNR, RSSI [233]	✗	Locomotion mode recognition	Zero-Shot learning
2023	[236]	Testbed	Timestamp, SNR, RSSI, frame counter, and other sensory data [235]	✗	Smart city, people counting	KNN, LSTM.
2023	[237]	ns-3 [151]	RSSI, SNR, ED positions [114]	108,401	SF management	DNN, LSTM, GRU

✗ = not mentioned in the referenced paper.

6. ns-3-Based ML Frameworks

The ns-3 frameworks, mainly designed for ML, can be utilized or integrated with the LoRaWAN ns-3 module [151,199] to enhance the performance of LoRaWAN with ML. These frameworks are discussed in the remainder of this section.

6.1. ns-3-AI Framework

Currently, researchers are interested in applying ML techniques to wireless communication networks [115–117]. It is owing to most ML techniques heavily relying on open-source TensorFlow and PyTorch ML frameworks. These two frameworks are developed independently and are extremely hard to merge. Moreover, connecting these two frameworks with data interaction is more reasonable and convenient. Therefore, the ns3-AI framework was proposed in [243,244]. The ns3-AI framework provides an efficient workflow between ns-3 and Python-based modules, enabling seamless data transfer and interaction between the two modules. As an example, using the ns-3-AI framework: (a) LSTM has been utilized to predict the channel quality, and (b) RL method for controlling the congestion occurring in TCP [244].

6.2. ns-3-gym Framework

The ns3-gym is an open-source RL framework, integrating OpenAI Gym and ns-3 [245]. The OpenAI Gym is a popular and open-source RL toolkit providing an interface for interacting with RL environments. The OpenAI Gym offers predefined environments with well-defined state and action spaces, making developing and comparing RL algorithms easier. It supports various RL methods, allowing researchers from academia to focus on developing new learning algorithms. The ns-3 Gym fills the gap between ns-3 and OpenAI Gym by creating an interface. This interface allows researchers to leverage the capabilities of ns-3 within the OpenAI Gym framework. As a result, such integration enables researchers to apply RL techniques to network scenarios and train RL agents to make intelligent decisions in complex networking environments.

For example, the authors in [246] present two use cases of cognitive radio (CR) transmitters to solve the issue of radio channel selection in the IEEE 802.11 WLAN with external interference [247]. In case 1, the transmitter senses the entire BW, while case 2 is related to data transmission, where the transmitter monitors its channel to avoid collisions by selecting a channel free of interference.

6.3. Open Neural Network Exchange (ONNX) Framework

ML could be computationally costly in LoRaWAN owing to its low computational power. As a result, energy consumption increases and thereby reducing the network lifetime. Therefore, DL models can be trained on one-time generated data (using ns-3 or testbed), and the pre-trained model (e.g., inference model) can be utilized in LoRaWAN ns-3 modules [199]. The pre-trained model can be configured using an Open Neural Network Exchange (ONNX) [248]. ONNX is an open-source Application Programming Interface (API) based on the C++ programming language for DL and ML techniques. To use ONNX with ns-3, first, an ONNX-supported pre-trained model using TensorFlow and PyTorch can be generated. Then, the pre-trained model can be imported into ns-3 with the help of the ONNX API. The ONNX API will provide raw data during simulation (similar input samples used during ML model training), which can be used for resource management (e.g., SF or TP). One example of ONNX implementation in ns-3 can be found in [249], where it has been utilized to simulate and model the behavior of an Open Radio Access Network [250].

6.4. ns-3-FL: Federated Learning Framework

The ns-3-FL [251,252] is a new framework for simulating FL in a realistic network environment. FL is an ML technique that allows multiple devices to train a shared model without sharing their data. This is useful for privacy- and delay-sensitive applications like healthcare and finance.

The ns-3-FL framework is built on two existing simulators: FLSim [253,254] and ns-3. It provides a realistic and flexible way to simulate FL training and inference in various network settings. FLSim [253] is responsible for data distribution between client–server architecture and FL, whereas ns-3 simulates the network. As an example of ns-3-FL working, (1) the FLSim [253] requests network simulation and selects the number of EDs for the FL training round, (2) the ns-3 performs the simulation for the selected EDs, (3) the ns-3 transmits the latency and throughput of each ED to the FLSim [253], and (4) the FLSim utilizes the received data from ns-3 during computing the convergence time of the global model (using FedAvg and FedAsync algorithms [255,256]) and average throughput for this specified training round, as illustrated in Figure 3.

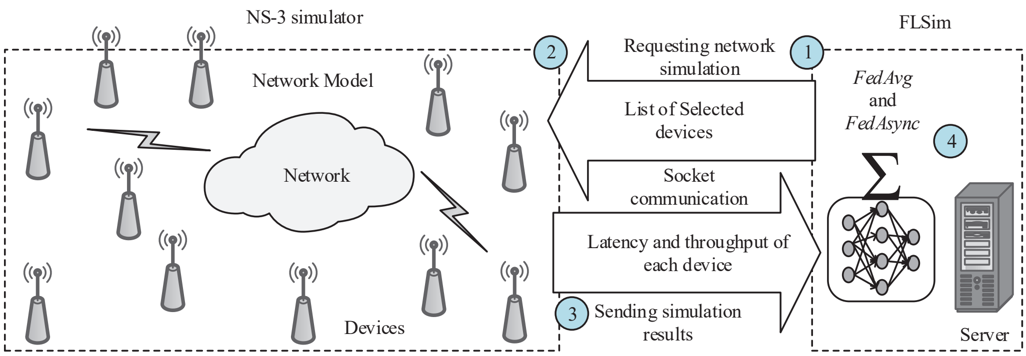

Figure 3. Working procedure of the ns-3-FL framework [252].

Furthermore, the ns-3-FL comprises three main components: the learning model, the network model, and the power control.

6.4.1. Learning Model

FL is an ML paradigm that allows multiple clients to train a shared model without sharing their data. The training is achieved by iteratively sending updates to a global model, which is then aggregated by the server using *FedAvg* and *FedAsync* algorithms [255,256]. The ns-3-FL supports two types of FL algorithms: synchronous and asynchronous. In synchronous FL, all clients update the model simultaneously, while in asynchronous FL, clients can update the model at different times.

6.4.2. Network Model

The ns-3 network simulator was used to model the latency and throughput between clients and the server, allowing to study of network conditions and their impact on the performance of FL.

6.4.3. Power Model

A power model calculates the energy consumption of FL training. This model considers the number of multiply–accumulate operations performed by the clients and the energy used to transmit the model to the server.

6.5. AI-ERA LoRaWAN Framework

Our previously published AI-Efficient Resource Allocation (AI-ERA) framework for SF classification [114,237], designed using AI and ns-3 modules, is a powerful framework, as illustrated in Figure 4. In the AI-ERA framework, the DNN model comprises five fully connected layers, trained using X and Y coordinates, SNR, and received power (P_{rx}). After achieving the desired level of classification accuracy, the pre-trained model is deployed on the ED side, where (1) a similar input sequence (utilized during training) is used as input to the pre-trained model, (2) the pre-trained model processes the input and classifies a suitable SF based on the learned knowledge, and (3) a mobile or static ED adapts the classified SF and start transmitting data in UL direction, as shown in Figure 4.

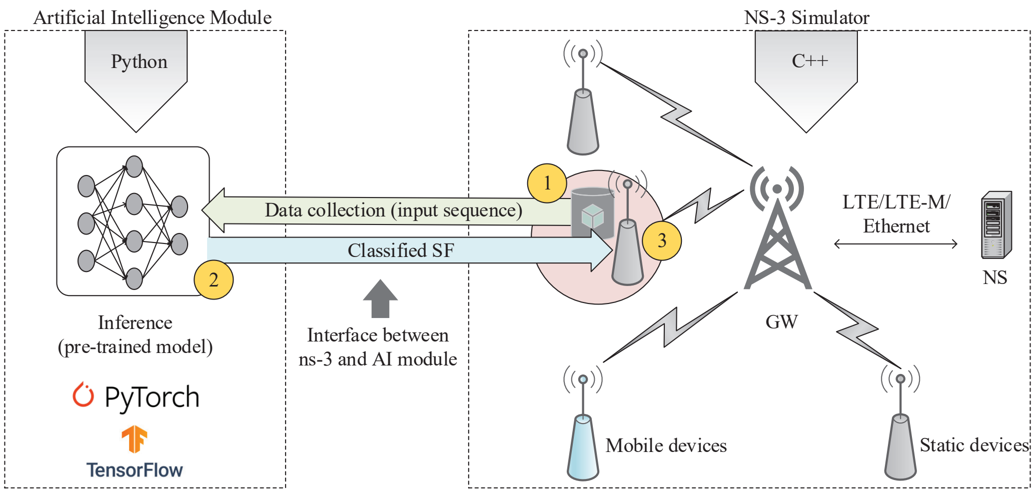

Figure 4. Illustration of the AI-ERA classification framework for spreading factor: (1) inference model deployed on the ED side, where ED prepares input sequence for the model, (2) SF classification by the pre-trained model, and (3) SF adaptation by the ED for uplink packet transmission [114].

In addition, the AI-ERA framework [237] provides three major components: AI module, dataset, and data labeling.

6.5.1. AI Module

As illustrated in Figure 4, the AI-ERA module is comprised of a pre-trained DNN model, which is deployed on the ED side for efficient SF classification to EDs during simulation.

6.5.2. Dataset

During the dataset generation, the AI-ERA framework utilized a regular ADR, where EDs transmit a packet with $SF_7 \sim SF_{12}$ at a regular interval of 10 min, as shown in Figure 5. Over a period of 10 days, a dataset was generated with a UL interval of 10 min. The dataset mainly consists of the X and Y coordinates of the ED locations, along with RSSI, SNR, the distance between ED and GW, and the ACK status of each SF in every UL packet transmitted.

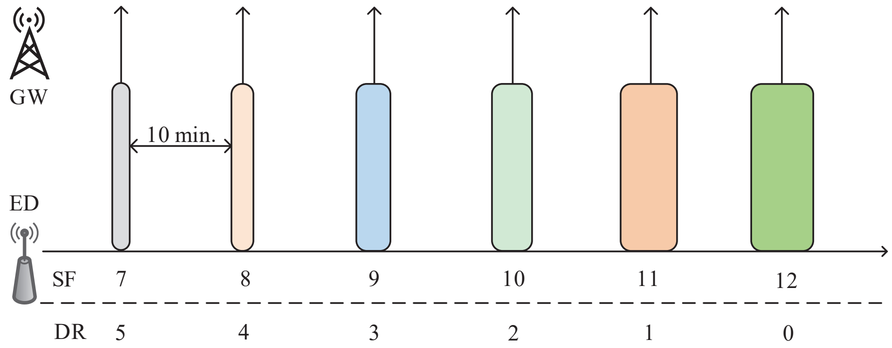

Figure 5. Regular ADR utilized for dataset collection in AI-ERA framework.

6.5.3. Data Labeling

To train the DNN model, the SF was labeled based on the successful ACK reception by the ED. There could be multiple ACK responses for the same packet transmitted with $SF_7 \sim SF_{12}$. As a result, the lowest SF is chosen for labeling, and a sequence of six groups as input is fed to the DNN model.

6.6. LoRaWAN Bandit Framework

LoRaWAN bandit provides an RL framework that can be utilized to allocate the optimal SF to EDs by leveraging a MAB approach [176,257]. The LoRaWAN bandit framework learns the trade-off between energy consumption for each SF. The framework is designed to work in two phases: exploration and exploitation. During the exploration phase, the framework utilizes all SF combinations and learns how the energy consumption and DR is affected during simulation. In the exploitation phase, the framework selects the optimal SF based on the learned information.

The framework utilizes delayed feedback, where it does not expect immediate feedback. However, it receives feedback after a delay caused by several factors, such as the time it takes to reach the GW and the time it takes to process the packet. The framework is implemented in the ns-3 simulator using the LoRaWAN module [151].

6.7. Remarks

The ns-3-based ML frameworks can be utilized by researchers and practitioners to analyze, optimize, and improve the performance of the LoRaWAN networks by efficiently managing the resource parameters. However, these ML frameworks [244,246,248,252] are designed for a different purpose. In addition, the ML frameworks in [114,148,237] and [176,257] are specifically designed for resource management utilizing the state-of-the-art LoRaWAN module [151]. These ML frameworks [114,148,176,237,257] can be adapted to improve the performance of LoRaWAN through resource management.

7. Discussion

In the current literature, ML-, DL-, and RL-based solutions have been extensively studied to tackle the critical challenge of resource allocation in LoRaWAN networks, aiming to enhance the performance of the LoRaWAN network. However, existing approaches predominantly focus on resolving resource allocation at the ED level or on the NS, leading to certain limitations and opportunities for improvement.

7.1. ML Methods at the ED Side

In the literature, several ML methods have been utilized at the ED side [114,127,148], bringing several advantages. The EDs can make autonomous decisions locally regarding the SF selection without constant communication with the NS, thereby reducing communication overhead. In addition, latency is particularly advantageous in scenarios with limited network bandwidth, unstable connections, and the availability of limited communication channels. Moreover, utilizing ML methods for SF classification can efficiently improve the convergence period under static and mobile IoT EDs, thus improving the packet success ratio [114].

However, utilizing ML methods for resource management on the ED side can be disadvantageous. For example, the primary concern is the computational load it places on resource-constrained EDs. Low-power IoT devices with limited processing capabilities may struggle to support ML models due to the significant computational power and memory requirements. Therefore, extra computational power can lead to excessive energy consumption. Moreover, training and maintaining the models on each ED can be challenging, particularly when EDs have different hardware and software configurations, making it difficult to ensure model consistency across the LoRa network.

7.2. ML Methods at the NS Side

When ML methods are utilized on the NS side, it can bring several advantages. For instance, the NS generally has more computational resources, allowing more complex and accurate models to be trained and deployed for resource management. Leveraging a centralized dataset, potentially containing data from massive EDs, can lead to a more comprehensive and accurate ML model for resource classification. Furthermore, updating and maintaining the ML model can be efficiently performed from a centralized location, ensuring consistency across the network.

However, implementing ML methods on the NS can have a negative impact on the network performance. In terms of mobility, if an ED receives a downlink $LinkADRReq$ MAC command from the NS that contains a new SF, and when the ED transmits a packet with the updated SF, it may not be delivered to the GW, resulting in packet loss. This is because the underlying propagation environment changes significantly when the ED is mobile [10,114]. In addition, communication between the EDs and the NS for resource allocation decisions may introduce latency in a large-scale LoRaWAN deployment. Relying on the NS for every resource allocation decision might lead to single points of failure and reduce network performance in terms of increased convergence period.

7.3. Remarks

Resource allocation through ML-, DL-, and RL-based solutions has promising potential to enhance the LoRaWAN network performance. However, addressing the challenges associated with dataset quality and considering the trade-offs of implementing the ML method on the EDs and the NS side is essential for developing effective and efficient resource allocation mechanisms in LoRaWAN networks. The choice between the two approaches must be made carefully, depending on the specific requirements and constraints of the LoRaWAN network. Both options present unique advantages and disadvantages that should be thoroughly evaluated for optimal performance and scalability.

8. Future Recommendations

This section presents future recommendations for SF and TP allocation to EDs using ML to improve the overall performance of LoRaWAN.

8.1. Spreading Factor Classification

The allocation of SF is dependent on few parameters, such as GW sensitivity (S_{GW}) [27] and ED sensitivity (S_{ED}) [105] thresholds (illustrated in Table 9), the distance between the GW and ED [7], path loss [129,146], ToA [133], interference/collision [201], ED positions with SNR [147,148], retransmission [10], the ratio of UL and downlink ACK [105], and packet drop ratio [258]. However, to apply ML/DL for SF allocation to EDs, multiple parameters have been adopted in the current literature, for example, the received power (i.e., RSSI), SNR, the distance between ED and GW, and ED position [114]. For mobile EDs, the ML methods should be deployed on the ED side since the propagation environment changes drastically. Therefore, the decision of efficient SF selection by ED will help to deliver a packet successfully, thereby improving the packet success ratio. However, deploying the ML on the ED side will increase the computational cost as low-power devices with limited processing capabilities may struggle to support ML models due to the significant computational power and memory requirements. On the other hand, it is recommended to utilize the ML method on the NS side for static EDs. In such a case, the propagation environment remains unchanged [10].

Table 9. Sensitivity and required SNR of EDs and GW with 125-kHz mode [27,200].

SF	GW Sensitivity (S_g) [dBm]	ED Sensitivity (S_e) [dBm]	SNR [dB]
12	−142.5	−137.0	−20
11	−140.0	−135.0	−17.5
10	−137.5	−133.0	−15
9	−135.0	−130.0	−12.5
8	−132.5	−127.0	−10
7	−130.0	−124.0	−7.5

8.2. Transmission Power Classification

In LoRaWAN, an ML model can be trained for efficient TP allocation to EDs in an intelligent manner. The input features for TP classification might include $RSSI$, link quality indicator (LQI), energy consumption, interference in the channel, and distance between the GW and ED. The TP level in LoRaWAN ranges from 2 dBm to 14 dBm and can be divided into five possible classes (2, 5, 8, 11, 14) dBm [152,155,167]. A packet successfully delivered with any SF and TP level can be labeled with a particular TP. For example, a DNN model can be trained to classify an appropriate TP level for the EDs based on the provided inputs.

8.3. Multiclass Multioutput Classification

Few existing works have investigated SF and TP classification problems individually. However, both SF and TP classification can be achieved simultaneously, which can be regarded as a multiclass multioutput classification problem, referred to as multi-resource classification (MRC). In the case of SF classification, there are six possible classes (i.e., SF_7, SF_8, SF_9, SF_{10}, SF_{11}, and SF_{12}). Similarly, the TP, ranging from 2 dBm to 14 dBm, can be classified into five possible classes (2, 5, 8, 11, 14) dBm [152,155,167]. During dataset collection, a packet would be transmitted with a pair of SF and TP. Based on the successful ACK reception by the ED for the lowest SF and TP pair, the features such as RSSI, SNR, the distance between ED and GW, ACK status, and X and Y coordinates will be labeled. Based on the requirements of the application (e.g., mobile or static), the ML/DL method can be implemented either on the ED side (in the case of mobile application) or on the NS side (for static application). It is because the underlying propagation environment changes drastically in the case of mobility, thereby the SF and TP selection decision should be taken by ED rather than NS.

9. Conclusions

LoRaWAN is a promising IoT protocol for long-range and ultra-low power consumption applications. However, a few challenges need to be addressed before LoRa and LoRaWAN can be widely deployed, such as LoRa parameters configuration, interference, and optimized ADR. One promising approach to overcoming these challenges and improving the performance of LoRaWAN is ML. ML can be used to develop robust, efficient, and intelligent ADRs responsible for resource parameter configurations (e.g., SF, TP, CR, etc.). Furthermore, the field of ML in LoRa and LoRaWAN is growing fast, with recent research and development focusing on various areas such as SF and TP classification, collision analysis, and interference mitigation.

In conclusion, this survey provides a detailed analysis of the state-of-the-art ML/DL/RL applications utilized for improving the performance of LoRaWAN. Further, the survey discusses the publicly available dataset collection frameworks and publicly available datasets. For the identified required features, the use of potential ML methods has been determined for improving the performance of LoRaWAN. Furthermore, the ns-3-based ML frameworks have been highlighted that can be integrated with the widely adopted LoRaWAN ns-3 module. Finally, a discussion on current ML research efforts is highlighted with features utilized for ML, DL, and RL, along with future recommendations that show how the LoRaWAN performance can be further improved using ML techniques.

Author Contributions: Conceptualization, A.F.; methodology, A.F.; software, A.F.; validation, A.F. and J.-Y.P.; investigation, A.F. and J.-Y.P.; resources, A.F. and J.-Y.P.; data curation, A.F. and J.-Y.P.; writing—original draft preparation, A.F.; writing—review and editing, A.F. and J.-Y.P.; visualization, A.F.; supervision, A.F. and J.-Y.P.; project administration, A.F. and J.-Y.P.; funding acquisition, A.F. and J.-Y.P. All authors have read and agreed to the published version of the manuscript.

Funding: This work was supported by the Research Fund from Chosun University, 2022.

Institutional Review Board Statement: Not applicable.

Informed Consent Statement: Not applicable.

Data Availability Statement: Not applicable.

Conflicts of Interest: The authors declare no conflict of interest.

References

1. Ducrot, N.; Ray, D.; Saadani, A.; Hersent, O.; Pop, G.; Remond, G. Lora Device Developer Guide. 2016. Available online: https://developer.orange.com/od-uploads/LoRa-Device-Developer-Guide-Orange.pdf (accessed on 16 June 2023).
2. Telagam, N.; Kandasamy, N.; Ajitha, D. Smart Healthcare Monitoring System Using LoRaWAN IoT and Machine Learning Methods. In *Practical Artificial Intelligence for Internet of Medical Things*; CRC Press: Boca Raton, FL, USA, 2023; pp. 85–104.
3. Islam, K.Z.; Murray, D.; Diepeveen, D.; Jones, M.G.; Sohel, F. Machine learning-based LoRa localisation using multiple received signal features. *IET Wirel. Sens. Syst.* **2023**, 1–18. [CrossRef]
4. Farhad, A.; Pyun, J.Y. Resource Management for Massive Internet of Things in IEEE 802.11 ah WLAN: Potentials, Current Solutions, and Open Challenges. *Sensors* **2022**, *22*, 9509. [CrossRef]
5. Mekki, K.; Bajic, E.; Chaxel, F.; Meyer, F. A comparative study of LPWAN technologies for large-scale IoT deployment. *ICT Express* **2019**, *5*, 1–7. [CrossRef]
6. Gomez, C.; Veras, J.C.; Vidal, R.; Casals, L.; Paradells, J. A sigfox energy consumption model. *Sensors* **2019**, *19*, 681. [CrossRef]
7. Farhad, A.; Kim, D.H.; Kim, B.H.; Mohammed, A.F.Y.; Pyun, J.Y. Mobility-Aware Resource Assignment to IoT Applications in Long-Range Wide Area Networks. *IEEE Access* **2020**, *8*, 186111–186124. [CrossRef]
8. Singh, R.K.; Puluckul, P.P.; Berkvens, R.; Weyn, M. Energy consumption analysis of LPWAN technologies and lifetime estimation for IoT application. *Sensors* **2020**, *20*, 4794. [CrossRef]
9. RP002-1.0.2 LoRaWAN® Regional Parameters. 2020. Available online: https://hz137b.p3cdn1.secureserver.net/wp-content/uploads/2020/11/RP_2-1.0.2.pdf?time=1672853176 (accessed on 9 January 2023).
10. Farhad, A.; Kim, D.H.; Pyun, J.Y. R-ARM: Retransmission-Assisted Resource Management in LoRaWAN for the Internet of Things. *IEEE Internet Things J.* **2022**, *9*, 7347–7361. [CrossRef]
11. Farhad, A.; Pyun, J.Y. Terahertz Meets AI: The State of the Art. *Sensors* **2023**, *23*, 5034.
12. Farahsari, P.S.; Farahzadi, A.; Rezazadeh, J.; Bagheri, A. A survey on indoor positioning systems for iot-based applications. *IEEE Internet Things J.* **2022**, *9*, 7680–7699. [CrossRef]
13. Torres-Sospedra, J.; Gaibor, D.P.Q.; Nurmi, J.; Koucheryavy, Y.; Lohan, E.S.; Huerta, J. Scalable and Efficient Clustering for Fingerprint-Based Positioning. *IEEE Internet Things J.* **2022**, *10*, 3484–3499. [CrossRef]
14. LoRa Simulator (LoRaSim). Available online: https://github.com/AlexSartori/LoRaSim (accessed on 3 May 2023).
15. Zorbas, D.; Caillouet, C.; Abdelfadeel Hassan, K.; Pesch, D. Optimal data collection time in LoRa networks—A time-slotted approach. *Sensors* **2021**, *21*, 1193. [CrossRef]
16. Beltramelli, L.; Mahmood, A.; Österberg, P.; Gidlund, M.; Ferrari, P.; Sisinni, E. Energy efficiency of slotted LoRaWAN communication with out-of-band synchronization. *IEEE Trans. Instrum. Meas.* **2021**, *70*, 1–11. [CrossRef]

17. Loh, F.; Mehling, N.; Metzger, F.; Hoßfeld, T.; Hock, D. LoRaPlan: A Software to Evaluate Gateway Placement in LoRaWAN. In Proceedings of the 17th International Conference on Network and Service Management (CNSM), Izmir, Turkey, 25–29 October 2021; pp. 385–387. [CrossRef]
18. Casals, L.; Gomez, C.; Vidal, R. The SF12 Well in LoRaWAN: Problem and End-Device-Based Solutions. *Sensors* **2021**, *21*, 6478. [CrossRef]
19. Zorbas, D.; Abdelfadeel, K.; Kotzanikolaou, P.; Pesch, D. TS-LoRa: Time-slotted LoRaWAN for the industrial Internet of Things. *Comput. Commun.* **2020**, *153*, 1–10. [CrossRef]
20. Abdelfadeel, K.Q.; Zorbas, D.; Cionca, V.; Pesch, D. *FREE*—Fine-grained scheduling for reliable and energy-efficient data collection in LoRaWAN. *IEEE Internet Things J.* **2019**, *7*, 669–683. [CrossRef]
21. Ta, D.T.; Khawam, K.; Lahoud, S.; Adjih, C.; Martin, S. LoRa-MAB: A Flexible Simulator for Decentralized Learning Resource Allocation in IoT Networks. In Proceedings of the 2019 12th IFIP Wireless and Mobile Networking Conference (WMNC), Paris, France, 11–13 September 2019; pp. 55–62. [CrossRef]
22. Reynders, B.; Wang, Q.; Pollin, S. A LoRaWAN module for ns-3: Implementation and evaluation. In Proceedings of the 10th Workshop on ns-3, Surathkal, India, 13–14 June 2018; pp. 61–68.
23. To, T.H.; Duda, A. Simulation of LoRa in NS-3: Improving LoRa Performance with CSMA. In Proceedings of the IEEE International Conference on Communications (ICC), Kansas City, MO, USA, 20–24 May 2018; pp. 1–7. [CrossRef]
24. Slabicki, M.; Premsankar, G.; Di Francesco, M. Adaptive configuration of lora networks for dense IoT deployments. In Proceedings of the NOMS 2018—2018 IEEE/IFIP Network Operations and Management Symposium, Taipei, Taiwan, 23–27 April 2018; pp. 1–9. [CrossRef]
25. Bounceur, A.; Marc, O.; Lounis, M.; Soler, J.; Clavier, L.; Combeau, P.; Vauzelle, R.; Lagadec, L.; Euler, R.; Bezoui, M. CupCarbon-Lab: An IoT emulator. In Proceedings of the 15th IEEE Annual Consumer Communications & Networking Conference (CCNC), Las Vegas, NV, USA, 12–15 January 2018; pp. 1–2. [CrossRef]
26. Croce, D.; Gucciardo, M.; Mangione, S.; Santaromita, G.; Tinnirello, I. Impact of LoRa imperfect orthogonality: Analysis of link-level performance. *IEEE Commun. Lett.* **2018**, *22*, 796–799. [CrossRef]
27. Magrin, D.; Centenaro, M.; Vangelista, L. Performance evaluation of LoRa networks in a smart city scenario. In Proceedings of the 2017 IEEE International Conference on Communications (ICC), Paris, France, 21–25 May 2017; pp. 1–7. [CrossRef]
28. Van den Abeele, F.; Haxhibeqiri, J.; Moerman, I.; Hoebeke, J. Scalability analysis of large-scale LoRaWAN networks in ns-3. *IEEE Internet Things J.* **2017**, *4*, 2186–2198. [CrossRef]
29. Pop, A.I.; Raza, U.; Kulkarni, P.; Sooriyabandara, M. Does Bidirectional Traffic Do More Harm Than Good in LoRaWAN Based LPWA Networks? In Proceedings of the GLOBECOM 2017—2017 IEEE Global Communications Conference, Singapore, 4–8 December 2017; pp. 1–6. [CrossRef]
30. Bor, M.C.; Roedig, U.; Voigt, T.; Alonso, J.M. Do LoRa low-power wide-area networks scale? In Proceedings of the 19th ACM International Conference on Modeling, Analysis and Simulation of Wireless and Mobile Systems, Malta, 13–17 November 2016; pp. 59–67.
31. Sigfox Simulator. Available online: https://github.com/maartenweyn/lpwansimulation (accessed on 26 May 2023).
32. NS-3 Module for Sigfox. Available online: https://github.com/DEIS-Tools/ns3-sigfox (accessed on 26 May 2023).
33. Blockchain-Based IoT Simulator. Available online: https://github.com/sapgan/NS3-IoT-Simulator (accessed on 26 May 2023).
34. NS-3-Based NB-IoT Simulator Module. Available online: https://github.com/gdbranco/RA5G_NS3 (accessed on 26 May 2023).
35. NS-3-Based Framework for Narrow Band-IoT and LTE. Available online: https://github.com/a3794110/ns-3-NB-IoT (accessed on 30 May 2023).
36. NS-3-Based Framework for 5G. Available online: https://github.com/QiuYukang/5G-LENA (accessed on 26 May 2023).
37. LENA Framework for LTE and Vehicle-to-Everything (V2X). Available online: https://github.com/signetlabdei/lena-plus (accessed on 26 May 2023).
38. Polese, M.; Centenaro, M.; Zanella, A.; Zorzi, M. M2M massive access in LTE: RACH performance evaluation in a Smart City scenario. In Proceedings of the 2016 IEEE International Conference on Communications (ICC), Kuala Lumpur, Malaysia, 22–27 May 2016; pp. 1–6. [CrossRef]
39. Sinha, R.S.; Wei, Y.; Hwang, S.H. A survey on LPWA technology: LoRa and NB-IoT. *ICT Express* **2017**, *3*, 14–21. [CrossRef]
40. Raza, U.; Kulkarni, P.; Sooriyabandara, M. Low power wide area networks: An overview. *IEEE Commun. Surv. Tutor.* **2017**, *19*, 855–873. [CrossRef]
41. Piroddi, A.; Torregiani, M. Machine Learning Applied to LoRaWAN Network for Improving Fingerprint Localization Accuracy in Dense Urban Areas. *Network* **2023**, *3*, 199–217. [CrossRef]
42. LoRaWAN L2 1.0.4 Specification. 2020. Available online: https://hz137b.p3cdn1.secureserver.net/wp-content/uploads/2021/11/LoRaWAN-Link-Layer-Specification-v1.0.4.pdf?time=1672853176 (accessed on 7 January 2023).
43. Haxhibeqiri, J.; De Poorter, E.; Moerman, I.; Hoebeke, J. A survey of lorawan for iot: From technology to application. *Sensors* **2018**, *18*, 3995. [CrossRef]
44. Butun, I.; Pereira, N.; Gidlund, M. Security risk analysis of LoRaWAN and future directions. *Future Internet* **2018**, *11*, 3. [CrossRef]
45. Saari, M.; bin Baharudin, A.M.; Sillberg, P.; Hyrynsalmi, S.; Yan, W. LoRa—A survey of recent research trends. In Proceedings of the 41st International Convention on Information and Communication Technology, Electronics and Microelectronics (MIPRO), Opatija, Croatia, 21–25 May 2018; pp. 872–877. [CrossRef]

46. Muteba, F.; Djouani, K.; Olwal, T. A comparative Survey Study on LPWA IoT Technologies: Design, considerations, challenges and solutions. *Procedia Comput. Sci.* **2019**, *155*, 636–641. [CrossRef]
47. Khalifeh, A.; Aldahdouh, K.A.; Darabkh, K.A.; Al-Sit, W. A Survey of 5G Emerging Wireless Technologies Featuring LoRaWAN, Sigfox, NB-IoT and LTE-M. In Proceedings of the International Conference on Wireless Communications Signal Processing and Networking (WiSPNET), Chennai, India, 21–23 March 2019; pp. 561–566. [CrossRef]
48. Sarker, V.K.; Queralta, J.P.; Gia, T.N.; Tenhunen, H.; Westerlund, T. A Survey on LoRa for IoT: Integrating Edge Computing. In Proceedings of the 2019 Fourth International Conference on Fog and Mobile Edge Computing (FMEC), Rome, Italy, 10–13 June 2019; pp. 295–300. [CrossRef]
49. Ntseane, L.; Isong, B. Analysis of LoRa/LoRaWAN Challenges: Review. In Proceedings of the International Multidisciplinary Information Technology and Engineering Conference (IMITEC), Vanderbijlpark, South Africa, 21–22 November 2019; pp. 1–7. [CrossRef]
50. Ayoub, W.; Samhat, A.E.; Nouvel, F.; Mroue, M.; Prévotet, J.C. Internet of mobile things: Overview of lorawan, dash7, and nb-iot in lpwans standards and supported mobility. *IEEE Commun. Surv. Tutor.* **2018**, *21*, 1561–1581. [CrossRef]
51. Qin, Z.; Li, F.Y.; Li, G.Y.; McCann, J.A.; Ni, Q. Low-Power Wide-Area Networks for Sustainable IoT. *IEEE Wirel. Commun.* **2019**, *26*, 140–145. [CrossRef]
52. Marais, J.M.; Abu-Mahfouz, A.M.; Hancke, G.P. A Review of LoRaWAN Simulators: Design Requirements and Limitations. In Proceedings of the 2019 International Multidisciplinary Information Technology and Engineering Conference (IMITEC), Vanderbijlpark, South Africa, 21–22 November 2019; pp. 1–6. [CrossRef]
53. Ertürk, M.A.; Aydın, M.A.; Büyükakkaşlar, M.T.; Evirgen, H. A survey on LoRaWAN architecture, protocol and technologies. *Future Internet* **2019**, *11*, 216. [CrossRef]
54. Gambiroža, J.Č.; Mastelić, T.; Šolić, P.; Čagalj, M. Capacity in LoRaWAN Networks: Challenges and Opportunities. In Proceedings of the 2019 4th International Conference on Smart and Sustainable Technologies (SpliTech), Split, Croatia, 18–21 June 2019; pp. 1–6. [CrossRef]
55. Bouras, C.; Gkamas, A.; Katsampiris Salgado, S.A.; Kokkinos, V. Comparison of LoRa simulation environments. In Proceedings of the 14th International Conference on Broad-Band Wireless Computing, Communication and Applications (BWCCA-2019), Antwerp, Belgium, 7–9 November 2019 ; Springer: Berlin/Heidelberg, Germany, 2019; pp. 374–385.
56. Kufakunesu, R.; Hancke, G.P.; Abu-Mahfouz, A.M. A Survey on Adaptive Data Rate Optimization in LoRaWAN: Recent Solutions and Major Challenges. *Sensors* **2020**, *20*, 5044. [CrossRef]
57. Lehong, C.; Isong, B.; Lugayizi, F.; Abu-Mahfouz, A.M. A Survey of LoRaWAN Adaptive Data Rate Algorithms for Possible Optimization. In Proceedings of the 2nd International Multidisciplinary Information Technology and Engineering Conference (IMITEC), Kimberley, South Africa, 25–27 November 2020; pp. 1–9. [CrossRef]
58. Sundaram, J.P.S.; Du, W.; Zhao, Z. A survey on lora networking: Research problems, current solutions, and open issues. *IEEE Commun. Surv. Tutor.* **2019**, *22*, 371–388. [CrossRef]
59. Alenezi, M.; Chai, K.K.; Chen, Y.; Jimaa, S. Ultra-dense LoRaWAN: Reviews and challenges. *IET Commun.* **2020**, *14*, 1361–1371. [CrossRef]
60. Staikopoulos, A.; Kanakaris, V.; Papakostas, G.A. Image Transmission via LoRa Networks—A Survey. In Proceedings of the IEEE 5th International Conference on Image, Vision and Computing (ICIVC), Beijing, China, 10–12 July 2020; pp. 150–154. [CrossRef]
61. Cotrim, J.R.; Kleinschmidt, J.H. LoRaWAN mesh networks: A review and classification of multihop communication. *Sensors* **2020**, *20*, 4273. [CrossRef]
62. Noura, H.; Hatoum, T.; Salman, O.; Yaacoub, J.P.; Chehab, A. LoRaWAN security survey: Issues, threats and possible mitigation techniques. *Internet Things* **2020**, *12*, 100303. [CrossRef]
63. Osorio, A.; Calle, M.; Soto, J.D.; Candelo-Becerra, J.E. Routing in LoRaWAN: Overview and challenges. *IEEE Commun. Mag.* **2020**, *58*, 72–76. [CrossRef]
64. Marais, J.M.; Abu-Mahfouz, A.M.; Hancke, G.P. A Survey on the Viability of Confirmed Traffic in a LoRaWAN. *IEEE Access* **2020**, *8*, 9296–9311. [CrossRef]
65. Raychowdhury, A.; Pramanik, A. Survey on LoRa Technology: For Internet of Things. In *Intelligent Systems, Technologies and Applications*; Thampi, S.M., Trajkovic, L., Mitra, S., Nagabhushan, P., El-Alfy, E.S.M., Bojkovic, Z., Mishra, D., Eds.; Springer: Berlin/Heidelberg, Germany, 2020; pp. 259–271.
66. Abd Elkarim, S.I.; Basem, M. Machine Learning Approaches for LoRa Networks: A Survey. Available online: https://www.researchgate.net/profile/Basem-Elhalawany/publication/370510570_Machine_Learning_Approaches_for_LoRa_Networks_A_survey/links/645b475ef3512f1cc58856de/Machine-Learning-Approaches-for-LoRa-Networks-A-survey.pdf (accessed on 19 July 2023).
67. Silva, F.S.D.; Neto, E.P.; Oliveira, H.; Rosário, D.; Cerqueira, E.; Both, C.; Zeadally, S.; Neto, A.V. A Survey on Long-Range Wide-Area Network Technology Optimizations. *IEEE Access* **2021**, *9*, 106079–106106. [CrossRef]
68. Ghazali, M.H.M.; Teoh, K.; Rahiman, W. A systematic review of real-time deployments of UAV-based Lora communication network. *IEEE Access* **2021**, *9*, 124817–124830. [CrossRef]
69. Benkahla, N.; Tounsi, H.; Song, Y.Q.; Frikha, M. Review and experimental evaluation of ADR enhancements for LoRaWAN networks. *Telecommun. Syst.* **2021**, *77*, 1–22. [CrossRef]
70. Lalle, Y.; Fourati, M.; Fourati, L.C.; Barraca, J.P. Routing Strategies for LoRaWAN Multi-Hop Networks: A Survey and an SDN-Based Solution for Smart Water Grid. *IEEE Access* **2021**, *9*, 168624–168647. [CrossRef]
71. Ugwuanyi, S.; Paul, G.; Irvine, J. Survey of IoT for developing countries: Performance analysis of LoRaWAN and cellular NB-IoT networks. *Electronics* **2021**, *10*, 2224. [CrossRef]

72. Gkotsiopoulos, P.; Zorbas, D.; Douligeris, C. Performance Determinants in LoRa Networks: A Literature Review. *IEEE Commun. Surv. Tutor.* **2021**, *23*, 1721–1758. [CrossRef]
73. da Silva, J.C.; Flor, D.d.L.; de Sousa Junior, V.A.; Bezerra, N.S.; de Medeiros, A.A. A Survey of LoRaWAN Simulation Tools in ns-3. *J. Commun. Inf. Syst.* **2021**, *36*, 17–30. [CrossRef]
74. Maurya, P.; Singh, A.; Kherani, A.A. A review: Spreading factor allocation schemes for LoRaWAN. *Telecommun. Syst.* **2022**, *80*, 449–468. [CrossRef]
75. Almuhaya, M.A.; Jabbar, W.A.; Sulaiman, N.; Abdulmalek, S. A survey on Lorawan technology: Recent trends, opportunities, simulation tools and future directions. *Electronics* **2022**, *11*, 164. [CrossRef]
76. Li, C.; Cao, Z. Lora networking techniques for large-scale and long-term iot: A down-to-top survey. *ACM Comput. Surv. (CSUR)* **2022**, *55*, 1–36. [CrossRef]
77. Banti, K.; Karampelia, I.; Dimakis, T.; Boulogeorgos, A.A.A.; Kyriakidis, T.; Louta, M. LoRaWAN Communication Protocols: A Comprehensive Survey under an Energy Efficiency Perspective. *Telecom* **2022**, *3*, 322–357. [CrossRef]
78. Cheikh, I.; Aouami, R.; Sabir, E.; Sadik, M.; Roy, S. Multi-Layered Energy Efficiency in LoRa-WAN Networks: A Tutorial. *IEEE Access* **2022**, *10*, 9198–9231. [CrossRef]
79. Idris, S.; Karunathilake, T.; Förster, A. Survey and Comparative Study of LoRa-Enabled Simulators for Internet of Things and Wireless Sensor Networks. *Sensors* **2022**, *22*, 5546. [CrossRef] [PubMed]
80. Almuhaya, M.A.; Jabbar, W.A.; Sulaiman, N.; Sulaiman, A. An Overview on LoRaWAN Technology Simulation Tools. In *International Conference of Reliable Information and Communication Technology*; Springer: Berlin/Heidelberg, Germany, 2022; Volume 127, pp. 345–358.
81. Hessel, F.; Almon, L.; Hollick, M. LoRaWAN Security: An Evolvable Survey on Vulnerabilities, Attacks and their Systematic Mitigation. *ACM Trans. Sens. Netw.* **2022**, *18*, 1–55. [CrossRef]
82. Sun, Z.; Yang, H.; Liu, K.; Yin, Z.; Li, Z.; Xu, W. Recent advances in lora: A comprehensive survey. *ACM Trans. Sensor Netw.* **2022**, *18*, 1–44. [CrossRef]
83. Jouhari, M.; Saeed, N.; Alouini, M.S.; Amhoud, E.M. A Survey on Scalable LoRaWAN for Massive IoT: Recent Advances, Potentials, and Challenges. *IEEE Commun. Surv. Tutor.* **2023**. [CrossRef]
84. Baker, S.; Xiang, W. Artificial Intelligence of Things for Smarter Healthcare: A Survey of Advancements, Challenges, and Opportunities. *IEEE Commun. Surv. Tutor.* **2023**, *25*, 1261–1293. [CrossRef]
85. Kitchenham, B.A.; Charters, S. *Guidelines for Performing Systematic Literature Reviews in Software Engineering*; Technical Report EBSE 2007-001, Keele University and Durham University Joint Report; Department of Computer Science, University of Durham: Durham, UK, 2007.
86. Semtech. LoRa® and LoRaWAN®: A Technical Overview. Available online: https://lora-developers.semtech.com/uploads/documents/files/LoRa_and_LoRaWAN-A_Tech_Overview-Downloadable.pdf (accessed on 16 June 2023).
87. Pasolini, G. On the LoRa chirp spread spectrum modulation. Signal properties and their impact on transmitter and receiver architectures. *IEEE Trans. Wirel. Commun.* **2021**, *21*, 357–369. [CrossRef]
88. Goursaud, C.; Gorce, J.M. Dedicated networks for IoT: PHY/MAC state of the art and challenges. *EAI Endorsed Trans. Internet Thingsl.* **2015**, *1*, 1–11.
89. Xie, B.; Yin, Y.; Xiong, J. Pushing the Limits of Long Range Wireless Sensing with LoRa. *Proc. ACM Interact. Mob. Wearable Ubiquitous Technol.* **2021**, *5*, 1–21. [CrossRef]
90. Avila-Campos, P.; Astudillo-Salinas, F.; Vazquez-Rodas, A.; Araujo, A. Evaluation of LoRaWAN transmission range for wireless sensor networks in riparian forests. In Proceedings of the 22nd International ACM Conference on Modeling, Analysis and Simulation of Wireless and Mobile Systems, Miami Beach, FL, USA, 25–29 November 2019; pp. 199–206.
91. Lavric, A.; Popa, V. Internet of things and LoRa™ low-power wide-area networks: A survey. In Proceedings of the 2017 International Symposium on Signals, Circuits and Systems (ISSCS), Iasi, Romania, 13–14 July 2017; pp. 1–5.
92. LoRaWAN Regional Parameters (RP002-1.0.3). 2021. Available online: https://hz137b.p3cdn1.secureserver.net/wp-content/uploads/2021/05/RP002-1.0.3-FINAL-1.pdf?time=1672853176 (accessed on 8 January 2023).
93. Marais, J.M.; Malekian, R.; Abu-Mahfouz, A.M. LoRa and LoRaWAN testbeds: A review. In Proceedings of the IEEE AFRICON, Cape Town, South Africa, 18–20 September 2017; pp. 1496–1501. [CrossRef]
94. Cuomo, F.; Gámez, J.C.C.; Maurizio, A.; Scipione, L.; Campo, M.; Caponi, A.; Bianchi, G.; Rossini, G.; Pisani, P. Towards traffic-oriented spreading factor allocations in LoRaWAN systems. In Proceedings of the 2018 17th Annual Mediterranean Ad Hoc Networking Workshop (Med-Hoc-Net), Capri, Italy, 20–22 June 2018; pp. 1–8. [CrossRef]
95. Fair Access Policy. Available online: https://www.thethingsnetwork.org/forum/t/fair-use-policy-explained/1300 (accessed on 9 January 2023).
96. Migabo, E.; Djouani, K.; Kurien, A.; Olwal, T. A comparative survey study on LPWA networks: LoRa and NB-IoT. In Proceedings of the Future Technologies Conference (FTC), Vancouver, BC, Canada, 29–30 November 2017; pp. 29–30.
97. de Carvalho Silva, J.; Rodrigues, J.J.P.C.; Alberti, A.M.; Solic, P.; Aquino, A.L.L. LoRaWAN—A low power WAN protocol for Internet of Things: A review and opportunities. In Proceedings of the 2017 2nd International Multidisciplinary Conference on Computer and Energy Science (SpliTech), Split, Croatia, 12–14 July 2017; pp. 1–6.

98. Farhad, A.; Kwon, G.R.; Pyun, J.Y. Mobility Adaptive Data Rate Based on Kalman Filter for LoRa-Empowered IoT Applications. In Proceedings of the 2023 IEEE 20th Consumer Communications & Networking Conference (CCNC), Las Vegas, NV, USA, 8–11 January 2023; pp. 321–324. [CrossRef]
99. Semtech. LoRaWAN Mobile Applications: Blind ADR. 2019. Available online: https://lora-developers.semtech.com/documentation/tech-papers-and-guides/blind-adr/ (accessed on 31 May 2023).
100. Farhad, A.; Kim, D.H.; Kwon, D.; Pyun, J.Y. An Improved Adaptive Data Rate for LoRaWAN Networks. In Proceedings of the 2020 IEEE International Conference on Consumer Electronics—Asia (ICCE-Asia), Seoul, Republic of Korea, 1–3 November 2020; pp. 1–4. [CrossRef]
101. Airtime Calculator for LoRaWAN. Available online: https://avbentem.github.io/airtime-calculator/ttn/eu868/51,12 (accessed on 9 January 2023).
102. TTN Airtime Calculator for LoRaWAN. Available online: https://www.thethingsnetwork.org/airtime-calculator (accessed on 9 January 2023).
103. Bor, M.; Roedig, U. LoRa Transmission Parameter Selection. In Proceedings of the 2017 13th International Conference on Distributed Computing in Sensor Systems (DCOSS), Ottawa, ON, Canada, 5–7 June 2017; pp. 27–34. 2017.10. [CrossRef]
104. Al-Gumaei, Y.A.; Aslam, N.; Chen, X.; Raza, M.; Ansari, R.I. Optimizing Power Allocation in LoRaWAN IoT Applications. *IEEE Internet Things J.* **2022**, *9*, 3429–3442. [CrossRef]
105. Farhad, A.; Kim, D.H.; Pyun, J.Y. Resource Allocation to Massive Internet of Things in LoRaWANs. *Sensors* **2020**, *20*, 2645. [CrossRef]
106. Marini, R.; Cerroni, W.; Buratti, C. A Novel Collision-Aware Adaptive Data Rate Algorithm for LoRaWAN Networks. *IEEE Internet Things J.* **2021**, *8*, 2670–2680. [CrossRef]
107. Anwar, K.; Rahman, T.; Zeb, A.; Khan, I.; Zareei, M.; Vargas-Rosales, C. RM-ADR: Resource Management Adaptive Data Rate for Mobile Application in LoRaWAN. *Sensors* **2021**, *21*, 7980. [CrossRef]
108. Moysiadis, V.; Lagkas, T.; Argyriou, V.; Sarigiannidis, A.; Moscholios, I.D.; Sarigiannidis, P. Extending ADR mechanism for LoRa enabled mobile end-devices. *Simul. Model. Pract. Theory* **2021**, *113*, 102388. [CrossRef]
109. Park, J.; Park, K.; Bae, H.; Kim, C.K. EARN: Enhanced ADR with Coding Rate Adaptation in LoRaWAN. *IEEE Internet Things J.* **2020**, *7*, 11873–11883. [CrossRef]
110. Benkahla, N.; Tounsi, H.; Ye-Qiong, S.; Frikha, M. Enhanced ADR for LoRaWAN networks with mobility. In Proceedings of the 2019 15th International Wireless Communications & Mobile Computing Conference (IWCMC), Tangier, Morocco, 24–28 June 2019; pp. 1–6.
111. Semtech. Understanding the LoRa Adaptive Data Rate. Available online: https://lora-developers.semtech.com/uploads/documents/files/Understanding_LoRa_Adaptive_Data_Rate_Downloadable.pdf (accessed on 16 June 2023).
112. ETSI. System Reference Document (SRdoc); Technical Characteristics for Low Power Wide Area Networks and Chirp Spread Spectrum (LPWAN-CSS) Operating in the UHF Spectrum below 1 GHz; ETSI TR 103 526 V1.1.1 (2018-04). Available online: https://www.etsi.org/deliver/etsi_tr/103500_103599/103526/01.01.01_60/tr_103526v010101p.pdf (accessed on 16 June 2023).
113. Farhad, A.; Kim, D.H.; Yoon, J.S.; Pyun, J.Y. Feasibility Study of the LoRaWAN blind Adaptive Data Rate. In Proceedings of the Twelfth International Conference on Ubiquitous and Future Networks (ICUFN), Jeju Island, Republic of Korea, 17–20 August 2021; pp. 67–69. [CrossRef]
114. Farhad, A.; Pyun, J.Y. AI-ERA: Artificial Intelligence-Empowered Resource Allocation for LoRa-Enabled IoT Applications. *IEEE Trans. Ind. Inform.* **2023**, 1–13.
115. Yu, P.; Zhou, F.; Zhang, X.; Qiu, X.; Kadoch, M.; Cheriet, M. Deep Learning-Based Resource Allocation for 5G Broadband TV Service. *IEEE Trans. Broadcast.* **2020**, *66*, 800–813. [CrossRef]
116. Ye, H.; Li, G.Y.; Juang, B.H.F. Deep Reinforcement Learning Based Resource Allocation for V2V Communications. *IEEE Trans. Veh. Technol.* **2019**, *68*, 3163–3173. [CrossRef]
117. Ahmed, K.I.; Tabassum, H.; Hossain, E. Deep Learning for Radio Resource Allocation in Multi-Cell Networks. *IEEE Netw.* **2019**, *33*, 188–195. [CrossRef]
118. Movassagh, A.A.; Alzubi, J.A.; Gheisari, M.; Rahimi, M.; Mohan, S.; Abbasi, A.A.; Nabipour, N. Artificial neural networks training algorithm integrating invasive weed optimization with differential evolutionary model. *J. Ambient. Intell. Humaniz. Comput.* **2021**, *4*, 6017–6025. [CrossRef]
119. Otynshin, A. Performance Enhancements of LoRaWAN Using Machine Learning on the Edge. Ph.D. Thesis, Nazarbayev University, Astana, Kazakhstan, 2021 .
120. Rodić, L.D.; Perković, T.; Škiljo, M.; Šolić, P. Privacy leakage of LoRaWAN smart parking occupancy sensors. *Future Gener. Comput. Syst.* **2023**, *138*, 142–159. [CrossRef]
121. Perković, T.; Dujić Rodić, L.; Šabić, J.; Šolić, P. Machine Learning Approach towards LoRaWAN Indoor Localization. *Electronics* **2023**, *12*, 457. [CrossRef]
122. Simeone, O. A Very Brief Introduction to Machine Learning With Applications to Communication Systems. *IEEE Trans. Cogn. Commun. Netw.* **2018**, *4*, 648–664. [CrossRef]
123. Hussain, F.; Hassan, S.A.; Hussain, R.; Hossain, E. Machine Learning for Resource Management in Cellular and IoT Networks: Potentials, Current Solutions, and Open Challenges. *IEEE Commun. Surv. Tutor.* **2020**, *22*, 1251–1275. [CrossRef]

124. Paredes, W.D.; Kaushal, H.; Vakilinia, I.; Prodanoff, Z. LoRa Technology in Flying Ad Hoc Networks: A Survey of Challenges and Open Issues. *Sensors* **2023**, *23*, 2403. [CrossRef]
125. Gomez, C.A.; Shami, A.; Wang, X. Machine learning aided scheme for load balancing in dense IoT networks. *Sensors* **2018**, *18*, 3779. [CrossRef]
126. TTN Mapper. 2020. Available online: https://ttnmapper.org/heatmap/ (accessed on 1 June 2023).
127. Yatagan, T.; Oktug, S. Smart spreading factor assignment for lorawans. In Proceedings of the 2019 IEEE Symposium on Computers and Communications (ISCC), Barcelona, Spain, 29 June–3 July 2019; pp. 1–7. [CrossRef]
128. Simulator for LoRa Spreading Factor (SimLoRaSF). Available online: https://github.com/tugrulyatagan/simlorasf (accessed on 26 May 2023).
129. Minhaj, S.U.; Mahmood, A.; Abedin, S.F.; Hassan, S.A.; Bhatti, M.T.; Ali, S.H.; Gidlund, M. Intelligent Resource Allocation in LoRaWAN Using Machine Learning Techniques. *IEEE Access* **2023**, *11*, 10092–10106. [CrossRef]
130. Voigt, T.; Bor, M.; Roedig, U.; Alonso, J. Mitigating Inter-Network Interference in LoRa Networks. *arXiv* **2016**, arXiv:1611.00688. [CrossRef]
131. LoRa Simulator. Available online: https://mcbor.github.io/lorasim/ (accessed on 3 June 2023).
132. González-Palacio, M.; Tobón-Vallejo, D.; Sepúlveda-Cano, L.M.; Rúa, S.; Le, L.B. Machine-Learning-Based Combined Path Loss and Shadowing Model in LoRaWAN for Energy Efficiency Enhancement. *IEEE Internet Things J.* **2023**, *10*, 10725–10739. [CrossRef]
133. Spathi, K.P.; Beletsioti, G.A.; Kantelis, K.F.; Valkanis, A.; Nicopolitidis, P.; Papadimitriou, G.I. Increasing device energy efficiency in LoRaWAN networks via a learning-automata-based approach. *Int. J. Sens. Netw.* **2023**, *42*, 87–101. [CrossRef]
134. Kim, D.Y.; Kim, S. Data transmission using K-means clustering in low power wide area networks with mobile edge cloud. *Wirel. Pers. Commun.* **2019**, *105*, 567–581. [CrossRef]
135. Cuomo, F.; Garlisi, D.; Martino, A.; Martino, A. Predicting LoRaWAN behavior: How machine learning can help. *Computers* **2020**, *9*, 60. [CrossRef]
136. Tsakmakis, A.; Valkanis, A.; Beletsioti, G.; Kantelis, K.; Nicopolitidis, P.; Papadimitriou, G. Learning-Automata-Based Hybrid Model for Event Detection in LoRaWAN Networks. In Proceedings of the 2022 IEEE 21st Mediterranean Electrotechnical Conference (MELECON), Palermo, Italy, 14–16 June 2022; pp. 1183–1188. [CrossRef]
137. Elbsir, H.; Kassab, M.; Bhiri, S.; Bedoui, M.H.; Castells-Rufas, D.; Carrabina, J. LoRaWAN Optimization using optimized Auto-Regressive algorithm, Support Vector Machine and Temporal Fusion Transformer for QoS ensuring. In Proceedings of the 2022 18th International Conference on Wireless and Mobile Computing, Networking and Communications (WiMob), Thessaloniki, Greece, 10–12 October 2022; pp. 302–307. [CrossRef]
138. Xiao, Y.; Song, Y.; Liu, J. Multi-Agent Deep Reinforcement Learning Based Resource Allocation for Ultra-Reliable Low-Latency Internet of Controllable Things. *IEEE Trans. Wirel. Commun.* **2023**. [CrossRef]
139. Chan, J.; Wang, A.; Krishnamurthy, A.; Gollakota, S. Deepsense: Enabling carrier sense in low-power wide area networks using deep learning. *arXiv* **2019**, arXiv:1904.10607.
140. Xiao, Y.; Chen, Y.; Nie, M.; Zhu, T.; Liu, Z.; Liu, C. Exploring LoRa and Deep Learning-Based Wireless Activity Recognition. *Electronics* **2023**, *12*, 629. [CrossRef]
141. Cui, S.; Joe, I. Collision prediction for a low power wide area network using deep learning methods. *J. Commun. Netw.* **2020**, *22*, 205–214. [CrossRef]
142. Alenezi, M.; Chai, K.K.; Alam, A.S.; Chen, Y.; Jimaa, S. Unsupervised learning clustering and dynamic transmission scheduling for efficient dense LoRaWAN networks. *IEEE Access* **2020**, *8*, 191495–191509. [CrossRef]
143. Li, C.; Guo, H.; Tong, S.; Zeng, X.; Cao, Z.; Zhang, M.; Yan, Q.; Xiao, L.; Wang, J.; Liu, Y. NELoRa: Towards ultra-low SNR LoRa communication with neural-enhanced demodulation. In Proceedings of the 19th ACM Conference on Embedded Networked Sensor Systems, Coimbra, Portuga, 15–17 November 2021; pp. 56–68.
144. Shen, G.; Zhang, J.; Marshall, A.; Peng, L.; Wang, X. Radio frequency fingerprint identification for LoRa using spectrogram and CNN. In Proceedings of the IEEE INFOCOM 2021-IEEE Conference on Computer Communications, Vancouver, BC, Canada, 10–13 May 2021; pp. 1–10.
145. Al-Shawabka, A.; Pietraski, P.; Pattar, S.B.; Restuccia, F.; Melodia, T. DeepLoRa: Fingerprinting LoRa devices at scale through deep learning and data augmentation. In Proceedings of the Twenty-Second International Symposium on Theory, Algorithmic Foundations, and Protocol Design for Mobile Networks and Mobile Computing, Shanghai, China, 26–29 July 2021; ACM: New York, NY, USA, 2021; pp. 251–260.
146. Liu, L.; Yao, Y.; Cao, Z.; Zhang, M. DeepLoRa: Learning accurate path loss model for long distance links in LPWAN. In Proceedings of the IEEE INFOCOM 2021—IEEE Conference on Computer Communications, Vancouver, BC, Canada, 10–13 May 2021; pp. 251–260. [CrossRef]
147. Elkarim, S.I.A.; Elsherbini, M.; Mohammed, O.; Khan, W.U.; Waqar, O.; ElHalawany, B.M. Deep Learning Based Joint Collision Detection and Spreading Factor Allocation in LoRaWAN. In Proceedings of the 2022 IEEE 42nd International Conference on Distributed Computing Systems Workshops (ICDCSW), Bologna, Italy, 10 July 2022; pp. 187–192. [CrossRef]
148. Farhad, A.; Kim, D.H.; Yoon, J.S.; Pyun, J.Y. Deep Learning-Based Channel Adaptive Resource Allocation in LoRaWAN. In Proceedings of the 2022 International Conference on Electronics, Information, and Communication (ICEIC), Jeju, Republic of Korea, 6–9 February 2022; pp. 1–5. [CrossRef]

149. Lee, S.; Lee, J.; Hwang, J.; Choi, J.K. A Novel Deep Learning-Based IoT Device Transmission Interval Management Scheme for Enhanced Scalability in LoRa Networks. *IEEE Wirel. Commun. Lett.* **2021**, *10*, 2538–2542. [CrossRef]
150. Intel Berkeley Research Lab Data. Available online: http://db.csail.mit.edu/labdata/labdata.html (accessed on 19 July 2023).
151. LoRaWAN ns-3 Module. Available online: https://github.com/signetlabdei/lorawan (accessed on 30 May 2023).
152. Fedullo, T.; Morato, A.; Tramarin, F.; Bellagente, P.; Ferrari, P.; Sisinni, E. Adaptive LoRaWAN transmission exploiting reinforcement learning: The industrial case. In Proceedings of the 2021 IEEE International Workshop on Metrology for Industry 4.0 & IoT (MetroInd4. 0&IoT), Rome, Italy, 7–9 June 2021; pp. 671–676.
153. Hamdi, R.; Baccour, E.; Erbad, A.; Qaraqe, M.; Hamdi, M. LoRa-RL: Deep reinforcement learning for resource management in hybrid energy LoRa wireless networks. *IEEE Internet Things J.* **2021**, *9*, 6458–6476. [CrossRef]
154. Carvalho, R.; Al-Tam, F.; Correia, N. Q-Learning ADR Agent for LoRaWAN Optimization. In Proceedings of the 2021 IEEE International Conference on Industry 4.0, Artificial Intelligence, and Communications Technology (IAICT), Bandung, Indonesia, 27–28 July 2021; pp. 104–108. [CrossRef]
155. Tellache, A.; Mekrache, A.; Bradai, A.; Boussaha, R.; Pousset, Y. Deep Reinforcement Learning based Resource Allocation in Dense Sliced LoRaWAN Networks. In Proceedings of the 2022 IEEE International Conference on Consumer Electronics (ICCE), Las Vegas, NV, USA, 7–9 January 2022; pp. 1–6. [CrossRef]
156. Soori, M.; Arezoo, B.; Dastres, R. Artificial intelligence, machine learning and deep learning in advanced robotics, a review. *Cogn. Robot.* **2023**, *3*, 54–70. [CrossRef]
157. Na, S.; Rouček, T.; Ulrich, J.; Pikman, J.; Krajník, T.s.; Lennox, B.; Arvin, F. Federated Reinforcement Learning for Collective Navigation of Robotic Swarms. *IEEE Trans. Cogn. Dev. Syst.* **2023**. [CrossRef]
158. Hellström, H.; da Silva, J.M.B., Jr.; Amiri, M.M.; Chen, M.; Fodor, V.; Poor, H.V.; Fischione, C. Wireless for machine learning: A survey. *Found. Trends® Signal Process.* **2022**, *15*, 290–399. [CrossRef]
159. Nisioti, E. Reinforcement Learning-Based Optimization of Multiple Access in Wireless Networks. Ph.D. Thesis, University of Essex, Colchester, UK , 2021.
160. Bonnefoi, R.; Moy, C.; Palicot, J. Improvement of the LPWAN AMI backhaul's latency thanks to reinforcement learning algorithms. *EURASIP J. Wirel. Commun. Netw.* **2018**, *2018*, 1–18. [CrossRef]
161. Aihara, N.; Adachi, K.; Takyu, O.; Ohta, M.; Fujii, T. Reinforcement Learning Aided Orthogonal Frequency Allocation in LoRaWAN. *IEICE Tech. Rep.* **2019**, *119*, 45–46.
162. Sandoval, R.M.; Garcia-Sanchez, A.J.; Garcia-Haro, J. Optimizing and updating lora communication parameters: A machine learning approach. *IEEE Trans. Netw. Serv. Manag.* **2019**, *16*, 884–895. [CrossRef]
163. Aihara, N.; Adachi, K.; Takyu, O.; Ohta, M.; Fujii, T. Q-learning aided resource allocation and environment recognition in LoRaWAN with CSMA/CA. *IEEE Access* **2019**, *7*, 152126–152137. [CrossRef]
164. Simpy. Event Discrete Simulation for Python. Available online: https://simpy.readthedocs.io/en/latest/ (accessed on 26 May 2023).
165. Bonnefoi, R.; Besson, L.; Manco-Vasquez, J.; Moy, C. Upper-Confidence Bound for Channel Selection in LPWA Networks with Retransmissions. In Proceedings of the 2019 IEEE Wireless Communications and Networking Conference Workshop (WCNCW), Marrakech, Morocco, 15–18 April 2019; pp. 1–7. [CrossRef]
166. Ilahi, I.; Usama, M.; Farooq, M.O.; Janjua, M.U.; Qadir, J. LoRaDRL: Deep Reinforcement Learning Based Adaptive PHY Layer Transmission Parameters Selection for LoRaWAN. In Proceedings of the 2020 IEEE 45th Conference on Local Computer Networks (LCN), Sydney, NSW, Australia, 16–19 November 2020; pp. 457–460. [CrossRef]
167. Yu, Y.; Mroueh, L.; Li, S.; Terré, M. Multi-Agent Q-Learning Algorithm for Dynamic Power and Rate Allocation in LoRa Networks. In Proceedings of the 2020 IEEE 31st Annual International Symposium on Personal, Indoor and Mobile Radio Communications, London, UK, 31 August–3 September 2020; pp. 1–5. [CrossRef]
168. Ilahi, I.; Usama, M.; Farooq, M.O.; Janjua, M.U.; Qadir, J. Intelligent resource allocation in dense lora networks using deep reinforcement learning. *arXiv* **2020**, arXiv:2012.11867.
169. Khalifeh, A.F.; Aldahdouh, K.; Alouneh, S. LoRaWAN energy optimization with security consideration. *Int. Arab J. Inf. Technol.* **2021**, *18*, 476–483. [CrossRef]
170. Ta, D.T.; Khawam, K.; Lahoud, S.; Adjih, C.; Martin, S. LoRa-MAB: Toward an intelligent resource allocation approach for LoRaWAN. In Proceedings of the 2019 IEEE global communications conference (GLOBECOM), Waikoloa, HI, USA, 9–13 December 2019; pp. 1–6.
171. Callebaut, G.; Ottoy, G.; van der Perre, L. Cross-Layer Framework and Optimization for Efficient Use of the Energy Budget of IoT Nodes. In Proceedings of the IEEE Wireless Communications and Networking Conference (WCNC), Marrakesh, Morocco, 15–18 April 2019; pp. 1–6. [CrossRef]
172. Azizi, F.; Teymuri, B.; Aslani, R.; Rasti, M.; Tolvaneny, J.; Nardelli, P.H.J. MIX-MAB: Reinforcement Learning-based Resource Allocation Algorithm for LoRaWAN. In Proceedings of the 2022 IEEE 95th Vehicular Technology Conference: (VTC2022-Spring), Helsinki, Finland, 19–22 June 2022; pp. 1–6. [CrossRef]
173. Zhong, H.; Ning, L.; Wang, J.; Suo, S.; Chen, L. Optimization of LoRa SF Allocation Based on Deep Reinforcement Learning. *Wirel. Commun. Mob. Comput.* **2022**, *2022*. [CrossRef]
174. Chen, M.; Mokdad, L.; Ben-Othman, J.; Fourneau, J.M. Dynamic Parameter Allocation With Reinforcement Learning for LoRaWAN. *IEEE Internet Things J.* **2023**, *10*, 10250–10265. [CrossRef]

175. Chen, M.; Mokdad, L.; Othman, J.B.; Fourneau, J.M. MULANE—A Lightweight Extendable Agent-oriented LoRaWAN Simulator with GUI. In Proceedings of the 2021 IEEE Symposium on Computers and Communications (ISCC), Athens, Greece, 5–8 September 2021, pp. 1–6. [CrossRef]
176. Navas, R.E.; Dandachi, G.; Hadjadj-Aoul, Y.; Maillé, P. Energy-Aware Spreading Factor Selection in LoRaWAN Using Delayed-Feedback Bandits. In Proceedings of the International Federation for Information Processing (IFIP) Networking 2023 Conference (NETWORKING 2023), Barcelona, Spain, 12–15 June 2023.
177. Zhao, G.; Lin, K.; Chapman, D.; Metje, N.; Hao, T. Optimizing energy efficiency of LoRaWAN-based wireless underground sensor networks: A multi-agent reinforcement learning approach. *Internet Things* **2023**, *22*, 100776. [CrossRef]
178. Garrido-Hidalgo, C.; Fürst, J.; Roda-Sanchez, L.; Olivares, T.; Fernández-Caballero, A. Lessons Learned on the Design of a Predictive Agent for LoRaWAN Network Planning. In *Proceedings of the International Conference on Practical Applications of Agents and Multi-Agent Systems, The PAAMS Collection*; PAAMS 2023; Lecture Notes in Computer Science; Springer: Berlin/Heidelberg, Germany, 2023; Volume 13955, pp. 88–99. _8. [CrossRef]
179. Teymuri, B.; Serati, R.; Anagnostopoulos, N.A.; Rasti, M. LP-MAB: Improving the Energy Efficiency of LoRaWAN Using a Reinforcement-Learning-Based Adaptive Configuration Algorithm. *Sensors* **2023**, *23*, 2363. [CrossRef]
180. Ayoub Kamal, M.; Alam, M.M.; Sajak, A.A.B.; Mohd Su'ud, M. Requirements, Deployments, and Challenges of LoRa Technology: A Survey. *Comput. Intell. Neurosci.* **2023**, *2023*. [CrossRef]
181. Farooq, M.O.; Pesch, D. Evaluation of Multi-Gateway LoRaWAN with Different Data Traffic Models. In Proceedings of the IEEE 43rd Conference on Local Computer Networks (LCN), Chicago, IL, USA, 1–4 October 2018; pp. 279–282. [CrossRef]
182. Francisco, S.; Pinho, P.; Luís, M. Improving LoRa Network Simulator for a More Realistic Approach on LoRaWAN. In Proceedings of the 2021 Telecoms Conference (ConfTELE), Leiria, Portugal, 11–12 February 2021; pp. 1–6. 50222.2021.9435570. [CrossRef]
183. Sugianto, S.; Anhar, A.A.; Harwahyu, R.; Sari, R.F. Simulation of Mobile LoRa Gateway for Smart Electricity Meter. In Proceedings of the 2018 5th International Conference on Electrical Engineering, Computer Science and Informatics (EECSI), Malang, Indonesia, 16–18 October 2018; pp. 292–297. [CrossRef]
184. Spinsante, S.; Gioacchini, L.; Scalise, L. A novel experimental-based tool for the design of LoRa networks. In Proceedings of the 2019 II Workshop on Metrology for Industry 4.0 and IoT (MetroInd4.0 & IoT), Naples, Italy, 4–6 June 2019; pp. 317–322. [CrossRef]
185. Borkotoky, S.; Bettstetter, C.; Schilcher, U.; Raffelsberger, C. Allocation of Repetition Redundancy in LoRa. In Proceedings of the European Wireless 2019—25th European Wireless Conference, Aarhus, Denmark, 2–4 May 2019; pp. 1–6.
186. Ferreira, C.M.S.; Oliveira, R.A.R.; Silva, J.S. Low-Energy Smart Cities Network with LoRa and Bluetooth. In Proceedings of the 2019 7th IEEE International Conference on Mobile Cloud Computing, Services, and Engineering (MobileCloud), Newark, CA, USA, 4–9 April 2019; pp. 24–29. [CrossRef]
187. Lee, G.; Youn, J. Group-based Transmission Scheduling Scheme for Building LoRa-based Massive IoT. In Proceedings of the 2020 International Conference on Artificial Intelligence in Information and Communication (ICAIIC), Fukuoka, Japan, 19–21 February 2020; pp. 583–586. [CrossRef]
188. Fam, P.A.; Faye, I. Towards More Energy Efficient MAC protocols for LoRaWAN Networks. In Proceedings of the 2020 XXXIIIrd General Assembly and Scientific Symposium of the International Union of Radio Science, Rome, Italy, 29 August–5 September 2020; pp. 1–4. [CrossRef]
189. Sallum, E.; Pereira, N.; Alves, M.; Santos, M. Performance optimization on LoRa networks through assigning radio parameters. In Proceedings of the 2020 IEEE International Conference on Industrial Technology (ICIT), Buenos Aires, Argentina, 26–28 February 2020; pp. 304–309. [CrossRef]
190. Charles, L.; Isong, B.; Lugayizi, F.; Abu-Mahfouz, A.M. Empirical Analysis of LoRaWAN-based Adaptive Data Rate Algorithms. In Proceedings of the IECON 2021—47th Annual Conference of the IEEE Industrial Electronics Society, Toronto, ON, Canada, 13–16 October 2021; pp. 1–7. [CrossRef]
191. Wongwatthanaroek, K.; Silapunt, R. Transmission Sequencing to Improve LoRaWAN Performance. In Proceedings of the 2021 18th International Joint Conference on Computer Science and Software Engineering (JCSSE), Lampang, Thailand, 30 June–2 July 2021; pp. 1–5. [CrossRef]
192. Alouneh, S.; Khalifeh, A.; Abou-Tair, D.E.D.I.; Aldahdouh, K.; Al-Hawari, F. An Open Source LoRaWAN Simulator Framework for the Internet of Things Applications. In Proceedings of the 2021 8th International Conference on Internet of Things: Systems, Management and Security (IOTSMS), Gandia, Spain, 6–9 December 2021; pp. 1–5. [CrossRef]
193. Helou, G.; Ibrahim, M.; Tawil, R.; Mohanna, Y. Are Existing Analytical Models for LoRa Networks Accurate? In Proceedings of the 2022 4th IEEE Middle East and North Africa COMMunications Conference (MENACOMM), Amman, Jordan, 6–8 December 2022; pp. 24–31. [CrossRef]
194. Faye, I.; Fam, P.A.; Ndiaye, M.L. Energy consumption of IoT devices: An accurate evaluation to better predict battery lifetime. *Radio Sci.* **2022**, *57*, 1–10. [CrossRef]
195. Lehong, C.; Isong, B.; Lugayizi, F.; Abu-Mahfouz, A. A spreading factor congestion status-aware adaptive data rate algorithm. *J. Sens. Actuator Netw.* **2021**, *10*, 70. [CrossRef]
196. Sallum, E.; Pereira, N.; Alves, M.; Santos, M. Improving Quality-of-Service in LoRa Low-Power Wide-Area Networks through Optimized Radio Resource Management. *J. Sens. Actuator Netw.* **2020**, *9*, 10. [CrossRef]

197. Marini, R.; Mikhaylov, K.; Pasolini, G.; Buratti, C. LoRaWanSim: A flexible simulator for LoRaWAN networks. *Sensors* **2021**, *21*, 695. [CrossRef] [PubMed]
198. LoRaWANSim: LoRaWAN Simulator. Available online: https://github.com/kvmikhayl/LoRaWAN_simulator (accessed on 1 May 2023).
199. Magrin, D.; Capuzzo, M.; Zanella, A. A thorough study of LoRaWAN performance under different parameter settings. *IEEE Internet Things J.* **2019**, *7*, 116–127. [CrossRef]
200. Farhad, A.; Kim, D.H.; Subedi, S.; Pyun, J.Y. Enhanced LoRaWAN Adaptive Data Rate for Mobile Internet of Things Devices. *Sensors* **2020**, *20*, 6466. [CrossRef] [PubMed]
201. Farhad, A.; Kim, D.H.; Sthapit, P.; Pyun, J.Y. Interference-Aware Spreading Factor Assignment Scheme for the Massive LoRaWAN Network. In Proceedings of the International Conference on Electronics, Information, and Communication (ICEIC), Auckland, New Zealand, 6 May 2019; pp. 1–2.
202. Farhad, A.; Kim, D.; Pyun, J. Scalability of LoRaWAN in an Urban Environment: A Simulation Study. In Proceedings of the Eleventh International Conference on Ubiquitous and Future Networks (ICUFN), Zagreb, Croatia, 2–5 July 2019; pp. 677–681. [CrossRef]
203. Farhad, A.; Pyun, J.Y. HADR: A Hybrid Adaptive Data Rate in LoRaWAN for Internet of Things. *ICT Express* **2022**, *8*, 283–289. [CrossRef]
204. Aernouts, M.; Berkvens, R.; Van Vlaenderen, K.; Weyn, M. Sigfox and LoRaWAN datasets for fingerprint localization in large urban and rural areas. *Data* **2018**, *3*, 13. [CrossRef]
205. Sigfox and LoRaWAN Datasets. Available online: https://zenodo.org/record/3342253 (accessed on 10 July 2023).
206. Janssen, T.; Berkvens, R.; Weyn, M. Comparing Machine Learning Algorithms for RSS-Based Localization in LPWAN. In *Advances on P2P, Parallel, Grid, Cloud and Internet Computing*; Barolli, L., Hellinckx, P., Natwichai, J., Eds.; Springer: Berlin/Heidelberg, Germany, 2020; pp. 726–735.
207. Anagnostopoulos, G.G.; Kalousis, A. A Reproducible Comparison of RSSI Fingerprinting Localization Methods Using LoRaWAN. In Proceedings of the 2019 16th Workshop on Positioning, Navigation and Communications (WPNC), Bremen, Germany, 23–24 October 2019; pp. 1–6. [CrossRef]
208. Aernouts, M.; BniLam, N.; Berkvens, R.; Weyn, M. TDAoA: A combination of TDoA and AoA localization with LoRaWAN. *Internet Things* **2020**, *11*, 100236. [CrossRef]
209. Li, Y.; Barthelemy, J.; Sun, S.; Perez, P.; Moran, B. Urban Vehicle Localization in Public LoRaWan Network. *IEEE Internet Things J.* **2022**, *9*, 10283–10294. [CrossRef]
210. Janssen, T.; Berkvens, R.; Weyn, M. Benchmarking RSS-based localization algorithms with LoRaWAN. *Internet Things* **2020**, *11*, 100235. [CrossRef]
211. Aqeel, I.; Iorkyase, E.; Zangoti, H.; Tachtatzis, C.; Atkinson, R.; Andonovic, I. LoRaWAN-implemented node localisation based on received signal strength indicator. *IET Wirel. Sens. Syst.* **2022**. [CrossRef]
212. Purohit, J.; Wang, X.; Mao, S.; Sun, X.; Yang, C. Fingerprinting-based Indoor and Outdoor Localization with LoRa and Deep Learning. In Proceedings of the GLOBECOM 2020—2020 IEEE Global Communications Conference, Taipei, Taiwan, 7–11 December 2020; pp. 1–6. [CrossRef]
213. Liu, Y.; Tsang, K.F.; Zhu, H.; Chi, H.R.; Wei, Y.; Wang, H.; Wu, C.K. Efficient load balancing for heterogeneous radio-replication-combined LoRaWAN. *IEEE Trans. Ind. Inform.* **2022**, *18*, 7400–7411. [CrossRef]
214. Goldoni, E.; Prando, L.; Vizziello, A.; Savazzi, P.; Gamba, P. Experimental data set analysis of RSSI-based indoor and outdoor localization in LoRa networks. *Internet Technol. Lett.* **2019**, *2*, e75. [CrossRef]
215. Experimental Datasets of LoRa/LoRaWAN RSSI Measurements. Available online: https://github.com/emanueleg/lora-rssi (accessed on 11 July 2023).
216. Bhatia, L.; Breza, M.; Marfievici, R.; McCann, J.A. LoED: The LoRaWAN at the edge dataset: Dataset. In Proceedings of the Third Workshop on Data: Acquisition To Analysis (ACM, New York, United States), Virtual Event, Japan, 16–19 November 2020; pp. 7–8. [CrossRef]
217. Spadaccino, P.; Crinó, F.G.; Cuomo, F. LoRaWAN Behaviour Analysis through Dataset Traffic Investigation. *Sensors* **2022**, *22*, 2470. [CrossRef] [PubMed]
218. LoED: The LoRaWAN at the Edge Dataset: Dataset. Available online: https://zenodo.org/record/4121430 (accessed on 10 July 2023).
219. Elmaghbub, A.; Hamdaoui, B. LoRa device fingerprinting in the wild: Disclosing RF data-driven fingerprint sensitivity to deployment variability. *IEEE Access* **2021**, *9*, 142893–142909. [CrossRef]
220. Elmaghbub, A.; Hamdaoui, B. Comprehensive RF Dataset Collection and Release: A Deep Learning-Based Device Fingerprinting Use Case. In Proceedings of the 2021 IEEE Globecom Workshops (GC Wkshps), Madrid, Spain, 7–11 December 2021; pp. 1–7. [CrossRef]
221. Release Note: Comprehensive LoRa RF Datasets for Device Fingerprinting Using Deep Learning. Available online: https://research.engr.oregonstate.edu/hamdaoui/sites/research.engr.oregonstate.edu.hamdaoui/files/release_note_rf_dataset_oct2022.pdf (accessed on 11 July 2023).
222. Masek, P.; Stusek, M.; Svertoka, E.; Pospisil, J.; Burget, R.; Lohan, E.S.; Marghescu, I.; Hosek, J.; Ometov, A. Measurements of LoRaWAN technology in urban scenarios: A data descriptor. *Data* **2021**, *6*, 62. [CrossRef]
223. Measurements of LoRaWAN Technology in Urban Scenarios. Available online: https://github.com/BUTResearch/MDPI_Data_Urban_LPWA_Measurement (accessed on 11 July 2023).
224. Svertoka, E.; Rusu-Casandra, A.; Burget, R.; Marghescu, I.; Hosek, J.; Ometov, A. LoRaWAN: Lost for Localization? *IEEE Sens. J.* **2022**, *22*, 23307–23319. [CrossRef]

225. LoRaWAN: Lost for Localization? Available online: https://zenodo.org/record/7236698 (accessed on 11 July 2023).
226. Goldoni, E.; Savazzi, P.; Favalli, L.; Vizziello, A. Correlation between weather and signal strength in Lorawan Networks: An extensive dataset. *Comput. Netw.* **2022**, *202*, 108627. [CrossRef]
227. Lagat, S.J. Detecting Denial of Service Attacks in LoRaWAN. Master's Thesis, St. Pölten University of Applied Sciences, Pölten, Austria, 2022.
228. González-Palacio, M.; Tobón-Vallejo, D.; Sepúlveda-Cano, L.M.; Rúa, S.; Pau, G.; Le, L.B. LoRaWAN Path Loss Measurements in an Urban Scenario including Environmental Effects. *Data* **2022**, *8*, 4. [CrossRef]
229. LoRaWAN Path Loss Dataset. Available online: https://github.com/magonzalezudem/MDPI_LoRaWAN_Dataset_With_Environmental_Variables (accessed on 11 July 2023).
230. Ren, Y.; Liu, L.; Li, C.; Cao, Z.; Chen, S. Is LoRaWAN Really Wide? Fine-grained LoRa Link-level Measurement in An Urban Environment. In Proceedings of the 2022 IEEE 30th International Conference on Network Protocols (ICNP), Lexington, KY, USA, 30 October 2022–2 November 2022; pp. 1–12. [CrossRef]
231. Yao, Y.; Ma, Z.; Cao, Z. LoSee: Long-Range Shared Bike Communication System Based on LoRaWAN Protocol. In Proceedings of the EWSN, Beijing, China, 25–27 February; pp. 407–412.
232. LoSee Dataset. Available online: https://github.com/lilygeek/LoSee_ICNP (accessed on 9 July 2023).
233. Kumar, R.; Mishra, R.; Gupta, H.P. A Federated Learning Approach With Imperfect Labels in LoRa-Based Transportation Systems. *IEEE Trans. Intell. Transp. Syst.* **2023**, 1–9. [CrossRef]
234. Signal Quality Measurement (SQM) Dataset. 2023. Available online: https://dx.doi.org/10.21227/aysz-nq69 (accessed on 10 July 2023).
235. Eldeeb, E.; Alves, H. LoRaWAN-enabled Smart Campus: The Dataset and a People Counter Use Case. *arXiv* **2023**, arXiv:2304.13366.
236. The Smart Campus Dataset. 2023. Available online: https://dx.doi.org/10.21227/xe4q-ax22 (accessed on 10 July 2023).
237. Farhad, A. AI-ERA: Artificial Intelligence-Empowered Resource Allocation for LoRa-Enabled IoT Applications. Available online: https://github.com/afarhad/AI-ERA (accessed on 8 July 2023).
238. LoRaWAN Traffic Analysis Dataset. Available online: https://zenodo.org/record/8090619 (accessed on 9 July 2023).
239. Outdoor LoRa RSSI Dataset. Available online: https://github.com/oliveiraleo/LoRa-RSSI-dataset-outdoor (accessed on 11 July 2023).
240. LoRa RSSI Measurements. Available online: https://github.com/oliveiraleo/RSSignal-LoRa (accessed on 11 July 2023).
241. LoRaWAN Dataset for Spreading Factor. Available online: https://github.com/IbrahimAqeel2023/LoRaWAN-Dataset-Combine-SFs/tree/main (accessed on 11 July 2023).
242. LoRa Time Series Dataset. Available online: https://github.com/akapet00/lora-time-series/tree/master (accessed on 11 July 2023).
243. ns3-AI Module. Available online: https://github.com/hust-diangroup/ns3-ai (accessed on 18 January 2023).
244. Yin, H.; Liu, P.; Liu, K.; Cao, L.; Zhang, L.; Gao, Y.; Hei, X. Ns3-Ai: Fostering Artificial Intelligence Algorithms for Networking Research. In Proceedings of the 2020 Workshop on Ns-3, Gaithersburg, MD, USA, 17–18 June 2020; pp. 57–64. [CrossRef]
245. API for Reinforcement Learning. Available online: https://www.gymlibrary.dev/i (accessed on 18 January 2023).
246. Gawłowicz, P.; Zubow, A. ns-3 meets OpenAI Gym: The Playground for Machine Learning in Networking Research. In Proceedings of the ACM International Conference on Modeling, Analysis and Simulation of Wireless and Mobile Systems (MSWiM), Miami Beach, FL, USA, 25–29 November 2019.
247. Demeslay, C.; Rostaing, P.; Gautier, R. Theoretical Performance of LoRa System in Multi-Path and Interference Channels. *IEEE Internet Things J.* **2022**, *9*, 6830–6843. [CrossRef]
248. Open Neural Network Exchange (ONNX). Available online: https://github.com/onnx/onnx (accessed on 28 December 2022).
249. ORAN: Ns-3 Module for Open Radio Access Network. Available online: https://github.com/usnistgov/ns3-oran/ (accessed on 1 June 2023).
250. Singh, S.K.; Singh, R.; Kumbhani, B. The Evolution of Radio Access Network Towards Open-RAN: Challenges and Opportunities. In Proceedings of the IEEE Wireless Communications and Networking Conference Workshops (WCNCW), Seoul, Republic of Korea, 6–9 April 2020; pp. 1–6. [CrossRef]
251. $NS3-FL$: Federated Learning Simulator. 2020. Available online: https://github.com/eekaireb/ns3-fl-network/tree/ec4276cc861f2ff5afdba23571790b8783d56790 (accessed on 7 May 2023).
252. Ekaireb, E.; Yu, X.; Ergun, K.; Zhao, Q.; Lee, K.; Huzaifa, M.; Rosing, T. ns3-fl: Simulating Federated Learning with ns-3. In Proceedings of the 2022 Workshop on ns-3, Virtual Event, 22–23 June 2022; pp. 97–104.
253. *FLSim*: A Federated Learning Simulator. 2020. Available online: https://github.com/eekaireb/flsim/tree/a81520201905881f88b8940dd6d041ef12a3f1fa (accessed on 31 May 2023).
254. Wang, H.; Kaplan, Z.; Niu, D.; Li, B. Optimizing Federated Learning on Non-IID Data with Reinforcement Learning. In Proceedings of the IEEE INFOCOM 2020—IEEE Conference on Computer Communications, Toronto, ON, Canada, 6–9 July 2020; pp. 1698–1707. [CrossRef]
255. McMahan, B.; Moore, E.; Ramage, D.; Hampson, S.; y Arcas, B.A. Communication-efficient learning of deep networks from decentralized data. In Proceedings of the Artificial Intelligence and Statistics, Fort Lauderdale, FL, USA, 20–22 April 2017; pp. 1273–1282.
256. Chen, Y.; Ning, Y.; Slawski, M.; Rangwala, H. Asynchronous Online Federated Learning for Edge Devices with Non-IID Data. In Proceedings of the 2020 IEEE International Conference on Big Data (Big Data), Atlanta, GA, USA, 10–13 December 2020; pp. 15–24. [CrossRef]

257. LoRaWAN Bandits. Available online: https://github.com/renzoe/LoRaWAN-Bandits/tree/main (accessed on 7 July 2023).
258. Finnegan, J.; Farrell, R.; Brown, S. Analysis and enhancement of the lorawan adaptive data rate scheme. *IEEE Internet Things J.* **2020**, *7*, 7171–7180. [CrossRef]

sensors

Article

LoRaWAN for Vehicular Networking: Field Tests for Vehicle-to-Roadside Communication

Gabriele Di Renzone [1], Stefano Parrino [2], Giacomo Peruzzi [3], Alessandro Pozzebon [3,*] and Lorenzo Vangelista [3]

1 Department of Information Engineering, University of Pisa, 56122 Pisa, Italy; gabriele.direnzone@phd.unipi.it
2 Department of Information Engineering and Mathematics, University of Siena, 53100 Siena, Italy; parrino2@unisi.it
3 Department of Information Engineering, University of Padova, 35131 Padova, Italy; giacomo.peruzzi@unipd.it (G.P.); lorenzo.vangelista@unipd.it (L.V.)
* Correspondence: alessandro.pozzebon@unipd.it

Abstract: Vehicular wireless networks are one of the most valuable tools for monitoring platforms in the automotive domain. At the same time, Internet of Things (IoT) solutions are playing a crucial role in the same framework, allowing users to connect to vehicles in order to gather data related to their working cycle. Such tasks can be accomplished by resorting to either cellular or non-cellular wireless technologies. While the former can ensure low latency but require high running costs, the latter can be employed in quasi-real-time applications but definitely reduce costs. To this end, this paper proposes the results of two measurement campaigns aimed at assessing the performance of the long-range wide-area network (LoRaWAN) protocol when it is exploited as an enabling technology to provide vehicles with connectivity. Performances are evaluated in terms of packet loss (PL) and received signal strength indicator (RSSI) in wireless links. The two testing scenarios consisted of a transmitter installed on a motorbike running on an elliptical track and a receiver placed in the centre of the track, and a transmitter installed on the roof of a car and a receiver placed next to a straight road. Several speeds were tested, and all the spreading factors (SFs) foreseen by the protocol were examined, showing that the Doppler effect has a marginal influence on the receiving performance of the technology, and that, on the whole, performance is not significantly affected by the speed. Such results prove the feasibility of LoRaWAN links for vehicular network purposes.

Keywords: IoT; LoRaWAN; transmission performance analysis; wireless links in motion; vehicular wireless networks

1. Introduction

Vehicular networks represent a paradigm in which the fundamentals of mobile wireless networks are applied to the field of vehicles, meaning that they represent the nodes of wireless sensor networks (WSNs) that are capable of transmitting sundry information (e.g., the state of the vehicles, environmental variables of the cabins, parameters related to loaded goods, etc.). In addition, and thanks to the advent of the Internet of Things (IoT), vehicular networks have evolved into the broader framework of the Internet of Vehicles (IoV), stressing the paradigm in which vehicles equipped with sensors and actuators are given Internet connectivity to fulfil, for instance, remote monitoring and control. More generally, vehicular networks include the architectures of vehicle-to-vehicle (V2V) and vehicle-to-roadside (V2R) communications models; the latter is under investigation in this paper.

Concerning the enabling technologies, they can be distinguished into two broad categories: cellular and non-cellular. The former, like long-term evolution (LTE) or 5G, are nearly mandatory whenever ultra-reliable low-latency communications (URLLC) or massive IoV applications are needed. However, using cellular technologies implicitly implies a notable increment of running costs since data transmission plans must be subscribed to. On the other hand, employing non-cellular technologies, like long range (LoRa) modulation and long-range wide-area network (LoRaWAN) protocol, results in a lower quality of service (QoS), thus limiting the range of application scenarios but at the same time drastically cutting the running costs. Therefore, a trade-off has to be usually reached in the design phase of vehicular network infrastructures.

Thanks to their reliability and robustness, LoRa modulation and the LoRaWAN protocol have been widely exploited in a plethora of distributed monitoring applications, thus becoming an almost de facto standard low-power wide-area network (LPWAN) technology within the IoT framework. Such a result is achieved because of the fact that LoRa is grounded on the chirp spread spectrum (CSS) modulation, which has the capability of demodulating signals to which a notable level of noise was added during transmission. Indeed, LoRa modulation can fully operate below the noise floor level, meaning that signals that have very low signal-to-noise ratio (SNR) (e.g., in the order of magnitude of -20 dB) can be demodulated. This also translates into a maximum receiver sensitivity of -137 dBm, depending on the exploited transmission parameters like the spreading factor (SF), the bandwidth, and the coding rate (CR). Such a feature resulted in the adoption of LoRaWAN in a myriad of application scenarios, and especially in the harsher ones: in non-line-of-sight (NLOS) conditions [1,2], in industrial contexts [3,4], in underground applications [5,6], in marine and offshore environments [7,8], and in search and rescue procedures in remote areas [9,10].

This paper extends a previous work [11], in which the behaviour of LoRa modulation and LoRaWAN protocol was investigated in cases of vehicles in motion. Specifically, a transmitter was installed onboard a motorcycle, and while it was transmitting data, the vehicle was driven along an elliptical track at several testing speeds. At the same time, a LoRaWAN gateway was placed at the centre of the track, and the packet loss (PL) and received signal strength indicators (RSSIs) were measured. Such results are reported herein to be compared with the ones related to a new measurement campaign in which the LoRaWAN transmitter was installed on the roof of a car. Similarly, the transmitter sent data while the car was driven on a straight road at several velocities, and the gateway was placed next to the road at the halfway point. This testing setup allowed us to assess the performance of the transmitting technology from the point of view not only of the PL and RSSI, like the former experiments, but also of the Doppler effect. Indeed, this phenomenon was hardly assessable in the former campaign since the distance between the transmitter and the receiver remained almost constant throughout the tests. Therefore, by means of the results related to the field measurement campaigns, this paper contributes a deeper assessment of the capabilities of the LoRaWAN protocol in enabling V2R networks by analysing metrics related to the receiver side (i.e., PL and RSSI) and by investigating whether the Doppler effect affects such wireless links and, if so, evaluating to what extent. In particular, these results, which at first glimpse appear to be contradictory with respect to the expected theoretical behaviour, allow us to fully understand and demonstrate the actual behaviour and performances of LoRaWAN receivers in terms of frequency tolerance, showing the possibilities that they offer within the field of vehicular networks. Moreover, another goal of this work is to preliminary validate the feasibility of V2R links exploiting LoRa modulation and the LoRaWAN protocol (i.e., two technologies that were not designed and developed for this particular application scenario).

The rest of the paper is drawn up as follows. Section 2 presents related works about the topic, highlights their similarities and discrepancies with this work, and clarifies how this paper advances the current state-of-the-art. Section 3 briefly explains the Doppler effect, while Section 4 presents the experimental setup from the point of view of the hardware and the instruments that were exploited for the field tests, which are shown in Section 5. Then, Section 6 is devoted to proposing the obtained results, their comparison, and their discussion. Finally, Section 8 highlights conclusions and final remarks.

2. Related Works

Vehicular networks can be enabled by the most diverse wireless communication technologies. Of course, the requirements of the application scenario at hand prescribe the most suitable transmission protocol. For instance, if low latency is mandatory, then 5G is by far the most appropriate. On the other hand, if low power consumption and low running costs are at a premium, then LPWAN technologies (e.g., LoRaWAN) are the most suitable choice. However, provided that a plethora of wireless transmitting technologies can do the job, only related works dealing with LoRa modulation and LoRaWAN protocol are herein treated because this work is focused on such solutions. In doing so, a complete and fair comparison can be made, since, for example, from the mere perspective of receiving performances, a communication technology operating in licensed frequency bands (e.g., 5G) generally outperforms another standards operating in industrial, scientific, and medical (ISM) frequency bands (e.g., LoRaWAN).

Providing vehicles with wireless connectivity may be useful in order to perform remote monitoring of their state, achieving onboard diagnostics in a quasi-real-time fashion when LoRaWAN is exploited for data transmission, provided that enough gateways are densely installed, for instance, in a smart city paradigm [12]. Similarly, connected vehicles may be critical in emergency or rescue situations. For instance, road accidents can be prevented by setting up V2V communications: vehicles can autonomously recognise whether other vehicles are present in their blind spot and eventually signal to them in such an event by means of LoRaWAN links [13]. Moreover, in cases in which car crashes occur, vehicles can automatically detect such events and consequently call for rescue and emergency personnel, aiming to avoid casualties [14].

Within the smart cities' domain, vehicular networks play a key role too, for instance, in public transport and shared mobility. Considering a bike-sharing system, although it applies to any other vehicles, one of the most compelling problems to address is the tracking of the vehicles in order to counteract vandalism and thefts. Each bike can be given a Global Positioning System (GPS) module and a wireless transceiver that sends its geographic coordinates on a fixed-time basis. In order to reduce running costs for data transmission, the LoRaWAN protocol can be exploited instead of cellular technologies, as was shown and tested in [15]. Similarly, public transport vehicles (e.g., buses [16,17]) can be tracked by employing a similar infrastructure. However, the localisation of mobile assets like vehicles can be accomplished not only by resorting to GPS but also by analysing fingerprinting of multiple RSSI measurements, provided that multiple gateways are installed [18].

So far, related work has been shown to deal with application use cases. However, the literature also proposes the contribution of analysing the transmission performance of LoRaWAN-enabled vehicular networks, which can be assessed by means of both simulations and field tests, thus more closely resembling the topic of this paper. For instance, in [19], the LoRaWAN protocol was evaluated by means of simulations, accounting for three different sets of transmission parameters (two values of SF and bandwidth were tested) over six different testing setups (simulating several road types and several velocities), and accounting for bit error rate (BER) and SNR as metrics. This study highlighted that transmissions that have a longer symbol time are characterised by worse performance due to the Doppler effect, since, especially at high speed, the coherence time related to the Doppler effect is shorter than the symbol time. However, no field tests were performed. On the other hand, in [20] field tests were accomplished by testing LoRaWAN links between electric vehicle charging stations, which act as gateways, and moving electric vehicles, which act as transmitters, within a smart city environment in Pamplona, Spain. The tests accounted for several NLOS links (due to buildings, trees, cars, etc.) covering the maximum distance of 350 m and proving the feasibility of the communication technology from both the point of view of RSSI and SNR measurements. However, no extensive experiments varying the vehicles speed and the adopted SF were performed. Contrarily, in [21], field tests were performed evaluating the effectiveness of LoRa links for vehicular networks in a medium-sized city. Such tests assessed the PL and RSSI when the number of transmitters (installed onboard as many vehicles), the covered distance, the speed of the vehicles, and the transmission parameters (i.e., SF, CR, and bandwidth) varied. The obtained results showed that the performance of LoRa modulation is affected when the distance and the number of transmitters are scaled up for a given SF, CR, and bandwidth. At the same time, when SF = 9, CR = 4/5, and a bandwidth of 250 kHz is selected, then the best RSSIs were recorded on average. Although such a result is valuable when IoV infrastructures are designed, it should be noted that the LoRaWAN protocol allows for the exploitation of a 125 kHz bandwidth for uplinks (at least in Europe), and this is the reason why we did not test other values for such a parameter. Also, [22] performed field tests setting up an architecture in which a LoRaWAN transmitter was installed onboard a car and several gateways were placed on the road. Concerning the PL, it was found out that it proportionally increased with the car speed, still proving the feasibility of wireless technology for such an application scenario.

Simulations aimed at studying the LoRa channel for vehicular networks, as well as field tests, were accomplished in [23], whose results highlighted that exploiting lower SFs helps in making LoRa links more robust towards the Doppler effect. This is reasonable since symbol time becomes shorter for lower SFs, and at a given speed, the coherence time will be more likely to be longer than the symbol time. This condition became more evident in V2V links whenever the two endpoints were in motion. However, [23] only tested the minimum and the maximum SF, thus providing results for the two extrema but missing a proper analysis for all the SFs in between, as was performed in this paper. On the other hand, in [24] only simulations were performed and accounted for a workspace of 1 km^2 and 2500 moving nodes at a speed up to 90 km/h. The relative results showed that performance, in terms of PL, became worse when the number of transmitters increased, as well as when the speed and the payload length increased. But, on the whole, the LoRaWAN protocol proved to be suitable for the application scenario, but no field tests were performed. Similarly, by resorting to simulations, [25] devised an algorithm implementing an alternative adaptive data rate (ADR) scheme to be employed in LoRaWAN-enabled vehicular networks, whose aim was twofold: enhancing performance and reducing power consumption by limiting retransmissions in case of communication breakdown. But, once again, no field tests were performed. Similarly, [26] proposed an alternative version of ADR, pursuing the same goals and obtaining similar results. Another contribution supporting the thesis that better performance can be achieved with lower SFs is [27], where simulations and field tests were performed by testing mobile gateways rather than transmitters. Once again, the authors' claims were supported by the theory standing behind the Doppler effect and, especially, the relation between the coherence time as varying with speed and the symbol time as primarily varying with the SF for a given payload length. The same authors continued investigating the problem in [28] by setting up several measurement campaigns; one of those resembled one in this paper. Indeed, from this point of view, [28] turned out to be the most similar related work with respect to this paper, although in [28], gateways played the role of moving agents while we exploited moving transmitters. But, at least theoretically, this can be considered as a minor diversity. From the perspective of the obtained results, similarities arose. Despite the viability of a LoRaWAN infrastructure for vehicular networks being fully proven, a performance degradation occurred for high speeds and high SFs. From this, although it is a niche application scenario, even boats were shown to form vehicular networks enabled by LoRa modulation, as in [29] for fluvial contexts. Such a study proved the feasibility of LoRa links in these frameworks, where a transmitter was installed onboard a boat sailing on a river and several gateways were placed on the banks of the river. The relative results showed that an average PL of 22% was experienced. However, apart from the fact that such a measurement campaign was structured in a different way with respect to the one in this paper, the application scenario of [29] is harsh in itself since wireless links are taking place above a water basin, thus introducing an additional variable hindering the wireless channel, as was also proven in a previous work [30].

The literature proposes a plethora of work dealing with LoRaWAN-enabled vehicular networks. The bulk of it is focused more on the application scenario and the monitoring infrastructure as the big picture than on the analysis of transmission performance. Some contributions belonging to the former case were described above to provide readers with a broader perspective on the topic. On the other hand, fewer studies belonging to the latter case can be retrieved, and the most valuable and significant were introduced above. Although the results obtained by such related works are all meaningful and beneficial, to the best of our knowledge, we found a lack in the state-of-the-art concerning a comparative performance analysis like the one we are presenting, especially tackling two use cases (i.e., vehicles travelling on tracks and vehicles travelling on roads) that are of typical interest in real-world applications whenever V2R networks are needed.

3. Doppler Shift

LoRa modulation directly derives from CSS modulation, entailing high sensitivity at the receiver side as well as robustness towards multipath interference and fading. However, as the relative transceivers may traverse varying environments at given velocities, the Doppler effect occurs, potentially influencing the performance of LoRa links. Such a phenomenon is observed whenever there is relative motion between a signal source and an observer, where, in this case, they respectively translate into a transmitter and a receiver. In the context of LoRa communication, this effect manifests as a frequency shift in the received signal due to the motion of either the transmitter or the receiver. Understanding the impact of the Doppler effect is pivotal to ensuring reliable LoRa links in all contexts in which devices are in motion (e.g., vehicular networks, asset tracking, mobile sensor networks, etc.). This section delves into the intricacies of the Doppler effect occurring for LoRa links by examining how frequency shifts take place and affect signal quality, thus shedding light on the challenges and potential solutions for maintaining reliable connectivity where mobile transceivers are concerned. LoRa packets are composed of modulated chirps (i.e., symbols) with a given SF quantifying the number of bits per symbol over a given bandwidth BW. This implicitly implies that SF and BW do affect the symbol duration t_s as

$$t_s = \frac{BW}{2^{SF}}. \tag{1}$$

Generally, whenever a transmitter and a receiver move while they are communicating, the Doppler effect comes into play. In particular, and without losing generality, let us consider a moving LoRa transmitter at speed v_{tx} and a LoRa receiver (i.e., the gateway) standing still. In addition, if the gateway is not on the transmitter trajectory, then the gateway observes the transmitter moving at its radial velocity $v_{rad} = v_{tx}cos(\theta)$, where θ is the angle between the transmitter's forward velocity (i.e., v_{tx}) and the line of sight from the transmitter to the gateway. Thus, if the transmitter sends a signal with a carrier frequency f_0, then the receiver detects the frequency f according to

$$f = \frac{c}{c \pm v_{rad}} f_0, \tag{2}$$

where v_{rad} is subtracted when the transmitter becomes closer to the gateway, while it is summed otherwise.

Alternatively, this phenomenon can be described by means of the frequency shift Δf (i.e., the Doppler shift)

$$\Delta f = f - f_0 = \left[\frac{c}{c \pm v_{rad}} - 1\right] f_0. \tag{3}$$

Moreover, in a digital communication system (e.g., LoRaWAN networks), the channel response may change over time. However, a timespan during which the channel impulse response can be considered to be invariant can be defined. It is named as coherence time, T_C, and it is related to Doppler shift since it is its dual in the time domain, in other words,

$$T_C = \frac{1}{\Delta f}. \tag{4}$$

Therefore, in order to avoid distortion at the gateway side as a result of the amplitude and phase changes entailed by the alteration of the channel response that occurs due to the Doppler effect, the symbol duration t_s should be smaller than the coherence time T_C. We are going to comment on this in Section 5.2.

4. Experimental Setup

Both measurement campaigns share the same experimental setup from the point of view of the transmitter and the receiver. The transmitter included a LoRa transceiver (i.e., the RFM95 from HopeRF) driven by a microcontroller (i.e., the ATtiny84-A from Microchip). Such components were powered exploiting a Panasonic NCR18650B battery proving 3.7 V and 3400 mAh. However, two different antennas were adopted due to constraints related to the vehicles involved in the two testing scenarios. The tests performed in a velodrome and on a straight road were carried out using, respectively, a motorcycle and a car. The reasons motivating this choice will be provided in the next section. For the tests carried out in the velodrome, a 2 dBi $\lambda/8$ omnidirectional whip antenna was exploited, while for the tests on the straight road, a 2 dBi $\lambda/2$ omnidirectional whip antenna was adopted. Despite being different sizes, they provided the same gain, thus reducing the number of involved variables. Unfortunately, using the same transmitting antenna for both measurement campaigns was unfeasible because the $\lambda/8$ antenna was placed inside the plastic tail trunk of the motorcycle, which was not big enough to contain the $\lambda/2$ antenna. On the other hand, exploiting the $\lambda/8$ antenna from the car cabin was not an optimal solution since, contrary to the plastic tail trunk, the car chassis inevitably acts as a source of loss (which cannot be ascribed to movement) within the wireless path loss. Instead, the $\lambda/2$ antenna had a permanent magnet at its bottom that was exploited to attach the antenna to the car roof.

The receiver was a LoRaWAN gateway, and included a LoRaWAN concentrator (i.e., the RAK831 from RAKWireless) driven by a Raspberry Pi 3 model B. The concentrator was connected to a 10 dBi omnidirectional antenna, while the gateway was mains-powered via an inverter drawing power from a 12 V 80 Ah lead acid battery.

Several speeds were tested in both scenarios, and for each velocity, many LoRaWAN packets were broadcast by exploiting the following transmission parameters: 6 SFs ranging from 7 to 12, CR of 4/5, bandwidth of 125 kHz, payload of 10 B, and transmitter power output of 14 dBm. Such a configuration was selected to reproduce a worst-case scenario; indeed, lower CRs theoretically improve the ability to correctly restore data at the receiver side. Concerning the number of transmitted packets, two approaches were followed. In the velodrome, 200 packets were sent for each speed and for each SF. Conversely, on the straight road, it was not feasible to fix a predetermined number of packets since the time that the car spent travelling on the straight road decreased as the speed increased, meaning that the higher the speed, the fewer the transmittable packets on the straight road. In addition, owing to the frequency hopping scheme established by the LoRaWAN protocol, 8 different channels belonging to the 863–870 MHz ISM band (i.e., 867.1 MHz, 867.3 MHz, 867.5 MHz, 867.7 MHz, 867.9 MHz, 868.1 MHz, 868.3 MHz, and 868.5 MHz) were exploited for the transmissions in both measurement campaigns.

The gateway was in charge of receiving, demodulating, and forwarding the incoming packet towards a remote network server by making use of the message queue telemetry transport (MQTT) protocol. To this end, the gateway was provided with a 4G dongle, proving Internet connectivity. Moreover, upon receiving, the gateway also measured the RSSIs associated with each of the correctly demodulated packets.

5. Field Tests

As anticipated, LoRaWAN links' feasibility in motion was validated in a velodrome to test cases in which the transmitter orbits around the gateway and on a straight road to analyse cases in which the transmitter passes by the gateway. As was previously stated, a motorbike was exploited in the velodrome, while a car was used on the straight road. Although employing a car would have been optimal because its cruise control could have been exploited to maintain a stable speed, the shape and radius of the velodrome would have significantly limited the maximum reachable speed. On the other hand, this constraint was not present for the tests on the straight road.

5.1. Velodrome Measurement Campaign

The velodrome is an elliptical track located in Siena, Italy, whose axes have dimensions of 135 m and 70 m (see Figure 1). The gateway was placed in the centre of the ellipse in order to limit the variation in the distance between it and the transceiver, consequently reducing the effect of path loss. Moreover, since the transmitter and gateway antennas were omnidirectional and because the transmitter revolved around the gateway, maintaining an almost constant distance, the Doppler effect could be considered negligible. The motorbike was driven along the track at different velocities while the transmitter was broadcasting packets sweeping SFs from 7 to 12 for each of the tested speeds. This measurement campaign accounted for six test sets, during which the motorbike was kept at constant velocities (i.e., 20 km/h, 30 km/h, 40 km/h, 50 km/h, and 60 km/h) for the former five, while during the last set (marked as 'Max'), the motorbike was driven at a variable speed spanning 60 km/h to 90 km/h. Keeping a constant speed greater than 60 km/h for the entire track was not feasible for safety reasons. In so doing, the effect of movement on both RSSI and PL can be assessed in all those cases in which the distance separating the transmitter and the gateway remains almost constant over time by analysing speed and SF.

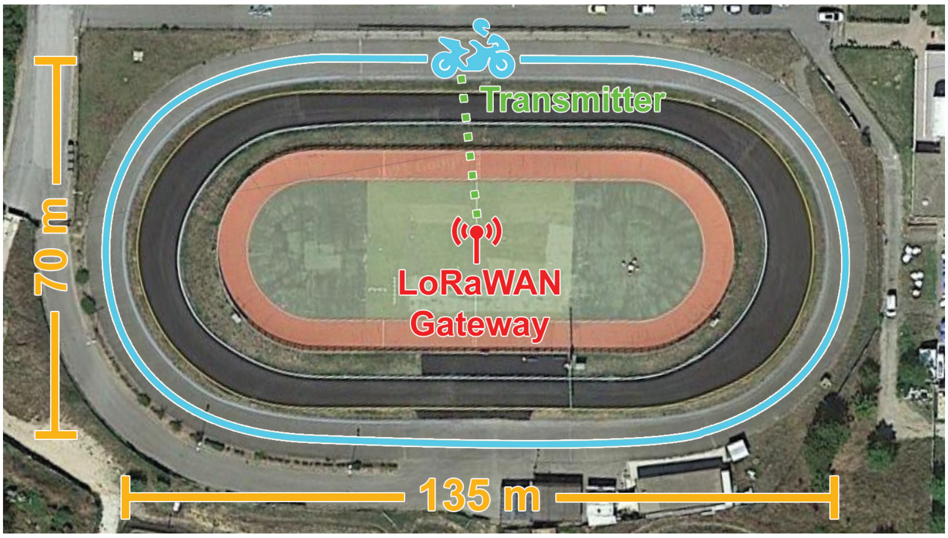

Figure 1. Aerial view of the elliptical track on which the velodrome measurement campaign was conducted (picture taken from [11]).

5.2. Straight Road Measurement Campaign

The straight road test site is located near Siena, Italy, in the locality of Le Corneta. It is a 1200 m long straight road on which no traffic was experienced during the tests since it is a secondary road (see Figure 2). The gateway was placed halfway (i.e., at 600 m from both of the endpoints of the road) in a lateral position at 6 m from the road. In such settings, the Doppler effect can be perceived on the gateway side. Indeed, this measurement campaign had a twofold scope by accounting for several speeds and all of the SFs: on the one hand, we assessed the Doppler effect on PL considering both the leg in which the transmitter approaches the gateway, and the one in which it leaves the gateway; on the other hand, we assessed the effect of movement on RSSI whenever the distance separating the transmitter and the gateway varied over time.

Tests were carried out by travelling the straight road several times in the same direction. The car was driven at 50 km/h, 70 km/h, 90 km/h, and 110 km/h by setting its cruise control. Each speed was tested twice by travelling the straight road for as long as all of the SFs were tested. Prior to the tests involving movement, some RSSI measurements were taken by placing the transmitter at fixed points in order to assess whether movement can significantly affect RSSI. Such spots were at the starting point and, in turn, at 300 m, 600 m, 900 m, and 1200 m from the starting point (therefore, the last spot corresponded with the finishing point of the road), and at each location, 100 packets per SF were broadcast by the transmitter.

Figure 2. Aerial view of the road on which the straight road measurement campaign was conducted.

Doppler Effect Analysis for the Straight Road Measurement Campaign

As discussed in Section 5.1, the Doppler effect can be considered negligible in the case of the velodrome. Conversely, it has to be taken into account in the case of the straight road. Therefore, in order to forecast the expected behaviour of LoRa technology in this context and the expected capability of correctly receiving packets in the presence of the Doppler effect for different radio settings, the relation between coherence time T_C and speed was calculated. Then, this was compared with the actual symbol duration t_s for a LoRaWAN transmission, taking into account the different SFs, which impact the actual t_s, as discussed in Section 3.

In particular, in Figure 3, the T_C trend is compared with the t_s achievable for the six SFs, while Figure 4 focuses explicitly on the six speeds at which the tests were carried out. Concerning this last figure, the relative speed between the transmitter and the gateway has to be taken into account. While this speed can be considered constant when the transmitter is far from the gateway, it rapidly decreases to 0 km/h and then increases again when the transmitter transmits in front of the gateway. At this point, the car switches from approaching to leaving the gateway; this is the reason for the peak of the coherence time in the middle of the path.

Looking at the two figures, one can see that, resorting only to the theory, successful transmission is expected to be possible when in motion only for SFs from 7 to 9 and for the two lowest speeds (i.e., at 50 km/h and 70 km/h). At 90 km/h, the transmission is expected to also become problematic for SF 9, while at 110 km/h, the transmission at this SF appears to be totally unfeasible.

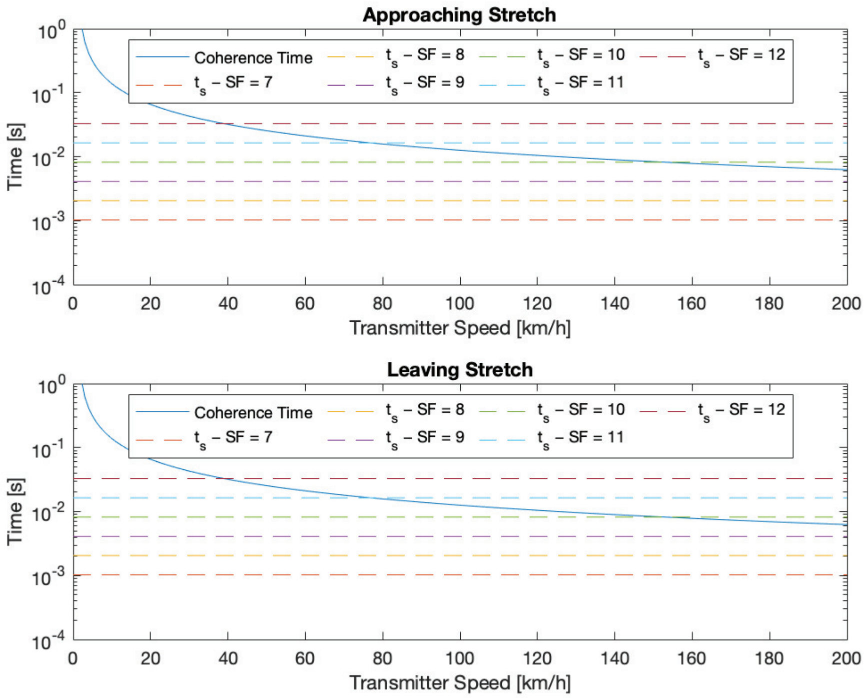

Figure 3. Comparison between symbol time t_s for each SF and coherence time T_C in function of the speed.

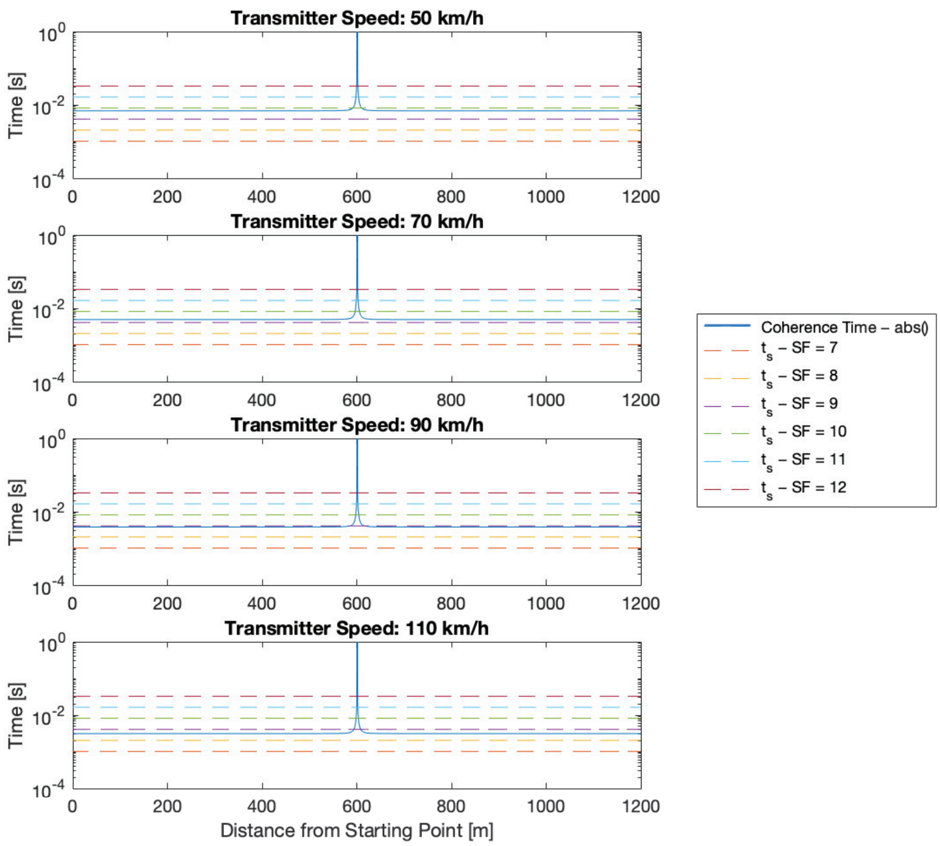

Figure 4. Comparison between symbol time t_s for each SF and coherence time T_C for each tested speed.

6. Results

6.1. Velodrome Measurement Campaign

The test results related to the velodrome measurement campaign are reported in Figures 5 and 6. First of all, the robustness of the LoRa modulation, and therefore of the LoRaWAN protocol, was confirmed. This hints at the potential feasibility of a vehicular network relying on such technologies, provided that low latency and high QoS are not requisites of utmost importance for the application at hand, since it is well known that the LoRaWAN protocol is lacking in these regards. The analysis of RSSIs highlighted that no macroscopic correlation with speed can be observed. However, RSSIs varied throughout the tests, although they did not hinder the wireless link. Particularly, the mean RSSIs spanned from −59 dBm to −72 dBm, meaning that a considerable link margin was experienced. Indeed, the LoRaWAN gateway had a sensitivity ranging from −137 dBm at SF = 12 to −126 dBm at SF = 7 (which are common values for many other commercial LoRaWAN gateways). Moreover, the measured RSSI excursion of 13 dB is almost a tenth of the receiver sensitivity. Finally, the technology's robustness was also validated by the limited values of RSSI standard deviations, which were approximately constant during the tests forming the measurement campaign.

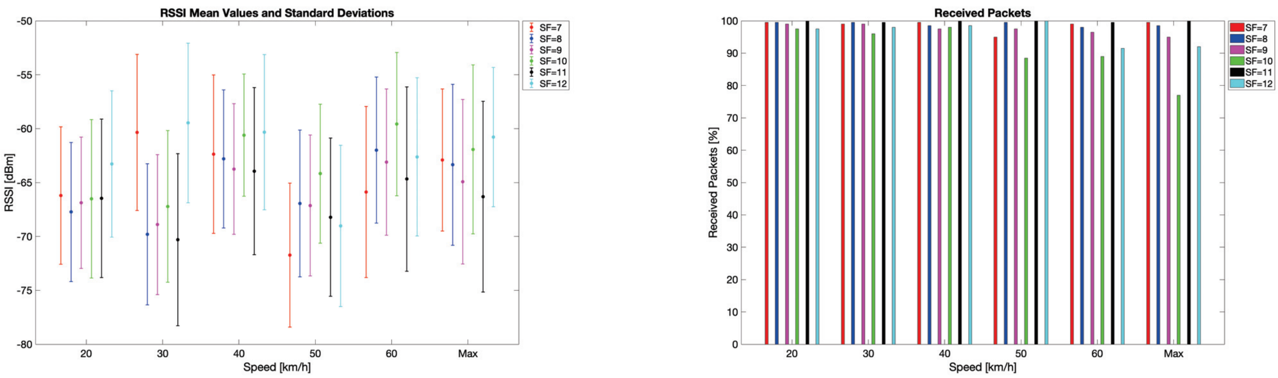

(**a**) (**b**)

Figure 5. Test results related to the velodrome measurement campaign's quantitative analysis: (**a**) RSSI and (**b**) received packets (picture taken from [11]).

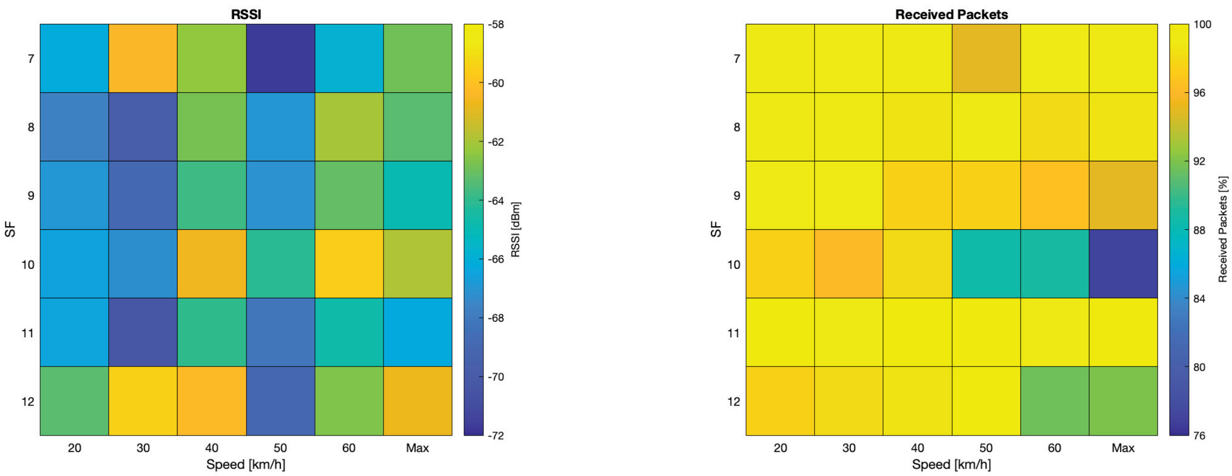

(**a**) (**b**)

Figure 6. Test results related to the velodrome measurement campaign's qualitative analysis: (**a**) RSSI and (**b**) received packets (picture taken from [11]).

The percentage of received packets was almost always 100% apart from a few minima: 97.5% at 20 km/h and 40 km/h, 96.0% at 30 km/h, 88.5% at 50 km/h, and 89.0% at 60 km/h; the overall minimum (i.e., 77.0%) was recorded during the 'Max' test set. Nonetheless, such results are far from being unexpected since a PL spanning from 20% to 30% should be taken into account in applications involving radio technologies operating in unlicensed frequencies (e.g., LoRa).

Finally, the test results can be analysed from the point of view of the SF. According to the tests, a worst-case scenario can be identified for SF = 10 because transmission performances marginally deteriorate as speed increases. However, owing to the limited number of transmitted packets (i.e., 200 per SF per speed), such a result can likely be ascribed to statistical fluctuations rather than to movement.

6.2. Straight Road Measurement Campaign

The test results related to the straight road measurement campaign are shown in Figures 7 and 8. Similarly to the other set of tests, the robustness and feasibility of LoRa modulation in this application scenario were proven. However, such viability may fail if the specific application scenario cannot tolerate high latency and low QoS because the LoRaWAN protocol implicitly entails such characteristics. Since the distance covered by the uplinks varied throughout the tests, the relative results are analysed by considering two stretches: the approaching one, meaning that the transmitter was getting closer to the gateway, and the leaving one, during which it was getting further away. This distinction helps in assessing probable effects due to Doppler.

Firstly, let us take into account the performance from the perspective of the received packets. On the whole, Figure 7a shows that, apart from a few cases in which the received packets ranged from 84% to 88%, the bulk of the tested settings recorded a percentage of received packets ranging from 90% to 100%, underlining the robustness of LoRaWAN for this application. Specifically, for speeds greater than or equal to 90 km/h, the PL increased, as was suggested in the literature. However, contrary to related works, adopting higher SFs ensured better reception capabilities, although the symbol time increased. This is justified by the fact that LoRa modulation is intrinsically robust against the Doppler effect (see Section 5.2), thus making it eligible for V2R communications. This is also confirmed by analysing Figure 7b,c: if compared, no significant discrepancies arise between what concerns the approaching and the leaving stretches and what concerns the percentage of received packets; moreover, these results are consistent with the results of Figure 7a, meaning that the transmission architecture worked similarly in both stretches.

Secondly, let us take into account the performance from the point of view of the RSSI measurements. Such results are displayed for each of the tested SFs, and they are compared with the set of RSSI measurements performed by keeping the transmitter still at the fixed points, thus allowing us to be able to assess the probable effects of movement and of the Doppler effect. In each of the charts of Figure 8, such measurements are plotted with a solid green line, while the RSSIs related to the tests accounting for movement are represented with dashed and dotted lines, with the colour representing the tested speed. Since the wireless links had variable distances, evaluating the RSSIs by looking for the best values is not meaningful (i.e., it is trivial that the best RSSIs were observed at halfway, close to where the gateway was installed). Conversely, the aim of this test is to spot whether, for a given SF, movement played a significant detrimental role, and to evaluate whether the RSSIs significantly varied for each of the SFs. Tests related to SF = 7 (see Figure 8a) showed that RSSIs varied, regardless of the speed, with respect to those recorded with no motion. Specifically, some of them were slightly worse with respect to those at 0 km/h, while some others were slightly better. This indicates that no significant variations can be perceived, and that a minimal link margin was experienced since the receiver sensitivity at SF = 7 is −126 dBm (which is the worst achievable for the tested transmitting parameters). The same conclusion can be drawn for the measurements performed at SFs of 8, 9, and 11. But, for those SFs, better receiver sensitivity was available, meaning that larger link margins were present. On the other hand, measurements related to SFs of 10 and 12 exhibited a slightly different behaviour, since the RSSIs recorded when the transmitter was still were higher for some tested spots with respect to those of the other SFs. However, such an outcome can be due to exogenous factors due to environmental conditions that cannot be controlled since tests were performed outside a laboratory, and it does not imply that movement played a significant beneficial role in the wireless links. Therefore, on the whole and on the face of such tests, it can be concluded that movement and the Doppler effect had a limited effect on RSSIs and a marginal effect on PL when low SFs were exploited and high speeds were tested. We are aware that several speeds could have been tested, but testing lower speeds would have modelled better-case scenarios, while testing higher ones would have been dangerous owing to the morphology of the straight road. Moreover, and at least in Italy, the maximum speed limit is 130 km/h, which can be achieved in motorways only.

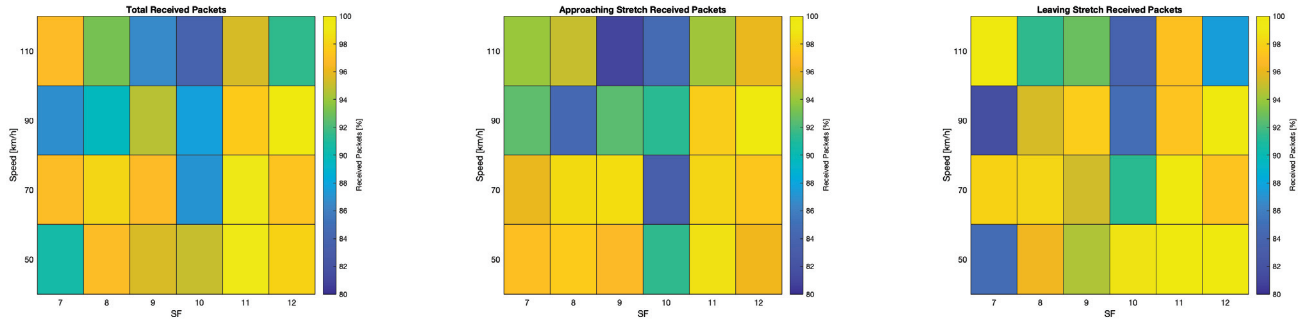

(**a**) (**b**) (**c**)

Figure 7. Test results related to the straight road measurement campaign's qualitative analysis of the received packets: (**a**) total; (**b**) approaching stretch; (**c**) leaving stretch.

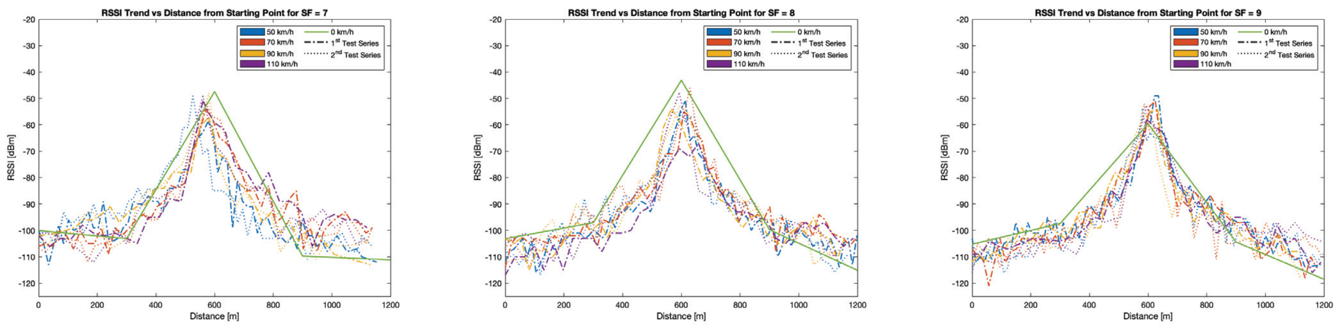

(**a**) (**b**) (**c**)

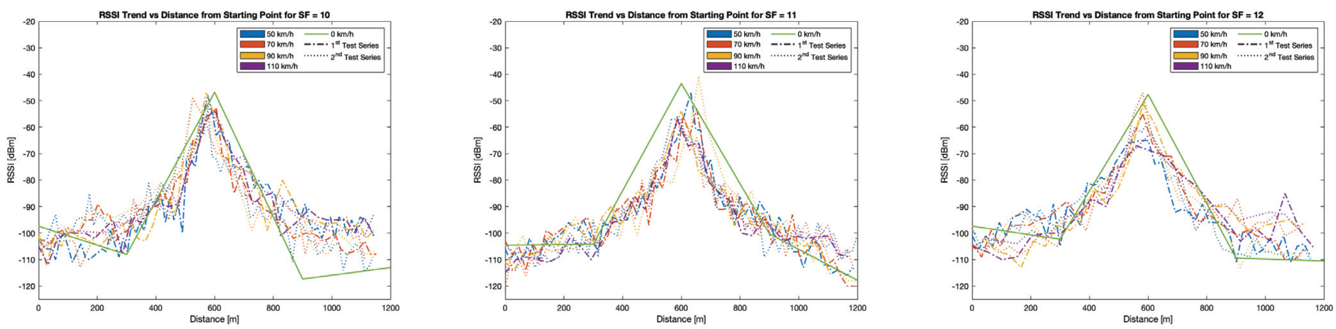

(**d**) (**e**) (**f**)

Figure 8. Test results related to the straight road measurement campaign's quantitative analysis of the RSSIs: (**a**) SF = 7; (**b**) SF = 8; (**c**) SF = 9; (**d**) SF = 10; (**e**) SF = 11; (**f**) SF = 12.

7. Discussion

The most promising result that emerged from the two measurement campaigns is that LoRa modulation and the LoRaWAN protocol can potentially enable vehicular networks, at least for the V2R paradigm. Indeed, PL, and in general performance decrease, was in line with the intrinsic behaviour of the technology, where operating in ISM bands is inevitably subject to interference and noise. Thus, if the application scenario allows a minimal amount of data loss along with a negligible latency, LoRaWAN can be a valuable alternative.

During the first measurement campaign, a quantitative analysis of the RSSI was possible since the length of the wireless path was almost constant throughout all the experiments. Conversely, RSSIs of the second measurement campaign could only be examined from a qualitative point of view since the path length varied over the trials. Indeed, just a comparison with the RSSI measurements performed with the transmitter kept still could be made. However, tests on RSSIs showed, on the one hand, that minimal variation was experienced when the speed changed, which did not mind the effectiveness of LoRa owing to its robustness, and on the other hand, that such measurements marginally varied for a given spot when the transmitter was moved with respect to when it was still. Both of these outcomes were independent of the SF, since for the velocity at hand, minor changes were experienced for different SFs. Of course, a deep analysis of link margin is superfluous and not pertinent because, in both measurement campaigns, the path length was particularly limited: in the first one, from a minimum of 35.0 m to a maximum of 67.5 m, and in the second one, from 6 m to 600 m.

The other metric under investigation was the PL or, alternatively, the percentage of received packets. For the measurement campaign conducted in the velodrome, the PL was almost always negligible, apart from five testing setups. For all of the other settings, the percentage of received packets ranged from 96% to 100%. A similar behaviour was observed also in the tests held on the straight road, although the number of testing setups registering a percentage of received packets below 96% was more consistent, but in the worst case, 84% of transmitted packets were received, meaning that the technology can be considered robust nonetheless since it performed according to what other related works dealing with LoRa links in harsh contexts reported. Moreover, for the latter campaign, the PL was analysed by considering the approaching and leaving stretches in addition to the overall performance. This was performed in order to assess probable detrimental effects due to the Doppler effect. However, since the results related to the three analyses (i.e., overall, the approaching stretch, and the leaving stretch) were similar, it can be concluded that the Doppler effect had a limited, almost negligible effect. Nevertheless, an additional fact must also be stressed. Since a gateway was exploited as the receiver rather than a spectrum analyser, it is reasonable that many of the lost packets could have been received, but they could have been corrupted, thus being marked as lost by the gateway due to its inability to demodulate them. Contrarily, if a spectrum analyser was exploited, then the PL would be far lower. This would have been a best-case scenario apart from the fact that, in real-life applications, gateways are almost always employed in place of spectrum analysers, and that the ability to retrieve information coded within the packet payloads is what is actually needed to consider the application satisfactory and effective. The usage of a spectrum analyser would have been beneficial to assess whether some potential interference was present during experiments. However, since the tests for both measurement campaigns took place over a limited timespan (i.e., a few hours), if some interference affected the communication channel, thus acting as background noise, this would have been experienced over all of the RSSI measurements, hence making it negligible when such results are analysed from a relative perspective, as was proposed above. In light of this, we opted for the usage of just a gateway, thus testing at the same time a worst-case scenario (also because the maximum CR was selected) and a real-life application scenario.

Concerning the Doppler effect, from Figures 3 and 4, one can see that the coherence time related to the Doppler effect is shorter than the symbol time, but the performance in terms of packet delivery does not degrade. This seems like a surprising result, but, in fact, it is not. The explanation of this result comes from the fact that Semtech's LoRa receivers that are employed in the experiments can cope with a considerable Doppler shift.

The technical possibility of a LoRaWAN receiver of coping with Doppler shifts of up to $BW/4$ is confirmed in the scientific literature. Quoting from [31]:

the LoRa receiver studied in this work can only estimate a CFO $\Delta f_c \in [-(B/4),(B/4)]$,

where CFO stands for Carrier Frequency Offset (equivalent in this context to the Doppler shift) and B denotes the bandwidth BW.

In Section 2.1 of [32], an application note covering Semtech's components used in the experiments, it is first of all confirmed that the maximum allowed Doppler shift is 1/4 of the bandwidth. A budget of the residual allowed frequency shift resulting after the consideration of an error of 5 ppm for the gateway and an error of 25 ppm for the transmitter is provided. In the case of $BW = 125$ kHz, the remaining frequency drift budget allowed is 5.21 kHz; considering a centre frequency for the communication of 868 MHz, a Doppler shift of 5.21 kHz corresponds to a speed of 6482.52 km/h or 5.3 Mach. Of course, with a larger bandwidth, the limit increases. The tolerance of LoRa receivers to Doppler shifts is also confirmed by other related works in the literature, whose results support those of this paper, along with those of [20–23,26–28], which were extensively analysed in Section 2. For instance, [33] performed tests investigating the performance of off-the-shelf LoRa transceivers in real-life contexts (that match with the measurement campaigns of Section 5), finding comparable results with the ones of this paper, although only the maximum SF was tested. In the same vein, [34] also performed similar experiments with respect to those of Section 5.2 and obtained analogous results, although a different bandwidth was exploited for the uplinks. Therefore, it is reasonable to deem that the minimal receiving performance decay experienced in the straight road measurement campaign, where the RSSIs related to the moving transmitter were compared with the ones of the still transmitter, can be ascribed to other detrimental effects (e.g., multipath fading) rather than to the Doppler effect that typically hinder wireless communications enabled by radio frequency technologies like LoRa modulation. Moreover, such an effect becomes more prominent whenever unlicensed frequency bands, like ISM bands, are exploited.

We can conclude then that, thanks to the possibility of LoRaWAN receivers, even those that are commercially available such as those that have been used in the experiments, to tolerate high Doppler shifts, the results of our experiments are perfectly justified. However, these promising results do not compensate for the intrinsic limitations of LoRa modulation and the LoRaWAN protocol when applied to the context of vehicular networks. For instance, this may not be the best alternative when the application scenario requires URLLC or massive IoV, since the LoRaWAN protocol implicitly entails a non-negligible latency and a low QoS. In such cases, cellular technologies (e.g., 5G) are definitely better suited. But this also implies a rise in running costs since, conversely to LoRaWAN, data transmission plans must be subscribed to. Thus, during the design phase of the network enabling the application, a thorough trade-off has to be generally achieved bearing in mind all of the use case requirements.

8. Conclusions

This paper aimed at assessing the feasibility, effectiveness, robustness, and reliability of the LoRa modulation and of the LoRaWAN protocol when exploited for enabling vehicular networks, specifically for V2R paradigms. To this aim, two measurement campaigns were conducted: the former took place in a velodrome, by putting a LoRaWAN transmitter inside the tail trunk of a motorcycle and by installing a LoRaWAN gateway in the centre of the velodrome; the latter was performed on a straight road, by placing a transmitter in a car with the antenna on the car roof and by installing the gateway at the halfway point in a lateral position with respect to the road. Several speeds were examined, and all of the SFs were tested in order to validate as many configurations as possible. Moreover, during the second set of tests, the Doppler effect was evaluated. The test results proved the overall feasibility of the transmission system for the specific application scenario, highlighting a degradation in reception performance in terms of PL and RSSI as the speed increased that, however, did not undermine the effectiveness of the wireless communication technology. Moreover, during the latter testing campaign, it was found that the Doppler effect played a marginal detrimental role, thus remarking the robustness of the LoRa modulation in terms of the frequency tolerance of the receivers.

Future work will address the current limitations of this study. Tests accounting for multiple moving transmitters will be conducted, as well as those accounting for multiple gateways. This can potentially pave the way for further tests within a smart city scenario, in which a multitude of attenuation sources are present (e.g., buildings, trees, other vehicles, etc.). In so doing, a broader perspective could be obtained, thus extensively validating the results obtained so far. Another limitation of the proposed approach is that the aforementioned presented and discussed results derive from measurement campaigns conducted in a velodrome and on a straight road. Although such results can be fully exploited to provide readers and practitioners in the field with useful insight about the topic, they could not be potentially extended to further contexts, at least as a first instance, unless additional efforts or assumptions are made. Nonetheless, future work addressing multiple moving transmitters and multiple gateways will shed light on this.

Author Contributions: Conceptualisation and methodology, G.D.R., G.P. and A.P.; software, S.P.; validation, G.D.R., S.P., G.P. and A.P.; formal analysis, G.P. and L.V.; investigation, G.D.R., S.P., G.P., A.P. and L.V.; data curation, G.P.; writing—original draft preparation, G.P., A.P. and L.V. All authors have read and agreed to the published version of the manuscript.

Funding: This research received no external funding.

Institutional Review Board Statement: Not applicable.

Informed Consent Statement: Not applicable.

Data Availability Statement: Data are contained within the article.

Acknowledgments: The authors would like to sincerely thank the Municipality of Siena, Italy, and the Polisportiva Mens Sana for granting us free usage of the velodrome testing site.

Conflicts of Interest: The authors declare no conflicts of interest.

References

1. Inagaki, K.; Narieda, S.; Fujii, T.; Umebayashi, K.; Naruse, H. Measurements of lora propagation in harsh environment: Numerous nlos areas and ill-conditioned lora gateway. In Proceedings of the 2019 IEEE 90th Vehicular Technology Conference (VTC2019-Fall), Honolulu, HI, USA, 22–25 September 2019; pp. 1–5.
2. Anugrah, T.W.; Rakhmatsyah, A.; Wardana, A.A. Non-Line of Sight LoRa–Based Localization using RSSI-Kalman-Filter and Trilateration. *Int. J. Inf. Commun. Technol. (IJoICT)* **2020**, *6*, 52–63. [CrossRef]
3. Aarif, L.; Tabaa, M.; Hachimi, H. Performance Evaluation of LoRa Communications in Harsh Industrial Environments. *J. Sens. Actuator Netw.* **2023**, *12*, 80. [CrossRef]
4. Zorbas, D.; Abdelfadeel, K.; Kotzanikolaou, P.; Pesch, D. TS-LoRa: Time-slotted LoRaWAN for the industrial Internet of Things. *Comput. Commun.* **2020**, *153*, 1–10. [CrossRef]
5. Emmanuel, L.; Farjow, W.; Fernando, X. Lora wireless link performance in multipath underground mines. In Proceedings of the 2019 International Conference on Innovation and Intelligence for Informatics, Computing, and Technologies (3ICT), Sakhier, Bahrain, 22–23 September 2019; pp. 1–4.
6. Gineprini, M.; Parrino, S.; Peruzzi, G.; Pozzebon, A. LoRaWAN performances for underground to aboveground data transmission. In Proceedings of the 2020 IEEE International Instrumentation and Measurement Technology Conference (I2MTC), Dubrovnik, Croatia, 25–28 May 2020; pp. 1–6.
7. Chen, B.; Wang, J. Long-Range Wireless Sensor Network-based Remote Marine Environmental Monitoring System. In Proceedings of the 2021 International Conference on Computer, Internet of Things and Control Engineering (CITCE), Guangzhou, China, 12–14 November 2021; pp. 100–106.
8. Radeta, M.; Ribeiro, M.; Vasconcelos, D.; Noronha, H.; Nunes, N.J. LoRaquatica: Studying range and location estimation using LoRa and IoT in aquatic sensing. In Proceedings of the 2020 IEEE International Conference on Pervasive Computing and Communications Workshops (PerCom Workshops), Austin, TX, USA, 23–27 March 2020; pp. 1–6.
9. Bianco, G.M.; Giuliano, R.; Marrocco, G.; Mazzenga, F.; Mejia-Aguilar, A. LoRa system for search and rescue: Path-loss models and procedures in mountain scenarios. *IEEE Internet Things J.* **2020**, *8*, 1985–1999. [CrossRef]

10. Bouras, C.; Gkamas, A.; Salgado, S.A.K. Exploring the energy efficiency for Search and Rescue operations over LoRa. In Proceedings of the 2021 11th IFIP International Conference on New Technologies, Mobility and Security (NTMS), Paris, France, 19–21 April 2021; pp. 1–5.
11. Di Renzone, G.; Parrino, S.; Peruzzi, G.; Pozzebon, A. LoRaWAN in motion: Preliminary tests for real time low power data gathering from vehicles. In Proceedings of the 2021 IEEE International Workshop on Metrology for Automotive (MetroAutomotive), Bologna, Italy, 1–2 July 2021; pp. 232–236.
12. Ferrari, P.; Sisinni, E.; Carvalho, D.F.; Depari, A.; Signoretti, G.; Silva, M.; Silva, I.; Silva, D. On the use of LoRaWAN for the Internet of Intelligent Vehicles in Smart City scenarios. In Proceedings of the 2020 IEEE Sensors Applications Symposium (SAS), Kuala Lumpur, Malaysia, 9–11 March 2020; pp. 1–6.
13. Suriyan, G.R.; Rahul, K.; Rajesh, S.; Dhanalakshmi, C.; Udhayakumar, G. Prevention of Road Accidents by Interconnecting Vehicles using LiFi and LoRaWAN Technologies. In Proceedings of the 2023 International Conference on Sustainable Computing and Smart Systems (ICSCSS), Coimbatore, India, 14–16 June 2023; pp. 1383–1387.
14. Vinodhini, M.; Rajkumar, S.; Subramaniam, S.K. Real-time Internet of LoRa Things (IoLT)-based accident detection and prevention system in vehicular networks towards smart city. *Int. J. Commun. Syst.* **2023**, 1–11. [CrossRef]
15. Croce, D.; Garlisi, D.; Giuliano, F.; Valvo, A.L.; Mangione, S.; Tinnirello, I. Performance of lora for bike-sharing systems. In Proceedings of the 2019 AEIT International Conference of Electrical and Electronic Technologies for Automotive (AEIT AUTOMOTIVE), Turin, Italy, 2–4 July 2019; pp. 1–6.
16. Boshita, T.; Suzuki, H.; Matsumoto, Y. IoT-based bus location system using LoRaWAN. In Proceedings of the 2018 21st International Conference on Intelligent Transportation Systems (ITSC), Maui, HI, USA, 4–7 November 2018; pp. 933–938.
17. Salazar-Cabrera, R.; Pachón de la Cruz, Á.; Madrid Molina, J.M. Proof of concept of an iot-based public vehicle tracking system, using lora (long range) and intelligent transportation system (its) services. *J. Comput. Netw. Commun.* **2019**, *2019*, 9198157. [CrossRef]
18. Li, Y.; Barthelemy, J.; Sun, S.; Perez, P.; Moran, B. Urban vehicle localization in public LoRaWan network. *IEEE Internet Things J.* **2021**, *9*, 10283–10294. [CrossRef]
19. Li, Y.; Han, S.; Yang, L.; Wang, F.Y.; Zhang, H. LoRa on the move: Performance evaluation of LoRa in V2X communications. *IEEE Internet Things J.* **2022**, *9*, 10283–10294. [CrossRef]
20. Klaina, H.; Guembe, I.P.; Lopez-Iturri, P.; Astrain, J.J.; Azpilicueta, L.; Aghzout, O.; Alejos, A.V.; Falcone, F. Aggregator to electric vehicle LoRaWAN based communication analysis in vehicle-to-grid systems in smart cities. *IEEE Access* **2020**, *8*, 124688–124701. [CrossRef]
21. Jurado Murillo, F.; Quintero Yoshioka, J.S.; Varela López, A.D.; Salazar-Cabrera, R.; Pachón de la Cruz, Á.; Madrid Molina, J.M. Experimental evaluation of lora in transit vehicle tracking service based on intelligent transportation systems and IoT. *Electronics* **2020**, *9*, 1950. [CrossRef]
22. Haque, K.F.; Abdelgawad, A.; Yanambaka, V.P.; Yelamarthi, K. Lora architecture for v2x communication: An experimental evaluation with vehicles on the move. *Sensors* **2020**, *20*, 6876. [CrossRef] [PubMed]
23. Torres, A.P.A.; Da Silva, C.B.; Tertuliano Filho, H. An experimental study on the use of LoRa technology in vehicle communication. *IEEE Access* **2021**, *9*, 26633–26640. [CrossRef]
24. Al mojamed, M. On the use of LoRaWAN for mobile Internet of Things: The impact of mobility. *Appl. Syst. Innov.* **2021**, *5*, 5. [CrossRef]
25. Anwar, K.; Rahman, T.; Zeb, A.; Khan, I.; Zareei, M.; Vargas-Rosales, C. Rm-adr: Resource management adaptive data rate for mobile application in lorawan. *Sensors* **2021**, *21*, 7980. [CrossRef] [PubMed]
26. Adi, P.D.P.; Purnama, I.; Siregar, A.A.; Juledi, A.P.; Edi, F.; Karim, A.; Wahyu, Y.; Maulana, F.I.; Susilo, S.A.B.; Harahap, I.M.; et al. Performance LoRa Technology for Autonomous Vehicles. In Proceedings of the 2023 International Seminar on Intelligent Technology and Its Applications (ISITIA), Surabaya, Indonesia, 26–27 July 2023; pp. 703–709.
27. Sobhi, S.; Elzanaty, A.; Ghuniem, A.M.; Abdelkader, M.F. Vehicle-Mounted Fog-Node with LoRaWAN for Rural Data Collection. In Proceedings of the 2022 IEEE 33rd Annual International Symposium on Personal, Indoor and Mobile Radio Communications (PIMRC), Kyoto, Japan, 12–15 September 2022; pp. 1438–1444.
28. Sobhi, S.; Elzanaty, A.; Selim, M.Y.; Ghuniem, A.M.; Abdelkader, M.F. Mobility of LoRaWAN gateways for efficient environmental monitoring in pristine sites. *Sensors* **2023**, *23*, 1698. [CrossRef] [PubMed]
29. da Rocha Santos, L.C.; Bruschi, S.M.; de Souza, P.S.L.; Ueyama, J.; dos Santos, A.d.J.; Barbosa, J.S. Performance analysis of a Vehicular Ad Hoc network Using LoRa technology and IoT devices in Amazon Rivers. *Ad Hoc Netw.* **2024**, *152*, 103301. [CrossRef]
30. Parri, L.; Parrino, S.; Peruzzi, G.; Pozzebon, A. Low power wide area networks (LPWAN) at sea: Performance analysis of offshore data transmission by means of LoRaWAN connectivity for marine monitoring applications. *Sensors* **2019**, *19*, 3239. [CrossRef] [PubMed]
31. Xhonneux, M.; Afisiadis, O.; Bol, D.; Louveaux, J. A Low-Complexity LoRa Synchronization Algorithm Robust to Sampling Time Offsets. *IEEE Internet Things J.* **2022**, *9*, 3756–3769. [CrossRef]
32. Semtech. Application Note: AN1200.80 LoRa ® Modem Doppler Immunity. 2023. Available online: https://semtech.my.salesforce.com/sfc/p/#E0000000JelG/a/3n000000l9Iq/6u0F6F4gEJ4jAjuUJyPm1HkISznAbzAluV.SBa7iT1U (accessed on 1 February 2024).

33. Petäjäjärvi, J.; Mikhaylov, K.; Pettissalo, M.; Janhunen, J.; Iinatti, J. Performance of a low-power wide-area network based on LoRa technology: Doppler robustness, scalability, and coverage. *Int. J. Distrib. Sens. Netw.* **2017**, *13*, 1550147717699412. [CrossRef]
34. Doroshkin, A.A.; Zadorozhny, A.M.; Kus, O.N.; Prokopyev, V.Y.; Prokopyev, Y.M. Experimental study of LoRa modulation immunity to Doppler effect in CubeSat radio communications. *IEEE Access* **2019**, *7*, 75721–75731. [CrossRef]

sensors

MDPI

Article

An Environment-Aware Adaptive Data-Gathering Method for Packet-Level Index Modulation in LPWA

Osamu Takyu [1], Keita Takeda [1], Ryuji Miyamoto [1], Koichi Adachi [2], Mai Ohta [3] and Takeo Fujii [2,*]

[1] Department of Electrical & Computer Engineering, Shinshu University, Nagano 380-8553, Japan; takyu@shinshu-u.ac.jp (O.T.); 22w2062e@shinshu-u.ac.jp (K.T.); 22w2105b@shinshu-u.ac.jp (R.M.)
[2] Advanced Wireless & Communication Research Center, University of Electrocommunications, Tokyo 182-8585, Japan; adachi@awcc.uec.ac.jp
[3] Department of Electronics Engineering and Computer Science, Fukuoka University, Fukuoka 814-0180, Japan; maiohta@fukuoka-u.ac.jp
* Correspondence: fujii@awcc.uec.ac.jp; Tel.: +81-42-443-5872

Abstract: Low-power wide-area (LPWA) is a communication technology for the IoT that allows low power consumption and long-range communication. Additionally, packet-level index modulation (PLIM) can transmit additional information using multiple frequency channels and time slots. However, in a competitive radio access environment, where multiple sensors autonomously determine packet transmission, packet collisions occur when transmitting the same information. The packet collisions cause a reduction in the throughput. A method has been proposed to design a mapping table that shows the correspondence between indexes and information using a packet collision minimization criterion. However, the effectiveness of this method depends on how the probability of the occurrence of the information to be transmitted is modeled. We propose an environment-aware adaptive data-gathering method that identifies the location of factors affecting sensor information and constructs a model for the probability of the occurrence of sensor information. The packet collision rate of the environment-aware adaptive data-gathering method was clarified through computer simulations and actual experiments on a 429 MHz LPWA. We confirm that the proposed scheme improves the packet collision rate by 15% in the computer simulation and 30% in the experimental evaluation, respectively.

Keywords: LPWA; PLIM; mathematical optimization

1. Introduction

In recent years, low-power wide-area (LPWA) communication technology has attracted attention as a wireless sensor network for the internet of things (IoT) due to its long-range capability and low power consumption. LPWA operates without a license, enabling the deployment of wireless networks virtually anywhere [1]. In particular, the event detection scheme that detects the environmental changes in IoT has been considered in [2]. In the IoT for agriculture, the event detection based on machine learning is considered in [3]. For the IoT of the inside of a car, the error detection of the equipment system is considered in [4]. For monitoring the water level, the highly accurate error detection based on a machine learning scheme is proposed in [5]. Event detection from the open sky using an unmanned aerial vehicle is proposed in [6]. Various frame works for highly accurate event detection are proposed in [7]. In addition, the process flow of event detection with the analysis of the gathered data is shown in [8]. The analysis of time and frequency domains for the robustness of noise is proposed and thus the detection accuracy is improved in [9]. Event detection based on the compressed sensing is proposed in [10]. The variable sampling rate adapted to the conditions of events is considered in [11]. However, as the event or the change in the monitored environment occurs, a lot of sensors recognize it and then access the channel, simultaneously. The packet collisions frequently occur and thus it is quite difficult to gather the sensing data [12]. In addition, LPWAs have the limitation of a data transmission duty cycle to secure a time for other systems to gain access. However, there is also the problem that the limitation of duty cycle reduces throughput.

Various schemes for reducing the packet collision and improving the packet delivery rate have been considered. The performance of LoRa under the industrial application with various algorithms of the adaptive data rate (ADR) is clarified in [13]. When the parameters of the LoRa format, such as packet length and spreading factor, are changed, the packet error rate is evaluated [14]. In the dense sensor nodes, the suitable spreading factor assigned to each sensor in accordance with the criterion of maximal delivery rate is considered [15]. In addition, in the dense sensor nodes, the adaptive switching of spreading factor and transmit power control is proposed for improving the packet delivery rate in [16]. The avoidance of packet collision based on the prediction of packet access is considered in [17]. The construction of a transmitting packet using the period of packet transmission is considered for avoiding the packet collision in [18]. For increasing the throughput, the interleaved chirp pattern of LoRa modulation is considered in [19]. In the transmission range under the 1 km, the packet collisions frequently occur and then the packet retransmission in the application layer is considered in [20]. The distributed control of the packet access parameters improves the packet delivery when late in [21].

One method to enhance the throughput of LPWA within the confines of the duty cycle limitation is through packet-level index modulation (PLIM) [22]. PLIM maintains the packet format while dynamically adjusting the channel and timing of packet transmission according to the information to be transmitted. This effectively utilizes the idle periods created by duty cycle limitations as indices for information transmission, thereby expanding throughput. Additionally, as PLIM adheres to the LPWA wireless standard, it can seamlessly integrate with existing LPWA deployments.

The conventional schemes for avoiding packet collision and compensating the degradation of the delivery rate assume the periodic packet access or the ability to directly controlling the parameters of the packet access. However, in the PLIM, the packet access depends on the sensing information. The conventional scheme cannot directly apply to the LoRa with PLIM. Therefore, the scheme for suppressing the packet collision as well as applying the LoRa PLIM is required.

We consider the application of PLIM in a competitive wireless environment where multiple sensors can transmit packets simultaneously on the same channel and with the same timing. When multiple sensors use PLIM to transmit identical information, they concurrently send packets over the same transmission channel and timing, resulting in packet collisions. Therefore, the mapping table, showing the correspondence between transmitted information and indices, is adapted for each sensor, thereby mitigating packet collisions. A method has been proposed to design a mapping that minimizes the packet collision probability by mathematical optimization [23]. Establishing a model of packet collision probability necessitates understanding the statistical trends of the sensor information to be transmitted beforehand. To achieve this, a method has been proposed that uses previously collected data and prior observations to construct a model of the probability of information occurrence [23]. However, if the information pattern transmitted by each sensor follows a uniform probability distribution, there is a chance that other sensors may select the same index, thereby limiting the effectiveness of packet collision suppression.

In this study, our focus is on identifying the factors influencing each piece of sensor information to understand the statistical trends of prior sensor data. While our explanation primarily pertains to radio sensors, the methodology is applicable to other phenomena that exhibit spatial spillover. Radio sensors are being explored for frequency-sharing applications [24]. In the context of radio sensors, when a radio source emits a signal, the sensor measures the receive signal strength indicator (RSSI) at its location. Subsequently, each radio sensor transmits the RSSI to a gateway (GW) using PLIM. The RSSI observed by each radio sensor varies depending on the location of the radio source. Therefore, we analyzed the statistical trend of RSSI by limiting the presence of radio sources to a narrower area within the overall observation range. Consequently, RSSI tends to exhibit a narrow spread and concentrate around a specific value. Therefore, we analyzed RSSI trends using radio sensors. Here, we divided the entire observation space into uniformly sized sections to form areas. Therefore, the statistical trend of RSSI for each sensor was analyzed according to the presence of radio sources in each area. Upon identifying the area where the radio source was located, the corresponding RSSI trend was used to design the PLIM mapping table. Therefore, each radio sensor focuses on a specific RSSI value and rarely sends other RSSI values to the GW. The vacant indices, which are not used for PLIM, are secured and then used by other sensors, thereby suppressing packet collisions. In the proposed method, the position estimation of the radio source and the selection of a suitable mapping table corresponding to the estimated position are iteratively used. Therefore, the proposed method adaptively switches the mapping table based the radio environment, referred to as an environment-aware adaptive data-gathering method. In this research, the packet collision rate is evaluated by computer simulation to elucidate the effect of reducing the packet collisions using the environment-aware adaptive data-gathering method. Furthermore, the environment-aware adaptive data-gathering method was implemented using 429 MHz-LoRa/FSK modules, and its effects were also assessed in the experimental evaluation.

The difference among our papers [22,23] and this paper is shown as follows. In Ref. [22], we initially proposed the packet-level index modulation. We did not consider the packet collision under the competitive wireless access environment among multiple sensors. Ref. [23] proposed the construction of the mapping table between the indexes, and the sensing information was constructed to minimize the packet collision rate in the PLIM. It confirmed the effect of reducing packet collisions in the computer simulation. However, this has not been confirmed in an experimental evaluation with the actual wireless equipment. In addition, the effect of reducing the packet collisions by the proposed construction of mapping table depends on the tendency of sensing information. Ref. [23] did not consider this in detail. This paper pays attention to the relationship between the position of the event source and the statistical tendency of the sensing information. It proposes the adaptive data-gathering scheme based on the positioning of the event source. In addition, this paper clarifies the effect of the optimal mapping table in an experimental evaluation with the actual wireless equipment, which is 429 MHz LoRa/FSK.

The main contributions of our paper are shown below.

- We propose the adaptive data-gathering scheme in which the mapping table of PLIM is adaptively changed in accordance with the position of event source. The proposed adaptive data gathering can effectively reduce the packet collisions.
- We implement the proposed adaptive data-gathering scheme in the actual equipment of 429 MHz LoRa/FSK. In the practical experiment, the effects of optimizing the mapping table of PLIM and the adaptive data-gathering scheme are clarified.
- In the computer simulation and the experimental evaluations, we confirm the improving effect of the proposed adaptive data-gathering scheme in terms of the reduction in packet collision rate and the packet delivery rate.

The necessity of the experimental evaluation is shown as follows. In computer simulation, the ray-tracing simulator is used for simulating the radio environment. As the number of reflections becomes large, its computational complexity is explosively increased and thus the results cannot be obtained within a practical and finite time duration. Instead, the simple simulation with a smaller number of reflections is used. However, a mismatch between the simple simulation and the actual radio environment occurs. In the proposed data-gathering method, the spatial correlation of the radio environment is used and thus the highly accurate simulation of the radio environment is necessary. Therefore, the experimental evaluation with the actual radio sensor measuring the RSSI can clarify the practicality of the proposed method. In the evaluation of Ref. [23], the packet access from each sensor to the GW is assumed as the ideal model with no packet loss. The LPWA is the wide area network and thus the sensor located in each site suffers from the various obstacles around it. Therefore, the channel model is different for each sensor. For simulating the highly accurate wireless communication, the channel model is constructed sensor by sensor and thus the process time of evaluation and constructing the program are significantly large. In the experimental evaluation with the packet transmission based on LPWA, the particular channel model in each sensor is considered and then the effect of the proposed data-gathering method can be evaluated. In addition, the processes of the proposed data-gathering method are composed of the positioning of the radio source, the selection of the suitable mapping in the PLIM, the informing from the GW to each sensor about the selected mapping, and the switch of the mapping in each sensor. These consume a certain amount of time as the processing time. As the adaptation of the proposed data-gathering method to the radio environment is evaluated, the processing time should be considered and thus the actual implementation of the proposed method is necessary.

2. System Model

In the sensor networks considered in this study, there was one GW and multiple sensor nodes. Each sensor converted its observation information into digital data and notified the GW. The GW periodically broadcasted time synchronization signals to all the sensors, ensuring time synchronization across the network. Each sensor transmitted its observation information once at periodic intervals, defining the transmission cycle as a frame. The observation information was encapsulated within packets containing necessary control information for communication. Therefore, each sensor sent a packet only once per frame. However, the packet access timing could be chosen arbitrarily as long as it fell within one frame time; the frame time was assumed to be significantly longer than the packet length.

LoRa is assumed to be the transmission method for LPWA, where a chirp pattern corresponding to the digital information is selected for transmission. This modulation is referred to as LoRa modulation. The duration of the chirp pattern is determined by the spreading factor (SF). As the SF increases, the symbol length of the chirp pattern expands, and the number of chirp pattern types increases. Consequently, the number of bits that can be transmitted per symbol also increases. Furthermore, as the energy per symbol is enlarged, the transmission distance is increased. However, when the SF is set to 1, two different frequencies are switched for and sensors autonomously select one channel each, which is equivalent to Frequency Shift Keying (FSK).

2.1. Packet Level Index Modulation (PLIM) [22]

PLIM is an index modulation technique where the index is determined by the transmission timing and frequency channel of the packet. Figure 1a shows the relationship between the channel and time. The frame is divided into short, equally spaced segments called slots, with each slot being shorter than the frame length but longer than the packet length. The frame start time for each sensor is detected using a synchronization signal from the GW. Each sensor sets the waiting time for packet transmission in slots from the frame's start time, allowing them to select a specific slot for packet transmission by adjusting their transmission waiting time. Moreover, multiple orthogonal frequency channels are prepared, and sensors autonomously select one channel each. Consequently, the total number of indices that can be formed is the product of the total number of frequency channels and the total number of time slots. The digital information is assigned to the index formed in this manner, a process called mapping table. Figure 1b presents an example of a mapping table. Each sensor can independently set its own mapping.

Information transmission in PLIM operates as follows: The sensor constructs a digital pattern, which is a combination of multiple pieces of digital information to be transmitted. In the case of transmitting two bits, there are four possible patterns: 00, 01, 10, and 11. Subsequently, the sensor selects the index corresponding to the digital pattern by referring to the mapping table. The packet is then transmitted in the timeslot and frequency channel indicated by the selected index. Upon reception, the receiver identifies the number of received frequency channels and the timing of reception. Since time synchronization between the receiver, GW, and each sensor node has been established, the difference between the start time of the frame and the arrival time of the packet indicates the timeslot selected by the transmitter, i.e., the sensor. The index is obtained from the detected frequency channel and timeslot. The GW refers to the mapping table used by the sensor whose ID is recognized from the header of the received packet. It then identified the digital pattern corresponding to the received index, thus receiving this digital pattern as the digital information from the sensor.

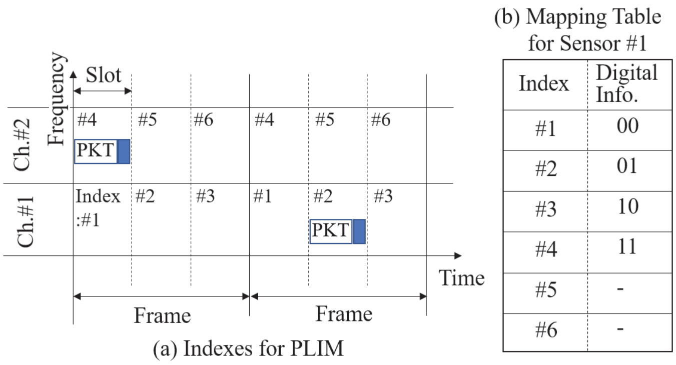

Figure 1. Image of PLIM.

In PLIM, besides the packet payload, additional information can be transmitted using the index, thereby expanding the throughput. Furthermore, the modulation format of the packet does not need to be altered, making it compliant with the LoRa standards.

2.2. Optimization of Mapping in PLIM [23]

One of the challenges of PLIM is the occurrence of packet collisions when multiple sensors select the same index, resulting in missing information. To mitigate packet collisions, the construction of the mapping table based on mathematical optimization techniques has been constructed. A quadratic programming problem is formulated by deriving the probability of packet collision between any two sensors and using the mapping pattern rules in PLIM as constraints. The specific model equation is as follows:

$$\min \sum_{k=1}^{K} \sum_{i_1=1}^{I} \sum_{i_2=i_1+1}^{I} \sum_{j_1=1}^{J} \sum_{j_2=1}^{J} P_{i_1,j_1} P_{i_2,j_2} x_{i_1,j_1,k} x_{i_2,j_2,k} \tag{1}$$

$$\text{subject to} \quad x_{i,j,k} \in \{0,1\} \quad \forall i \in I, \forall j \in J, \forall k \in K$$

$$\sum_{k=1}^{K} x_{i,j,k} = 1 \quad \forall i \in I, \forall j \in J \tag{2}$$

$$\sum_{j=1}^{J} x_{i,j,k} \leq 1 \quad \forall i \in I, \forall k \in K \tag{3}$$

$$1 \leq \sum_{j=1}^{J} \sum_{i=1}^{I} x_{i,j,k} \leq I \quad \forall k \in K \tag{4}$$

Here, i indicates the sensor number, j indicates the digital pattern number assigned by a particular decimal number, and k indicates the index number, respectively. Additionally, I, J, and K denote the total number of sensors, the total number of digital patterns, and indices, respectively. $P_{i,j}$ indicates the probability that the ith sensor will send the jth digital pattern. When $x_{i,j,k}$ is one, the kth index is assigned to the jth digital pattern of the ith sensor. Conversely, zero indicates no assignment. Note that $x_{i,j,k}$ is the optimization variable.

Equation (2) indicates that each digital pattern is assigned an index for each sensor. Equation (3) indicates that at most, one digital pattern is assigned to one index at each sensor. Equation (4) also ensures that each index is assigned at most one digital pattern for any one sensor, and at most up to the number of sensors. The optimization solver can be used to determine the design variables $x_{i,j,k}$.

In Ref. [23], the construction of mapping in the PLIM is modeled as the quadratic programming problem. The Gurobi Optimization [25], which is the solver of the quadratic problem, is used for deriving the optimal variables [23]. We also use the Gurobi Optimization as the solver of the quadratic programming problem. The computational cost of constructing mapping table is more significant as the number of variables becomes large [23]. Therefore, we also use the quasi-optimization solution with low complexity, as Ref. [23] also uses it.

The model equation requires a prior estimation of $P_{i,j}$. Estimation methods include prior observations and analogous methods based on previously gathered results. Here, we consider a case where a particular digital pattern in $P_{i,j}$ exhibits a higher probability of occurrence than the other patterns. Maintaining a low collision probability entails assigning a digital pattern with low occurrence probability to the index assigned to the digital pattern with high occurrence probability. This concept yields the mapping table derived from optimal design, which can effectively suppress packet collisions. Conversely, if the occurrence probability of any digital pattern is uniform, the probability of selecting any index is not low, even with the mapping changes. Therefore, the probability of multiple sensors selecting the same index is high, limiting the effectiveness of collision suppression. Therefore, when the occurrence probability of a particular digital pattern is high, the collision-suppression effect of the mapping design can be enhanced. In this study, we established an environment-aware adaptive data-gathering method where the occurrence probability of a digital pattern is concentrated on a specific pattern.

2.3. An Environment-Aware Adaptive Data-Gathering Method

This study assumes that a sensor observes the RSSI of a radio wave and transmits it via PLIM. The same concept can be applied to cases where temperature, humidity, etc., are transmitted. The magnitude of RSSI observed by the radio sensor is quantized at regular intervals, making RSSI a discrete value. Each discrete value corresponds to a digital pattern of PLIM. Therefore, a unique index is assigned to each discrete value, and then the RSSI is transmitted by PLIM. Each discrete value of RSSI is associated with a decimal number, referred to as the RSSI number.

By uniformly placing sensors in the observation area and measuring RSSI, the spatial spread of radio waves emitted by a radio source is observed. Radio wave propagation is subject to shielding effects from buildings and attenuation corresponding to the propagation distance [26]. Therefore, the shielding effect of each building differs depending on the position from which the radio waves are emitted, resulting in inherent variability in radio propagation depending on the location of the radio source. The RSSI dataset, which aggregates the occurrence probability of the RSSI observed by each sensor, can be considered to have specificity depending on the location of the radio source. A method using this RSSI-spatial specification for location positioning has also been investigated [27]. In this study, we develop a probabilistic model of RSSI corresponding to the location of the radio source.

Figure 2 shows the past locations of radio sources and the probability distribution of RSSI observed by a certain single sensor. Note that each figure for a radio source shows the cumulative past locations, and these sources do not emit radio waves simultaneously. Figure 2a shows the case where radio sources are uniformly distributed within the observation range for evaluating the frequency distribution to determine the probability of RSSI for each sensor. Conversely, Figure 2b shows the case where radio sources are uniformly distributed within the observable range for evaluating the frequency distribution to determine the probability of RSSI for each sensor. This represents a case where the occurrence range of past radio sources is restricted to an area smaller than the observation range. From the figures, it is evident that the probability distribution of RSSI in Figure 2b converges more narrowly than that in Figure 2a. Therefore, if the range of occurrence of a radio source can be limited to a certain area, the probability distribution of transmitted information can be constrained more narrowly.

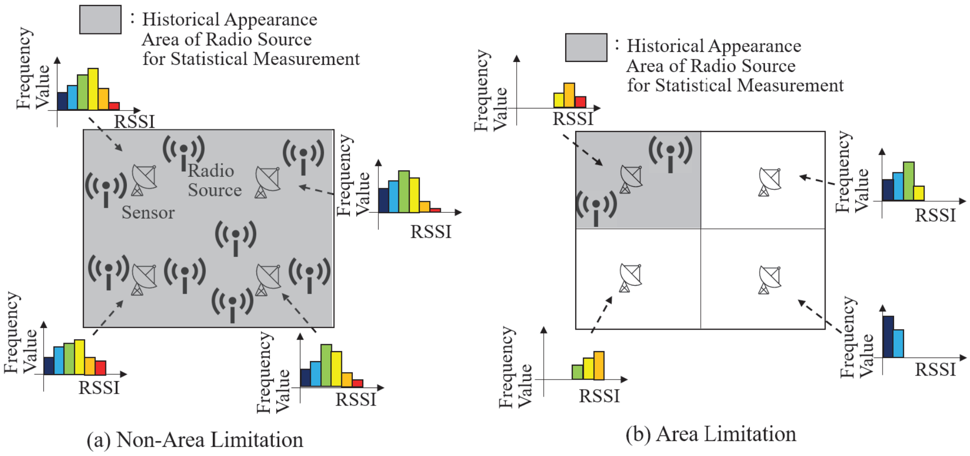

Figure 2. Stochastic tendency of detected RSSI depending on concentration level of appearing radio source. The colors indicate the level of RSSI.

Therefore, we propose the following environment-aware adaptive data-gathering method: We divided the observed space of radio waves into equally sized small areas. Then, we recorded the RSSI of each sensor corresponding to the occurrence of radio sources at various locations within each area. The RSSI recorded by each sensor was analyzed using histogram analysis to obtain the probability of occurrence of each RSSI value. Consequently, a probability model for the occurrence of the RSSI for each sensor can be obtained for each area. This provides the prior RSSI occurrence probability necessary for designing the optimal mapping. Next, the optimal mapping was derived based on the reference [23]. As a result of these processes, the optimal mapping was established for each area. The mapping corresponding to each area was recorded for each sensor and GW.

For the information gathered by PLIM, mappings are selected adaptively according to the process flow shown in Figure 3. As we can see this figure, the selecting mapping is composed of the iterative process. Each sensor first informs PLIM of its observed RSSI using the default mapping. Here, a random mapping table is used as the default mapping, constructed by establishing random correspondence between the RSSI numbers and the indices. The RSSI gathered by all sensors is then utilized by the GW to estimate the area where the radio source is located. In the method of estimating the radio source's location, the sensor observing the maximum RSSI can be considered as the location of the radio source, or the center-of-gravity addition method [28] can be used. The estimated area where the radio source exists is then communicated from the GW to each sensor. Subsequently, the GW and each sensor select a mapping designed according to the RSSI probability distribution for each area. The selected mapping is used to notify PLIM of the RSSI. This series of processes is then repeated: radio source location estimation, area location estimation, GW notifying each sensor of the estimated area, switching the mapping, and PLIM transmission.

By proceeding the iterative process of the proposed method, it becomes possible to select an appropriate mapping table according to the radio source and transmit it by PLIM. Due to the limited range of radio sources, packet collisions among sensors can be suppressed using a mapping table with an optimized design that uses the converged RSSI distribution. Additionally, as the location of the radio source is monitored, mapping can be adjusted to accommodate changes in the radio environment resulting from the movement of the radio source. Therefore, the success rate of sensor information collection can be maintained at a high level.

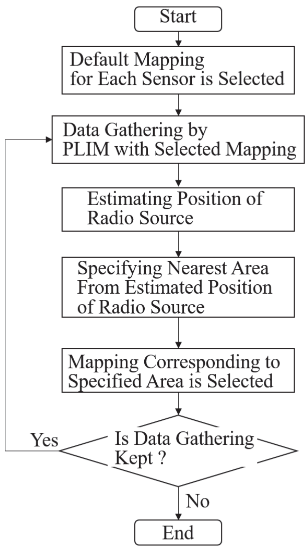

Figure 3. System flow of environment-aware adaptive data-gathering method.

The proposed method was unable to prevent packet collisions resulting from multiple sensors transmitting packets with the same index when using the initial default mapping. This resulted in missing RSSI data, leading to errors in the estimation of radio source locations. To mitigate these errors, the area can be expanded within a certain range to provide a margin against location estimation errors. However, enlarging the area reduces the collision-avoidance efficacy of the mapping design as the probability distribution of RSSI widens. Hence, there exists a tradeoff between the margin for position estimation error and the collision avoidance effect of the mapping design.

3. Implementation of Environment-Aware Adaptive Data-Gathering Method to 429 MHz LoRa/FSK

The proposed environment-aware adaptive data-gathering method was implemented using a 429 MHz LoRa/FSK. Figure 4 shows an overview of the proposed method for 429 MHz LoRa/FSK. The 429 MHz LoRa/FSK utilizes a LoRa-BAR module manufactured by Circuit Design, Inc. This module integrates an antenna and a modulation, and demodulation circuity, allowing it to emit radio waves in compliance with the LoRa standard.

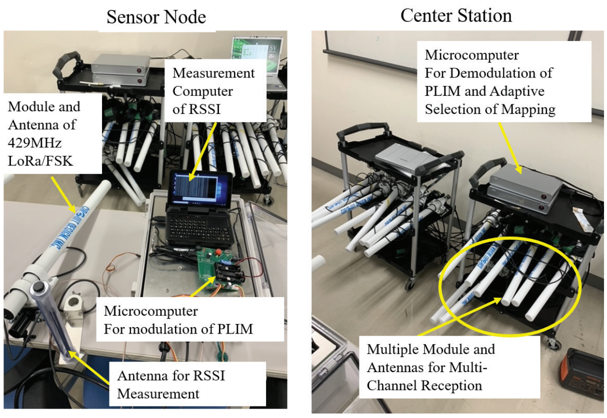

Figure 4. Overview of constructed method to 429 MHz LoRa/FSK.

The sensor was equipped with a microcontroller for PLIM control. This microcontroller managed the LoRa-BAR channel and transmission timing to realize the PLIM. Additionally, the sensor featured an antenna for RSSI observation and a universal software radio peripheral for RSSI calculation. Based on the RSSI value obtained, the sensor referred to the mapping table to select an appropriate index. Subsequently, it determined the transmission timing and channel for the packet corresponding to the selected index and transmitted the packet accordingly. A mapping table was designed, with one assigned to each area, where the radio source was present. Consequently, each sensor has a mapping table equal to the number of areas. The GW stored a mapping table recorded for each sensor categorized by area. By employing methods like the maximum RSSI method or the center-of-gravity addition [28], the GW determined the mapping for each sensor corresponding to the identified area. Furthermore, it informed all the sensors within the identified area accordingly. Since each sensor's LoRa-BAR supported half-duplex communication, the GW received and processed data from each sensor at the time of the announcement. Time synchronization was established during periodic beacon transmissions. Subsequently, each sensor selected a mapping corresponding to the area notified by the GW and used it for PLIM modulation.

The GW has a number of LoRa-BARs equal to the number of channels, allowing the simultaneous reception of multiple channels. All LoRa-BARs are connected to a microcontroller for PLIM demodulation. When a LoRa-BAR successfully receives a packet, it notifies the source information and the received data to the PLIM demodulator microcontroller. Since each LoRa-BAR corresponds to one channel, the LoRa-BAR that notifies the information is distinguished, and the channel number used by the sensor to transmit the packet. Next, the time of data arrival of the information to the microcontroller was determined as the packet arrival time, and the time slot in which the sensor transmitted the packet was identified. Identification of the channel number and time slot helps to identify the index that the sensor chooses in its transmission. The sensor that sends the packet is identified by the ID provided in the packet header. The mapping table for the identified sensor is then used to identify the transmitted information corresponding to the index, and PLIM demodulation is completed. In this implementation, transmission and reception by PLIM modulation, estimation of the area of the radio source, notification of the estimated area to all sensors, and switching of the mapping table by each sensor according to the notified area were completed within the frame time length defined by PLIM. When these flows were repeated, the GW tracked the position of the radio source. Therefore, the proposed method can select a suitable mapping table for a radio environment that is affected by the mobility of the radio source.

4. Computer Simulation

A simulation is conducted assuming a radio sensor that measures the RSSI of radio waves emitted by 920 a band LPWA source. Figure 5 presents an image of the proposed sensor network. Thirty sensors were deployed on the site. Radio sources were placed uniformly and randomly on the site, and the sensors measured the RSSI of the radio waves emitted by the sources. A three-dimensional map of the site was applied to a ray-tracing simulation, and the RSSI at the point where each sensor is placed was determined by the radio sensors. The ray-tracing simulation assumed four reflections, zero refractions, and one diffraction. The measured RSSI was considered to be the RSSI measured by the sensor. Each antenna was assumed omni-directional. The arrangement of the radio sensors and sources is shown in Figure 5. Among the 30 sensors, the number of terminals transmitting in the same frame in PLIM was set from 4 to 8. When x(=4, 5, 6, 7, 8) sensors compete for access in the same frame, the site is divided into x equal parts, and one sensor is randomly selected from each divided area. Of the total radio sources (411 points), 240 points were used as radio emission sources to determine the probability of RSSI generation for each sensor in the proposed method. The remaining 171 points were used to evaluate the packet collision rate when gathering RSSI by PLIM with a generated radio source. Note that two or more radio sources do not emit radio simultaneously; instead, a single radio source emits waves each time. The proposed radio source is divided into nine equal parts, and the positioning method used was center-of-gravity addition. There were a total of 10 values and 10 indexes.

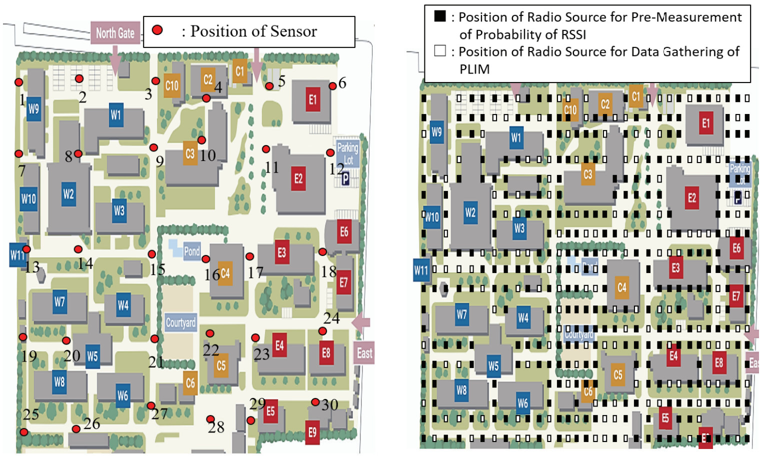

(a) Position of Sensors (b) Position of Radio Sources

Figure 5. Assumed wireless sensor networks for simulation. In (**a**), the number of sensors is 30, and in (**b**), the numbers of radio sources for pre-measurement of the probability of RSSI and for data gathering of PLIM are 240 and 171, respectively.

The packet collision probability against the number of sensors is shown in Figure 6. The figure shows four mapping tables: Common mapping, random mapping, optimal mapping without area division, and optimal mapping with area division. In a common mapping table, all sensors use a single common mapping table. In the random mapping table, the correspondence between the information and index is randomly constructed for each sensor. In the optimal mapping table without area division, the construction of the mapping table is based on minimizing the occurrence probability of packet collisions using the pre-measured tendency of RSSI without area division of the radio source. By contrast, the optimal mapping table with area division is based on the area division. In the optimal mapping table with area division, we also show the two results when the area of the radio source is estimated without error and when it is estimated. From the figure, the optimal mapping table with area division and ideal estimation achieves a 15% reduction in the packet collision rate than the common mapping table. Additionally, the optimal mapping table with area division and the actual estimation achieved a 13% reduction. Moreover, the optimal mapping table with area division and actual estimation can achieve about 5% drop from that with area division and ideal estimation. The proposed method effectively suppressed packet collision probability.

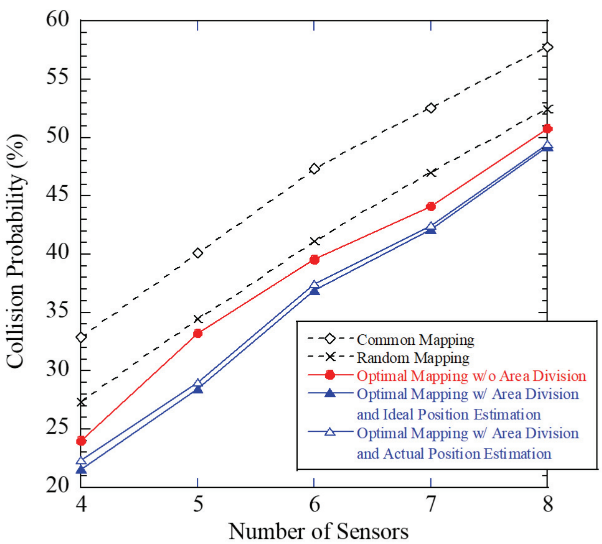

Figure 6. Performance between number of sensors and packet collision rate.

5. Experimental Evaluation

An experiment was conducted to clarify the accuracy of the information gathered by the 429 MHz LoRa/FSK implementing the proposed method. In this study, we observed RSSI using a radio wave sensor in two wireless environments. The first was to measure the RSSI of radio waves emitted by a 5 GHz wireless LAN access point in a typical indoor environment. The second measured the RSSI of radio waves emitted by a 5 GHz wireless LAN access point in an electro-magnetic anechoic chamber. In the latter case, when the emitted radio wave arrives at the wall surface, it is completely absorbed. Radio wave reflections occur from devices in the same room; therefore, radio wave reflections cannot be completely suppressed. However, the radio waves observed by the sensor were in a radio environment where direct waves were dominant.

Figure 7 shows the arrangement of the sensors in Experiment 1 and their images. Eight sensor terminals were used in Experiment 1. Each sensor observes the RSSI of the radio waves emitted by the 5 GHz Wi-Fi and notifies the GW via PLIM. The RSSI is quantized at 4 dB intervals from −94 dBm, the minimum value, and quantized into 10 units. In this experiment, both in estimating the prior probability of RSSI occurrence and in aggregating RSSI information using PLIM, the radio sources were assumed to be in the same location. In the trend analysis to determine the probability of RSSI occurrence, the radio source communicated data for 10 consecutive min. Each sensor repeatedly measured the RSSI of radio waves emitted by the source at regular time intervals. The RSSI measured by each sensor was subjected to a histogram analysis to determine the frequency of occurrence of each quantized RSSI, and the probability of occurrence of quantized RSSI was calculated. We repeated this process for each radio source to obtain the occurrence probability of RSSI for each radio source. In other words, we created a database showing the relationship between the occurrence probability of RSSI for each sensor corresponding to a radio wave source. Then, using the occurrence probability of RSSI corresponding to each radio source, we designed a mapping that minimizes the packet collision rate using the proposed method. Through this process, optimal mapping for each sensor was designed based on the location of each radio source. The designed mapping is pre-recorded in the GW and each sensor and used in PLIM.

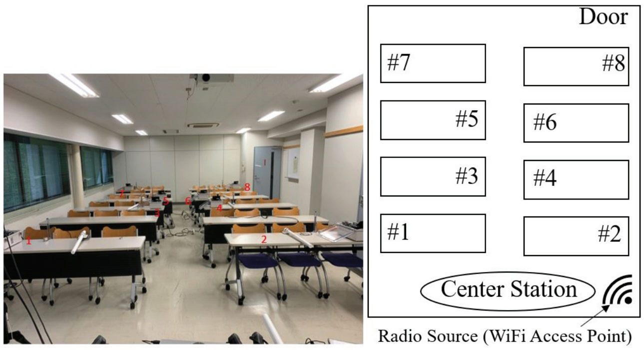

(a) Image of Actual Machine Experiment

(b) Position of Sensors, Center Station, and Radio Source

Figure 7. Arrangement of sensors in Experiment 1.

The parameters used in Experiment 1 are listed in Table 1. A total of 10 indices were used: 1 frequency channel with 10 time slots. To evaluate the packet delivery rate (PDR), the radio sources communicated data continuously for 10 min. During this time, each sensor sent one RSSI measurement and notification to the GW every 5 s. Therefore, the RSSI data were sent to the GW 120 times during the measurement period, and the PDR was evaluated. To confirm the effectiveness of the optimization, we assumed that the location of the radio source was known. Therefore, the proposed method uses an optimal mapping that minimizes the collision probability corresponding to the radio source.

Table 1. Experimental parameters for Experiment 1.

Parameters	Value
Quantization Interval for RSSI	4 [dB]
Number of Indexes	10
Number of RSSI values	10
Minimum RSSI Level	−94 [dBm]
Maximum RSSI Level	−54 [dBm]

Experiment 2 was conducted in an electromagnetic anechoic chamber with a sensor network and Wi-Fi as the radio source. Figure 8 shows the actual locations of the radio sources and sensors. The radio sources were placed at two locations, each with a radio source device. However, these two radio sources did not emit radio waves simultaneously. In other words, when one radio wave was emitted, the other ceased emitting radio waves. Thus, there was no physical movement of the radio sources and no misalignment between them. Following the same procedure as in Experiment 1, a preliminary trend analysis of radio wave emissions were performed at the placement location of one radio wave source, and measured the RSSI. This process was then repeated at the location of another radio source. A histogram of the quantized RSSI of each radio sensor was then analyzed to obtain the occurrence probability of the quantized RSSI. Using the occurrence probability, an optimal mapping was derived under the packet collision probability minimization condition. Therefore, a mapping table was obtained for each sensor corresponding to the locations of the two radio sources. This resulting table was then stored at the GW and each sensor. In the proposed method, one of the two designed mapping tables was selected and used for information gathered by the PLIM, based on the location estimation of radio sources. Two methods were used to estimate the position of the radio source: one used the position information of the sensor with the largest RSSI as the position of the radio source, and the other estimated the position by adding the centers of gravity [28].

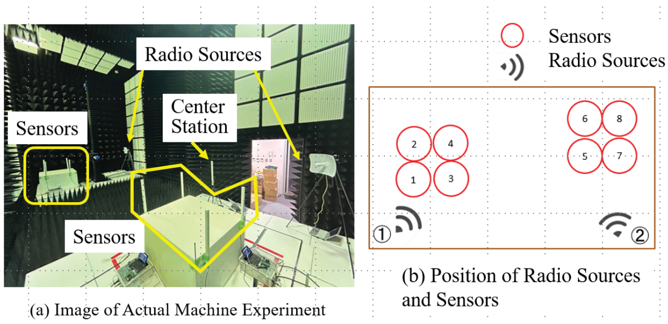

Figure 8. Arrangement of sensors in Experiment 2.

The GW estimates the position of the radio source at each frame time, as defined by PLIM. In this experiment, there are two locations where the radio sources were located, each assigned a unique identifier. Subsequently, the location coordinates of the estimated radio sources and the squared distance between the location coordinates of the two radio source placement locations were calculated. The placement location with the smaller distance was set as the most promising radio source location. Subsequently, the location numbers of the estimated radio sources were recorded in a FIFO-type memory. Here, the memory size is 3. The location number with the highest frequency among the recorded location information was estimated as the location where the radio source was emitting, and PLIM was performed using the mapping corresponding to that location. The simulation parameters for Experiment 2 are the same as those used for Experiment 1.

6. Experimental Results

Table 2 lists the PDR for Experiment 1. Here, the PDR represents the ratio of the total number of packets transmitted to the number of packets that are successfully demodulated. The terms "optimal mapping", "random mapping", and "common mapping" correspond to cases where the mapping is randomly assigned and where all sensors use the same mapping, respectively.

Table 2. Results of Experiment 1.

Mapping Method	PDR [%]
Optimal Mapping	93.75
Random Mapping	59.58
Common Mapping	51.98

From the table, it is evident that the optimal mapping achieves a higher PDR than the fixed and random mappings by more than 30%. To clarify the reason behind this, the frequency distribution of index selection made by each sensor is shown in Figures 9 and 10. The former represents the case with the proposed optimal mapping, while the latter depicts the common mapping. From the figures, it is evident that in the fixed mapping, multiple sensors frequently select the same index, resulting in frequent packet collisions. However, the proposed mapping shows that each sensor uses a different index, thereby avoiding packet collisions. Since this experiment was conducted indoors with a single radio source and fixed placement, the RSSI value observed by each sensor remains within a certain range. Therefore, sensors located at the same distance from the source tend to have the same RSSI, leading to frequent packet collisions when selecting the same index in the fixed mapping. Conversely, random mapping is more effective than fixed mapping in avoiding collisions, but it is inferior to the proposed method. Therefore, we confirmed the collision-suppression effect of the proposed method by designing mappings based on minimum collision probability conditions.

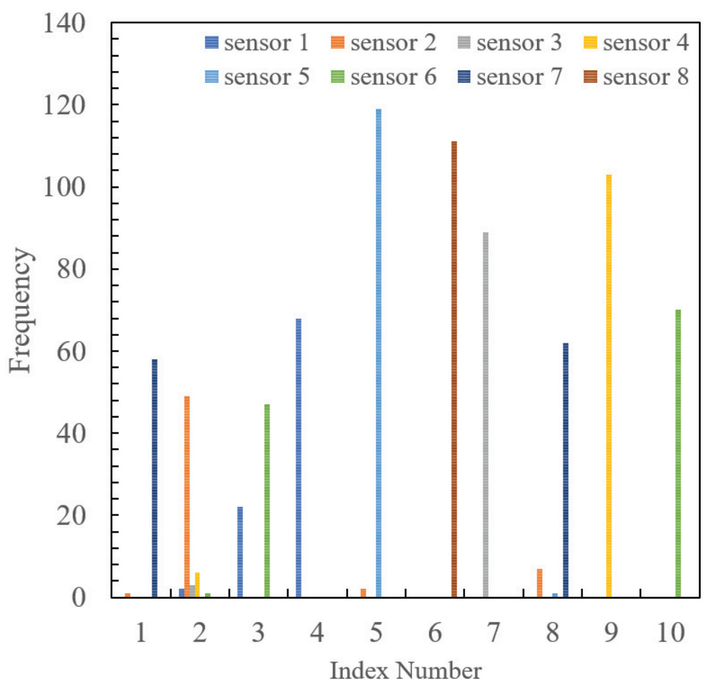

Figure 9. Frequency numbers of indexes selected by each sensor in optimal mapping.

Table 3 presents the PDR for Experiment 2. Here, position 1 and 2 indicate the launch positions of the radio source, and the PDR is evaluated for each launch position of each radio source. Position 1 corresponds to Area 1, and Position 2 corresponds to Area 2. The "w/Area Division" column shows the PDR of the PLIM using the mapping optimized by evaluating the probability of RSSI occurrence at position 1 and position 2, respectively. The " w/o Area Division" shows the PDR of the PLIM using the mapping optimized by evaluating the prior probability of RSSI occurrence for the two emission sources, regardless of their locations. The table shows that the optimal mapping with Area Division achieves the highest PDR for both Positions 1 and 2. Specifically, compared to random mapping, the optimal mapping without Area Division yields an improvement in PDR of approximately 18% to 20%. Conversely, the optimal mapping with Area Division exhibits an improvement from approximately 17% to 19% compared to the optimal mapping without Area Division. Thus, the superior PDR is achieved by harnessing the packet collision-suppression effect of the optimal mapping design and by limiting the launch position of the radio source to specific areas, thereby limiting the probability of RSSI occurrence.

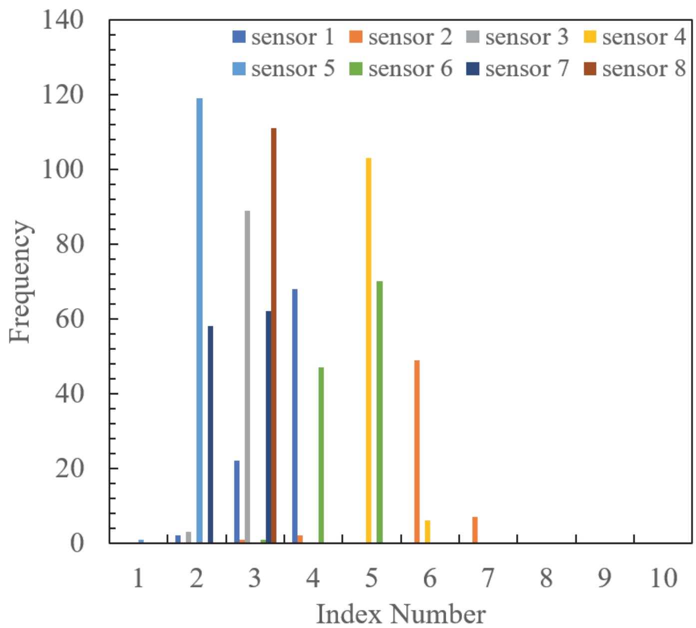

Figure 10. Frequency numbers of indexes selected by each sensor in common mapping.

Table 3. Experimental results: part 1 of Experiment 2.

Position and Mapping	PDR
Position 1 and Optimal Mapping w/Area Division	69.48 [%]
Position 1 and Optimal Mapping w/o Area Division	50.83 [%]
Position 1 and Random Mapping	30.21 [%]
Position 2 and Optimal Mapping w/Area Division	95.73 [%]
Position 2 and Optimal Mapping w/o Area Division	72.19 [%]
Position 2 and Random Mapping	54.69 [%]

Figures 11 and 12 show the quantized RSSI generation rates for each sensor when the radio source is positioned at 1 and 2, respectively. It is evident that at both radio source positions, each sensor generates a high percentage of specific RSSI values, with a narrow and limited spread of quantized RSSI. Consequently, the optimal design using the proposed method ensures that each sensor transmits high-frequency RSSI at different indices, effectively mitigating packet collisions. Furthermore, the RSSI distribution at position 1 is more widely spread than that at position 2, with a higher proportion of RSSI failing within multiple quantization intervals. This disparity arises because when quantizing RSSI, the RSSI value measured at position 1 corresponds to the boundary of the quantization interval. This may lead to slight fluctuations triggering RSSI quantization switches, thereby obtaining a variety of RSSIs compared to position 2.

Table 4 lists the PDR for each method in Experiment 2. Here, Optimal Mapping refers to the scenario where the optimal mapping is selected based on area estimation derived from the radio source's location estimation. Nearest Maximal RSSI Sensor indicates the case where the area closest to the sensor, which observed the maximum RSSI, is selected during location estimation. Conversely, Center of Gravity Addition represents the case where location estimation is performed using the method outlined in Ref. [28], and the area nearest to the estimated radio source location is estimated. The table shows that the Nearest Maximal RSSI Sensor achieved a higher gathering success rate than Optimal Mapping without Area Division by 20% and random mapping by 40%. Hence, we have confirmed the improvement of the proposed mapping method, including the location estimation process. However, Optimal Mapping w/Area Division "center-of-gravity addition" degraded by about 6% compared to "Nearest Maximal RSSI Sensor". This discrepancy can be attributed to the accuracy of the area estimation, where the Nearest Maximal RSSI Sensor exhibited close to 100% accuracy, whereas the Center of Gravity Addition achieved a lower accuracy of 92%. In the nearest maximal RSSI sensor, the position of the sensor measuring the maximal RSSI is considered as the position of the radio source and thus the gap between the actual position of radio source and the estimated one is not smaller than the half of the distance between the two sensors. In the center of gravity addition scheme, as the compensation of positioning the radio sources based on the measured RSSI of each sensor is effective, this gap could be smaller than the maximal RSSI sensor. In the experimental evaluation of this paper, we confirmed the maximal RSSI sensor is better than the center of gravity addition. In this experimental setup, each of the four units was placed in the vicinity of Areas 1 and 2; resulting in a strong relationship between the sensor with the largest RSSI and the Area 2, thereby achieving high estimation accuracy. However, the center of gravity addition tended to use the midpoint between the two separate sensor arrangements as the estimation position, resulting in an indeterminate distinction between areas and degradation of estimation accuracy.

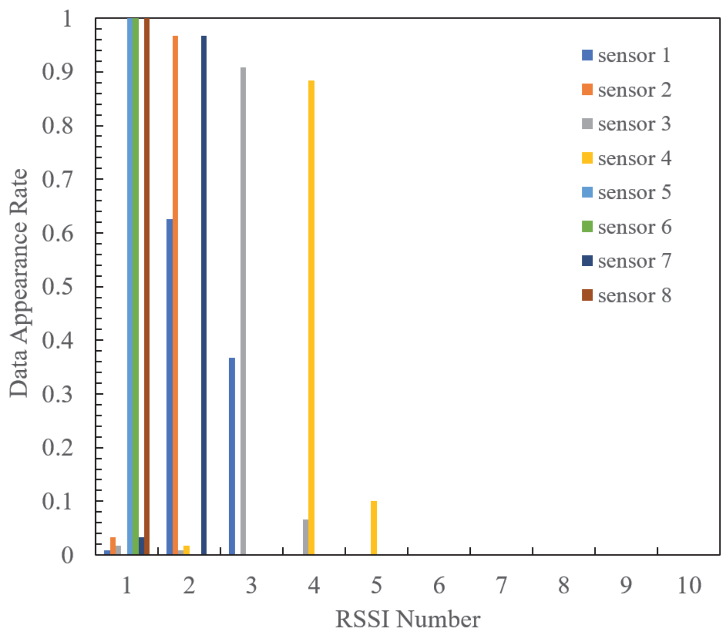

Figure 11. Quantized RSSI generation rates for each sensor in Position 1.

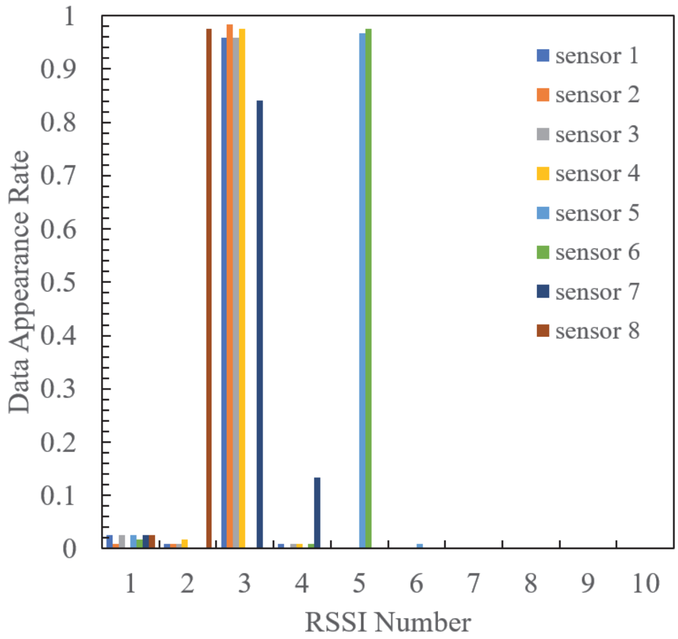

Figure 12. Quantized RSSI generation rates for each sensor in Position 2.

Table 4. Experimental results: part 2 of Experiment 2.

Mapping	PDR
Optimal Mapping with Nearest Maximal RSSI Sensor	82.96 [%]
Optimal Mapping with Center of Gravity Addition	76.56 [%]
Optimal Mapping w/o Area Division	61.51 [%]
Random Mapping	42.45 [%]

7. Conclusions

In this study, we proposed a mapping design for packet-level index modulation (PLIM) that uses pre-observation results of environmental conditions. In a wireless environment where multiple sensors contend for access, packet collisions can result in information loss if the same information is transmitted by PLIM. We introduced a method in which each sensor dynamically switches the mapping, defining the relationship between the index and information assignment, to reduce the probability of packet collision. Our focus was on understanding the change in the statistical trend of sensor information depending on the influencing factor's locations. Subsequently, we established a method to estimate the location of these factors within a certain range and dynamically switch the mapping according, referred to as an environment-aware adaptive data-gathering method. The effectiveness of our proposed method was verified through computer simulations and actual experiments.

In the proposed method, we use the uniform area division for the initial studies. In the practical situation, the area division depends on the appearance tendency of the event source and thus the suitable area division in accordance with the appearance tendency of the event source is a powerful for additional performance improvement. Therefore, the construction of the suitable area division is important future work.

In the wireless access to the multiple channels, the adjacent channel interference causes the packet drop. This paper tackles the recover of the packet collision under the co-channel wireless access. For clarifying the effect of the proposed scheme, the single channel access is assumed in the experimental evaluation. In practical LPWA, the adjacent channel interference is also serious problem. The recovering of the adjacent channel interference is also important future work.

The adaptation of the proposed data-gathering method to the radio environment has not been evaluated yet. For evaluation, the mobility model of the radio source is required but the suitable model is not determined. The evaluation of the adaptation of the proposed data-gathering method to the radio environment is also important future work.

Author Contributions: Conceptualization, O.T., K.A., M.O. and T.F.; methodology, O.T.; software, K.T. and R.M.; validation, K.T. and R.M.; formal analysis, K.T., R.M. and O.T.; investigation, K.T., R.M. and O.T.; resources, K.T., R.M. and O.T.; data curation, K.T., R.M. and O.T.; writing—original draft preparation, O.T.; writing—review and editing, O.T.; visualization, K.T., R.M. and O.T.; supervision, K.A., M.O. and T.F.; project administration, O.T.; funding acquisition, O.T. All authors have read and agreed to the published version of the manuscript.

Funding: This research was funded by the Ministry of Internal Affairs and Communications in Japan, under the project name Strategic Information and Communications R&D Promotion Programme (SCOPE) JP235004002.

Institutional Review Board Statement: Not applicable.

Informed Consent Statement: Not applicable.

Data Availability Statement: The data presented in this study are available on request from the corresponding author.

Conflicts of Interest: The authors declare no conflicts of interest.

References

1. Homssi, B.A.; Al-Hourani, A.; Magowe, K.; Delaney, J.; Tom, N.; Ying, J.; Wolf, H.; Maselli, S.; Kandeepan, S.; Wang, K.; et al. A Framework for the Design and Deployment of Large-Scale LPWAN Networks for Smart Cities Applications. *IEEE Internet Things Mag.* **2021**, *4*, 53–59. [CrossRef]
2. Gupta, U.; Sharma, R. A Survey of Event Detection Techniques in Intelligent IoT System. In Proceedings of the 2023 14th International Conference on Computing Communication and Networking Technologies (ICCCNT), Delhi, India, 6–8 July 2023.
3. Karras, A.; Karras, C.; Giannaros, A.; Giotopoulos, K.C.; Tsolis, D. TinyML-based Event Detection: An Edge-Cloud Approach for Smart Agriculture over LoRa WSNs. In Proceedings of the 2023 8th South-East Europe Design Automation, Computer Engineering, Computer Networks and Social Media Conference (SEEDA-CECNSM), Piraeus, Greece, 10–12 November 2023.
4. Sagala, A.; Putra, J.A.; Silalahi, J.K.A.; Sianipar, R.A.T.T. Vehicle Accident Detection System with LPWAN Technology for Information Transmission. In Proceedings of the 2023 IEEE 9th Information Technology International Seminar (ITIS), Batu Malang, Indonesia, 18–20 October 2023.
5. Gonzalez-Vidal, A.; Cuenca-Jara, J.; Skarmeta, A.F. IoT for Water Management: Towards Intelligent Anomaly Detection. In Proceedings of the 2019 IEEE 5th World Forum on Internet of Things (WF-IoT), Limerick, Ireland, 15–18 April 2019; pp. 858–863.
6. Bhoi, S.K.; Jena, K.K.; Jena, A.; Panda, B.C.; Singh, S.; Behera, P. A Reputation Deterministic Framework for True Event Detection in Unmanned Aerial Vehicle Network (UAVN). In Proceedings of the 2019 International Conference on Information Technology (ICIT), Bhubaneswar, India, 19–21 December 2019; pp. 257–262. [CrossRef]
7. Yahyaoui, A.; Abdellatif, T.; Yangui, S.; Attia, R. READ-IoT: Reliable Event and Anomaly Detection Framework for the Internet of Things. *IEEE Access* **2021**, *9*, 24168–24186. [CrossRef]
8. Kolios, P.; Panayiotou, C.; Ellinas, G.; Polycarpou, M. Data-Driven Event Triggering for IoT Applications. *IEEE Internet Things J.* **2016**, *3*, 1146–1158. [CrossRef]
9. Ge, J.; Rui, J.; Ma, H.; Li, B.; He, Y. HySense: Hybrid Event Occurrence Detection Method for IoT Devices. In Proceedings of the ICASSP 2024—2024 IEEE International Conference on Acoustics, Speech and Signal Processing (ICASSP), Seoul, Republic of Korea, 14–19 April 2024; pp. 4905–4909.
10. Sun, X.; Gao, X.; Li, C. A joint abnormal event detection scheme based on compressed sensing for Internet of Things. In Proceedings of the 2016 16th International Symposium on Communications and Information Technologies (ISCIT), Qingdao, China, 26–28 September 2016; pp. 509–513.
11. Bunaiyan, S.; Al-Dirini, F. Real-Time Analog Event-Detection for Event-Based Synchronous Sampling of Sparse Sensor Signals. In Proceedings of the 2021 IEEE International Midwest Symposium on Circuits and Systems (MWSCAS), Lansing, MI, USA, 8–11 August 2021; pp. 1053–1057.
12. Asteriou, V.; Valkanis, A.; Beletsioti, G.; Kantelis, K.; Papadimitriou, G.; Nicopolitidis, P. LoRaWAN-Based Adaptive MACs for Event Response Applications. *IEEE Access* **2022**, *10*, 97465–97480. [CrossRef]

13. Soto-Vergel, A.; Arismendy, L.; Bornacelli-Durán, R.; Cardenas, C.; Montero-Arévalo, B.; Rivera, E.; Calle, M.; Candelo-Becerra, J.E. LoRa Performance in Industrial Environments: Analysis of Different ADR Algorithms. *IEEE Trans. Ind. Inform.* **2023**, *19*, 10501–10511. [CrossRef]
14. Mahjoub, T.; Said, M.B.; Boujemaa, H. On the Performances of Packet Error Rate for LoRa Networks. In Proceedings of the 2022 International Wireless Communications and Mobile Computing (IWCMC), Dubrovnik, Croatia, 30 May–3 June 2022; pp. 372–377.
15. Gusev, O.; Turlikov, A.; Kuzmichev, S.; Stepanov, N. Data Delivery Efficient Spreading Factor Allocation in Dense LoRaWAN Deployments. In Proceedings of the 2019 XVI International Symposium "Problems of Redundancy in Information and Control Systems" (REDUNDANCY), Moscow, Russia, 21–25 October 2019; pp. 199–204.
16. Babaki, J.; Rasti, M.; Aslani, R. Dynamic Spreading Factor and Power Allocation of LoRa Networks for Dense IoT Deployments. In Proceedings of the 2020 IEEE 31st Annual International Symposium on Personal, Indoor and Mobile Radio Communications, London, UK, 31 August–3 September 2020.
17. Rezazadeh, R.; Sedaahat, Y.; Ghodsollahee, I.; Azizi, F. Improving Fault Tolerance of LoRaWAN With Predicting Packet Collision. In Proceedings of the 2023 28th International Computer Conference, Computer Society of Iran (CSICC), Tehran, Iran, 25–26 January 2023.
18. Xu, Z.; Luo, J.; Yin, Z.; He, T.; Dong, F. S-MAC: Achieving High Scalability via Adaptive Scheduling in LPWAN. In Proceedings of the IEEE INFOCOM 2020—IEEE Conference on Computer Communications, Toronto, ON, Canada, 6–9 July 2020; pp. 506–515.
19. Edward, P.; Tarek, E.; El-Aasser, M.; Ashour, M.; Elshabrawy, T. Further LoRa Capacity Enhancement through Interleaved Chirp Spreading LoRa Expansion. In Proceedings of the 2019 International Conference on Wireless and Mobile Computing, Networking and Communications (WiMob), Barcelona, Spain, 21–23 October 2019.
20. Wang, S.-Y.; Chen, T.-Y. Increasing LoRaWAN Application-Layer Message Delivery Success Rates. In Proceedings of the 2018 IEEE Symposium on Computers and Communications (ISCC), Natal, Brazil, 25–28 June 2018; pp. 148–153.
21. Alahmadi, H.; Bouabdallah, F.; Ghaleb, B.; Al-Dubai, A. Sensitivity-Aware Configurations for High Packet Generation Rate LoRa Networks. In Proceedings of the 2021 20th International Conference on Ubiquitous Computing and Communications (IUCC/CIT/DSCI/SmartCNS), London, UK, 22 December 2021; pp. 240–246.
22. Adachi, K.; Tsurumi, K.; Kaburaki, A.; Takyu, O.; Ohta, M.; Fujii, T. Packet-Level Index Modulation for LoRaWAN. *IEEE Access* **2020**, *9*, 12601–12610. [CrossRef]
23. Miyamoto, R.; Takyu, O.; Fujiwara, H.; Adachi, K.; Ohta, M.; Fujii, T. Data Gathering Method with High Accuracy of Environment Recognition Using Mathematical Optimization in Packet-level Index Modulation. *IEICE Trans. Commun.* **2023**, *E106-B*, 1337–1349. [CrossRef]
24. Shinbo, H.; Yamazaki, K.; Kishi, Y. Research & Development of the Advanced Dynamic Spectrum Sharing System between Different Radio Services. *IEICE Trans. Commun.* **2021**, *E104-B*, 1198–1206.
25. *Gurobi Optimization: Gurobi Optimizer Reference Manual Version 9.5*; Gurobi Optimization, LLC: Beaverton, OR, USA, 2021.
26. Jang, J.; Xu, L.; Yee, B.; Petsalis, E.; Beck, S.; Lang, V.I.; Chew, H. Propagation Models: Large Scale and Site-Specific. In Proceedings of the 2018 IEEE International Symposium on Antennas and Propagation & USNC/URSI National Radio Science Meeting, Boston, MA, USA, 8–13 July 2018; pp. 93–94.
27. Tsujino, T.; Fujii, T. Precise position estimation using position fingerprinting using time-series received data. *IEICE Tech. Rep.* **2020**, *120*, 169–174.
28. Matsuno, H.; Kunisawa, Y.; Hayashi, T. Direction and location estimation algorithm with power gravity point for spectrum sharing. In Proceedings of the 2020 International Symposium on Antennas and Propagation (ISAP), Osaka, Japan, 25–28 January 2021; pp. 679–680.

sensors

MDPI

Article

Application of Artificial Neural Networks for Prediction of Received Signal Strength Indication and Signal-to-Noise Ratio in Amazonian Wooded Environments

Brenda S. de S. Barbosa [1,*], Hugo A. O. Cruz [1], Alex S. Macedo [1], Caio M. M. Cardoso [1], Filipe C. Fernandes [1], Leslye E. C. Eras [2], Jasmine P. L. de Araújo [1], Gervásio P. S. Calvacante [1] and Fabrício J. B. Barros [1]

1 Electrical Engineering Graduate Department, Universidade Federal do Pará, Rua Augusto Corrêa, 01, Guamá, Belém 66075-110, Brazil; hugo1822@gmail.com (H.A.O.C.); alexsanchess@gmail.com (A.S.M.); caio.cardoso@itec.ufpa.br (C.M.M.C); filipe.fernandes@itec.ufpa.br (F.C.F.); jasmine@ufpa.br (J.P.L.d.A.); gervasio@ufpa.br (G.P.S.C.); fbarros@ufpa.br (F.J.B.B.)

2 Institute of Geoscience and Engineering, Universidade Federal do Sul e Sudoeste do Pará, Marabá 68505-080, Brazil; lecastro@unifesspa.edu.br

* Correspondence: brendabarb@gmail.com; Tel.: +55-91-98121-9351

Abstract: The presence of green areas in urbanized cities is crucial to reduce the negative impacts of urbanization. However, these areas can influence the signal quality of IoT devices that use wireless communication, such as LoRa technology. Vegetation attenuates electromagnetic waves, interfering with the data transmission between IoT devices, resulting in the need for signal propagation modeling, which considers the effect of vegetation on its propagation. In this context, this research was conducted at the Federal University of Pará, using measurements in a wooded environment composed of the Pau-Mulato species, typical of the Amazon. Two machine learning-based propagation models, GRNN and MLPNN, were developed to consider the effect of Amazonian trees on propagation, analyzing different factors, such as the transmitter's height relative to the trunk, the beginning of foliage, and the middle of the tree canopy, as well as the LoRa spreading factor (SF) 12, and the co-polarization of the transmitter and receiver antennas. The proposed models demonstrated higher accuracy, achieving values of root mean square error (RMSE) of 3.86 dB and standard deviation (SD) of 3.8614 dB, respectively, compared to existing empirical models like CI, FI, Early ITU-R, COST235, Weissberger, and FITU-R. The significance of this study lies in its potential to boost wireless communications in wooded environments. Furthermore, this research contributes to enhancing more efficient and robust LoRa networks for applications in agriculture, environmental monitoring, and smart urban infrastructure.

Keywords: Amazon; dense vegetation; LoRa; machine learning; propagation models

1. Introduction

The Internet of Things (IoT) is a reality that impacts all the telecommunication sectors, contributing to the evolution of numerous applications, such as smart cities, smart campuses, and smart agriculture. The connected things gather information that helps improve every type of process, saving financial resources and energy. Furthermore, the IoT market is expected to reach USD 1.5 trillion by 2030 [1].

In summary, the Internet of Things is an idea that has already impacted and will continue to impact all aspects of human life significantly [2]. Moreover, most devices used in IoT will employ non-cellular wireless technologies, such as Bluetooth®, Wi-Fi, ZigBee, THREAD, EnOcean, Sigfox®, and LoRa™, among others [3].

IoT devices have different bandwidth, rate, and transmission power requirements. Additionally, they are subject to interference from other wireless transmitters, path loss, random fluctuations caused by shadowing, and obstacles in the communication path [4].

These factors cause high variability in the quality of the received signal, affecting the reliability and performance of wireless communication systems. Therefore, it is necessary to carry out studies to guarantee the reliability and coverage of the connection, making it essential to develop propagation loss models for the most diverse environments [4].

Several studies have addressed the modeling of communication channels, considering different wireless communication technologies. Among these technologies, Long-Range (LoRa) has stood out, as it provides long-range communication and low energy consumption, as pointed out by [5,6]. Moreover, a single receiver in the LoRa network can manage multiple nodes distributed in the environment, leading to significant improvements in IoT applications and contributing to reduce the costs associated with IoT systems deployment.

In addition, channel modeling also varies according to the characteristics of the surrounding area. The combination of dense vegetation, topographical variations, high humidity, remote locations, and wildlife interference makes the Amazon rainforest a particularly challenging environment for wireless signal propagation. This environmental diversity represents a challenge for planning systems to design and deploy IoT applications efficiently. Without understanding the appropriate channel model, it is difficult to analyze coverage and predict optimal deployment configurations.

Empirical propagation loss models in different outdoor environments have been proposed in [7–9], acknowledging that the type of terrain significantly interferes with signal propagation and the importance of accurate models to assist in decision-making for the wireless sensor networks' (WSN) deployment. Therefore, outdoor environments with heterogeneous vegetation have the special characteristic of acting as spreaders of electromagnetic waves. The excessive spread attenuates the signal, limiting the performance expected for 5G mobile wireless communications [10].

Works such as [11–13] mentioning the use of machine learning (ML) techniques to predict propagation loss has been progressively growing. The use of ML techniques to model the wireless signal channel improves the propagation loss prediction in different environments. However, to use ML models, it is necessary to realize data acquisition, which will be employed to train different models. In addition, to the best of the authors' acknowledge, few are the works that collect data to represent signal propagation in an Amazon wooded environment, as seen in [14–19].

In this context, this research aims to develop an ML model that represents the channel behavior in an Amazon wooded environment. For this purpose, a measurement campaign was conducted in the Camilo Vianna forest, located within the Federal University of Pará (UFPA). Furthermore, the developed ML model was compared with classical models present in the literature to verify the model quality.

Thus, the main contributions of this research are as follows:

- Extensive measurements in the Amazon environment with the transmitter at different heights: 6 m (tree trunk level), 12 m (beginning of the tree canopy), and 18 m (middle of the tree canopy);
- Analysis of signal propagation in the Amazon environment considering different polarizations of the transmitting and receiving antennas, vertical–vertical (VV) and horizontal–horizontal (HH);
- Analysis of the RSSI (received signal strength indication) and SNR (signal-to-noise ratio) variation for Amazonian environments;
- Calculation of coefficients, Alpha and Beta, for the Floating Intercept (FI) model and Path Loss Exponent (PLE) for the Close-In (CI) considering the frequency of 915 MHz for environments with heterogeneous and dense vegetation;
- Development of two ML models using a general regression neural network (GRNN) and a multilayer perceptron neural network (MLPNN), based on data measured in a densely wooded scenario.

The rest of this article is organized as follows. Section 2 discusses with details the related works showing the main works with propagation in wooded environments and addresses ML-based propagation models. Section 3 describes the materials and methods used in this research. Section 4 presents the main empirical propagation models, used to compare with the proposed model. Section 5 explains the machine learning techniques employed in this work. Section 6 details the evaluation of the results found by this work. Finally, Section 7 provides the conclusions of the research and suggest future works.

2. Related Works

The performance of LoRa technology in both indoor and outdoor environments has been the subject of various research studies. However, there is a limited number of articles specifically addressing LoRa in vegetated environments. The authors in [20] explore LoRa performance in a unique environment, namely the ISTAC-IIUM Campus, featuring a row of five palm trees. Utilizing different spreading factors (SF7-SF12) at 868 MHz, 125 KHz bandwidth, and a transmission power of 14 dBm, the study measures the received signal strength indication (RSSI). It highlights factors impacting LoRa propagation through vegetation, including diffraction, foliage scattering, and reflection, emphasizing the importance of considering these aspects to optimize LoRa performance in vegetated areas and overcome associated challenges.

The article [21] presents a study about LPWAN for smart agriculture applications, evaluating the performance of LoRa transmission technology operating in the 433 MHz and 868 MHz bands, intended for wildlife monitoring in a forested vegetation area. The study analyzed signal-to-noise ratio (SNR), RSSI, and packet delivery rate (PDR), showing that the stability of the LoRa signal significantly depends on the environment and is more stable in less dense forest environments than in highly dense forest environments. Furthermore, it suggests future research regarding the study of environmental impact, considering atmospheric conditions (humidity, pressure, rainfall, etc.), LoRa performance, and proposing a suitable propagation model for forested environments based on the obtained results.

Aiming to obtain a suitable propagation model for vegetated environments, the article [22] investigates the use of empirical propagation models in precision agriculture. Models such as the Free Space Path Loss (FSPL) for large-scale loss in free space, the Flat Earth (FE) model, and vegetation models like Weissberger, ITU-R, FITU-R, and COST235 are explored in a simulation, assuming flat terrain greenhouse with an area of 100 m × 100 m and operation frequency of 2.5 GHz. The study considers variations in antenna heights, distance between transceivers, and vegetation depth to predict signal propagation loss. At the end of the simulation, the study explains that propagation losses decrease with great antenna heights and increase with large distances between transceivers and deeper vegetation. The total loss is calculated as the sum of free space loss and vegetation loss in greenhouse-style environments.

The article [23] proposes a method to improve the accuracy of path loss for wireless communication in a mountainous forest area called Takakuma at Kagoshima University, Tarumizu City, southern Japan, at an elevation of 2000 m. The devices operate at a frequency of 920 MHz, SF12, transmission power of 13 dBm, a bandwidth of 400 KHz, and monopole antennas with vertical polarization at heights of 2 m and 2.5 m for the receiver and transmitter, respectively. This method divides the total distance between the transmitter and receiver into two parts: one is the total transmission distance through the forest, and the other is the total distance considering free space. Subsequently, it calculates the path losses for the forested area and the open space, and then sums them to obtain the total path loss. Finally, the study compares the proposed method with five literature models Weissberger, ITU-R, FITU-R, LITU-R, and COST235, and concludes that the proposed method exhibits a reasonable level of path loss accuracy in mountainous forest environments and has the potential to enhance the accuracy of wireless communication in such environments.

In [24], the behavior of wireless channels at frequencies of 433 MHz and 2.4 GHz is investigated, considering the effects of distance and antenna height on signal strength and packet loss rate in agricultural areas. The study compares modified models of exponential decay for vegetation environments, including Weissberger, ITU-R, and COST235, along with a linear logarithmic model, through Matlab simulations. An ideal fitting model, namely the parametric exponential decay model (OFPED), is obtained. Measurements are conducted in a wheat field using Zigbee technology, with a transmission power of 0 dBm and a 4 dB gain omnidirectional antenna. RSSI and Packet Loss Rate (PLR) are obtained at different distances from the transceivers and various heights of the transmitter and receiver antennas, considering three stages of wheat growth. The findings reveal that the RSSI decreases as the distance from the transceiver increases, and the PLR increases with the distance from the transceiver. Additionally, path loss decreases with increasing antenna height, and the path loss at 2.4 GHz is higher than that at 433 MHz. Finally, the validation results indicate that modified exponential decay (MED) models can be used as conservative upper and lower limits for path loss, at least for the wheat field.

In [25], the study focuses on deploying WSN in high grass environments. Received signal strength (RSS) measurements were collected on an 80 m $\times$ 80 m high grass farm, where the transmitter and receiver were always in line-of-sight (LOS). The transmission antenna was placed at the center of the grassy area, and the receiving antennas were positioned at eight different distances. These antennas' height was 20 cm, with omnidirectional radiation patterns. Data collection was carried out at a frequency of 1925 MHz, at a total of 128 measurement points, with 300 RSS samples collected at each point. As a result, it was possible to propose an empirical propagation loss model for this type of scenario, which was compared to classical models such as FSPL and Two-Ray Ground, both of which were less accurate in predicting RSS in high grass environments.

The article [26] provides a systematic literature review of propagation models for WSN in vegetated environments, including references to articles such as [20,22–25]. The review indicates that, from 2011 to 2021, Zigbee technology was preferred for such environments, but currently, the use of LoRa technology is on the rise. Furthermore, the article suggests employing techniques not previously used in wireless communication propagation studies in these scenarios, such as machine learning.

In addition, the article [27] provides an overview of recent developments in radio wave propagation modeling using ML algorithms. It emphasizes the importance of selecting the appropriate ML method for the propagation model accuracy and notes the significant number of propagation modeling articles that have utilized artificial neural networks (ANNs). The article anticipates a further growth in this trend, highlighting the challenges, prospects, and open issues in this research direction.

Some related articles cited, such as [28], employ the back-propagation (BP) neural network to predict the received signal power in a suburban environment. This model is based on field measurements obtained from the base station (BS) and the receiver (Rx), including information on topography, frequency, transmitted power, antenna angle, and received power at all locations. The results demonstrate that the proposed model accurately predicts the received signal power for this type of environment.

The article [29] uses a combination of three techniques: multidimensional regression based on ANN, analysis of variance based on Gaussian process, and feature selection aided by principal component analysis (PCA), and path loss data measured in a suburban area in Korea are used. The collected data show that the proposed combined path loss and shading model is more accurate and flexible compared to the conventional log-normal path loss model. The article [11] presents a study on the prediction of digital terrestrial television (DTT) coverage using ML regression techniques, through electric field intensity measurements in eight DTT channels operating in the city of Quito in Ecuador, showing the efficiency of using ML in this application.

Furthermore, the article [30] conducted measurements in Cyprus considering six transceiver BSs, at frequencies of 433 MHz and 2.4 GHz. The mobile devices used in these field measurements were Sony Z2 phones equipped with TEMS for measuring received power and other key performance indicators (KPIs) of the investigated network. The mobile device's height was 1.5 m, with an average propagation distance of around 3.0 km and a specified measurement time of about 60 s on average. The aim was to investigate the impact of the plants' height and antenna height, at various stages of plants growth, on signal propagation through RSSI and PLR analysis. From these data, two ML models are proposed: the radial basis function neural network (RBFNN) and the multilayer perception neural network (MLPNN), compared with the following empirical models: free space, COST231 Hata, ECC-33, Ericsson, and ITU-R, through the metrics RMSE, MAPE, MAE, and R^2, showing that RBFNN performed better than MLPNN and predicts the loss propagation closest to the measured data with minimal error.

As can be seen in the works cited above, none of them addressed the analysis of the transmission and reception antennas matching polarizations. Moreover, the works do not analyze the different heights of the transmitter in environments with dense vegetation, relating the transmitter height to different parts of the trees. Furthermore, although some already employ machine learning techniques, none of them use a general regression neural network (GRNN).

Therefore, from this overview of related works, it is noted that this research uses an trending approach, as it presents two neural network models, GRNN and MLPNN, using LoRa technology at the frequency of 915 MHz and considering the co-polarization of antennas, both transmitter and receiver, in Amazonian forest environments, to predict RSSI and SNR with greater accuracy.

3. Materials and Methods

The methodology applied in this research is divided into the following stages: data collection (RSSI, SNR, and geolocations) related to signal transmission in an area of dense vegetation, followed by data pre-processing to handle and apply the proposed ML techniques for RSSI and SNR prediction. Subsequently, propagation loss is calculated according to the flowchart in Figure 1.

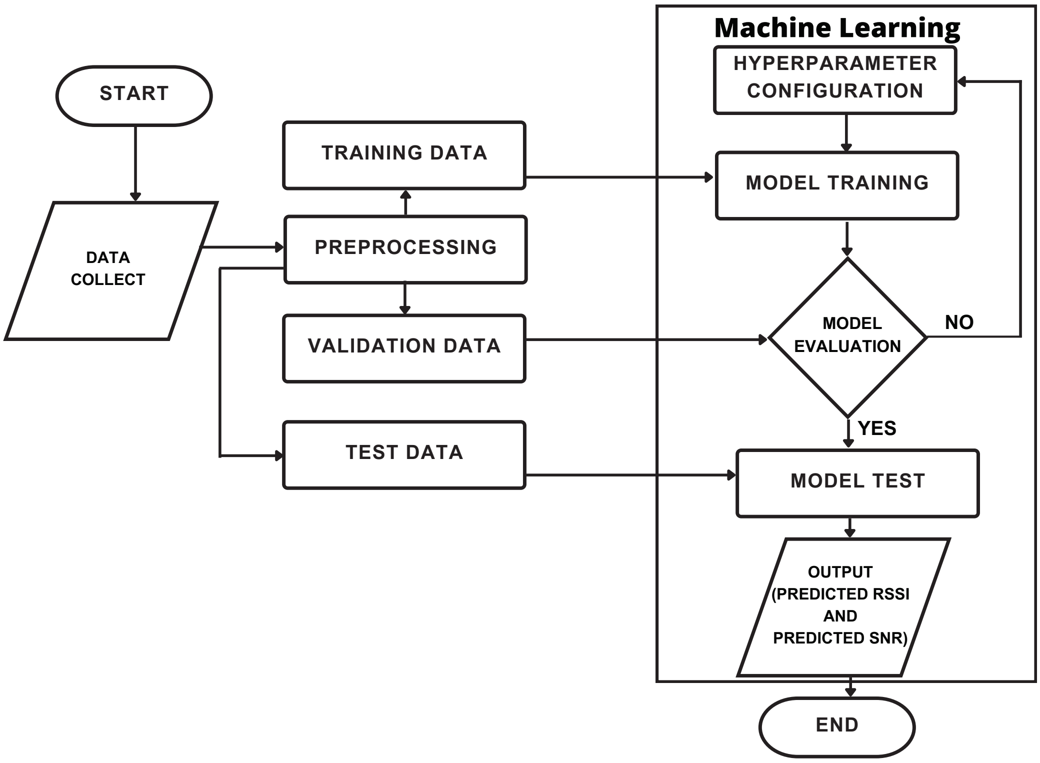

Figure 1. Flowchart of the applied methodology.

3.1. Description of the Measurement Campaign

This section will present the methodology applied for data collection of the wireless signal in a wooded scenario, describing the devices and configurations for transmitting the LoRa signal. This will take into account the distance between Tx-Rx, Tx height, and detailing the pre-processing steps of the data obtained.

3.1.1. Scenario

The measurements were conducted in Belém, Pará, at the campus of the Federal University of Pará (UFPA). The University City contains small forests formed by native species with tree, shrub, and forage vegetation. Among these forests, the Camillo Vianna forest or Pau-Mulato forest, which occupies an area of 16.700 m^2, was chosen due to the presence of several specimens of Pau-Mulato trees, a typical Amazonian tree [31], as shown in Figure 2.

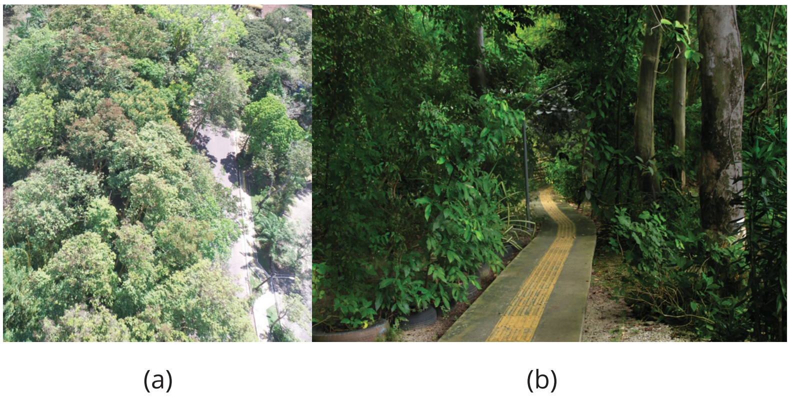

Figure 2. Measurement scenario Camilo Vianna forest (UFPA): (**a**) Aerial view of the Amazon rainforest grove. (**b**) Path of the tree-lined corridor traversed for data collection within the grove.

3.1.2. Equipment Setup and Configuration

For the data collection, three sets of LoRa Dragino shields were used. The shields were coupled to an arduino and used the chip sx1276 from SEMTECH and monopole and omnidirectional antennas [32]. At transmission, a 9 V battery is used, and at reception two smartphones are used to power the circuit and record the transmission log. Table 1 shows the parameters used in measurements and Figure 3 shows the equipment.

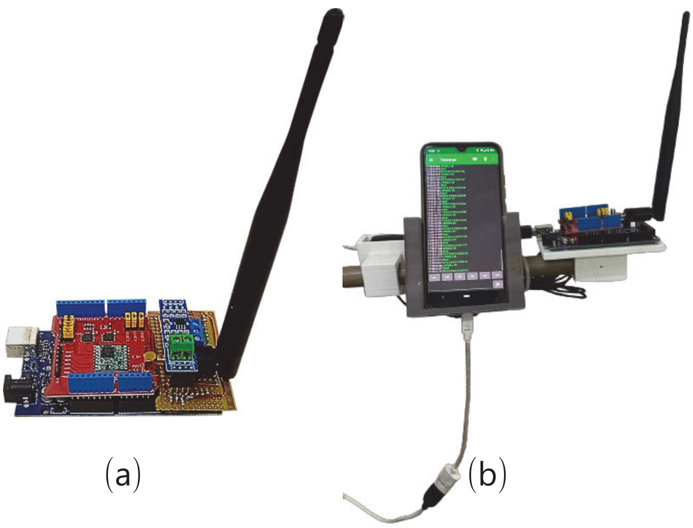

Figure 3. Transmission and reception equipment: (**a**) Arduino Uno module + Dragino 915 MHz LoRa module + omnidirectional antenna. (**b**) Arduino Uno module + Dragino 915 MHz LoRa module + omnidirectional antenna + GPS + smartphone.

Table 1. Configuration of the measurement setup parameters.

Operating Frequency	Effective Radiated Power	Spreading Factor	Bandwidth	Coding Rate
915 MHz	5 dBm	12	125 KHz	4/5

The equipment settings shown in Table 1 were chosen for the following reason. The lowest feasible transmit power of 5 dBm was chosen to preserve the device energy, allowing for more measurements to be taken before battery recharging. Moreover, this approach minimizes potential interference with the animals' natural habitat and aligns with our sustainability goals.

In addition, the bandwidth of 125 kHz and the coding rate of 4/5 were selected because they are the standard for LoRa devices in the AUS915-928 region [33]. Moreover, the 915 MHz frequency was chosen for our study because it is part of the ISM (Industrial, Scientific, and Medical) band allocated for such unlicensed communication purposes in Brazil.

Finally, the SF determines the transmission rate and the sensitivity of the LoRa receiver. For densely wooded environments, SF12 is an ideal option for several important reasons. Firstly, trees and other types of dense vegetation act as physical obstacles that can weaken and attenuate the radio signal. A high SF offers a greater communication range. In addition, the high SF spreads the LoRa signal over a wider bandwidth, which increases the signal's resilience and extends the transmission range [34].

3.1.3. Measurement Methodology

The measurements were based on the transmission and reception of the signal, with the transmitter mounted on a DJI Inspire 1 drone located outside the forest at different heights (6 m, 12 m, and 18 m) and the receivers mounted on a pole with a height of 2 m, being moved by a person walking inside the forest. Both transmitter and receivers had antennas in both vertical and horizontal polarizations, as illustrated in Figure 4.

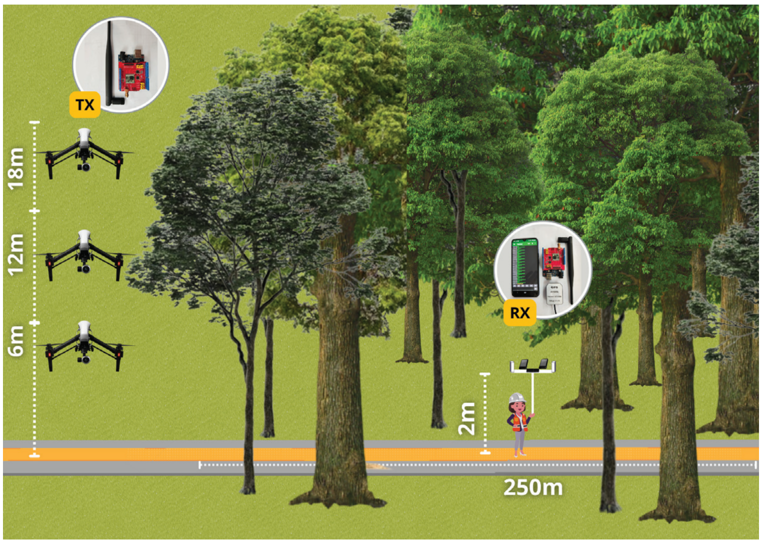

Figure 4. Measurement methodology scenario.

Considering the morphology of the forest, predominantly composed of the Pau-Mulato tree species, a typical tree of the Amazon [35] has an average height of 24 m. The transmitter heights were defined at 6 m (tree trunk level), 12 m (beginning of the tree canopy), and 18 m (middle of the tree canopy). The aim was to analyze the influence of transmitter heights and antenna polarizations in the forest. Table 2 shows all possible combinations of transmission and reception parameters.

Table 2. Configuration corresponding to the measurement methodology.

SF	Heights	Antenna Polarization
12	6 m 12 m 18 m	VV HH

Given that there are one SF, three heights, and two polarizations in a non-line-of-sight (NLOS) scenario, six combinations were tested. For each combination, the 250 m route inside the forest was traveled six times, totaling 36 repetitions of the same route. Approximately 4.525 samples were collected in total, averaging about 358 samples per route, which corresponds to approximately one sample every 2 m while walking at an average speed of approximately 1.67 m/s. Each sample comprised latitude and longitude values, RSSI, and SNR.

3.2. Data Processing

Data processing consists of a set of techniques and steps applied to improve, organize, clean, and transform raw data to be analyzed. In addition, it helps to identify and correct errors, noise, and missing values in the data. Furthermore, data processing also addresses the integration and combination of data from different sources, allowing one to create a unified and coherent dataset.

In this research, to carry out data processing, the rule 3-sigma ($3 - \sigma$) was used to identify and remove outliers. This rule uses three times the standard deviation value from the mean (μ) in a window of 25 samples, sliding this window through the series of measurements. The values $\mu + (3 \cdot \sigma)$ and $\mu - (3 \cdot \sigma)$ define the upper and lower limits of outliers detection [36].

3.2.1. Distance Calculation

The distance calculation of latitude and longitude using the Haversine equation is a fundamental tool in the field of geolocation and navigation. The Haversine equation is a mathematical formula that allows for estimating the distance between two points on the Earth's surface, considering their location in terms of latitude and longitude coordinates. This equation takes into account the curvature of the Earth and considers the average radius of the planet to calculate the distance on a sphere. Equation (1) calculates the distance between two geolocations [19]:

$$D_r = \sqrt{\left(2r \cdot arcsin\left(\sqrt{sin^2\left(\frac{\varphi_2 - \varphi_1}{2}\right) + cos\varphi_1 cos\varphi_2 sin^2\left(\frac{\lambda_2 - \lambda_1}{2}\right)}\right)\right)^2 + h^2} \quad (1)$$

where D_r represents the distance between Tx-Rx, r is the average radius of the Earth (e.g., approximately 6371 km); φ_1 and λ_1 are the latitude and longitude coordinates of the first point, respectively; φ_2 and λ_2 are the latitude and longitude coordinates of the second point, respectively; h is the height difference between Tx and Rx relative to the ground.

3.2.2. Propagation Loss Calculation

The expected signal power (ESP) according to [37] is defined as the signal power at the receiver Equation (2):

$$ESP_{(dB)} = RSSI_{(dBm)} + SNR_{(dB)} - 10 \cdot log_{10}^{\left(1+10^{\frac{SNR_{(dB)}}{10}}\right)} \quad (2)$$

Thus, we can calculate the propagation loss using the link balance Equation (3), as follows:

$$PL_{(dB)} = P_{Tx(dBm)} + G_{(dBi)} - ESP_{(dB)} \quad (3)$$

ESP is the expected signal power at a certain point in dB; P_{Tx} is the power transmitted by the gateway in dBm; G is the sum of the transmission and reception gains, usually in dBi, and finally, PL represents the propagation loss of the signal in dB.

4. Empirical Propagation Models

In this section, we will describe the empirical models from the literature used in this work for comparison with the ML models.

4.1. Floating–Intercept Model (FI)

The floating–intercept (FI) propagation model, also known as the alpha–beta (AB) model, does not have parameters based on physical fundamentals. It utilizes curve-fitting factors calculated by the minimum mean square error (MMSE) method. The model has been adopted by the 3rd Generation Partnership Project (3GPP) and the WINNER II association, which provide standard propagation models. The 3GPP and WINNER II models are widely used in the industry as they cover various types of scenarios. However, they are only used for frequencies below 6 GHz and need to be enhanced for higher frequency bands [38].

For this reason, the FI model has been extensively studied. It can be used to characterize millimeter-wave frequencies, where channels may be in line-of-sight or non-line-of-sight environments [38,39]. The equation of the FI model is given in (4):

$$PL_{FI(dB)} = \alpha + 10\beta log_{10}\left(\frac{d}{d_0}\right) - X_{\sigma FI} \tag{4}$$

In which α is the floating intercept coefficient in dB, known as the offset, β is the slope of the line, d is the distance between the antennas in meters, and $X_{\sigma FI}$ is the slow fading variable, which describes large-scale signal fluctuations over the average path loss, with zero mean and standard deviation σ. The values of α and β are calculated by MMSE to minimize the value of $X_{\sigma FI}$ [40]. A dataset obtained from measurements is necessary to compute the path loss values. The coefficients are then obtained from these values using established formulas [38] that minimize the standard deviation.

The FI model can be further expanded into another model known as ABG (alpha–beta–gamma), which adds another fitting parameter for frequency. Like the FI model, it has no physical anchoring and provides a curve that best fits the dataset across multiple frequencies simultaneously.

4.2. Close-in Model (CI)

This path loss model is referenced as the Free Space Path Loss ($FSPL$) provided in the equation and parameterized by the model parameter "n", also known as the Path Loss Exponent (PLE) [41]. In this model, the PLE is modeled through MMSE [40], aiming to minimize the standard deviation (σ) between the Path Loss and the measured data. This model has been used for frequencies on the order of gigahertz (GHz), and it is based on the fundamental principles of propagation, linked to the Friis and Bullington formulas related to Free Space Path Loss ($FSPL$) [38]. While the FI model uses constants based on curve fitting, the CI model has the $FSPL$ as a physical anchor, ensuring a fixed and continuous relationship between transmitted power and distance. Its equation is given in (5):

$$PL^{CI}(f,d) = FSPL(f,d_0) + 10nlog_{10}\left(\frac{d}{d_0}\right) + X_{\sigma}^{CI} \tag{5}$$

In which d is the distance between the antennas in meters, n is the path loss exponent, which typically has values less than 2 in indoor environments with line-of-sight, and X_{σ} represents large-scale shadowing. The $FSPL(f,d_0)$ is defined as follows:

$$FSPL(f,d) = 10nlog_{10}\left(\frac{4\pi d_0}{\lambda}\right)^2 \tag{6}$$

where λ is the wavelength, and the distance d_0 is equal to 1 m, as it is a reference adopted in various models capable of providing a standardized modeling approach.

4.3. Empirical Models for Vegetation

The article [42,43] shows the most commonly used propagation models in vegetated environments for planning and deploying WSNs. These models exhibit high efficiency in path loss estimation, along with low mathematical complexity. They are known as the "Modified Exponential Decay Model (MED)" due to their format:

$$Att_{MED} = x f^{y} d^{z} \tag{7}$$

where Att_{MED} is the attenuation in dB added by vegetation on top of the Free Space Path Loss (FSPL), f is the frequency in GHz for the Weissberger model and in MHz for the other models, d is the depth distance into the vegetation in meters, and x, y, and z are parameters that should be adjusted based on measurements taken in each scenario where their use is required, as stated in [38].

4.3.1. Weissberger Model

This model is applicable in situations where wireless signal propagation occurs in wooded environments, and the distance between the transmitting and receiving antennas must be up to 400 m, in the frequency range from 230 MHz to 96 GHz [44]. Its equation for calculating excess loss, added to the free space loss, is given by:

$$Att_{WEIS} = \begin{cases} 1.33 \times f^{0.284} \times d^{0.588}, se & 14\text{ m} < d < 400\text{ m} \\ 0.45 \times f^{0.284} \times d, se & 0\text{ m} < d < 14\text{ m} \end{cases} \tag{8}$$

where

- Att_{WEIS} is the excess attenuation according to the Weissberger model (dB);
- d is the distance between Tx and Rx (m);
- f is the system's operating frequency (MHz).

4.3.2. ITU-R Model

This model became known as the Early ITU model, proposed by the International Telecommunication Union (ITU) based on measurement campaigns in 1988. It is valid for frequencies between 200 MHz and 95 GHz and for distances between the transmitting and receiving antennas of less than 400 m [45]. Its equation for calculating excess loss, added to the free space loss, is given by (9):

$$Att_{ITU-R} = 0.2 \times f^{0.3} \times d^{0.6}, \qquad d < 400\text{ m} \tag{9}$$

- Att_{ITU-R} is the excess attenuation according to the ITU-R model (dB);
- d is the distance between Tx and Rx (m);
- f is the system's operating frequency (MHz).

4.4. COST 235 Model

This model distinguishes between wooded environments with the presence of leaves and those without. In this study, the equation with the presence of leaves is considered [44]. The equations for calculating excess loss added to the free space loss are given by:

$$Att_{COST} = \begin{cases} 26.6 \times f^{-0.2} \times d^{0.5}, se & sem folhas \\ 15.6 \times f^{-0.009} \times d^{0.26}, se & com folhas \end{cases} \tag{10}$$

- Att_{COST} is the excess attenuation according to the COST235 model (dB);
- d is the distance between Tx and Rx (m);
- f is the system's operating frequency (MHz).

4.5. Fitted ITU-R (FITU-R) Model

This model, originated as an enhancement of the ITU-R model, introduced the concept of differentiating prediction model equations based on the seasonality experienced by vegetation [44]. In this study, the equation with the presence of leaves is considered. The equations for calculating excess loss added to the free space loss are as follows:

$$Att_{FITUR} = \begin{cases} 0.37 \times f^{-0.18} \times d^{0.59}, se \quad semfolhas \\ 0.39 \times f^{-0.39} \times d^{0.25}, se \quad comfolhas \end{cases} \tag{11}$$

- Att_{FITUR} is the excess attenuation according to the FITU-R model (dB);
- d is the distance between Tx and Rx (m);
- f is the system's operating frequency (MHz).

5. Machine Learning (ML) Techniques

According to [46], ML techniques can be classified into supervised and unsupervised. Supervised techniques are the most commonly used and are associated with data pairs (x, y), where x is the input to the ML model mapped to a specific output y, unlike unsupervised techniques where only the input x is known. In this research, two supervised ML techniques, MLPs and GRNNs, were used.

5.1. Multilayer Perceptrons (MLPs)

MLPs are an artificial neural network architecture composed of multiple layers of neurons, which are basic processing units. These networks are designed to solve complex classification and regression problems and are known for their ability to handle nonlinear data [47].

The main characteristic of MLPs is the presence of one or more hidden layers, situated between the input layer and the output layer. Each layer consists of interconnected neurons, where the connections between neurons have associated weights. These weights are adjusted during the network training process to optimize performance and enhance accuracy [47].

MLPs are capable of learning from examples provided during training. Data propagation occurs directly from the input layer to the output layer through a weighted linear combination of input values and synaptic weights. Subsequently, the output undergoes a nonlinear activation function, introducing nonlinearity into the network and enabling it to learn complex relationships among the data.

During the training process, synaptic weights are adjusted using learning algorithms such as back-propagation, which calculate the error between the network outputs and expected values, and iteratively update the weights to minimize this error. Once the network has been trained, it can be used to make predictions or classify new input examples. Through the process of forward propagation, the network performs a series of mathematical operations and neuron activations, processing the input data and generating a final output [47].

MLPs are widely used in areas such as pattern recognition, natural language processing, computer vision, and many other applications involving analysis and learning from complex data. Their ability to learn and generalize from examples makes them powerful models for classification and regression problems.

Many tests were conducted considering different ANN topologies to determine the best network. The test considered neuron numbers from 1 to 30 in the hidden layer, and for each neuron in the hidden layer the test was repeated for 100 different random seeds. Finally, the topology with one hidden layer with 24 neurons yielded the best accuracy, as seen in Figure 5.

Figure 6 represents the MLP neural network modeled for this research, in which the input layer has three neurons, which represent the distance between the transmitter (Tx) and the receiver (Rx) in meters (m), the heights of the Tx, 6, 12, and 18, in meters (m) and the co-polarizations of the transmitting and receiving antennas (VV and HH), with sigmoid function in the hidden layer and linear activation function for the output layer.

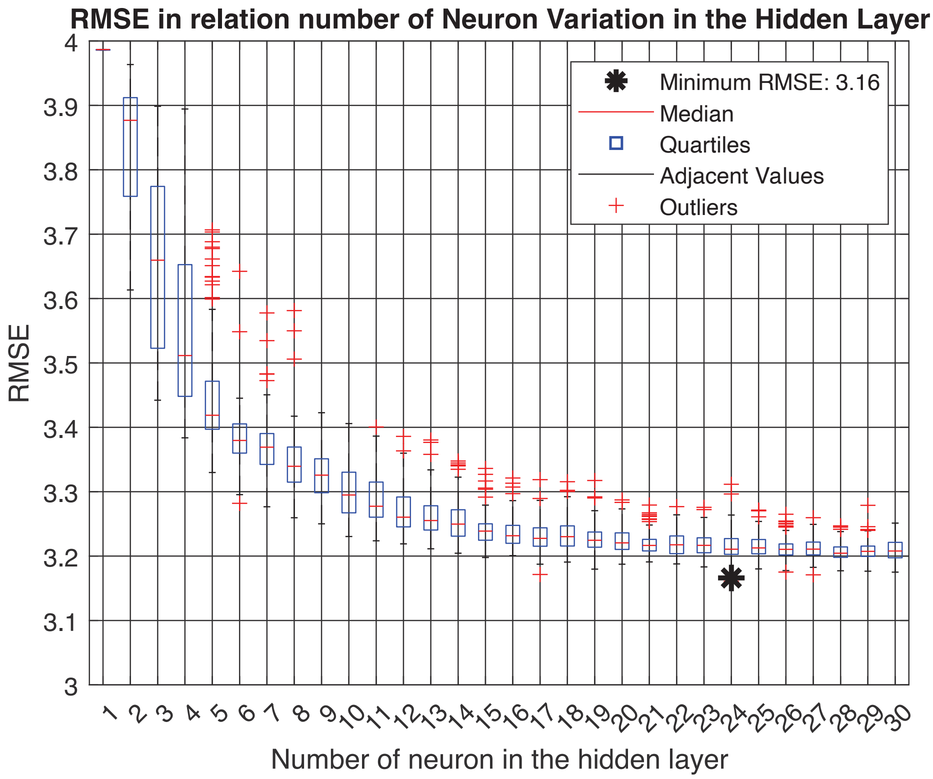

Figure 5. RMSE in relation to the number of neurons in the hidden layer.

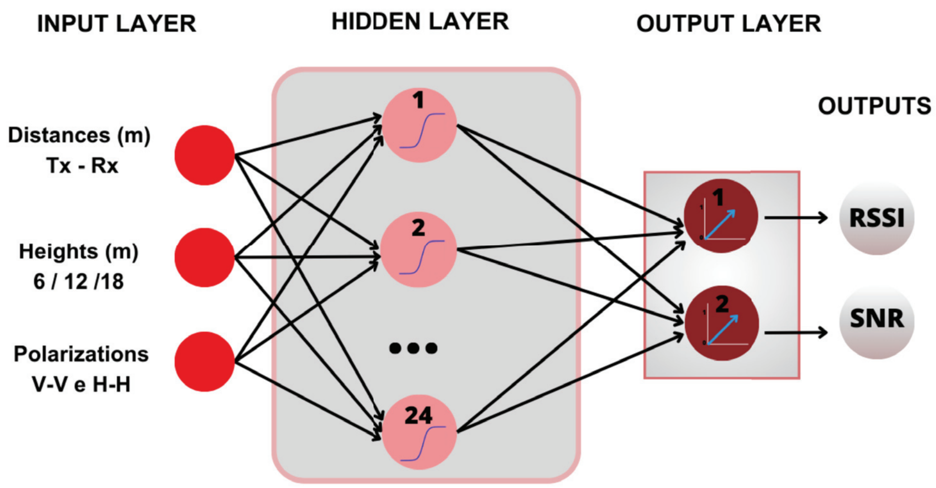

Figure 6. MLP network implemented.

5.2. General Regression Neural Network (GRNN)

The general regression neural network (GRNN) is a type of artificial neural network developed to solve regression problems, i.e., predict continuous values in response to a set of input variables. The GRNN was originally proposed by Donald F. Specht in 1991 as an extension of the probabilistic classification algorithm called probabilistic neural network (PNN) [48].

GRNN is a feedforward neural network that stands out for its simplicity and ease of implementation. It is a variant of the RBF network, which uses radial basis functions to perform interpolation and extrapolation of data and consists of four main layers: the input layer, the pattern layer, the summation layer, and the output layer [48].

In the input layer, the input variables are normalized and provided as input to the network. Then, in the pattern layer, the network compares the input patterns with stored training patterns. These training patterns consist of the input and corresponding output values' combination. Each training pattern has an associated activation function that measures the similarity between the input pattern and the training pattern. Typically, the Gaussian activation function is used where the output is a measure of the distance between the input pattern and the training pattern.

The summation layer receives the activation values calculated in the pattern layer and performs a weighted sum of these values. The weights associated with the activation values are determined by the Gaussian activation function, which assigns a higher weight to training patterns closer to the input pattern.

Finally, the output layer combines the outputs from the summation layer to generate a final response, which is the value predicted by the GRNN. The output is calculated by the patterns layer's output values' weighted average, where the weights are determined by the Gaussian activation function.

One of the advantages of GRNN is its ability for fast and efficient learning. Once the network is trained with corresponding input and output patterns, it can rapidly predict output values for new input patterns without the need for an iterative process of weight adjustment [48].

Additionally, the GRNN is known for being a robust neural network capable of handling noise and incomplete data. It also has a low number of hyper-parameters. In this case, it had only one, the smooth parameter, which for this model was set to 0.0039, making it easier to implement and adjust.

However, it is important to note that the GRNN may be more suitable for simple regression problems with a limited number of input variables. For more complex problems or large datasets, other neural network architectures such as deep neural networks may be more appropriate.

Figure 7 represents the architecture of the GRNN used in this research, considering the same inputs as the MLP and also predicting RSSI and SNR as output.

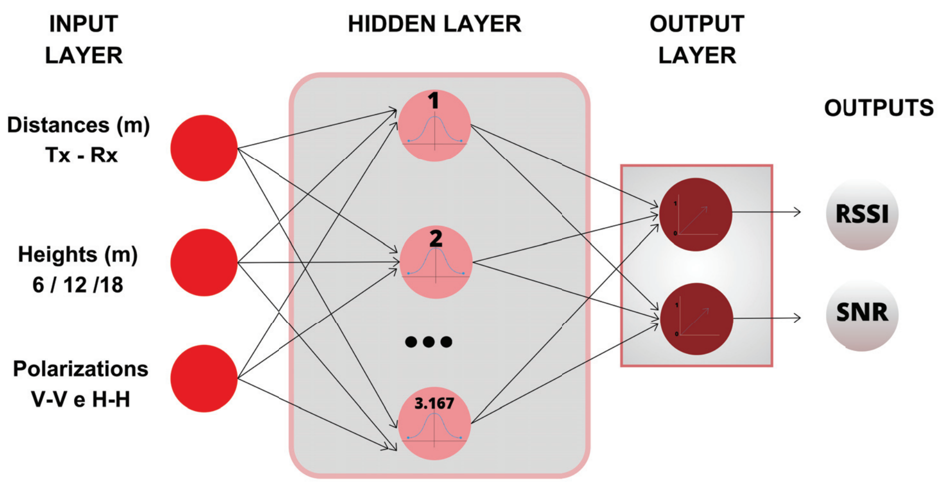

Figure 7. GRNN network implemented.

5.3. Dataset

The dataset used for implementing both techniques, MLP and GRNN, consists of 4525 samples distributed across three randomly generated datasets: the training set containing 3167 points, which corresponds to 70% of the total data; and the validation set and the test set, each containing 679 points, amounting to 30% of the total samples, as shown in Table 3.

The training process involves presenting a pattern to the input layer units, where the units compute their response and present it to the output layer to obtain the network answer. Then, the error is computed and propagated from the output layer back to the input layer, and the weights of the connections in hidden layer units are adjusted, gradually decreasing the error to achieve the best generalization rate of the MLP. In the supervised training of the MLP, the Levenberg–Marquardt algorithm was used.

Table 3. Splitting the dataset.

Sample Set	Number of Samples	% in Relation to the Total
Training	3167	70%
Validation	679	15%
Test	679	15%

6. Results

In this section, the results obtained in the typical Amazonian forest, where the vegetation has an average height of 24 m, and the transmitter heights are defined at 6 m (tree trunk), 12 m (beginning of the tree canopy), and 18 m (mid-canopy), will be presented. The influence of these antenna's heights and polarizations in signal propagation will be analyzed; following this, comparisons will be made between the proposed RNA-based models with other propagation loss models such as CI, FI, Weissberger, Early ITU-R, Cost235, and FITU-R models, aiming to demonstrate the efficiency of using ML techniques such as MLP and GRNN in estimating propagation loss in wooded environments.

6.1. Analysis of the Influence of Heights and Polarizations in Densely Wooded Environments

Wireless communication in densely vegetated environments has been gaining increasing importance due to applications such as environmental monitoring, fire prevention, and search and rescue systems. However, dense vegetation, especially tree canopies, can cause signal attenuation and interference, making it essential to properly select the polarization and height of the transmitter to improve the reliability and quality of transmissions.

Wireless signal transmissions in such environments pose unique challenges, where the proper choice of electromagnetic wave polarization can significantly affect transmission performance in this scenario. This section explores the effectiveness of HH (horizontal transmitted and horizontal received) and VV (vertical transmitted and vertical received) polarizations at different heights relative to transmissions at both trunk and canopy levels of trees.

The choice of microwave polarization (such as HH and VV) at different heights of transmissions below tree canopies is related to the interaction of electromagnetic waves with vegetation. This interaction can vary depending on the structure and density of the vegetation, as well as the characteristics of the waves used.

The relationship between RSSI and SNR in LoRa technology is that RSSI provides information about the overall signal strength, while SNR complements this information by indicating the signal quality relative to background noise. To obtain a more comprehensive and accurate view of the LoRa communication link quality, it is important to consider both parameters. In some LoRa implementations, SNR may be more significant in determining data reception capability than RSSI, especially in environments with high noise or interference.

Figure 8 illustrates the measurement points which are in the middle of a dense forest. The transmitter is at the beginning of the way and has a static longitude and latitude; in contrast, the receiver varies in longitude and latitude since it is moving across the way. Figure 8a,b show the RSSI and SNR values, respectively. A detailed analysis of RSSI and SNR according to the transmitter height is below.

According with Figure 9, the lowest value for RSSI with vertical polarization is -133 dBm and the highest value is -75 dBm; on the other hand, for horizontal polarization, the lowest value is -135 dBm and the highest value is -75 dBm. In addition, it can be seen that the RSSI values are similar for both polarizations; however, RSSI values for VV show higher values, especially for distances greater than 150 m.

Additionally, four VV RSSI values show a decreasing trend around 20 dB each 100 m. For HH, the decrease in RSSI values is around 25 dB each 100 m. This means that the forest plays a significant attenuation role, even over short distances.

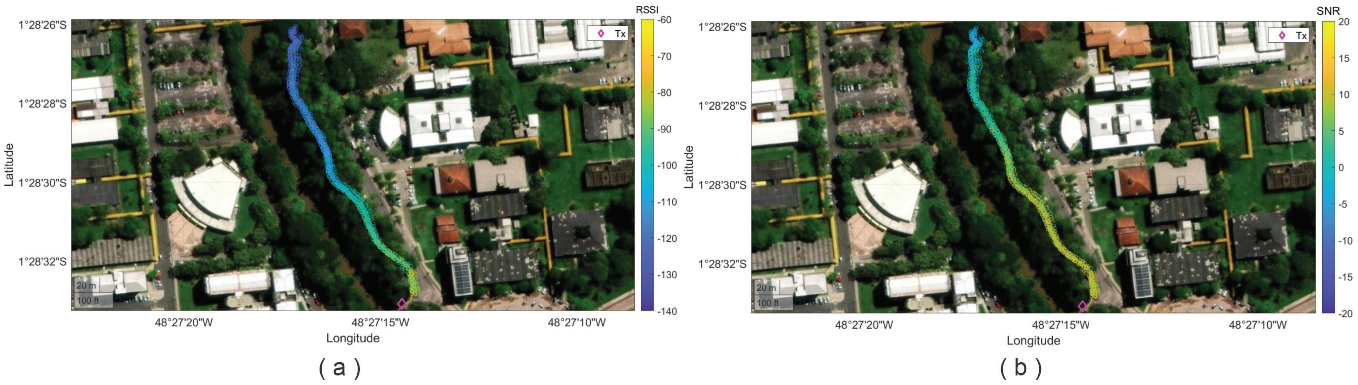

Figure 8. (**a**) The collected GPS data corresponding to RSSI levels vs. distance in the studied environment. (**b**) The collected GPS data corresponding to SNR levels vs. distance in the studied environment.

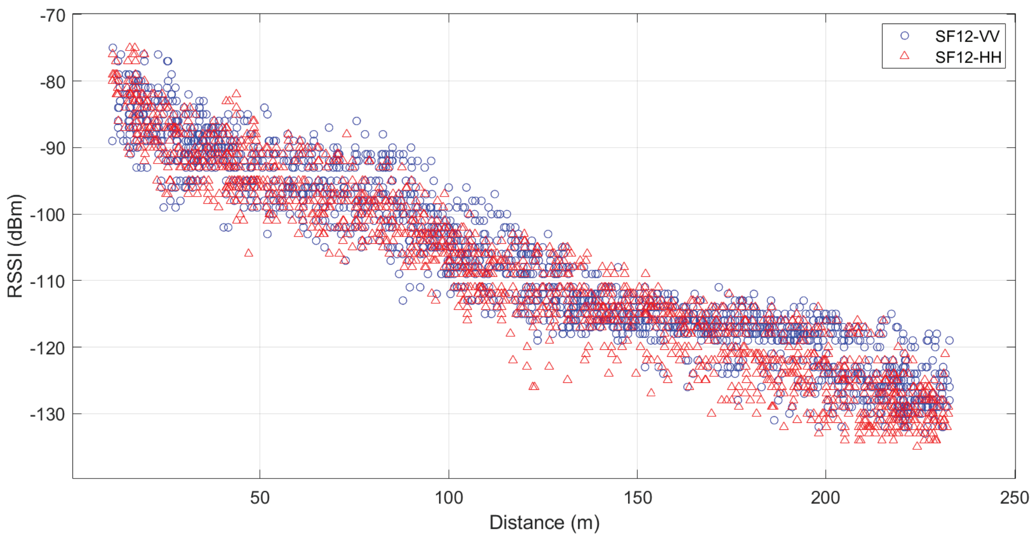

Figure 9. Distribution of the measured RSSI data with respect to distance for SF12 at all heights for HH and VV polarizations.

Figure 10 shows that the minimum SNR for HH is −13, and for VV is −9, the maximum value for HH is 13, and for VV it is 14. Also, the SNR for both polarizations begins decreasing for distances greater than 100 m for SF12 at all heights. However, VV polarization has a stronger and better signal quality in a densely wooded environment, which means that the signal RSSI is stronger relative to the noise, resulting in better communication performance. Additionally, when observing the variations in RSSI and SNR values with distance, it is noted that the forest environment affects both RSSI and SNR even at short distances.

In summary, according to Figures 9 and 10, it can be observed that VV polarization performs better in transmission compared to HH polarization for all heights. Furthermore, in all these situations, it is observed that RSSI exhibited a linear behavior, and SNR exhibited an exponential behavior for a distance over 250 m.

Analysis of RSSI and SNR Values with Respect to Heights

The results of RSSI and SNR for SF12 in densely wooded environments for IoT networks in the 915 MHz frequency band are presented and analyzed for each height. A new graph that condenses the information of RSSI, mean, and standard deviation values for fixed distance intervals is presented to make it easy to compare for different heights and polarizations. The mean and standard deviation are calculated considering all RSSI values contained within the distance interval covered by a sliding window.

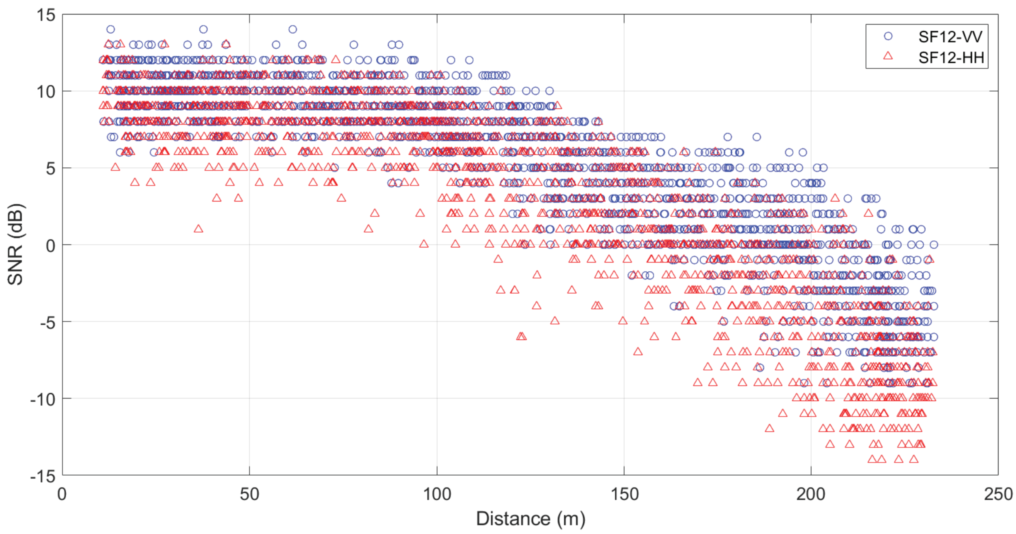

Figure 10. Distribution of the measured SNR data with respect to distance for SF12 at all heights for HH and VV polarizations.

The RSSI and SNR values along the traveled path are displayed for the SF12 combination heights of 6, 12, and 18 m in Figures 11 and 12. First, while analyzing the horizontal antenna polarization (HH), for a height of 6 m, where the transmitter is located at the tree trunk level, it can observed that the RSSI values range from −131 to −80 dBm , while the SNR ranges from −8 to 11 dB.

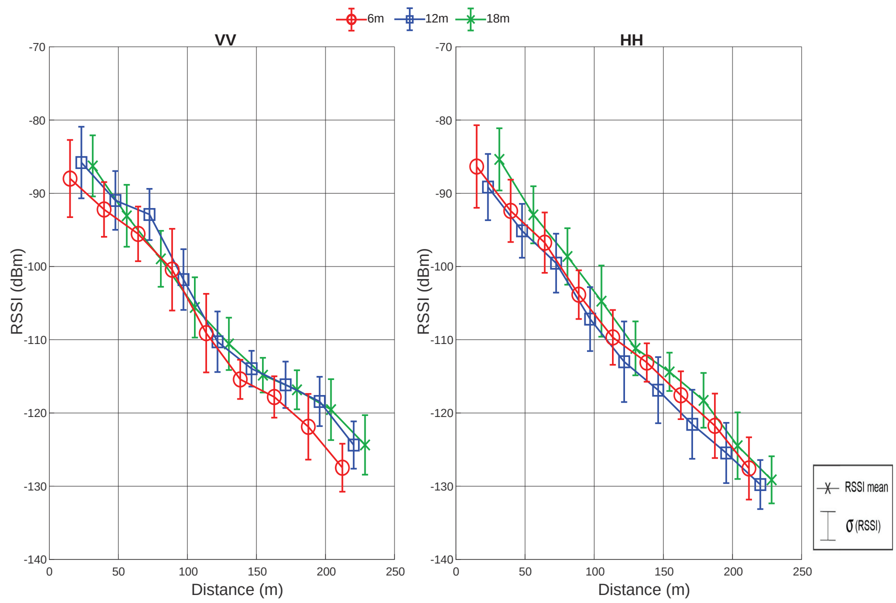

Figure 11. Analysis of the mean and standard deviation values of RSSI for SF12 at all heights and for VV and HH polarizations.

At a height of 12 m, corresponding to the beginning of the tree canopy , the RSSI values range from −133 to −85 dBm, while the SNR ranges from −11 to 8 dB. Finally, at a height of 18 m, corresponding to the middle of the tree canopy, the RSSI values range from −132 to −82 dBm, while the SNR ranges from −12 to 8 dB.

Analyzing the vertical antenna polarization (VV), the RSSI and SNR values at a height of 6 m range from −131 to −83 dBm and from −7 to 12 dB, respectively. At a height of 12 m, the RSSI values are in a range from −128 to −81 dBm, and the SNR values are in a range from −3 to 11 dB. Finally, for a height of 18 m, the RSSI values are in a range from −129 to −82 dBm, and the SNR values are in a range from −5 to 10 dB.

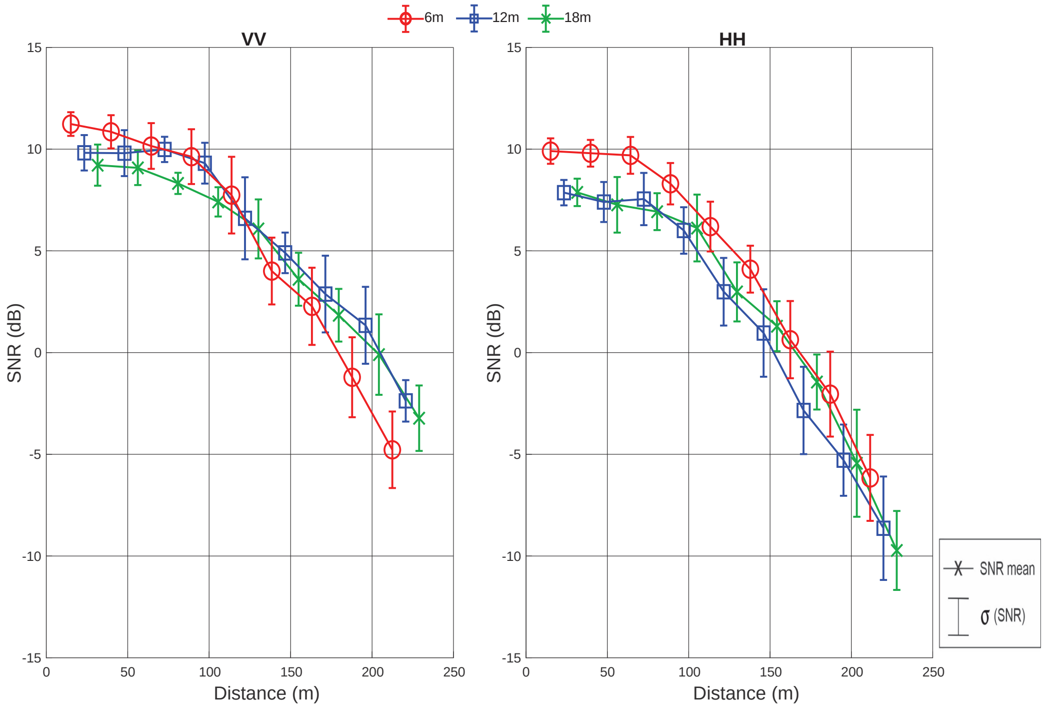

Figure 12. Analysis of the mean and standard deviation values of SNR for SF12 at all heights and for VV and HH polarizations.

From Figures 11 and 12, it is possible to observe that the VV polarization presents RSSI and SNR values similar to the HH polarization. However, the decay in the VV signal level over the distance is smaller compared to the HH signal. In addition, analyzing Table 4, it can also be verified that, on average, the lowest value of VV polarization (at a height of 18 m) shows a result practically equal to the highest value of HH polarization (at a height of 6 m).

Table 4. Statistical metrics of the collected signal.

Height	σ-RSSI (dBm)		Mean RSSI (dBm)		σ-SNR (dB)		Mean SNR (dB)	
	HH	VV	HH	VV	HH	VV	HH	VV
6 m	14.84	16.62	−107.24	−105.76	6.68	6.93	4.32	5.36
12 m	14.86	15.01	−111.09	−106.24	6.87	5.13	1.16	5.10
18 m	15.91	14.90	−108.76	−107.31	7.22	5.96	1.08	4.28

In summary, when placing the transmitter at heights of 12 and 18 m, corresponding to the beginning and middle of the leaves, respectively, a worse SNR is observed. Therefore, what most affects the signal quality in a wooded environment are the leaves. Furthermore, analyzing the mean values of RSSI and SNR for each situation, it is observed that, as the heights increase, the mean values of both RSSI and SNR decrease, as shown in Table 4.

6.2. Adjustments to CI and FI Propagation Models

The values of PLE and the coefficients alpha (α) and beta (β) are crucial for improving the accuracy of signal propagation predictions in real environments, which enhances the performance of wireless networks in vegetated areas. All values of PLE for the CI model and the coefficients (α and β) and initial distance (d_0) for the FI model are displayed in Table 5.

Table 5. Adjusted coefficient values for FI and CI.

SITUATIONS	FI (d_0 (m)|α|β)	CI (PLE)
SF12-6 m-HH	10.92|69.02|4.98	3.93
SF12-6 m-VV	10.92|68.29|4.91	3.85
SF12-12 m-HH	17.32|76.56|5.87	4.15
SF12-12 m-VV	12.45|68.34|4.79	3.73
SF12-18 m-HH	14.13|71.43|5.66	4.08
SF12-18 m-VV	12.47|73.30|4.71	3.86

According to the values of FI(β) and CI (PLE), at a height of 6 m (tree trunk), the propagation loss for both VV and HH polarizations is similar. However, at heights of 12 m (beginning of the tree canopy) and 18 m (middle of the tree canopy), the VV polarization has the lowest decay with distance.

6.3. Evaluation of the Proposed Propagation Models Based on Artificial Neural Networks (ANNs)

The proposed models use three input variables: distance (5 to 250 m), transmitter height (6, 12, and 18 m), and the co-polarization of the transmitting and receiving antennas (HH-VV). To evaluate the accuracy and precision of the proposed models, two metrics were applied: root mean square error (RMSE) and standard deviation (σ).

RMSE measures the square root of the squared errors' average between the values predicted by the model and the measured values. Its goal is to predict a continuous numerical value, such as propagation loss in a wireless communication system. The RMSE is calculated using Equation (12) [49]:

$$RMSE = \sqrt{\frac{1}{n}\sum_{i=1}^{n}(y_i - \hat{y}_i)^2} \tag{12}$$

in which $\sum$ indicates the sum of all elements for each sample i, y_i represents the actual observed value in sample i, $\hat{y}_i$ represents the value predicted by the model for the $i - th$ sample, and n is the total number of samples or observations in the dataset.

The σ is a measure of dispersion or variability in the data relative to the mean. In simple terms, it tells us how far the values are from the mean. The standard deviation is calculated using the Formula (13) [50]:

$$\sigma = \sqrt{\frac{\sum_{i=1}^{n}(x_i - \bar{x})^2}{n}} \tag{13}$$

in which $\sum$ indicates the sum of all elements, x_i is the individual value in the dataset, $\bar{x}$ is the mean of the values, and n is the total number of examples.

The importance of standard deviation in the evaluation of RNA-based propagation loss models is related to its ability to show us the variability of observed propagation loss values. The smaller the standard deviation, the more consistent and accurate the results predicted by the model.

To properly evaluate an RNA-based propagation loss model, it is essential to consider both RMSE and standard deviation. RMSE provides a general idea of the model's predictions accuracy, while the standard deviation helps to understand the variability in the data and the prediction's reliability across different scenarios.

Furthermore, it is important to emphasize that the choice of evaluation metrics also depends on the context and specific requirements of the problem at hand. For example, in critical applications such as communication systems, it is essential to have propagation loss prediction models with high accuracy and low standard deviation to ensure the proper performance of the system.

The obtained results were close in terms of performance, as shown in Figure 13, and the MLP responses, represented by the red x, are close to GRNN responses, represented by the black square. Moreover, the RMSE of 3.86 for the GRNN and 3.8614 for the MLPNN suggests that both networks were able to effectively capture patterns in the data and generalize to new samples. This closeness in results may also indicate that the problem is relatively well-behaved and that both networks are providing consistent and accurate solutions.

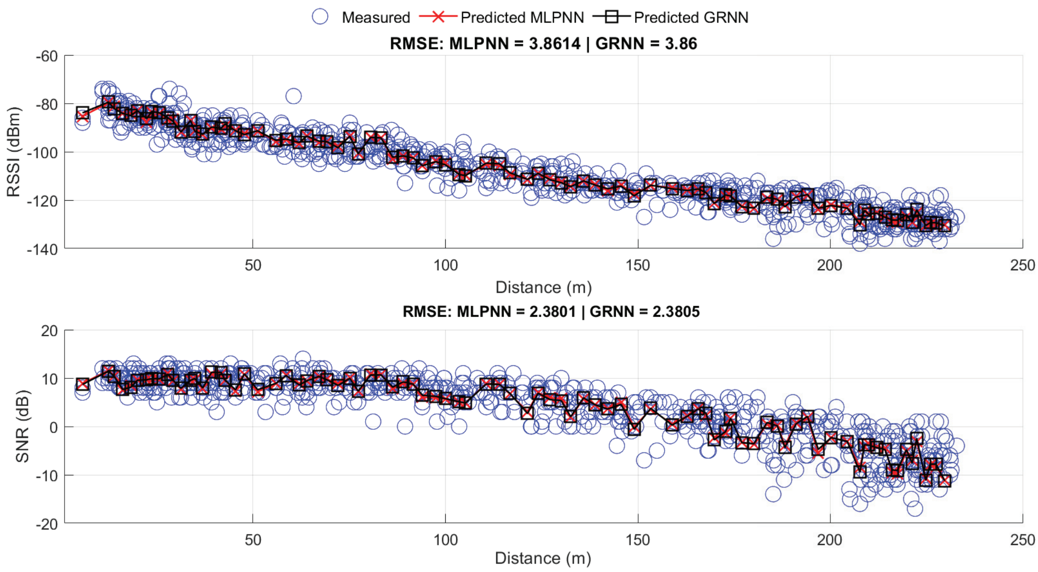

Figure 13. Measured data and prediction of MLPNN and GRNN.

Table 6 shows the values of the evaluated metrics. It can be observed that both ANNs were very close in terms of accuracy and precision. However, regarding training time, the GRNN was approximately 82% faster than the MLPNN. Both were trained using a notebook equipped with a Core i5 12500H processor. The advantage of the GRNN in requiring lower computational cost is an important characteristic to consider, especially when addressing large volumes of data or when optimizing available resources.

Table 6. Evaluation metrics for the ANNs.

ANNs	RMSE	σ	Training Time (s)
GRNN	3.8600	3.8558	0.3634
MLPNN	3.8614	3.8564	2.0839

6.4. Comparison with Propagation Loss Models from the Literature

The results presented by the proposed RNA-based models for densely forested environments for IoT networks in the 915 MHz frequency range were compared with empirical models CI and FI, as well as with models adapted for vegetated environments, namely Weissberger, Early ITU-R, Cost235, and FITU-R.

Figure 14 shows the comparison of the proposed RNA-based models and vegetation-adapted models to the measured data for a height of 6 m VV. As seen in Figure 13, the

MLPNN and GRNN models better represented the average behavior of the measured data, obtaining RMSE and standard deviation values that were similar and lower than the other analyzed models. This is due to RNA-based propagation models being able to estimate the variability in propagation loss more accurately at a single point, as well as representing the signal behavior in the studied environment.

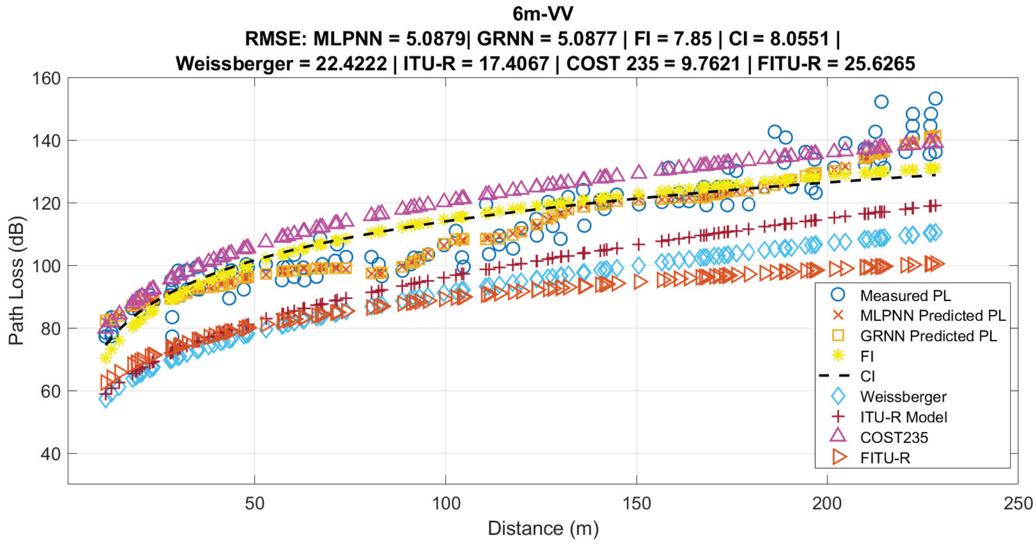

Figure 14. Propagation loss models and applied and proposed MLPNN and GRNN models.

The other empirical propagation models obtained higher RMSE and standard deviation values than the proposed models. In particular, the FI and CI models, which were adjusted according to the measured data using the linear least squares technique, showed higher RMSE values. However, the FI model performed slightly better than the CI model, as it considers the measured initial point as its own reference, while the CI model considers the value of FSPL as the initial reference point.

For the propagation loss models in vegetated environments, the one that best represented the measured data was COST235, followed by ITU-R, Weissberger, and finally the FITU-R model. The FITU-R model performs better than the ITU-R and Weissberger models up to the first 50 m. The comparisons of propagation models, through the RMSE and σ metrics, for the other heights and polarizations, are presented in Table 7.

Table 7. Results of the propagation models' comparison.

Type	Metrics	GRNN	MLPNN	CI	FI	WEISSB.	ITU-R	COST 235	FITU-R
SF12-6 m-HH	RMSE	3.46	3.39	7.83	7.69	22.12	16.90	9.91	25.70
	σ	4.21	4.14	7.86	7.73	6.51	6.17	17.23	9.30
SF12-6 m-VV	RMSE	4.12	4.11	8.05	7.85	22.42	17.40	9.76	25.62
	σ	4.97	4.96	8.08	7.88	6.95	6.46	18.73	9.95
SF12-12 m-HH	RMSE	4.11	4.19	8.11	7.84	26.70	21.30	7.83	30.40
	σ	5.71	5.80	8.15	7.89	7.35	6.73	17.77	10.21
SF12-12 m-VV	RMSE	3.66	3.61	7.44	7.42	19.59	14.50	11.75	23.32
	σ	4.29	4.24	7.45	7.45	6.09	6.35	16.00	8.16
SF12-18 m-HH	RMSE	4.01	4.04	9.38	8.53	23.99	18.43	10.01	28.26
	σ	5.30	5.31	9.41	8.58	8.20	7.30	19.13	11.48
SF12-18 m-VV	RMSE	3.82	3.86	7.24	7.10	21.42	16.21	10.10	25.10
	σ	5.11	5.16	7.27	7.13	6.22	6.12	16.72	8.77

7. Conclusions

This work aimed to develop two propagation models using machine learning techniques, MLPNN and GRNN, for densely forested environments at a frequency of 915 MHz, and to evaluate them in relation to measured data and existing models in the literature. To achieve this, an extensive measurement campaign was conducted in the Camillo Vianna forest, located within the Federal University of Pará, which features various tree species, predominantly the Pau-Mulato type.

In this measurement campaign, data related to geolocation, RSSI, and SNR were collected along a 250 m path. Subsequently, there was a need for data processing, such as calculating the distance using geolocations and calculating propagation loss using RSSI and SNR data.

Furthermore, artificial neural networks (MLPNN and GRNN) were trained, in addition to the application of least squares technique to adjust the CI and FI propagation models. The objective was to predict the average behavior of signal propagation and evaluate them in relation to the measured data. Subsequently, they were compared with models adapted for vegetation (ITU-R, Weissberger, COST235, and FITU-R).

Thus, the proposed propagation models, MLPNN and GRNN, achieved better accuracy and precision, with RMSE values of 3.8614 and 3.86, and standard deviation values of 3.8564 and 3.8558, respectively, for RSSI. In addition, for the SNR prediction, the RMSE values were 2.3801 and 2.3805, and the standard deviation values were 2.3788 and 2.3798, respectively.

The results show the models' ability to learn from data and capture nonlinear relationships. This ability allows these models to achieve greater predictive capability of the average signal behavior compared to classical models in the literature.

The satisfactory results obtained by the MLPNN and GRNN ANNs in modeling propagation loss indicate that both are viable options for this regression task. With minimal difference in the RMSE results, the choice between the two can be guided by training speed and resource demand, with the GRNN having an advantage in these aspects.

While the CI and FI models performed overall better than vegetation-adapted propagation models, it is worth noting that both were adjusted with measured data from the environment, as shown in Table 5. As for models adjusted for vegetated environments, the COST235 propagation model generally better fitted the measured data than other vegetation models.

Another significant contribution of the work was the analysis regarding heights and co-polarizations. The appropriate choice of electromagnetic wave polarization for wireless signal transmissions in vegetated environments is crucial to optimize the efficiency and reliability of communications. This research demonstrated that VV polarization is more suitable for all heights. Understanding these differences allows for the design of more efficient and resilient communication networks, contributing to advancements in monitoring and research applications in densely forested environments. Finally, another contribution was calculating the values of PLE, α, and β for the study environment, as shown in Table 5.

For future work, the intention is to analyze the impact of spreading factor, and consequently, the bit rate, as the two are directly related. Also, analyze the heights higher than 18 m and lower than 6 m to quantify the impact of dense vegetation on electromagnetic signals. To examine the cross-polarizations of transmitter and receiver, antennas for different heights need to be used in order to understand which polarization type experiences less loss through the forest. Additionally, due the propagation loss imposed by vegetation on transmission across these various scenarios, the intention is to utilize other machine learning techniques (such as ANFIS) and statistical metrics (including MAE, MPE, MAPE, and GRG-MAPE), as well as employ the ITU-R P.1546-6 model as it is the new extension of the 1546 model for distances shorter than 1000 km.

Author Contributions: Conceptualization, B.S.d.S.B., J.P.L.d.A., F.J.B.B. and G.P.S.C.; Methodology, B.S.d.S.B., H.A.O.C., J.P.L.d.A., F.J.B.B. and G.P.S.C.; Software, B.S.d.S.B., H.A.O.C., F.C.F. and J.P.L.d.A.; Validation, B.S.d.S.B., H.A.O.C., J.P.L.d.A. and F.J.B.B.; formal analysis, B.S.d.S.B., J.P.L.d.A., F.J.B.B. and G.P.S.C.; Investigation, B.S.d.S.B., H.A.O.C., C.M.M.C., A.S.M. and F.J.B.B.; data curation, B.S.d.S.B., H.A.O.C., C.M.M.C. and F.C.F.; writing—original draft, B.S.d.S.B., H.A.O.C., A.S.M. and J.P.L.d.A.; writing—review and editing, B.S.d.S.B., A.S.M., H.A.O.C., C.M.M.C., L.E.C.E., J.P.L.d.A. and F.J.B.B.; Visualization, B.S.d.S.B., L.E.C.E., A.S.M., H.A.O.C., J.P.L.d.A. and F.J.B.B.; Supervision, J.P.L.d.A., G.P.S.C. and F.J.B.B.; project administration, J.P.L.d.A., G.P.S.C. and F.J.B.B.; funding acquisition, B.S.d.S.B., J.P.L.d.A., G.P.S.C. and F.J.B.B. All authors have read and agreed to the published version of the manuscript.

Funding: The authors would like to thank LCT (Computer and Telecommunications Laboratory) members, PROPESP/UFPA, CAPES, and CNPq for the support given to the research.

Institutional Review Board Statement: Not applicable.

Informed Consent Statement: Not applicable.

Data Availability Statement: The authors reserve the right not to disclose the private dataset used in this study.

Conflicts of Interest: The authors declare no conflict of interest.

Abbreviations

The following abbreviations are used in this manuscript:

UFPA	Federal University of Pará
LOS	Line-of-sight
NLOS	Non-line-of-sight
IOT	Internet of Things
LoRA	Long Range
MMSE	Minimum mean square error
RMSE	Root mean squared error
WSNs	Wireless sensor
5G	Fifth generation
ML	Machine learning
RNAs	Artificial neural networks
SF	Spreading factor
GRG-MAPE	Maximization of gray relationship degree and mean absolute percentage error
UAVs	Unmanned aerial vehicles
LoRaWan	Long range wide area network
SNR	Signal-to-noise ratio
Tx	Transmitter
Rx	Receiver
VV	Vertical–vertical
HH	Horizontal–horizontal
PLE	Path loss exponent
FI	Floating intercept
CI	Close in
RSSI	Received signal strength indicator
GRNN	General regression neural network
MLPNN	Multi-layer perceptron neural network

References

1. Alwis, C.D.; Kalla, A.; Pham, Q.V.; Kumar, P.; Dev, K.; Hwang, W.J.; Liyanage, M. Survey on 6G Frontiers: Trends, Applications, Requirements, Technologies and Future Research. *IEEE Open J. Commun. Soc.* **2021**, *2*, 836–886. [CrossRef]
2. Gava, M.A.; Rocha, H.R.O.; Faber, M.J.; Segatto, M.E.V.; Wörtche, H.; Silva, J.A.L. Optimizing Resources and Increasing the Coverage of Internet-of-Things (IoT) Networks: An Approach Based on LoRaWAN. *Sensors* **2023**, *23*, 1239. [CrossRef]

3. Abdallah, W.; Mnasri, S.; Nasri, N.; Val, T. Emergent IoT Wireless Technologies beyond the year 2020: A Comprehensive Comparative Analysis. In Proceedings of the International Conference on Computer and Information Technology (ICCIT 2020), Dhaka, Bangladesh, 19–21 December 2020; pp. 2–6.
4. Alobaidy, H.A.H.; Jit Singh, M.; Behjati, M.; Nordin, R.; Abdullah, N.F. Wireless Transmissions, Propagation and Channel Modelling for IoT Technologies: Applications and Challenges. *IEEE Access* **2022**, *10*, 24095–24131. [CrossRef]
5. Zourmand, A.; Hing, A.L.K.; Hung, C.W.; AbdulRehman, M. Internet of Things (IoT) using LoRa technology. In Proceedings of the 2019 IEEE International Conference on Automatic Control and Intelligent Systems (I2CACIS), Selangor, Malaysia, 29 June 2019. [CrossRef]
6. Consultimer Group, (2012–2023). Available online: https://consultimer.com/o-que-e-lora-conheca-a-tecnologia-de-1080 radiofrequencia-de-longo-alcance (accessed on 29 June 2023).
7. Rao, T.R.; Balachander, D.; Kiran, A.N.; Oscar, S. RF propagation measurements in forest & plantation environments for Wireless Sensor Networks. In Proceedings of the 2012 International Conference on Recent Trends in Information Technology, Chennai, India, 19–21 April 2012. [CrossRef]
8. Olasupo, T.; Otero, C.E.; Olasupo, K.O.; Kostanic, I. Empirical Path Loss Models for Wireless Sensor Network Deployments in Short and Tall Natural Grass Environments. *IEEE Trans. Antennas Propag.* **2016**, *64*, 4012–4021. [CrossRef]
9. Cheffena, M.; Mohamed, M. Empirical Path Loss Models for Wireless Sensor Network Deployment in Snowy Environments. *IEEE Antennas Wirel. Propag. Lett.* **2017**, *16*, 2877–2880. [CrossRef]
10. Lopez-Iturri, P.; Aguirre, E.; Celaya-Echarri, M.; Azpilicueta, L.; Eguizábal, A.; Falcone, F.; Alejos, A. Radio Channel Characterization in Dense Forest Environments for IoT-5G. In Proceedings of the 5th International Electronic Conference on Sensors and Applications, online, 15–30 November 2018; MDPI: Basel, Switzerland, 2018. [CrossRef]
11. Moreta, C.E.G.; Acosta, M.R.C.; Koo, I. Prediction of Digital Terrestrial Television Coverage Using Machine Learning Regression. *IEEE Trans. Broadcast.* **2019**, *65*, 702–712. [CrossRef]
12. Alimpertis, E.; Markopoulou, A.; Butts, C.; Psounis, K. City-Wide Signal Strength Maps: Prediction with Random Forests. In Proceedings of the The World Wide Web Conference, San Francisco, CA, USA, 13–17 May 2019; pp. 2536–2542. [CrossRef]
13. Thrane, J.; Zibar, D.; Christiansen, H.L. Model-Aided Deep Learning Method for Path Loss Prediction in Mobile Communication Systems at 2.6 GHz. *IEEE Access* **2020**, *8*, 7925–7936. [CrossRef]
14. Castro, B.S.L.; Pinheiro, M.R.; Cavalcante, G.P.S.; Gomes, I.R.; de O. Carneiro, O. Comparison between known propagation models using least squares tuning algorithm on 5.8 GHz in Amazon region cities. *J. Microwaves Optoelectron. Electromagn. Appl.* **2011**, *10*, 106–113. [CrossRef]
15. Carvalho, A.A.P.d.; Batalha, I.; Alcantara, M.; Castro, B.; Barros, F.; Araujo, J.; Cavalcante, G. Empirical Path Loss Model in City-forest Environment for Mobile Communications. *J. Commun. Inf. Syst.* **2021**, *36*, 70–74. [CrossRef]
16. Castro Eras, L.E.; Nakata da Silva, D.K.; Correia, L.; Brito Barros, F.J.; Leite de Araujo, J.P.; Protasio dos Santos Cavalcante, G. A Radio Propagation Model for a Rainforest–River Environment Using UTD and Geometrical Optics. *IEEE Antennas Wirel. Propag. Lett.* **2022**, *21*, 54–58. [CrossRef]
17. Nakata da Silva, D.K.; Castro Eras, L.E.; Moreira, A.A.; Correia, L.M.; Brito Barros, F.J.; Protásio dos Santos Cavalcante, G. A Propagation Model for Mixed Paths Using Dyadic Green's Functions: A Case Study Over the River for a City–River–Forest Path. *IEEE Antennas Wirel. Propag. Lett.* **2018**, *17*, 2364–2368. [CrossRef]
18. Cruz, H.A.O.; Ferreira, S.C.B.; Araújo, J.P.L.; Barros, F.J.B.; Farias, F.S.; Neto, M.C.A.; Tostes, M.E.L.; Nascimento, A.A.; Cavalcante, G.P.S. Methodology for LoRa Gateway Placement Based on Bio-Inspired Algorithmsfor a Smart Campus in Wooded Area. *Sensors* **2022**, *22*, 6492. [CrossRef] [PubMed]
19. Cardoso, C.M.M.; Barros, F.J.B.; Carvalho, J.A.R.; Machado, A.A.; Cruz, H.A.O.; de Alcântara Neto, M.C.; Araújo, J.P.L. SNR Prediction with ANN for UAV Applications in IoT Networks Based on Measurements. *Sensors* **2022**, *22*, 5233. [CrossRef]
20. Anzum, R. Factors that affect LoRa Propagation in Foliage Medium. *Procedia Comput. Sci.* **2021**, *194*, 149–155. [CrossRef]
21. Ojo, M.O.; Adami, D.; Giordano, S. Experimental Evaluation of a LoRa Wildlife Monitoring Network in a Forest Vegetation Area. *Future Internet* **2021**, *13*, 115. [CrossRef]
22. Sabri, N.; S, M.S.; Fouad, S.; A, S.A.; AL-Dhief, F.T.; Raheemah, A. Investigation of Empirical Wave Propagation Models in Precision Agriculture. *MATEC Web Conf.* **2018**, *150*, 06020. [CrossRef]
23. Myagmardulam, B.; Tadachika, N.; Takahashi, K.; Miura, R.; Ono, F.; Kagawa, T.; Shan, L.; Kojima, F. Path Loss Prediction Model Development in a Mountainous Forest Environment. *IEEE Open J. Commun. Soc.* **2021**, *2*, 2494–2501. [CrossRef]
24. Wu, H.; Zhang, L.; Miao, Y. The Propagation Characteristics of Radio Frequency Signals for Wireless Sensor Networks in Large-Scale Farmland. *Wirel. Pers. Commun.* **2017**, *95*, 3653–3670. [CrossRef]
25. Alsayyari, A.; Aldosary, A. Path Loss Results for Wireless Sensor Network Deployment in a Long Grass Environment. In Proceedings of the 2018 IEEE Conference on Wireless Sensors (ICWiSe), Langkawi, Malaysia, 21–22 November 2018. [CrossRef]
26. Barrios-Ulloa, A.; Ariza-Colpas, P.; Sánchez-Moreno, H.; Quintero-Linero, A.; la Hoz-Franco, E.D. Modeling Radio Wave Propagation for Wireless Sensor Networks in Vegetated Environments: A Systematic Literature Review. *Sensors* **2022**, *22*, 5285. [CrossRef] [PubMed]
27. Seretis, A.; Sarris, C.D. An Overview of Machine Learning Techniques for Radiowave Propagation Modeling. *IEEE Trans. Antennas Propag.* **2022**, *70*, 3970–3985. [CrossRef]

28. Wu, L.; He, D.; Guan, K.; Ai, B.; Briso-Rodriguez, C.; Shui, T.; Liu, C.; Zhu, L.; Shen, X. Received Power Prediction for Suburban Environment based on Neural Network. In Proceedings of the 2020 International Conference on Information Networking (ICOIN), Barcelona, Spain, 7–10 January 2020. [CrossRef]
29. Jo, H.S.; Park, C.; Lee, E.; Choi, H.K.; Park, J. Path Loss Prediction Based on Machine Learning Techniques: Principal Component Analysis, Artificial Neural Network, and Gaussian Process. *Sensors* **2020**, *20*, 1927. [CrossRef] [PubMed]
30. Ojo, S.; Imoize, A.; Alienyi, D. Radial basis function neural network path loss prediction model for LTE networks in multitransmitter signal propagation environments. *Int. J. Commun. Syst.* **2020**, *34*, e4680. [CrossRef]
31. Paiva, B.S.; da Luz, L.M.; da Silva, C.N. Sistemas de Áreas Verdes da Cidade Universitária ProfessorJosé da Silveira Netto, da UFPA, em Belém (PA); v. 25, n. 1, p. 297–323. jan-abr 2022. Available online: https://periodicos.ufpa.br/index.php/ncn/article/view/8988 (accessed on 30 June 2023). [CrossRef]
32. GSM-8696-2.pdf. Available online: https://cdn.sparkfun.com/assets/1/0/d/3/1/GSM-8696-2.pdf (accessed on 20 March 2023).
33. LoRaWAN Regional Parameters RP002-1.0.4. Available online: https://resources.lora-alliance.org/technical-specifications/rp002-1-0-4-regional-parameters (accessed on 20 March 2023).
34. LoRa™ Modulation Basics Note An1200.22. Available online: https://www.semtech.com/uploads/documents/an1200.22.pdf (accessed on 20 March 2023).
35. Stehmann, J.R.; Faria, F.S.; Bragioni, T.L.S. 50 Árvores do Museu. 2019. Available online: http://hdl.handle.net/1843/40587 (accessed on 20 March 2023).
36. Gras López, S. Detection of Unsupervised Anomalies in Light Sensors. Bachelor's Thesis, Universitat Politècnica de Catalunya, Barcelona, Spain, 2023.
37. González-Palacio, M.; Tobón-Vallejo, D.; Sepúlveda-Cano, L.M.; Rúa, S.; Pau, G.; Le, L.B. LoRaWAN Path Loss Measurements in an Urban Scenario including Environmental Effects. *Data* **2022**, *8*, 4. [CrossRef]
38. Sun, S.; Rappaport, T.S.; Thomas, T.A.; Ghosh, A.; Nguyen, H.C.; Kovacs, I.Z.; Rodriguez, I.; Koymen, O.; Partyka, A. Investigation of Prediction Accuracy, Sensitivity, and Parameter Stability of Large-Scale Propagation Path Loss Models for 5G Wireless Communications. *IEEE Trans. Veh. Technol.* **2016**, *65*, 2843–2860. [CrossRef]
39. Maccartney, G.R.; Rappaport, T.S.; Sun, S.; Deng, S. Indoor Office Wideband Millimeter-Wave Propagation Measurements and Channel Models at 28 and 73 GHz for Ultra-Dense 5G Wireless Networks. *IEEE Access* **2015**, *3*, 2388–2424. [CrossRef]
40. Rappaport, T.S.; MacCartney, G.R.; Samimi, M.K.; Sun, S. Wideband Millimeter-Wave Propagation Measurements and Channel Models for Future Wireless Communication System Design. *IEEE Trans. Commun.* **2015**, *63*, 3029–3056. [CrossRef]
41. Macedo, A.; Costa, T.; de Matos, E.; Eras, L.C.; de Araujo, J.; Castellanos, P.V.G.; Barros, F. Channel Analysis for 3.5 GHz Frequency in Airport. *J. Commun. Inf. Syst.* **2023**, *38*, 115–120. [CrossRef]
42. Rappaport, T.S. (Ed.) *Wireless Communications Principles and Practice*; Prentice Hall PTR: Hoboken, NJ, USA, 2002.
43. Ndzi, D.; Munirah Kamarudin, L.; Mohammad, E.; Zakaria, A. Vegetation attenuation measurements and modeling in plantations for wireless sensor network planning. *Prog. Electromagn. Res. B* **2012**, *36*, 283–301. [CrossRef]
44. Silva, J.C.; Siqueira, G.L.; Castellanos, P. Propagation model for path loss through vegetated environments at 700–800 MHz band. *J. Microwaves Optoelectron. Electromagn. Appl.* **2018**, *17*, 179–187. [CrossRef]
45. Carvalho, N.P.; Matos, L.J.; Cataldo, E. Rede Neural Artificial Aplicada na Predição de Cobertura de Sinal em Vegetação. In Proceedings of the XXXVIII Simpósio Brasileiro de Telecomunicações e Processamento de Sinais —-SBrT, Florianopolis, Brazil, 22–25 November 2020. [CrossRef]
46. Murphy, K.P. *Machine Learning a Probabilistic Perspective*; MIT Press: Cambridge, MA, USA, 2012.
47. Haykin, S. *Neural Networks: A Comprehensive Foundation. 1999*; Mc Millan: Haddon Township NJ, USA, 2010; pp. 1–24.
48. Specht, D. A general regression neural network. *IEEE Trans. Neural Netw.* **1991**, *2*, 568–576. [CrossRef] [PubMed]
49. Montgomery, D.C.; Runger, G. *Estatística aplicada e Probabilidade Para Engenheiros*, 5th ed.; Livros Técnicos e Científicos Ltda: Centro Rio de Janeiro, Brazil, 2012.
50. Haykin, S. *Neural Networks and Learning Machines, 3/E*; Pearson Education India: Delhi Noida, India, 2009.

sensors

MDPI

Article

Design and Evaluation of a Low-Power Wide-Area Network (LPWAN)-Based Emergency Response System for Individuals with Special Needs in Smart Buildings

Habibullah Safi [1], Ali Imran Jehangiri [1], Zulfiqar Ahmad [1,*], Mohammed Alaa Ala'anzy [2,*], Omar Imhemed Alramli [3] and Abdulmohsen Algarni [4]

1 Department of Computer Science and Information Technology, Hazara University, Mansehra 21300, Pakistan; habibullah.hairan@gmail.com (H.S.); ali_imran@hu.edu.pk (A.I.J.)
2 Department of Computer Science, SDU University, Almaty 040900, Kazakhstan
3 Department of Networks and Communications, Faculty of Information Technology, Misurata University, Misurata P.O. Box 2478, Libya; omar.alramli@it.misuratau.edu.ly
4 Department of Computer Science, King Khalid University, Abha 61421, Saudi Arabia; a.algarni@kku.edu.sa
* Correspondence: zulfiqarahmad@hu.edu.pk (Z.A.); m.alanzy.cs@gmail.com (M.A.A.)

Abstract: The Internet of Things (IoT) is a growing network of interconnected devices used in transportation, finance, public services, healthcare, smart cities, surveillance, and agriculture. IoT devices are increasingly integrated into mobile assets like trains, cars, and airplanes. Among the IoT components, wearable sensors are expected to reach three billion by 2050, becoming more common in smart environments like buildings, campuses, and healthcare facilities. A notable IoT application is the smart campus for educational purposes. Timely notifications are essential in critical scenarios. IoT devices gather and relay important information in real time to individuals with special needs via mobile applications and connected devices, aiding health-monitoring and decision-making. Ensuring IoT connectivity with end users requires long-range communication, low power consumption, and cost-effectiveness. The LPWAN is a promising technology for meeting these needs, offering a low cost, long range, and minimal power use. Despite their potential, mobile IoT and LPWANs in healthcare, especially for emergency response systems, have not received adequate research attention. Our study evaluated an LPWAN-based emergency response system for visually impaired individuals on the Hazara University campus in Mansehra, Pakistan. Experiments showed that the LPWAN technology is reliable, with 98% reliability, and suitable for implementing emergency response systems in smart campus environments.

Keywords: emergency response; Heltec; WiFi; LoRa 32; IoT; LPWAN; wireless sensor networks

1. Introduction

Throughout history, emergency response systems have been significant in mitigating the negative impacts of natural disasters. Environmental emergencies, such as earthquakes, panic situations, theft, and navigation for the visually impaired, can be particularly challenging [1]. Furthermore, obstacles, including oil spills, chemical spills, attacks, pandemics, nuclear disasters, heavy snowfalls, storms, hurricanes, floods, wild or bush fires, and tsunamis, endanger the safety and welfare of the public at large [2]. Typically, emergency medical services, the fire department, police, and community volunteers initially address these incidents [3]. Effective communication between disaster-stricken areas and disaster management offices is critical, and restoring network services immediately following a disaster is essential for facilitating first responder activities [4]. With the advent of distributed technologies such as the IoT, big data, cloud computing, and 5G cellular networks, the internet has undergone a significant evolution. This transformation has led to the development of cost-effective networks with the capacity to cover large areas. One such network is the Long-Range (LoRa) network, which belongs to the family of low-power wide-area networks (LPWANs) [5,6]. These cutting-edge technologies allow for the placement and maintenance of sensors using a low-power wide-area client, with a maximum range of 30 km in sensor network operational areas [7]. This capability could enable the monitoring of almost all habitable regions without requiring additional management systems. In other words, this can be achieved through device self-communication, such as device-to-device (D2D) and machine-to-machine (M2M) communication technologies. If a mobile device is outside the range of a cellular network, it can communicate using D2D communication with a peer-to-peer wireless communications network. In an emergency, if there is a network connection between the mobile device and the network element, the device sends a message to the network element. If there is no network connection, the device transmits the data to a second mobile device, which connects to a third mobile device using D2D communication [8–10]. In an emergency, time is critical and reliability is paramount. Therefore, it is essential to establish an emergency action plan that ensures the prompt provision of rescue resources. To address the challenges posed by such scenarios, we conducted research into an LPWAN-based emergency response system for people with special needs on smart campuses. The experimental results indicate that LPWAN technology is an effective solution for the implementation of emergency response systems on smart campuses.

LPWAN technology has gained significant attention in scientific communities and industry because of its low power consumption, low cost, and long-range communication capabilities, allowing for reliable communication up to 30 km [7,11]. These features make LPWAN ideal for IoT-based wireless sensor networks (WSNs) that transmit minimal data at low rates over long distances with a radio chipset cost of less than USD 2 and an operating cost of USD 1 per device per year [8,9]. LPWAN technology encompasses various low-powered networks that come in different forms and sizes. The increasing demand for IoT in fields such as emergency response systems for individuals with special needs has driven the development of LPWAN-based solutions that address issues like the limited range, high power consumption, and expensive hardware. To improve the reliability and reduce the latency, we propose an LPWAN-based emergency response system for people with special needs on a smart campus. The "smart campus" concept involves integrating smart technologies with physical structures to expand facilities, make decisions, and ensure campus sustainability. Smart classrooms, facial recognition-based attendance systems, and other small-scale solutions have been implemented on campuses. However, there is still no universal model for smart campuses, and the educational industry continues to benefit from digital technologies and smart applications that control various appliances and networked devices [5,12–14]. The proposed emergency response system can be utilized by anyone, including regular individuals. Our focus on people with special needs, particularly the visually impaired, stems from the recognition that they may encounter more challenges and face higher risks in emergency situations within a smart campus environment.

This research work makes three main contributions:

- We establish a framework for implementing an LPWAN-based emergency response system for people with special needs on smart campuses.
- We deploy Heltec WiFi LoRa 32 devices to improve communication and enable individuals with special needs to exchange information with their family and caregivers regarding their safety in the case of a risky or dangerous situation.
- We evaluate the performance of the proposed framework in terms of the latency and reliability.

The rest of the paper is structured as follows: Section 2 covers the related work. Section 3 highlights the background knowledge of LPWAN technologies. Section 4 explains the system model and design. Section 5 describes the experiments and results. Section 6 presents a discussion on the results, and finally, Section 7 concludes the paper.

2. Related Work

In this section, we provide an overview of existing research related to the LPWAN-based emergency response system proposed in this study.

The incorporation of technology into emergency response systems is important, and the IoT holds significant potential for supplying sensitive information during rescue and relief efforts in the event of natural disasters. While the LPWAN has been successfully integrated into various intelligent environments like smart buildings, banks, agriculture, smart vehicles, traffic management, smart cities, healthcare, and sensitive infrastructure [5,8,9,12–14], its implementation has not been geared toward providing LPWAN-based emergency response systems for individuals with special needs on a smart campus. Furthermore, ad hoc networks have not been utilized to reduce the latency and enhance the reliability. To address these concerns, we propose an LPWAN-based emergency response system that caters to people with special needs on the smart campus, using Hazara University in Pakistan as a case study.

According to research conducted by [15], there are specific requirements for an efficient emergency rescue and response mechanism for oceanic disasters, along with obstacles encountered when attempting to implement disaster management solutions in such situations. The authors suggest an approach based on the IoT that can be integrated with the existing oceanic network architecture to provide contextual information about the fishermen and their vessels. This approach provides partial context-awareness and can help address the challenges. This information can help with search and rescue operations by detecting any unusual activity on the fishing vessels. The study emphasizes the significance of technology acceptance and community participation in successfully adopting such an approach. By leveraging the advantages of the large-scale deployment of IoT solutions, coupled with community involvement, it is possible to bring about positive transformations in the community, which can be extremely beneficial in managing disasters in the ocean.

The authors of [16] suggested a model that employs Dragino shields to implement LoRa wireless communication technology for localization. This model utilizes Arduino microcontrollers to incorporate additional sensing mechanisms, improving the localization accuracy and reducing the power consumption in GPS-less environments. The experiments conducted in outdoor environments yielded positive outcomes, and the low power consumption and easy integration of localized environmental sensory data make LoRa technology a valuable resource for emergency services. In [17], the authors presented a WiFi-enabled microcontroller system that interfaces with several sensors, with the number of sensors scalable but limited by the microcontroller's capabilities. The collected data are stored and visualized using the cloud platform Thinger.io, with endpoints available for sending emails and pushing data to external services. The system also uses the web-based service IFTTT to send alerts with a full emergency response profile to responders during emergency situations. This smart emergency response system is designed for use by individuals such as athletes, people with disabilities, and the elderly. The authors of [18] presented an assistive system called the "Online Blind Assistive System using Object Recognition", which enables individuals with visual impairments to traverse unknown indoor and outdoor areas using an object recognition system. The implementation of a DNN using Python proved to be an accurate tool for object identification. However, the speed of the network may be a potential issue.

In [19], the authors introduced a mobile emergency response system to reduce the response time in the gas and oil industries. Ensuring low latency and robust security measures has been a critical challenge in emergency response, as any delay in the response time may have severe consequences and can also potentially result in data breaches in the case of cyber-attacks or theft. Informing people about emergencies needs to be faster. The authors proposed a method for controlling the motion in SNOW (Sensor Network Over White Spaces) in [20], which is an LPWAN operating in TV white spaces. This LPWAN utilizes Orthogonal Frequency-Division Multiplexing (OFDM) for synchronous communication between a base station and numerous low-power nodes. However, inter-carrier interference (ICI) can be an issue due to the OFDM-based design. Nevertheless, the OFDM-based architecture of SNOW leads to more pronounced inter-carrier interference (ICI). Hence, the authors put forward a solution for handling motion in SNOW to mitigate the impact of ICI and enhance the network's overall functionality. In [21], the authors conducted an investigational analysis to examine the impact of mobility on LPWAN performance in mobile IoT applications. The study revealed that even minor mobility, such as human movement, has a significant impact on LPWANs. The authors found that mobility in various scenarios, such as the gateway's location, the speed of the vehicle, and the placement of the end devices, can have a considerable effect on the LPWAN performance.

In [22], the authors investigated the mobility management of LPWAN systems and proposed a new IPv6-based solution to ensure communication continuity during changes in connection layer technology. This solution enables users to migrate between different LPWA networks and technologies, while optimizing the communication paths and preserving the bandwidth to reduce the data transfer time. The proposed method was validated through simulations and testing of the end-device handovers between LoRaWAN and NB-IoT. To assist first responders, a real-time communication system has been developed [23]. The centralized data hub known as the First Responder Units (FRUs) collects and distributes data from numerous connected peripherals. Additionally, a mobile emergency operations center (MEOC) is equipped and deployed with essential communication tools such as visual display devices and computers to provide support to first responders during their actions. The author of [24] presented the Emergency Communication System (ECS), which uses LoRa technology to provide infrastructure-free phone-based networks with long-range D2D communication. The LOCATE system comprises a mobile application that allows users to input critical emergency-related information and a distribution protocol that delivers emergency requests via multi-hop LoRa networks.

We summarized the related work in Table 1, and based on existing studies, we proposed research that focuses on the integration of IoT technology, particularly LPWANs, into emergency response systems. A specific emphasis is placed on addressing the needs of individuals with special requirements within smart campus environments. While the existing literature highlights the potential of the IoT, including LPWANs, in various sectors, such as disaster management, healthcare, and mobility, few studies have delved into the application of LPWANs for emergency response systems tailored to smart campuses. Prior work has explored diverse aspects of IoT technologies, including LoRa-based communication for localization, assistive systems for the visually impaired, and real-time communication systems for first responders.

Smart campus emergency response systems for individuals with special needs are worth considering to promote quality education for individuals with special needs by ensuring their safety and well-being. Several solutions have been proposed to address such problems, but many of these solutions come with significant limitations:

- IoT-Based Emergency Response Systems: Existing studies have discussed the potential of IoT technologies in emergency response systems. These networks have a significant role in the response and coordination of relief efforts for emergencies by using sensors, actuators, and communication networks. Nevertheless, IoT-based systems will have pros and cons, such as real-time monitoring and alerts, but they will also experience problems of scalability, reliability, and interoperability. In addition, IoT deployment and maintenance can be a burden and a challenge to the implementation of the technology, which may, in turn, hamper its acceptance, especially when resources are scarce.
- LPWAN-Based Solutions: The characteristic of LPWAN (Low-Power Wide-Area Network) technologies including LoRaWAN and NB-IoT is their long-distance data transmission with low power consumption, which makes them attractive to use. LPWAN-based emergency response systems can be considered a better solution as they are characterized by wide-range coverage and low energy consumption, which makes them suitable for a smart campus environment. However, they may be constrained by

several problems, like network congestion, latency, and data throughput, particularly in areas with a high density of inhabitants and when there is a high demand.

- Assistive Technologies for Special Needs Individuals: Several efforts have been undertaken to design user-friendly and individualized assistive devices that can serve people who have disabilities, such as those with visual impairments. This technology, in the form of wearable devices, mobile applications, or sensory aids, is aimed at improving accessibility and safety. On the other hand, assistive technologies may be disadvantageous in terms of the usability, affordability, and compatibility with the existing infrastructure.
- Real-Time Communication Systems: During times of emergencies, real-time communication systems will allow the quick sending of critical data for the first responders and the people who are affected. The existing networks are often wirelessly linked via mobile apps and centralized data hubs in order to provide communication and coordination. Instant communication systems do provide quick response features, but they may also have some challenges, such as network congestion, privacy risks, and dependence on the internet, which can be interrupted during emergencies.
- Localization and Tracking Solutions: Localization and tracking technologies such as GPS and RFID can locate the position of individuals in the event of an emergency. Thus, the optimal use of resources and the best way of organizing the evacuation can be ensured. However, GPS-less environments or poor GPS reception may pose limitations to the indoor localization technologies, which might negatively affect their accuracy and reliability.

The existing studies primarily focus on specific applications or technical aspects, whereas our research aims to bridge the gap by proposing and evaluating an LPWAN-based emergency response system specifically designed for smart campuses, with a particular focus on addressing the needs of visually impaired individuals.

Table 1. An overview of related works.

Reference	Contributions	Limitations
[15]	The authors implemented a partial context-aware algorithm to manage emergencies in the ocean by detecting any atypical movements of fishing vessels.	There is a problem of latency in determining the state of the vessel.
[16]	The proposed system was developed using Dragino LoRa v1.3 Shield devices, which are specifically designed to be easily programmed and integrated with an Arduino Uno microcontroller.	The system is not reliable because the system accuracy is not good.
[17]	The author connected several sensors to a microcontroller that is equipped with WiFi capabilities to detect various conditions, such as motion, vibration, and pulse rate. Additionally, a GPS module was integrated with the WiFi-enabled microcontroller to enable positioning and tracking functionalities.	The reliability of the system may be limited in certain environments where GPS signals cannot penetrate, such as underground or underwater, as GPS is used as part of the system.
[20]	The D-OFDM technique, which utilizes TV white spaces, was implemented by the authors. SNOW, a communication technology that permits extensive and simultaneous communication between multiple nodes and a base station (BS), was also utilized.	The hardware is very expensive.
[23]	A Mobile Emergency Operations Center (MEOC) was established to aid the activities of first responders and to provide support with the development of a real-time communication technology.	Neglecting the aspects of latency and reliability.

3. LPWAN Technologies

An LPWAN is a wireless communication technology that enables low-power devices with limited bandwidth to transmit data over long distances using low data rates. It is designed to support M2M and IoT networks and is typically more cost-effective and power-efficient than traditional mobile networks. This technology can support a large number of devices over a wide geographical area. LPWANs are classified into two main groups based on their protocols and technologies. The initial set of LPWAN technologies operates on unlicensed frequency bands and does not require cellular infrastructure. This group includes protocols such as LoRaWAN and Sigfox. The second group uses cellular technologies based on 3GPP standards and uses the licensed spectrum of mobile operators.

There are three types of cellular-based LPWANs: LTE-M, NB-IoT, and EC-GSM-IoT. LTE-M supports applications that require low to medium bandwidth and can achieve data rates of up to 1 Mbps. NB-IoT is optimized for low power consumption, long battery life, and deep indoor penetration, with data rates of up to 250 Kbps. EC-GSM-IoT is a modification of the GSM standard that offers extended coverage and better indoor penetration for IoT devices, with data rates of up to 240 Kbps. The choice of LPWAN technology and protocol depends on various factors, such as the application requirements, coverage area, data rate, power consumption, and network deployment cost.

Non-cellular LPWANs such as LoRaWAN and Sigfox are well-suited for applications that require low power consumption, long-range coverage, and low-cost deployment [25, 26]. Cellular-based LPWANs such as LTE-M, NB-IoT, and EC-GSM-IoT are ideal for applications that require higher data rates, deeper indoor penetration, and better network reliability, but they may come with higher deployment costs [27,28]. Therefore, it is important to evaluate the advantages and disadvantages of each LPWAN technology and protocol before selecting the most appropriate one for a given application. Non-cellular LPWANs, such as LoRaWAN and Sigfox, operate on unlicensed spectrum bands and support devices with low power consumption and low data rates. They have a wide coverage range of up to 10 km in urban areas and up to 30 km in rural areas. The cellular-based LPWANs, on the other hand, utilize the licensed spectrum of mobile operators and provide a more reliable and secure connection. LTE-M is designed to support higher data rates than non-cellular LPWANs and has better coverage in urban areas. NB-IoT is specifically designed for low-power, low-data-rate applications, while EC-GSM-IoT is designed to provide better coverage in rural areas. LPWAN technology offers a flexible and scalable solution for a wide range of IoT applications, providing low-cost, low-power, and long-range connectivity [15]. A comprehensive description of the LPWAN technologies is provided below:

A. Sigfox

Sigfox offers LPWAN solutions that operate in license-free sub-GHz bands across various regions, such as 433 MHz in Asia, 868 MHz in Europe, and 915 MHz in North America. The technology used in Sigfox involves base stations that are equipped with software-defined radios, which connect to back-end servers through an IP network. For uplink communication, terminal devices use a 100 Hz bandwidth (BPSK) modulation in a 100 Hz data band, taking advantage of the sub-GHz spectrum's Ultra Narrow Band (UNB) to maximize the frequency band utilization with low noise levels. This leads to better receiver sensitivity and lower energy consumption. Although Sigfox originally only supported uplink communication, it later upgraded to two-way communication. However, regional regulations limit the number of notifications sent via the uplink to 140 messages, with a message size of 12 bytes. Only four messages per day are allowed on the downlink, and the base station cannot verify each uplink message. The payload size of the downlink message is eight bytes without authentication, and the reliability of the uplink communication improves with message resending and time variation. This simplified approach reduces the overall cost of the solution [14,27,29].

B. NB-IOT

The narrowband Internet of Things (NB-IoT) is an LPWAN technology that operates in licensed frequency bands and is compatible with LTE and GSM. It offers three operational modes: Standalone, Guard Band, and In-Band, with a bandwidth of 200 kHz. The Standalone mode is intended to work with the current GSM frequency spectrum, while the Guard Band mode utilizes the inactive resource block of the LTE carrier. In contrast, the In-Band mode uses the resource block in the LTE carrier [30,31]. The NB-IoT communication protocols offer a range of benefits for IoT devices and their applications, as they are based on LTE concepts. Despite the limitation on the integration of BPSK and QPSK functions, NB-IoT carriers can support up to 100,000 appliances, making them a highly scalable option [14]. Using frequency division multiple access (FDMA), up to 20 kbps of data can be transmitted from a node to a base station, while Orthogonal Frequency Division Multi-Access (OFDMA) enables a maximum throughput range of 200 kbps to 1600 bytes for downlink connections. As such, NB-IoT represents a reliable and efficient solution for connecting IoT devices to the network, offering improved performance and functionality [32,33].

C. LoRaWAN

LoRaWAN is a spread-spectrum technology that uses the chirp spread spectrum (CSS) to modify signals in the sub-GHz range for two-way communication. This LPWAN technology is based on the LoRa standard that was introduced by Semtech in 2015 and was later standardized by the LoRa Alliance [34]. The signal model is tailored to accommodate channel noise and interference, and the transmitter generates a chirp signal that causes the frequencies of symbols to fluctuate over time while keeping their phases constant. The receiver can decrypt the chirp signal by varying the frequency shift, resulting in improved chipping symbols for each chirp signal. Furthermore, forward error correction (FEC) is employed to enhance the receiver's sensitivity. LoRa technology boasts an impressive range of 1–30 km across both land and sea [35–37]. LoRaWAN, an open standard network stack, capitalizes on the physical layer characteristics of LoRa. Its objective is to enable sensors to exchange data frames through a server at a low data rate with relatively independent time intervals between transfers, such as one transmission per hour or per day. The network structure follows a star-star topology (GW), and the endpoints are connected to the network servers (NS) via the gateway. LoRaWAN adjusts its bitrate according to the quality of the available channels. LoRaWAN utilizes the SF (spreading factor) function to adjust the signal and battery strength. If the sensor node encounters poor connection quality, LoRaWAN increases the SF to transmit the modeled signal over longer distances, but this results in a lower bitrate. The transition is controlled by the LoRaWAN parameter DR (data rate), which ranges from DR0 (low bitrate, SF12) to DR5 in the EU (high bitrate, SF7) [38–41].

D. TELENSA

Telensa, a UK-based firm, offers IoT-based private and public network solutions that cater to smart cities, smart metering, and smart lighting needs. The company has successfully installed millions of linked street lighting systems across different countries and employs IoT technology for tracking, detection, and monitoring in smart cities and homes. Telensa's technology is similar to that of Sigfox and is widely used to regulate millions of lights and other products. Recently, Telensa has been focused on creating innovative applications for smart cities, such as urban data insight and urban IQ, using next-generation light pole sensors that employ artificial intelligence technology. These multi-sensor pods use the latest smartphone artificial intelligence capabilities and automobile camera and radar-imaging technology to provide a comprehensive understanding of road infrastructure. In addition, Telensa is leading an urban data initiative that aims to change the way data are collected and utilized by local governments, creating what they call a "digital twin of a city". Telensa has designed a modulation mechanism specifically for the UNB (Ultra Narrow Band) that enables low-data-rate wireless connections between end nodes and base stations operating in the unlicensed sub-GHz ISM (Industrial, Scientific, and

Medical) band. UNB technology is designed for low-bandwidth transmission, and Telensa has developed a vertical grid stack for its network, which allows for easy integration with third-party software and end-to-end solutions for LPWAN applications. The company has more than 8 million UNBs operating in 30 countries, and its technology is low risk and top-notch. To ensure seamless integration into applications, the company is standardizing its technology to meet ETSI (LTN) network requirements. Telensa's UNB device has an uplink rate of 62.5 bps and a downstream rate of 500 bps. The company is working with Sigfox in the ETSI LTN group [27].

E. INGENU RPMA

INGENU, formerly known as On-Ramp Wireless, uses a patented LPWAN technology that differs from many other LPWAN technologies on the market by operating in the 2.4 GHz ISM band instead of the sub-GHz band. INGENU's LPWAN technology has the advantage of improved throughput and capacity in regions where the work-cycle maximum regulations do not limit the 2.4 GHz band. Additionally, the Random Phase Multiple Access (RPMA) physical access technique used by INGENU's LPWAN technology is a distinctive feature that differentiates it from other LPWAN technologies. RPMA employs a wide range of direct sequences for uplink communication, enabling multiple transmitters to use a single time slot. This form of code division multiple access (CDMA) increases the signal-to-interference ratio for each link by ensuring that the channel does not align the transmitters exactly at the same time. The exceptional receptor sensitivity of -142 dB and a bond budget of 168 dB make RPMA unmatched in the industry. Multiple demodulators on the receiving end of base stations decode signals that arrive at different times in a slot. While there may be some link asymmetry, INGENU's technology enables two-way communication. Downlink communication is accomplished by base stations transmitting signals to specific end devices, which are subsequently sent utilizing CDMA. The end nodes can also modify their broadcast strength to reach the nearest base station without interfering with surrounding devices. INGENU is leading the way in standardizing the physical layer requirements according to the IEEE 802.15.4k, with RPMA technology developed in compliance with these requirements [27].

Table 2 presents a comparison of the primary technical features of various LPWAN technologies, such as the availability, bandwidth, link budget, battery life, energy usage, frequency, security, and private network allocation [27,34]. The appropriate LPWAN technology for IoT applications is determined by these key factors. Telensa, Sigfox, and NB-IoT do not support private network deployment as the signal strength relies on the service provider base stations, while RPMA and LoRa enable the creation of private networks for these applications. Telensa, Sigfox, and LoRaWAN utilize sub-GHz frequencies that are not licensed, and their communication capabilities are designed to overcome multi-path interference and fading. This allows them to provide effective communication. In contrast, NB-IoT uses licensed frequencies to provide high-quality service, but at a higher cost. However, NB-IoT devices have a shorter service life due to the OFDM/FDMA approach, which requires a higher current for simultaneous communication from its terminal tools. Despite being released in 2016, the NB-IoT standard is still in its supply phase, while other LPWAN deployment models have already matured. At present, LoRaWAN is the most widely used LPWAN technology, with deployments in over 160 countries. LoRaWAN can establish public networks, local area networks, and a hybrid operating model that combines a local LoRaWAN network with a base station public network. LoRa uses unlicensed frequencies, is energy-efficient and affordable, and offers a communication range of 1–30 km over ground and water, respectively [27,34].

Table 2. Comparison of key technical specifications for LPWAN technologies [27,34].

Technologies	Sigfox	NB-IoT,	Telensa	LoRa	INGENU RPMA,
Creator	**Sigfox**	3 GPP	Telensa	Semtech	Ingenu
Modulation	BPSK	QPSK	UNB 2-FSK	CSS	UL: RPMA-DSSS DL: CDMA
Frequency	Sub-GHz ISM EU 868 MHz US 902 MHz	Licensed LTE Frequency bands	Sub-GHz, ISM EU: 868 MHz US: 915 MHz AS: 430 MHz	Unlicensed ISM EU 868 MHz US 915 MHz	2.4 GHz ISM
Data Rate.	100 bps (UL) 600 bps (DL)	200 kbps	UL: 62.5 bps DL: 500 bps	0.3–50 kbps	UL: 624 kbps DL: 156 kbps
Energy consumption	Very low	Low	Low	Very low	High
Bandwidth	100 or 600 Hz DL: 1.5 kHz	180 kHz	100 kHz	125, 250, 500 kHz	1 MHz
Link budget (dB)	EU: 162 US: 146	189	EU: 161 US: 149	EU: 151 US: 171	EU: 168 US: 180
Range	10 km (Urban) 50 km (Rural)	1 km (Urban) 10 km (Rural)	Urban: 3 km Rural: 16 km	1–30 km	Urban: 15 km Rural: 48 km
Allow private networks	No	NO	NO	YES	YES

4. System Model and Design

In our study, we designed an LPWAN-based emergency response (LBER) system to meet the needs of people with special requirements on a smart campus. To ensure data distribution in areas with WiFi coverage and to fill gaps in areas without, we utilized WiFi as the primary means of communication and LoRaWAN as a backup. In the event of an emergency, WiFi may become unreliable and the electricity supply may be disrupted, but the LoRaWAN network will remain functional. Our solution utilizes two Heltec WiFi LoRa 32 V2 devices, each equipped with BLE, WiFi, and LoRa technology with one serving as the sender and the other as the receiver of data. To initiate an emergency response, the user simply presses a panic button, and the message is transmitted to the recipient. This approach allows for the reduced latency and improved reliability of the emergency response system on a smart campus. Figure 1 provides a visual representation of our proposed model to facilitate better understanding.

A. WiFi LoRa

The WiFi LoRa 32 V2, a well-known IoT development board, is produced by Heltec Automation (TM) and is depicted in Figure 2. This highly integrated board is based on ESP32 + SX127x and has WiFi, Bluetooth Low Energy (BLE), and LoRa capabilities, as well as a Li-Po battery management system and a 0.96″ Organic Light-Emitting Diode (OLED). It is an extremely low-power solution board that is ideal for IoT creators working on projects such as smart cities, smart farms, and smart homes [25].

The ESP32 chip has the capability to support the Transmission Control Protocol/Internet Protocol (TCP/IP), the 802.11 b/g/n WiFi Medium Access Control (MAC) protocol, and the WiFi Direct specification. Meanwhile, the SX127647 is a half-duplex transceiver that operates at a low intermediate frequency and utilizes Semtech's patented LoRa modulation technique, along with a low-cost crystal, to achieve a sensitivity level that surpasses −148 dBm. It is pertinent to mention that the sensitivity depends on the spreading factor and bandwidth. Additionally, the SX1276 has two modems—one for Frequency Shift Keying (FSK) and one for LoRa spread spectrum modulation—which can be utilized based on the selected modes. By utilizing the LoRa modulation technique, the device can gain greater immunity to in-band interference.

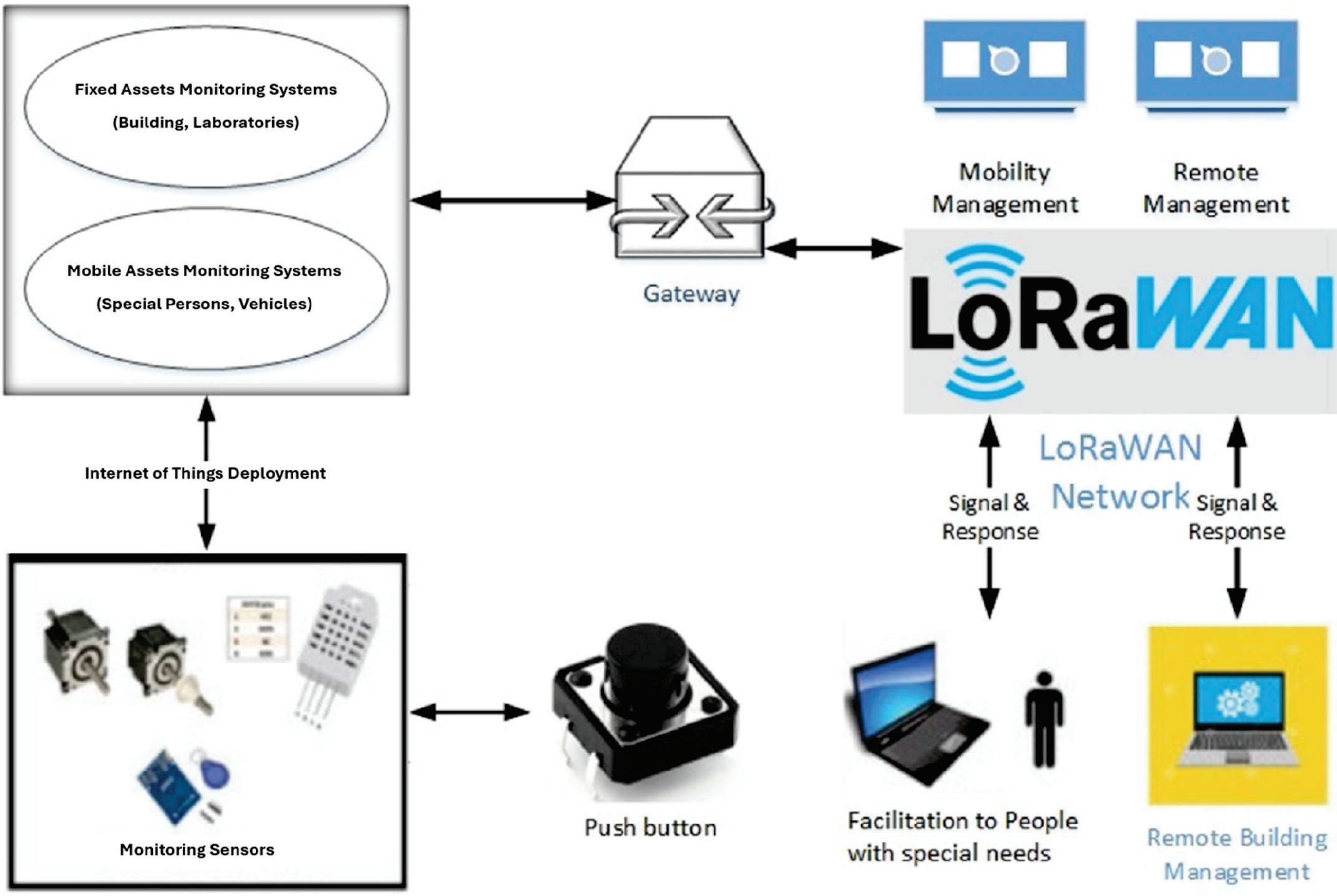

Figure 1. An LPWAN-based emergency response system for individuals with special needs in smart buildings.

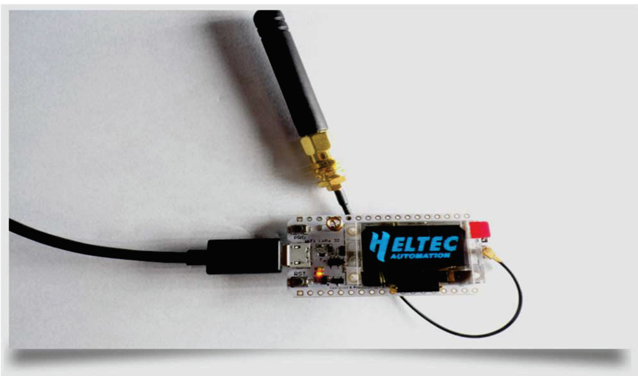

Figure 2. Heltec WiFi LoRa 32 board [42].

B. GPS Module

The GPS module is an adaptable and economical positioning device designed for wide-ranging applications. It offers a 2.5 m horizontal positioning accuracy and has the capability to store the device's configuration when it is powered off. It is equipped with an IPX interface for attaching various active antennas that provide a strong signal, and it has 50 channels for signal reception. It features four-pin connections for VCC, GND, TX, and RX. Customized settings can be created using the u-center software provided by u-blox AG [26]. The module is primarily utilized for satellite navigation, and it can determine speed and location on land, air, and sea and provide precise maps, tracking systems, navigation, and aircraft positioning. NEO-6 modules are particularly suitable for mobile devices that have strict limitations on cost and space due to their compact design and power and memory options. The specifications of the GPS module are listed in Table 3 and Figure 3 illustrates the GPS module.

Table 3. GPS module specifications.

Parameters	Specification
Operating Voltage	2.7–5 V
Baud Rate	9600 (default)
Update Rate for Navigation	1 Hz (default) 5 Hz
Tracking Sensitivity	−161 dBm
Operating Current	45 Ma
Communication Protocol	NMEA (default), UBX library

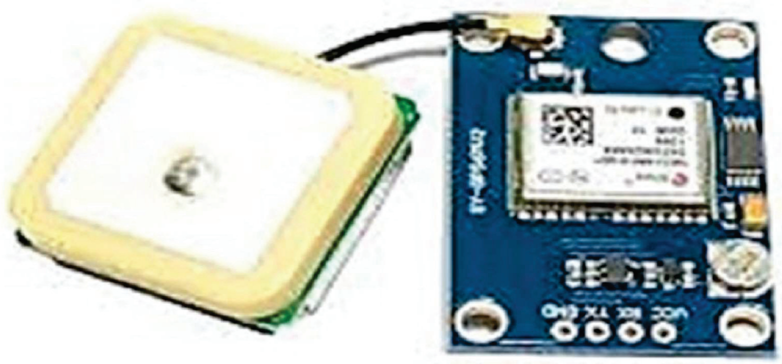

Figure 3. GPS NEO-6M u-blox module.

C. *Panic Button*

The panic button proposed in this study is designed to have the utmost effectiveness and efficiency as it is intended to be used in emergency or critical situations by individuals with special needs. The Wi-Fi LoRa 32 v2-based IoT panic button will be set up to address the needs of individuals with special needs who may be faced with various risks, including panic situations, fear of theft, or difficulty navigating due to blindness. Many of these individuals may lack technical proficiency in operating devices, hence necessitating the need for a simple and reliable device that can alert someone when help is needed. This IoT panic button will be enabled over LoRa, and we are using the WiFi LoRa 32 module to increase its portability and simplicity. The operation of this panic or push button is straightforward, requiring the user to push the button to trigger an alert, which will immediately send their location to the designated person. Figure 4 depicts the design of the push or panic button.

Figure 4. Push button.

There are several benefits of implementing a panic button, including but not limited to the following:

1. The ability to swiftly inform family members or relevant authorities in case of an emergency.
2. Expedite rescue efforts, thereby potentially saving a life.
3. Provide assistance to individuals facing potential risks.

5. Experiments, Results and Discussion

A. Experimental Setup

The experimental setup, as illustrated in Figure 5, involved ensuring the proper connection of all the components and devices according to the desired configuration. To enable the flow of current, the Heltec WiFi LoRa 32 development board utilized a Power Bank to receive external power. In the event of danger, the visually impaired person would activate the panic button. Subsequently, the GPS module would provide the location of the danger and send an alert to a designated emergency care provider.

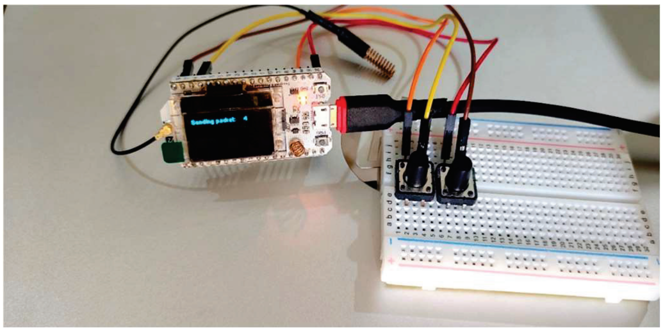

Figure 5. Experimental setup.

In our experimentation, we utilized LoRa modulation with specific transmission parameters, including the spreading factor (SF), bandwidth (BW), and coding rate (CR). For the spreading factor, we employed a default value throughout the trials, which was 7. The bandwidth was set at 125 kHz, and the coding rate was fixed at 4/5. As for the number of packets sent for each testing setup, we transmitted a total of 50 packets at each distance in every experiment, maintaining consistency across all the trials.

B. Results and Discussion

To evaluate the efficacy of the system, a total of 18 experiments were executed, comprising 9 trials in an open field and an additional 9 in IT Building No. 3 at Hazara University in Mansehra, Pakistan. The morphology of the testing site, as depicted on a map, is illustrated in Figure 6. The selected open field was elevated and proved demanding to test the system's performance in challenging environments. The experiments were conducted using three distinct antenna heights (0 m, 1 m, and 2 m) and three varied packet sizes (16 bytes, 32 bytes, and 64 bytes), while keeping the default TX power (dBm) of 15 for all the tests. The end device was tested at varying distances from 0 m to 600 m, with increments of 50 m. For each experiment, the antenna height was set at 0 m for the first experiment, 1 m for the second, and 2 m for the third experiment for a data packet size of 16 bytes. The same process was repeated for 32 and 64 bytes of data packets. To determine the system's performance based on the packet size and antenna height, 50 packets were transmitted at each distance in each experiment, and the average of the experiment results was used to evaluate the performance.

Figure 6. The morphology of the testing site shown through a map.

a. Reliability

Reliability pertains to the capability of consistently performing with dependability and trustworthiness. In the context of a network system, reliability can be determined by evaluating the probability of successful interaction between every pair of nodes or by measuring the operational efficacy and signal strength (RSSI) following the experiment. The RSSI represents the received signal power in milliwatts, expressed in dBm, and is utilized to assess data transmission across different settings and distances. The packet delivery ratio (PDR) is calculated as the ratio of valid received packets to the total number of transmitted packets, as demonstrated in Equation (1). The PDR is an indicative measure of communication reliability, which can be used in tandem with the RSSI to provide a comprehensive assessment of system performance. The RSSI value can be utilized to gauge the strength of the signal received by the receiver from the sender, and it is represented as a negative value, where a value closer to 0 signifies a stronger signal.

$$\text{PDR} = \frac{R}{S} \tag{1}$$

R: Total packets received successfully
S: Total packets sent.

In order to evaluate the collected data, we first summarized it and then presented it using figures and tables. Figures 7–12, along with Tables 4–7, display the reliability and RSSI for various antenna heights and distances. These visuals allow us to observe both high and low reliability and RSSI values. The experiment was conducted at Hazara University, covering an area of 1300 m^2, and yielded excellent results. We focused on the reliability data for a distance of 600 m in two different locations.

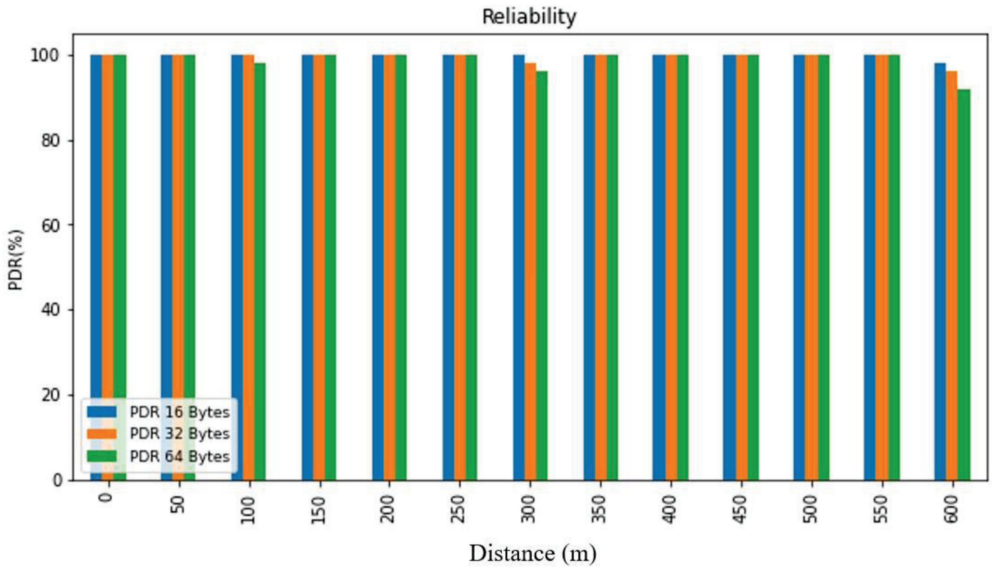

Figure 7. PDR according to distance and packet size when antenna height = 0 m.

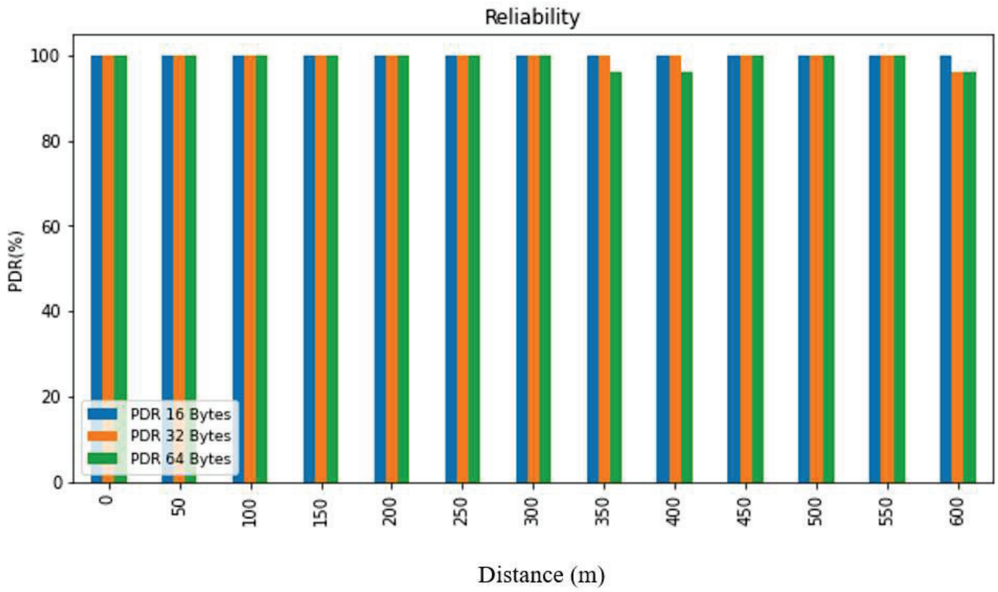

Figure 8. PDR according to distance and packet size when antenna height = 1 m.

Table 4. Reliability results for different distances and packet sizes when antenna height = 0 m.

Antenna Height = 0 m						
Distance	P-Size: 16 Bytes		P-Size: 32 Bytes		P-Size: 64 Bytes	
	PDR %	RSSI	PDR %	RSSI	PDR %	RSSI
0 m	100%	−22.0	100%	−27.42	100%	−35.18
50 m	100%	−81.0	100%	−92.82	100%	−99.80
100 m	100%	−92.3	100%	−99.24	98%	−104.54
150 m	100%	−95.6	100%	−94.84	100%	−92.48
200 m	100%	−106.9	100%	−99.98	100%	−102.00
250 m	100%	−103.3	100%	−99.98	100%	−106.34
300 m	100%	−108.9	98%	−111.62	96%	−121.92

Table 4. *Cont.*

Antenna Height = 0 m						
Distance	P-Size: 16 Bytes		P-Size: 32 Bytes		P-Size: 64 Bytes	
	PDR %	RSSI	PDR %	RSSI	PDR %	RSSI
350 m	100%	−114.9	100%	−111.64	100%	−120.20
400 m	100%	−118.2	100%	−114.00	100%	−127.42
450 m	100%	−115.9	100%	−115.60	100%	−131.00
500 m	100%	−122.6	100%	−111.66	100%	−120.70
550 m	100%	−120.6	100%	−113.00	100%	−121.50
600 m	98%	−130.9	96%	−123.00	92%	−135.60

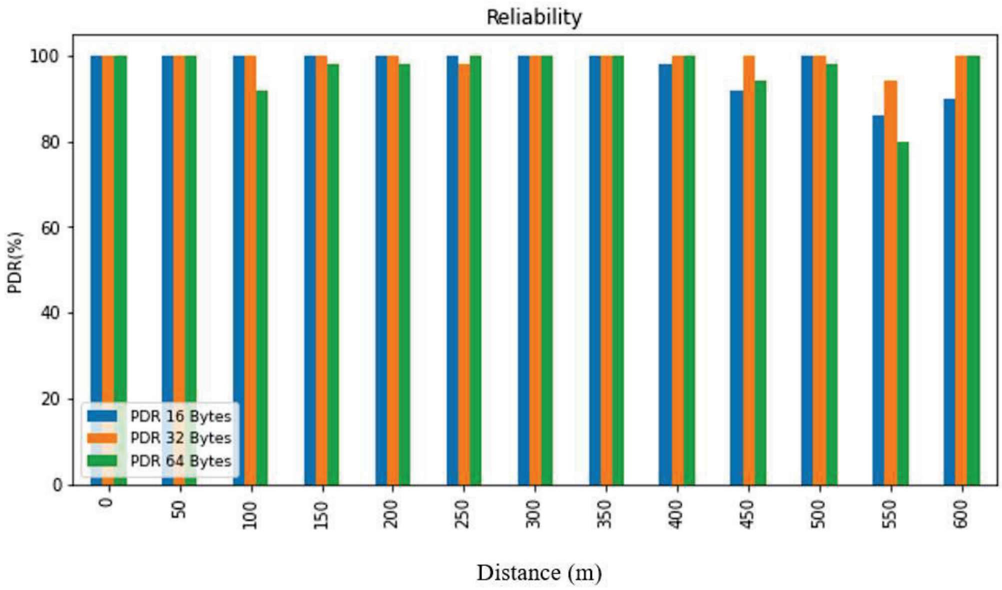

Figure 9. PDR according to distance and packet size when antenna height = 2 m.

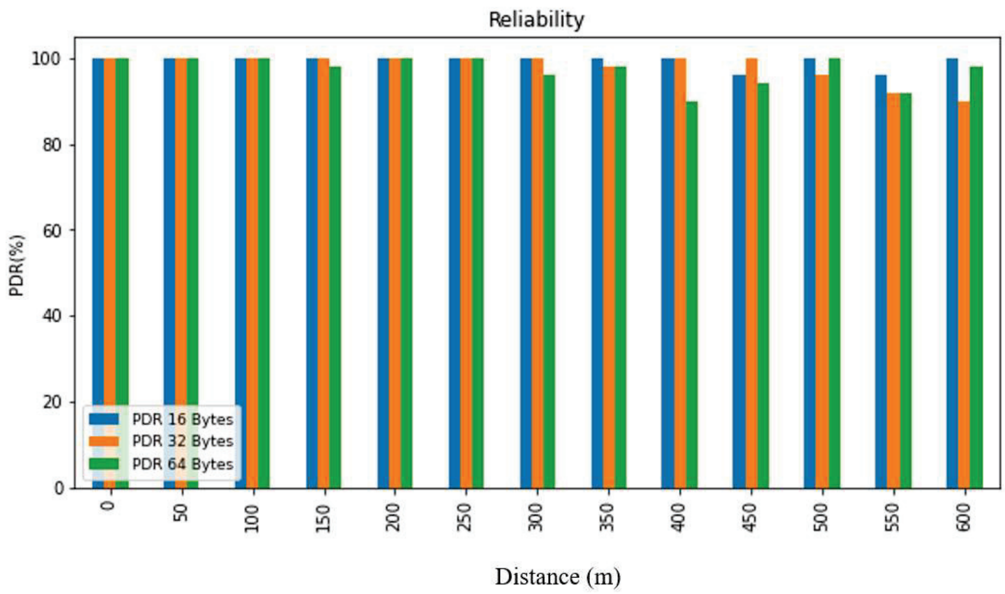

Figure 10. Reliability analysis of the first floor.

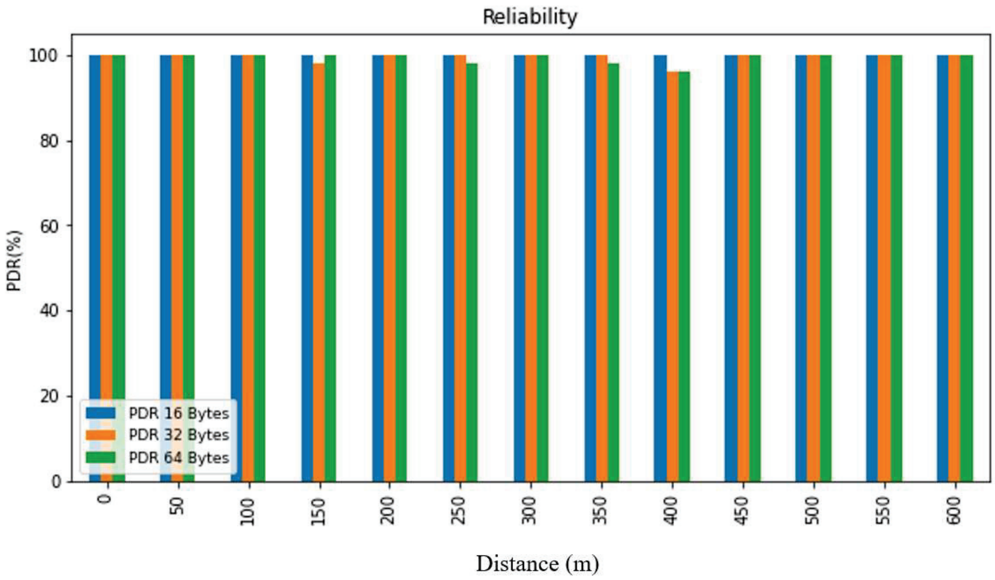

Figure 11. Reliability analysis of the second floor.

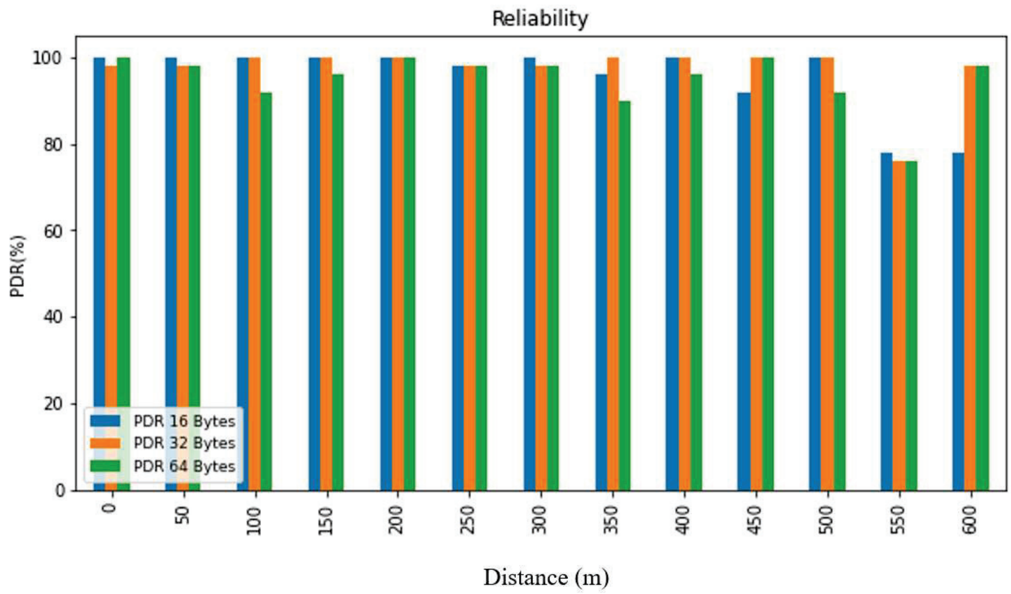

Figure 12. Reliability analysis of the third floor.

Table 5. Reliability results for different distances and packet sizes when antenna height = 1 m.

Antenna Height = 1 m						
Distance	**P-Size:16 Bytes**		**P-Size: 32 Bytes**		**P-Size: 64 Bytes**	
	PDR %	**RSSI**	**PDR %**	**RSSI**	**PDR %**	**RSSI**
0 m	100%	−41.3	100%	−24.88	100%	−56.6
50 m	100%	−99.06	100%	−78.82	100%	−76.86
100 m	100%	−108	100%	−89.88	100%	−91
150 m	100%	−109.8	100%	−86.32	100%	−93.52
200 m	100%	−110.42	100%	−92.52	100%	−86.44
250 m	100%	−112.84	100%	−97.5	100%	−104.32
300 m	100%	−117.28	100%	−100.66	100%	−107.9

Table 5. *Cont.*

Antenna Height = 1 m						
Distance	**P-Size:16 Bytes**		**P-Size: 32 Bytes**		**P-Size: 64 Bytes**	
	PDR %	**RSSI**	**PDR %**	**RSSI**	**PDR %**	**RSSI**
350 m	100%	−124.26	100%	−108.28	96%	−115.72
400 m	100%	−127	100%	−106.68	96%	−118.14
450 m	100%	−124.1	100%	−111.86	100%	−118.8
500 m	100%	−128.76	100%	−111.18	100%	−127.8
550 m	100%	−129.12	100%	−120	100%	−121.84
600 m	100%	−130.66	96%	−128.52	96%	−128.78

Table 6. Reliability results for different distances and packet sizes when antenna height = 2 m.

Antenna Height = 2 m						
Distance	**P-Size:16 Bytes**		**P-Size: 32 Bytes**		**P-Size: 64 Bytes**	
	PDR %	**RSSI**	**PDR %**	**RSSI**	**PDR %**	**RSSI**
0 m	100%	−48.16	100%	−42	100%	−55
50 m	100%	−85.86	100%	−84.00	100%	−77.10
100 m	100%	−86.58	100%	−96.48	100%	−86.72
150 m	100%	−89.8	98%	−92.8	100%	−90.66
200 m	100%	−103	100%	−92.42	100%	−94.96
250 m	100%	−104.54	100%	−106.66	98%	−105.74
300 m	100%	−113.38	100%	−111.18	100%	−106.54
350 m	100%	−113.96	100%	−115.88	98%	−114.72
400 m	100%	−117.48	96%	−112.88	96%	−121.16
450 m	100%	−118.2	100%	−117.72	100%	111.42
500 m	100%	−114.24	100%	−115.18	100%	112.32
550 m	100%	−118.46	100%	−114.8	100%	−111.52
600 m	100%	−116.86	100%	−124.28	100%	−117.82

i. The transmitter was positioned on the left side of a location, specifically Boys Hostel No. 2, situated in an unobstructed area.
ii. The transmitter was initially deployed outside IT Building No. 3 to extend the range of transmission to the receiver.

Hazara University is a verdant campus with an abundance of trees that form dense forests, and the central IT Building is surrounded by towering trees, which pose a significant impediment to D2D communication. To evaluate LoRa's reliability performance over varying distances, the receiver was placed at different distances ranging from 0 to 600 m in increments of 50 m, denoted as R0 to R600, with the transmitter fixed at one end. For each distance, 50 trials were conducted to determine the reliability, with 3 different packet sizes of 16, 32, and 64 bytes, and 3 different antenna heights of 0, 1, and 2 m in an open area and on the first, second, and third floors of IT Building 3.

Table 7. Reliability results for different distances and packet sizes with the antenna on the 1st, 2nd, and 3rd floor.

P-Size	P-Size: 16 Bytes						P-Size: 32 Bytes						P-Size: 64 Bytes					
A-Height	1st Floor		2nd Floor		3rd Floor		1st Floor		2nd Floor		3rd Floor		1st Floor		2nd Floor		3rd Floor	
Distance	PDR %	RSSI	PDR %	RSSI	PDR %	RSSI	PDR %	RSSI	PDR %	RSSI	PDR %	RSSI	PDR %	RSSI	PDR %	RSSI	PDR %	RSSI
0 m	100%	−72.3	100%	−53.78	100%	−14.58	98%	−73.24	100%	−36.12	100%	−30.48	100%	−67.2	100%	−29.52	100%	−40.66
50 m	100%	−75.32	100%	−87.20	100%	−79.46	98%	−74.66	100%	−64.72	100%	−81.68	98%	−74.88	100%	−72.16	100%	−85.90
100 m	100%	−89.14	100%	−89.72	100%	−97.16	100%	−85.7	100%	−81.3	100%	−90.3	92%	−83.54	92%	−80.76	100%	−90.44
150 m	100%	−103.58	100%	−115	100%	−91.72	100%	−93.24	100%	−89.36	100%	−104.86	96%	−65.64	98%	−92.16	98%	−97.12
200 m	100%	−109.38	100%	−119.26	100%	−97	100%	−101.34	100%	−90.1	100%	−101.44	100%	−99.58	98%	−94.74	100%	−94.92
250 m	98%	−118.58	100%	−119.46	100%	−107	98%	−112.56	98%	−108.72	100%	−99.54	98%	−103.38	100%	−102.3	100%	−104.32
300 m	100%	−116.76	100%	−119.8	100%	−102.28	98%	−116.8	100%	−106.58	100%	−104.96	98%	−105.26	100%	−104	96%	−102.22
350 m	96%	−124.34	100%	−117.82	100%	−109.24	100%	−113	100%	−105.52	98%	−111.42	90%	−112.8	100%	−106.8	98%	−109.5
400 m	100%	−117.64	98%	−123.86	100%	−114.18	100%	−104.46	100%	−114	100%	−107	96%	−111.98	100%	−103.4	90%	−117.92
450 m	92%	−124	92%	−127.9	96%	−118.5	100%	−108.34	100%	−116.34	100%	−116.84	100%	−110.44	94%	−120.24	94%	−119.22
500 m	100%	−124.28	100%	−123.34	100%	−119.26	100%	−120.72	100%	−118.9	96%	−119.38	92%	−119.36	98%	−113.46	100%	−112.3
550 m	78%	−131.16	86%	−124.28	96%	−124.54	76%	−126.14	94%	−119.76	92%	−124.72	76%	−116.64	80%	−118.22	92%	−126.68
600 m	78%	−131.12	90%	−128	100%	−127.6	98%	−115.36	100%	−121.4	90%	−124.98	98%	−125.2	100%	−112.6	98%	−121

This study's findings showed that the reliability of the system was affected by the distance, payload size, and antenna height. The reliability was found to decrease with an increase in the distance and payload size due to the longer airtime in LoRa transmission, while it increased with an increase in the antenna height. This study evaluated the reliability for different antenna heights and packet sizes and found that it was lowest for low antenna heights and large distances and highest for high antenna heights and small distances. Additionally, the reliability increased as the distance and packet size decreased. This study also found that the LoRa transmission range decreased with a decreasing antenna height in the case of indoor D2D-LoRa networks. Despite some distances exhibiting lower reliability due to high obstacles, the reliability results were stronger than expected, with more than 98% reliability demonstrated at all the distances and antenna heights in all the settings. As evident from the presented tables and figures, all the environments exhibited more than 98% reliability at all the distances and antenna heights, except for a few distances with high obstacles. Compared to similar studies [1,12,17], the measured distances and reliability results were remarkably strong.

b. Latency

Latency, the amount of time that has passed since an event, is an important factor in network performance, particularly in terms of the time it takes for data to travel from one point to another. This duration, commonly referred to as "round trip delay", encompasses both the transmission and reception times. The latency is calculated by summing together all sorts of delays, including transmitting and receiving delays. It is measured in ms [43]. Equation (2) is used to compute the latency.

$$Latency = REC_T - S_T \tag{2}$$

The REC_T denotes the receiving time and the sending time is denoted by S_T. The latency was evaluated in a test conducted at Hazara University, in which the receiver was positioned at various distances from the transmitter, located on the left side of Boys Hostel 2, to assess LoRa's performance at different ranges. The results are shown in Figures 13–18, along with Tables 8 and 9. The distances between the receiver and transmitter ranged from 0 m to 600 m, with a 50 m interval between them, represented as R0, R50, R100, R150 ... R600. The transmitter remained stationary, while the receiver was gradually moved away from it at the distances mentioned above. The results demonstrate that the latency of the LoRa transmission increases significantly as the payload size increases. For example, when the payload size increases from 16 bytes to 32 bytes and then to 64 bytes, the average latency increases by 8% and 17%, respectively, at 600 m and an antenna height of 0 m. Similarly, at 600 m and an antenna height of 0 m, the latency for 64 bytes of data is more than twice that of 16 bytes of data. This indicates that larger payload sizes may not be suitable for applications that require low latency, and smaller packet sizes should be used for low-latency applications. The experimental results demonstrate that the performance of LoRa in terms of the reliability and latency is affected by the distance, payload size, and antenna height. The results show that increasing the antenna height leads to higher reliability and lower latency, while larger payload sizes and longer distances result in lower reliability and higher latency. These findings can be used to optimize the design of LoRa-based IoT systems for specific use cases and environments.

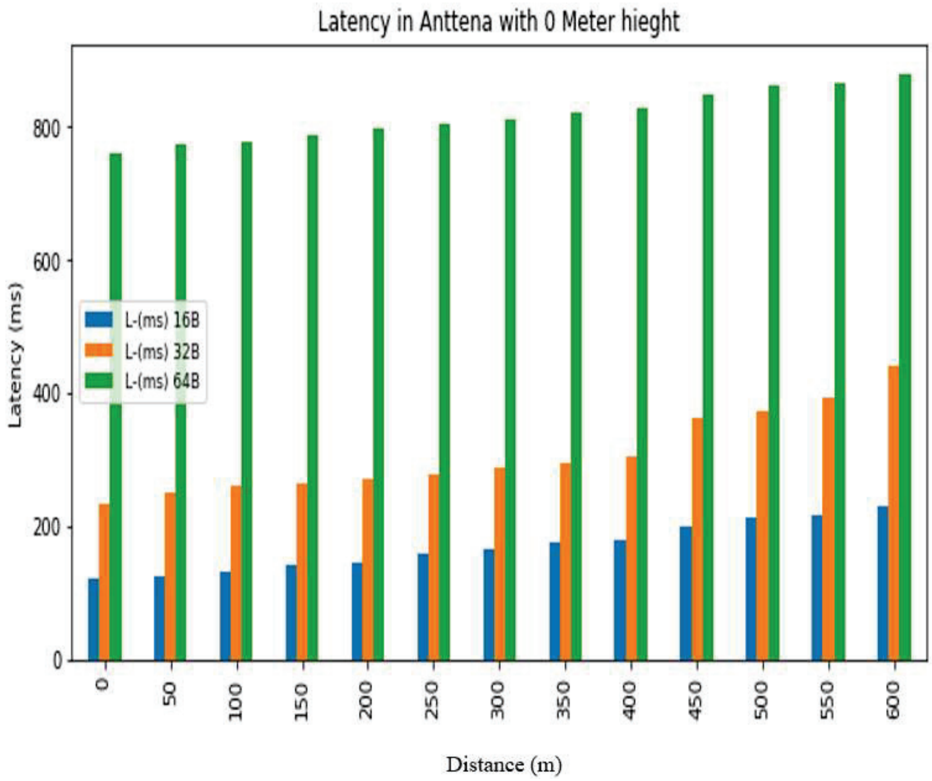

Figure 13. Latency analysis for antenna height = 0 m.

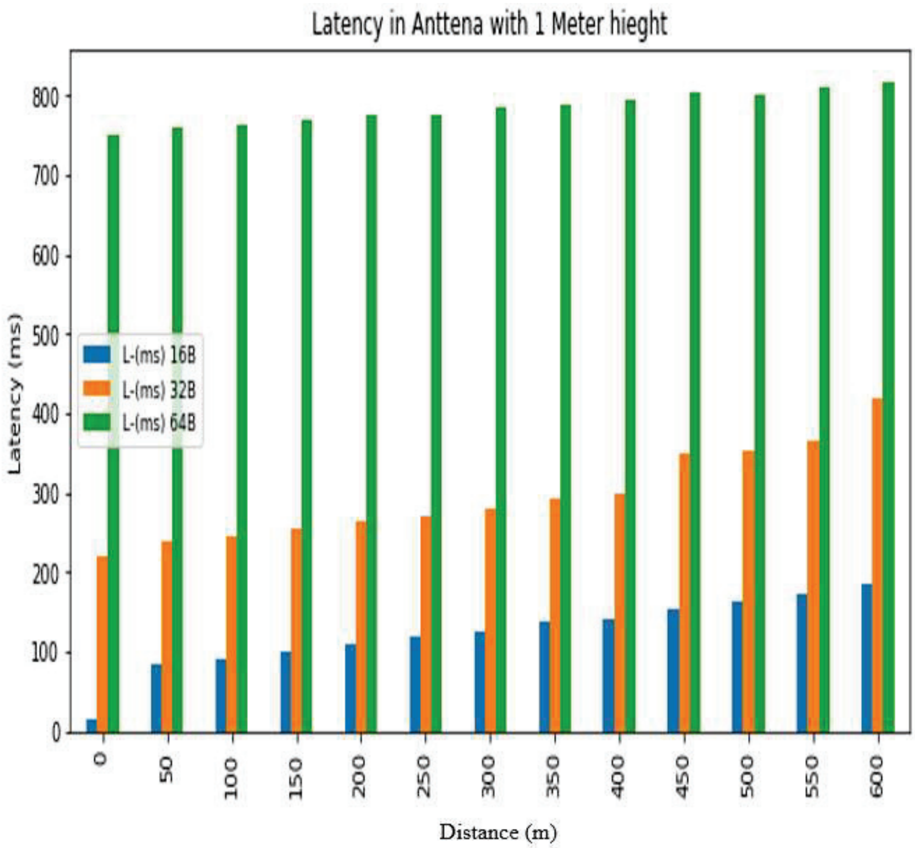

Figure 14. Latency analysis for antenna height = 1 m.

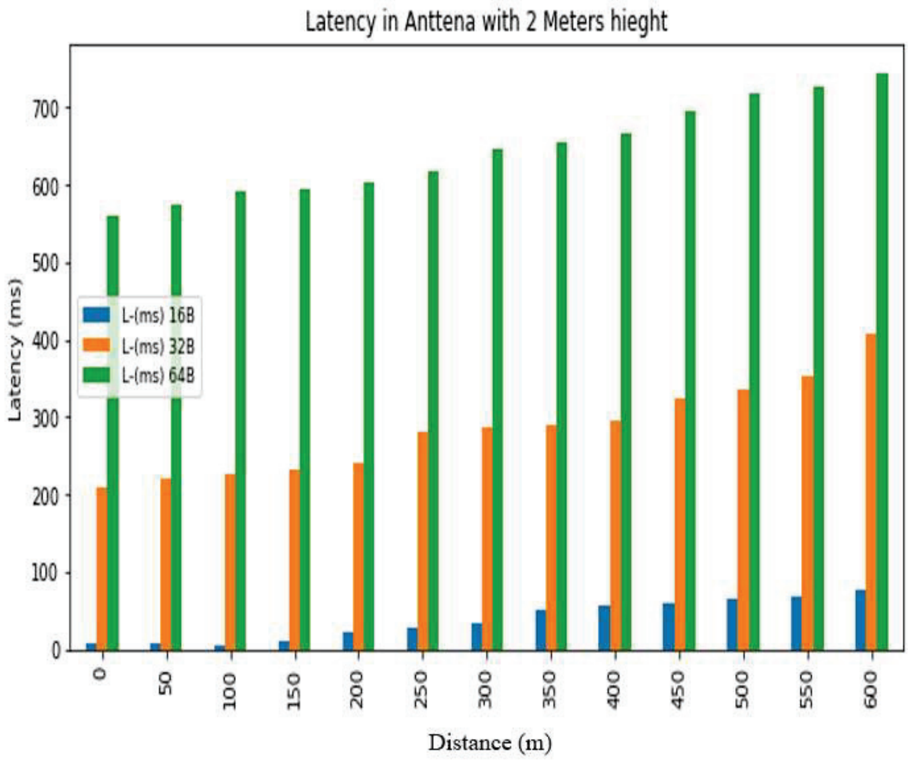

Figure 15. Latency analysis for antenna height = 2 m.

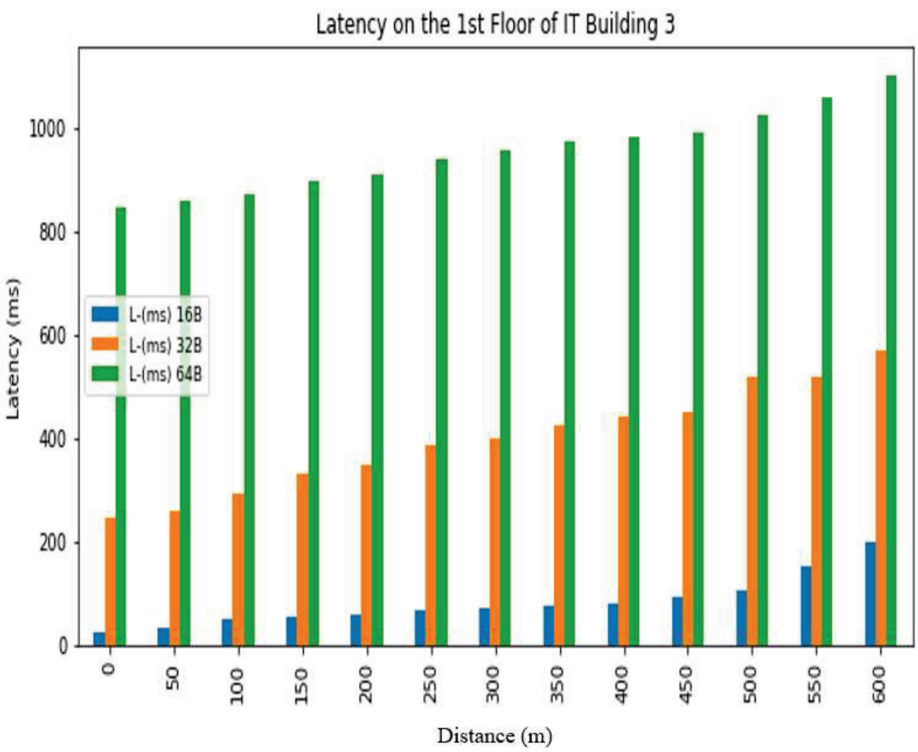

Figure 16. Latency analysis on 1st floor.

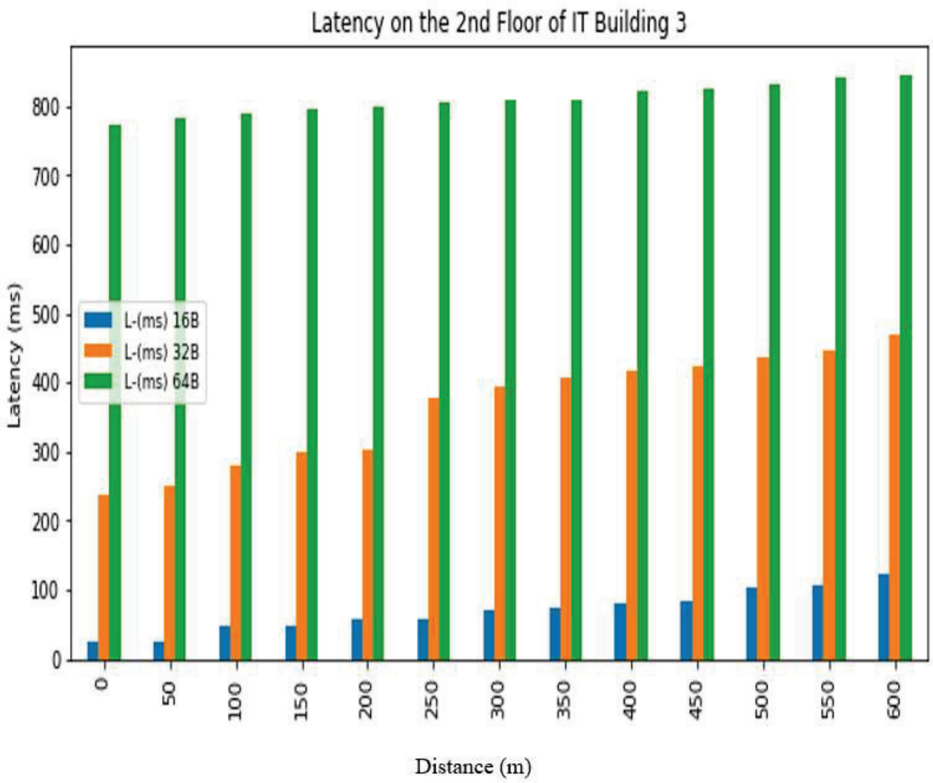

Figure 17. Latency analysis on 2nd floor.

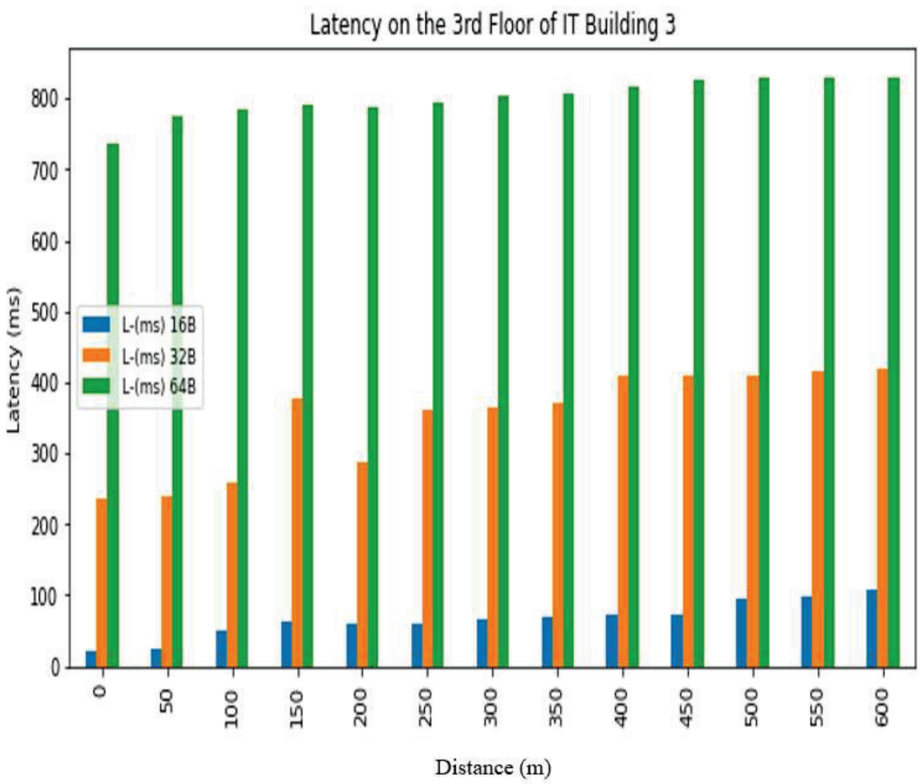

Figure 18. Latency analysis on 3rd floor.

Table 8. Latency results for different distances, packet sizes and antenna heights.

Packet Size	16 Bytes						32 Bytes						64 Bytes					
Antenna Height	0 m		1 m		2 m		0 m		1 m		2 m		0 m		1 m		2 m	
Distance	L (MS)	RSSI	L (MS)	RSSI	L (MS)	RSSI	L (MS)	RSSI	L (MS)	RSSI	L (MS)	RSSI	L (MS)	RSSI	L (MS)	RSSI	L (MS)	RSSI
0 m	120	−21.96	16	−41.3	8	−48.16	233	−27.42	220	−24.88	208	−42	760	−35.18	749	−56.6	560	−55
50 m	125	−80.98	84	−99.06	8	−85.86	252	−92.82	240	−78.82	222	−84.00	775	−99.80	760	−76.86	576	−77.10
100 m	133	−92.32	91	−108	5	−86.58	260	99.24	245	−89.88	226	−96.48	779	−104.54	764	−91	593	−86.72
150 m	141	−95.62	101	−109.8	10	−89.8	265	−94.84	255	−86.32	231	−92.8	788	−92.48	768	−93.52	595	−90.66
200 m	146	−106.94	111	−110.42	21	−103	272	−99.98	265	−92.52	240	−92.42	798	−102.00	774	−86.44	604	−94.96
250 m	157	−103.30	118	−112.84	29	−104.54	279	−99.98	270	−97.5	281	−106.66	806	−106.34	776	−104.32	618	−105.74
300 m	167	−108.94	126	−117.28	33	−113.38	287	−111.62	280	−100.66	287	−111.18	812	−121.92	785	−107.9	646	−106.54
350 m	176	−114.86	137	−124.26	50	−113.96	293	−111.64	291	−108.28	290	−115.88	820	−120.20	789	−115.72	655	−114.72
400 m	179	−118.20	142	−127	56	−117.48	306	−114.00	298	−106.68	295	−112.88	830	−127.42	794	−118.14	667	−121.16
450 m	199	−115.94	153	−124.1	60	−118.2	361	−115.60	349	−111.86	324	−117.72	848	−131.00	805	−118.8	695	−111.42
500 m	213	−122.60	164	−128.76	64	−114.24	373	−111.66	352	−111.18	335	−115.18	862	−120.70	800	−127.8	718	−112.32
550 m	218	−120.58	172	−129.12	69	−118.46	394	−113.00	366	−120	352	−114.8	867	−121.50	811	−121.84	726	−111.52
600 m	230	−130.92	186	−130.66	77	−116.86	442	−123.00	420	−128.52	409	−124.28	880	−135.60	817	−128.78	745	−117.82

Table 9. Latency results for different distances, packet sizes and antenna heights on different floors of IT Building 3.

Packet Size	16 Bytes						32 Bytes						64 Bytes					
Antenna Height	**1st Floor**		**2nd Floor**		**3rd Floor**		**1st Floor**		**2nd Floor**		**3rd Floor**		**1st Floor**		**2nd Floor**		**3rd Floor**	
Distance	**L (MS)**	**RSSI**	**L (MS)**	**RSSI**	**L (MS)**	**RSSI**	**L (MS)**	**RSSI**	**L (MS)**	**RSSI**	**L (MS)**	**RSSI**	**L (MS)**	**RSSI**	**L (MS)**	**RSSI**	**L (MS)**	**RSSI**
0 m	26	−72.3	24	−53.78	23	−14.58	244	−73.24	236	−36.12	237	−30.48	845	−67.2	771	−29.52	738	−40.66
50 m	33	−75.32	24	−87.20	25	−79.46	258	−74.66	249	−64.72	241	−81.68	858	−74.88	784	−72.16	776	−85.90
100 m	49	−89.14	47	−89.72	51	−97.16	291	−85.7	281	−81.3	260	−90.3	870	−83.54	788	−80.76	786	−90.44
150 m	54	−103.58	49	−115	62	−91.72	332	−93.24	299	−89.36	376	−104.86	898	−65.64	795	−92.16	790	−97.12
200 m	59	−109.38	57	−119.26	60	−97	347	−101.34	303	−90.1	288	−101.44	908	−99.58	798	−94.74	789	−94.92
250 m	66	−118.58	59	−119.46	59	−107	387	−112.56	379	−108.72	362	−99.54	938	−103.38	805	−102.3	795	−104.32
300 m	70	116.76	70	−119.8	65	−102.28	398	−116.8	393	−106.58	365	−104.96	958	−105.26	808	−104	805	−102.22
350 m	77	−124.34	73	−117.82	68	−109.24	425	−113	407	−105.52	371	−111.42	973	−112.8	809	−106.8	806	−109.5
400 m	80	−117.64	79	−123.86	72	−114.18	442	−104.46	417	−114	408	−107	980	−111.98	823	−103.4	817	−117.92
450 m	94	−124	85	−127.9	73	−118.5	451	−108.34	422	−116.34	409	−116.84	990	−110.44	825	−120.24	826	−119.22
500 m	104	−124.28	104	−123.34	94	−119.26	516	−120.72	436	−118.9	409	−119.38	1024	−119.36	831	−113.46	828	−112.3
550 m	152	−131.16	108	−124.28	97	−124.54	519	−126.14	447	−119.76	417	−124.72	1059	−116.64	840	−118.22	829	−126.68
600 m	198	131.12	124	−128	109	−127.6	570	−115.36	470	−121.4	419	−124.98	1102	−125.2	845	−112.6	830	−121

Numerous methods have been proposed in the literature to address wireless communication challenges during emergency response situations. However, these methods are limited in terms of the latency and reliability, particularly in densely populated areas like urban zones that are prone to natural disasters such as earthquakes, floods, and storms. For instance, communication systems based on WiFi and other radio technologies have shorter ranges, making it difficult to cover large areas such as those affected by urban emergencies. To address this research gap, we proposed an LPWAN-based emergency response system for people with special needs on a smart campus. To test the efficacy of the system, we conducted real-world experiments at Hazara University using Heltec WiFi LoRa 32 devices. Our experiments involved varying the distance and antenna height above the ground surface. We found that LoRaWAN technology is a promising choice for improving communication on smart campuses. Our results revealed that a higher antenna size and minimum distance improved the reliability and decreased the latency, as signals could easily pass through small objects and obstacles. Conversely, a lower antenna size and maximum distance resulted in lower reliability and increased latency, owing to the urban and green campus environment with different types of obstacles.

6. Discussion

This study aimed to propose and test an LPWAN-based emergency response system for people with special needs on a smart campus and to compare the performance of the LoRa-based system with other wireless communication technologies in terms of the latency, reliability, and range. The analysis of the performance of the proposed research work has been based on the benchmark proposed in studies [1,12,17]. We evaluated the proposed work using two parameters: reliability and latency. For data transmission, we utilized the WiFi LoRa 32 board with payload sizes of 16, 32, and 64 bits, and the results were compared at different heights. Additionally, experiments were conducted in both open environments and environments with obstacles such as buildings and trees. The results of our experiments suggest that LoRaWAN technology is a promising choice for better communication in smart campus emergency response systems. Our experiments involved the deployment of Heltec WiFi LoRa 32 devices at Hazara University, where we conducted several experiments at varying distances and heights above the ground's surface. We sent out 50 packets from each distance, with 50-m intervals in length, ranging from 0 to 600 m, and assessed their reception, RSSI, network latency, and reliability.

The experimental results indicate that the reliability and latency of LoRa-based communication systems are improved with a higher antenna size and minimum distance. This is because the signals are less likely to be obstructed by small objects and obstacles, resulting in better transmission quality. Conversely, with a lower antenna size and maximum distance, the reliability and latency suffer due to the green and urban environment of the campus, where signals face different types of objects and obstacles. It is worth noting that our results suggest that the performance of the LoRa-based system is not affected by cold and rainy weather, as the RSSI values approached zero, indicating a strong RSSI. This is in contrast to other cellular and satellite technologies, which are negatively affected by rainy weather. Thus, LoRaWAN technology appears to be more resilient in adverse weather conditions, making it a more reliable choice for emergency response systems.

We conducted extensive experiments to investigate the real-world implementations of LoRaWAN technology in the context of smart campus emergency response systems. By evaluating the performance of the proposed solution using these parameters, we aimed to provide insights into its practical applicability and effectiveness in addressing the unique challenges faced by individuals with special needs in emergency situations. Our study builds upon the existing literature by focusing specifically on LPWAN-based emergency response systems tailored for smart campuses, with a particular emphasis on addressing the needs of visually impaired individuals. We conducted experiments at Hazara University to assess the reliability and latency of LPWAN technology in various scenarios, including different distances and antenna heights. The findings from our experiments revealed that

LPWAN technology, particularly LoRaWAN, presents a viable option for implementing emergency response systems in smart campus environments, with a significant reliability. Our study contributes to the existing body of knowledge by providing insights into the performance of LoRa-based communication systems under different environmental conditions, such as urban and green campus environments with various obstacles. We observed that factors like the distance, payload size, and antenna height significantly impact the reliability and latency of LoRa communication, which can inform the design and optimization of emergency response systems for specific use cases and environments.

Our study has some limitations that should be addressed in future research. Firstly, the experiment was conducted in a single location, and the findings may not be generalizable to other environments. Secondly, the study only tested the performance of the LoRa-based system in terms of the reliability and latency, and other factors, such as the energy consumption, should be considered in future studies. Finally, the experiment was conducted in a controlled environment, while real-world scenarios may have more complex network conditions that may affect the system's performance. The experiments show that LoRaWAN technology is a promising choice for emergency response systems on smart campuses. The system's reliability and latency are improved with a higher antenna size and minimum distance, making it a more resilient choice for emergency response in adverse weather conditions. Future research should focus on addressing the limitations of this study and exploring the system's energy consumption and performance in real-world scenarios.

7. Conclusions

In this study, we successfully implemented an LPWAN-based emergency response system for people with special needs on the Hazara University campus, using Heltec WiFi LoRa 32 devices as the sender and receiver nodes. Our experimental evaluation of the system's performance has revealed valuable insights into the impact of various factors, such as the distance, antenna height, and packet size, on the reliability and latency of LoRa communication in an indoor D2D network. One of the key challenges of the system implementation was the presence of large trees surrounding the academic block buildings, which presented obstacles for D2D communication. Despite this challenge, our results have shown that LoRa technology can be a promising choice for reliable communication in emergency response scenarios, even in the presence of environmental barriers. Moreover, we observed that the data transmission quality of LoRa was positively affected by cold and rainy weather, suggesting that it may be more resilient to adverse weather conditions than other cellular and satellite technologies. Our findings have also highlighted the critical role of the antenna height in determining the reliability and latency of LoRa communication. Specifically, we found that the reliability of the system was highest for high antenna heights and small distances, while the latency was lowest for high antenna heights and small distances. These results suggest that optimizing the antenna height can significantly improve the performance of LoRa-based emergency response systems in indoor settings.

This study has provided valuable insights into the design and optimization of LPWAN-based emergency response systems for people with special needs. Future research in this area could focus on investigating the scalability and generalizability of our findings to different types of indoor environments and emergency scenarios. Further exploration of alternative LPWAN technologies and hybrid communication approaches may help to address some of the limitations of LoRa in high-density node environments.

Author Contributions: Conceptualization, H.S., A.I.J., Z.A., M.A.A. and O.I.A.; methodology, O.I.A.; software, H.S., A.I.J. and Z.A.; validation, A.I.J., Z.A., M.A.A. and A.A.; formal analysis, H.S., Z.A., M.A.A., O.I.A. and A.A.; investigation, O.I.A.; resources, A.A.; data curation, H.S. and M.A.A.; writing—original draft, H.S., A.I.J. and O.I.A.; writing—review and editing, Z.A., M.A.A. and A.A.; visualization, A.I.J., Z.A., M.A.A., O.I.A. and A.A.; supervision, A.I.J., Z.A. and A.A.; project administration, Z.A., O.I.A. and A.A.; funding acquisition, A.I.J., Z.A. and A.A. All authors have read and agreed to the published version of the manuscript.

Funding: This research was financially supported by the Deanship of Scientific Research at King Khalid University under research grant number (R.G.P.2/93/45).

Institutional Review Board Statement: Not applicable.

Informed Consent Statement: Not applicable.

Data Availability Statement: The original contributions presented in the study are included in the article, further inquiries can be directed to the corresponding authors.

Acknowledgments: The authors sincerely appreciate the support from the Deanship of Scientific Research at King Khalid University under research grant number (R.G.P.2/93/45). The authors also appreciate the support from Hazara University Mansehra, Pakistan, for the provision of funds to purchase and deploy the equipment used to perform experiments in this research.

Conflicts of Interest: The authors declare that they have no conflicts of interest.

References

1. Damaševičius, R.; Bacanin, N.; Misra, S. From Sensors to Safety: Internet of Emergency Services (IoES) for Emergency Response and Disaster Management. *J. Sens. Actuator Netw.* **2023**, *12*, 41. [CrossRef]
2. Khan, S.M.; Shafi, I.; Butt, W.H.; Diez, I.d.l.T.; Flores, M.A.L.; Galán, J.C.; Ashraf, I. A Systematic Review of Disaster Management Systems: Approaches, Challenges, and Future Directions. *Land* **2023**, *12*, 1514. [CrossRef]
3. Safi, A.; Ahmad, Z.; Jehangiri, A.I.; Latip, R.; Zaman, S.K.u.; Khan, M.A.; Ghoniem, R.M. A Fault Tolerant Surveillance System for Fire Detection and Prevention Using LoRaWAN in Smart Buildings. *Sensors* **2022**, *22*, 8411. [CrossRef] [PubMed]
4. Wang, Q.; Li, W.; Yu, Z.; Abbasi, Q.; Imran, M.; Ansari, S.; Sambo, Y.; Wu, L.; Li, Q.; Zhu, T. An Overview of Emergency Communication Networks. *Remote Sens.* **2023**, *15*, 1595. [CrossRef]
5. Cheimaras, V.; Peladarinos, N.; Monios, N.; Daousis, S.; Papagiakoumos, S.; Papageorgas, P.; Piromalis, D. Emergency Communication System Based on Wireless LPWAN and SD-WAN Technologies: A Hybrid Approach. *Signals* **2023**, *4*, 315–336. [CrossRef]
6. Jouhari, M.; Saeed, N.; Alouini, M.-S.; Amhoud, E.M. A Survey on Scalable LoRaWAN for Massive IoT: Recent Advances, Potentials, and Challenges. *IEEE Commun. Surv. Tutor.* **2023**, *25*, 1841–1876. [CrossRef]
7. Lima, W.G.; Lopes, A.V.R.; Cardoso, C.M.M.; Araújo, J.P.L.; Neto, M.C.A.; Tostes, M.E.L.; Nascimento, A.A.; Rodriguez, M.; Barros, F.J.B. LoRa Technology Propagation Models for IoT Network Planning in the Amazon Regions. *Sensors* **2024**, *24*, 1621. [CrossRef] [PubMed]
8. Areqi, M.A.; Zahary, A.T.; Ali, M.N. State-of-the-Art Device-to-Device Communication Solutions. *IEEE Access* **2023**, *11*, 46734–46764. [CrossRef]
9. Adibi, S.; Labrador, C.; Simmons, S. Method and System for Peer-to-Peer (P2P) ad-hoc Location Determination Routing Protocol 2014. US8843104B2, 23 September 2014.
10. Alanzy, M.; Latip, R.; Muhammed, A. Range wise busy checking 2-way imbalanced algorithm for cloudlet allocation in cloud environment. *J. Phys. Conf. Ser.* **2018**, *1018*, 012018. [CrossRef]
11. Yalçın, S. An artificial intelligence-based spectrum sensing methodology for LoRa and cognitive radio networks. *Int. J. Commun. Syst.* **2023**, *36*, e5433. [CrossRef]
12. Ortiz-Garcés, I.; Andrade, R.O.; Sanchez-Viteri, S.; Villegas-Ch, W. Prototype of an Emergency Response System Using IoT in a Fog Computing Environment. *Computers* **2023**, *12*, 81. [CrossRef]
13. Jain, K.; Saini, H.K. An Emergency Rescue Framework through Smart IoT LPWAN. In *Proceedings of the 2023 International Conference on Advancement in Computation & Computer Technologies (InCACCT), Punjab, India, 5–6 May 2023*; IEEE: New York, NY, USA, 2023; pp. 668–672.
14. Islam, M.; Jamil, H.; Pranto, S.; Das, R.; Amin, A.; Khan, A. Future Industrial Applications: Exploring LPWAN-Driven IoT Protocols. *Sensors* **2024**, *24*, 2509. [CrossRef] [PubMed]
15. Anand, S.; Vinodini Ramesh, M. An IoT Based Disaster Response Solution for Ocean Environment. In *Proceedings of the Adjunct Proceedings of the 2021 International Conference on Distributed Computing and Networking, Nara, Japan, 5–8 January 2021*; ACM: New York, NY, USA, 2021; pp. 19–24.
16. Mackey, A.; Spachos, P. LoRa-based Localization System for Emergency Services in GPS-less Environments. In *Proceedings of the IEEE INFOCOM 2019—IEEE Conference on Computer Communications Workshops (INFOCOM WKSHPS), Paris, France, 29 April–2 May 2019*; IEEE: New York, NY, USA, 2019; pp. 939–944.
17. Kodali, R.K.; Mahesh, K.S. Smart emergency response system. In *Proceedings of the TENCON 2017—2017 IEEE Region 10 Conference*; IEEE: New York, NY, USA, 2017; pp. 712–717.
18. Muhsin, A.; Alkhalid, F.F.; Oleiwi, B.K. Online Blind Assistive System using Object Recognition. *Int. Res. J. Innov. Eng. Technol.* **2019**, *3*, 47–51.

19. Kostyuk, A.; Tumanov, A.; Tumanov, V.; Zybina, O. Improving Emergency Response Systems in the Oil and Gas Industry to Reduce Environmental Damage. In *Proceedings of the E3S Web of Conferences, Semarang, Indonesia, 12–13 August 2020*; EDP Sciences: Les Ulis, France, 2020; Volume 221.
20. Ismail, D.; Saifullah, A. Handling Mobility in Low-Power Wide-Area Network. *arXiv* **2021**, arXiv:2101.01518.
21. Patel, D.; Won, M. Experimental Study on Low Power Wide Area Networks (LPWAN) for Mobile Internet of Things. *IEEE Veh. Technol. Conf.* **2017**, *2017*, 8108501. [CrossRef]
22. Ayoub, W.; Samhat, A.E.; Nouvel, F.; Mroue, M.; Jradi, H.; Prévotet, J.-C. Media independent solution for mobility management in heterogeneous LPWAN technologies. *Comput. Netw.* **2020**, *182*, 107423. [CrossRef]
23. Campana, T.; Casoni, M.; Marousis, A.; Maliatsos, K.; Karagiannis, A. E-SPONDER system: A new communication infrastructure for future emergency networks. In Proceedings of the International Conference on Wireless and Mobile Computing, Networking and Communications, Larnaca, Cyprus, 8–10 October 2014; pp. 136–143.
24. Sciullo, L.; Fossemo, F.; Trotta, A.; Felice, M. Di LOCATE: A LoRa-based mObile emergenCy mAnagement sysTEm. In Proceedings of the Proceedings—IEEE Global Communications Conference, GLOBECOM, Abu Dhabi, United Arab Emirates, 9–13 December 2018.
25. Onumanyi, A.J.; Abu-Mahfouz, A.M.; Hancke, G.P. Low Power Wide Area Network, Cognitive Radio and the Internet of Things: Potentials for Integration. *Sensors* **2020**, *20*, 6837. [CrossRef]
26. Peruzzi, G.; Pozzebon, A. A Review of Energy Harvesting Techniques for Low Power Wide Area Networks (LPWANs). *Energies* **2020**, *13*, 3433. [CrossRef]
27. Almuhaya, M.A.M.; Jabbar, W.A.; Sulaiman, N.; Abdulmalek, S. A Survey on LoRaWAN Technology: Recent Trends, Opportunities, Simulation Tools and Future Directions. *Electronics* **2022**, *11*, 164. [CrossRef]
28. Zanaj, E.; Caso, G.; De Nardis, L.; Mohammadpour, A.; Alay, Ö.; Di Benedetto, M.-G. Energy Efficiency in Short and Wide-Area IoT Technologies—A Survey. *Technologies* **2021**, *9*, 22. [CrossRef]
29. Iqbal, M.; Abdullah, A.Y.M.; Shabnam, F. An Application Based Comparative Study of LPWAN Technologies for IoT Environment. *2020 IEEE Reg. 10 Symp. (TENSYMP)* **2020**, *2020*, 1857–1860. [CrossRef]
30. Parrino, S.; Peruzzi, G.; Pozzebon, A. LoPATraN: Low Power Asset Tracking by Means of Narrow Band IoT (NB-IoT) Technology. *Sensors* **2021**, *21*, 3772. [CrossRef] [PubMed]
31. Zheng, Y.; Wu, Y.; Gao, J.; Cui, S. NB-IoT based method for monitoring the tilt status of transmission towers. *J. Phys. Conf. Ser.* **2021**, *2108*, 012033. [CrossRef]
32. Bima, W.I.W.K.; Suryani, V.; Wardana, A.A. Narrowband-IoT network for asset tracking system. *IOP Conf. Ser. Mater. Sci. Eng.* **2020**, *830*, 022087. [CrossRef]
33. Ferreira, B.; Gaspar, B.; Paiva, S.; Santos, A.; Cabral, J. Coverage and Deployment Analysis of NB-IoT Technology under Various Environment Scenarios. In *Proceedings of the 2020 2nd International Conference on Societal Automation (SA), Virtual Conference, 26–28 May 2021*; IEEE: New York, NY, USA, 2021; pp. 1–7.
34. LoRa Alliance. LoRaWAN® Network Coverage. Available online: https://lora-alliance.org/lorawan-network-coverage/ (accessed on 10 August 2023).
35. Piechowiak, M.; Zwierzykowski, P.; Musznicki, B. LoRaWAN Metering Infrastructure Planning in Smart Cities. *Appl. Sci.* **2023**, *13*, 8431. [CrossRef]
36. Anwar, K.; Rahman, T.; Zeb, A.; Khan, I.; Zareei, M.; Vargas-Rosales, C. RM-ADR: Resource Management Adaptive Data Rate for Mobile Application in LoRaWAN. *Sensors* **2021**, *21*, 7980. [CrossRef] [PubMed]
37. Di Renzone, G.; Parrino, S.; Peruzzi, G.; Pozzebon, A. LoRaWAN in Motion: Preliminary Tests for Real Time Low Power Data Gathering from Vehicles. In *Proceedings of the 2021 IEEE International Workshop on Metrology for Automotive (MetroAutomotive), Bologna, Italy, 2–3 July 2021*; IEEE: New York, NY, USA, 2021; pp. 232–236.
38. Al mojamed, M. On the Use of LoRaWAN for Mobile Internet of Things: The Impact of Mobility. *Appl. Syst. Innov.* **2021**, *5*, 5. [CrossRef]
39. Sobhi, S.; Elzanaty, A.; Selim, M.Y.; Ghuniem, A.M.; Abdelkader, M.F. Mobility of LoRaWAN Gateways for Efficient Environmental Monitoring in Pristine Sites. *Sensors* **2023**, *23*, 1698. [CrossRef] [PubMed]
40. Xiao, Y.; Chen, Y.; Nie, M.; Zhu, T.; Liu, Z.; Liu, C. Exploring LoRa and Deep Learning-Based Wireless Activity Recognition. *Electronics* **2023**, *12*, 629. [CrossRef]
41. Sobhi, S.; Elzanaty, A.; Ghuniem, A.M.; Abdelkader, M.F. Vehicle-Mounted Fog-Node with LoRaWAN for Rural Data Collection. In *Proceedings of the 2022 IEEE 33rd Annual International Symposium on Personal, Indoor and Mobile Radio Communications (PIMRC), Online, 12–15 September 2022*; IEEE: New York, NY, USA, 2022; pp. 1438–1444.
42. HELTEC AUTOMATION. WiFi LoRa 32(V3). Available online: https://heltec.org/project/wifi-lora-32/ (accessed on 10 August 2023).
43. Verba, N.; Chao, K.M.; Lewandowski, J.; Shah, N.; James, A.; Tian, F. Modeling industry 4.0 based fog computing environments for application analysis and deployment. *Futur. Gener. Comput. Syst.* **2019**, *91*, 48–60. [CrossRef]

sensors

MDPI

Article

Towards Mass-Scale IoT with Energy-Autonomous LoRaWAN Sensor Nodes

Roberto La Rosa [1,*], Lokman Boulebnane [2], Antonino Pagano [2,3,*], Fabrizio Giuliano [2,3] and Daniele Croce [2,3]

[1] STMicroelectronics, Stradale Primosole 50, 95121 Catania, Italy
[2] Department of Engineering, University of Palermo, 90128 Palermo, Italy; lokman.boulebnane@community.unipa.it (L.B.); fabrizio.giuliano@unipa.it (F.G.); daniele.croce@unipa.it (D.C.)
[3] Palermo Research Unit, CNIT (National Inter-University Consortium for Telecommunications), 90128 Palermo, Italy
* Correspondence: roberto.larosa@st.com (R.L.R.); antonino.pagano@unipa.it (A.P.)

Abstract: By 2030, it is expected that a trillion things will be connected. In such a scenario, the power required for the trillion nodes would necessitate using trillions of batteries, resulting in maintenance challenges and significant management costs. The objective of this research is to contribute to sustainable wireless sensor nodes through the introduction of an energy-autonomous wireless sensor node (EAWSN) designed to be an energy-autonomous, self-sufficient, and maintenance-free device, to be suitable for long-term mass-scale internet of things (IoT) applications in remote and inaccessible environments. The EAWSN utilizes Low-Power Wide Area Networks (LPWANs) via LoRaWAN connectivity, and it is powered by a commercial photovoltaic cell, which can also harvest ambient light in an indoor environment. Storage components include a capacitor of 2 mF, which allows EAWSN to successfully transmit 30-byte data packets up to 560 m, thanks to opportunistic LoRaWAN data rate selection that enables a significant trade-off between energy consumption and network coverage. The reliability of the designed platform is demonstrated through validation in an urban environment, showing exceptional performance over remarkable distances.

Keywords: battery-free; energy harvesting; IoT; wireless sensor node; LPWAN; LoRaWAN

1. Introduction

Wireless sensor nodes (WSNs) are rapidly becoming the most critical elements in IoT infrastructure for several domain-based solutions, aiming to enhance the quality of life by integrating cutting-edge technologies. Wireless devices possess versatile computing, communication, and control capabilities [1], making them adaptable to a wide range of IoT applications. While the requirements for WSNs can vary significantly, defining fixed criteria for nodes and networks is impractical. Nonetheless, common characteristics define WSNs, including deployment adaptability, mobility support, compactness, lightweight design, energy efficiency, wireless communication capability, and power optimization [2]. As the demands on wireless nodes continue to grow, these include increasingly performing complex and advanced functions [3]. Battery-powered sensor devices are commonly used in WSNs and often present challenges of power consumption and the need to replace batteries [4], which is a critical issue. Ongoing research efforts aim at increasing the energy density of batteries, and the search is on for solutions to extend the operational life of sensor nodes. However, even with the most advanced technology available, the lifetime of the entire network remains limited, typically ranging from a few months to a few years [5].

A promising approach to achieving perpetual and sustainable network operation is using energy-autonomous, battery-less wireless systems powered solely by energy harvesting (EH) from environmental sources like light, radio waves, temperature variations, vibrations, motion, wind, and water currents. These approaches provide a practical solution for efficiently harnessing energy from the environment, ensuring the sustainable power supply for wireless sensor nodes, and enabling uninterrupted network operation [1,4,6,7]. Energy-autonomous wireless systems focus on efficiency through the use of a variety of ultra-low-power design techniques. These techniques include the use of low-power microcontrollers and the implementation of operating modes that minimize or eliminate power consumption or efficient power control mechanisms to optimize internal energy use [3,6,8,9].

In WSNs, communication is generally the most energy-consuming operation, mainly due to the high power consumption associated with radio transmissions [5]. Adaptive transmission algorithms play a vital role in optimizing the efficiency and dependability of these sensors to address this issue. The goal is to find a trade-off between energy consumption and communication demands by considering design parameters such as transmission power, data rate, modulation scheme, and duty cycle [6]. A current trend is to adopt energy-efficient communication technologies such as ZigBee, Bluetooth Low Energy (BLE), and LoRaWAN. In particular, LoRaWAN is used in various applications due to its exceptional range and energy efficiency. It operates in the license-free Industrial, Scientific, and Medical (ISM) band [10–12]. LoRaWAN, on the other hand, builds on LoRa to provide long-range communications between LoRa devices and network gateways [13,14]. The literature presents numerous energy-conscious transmission algorithms designed to enhance the performance of battery-free IoT sensors [15–18]. Adaptive transmission algorithms are pivotal in this context, as they play a crucial role in maximizing both efficiency and reliability [6,9]. These approaches take into account parameters such as transmission power, data rate, and the modulation scheme (e.g., spreading factor and bandwidth) while using off-the-shelf components to eliminate the need for battery replacement in devices located in hazardous areas [3,19].

Taking advantage of the widespread availability and cleanliness of this renewable resource, this paper presents a novel battery-free EAWSN platform powered by solar energy. The platform comprises an STM32WL Nucleo 64 board with an STM32WLJC1 MCU that can support LPWAN with a dual-core 32-bit architecture (ARM CortexM4/M0) and a radio frequency (RF) transceiver that operates from 150 MHz through 960 MHz. Our design also incorporates a 2 mF to 16 mF amorphous silicon solar cell (AM1815) and storage condenser ($C_{storage}$) for testing and validation. We argue in favor of a measurement-based approach, which we consider to be more practical than mathematical models or simulation-based studies. In addition, our work is original in optimizing network parameters such as packet size and dedicated storage allocation along with the LoRaWAN configuration, tailoring each setup for self-powered and battery-free LoRaWAN devices. Finally, our work aims to address the following research questions: (I) How does a battery-free LoRaWAN sensor perform in terms of coverage and signal quality in an urban environment? (II) How does energy storage capacity influence the packet length and spreading factor of the battery-free sensor? (III) What are the limitations of real-world deployment of battery-free sensors in urban environments? (IV) How can these limitations be overcome through optimization of system design?

Our paper is structured in the following way: Section 2 presents the related works, focusing on the LoRaWAN background and battery-free devices for IoT. In Section 3, we analyze the architectural design of our EAWSN system, explaining its main components description, design, and detailed description of the microcontroller. Section 4 outlines the experimental objectives and setup, providing detailed information on tools, equipment, and base station (BS) configuration to effectively exploit the LoRaWAN protocol through a gateway and network server. Section 5 focuses on analyzing the experimental data, showing how variations in LoRaWAN parameters affect energy consumption, range, and packet length (PL). The results show the performance and efficiency of the system in transmitting data over a range of distances, in both base station and gateway environments, and within the power constraints imposed by the battery-free design. Section 6 discusses the recommended settings for the EAWSN under different lighting conditions, addresses possible limitations, and examines its mass scale capability. Finally, the concluding section summarizes the main findings and contributions.

2. Related Works

This section presents the background on LoRaWAN and provides a brief literature review on energy-autonomous and battery-free sensors for IoT, highlighting the potentialities and the challenges of this technology.

2.1. Background on LoRaWAN

LoRa technology represents a significant evolution in wireless communications, specifically designed to meet the needs of the IoT [20]. It is characterized by the ability to transmit data over long distances while using minimal energy [13]. LoRa is based on spread spectrum modulation technology, known for its remarkable signal propagation capabilities, ensuring reliable communications in diverse environments, including urban, rural, and industrial landscapes [21,22]. By optimizing the delicate balance between communication range and power efficiency, LoRa demonstrates adaptability through its control over transmit power, modulation rate, and payload size, making it highly suitable for various application scenarios [23]. Furthermore, the unique architecture of LoRa enables the creation of extensive networks over long distances, making it an effective choice for a variety of applications, such as smart cities, agriculture, asset tracking, and environmental monitoring [24]. LoRaWAN comprises two essential layers: the physical layer, utilizing Semtech's patented Chirp Spread Spectrum modulation (CSS), and the Media Access Control (MAC) layer, governed by the LoRa Alliance-defined LoRaWAN protocol. These combined technical aspects establish LoRa as a disruptive force within the realms of IoT and long-range wireless communications [25]. One of the most adopted MAC layers within LoRa technology is LoRaWAN [26,27]. It plays a pivotal role in overseeing access to shared media and ensuring efficient, dependable data transmission among connected devices [14]. This standard is designed to enhance communication across wide-area networks. As depicted in Figure 1a, the architecture of the LoRaWAN network shows how end devices establish communication with the gateway through the LoRa RF interface. Subsequently, the gateway transmits frames to the server via non-LoRaWAN networks like Ethernet, Cellular (e.g., 3G/4G/5G), Wi-Fi, and similar alternatives [28]. Figure 1b showcases the communication stack specific to LoRaWAN, where the physical layer delineates the ISM band (e.g., 868 MHz in Europe).

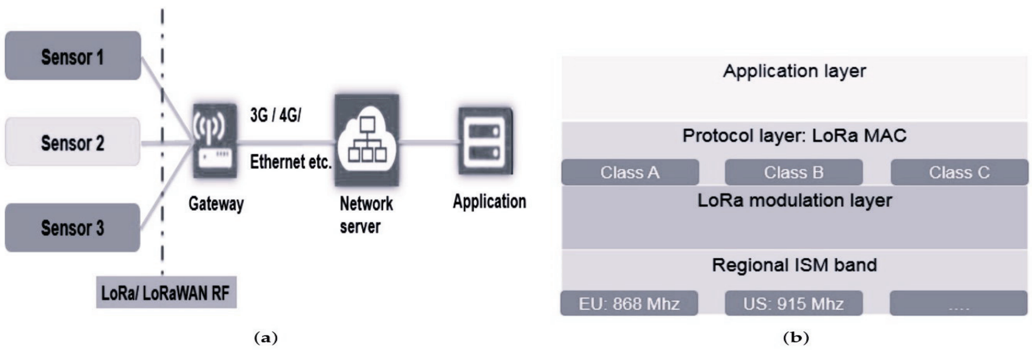

Figure 1. (**a**) LoRaWAN network architecture. (**b**) LoRaWAN protocol stack.

The LoRaWAN specification outlines three distinct classes designed to address various application demands. These classes determine the communication protocols between devices and the network and regulate power consumption management. An overview of each LoRaWAN device class can be found in [14] and is summarized in Table 1. Choosing which class to use depends on the specific requirements of the IoT application. Class A is ideal for battery-powered devices with minimal power consumption requirements [29,30], even if this means occasional downlink latency. For applications that require more predictable downlink communication at the expense of higher power consumption, Class B is suitable. Class C is used when low-latency downlink communication is essential and it is possible to relax the power restrictions.

Table 1. LoRaWAN Classes Comparison.

Class	Description	Energy Consumption
A	Sensor triggers, Followed by a downlink response.	Most efficient
B	Communication occurs in slots Simple-synchronized beacon	Controlled downlink
C	Communication without delay.ensuring Downlink communication without delay.	High power consumption

The spreading factor (SF) is a critical parameter in the LoRa physical layer that defines the ratio between symbol rate (Rs) Equation (1) and chip rate (Rc) Equation (2),

$$Rs = \frac{1}{Ts} = \frac{BW}{2^{SF}} \quad \text{symbols/sec} \tag{1}$$

$$Rc = Rs \cdot 2^{SF} \quad \text{chips/sec} \tag{2}$$

SF determines the number of chips used to encode a symbol. For each SF, Table 2 illustrates 2^{SF} chips per symbol.

Table 2. Spreading Factors and corresponding chips length.

Spreading Factor (SF)	Chips Length 2^{SF}
7	128
8	256
9	512
10	1024
11	2048
12	4096

Increasing the spreading factor (SF) value results in a higher sensitivity of the receiver and extends the range. However, this adjustment reduces the data bit rate (as illustrated in Equation (4)) and increases the time on air (ToA) of the packet. CR denotes the code rate determining the extent of forward error correction (FEC). LoRa provides CR values ranging from 0 to 4, with CR = 0 denoting no FEC.

$$Sensitivity = -174 + 10\log(BW) + SNR + NF \tag{3}$$

$$Rb = SF \cdot \frac{BW}{2^{SF}} \cdot \frac{4}{4+RC} \qquad \text{bits/sec} \tag{4}$$

Each incremental increase in spreading factor (SF) halves the transmission rate, doubling the transmission time and consequently increasing the power consumption [31,32].

LoRaWAN has a set of six orthogonal spreading factors in the range of 7 to 12, providing a dynamic balance between data rate and communication range, as represented in Table 2. Note that LoRA network conditions (e.g., power transmission or end-device position) can have significant impact on orthogonality of SF allocations [33–35].

2.2. Internet of Battery-Less Things

Batteries have limitations, presenting several challenges. As we progress into a future marked by countless IoT devices, this would lead to an economic burden due to the need to replace large quantities of depleted batteries and devices. Furthermore, it would also pose significant environmental concerns [36]. Indeed, an expansion of IoT based on trillions of new battery-powered devices could lead to an environmental catastrophe. Most of the batteries that are disposed of are deposited in landfills, with a mere 5% undergoing recycling [36,37]. As these discarded batteries break down, they emit harmful fumes into the atmosphere and leach chemicals into the soil. Additionally, the process of battery recycling introduces pollutants into water bodies [37].

Over the last decade, research has focused on a new system, widely deployed and battery-free. Similar to conventional sensors, battery-free IoT devices are equipped with modules for detection, processing, and communication. Instead of relying on batteries storing chemical energy, these devices use small capacitors as energy buffers. For instance, Delgado et al. [38] introduced a Markov model for assessing the performance of battery-free devices in uplink and downlink (UL/DL) transmissions, assessing their effectiveness regarding factors like device setup and environmental circumstances. The study demonstrated that with a 47 mF capacitor and a 1 mW energy harvesting rate, it is feasible to sustain 1 Byte transmissions every 60 s.

Moreover, in [39], the authors investigated the efficacy of energy-harvested battery-free sensors in case of random transmission patterns. Employing stochastic geometry and Markov chain analysis techniques, a mathematical model was devised for each system component, allowing for the analytical determination of the probabilities associated with energy and communication failures. The research underscored that the adaptive data rate (ADR) feature in LoRa networks could result in energy deficits when utilizing higher spreading factors. Consequently, they proposed adaptive charging time strategies as a potential remedy. In their work [40], the authors explored the ideal parameters for scheduling application tasks on battery-less IoT sensor devices. Through an environment emulator, they validated a mathematical model for selecting these parameters, aiming to minimize the application cycle completion time for sensing and transmission tasks under varying device and environmental conditions. Their analysis indicated that a device fitted with a 10 mF capacitor can perform temperature measurements and transmit data at intervals of at least once every 5 s while being capable of harvesting a minimum of 50 mW (equivalent to 10 mA of current). Battery-free IoT devices operate intermittently due to the high variability and unpredictability of the harvested ambient energy, leading to frequent power interruptions. This operating pattern can hinder the normal progression of computational operations, as energy interruptions prevent continuous monitoring. In these cases, the combined use of supercapacitors and adaptive algorithms can optimize monitoring even by dynamically adjusting key network parameters, including packet transmission time, data redundancy, and packet size, to enhance device performance, for instance, optimizing data monitoring and transmission even when the natural energy source is absent, such as during the night [6].

In the study by Sabovic et al. [40], the researchers delved into determining the best parameters for scheduling application tasks on battery-less IoT sensor devices. Utilizing an environment emulator, they confirmed the accuracy of a mathematical model designed to select these optimal parameters, to achieve the shortest completion time for application cycles, thereby facilitating sensing and transmission tasks across diverse device and environmental conditions. Their analysis demonstrated that a device furnished with a 10 mF capacitor is capable of performing temperature measurements and transmitting data at intervals of no more than once every 5 s, while being able to harvest a minimum of 50 mW (equivalent to 10 mA of current). Battery-free IoT devices operate intermittently due to the highly variable and unpredictable nature of harvested ambient energy, resulting in frequent power disruptions. Such operational interruptions can impede the smooth flow of computational tasks, as discontinuous energy availability prevents continuous monitoring.

In such scenarios, employing supercapacitors in conjunction with adaptive algorithms can optimize monitoring by dynamically adjusting key network parameters like packet transmission timing, data redundancy, and packet size, thereby enhancing device performance, for instance, optimizing data monitoring and transmission even during periods of natural energy absence, such as nighttime, as discussed in [6]. Finally, to the best of our knowledge, this study represents the first real-world validation of battery-free wireless sensors in a complex urban environment. However, these theoretical results, and in particular [38,39], might be overly optimistic in terms of interarrival times between packets and the size of the storage capacitor, requiring to be confirmed in a real-world implementation.

3. Design of the Energy-Autonomous and Battery-Free LoRaWAN Sensor Node

In a standard wireless sensor network (WSN), a sensor without a conventional battery must efficiently harvest, control, and store energy to perform tasks such as sensing, data processing, and wirelessly transmitting data to a remote base station.

The basic architecture of an energy-autonomous wireless node (EAWSN), powered solely by energy harvested from the environment, is shown in the block diagram in Figure 2. This diagram also shows the LORIOT cloud which includes a network server (NS) and an application server (AS). The LORIOT LoRaWAN network server integrates all the main output formats and several IoT platforms.

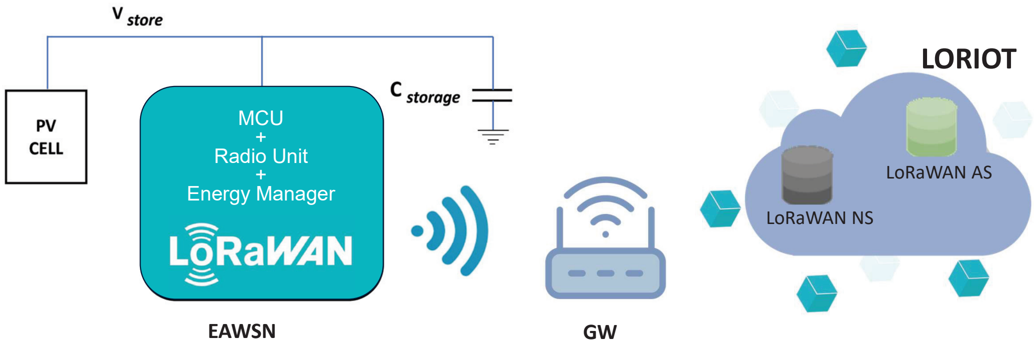

Figure 2. LoRaWAN architecture with block diagram of EAWSN, gateway (GW), and LORIOT cloud, which includes network server (NS) and application server (AS).

Figure 3 provides a visual depiction of the operation of the EAWSN, illustrating the alternating phases of energy harvesting and data transmission. In the energy harvesting phase, the node harvests energy from ambient light via the photovoltaic transducer and accumulates it in the storage capacitor ($C_{storage}$), gradually increasing the voltage (V_{store}). The energy stored is subsequently utilized to power the LoRaWAN radio during the data transmission phase.

The key design challenge in developing an EAWSN revolves around efficiently managing these limited energy resources, which, in this work, is primarily provided by the light-induced current generated by the photovoltaic cell.

Energy management in an EAWSN is the principal design challenge because the system relies uniquely on energy harvested from the environment, which is inherently limited. Therefore, the power consumption and energy efficiency of each component within the system are critical. For the system to operate sustainably and autonomously, it must ensure efficient energy utilization. For this reason, the design of these systems utilizes ultra-low-power architectures, with particular attention paid to the appropriate selection of devices in terms of power consumption. Based on these principles, the STM32WL5 microcontroller (by STMicroelectronics) was selected, as it is an ultra-low-power microcontroller device that offers comprehensive support for eight primary low-power modes, including Low-Power Run, Sleep, Low-Power Sleep, Stop 0, Stop 1, Stop 2, STANDBY with RAM retention, Standby, and Shutdown. Within each of these main modes, several configurable sub-modes provide a range of power-saving options [41]. The STM32WL5 microcontroller includes a programmable voltage detector (PVD) that can operate while the MCU is in a low-power mode. This PVD is fundamental for the development of battery-free sensors. The PVD continuously monitors the voltage level of the storage voltage (V_{store}). When the V_{store} reaches its highest value V_H, the system switches from the energy harvesting phase to the data transmission phase.

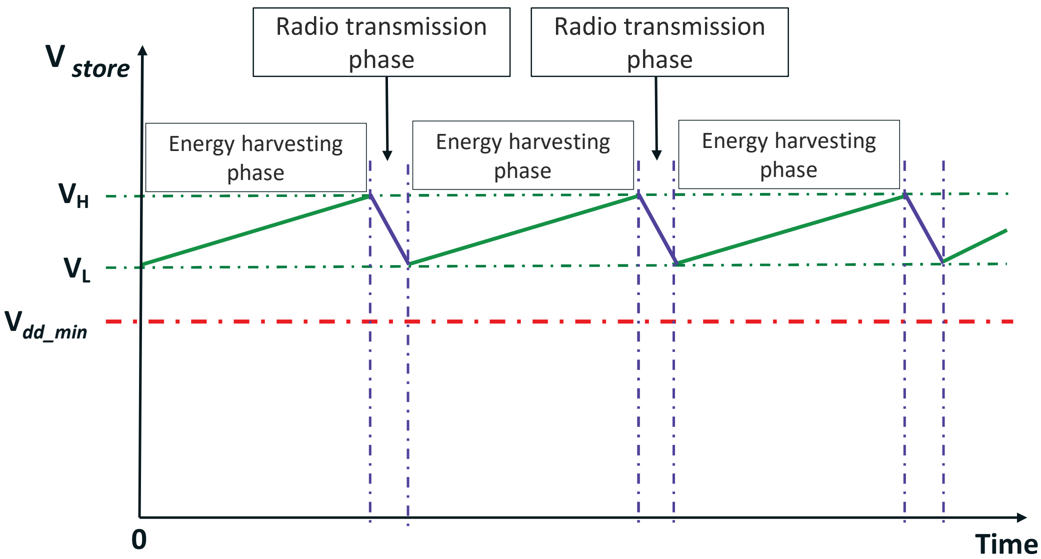

Figure 3. Functional description of the designed EAWSN platform.

During the data transmission phase, the current required to power the radio is tens of milliamperes, which exceeds, by more than an order of magnitude, the photovoltaic transducer's current generation, typically in the order of tens of microamperes. As a result, (V_{store}) drops rapidly and reaches its lowest point, V_L. To ensure uninterrupted operation and prevent MCU from resetting, V_L must never fall below the minimum MCU bias voltage, V_{dd_min}. Therefore, the design must ensure the following conditions for the voltage V_L and the storage capacitor $C_{storage}$, as expressed by Equations (5) and (6).

$$V_L > V_{dd\_min} \tag{5}$$

$$C_{storage} > \frac{1}{2} \cdot E_{LoRa\_TX} \cdot (V_H^2 - V_L^2) \tag{6}$$

where the energy required to transmit a data packet, denoted as E_{LoRa_TX}, is subject to various influencing factors. Among these, critical factors affecting energy consumption for transmitting LoRaWAN data packets include packet length, spreading factor (SF), bandwidth (BW), coding rate, and transmitted power. During the energy harvesting phase, the total quiescent current (I_q) of the system is approximately 1 µA, a crucial performance threshold for the limit of detection (LoD) of the system. While actively harvesting energy, the $C_{storage}$ capacitor is charged by the current supplied by the photovoltaic source. Maintaining a positive balance between the current generated by the photovoltaic source and the current supplied to the load is essential for successful charging, especially under low-light-intensity conditions, reaching as low as 200 lux. Consequently, the photovoltaic harvester must deliver a current higher than the quiescent current I_q. This requirement leads to the selection of the amorphous silicon solar cell AM-1815 by Panasonic [42]. This cell offers a typical output current I_{ope} of 45.7 µA at the voltage V_{ope} of 3.0 V under a light intensity of 200 lux, with maximum overall dimensions of 58.1 mm × 48.6 mm × 1.1 mm. In addition, the A108G Ultra Low ESR COTS-Plus tantalum capacitor was selected for its high-performance characteristics, including a capacitance value of 1 mF and a voltage rating of 4 VDC, making it an ideal choice for $C_{storage}$ [43].

4. System Configuration Setup and Experimental Procedure

The primary function of the designed EAWSN is to establish communication with a base station, which enables the transmission of data in an energy-efficient and self-sustaining manner. Figure 4 illustrates the system components of the LoRaWAN protocol standard. In particular, Figure 4a shows the EAWSN platform, and Figure 4b shows the gateway used. The gateway consists of the NUCLEO-F746ZG board and the RisingHF LoRaWAN GS&HF1 (868/915/923 MHz) extension board with antenna from STMicroelectronics [44]. To ensure compatibility with the LoRaWAN protocol, the EAWSN must be configured to comply with protocol standards. This configuration increases the versatility and adaptability of the designed EAWSN platform for different applications.

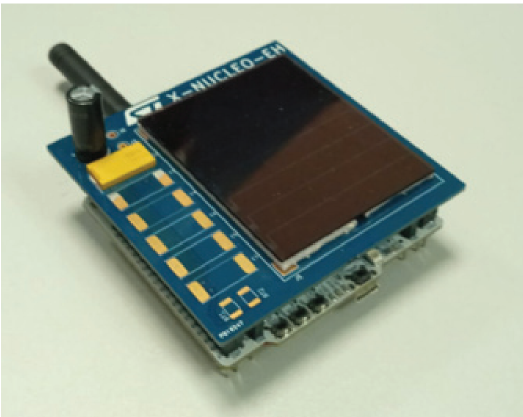

(a)

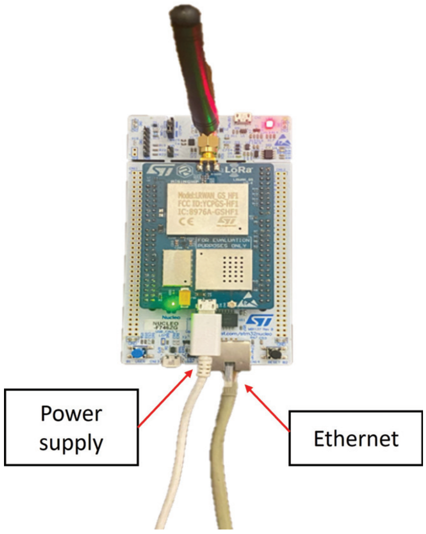

(b)

Figure 4. System components for LoRaWAN protocol configuration. (**a**) EAWSN platform with (NUCLEO-WL55JC) board, amorphous silicon solar cell (AM1815), and $C_{storage}$ ranging from 2 mF to 16 mF. (**b**) Gateway (NUCLEO-F746ZG) as receiver.

4.1. EAWSN Configuration for LoRaWAN Protocol

The battery-free node was configured in CLASS A mode of the LoRaWAN protocol, as it is preferred for its energy-efficient characteristics, as described in [29]. Additionally, activation by personalization (ABP) was set to eliminate the need to create a session between the gateway and the EAWSN, and all receive windows of the EAWSN system were disabled for energy efficiency. Finally, the transmitted packet was configured to conform to the LoRaWAN packet format, as defined in Equation (7), which is 255 bytes in length for SF7, with a payload of 242 bytes and a header of 13 bytes.

$$MHDR(1) + FHDR(7) + Port(1) + Payload(242) + MIC(4) \tag{7}$$

The transmit power level was set to 14 dBm, and adaptive data rate (ADR) was disabled to enable fixed spread factor transmission and avoid dynamic SF transmissions. In fact, the setting of transmission parameters such as spreading factor (SF) varied in the range of 7 to 12 between experiments. Finally, to improve data security through AES-256 encryption, a 16-byte application session key, network session key, and 4-byte device address were stored in the EAWSN's nonvolatile memory.

4.2. Gateway Setup and Configuration

In our setup, the gateway, an NUCLEO-F746ZG board, is preconfigured to send data packets to the LORIOT network server by default. However, it is important to emphasize the adaptability of the system. It is possible to change the configuration of the gateway to enable compatibility with other network servers that utilize the Semtech packet forwarder protocol. For example, this may involve modifying the LoRaWAN server, MAC address, and gateway extended unique identifier (EUI) [45].

4.3. Network Server Setup

The server used is LORIOT EU1, located in Frankfurt, Germany. The configuration process includes entering the LoRaWAN server settings, MAC address, and gateway EUI into the base platform (packet forwarder STM). Finally, sensor devices can be registered by inputting device-specific parameters such as device address, network session key, and application session key, corresponding to those provided to EAWSN.

4.4. Maximum Achievable Packet Length

The initial phase involves the determination of the maximum reliable packet length (PL) that the EAWSN system can accommodate using LoRaWAN connectivity while simultaneously measuring energy consumption. Through the manipulation of PL and LoRaWAN parameters, our objective is to pinpoint the optimal configuration that strikes a balance between data throughput and power consumption. This preliminary phase is integral in gaining essential insights into the system's data transmission capabilities under various conditions and will serve as a guiding factor for our battery-free sensor design in real-world implementations.

We started by setting up our equipment with some initial values: SF7, a PL = 10 bytes, and $C_{storage} = 2$ mF. We used an oscilloscope to check the minimum voltage drop V_L. Then, the step-by-step process was initiated. At each step, PL increased by 10 bytes V_L, measured again until V_L falls into the range of 1.8 to 2 volts to ensure the condition in Equation (5) when V_L reaches this voltage range, the maximum PL that the EAWSN platform could handle with that particular $C_{storage}$.

To expand the scope of our research, the energy storage $C_{storage}$ increased by 2 mF, and the entire process is repeated. This incremental adjustment of $C_{storage}$ was carried out iteratively until we reached a final value of 16 mF. This stepwise approach was designed to investigate the impact of increased stored energy on the maximum attainable PL in our study. Furthermore, this experiment covered all SF ranging from SF7 to SF12. This approach allowed for a comprehensive examination of how variations in SF values and specific energy storage $C_{storage}$ influenced the maximum achievable PL. These efforts contributed significantly to a more comprehensive understanding of the performance of EAWSN with LoRaWAN connectivity under different conditions and configurations.

4.5. Determining the Coverage

In the second phase, the aim is to determine the maximum achievable communication range of the EAWSN, building on our findings from the first phase. We wanted to investigate the ability of the system to achieve extended communication distances while maintaining a constant configuration. This experiment is of paramount importance in understanding the operational limits of the EAWSN, with particular emphasis on its range performance. By investigating the maximum achievable communication distance, we will gain valuable insight into the system's capabilities under varying conditions, thereby guiding our design choices for real-world implementations.

In this phase, the focus shifts to the evaluation of the EAWSN coverage in a specific environment an urban area in Catania, Italy, a noisy environment due to the presence of buildings and infrastructure. The configuration of the EAWSN includes fixed parameters: a BW of 125 kHz, a CR of 4/5, a transmit power (TP) of 14 dBm, and a PL of 20 bytes. The EAWSN will be maintained at a height of 15 m above ground.

The first test uses SF7 with an energy storage capacity ($C_{storage}$) of 2 mF. The next test will select SF8 and set $C_{storage}$ to 4 mF.

5. Experimental Results

In this section, experimental results regarding test coverage and the effect of storage capacitor dimensions on LoRaWAN packet length and spreading factor are presented.

5.1. Analyzing the Maximum Packet Length

In order to determine the maximum achievable packet length (PL) of the designed EAWSN platform, several parameters were kept constant during the measurement phase, including a bandwidth (BW) of 125 kHz, a transmit power (TP) of 14 dBm, and a code rate (CR) of 4/5. To determine the energy consumption E_{LoRaTX} for each transmitted packet, a PicoScope oscilloscope was used to monitor the minimum voltage drop at each transmission packet. As already discussed in Section 3, the design must meet the conditions expressed in Equations (6) and (5). In particular, Equation (5) shows how the minimum voltage V_L must always be above V_{dd_min}, i.e., 1.7 V for the STM32WL55JC1. Figure 5 shows the experimental measurements of the voltage V_{store} through an oscilloscope. This analysis explores various PL while keeping constant at 2 mF the $C_{storage}$ capacitance value. The radio is configured with spreading factor 7 (SF7), BW = 125 kHz, and TP = 14 dBm. The relationship between PL and voltage drop V_L reveals an inverse proportionality so that while increasing the packet length, the voltage level V_L decreases. As shown in Figure 5a,b when the radio transmits data with a packet length of 10 bytes (PL = 10 bytes), the voltage V_L decreases to ≈2.5 V, while for a higher packet length of 30 bytes, the voltage drop diminishes further to the value $V_L \approx 2$ V. Based on this observation, it is essential to avoid using a packet length greater than 30 bytes to prevent the system from entering reset mode.

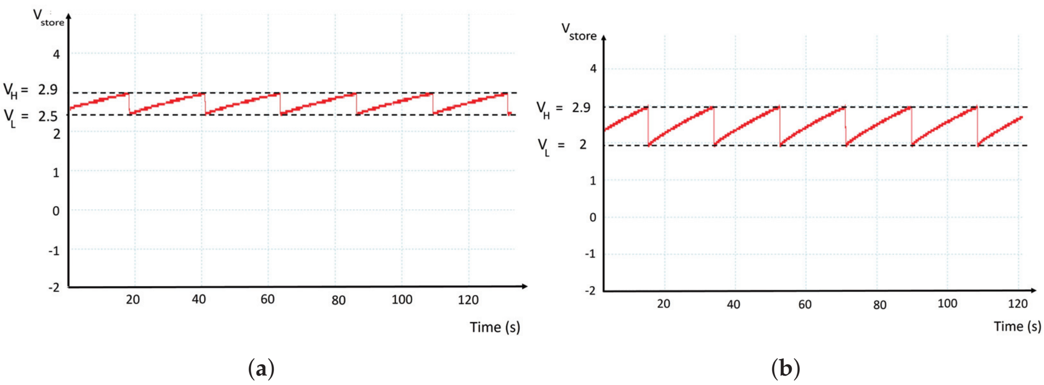

Figure 5. Experimental measurements with the oscilloscope of the voltage V_{store}. Setup conditions: SF = 7, BW = 125 kHz, TP = 14 dBm, $C_{storage}$ = 2 mF. Figure (**a**) shows the voltage V_{store} for PL = 10 bytes, $V_H \approx 3$ V. $V_L = 2.5$ V. Figure (**b**) shows the voltage V_{store} for PL = 30 bytes, $V_H \approx 3$ V. $V_L = 2.0$ V.

Figure 6a and Figure 6b show, respectively, the measurement results of the voltage V_L and the corresponding energy consumption during the transmission phase by varying PL. These experimental results were obtained using a 4 mF storage capacitor ($C_{storage}$). Doubling the storage capacitance from 2 mF to 4 mF results in a doubling of the stored energy, enabling an increase in packet length from 30 to 80 bytes.

Figure 7 shows the experimental results of measuring packet lengths corresponding to $C_{storage}$ values and their associated spreading factors (SF7 to SF12). The graph clearly shows that with a $C_{storage}$ of 4 mF, an SF of 7 allows a maximum PL of 80 bytes. This maximum PL is reduced to 30 bytes at SF8 and further reduced to only 10 bytes at SF9. Beyond SF9, the system shows an inability to transmit data packets of any length. This limitation is due to the modulation scheme associated; when SF increases, the time-on-air (TOA) also increases, resulting in higher power consumption.

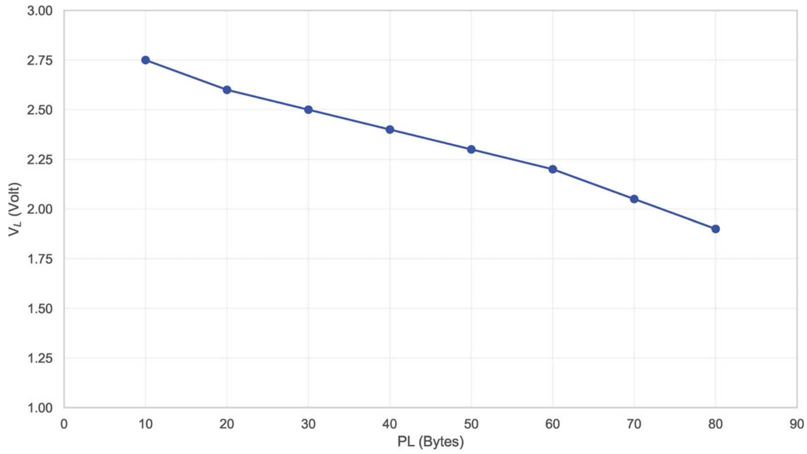

(**a**)

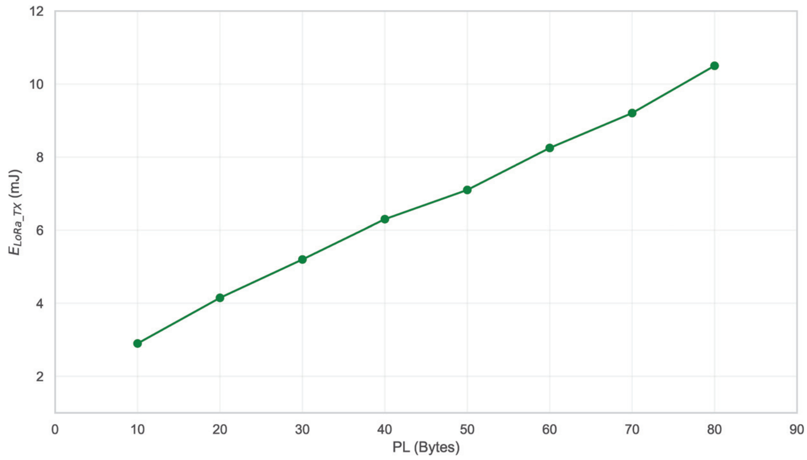

(**b**)

Figure 6. Measurement results: Variations in V_{store}, V_L, and E_{LoRa_TX} vs. packet length (PL). Setup conditions: SF = 7, BW = 125 kHz, TP = 14 dBm, $C_{storage}$ = 4 mF. Figure (**a**) shows minimum voltage V_L vs. PL. Figure (**b**) shows energy required E_{LoRa_TX} for transmission vs. PL.

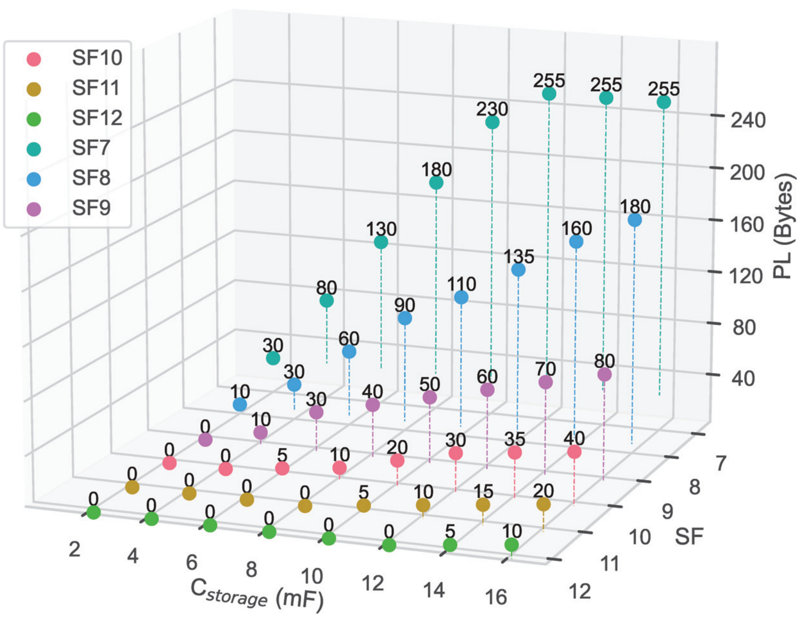

Figure 7. LoRaWAN maximum PL as function of $C_{storage}$ for SF from 7 to 12. Setup conditions: BW = 125 kHz, TX output power =İ14 dBm, CR = 4/5.

These measurements provide valuable insights into the behavior of the designed EAWSN platform. Increasing $C_{storage}$ extends the maximum PL while keeping SF constant. On the other hand, maintaining $C_{storage}$ at the same level but increasing SF approximately halves the required packet length. These results have important implications for optimizing the performance of our system.

5.2. Analyzing the Coverage

To evaluate the communication range of our EAWSN system, we carried out a series of tests in different locations in a busy urban environment in the central area of Catania. Table 3 shows a conductive test carried out in the scenario of Figure 8 with the following specific parameters: SF7, a bandwidth of 125 kHz, a transmission (TX) output power of 14 dBm, CR = 4/5, PL = 20 bytes and $C_{storage}$ = 2 mF. The GW is positioned at a height (h) = 15 m. The test provided detailed data on RSSI and SNR for each tested point (points 1 to 4). The data presented in the table indicate that at point 4 at a distance of ≈560 m, the minimum achievable SNR and RSSI were −8 dB and −110 dBm, respectively.

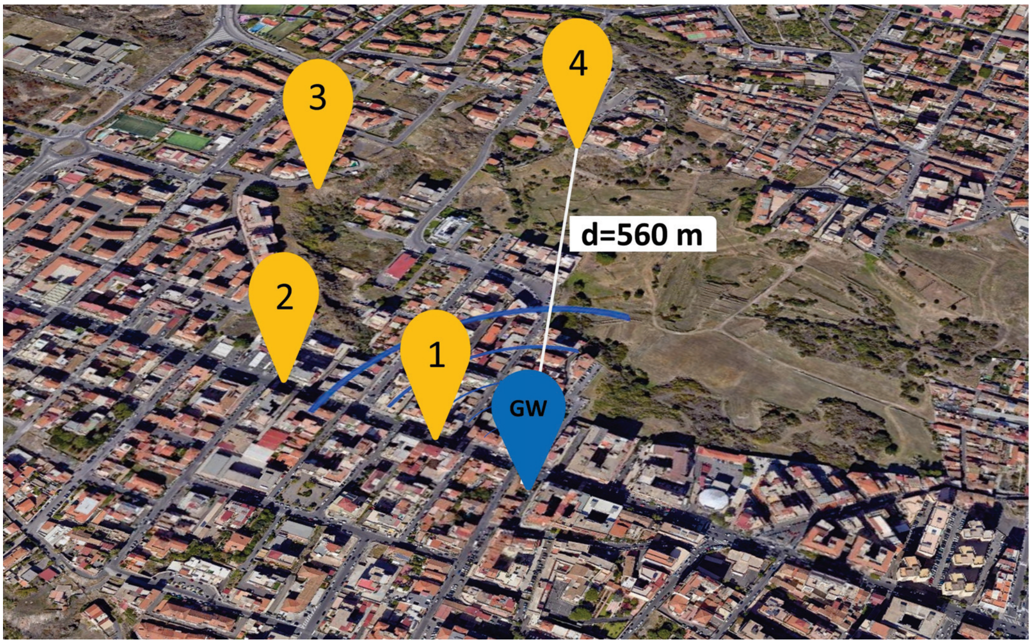

Figure 8. Communication distance in urban area for SF7, BW = 125 kHz, $C_{storage}$ = 2 mF, TX output power = 14 dBm, CR = 4/5, PL = 20 bytes, GW at h = 15 m.

Table 4 shows the test carried out in the urban scenario of Figure 9 with the following specific parameters: SF8, a BW of 125 kHz, a TP of 14 dBm, CR = 4/5, PL = 20 bytes and $C_{storage}$ = 4 mF. The test provided detailed data on RSSI and SNR for each tested point (points 1 to 5). The data indicate that at point 5 at a distance ≈1100 m, the minimum achievable SNR and RSSI were −13 dB and −113 dBm, respectively.

Table 3. Experimental results of coverage, SNR, and RSSI for various urban points in the Figure 8 scenario (SF7, $C_{storage}$ = 2 mF, PL = 20 bytes).

Point	Distance (m)	SNR (dB)	RSSI (dBm)
1	73	12	−71
2	265	7	−91
3	490	−1	−103
4	560	−8	−110

Figure 9. Communication distance in an urban area for SF8. Setup conditions: spreading factor SF = 8, BW = 125 kHz, $C_{storage}$ = 4 mF, TX output power = 14 dBm, CR = 4/5, PL = 20 bytes, GW at h = 15 m.

Table 4. Experimental results of coverage, SNR, and RSSI for various urban points in the Figure 9 scenario (SF8, $C_{storage}$ = 4 m F, PL = 20 bytes).

Point	Distance (m)	SNR (dB)	RSSI (dBm)
1	65	12	−68
2	240	7	−87
3	380	2	−98
4	600	−3	−105
5	1100	−13	−113

The results obtained are in line with the expected performance for LoRaWAN devices and demonstrate the practical performance of our EAWSN system in an urban environment. These results demonstrate the applicability of our system design in real-world scenarios, especially in challenging urban environments. Furthermore, we calculated the linear correlation coefficients (r) between RSSI and SNR for the two experimental scenarios SF7 and SF8, which were 0.95 and 0.94, respectively. These high correlations indicate consistent and coherent signal quality in both test scenarios. Based on the provided SNR and RSSI data, we have generated informative graphs representing the relationship between SNR and RSSI regarding distance. This inverse correlation is observed in Figure 10a,b. These results are consistent with the basic principles of LoRa technology and modulation techniques. They show that increasing the spread factor results in an extended communication range but at the cost of higher power consumption. These trade-offs highlight our EAWSN system's adaptability in different environmental conditions and provide valuable insights into its performance characteristics in the complex urban context we studied.

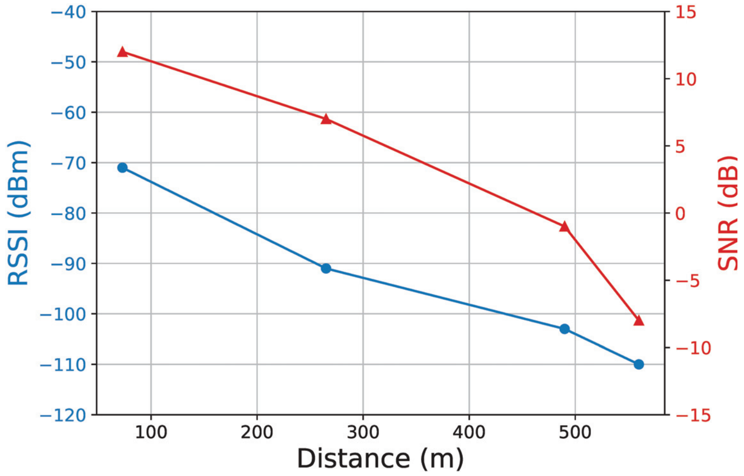

(a)

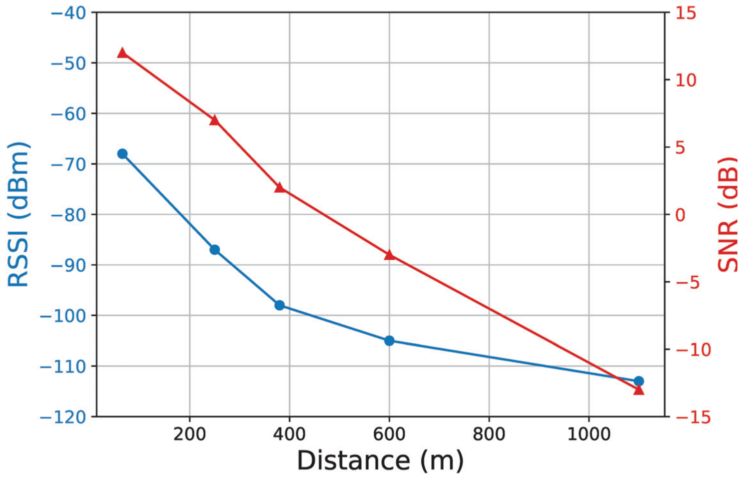

(b)

Figure 10. SNR and RSSI values at varied distances. Setup conditions: BW = 125 kHz, TP = 14 dBm, CR = 4/5, PL = 20 bytes, TX at h = 15 m. Panel (**a**) depicts SNR and RSSI values vs. distance with SF = 7. Panel (**b**) depicts SNR and RSSI values vs. distance with SF = 8.

6. Discussion

This section addresses the optimal configurations for the EAWSN under different lighting conditions, discusses potential constraints, and evaluates its scalability.

6.1. EAWSN under Different Light Condition and Recommended Setting

We tested the EAWSN system both in indoor environments, where the illuminance was approximately 500 lux (similar to a bright office), and in outdoor environments, where sunlight typically ranges from 32,000 lux to 100,000 lux. However, the EAWSN can also operate under low-light-intensity conditions, around 200 lux, as the solar cell can provide an operating voltage of 3 V and an operating current of 45.7 µA [42]. These tests demonstrate that the EAWSN system can maintain an acceptable level of energy autonomy in diverse environmental conditions, ensuring functionality even in low-light scenarios. Moreover, in our experiments, we evaluated various transmission configurations to determine the most suitable one for the needs of the EAWSN. Our study can help identify appropriate design parameters such as capacity and maximum package size. Along with these parameters, design optimization should also consider other factors, such as cost. However, the recommended design must take into account the use case. For example, the packet size can vary from a few bytes in smart agriculture [46,47] to 200 or more bytes in industrial contexts [48]. Therefore, a recommended choice should find a good compromise between maximum payload and device coverage radius. If flexibility on packet size, coverage, and spreading factor allocation is chosen, a 16 mF capacitor could be the recommended choice. With this configuration, the packet size ranged from a minimum of 10 bytes to a maximum of 255 bytes for SF12 and SF7, respectively. We identified that optimizing transmission strategies is crucial to ensure efficient operation of the system in autonomous mode. Conversely, if the goal is to reduce size and costs, a good compromise between coverage and maximum payload length could be achieved using an 8 mF capacitor with an SF8 setting. In this case, a packet size of 90 bytes and a maximum range of 1100 m in urban environments can be achieved.

6.2. Limitations and Possible Solutions

The possible limitations of the proposed system are basically twofold: the packet size is limited to a few bytes for higher spreading factors (e.g., 10 bytes at SF12), and the system does not operate in the absence of ambient light, such as at night. However, there are solutions for these two limitations. Both can be addressed by choosing a capacitor with a higher capacitance value, allowing for a larger packet size even at high SF values, according to the LoRa regional parameters policy in [49]. The size of the capacitor can be selected according to the specific use case, as discussed in Section 6.1. Furthermore, by integrating a supercapacitor into the system and jointly using adaptive transmission algorithms, as proposed in [6], it is possible to enable data transmission even during the night.

6.3. Mass-Scale Capability Eliminating Battery Replacement

The widespread adoption of IoT sensors has been favored by the almost ubiquitous availability of wireless connectivity and the rapid decline in sensor costs [50,51]. It is predicted that by 2025, there will be 75 billion IoT devices worldwide [52]. However, there are limitations to the massive deployment of IoT sensors. In fact, battery-powered sensors significantly increase the maintenance costs of IoT devices and reduce their lifespan [50,53]. The cost of replacing batteries is often higher than the cost of the IoT device itself, which limits the large-scale deployment of IoT devices. According to forecasts, there will be about 274 million battery replacements in IoT devices per day in a 10-year lifespan scenario, and the number would rise to 913 million per day in a 3-year lifespan scenario [50]. In this context, our work shows how the adoption of energy harvesting, together with ultra-low-power microcontroller systems, can eliminate the need for batteries, promoting a large-scale and environmentally friendly deployment of IoT sensors in the near future.

7. Conclusions

A self-powered wireless sensor node (WSN) was designed, built, and tested. This device exemplifies the EAWSN platform's capability to transmit data using LoRaWAN technology without relying on batteries or external power sources. The conducted experiments shed light on the significance of optimizing LoRaWAN transmission settings, including spreading factor (SF), bandwidth (BW), coding rate (CR), packet length (PL), and transmit power (TP), in managing energy consumption. The proposed solution lays the foundation for widespread deployment in mass-scale IoT scenarios.

The experimental trials conducted in Catania, Italy, showcased the exceptional performance of the EAWSN. Specifically, with carefully configured settings such as a transmit power of 14 dBm, SF7, 125 kHz BW, CR of 4/5, a PL of 20 bytes, and a 2 mF energy storage capacitor, the system achieved a communication range of 560 m. Furthermore, adopting a similar configuration with SF8 and a 4 mF energy storage capacitor, the system impressively extended its range to 1110 m. These achievements, coupled with the remarkable communication range, underscore the system's robustness and versatility, rendering it suitable for a multitude of applications. Additionally, this research highlights the EAWSN's adaptability to function effectively in two distinct environments. One environment entails direct communication between WSNs, while the other operates within the LoRaWAN protocol framework, each with its specific constraints. This showcases the system's versatility across various settings, making it a flexible choice for diverse scenarios.

In conclusion, the designed system represents a clean technology solution that not only offers sustainability and efficiency but also aligns with contemporary environmental concerns. By eliminating the need for batteries and offering maintenance-free operation, it presents an eco-friendly approach that is ideal for responsible and practical deployment across a wide spectrum of applications. Moreover, this sensor has the potential to revolutionize the field of mass-scale IoT sensing and enable new applications that were previously impossible due to power constraints.

In the future, research will continue, with a focus on specific areas of investigation. One such aspect is the potential implementation of this system using the LoRaWAN standard with OTAA authentication, which provides enhanced data security. In addition, research will continue into adapting the system to operate in low- or no-light conditions.

Author Contributions: Conceptualization, R.L.R. and L.B.; methodology, R.L.R. and D.C.; software, L.B. and R.L.R.; validation, L.B.; resources, R.L.R.; data curation, A.P., R.L.R. and L.B.; writing—original draft preparation, L.B.; writing—review and editing, A.P. and F.G.; supervision, D.C.; project administration, R.L.R.; funding acquisition, R.L.R. All authors have read and agreed to the published version of the manuscript.

Funding: This research was funded by the European Union under the Italian National Recovery and Resilience Plan (NRRP) of NextGenerationEU: partnership on "Telecommunications of the Future" (PE00000001—program "RESTART"), S14—Net4Future—Cross-project vision and results; and project PNRR M4—C2—investment 1.1: Projects of Significant National Interest (PRIN)—PRIN 2022 code 2022FYCNPT "IoTSensE: IoT-based Sensing Extension", CUP B53D23002610006.

Institutional Review Board Statement: Not applicable.

Informed Consent Statement: Not applicable.

Data Availability Statement: Data are contained within the article.

Conflicts of Interest: Author Roberto La Rosa is employed by the company STMicroelectronics. The remaining authors declare that the research was conducted in the absence of any commercial or financial relationships that could be construed as a potential conflict of interest

References

1. Rao, V. Ambient-Energy Powered Multi-Hop Internet of Things. Ph.D. Thesis, Delft University of Technology, Delft, The Netherlands, 2017. [CrossRef]
2. Romer, K.; Mattern, F. The design space of wireless sensor networks. *IEEE Wirel. Commun.* **2004**, *11*, 54–61. [CrossRef]
3. La Rosa, R.; Livreri, P.; Trigona, C.; Di Donato, L.; Sorbello, G. Strategies and Techniques for Powering Wireless Sensor Nodes through Energy Harvesting and Wireless Power Transfer. *Sensors* **2019**, *19*, 2660. [CrossRef] [PubMed]
4. Rosa, R.L.; Boulebnane, L.; Croce, D.; Livreri, P.; Tinnirello, I. An Energy-Autonomous and Maintenance-Free Wireless Sensor Platform with LoRa Connectivity. In Proceedings of the 2023 12th International Conference on Renewable Energy Research and Applications (ICRERA), Oshawa, ON, Canada, 29 August–1 September 2023. [CrossRef]
5. Wang, X.; Rao, V.S.; Prasad, R.V.; Niemegeers, I. Choose wisely: Topology control in Energy-Harvesting wireless sensor networks. In Proceedings of the 2016 13th IEEE Annual Consumer Communications & Networking Conference (CCNC), Las Vegas, NV, USA, 9–12 January 2016; pp. 1054–1059. [CrossRef]
6. Giuliano, F.; Pagano, A.; Croce, D.; Vitale, G.; Tinnirello, I. Adaptive algorithms for batteryless lora-based sensors. *Sensors* **2023**, *23*, 6568. [CrossRef] [PubMed]
7. Rosa, R.L.; Dehollain, C.; Burg, A.; Costanza, M.; Livreri, P. An Energy-Autonomous Wireless Sensor With Simultaneous Energy Harvesting and Ambient Light Sensing. *IEEE Sens. J.* **2021**, *21*, 13744–13752. [CrossRef]
8. Trigona, C.; Ando, B.; Baglio, S.; La Rosa, R.; Zoppi, G. Sensors for Kinetic Energy Measurement Operating on "Zero-Current Standby". *IEEE Trans. Instrum. Meas.* **2017**, *66*, 812–820. [CrossRef]
9. La Rosa, R.; Pandiyan, A.Y.S.; Trigona, C.; Andò, B.; Baglio, S. An integrated circuit to null standby using energy provided by MEMS sensors. *ACTA IMEKO* **2020**, *9*, 144. [CrossRef]
10. Alioto, M.; Shahghasemi, M. The Internet of Things on its edge: Trends toward its tipping point. *IEEE Consum. Electron. Mag.* **2018**, *7*, 77–87. [CrossRef]
11. Martinez, B.; Monton, M.; Vilajosana, I.; Prades, J.D. The power of models: Modeling power consumption for IoT devices. *IEEE Sens. J.* **2015**, *15*, 5777–5789. [CrossRef]

12. Garlisi, D.; Pagano, A.; Giuliano, F.; Croce, D.; Tinnirello, I. A Coexistence Study of Low-Power Wide-Area Networks based on LoRaWAN and Sigfox. In Proceedings of the 2023 IEEE Wireless Communications and Networking Conference (WCNC), Glasgow, UK, 26–29 March 2023; pp. 1–7. [CrossRef]
13. LoRa® and LoRaWAN®: A Technical Overview. Available online: https://lora-developers.semtech.com/uploads/documents/files/LoRa_and_LoRaWAN-A_Tech_Overview-Downloadable.pdf (accessed on 26 August 2023).
14. Lavric, A.; Popa, V. A LoRaWAN: Long range wide area networks study. In Proceedings of the 2017 International Conference on Electromechanical and Power Systems (SIELMEN), Iasi, Romania, 11–13 October 2017; pp. 417–420. [CrossRef]
15. Pizzotti, M.; Perilli, L.; Del Prete, M.; Fabbri, D.; Canegallo, R.; Dini, M.; Masotti, D.; Costanzo, A.; Franchi Scarselli, E.; Romani, A. A long-distance RF-powered sensor node with adaptive power management for IoT applications. *Sensors* **2017**, *17*, 1732. [CrossRef]
16. Karimi, M.; Wang, Y.; Kim, H. Energy-Adaptive Real-time Sensing for Batteryless Devices. In Proceedings of the 2022 IEEE 28th International Conference on Embedded and Real-Time Computing Systems and Applications (RTCSA), Taipei, Taiwan, 23–25 August 2022; pp. 205–211.
17. Chen, K.; Gao, H.; Cai, Z.; Chen, Q.; Li, J. Distributed energy-adaptive aggregation scheduling with coverage guarantee for battery-free wireless sensor networks. In Proceedings of the IEEE INFOCOM 2019-IEEE Conference on Computer Communications, Paris, France, 29 April–2 May 2019; pp. 1018–1026.
18. Yang, F.; Thangarajan, A.S.; Ramachandran, G.S.; Krishnamachari, B.; Joosen, W.; Huygens, C.; Hughes, D. Astar: Sustainable battery free energy harvesting for heterogeneous platforms and dynamic environments. In Proceedings of the 2019 International Conference on Embedded Wireless Systems and Networks, EWSN 2019, Beijing, China, 25–27 February 2019; pp. 71–82.
19. La Rosa, R.; Livreri, P.; Dehollain, C.; Costanza, M.; Trigona, C. An energy autonomous and battery-free measurement system for ambient light power with time domain readout. *Measurement* **2021**, *186*, 110158. [CrossRef]
20. Guo, Q.; Yang, F.; Wei, J. Experimental Evaluation of the Packet Reception Performance of LoRa. *Sensors* **2021**, *21*, 1071. [CrossRef]
21. Pasolini, G. On the LoRa Chirp Spread Spectrum Modulation: Signal Properties and Their Impact on Transmitter and Receiver Architectures. *IEEE Trans. Wirel. Commun.* **2022**, *21*, 357–369. [CrossRef]
22. Nguyen, T.T.; Nguyen, H.H.; Barton, R.; Grossetete, P. Efficient Design of Chirp Spread Spectrum Modulation for Low-Power Wide-Area Networks. *IEEE Internet Things J.* **2019**, *6*, 9503–9515. [CrossRef]
23. Li, Y.; Yang, J.; Wang, J. DyLoRa: Towards Energy Efficient Dynamic LoRa Transmission Control. In Proceedings of the IEEE INFOCOM 2020—IEEE Conference on Computer Communications, Toronto, ON, Canada, 6–9 July 2020; pp. 2312–2320. [CrossRef]
24. Loh, F.; Geißler, S.; Hoßfeld, T. LoRaWAN Network Planning in Smart Environments: Towards Reliability, Scalability, and Cost Reduction. 2022. Available online: https://d-nb.info/1266015175/34 (accessed on 30 June 2024).
25. Hoßfeld, T.; Raffeck, S.; Loh, F.; Geißler, S. Analytical model for the energy efficiency in low power iot deployments. In Proceedings of the 2022 IEEE 8th International Conference on Network Softwarization (NetSoft), Milan, Italy, 27 June–1 July 2022; pp. 19–24.
26. Loh, F.; Raffeck, S.; Geißler, S.; Hoßfeld, T. Generic Model to Quantify Energy Consumption for Different LoRaWAN Channel Access Methods. In Proceedings of the 2022 18th International Conference on Wireless and Mobile Computing, Networking and Communications (WiMob), Thessaloniki, Greece, 10–12 October 2022; pp. 290–295.
27. Pirri, A.; Pirri, M.; Leonardi, L.; Bello, L.L.; Patti, G. Towards Supporting Multiple MAC Protocols on a LoRaWAN End-Device for Industrial Applications. In Proceedings of the 2023 IEEE 28th International Conference on Emerging Technologies and Factory Automation (ETFA), Sinaia, Romania, 12–15 September 2023; pp. 1–4.
28. Vatcharatiansakul, N.; Tuwanut, P.; Pornavalai, C. Experimental performance evaluation of LoRaWAN: A case study in Bangkok. In Proceedings of the 2017 14th International Joint Conference on Computer Science and Software Engineering (JCSSE), NakhonSiThammarat, Thailand, 12–14 July 2017. [CrossRef]
29. Cheong, P.S.; Bergs, J.; Hawinkel, C.; Famaey, J. Comparison of LoRaWAN classes and their power consumption. In Proceedings of the 2017 IEEE Symposium on Communications and Vehicular Technology (SCVT), Leuven, Belgium, 14 November 2017; pp. 1–6. [CrossRef]
30. Augustin, A.; Yi, J.; Clausen, T.; Townsley, W. A Study of LoRa: Long Range, Low Power Networks for the Internet of Things. *Sensors* **2016**, *16*, 1466. [CrossRef] [PubMed]
31. Jebril, A.; Sali, A.; Ismail, A.; Rasid, M. Overcoming Limitations of LoRa Physical Layer in Image Transmission. *Sensors* **2018**, *18*, 3257. [CrossRef] [PubMed]
32. Bor, M.C.; Roedig, U.; Voigt, T.; Alonso, J.M. Do LoRa Low-Power Wide-Area Networks Scale? In Proceedings of the 19th ACM International Conference on Modeling, Analysis and Simulation of Wireless and Mobile Systems, Malta, 13–17 November 2016; pp. 59–67. [CrossRef]
33. Ferrari, P.; Flammini, A.; Rizzi, M.; Sisinni, E.; Gidlund, M. On the evaluation of LoRaWAN virtual channels orthogonality for dense distributed systems. In Proceedings of the 2017 IEEE International Workshop on Measurement and Networking, Naples, Italy, 27–29 September 2017; pp. 1–6. [CrossRef]
34. Caillouet, C.; Heusse, M.; Rousseau, F. Optimal SF Allocation in LoRaWAN Considering Physical Capture and Imperfect Orthogonality. In Proceedings of the 2019 IEEE Global Communications Conference (GLOBECOM), Waikoloa, HI, USA, 9–13 December 2019; pp. 1–6. [CrossRef]

35. Croce, D.; Gucciardo, M.; Mangione, S.; Santaromita, G.; Tinnirello, I. Impact of LoRa Imperfect Orthogonality: Analysis of Link-Level Performance. *IEEE Commun. Lett.* **2018**, *22*, 796–799. [CrossRef]
36. Ahmed, S.; Islam, B.; Yildirim, K.S.; Zimmerling, M.; Pawełczak, P.; Alizai, M.H.; Lucia, B.; Mottola, L.; Sorber, J.; Hester, J. The Internet of Batteryless Things. *Commun. ACM* **2024**, *67*, 64–73. [CrossRef]
37. Church, C.; Wuennenberg, L. *Sustainability and Second Life*; International Institute for Sustainable Development: Winnipeg, MB, Canada, 2019. Available online: https://www.iisd.org/sites/default/files/publications/sustainability-second-life-cobalt-lithiumrecycling.pdf (accessed on 30 June 2024).
38. Delgado, C.; Sanz, J.M.; Blondia, C.; Famaey, J. Batteryless LoRaWAN communications using energy harvesting: Modeling and characterization. *IEEE Internet Things J.* **2020**, *8*, 2694–2711. [CrossRef]
39. Georgiou, O.; Psomas, C.; Demarchou, E.; Krikidis, I. LoRa Network Performance Under Ambient Energy Harvesting and Random Transmission Schemes. In Proceedings of the ICC 2021-IEEE International Conference on Communications, Montreal, QC, Canada, 14–23 June 2021; pp. 1–6.
40. Sabovic, A.; Delgado, C.; Subotic, D.; Jooris, B.; De Poorter, E.; Famaey, J. Energy-aware sensing on battery-less lorawan devices with energy harvesting. *Electronics* **2020**, *9*, 904. [CrossRef]
41. STMicroelectronics. STM32WL5x Product Page. 2021. Available online: https://www.st.com/en/microcontrollers-microprocessors/stm32wl5x.html (accessed on 28 July 2023).
42. Panasonic. Amorton E Series Brochure. 2021. Available online: https://panasonic.net/electricworks/amorton/assets/pdf/Brochures_Amorton_E_2.pdf (accessed on 29 July 2023).
43. Electronics, M. Tantalum Ultra Low ESR COTS-Plus Capacitors. 2021. Available online: https://eu.mouser.com/pdfDocs/TBM-COTS-Plus.pdf (accessed on 1 July 2021).
44. STMicroelectronics: Our Technology Starts with You. 2023. Available online: https://www.st.com/content/st_com/en.html (accessed on 2 September 2023).
45. STMicroelectronics. Getting Started with the P-NUCLEO-LRWAN2 and P-NUCLEO-LRWAN3 Starter Packs. 2021. Available online: https://www.st.com/resource/en/user_manual/um2587-getting-started-with-the-pnucleolrwan2-and-pnucleolrwan3-starter-packs-stmicroelectronics.pdf (accessed on 1 July 2021).
46. Rachmani, A.F.; Zulkifli, F.Y. Design of iot monitoring system based on lora technology for starfruit plantation. In Proceedings of the TENCON 2018-2018 IEEE Region 10 Conference, Jeju, Republic of Korea, 28–31 October 2018; pp. 1241–1245.
47. Rivera Guzmán, E.F.; Mañay Chochos, E.D.; Chiliquinga Malliquinga, M.D.; Baldeón Egas, P.F.; Toasa Guachi, R.M. LoRa Network-Based System for Monitoring the Agricultural Sector in Andean Areas: Case Study Ecuador. *Sensors* **2022**, *22*, 6743. [CrossRef]
48. Ballerini, M.; Polonelli, T.; Brunelli, D.; Magno, M.; Benini, L. Experimental Evaluation on NB-IoT and LoRaWAN for Industrial and IoT Applications. In Proceedings of the 2019 IEEE 17th International Conference on Industrial Informatics (INDIN), Helsinki, Finland, 22–25 July 2019; Volume 1, pp. 1729–1732. [CrossRef]
49. LoRa-Alliance. RP002-1.0.4 Regional Parameters. 2022. Available online: https://resources.lora-alliance.org/technical-specifications/rp002-1-0-4-regional-parameters (accessed on 30 June 2024).
50. Deng, Y.; Chen, Z.; Yao, X.; Hassan, S.; Ibrahim, A.M. Parallel offloading in green and sustainable mobile edge computing for delay-constrained IoT system. *IEEE Trans. Veh. Technol.* **2019**, *68*, 12202–12214. [CrossRef]
51. Oliveira, M.; Chauhan, S.; Pereira, F.; Felgueiras, C.; Carvalho, D. Blockchain protocols and edge computing targeting industry 5.0 needs. *Sensors* **2023**, *23*, 9174. [CrossRef] [PubMed]
52. Rahmani, A.M.; Bayramov, S.; Kiani Kalejahi, B. Internet of things applications: Opportunities and threats. *Wirel. Pers. Commun.* **2022**, *122*, 451–476. [CrossRef] [PubMed]
53. Taha, A.; Elkotby, H.; Haque, T.; Pragada, R.; Castor, D. Eliminating battery replacement throughout the useful life of IoT devices with limited-capacity batteries: Analysis and design of a zero energy air interface. In Proceedings of the 2021 IEEE International Conference on Communications Workshops (ICC Workshops), Montreal, QC, Canada, 14–23 June 2021; pp. 1–6.

sensors

MDPI

Article

LoRa Resource Allocation Algorithm for Higher Data Rates

Hossein Keshmiri *, Gazi M. E. Rahman and Khan A. Wahid

Department of Electrical and Computer Engineering, University of Saskatchewan, Saskatoon, SK S7N 5A2, Canada; ehsan.rahman@usask.ca (G.M.E.R.); khan.wahid@usask.ca (K.A.W.)
* Correspondence: hossein.keshmiri@usask.ca

Abstract: LoRa modulation is a widely used technology known for its long-range transmission capabilities, making it ideal for applications with low data rate requirements, such as IoT-enabled sensor networks. However, its inherent low data rate poses a challenge for applications that require higher throughput, such as video surveillance and disaster monitoring, where large image files must be transmitted over long distances in areas with limited communication infrastructure. In this paper, we introduce the LoRa Resource Allocation (LRA) algorithm, designed to address these limitations by enabling parallel transmissions, thereby reducing the total transmission time (T_{tx}) and increasing the bit rate (BR). The LRA algorithm leverages the quasi-orthogonality of LoRa's Spreading Factors (SFs) and employs specially designed end devices equipped with dual LoRa transceivers, each operating on a distinct SF. For experimental analysis we choose an image transmission application and investigate various parameter combinations affecting T_{tx} to optimize interference, BR, and image quality. Experimental results show that our proposed algorithm reduces T_{tx} by 42.36% and 19.98% for SF combinations of seven and eight, and eight and nine, respectively. In terms of BR, we observe improvements of 73.5% and 24.97% for these same combinations. Furthermore, BER analysis confirms that the LRA algorithm delivers high-quality images at SNR levels above −5 dB in line-of-sight communication scenarios.

Keywords: image transmission; LoRa PHY; LoRa MAC layer; LoRa modulation; SF selection

1. Introduction

LoRa modulation is widely recognized for its long-range, low-power transmission capabilities, making it an attractive option for a broad spectrum of applications. Its efficiency and cost-effectiveness have made LoRa particularly suitable for use in cases that require low data rates, such as environmental monitoring, smart agriculture, and IoT networks. However, the low data rates inherent to LoRa present a challenge for applications that demand higher throughput, such as video surveillance, disaster monitoring, and plant phenotyping. These applications often require the transmission of large image files over long distances in areas where reliable communication infrastructure is lacking. Given its low complexity and energy efficiency, LoRa holds promise in such scenarios. Yet, the existing technology can result in prolonged transmission times, especially when dealing with high-resolution images or when operating under less-than-ideal channel conditions. To address these limitations, research has been focused on enhancing LoRa's performance, aiming to increase its data rate while maintaining its key advantages.

In 2016, C. Pham [1] took the first step towards transmitting images, only a year after the birth of the LoRa framework. In this research, a low-cost, low-power image sensor is presented that implements an image compression technique to reduce the data size for long-range transmissions. Wei et al. [2] proposed an image transmission technique with various spreading factors (SFs) which utilized three separate nodes operating on different SFs to collaborate in sending images to their designated peers on the receiver side. Each LoRa node is controlled by a dedicated Raspberry pi and the data segments of the image are distributed among the senders using MQTT protocol. Chen et al. [3] proposed a lightweight and reliable communication protocol called MPLR, specifically designed for image dispatching over LoRa networks in an agricultural IoT platform. The MPLR protocol optimizes packet transmission by grouping information packets and utilizing bit-vector acknowledgments, which reduces the number of acknowledgment packets required and the associated wait times. To further minimize packet collisions caused by network congestion, MPLR employs a separate channel for transmitting request packets, distinct from the channels used for data and acknowledgment signals.

Achieving higher data rates in LoRa communications is also possible by upgrading the modulation technique. However, any modifications to LoRa modulation will render the existing modules incompatible with current applications and new hardware design will be required, resulting in increased complexity. In this paper, we have introduced the LoRa Resource Allocation (LRA) algorithm capable of parallel transmissions of the same data, reducing the total transmission time (T_{tx}) and increasing the Bit Rate (BR). Inspired by the quasi-orthogonality of Spreading Factors (SFs) in LoRa [4,5], our proposed algorithm utilizes specially designed end devices that consist of two LoRa transceivers connected to a single controller unit, ensuring simple hardware implementation. For the experimental analysis, an image transmission application is chosen. We have investigated all possible parameter combinations affecting T_{tx} to identify the optimal results in terms of interference, BR, and received image quality. Experimental results show that the proposed algorithm can significantly improve the T_{tx} and BR compared to a typical LoRa framework for a Line of Sight (LoS) communication link while maintaining a high image quality. The main contributions of this research are as follows:

1. Proposes a specially designed end device (DED) to practically evaluate the quasi-orthogonality feature of LoRa in SF and RF channels and suggests optimal SF combinations for parallel transmission;
2. Proposes a lightweight, synchronized resource-allocation algorithm for transmission time and bit rate improvement;
3. Derives mathematical models for the proposed algorithm regarding SF allocation for the total parallel transmission time, data rate, and energy consumption;
4. Implements the identified SF combinations and evaluates the throughput improvement;
5. Gives insight about the Bit Error Rate (BER) performance of the parallel setup and the quality of the images received.

The rest of the paper is organized as follows. In Section 2 we have presented a literature review of the related studies in the field. Section 3 illustrates in detail the framework of the proposed algorithm. Section 4 presents the experimental study and the results are presented. Finally, Section 5 concludes the paper by summarizing the results and suggesting directions for future research.

2. Related Work

Recent studies in the literature have explored various methods to enhance the data rate of LoRa by modifying its Chirp Spread Spectrum (CSS) modulation. Edward et al. [6] proposed the use of Interleaved Chirp Spreading (ICS) alongside traditional chirp spreading. This technique incorporates an additional bit into the LoRa symbol for ICS, leading to a 42% increase in capacity. Building on this concept, a Slope Shift Keying (SSK) approach with ICS was introduced in [7], which utilizes a combination of up, down, and interleaved up-and-down chirp modulation. This method further boosts the data rate, achieving a 28.6% improvement compared to the standard CSS LoRa with the same SF and BW. Kang [8] proposed a new index modulation for LoRa that utilizes multiple quasi-orthogonal chirps modulated under different SFs, enabling it to carry more information compared to the conventional LoRa. Hanif et al. [9] introduced the frequency shift chirp spread spectrum modulation that exploits index modulation (FSCSS-IM) to increase the data rate. Instead of one chirp at a time, FSCSS-IM transmits multiple chirps simultaneously. In [10], Time-Domain Multiplexing (TDM) is employed for LoRa modulation, distributing bits of a symbol across different SFs. This method doubles the data rate with a minor degradation in BER, particularly at the lower SF of 7. Additionally, in [11], authors introduced a data rate enhancement approach known as PATCH (Phase-based Additional Channel), which utilizes the phase of the chirp signal as an additional channel. This technique can boost the BR by up to 28.57% for SF = 7. Nurbay et al. [12] introduced a cooperative framework for transmitting large files over LoRa. They developed an algorithm that leverages neighboring nodes, selecting them based on their SF and packet success rate to share portions of the data. To facilitate communication between nodes, the framework utilizes a high data rate medium like Wi-Fi for exchanging algorithmic messages among the neighbors.

Some research efforts have proposed enhancements to the network access techniques for the LoRa communication protocol. For instance, a dynamic spreading factor allocation algorithm was introduced in [13] to maximize the data rate for the communication link. This algorithm optimizes the data rate by considering the hop count, ensuring that higher SFs are assigned to links with fewer hops or clusters that are closer, thereby equalizing the packet travel time or Time on Air (ToA). The approach is capacity-focused, utilizing an iterative process to allocate SFs, enhancing overall network performance.

The LoRaWAN Gateway (GW) is not full-duplex, and relies on an Adaptive Data Rate (ADR) to adjust the SF. However, this adjustment becomes impractical when the GW is mobile at speeds above 2 km/h. In such scenarios, the GW must frequently switch SF and channels to communicate with end devices (EDs), leading to significant overhead and reducing goodput to as low as 20%. To address this, Cantor [14] was implemented in a single-GW LoRaWAN network to gather network parameters from EDs, optimize the Packet Reception Rate (PRR), and estimate the actual downlink (DL) PRR using an optimization algorithm. By employing a regression model (WW: Wane and Wax, representing alternate increase and decrease), Cantor more accurately determines PRR and improves goodput by up to 70%. Additionally, Cantor's use of windowing for acknowledgments (ACK) shows better performance with higher SFs.

The distance-based SF allocation using the Exponential Windowing Scheme (EWS) [15] is designed to reduce co-SF interference and improve network capacity. This approach utilizes an offline optimization algorithm, making it particularly effective for static EDs. The method achieves a PDR improvement of 18.2% to 55.25% compared to similar SF allocation algorithms. However, a significant drawback is the exponential decrease in data throughput as the number of EDs increases from 1000 to 8000. Additionally, EWS requires GPS-based location data, RSSI-based distance calculation, or manual distance measurement, adding complexity to its implementation. In contrast, the proposed LRA algorithm avoids offline calculations to maintain a lightweight protocol. Kang et al. [16] proposed Multiple-Input Multiple-Output (MIMO)-LoRa, which enhances BER at higher SFs of 10, 11, and 12 by utilizing multiple SFs for parallel transmission. This approach employs a precoding matrix to optimize the total SNR and peak transmit power to select the appropriate SFs.

The LoRa GW chip is designed to decode superimposed signals from different SFs, as proposed in [17]. The demodulator is divided into two groups, handling odd and even SFs separately. To efficiently utilize the MAC layer, which treats all packets from different SFs as a single transmission, strict synchronization across all EDs is required. However, using higher SFs increases the likelihood of network congestion. Since higher SFs result in longer transmission times, they can occupy the channel for extended periods, potentially leading to congestion in networks with multiple devices. As a result, it may be necessary to classify EDs to manage the SF-based packet distribution effectively and avoid congestion-related issues. Some research works have focused on lowering the size of the image by employing encoders and compression techniques to reduce the total data size required for the image transmission [18,19].

Some other works adopted machine-learning-based strategies for dynamic SF allocation. Scarvaglieri et al. [20] proposed an energy-efficient resource allocation strategy based on Q-Learning, enabling LoRa devices to make autonomous decisions on SF configurations. However, as Q-Learning algorithms require multiple iterations to converge to optimal decisions, in dynamic environments where conditions like interference and device density change frequently, this convergence time could limit performance. Ta et al. [21] focused on mitigating inter-SF interference using a Multi-Armed Bandit (MAB) model and EXP3 (Exponential Weights for Exploration and Exploitation) algorithm, enabling LoRa devices to autonomously select the least-congested SFs. Although the EXP3 algorithm is computationally efficient, it may require time to converge on optimal SF allocations, which could lead to inefficiencies during periods of high network changes or initialization phases.

A Deep Reinforcement Learning (DRL)-based SF optimization algorithm that dynamically adjusts SF by considering both node characteristics and channel conditions is proposed in [22]. The algorithm uses retransmission as a proxy for detecting collisions. This indirect method may introduce inaccuracies in environments where packet losses occur due to interference or poor signal conditions rather than collisions. Busacca et al. [23] introduced FedLoRa, a federated learning-based optimization scheme that balances resource allocation to minimize FML (Federated Machine Learning) round time and energy consumption by distributing network load across available SFs. A greedy algorithm is proposed to approximate the optimization problem of resource allocation.

3. LRA Algorithm Framework

3.1. Physical Layer

LoRa uses CSS modulation at various ISM bands such as 915 MHz for North America. LoRa transceivers, such as the SX1276, support programmable bandwidths (BW) from 7.8 to 500 kHz. Some of the most used BW settings are 125 kHz, 250 kHz, and 500 kHz. SF represents the number of bits carried by each symbol and is directly proportional to the symbol time or chirp duration. Longer SFs result in longer symbol times and vice versa. Signals modulated with different SFs are said to be quasi-orthogonal [4], thus they can co-exist and be decoded successfully at the same time. The quasi-orthogonality can be proved by following the principle of orthogonal functions. Assume that $s_n(t)$ is the time domain representation of a chirp signal with $SF = n$.

$$s_n(t) = Ae^{j2\pi(f_0 t + \frac{B}{2T_{s,n}} t^2)} \quad (1)$$

B is the BW, $T_{s,n}$ is the symbol time, and f_0 is the frequency offset that refers to the initial frequency of the chirp for $SF = n$ and are defined as below:

$$T_{s,n} = \frac{2^n}{B} \tag{2}$$

$$f_0 = \frac{B}{2^n}k \tag{3}$$

where $k \in \{0, \ldots, 2^n - 1\}$ is the chip decimal value. Two signals with $SF = n$ and $SF = p$, $n \neq p$ are quasi-orthogonal if their inner product is near zero.

$$< s_n(t).s_p^*(t) >= \int s_{n(t)} s_p^*(t) dt \cong 0 \tag{4}$$

Integral in (4) can be expanded as (5).

$$A^2 \int e^{j2\pi[(f_{0,n} - f_{0,p})t]} dt + A^2 \int e^{j2\pi[(\frac{1}{T_{s,n}} - \frac{1}{T_{s,p}})\frac{B}{2}t^2]} dt \tag{5}$$

Integrating the first term over interval $[0, T]$, $T = \max(T_{s,n}, T_{s,p})$ is zero. The phase of the second term is generally a large value (61.0352×10^6 for $B = 125$ kHz, $n = 7$, $p = 8$) causing rapid oscillations throughout the interval. Using the stationary phase approximation will yield the magnitude of $\sqrt{(\pi/a)}$ where $a = 2\pi(1/T_{s,n} - 1/T_{s,p})B/2$, indicating a near-zero value for the inner product.

The actual BR depends on the SF, Coding Rate (CR), and BW, and is calculated using (6) [24], which gives a maximum BR of 21.875 kbps for BW = 500 kHz, CR = 1, and SF = 7.

$$BR = SF \frac{4}{4 + CR} \frac{B}{2^{SF}} \tag{6}$$

The transmission power supported by LoRa is adjustable from −4 dBm to +20 dBm. The lowest receiver sensitivity is around −130 dBm, and it performs better at higher SF and lower BW (−136 dBm at SF = 12 and BW = 125 kHz) [24]. This sensitivity increases LoRa's range at higher SF and lower BW over other LPWAN technologies [25]. The range of LoRa transmission depends on the radio link conditions and the antenna height to reduce signal reflection and absorption by the ground.

Keeping the current LoRa modulation unchanged, its capacity in terms of the BR can be increased with parallel transmissions and receptions of the payload. Unlike the GW LoRa modem (such as SX13XX or similar), the existing LoRa EDs do not support multiple channels and SFs for simultaneous communication. However, LoRa link capacity and network goodput can be improved by utilizing its orthogonality features and by improving the MAC protocol. As shown in Figure 1a, the LoRa physical layer packet consists of two mandatory blocks called the Preamble and Payload, along with two optional blocks for the header and Payload-CRC (Cyclic Redundancy Check). Figure 1b shows our proposed parallel setup by grouping two LoRa physical channels. These channels have the same configuration (BW, RF and CR), except for the different SFs, and are highly synchronized to transfer the data stream.

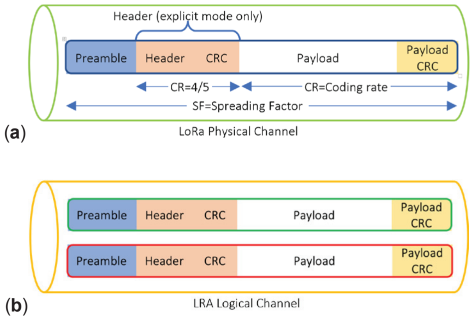

Figure 1. LoRa structure. (**a**) Physical channel, and (**b**) logical channel used in LRA algorithm.

Due to the similarity of configuration and operation, in the rest of this paper this channel is called a logical channel (LC), to facilitate describing the proposed method. All the block sizes are variable according to the transceiver configuration and the payload size ranges from 1 to 255 bytes.

3.2. Designed End Device (DED)

Based on the proposed LC (Figure 1b), a customized end device is designed that comprises two Semtech SX1276 LoRa transceivers connected and controlled by a single processor to avoid data processing/sharing complexity. As shown in Figure 2, the processor is a Texas Instrument Tiva C series unit and is programmed using Energia IDE 1.8.11, a fork of Arduino IDE. Both LoRa modules are connected to a shared Synchronous Peripheral Interface (SPI) bus and are equipped with identical dipole antennas for enhanced transmission power. The LRA algorithm, which is elaborated in the next section, is performed on this processor and the resulting data packets are fed to the radios to be transmitted simultaneously.

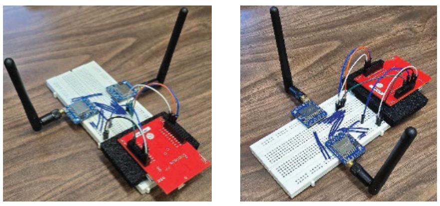

Figure 2. Lab prototype of the DED.

It is assumed that multiple SFs are used in the same RF channel, which are not assigned for any other link at the same time in the network to avoid co-channel interference. Figure 3 shows the hardware and software blocks of the DED with two LoRa transceiver modules used for the proposed LRA algorithm implementation. All the transceivers are configured to have the same LoRa parameters, except for SF. The transferred data are measured in bytes.

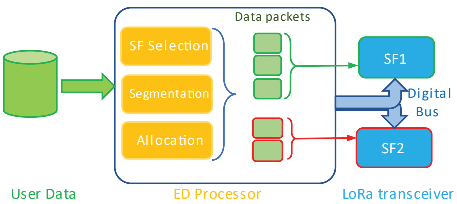

Figure 3. DED's block diagram for the LRA algorithm implementation.

To improve network capacity, the LRA algorithm improves the BR of a LoRa link and the goodput of the network by reducing the total data transmission time T_{tx} between EDs and GW, regardless of the application type. As shown in Figure 4, the physical layer utilizes the LoRa SF orthogonality for parallel data transmission by efficiently selecting multiple SFs. The proposed algorithm can act as a MAC layer that facilitates packet distribution and synchronization among the SFs.

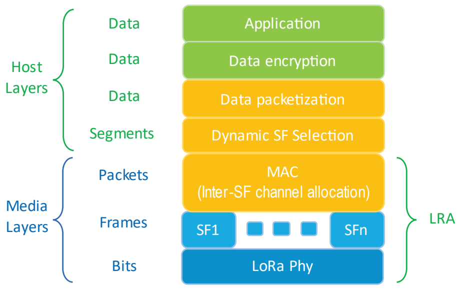

Figure 4. Proposed LoRa stack for the LRA algorithm.

3.3. Resource Allocation Algorithm

Based on the achievable BR for a given payload size, the ToA related to each SF can be derived. Assume that packets with the equal payload of 240 bytes are to be successively transmitted. Figure 5 shows the transmission times of 240-byte packets using different SFs, with each block representing the time of a single packet. The gaps between the blocks are packet processing times (t_u). In this example, the transmission takes about 300 ms if SF = 9, while it only takes approximately 60 ms for SF = 7. SF = 6 is not considered in our algorithm due to its unavailability in some transceivers. As indicated by the green dashed lines, packets transferred using SF = 7 achieve better synchronization with packets transferred concurrently using SF = 9, compared to those using SF = 8 or SF = 10. Therefore, synchronous access of LC can be maintained by allocating different portions of data with equal packet sizes to the physical channels.

The proposed algorithm assigns a specific number of data packets sequentially to the transmitters based on the amount of data they can send through the LC. As illustrated in Figure 5, while transmitting a single packet at SF = 9, it is possible to transmit three packets at SF = 7. However, by introducing a slight delay in packet processing, the system can transmit two packets at SF = 8 alongside three consecutive packets at SF = 7, contributing to a higher BR compared to other SF combinations. In other words, three out of five packets are sent by the transmitter with SF = 7 and two are sent by the one with SF = 8 per each round of parallel transmission. Thus, to maximize channel utilization and minimize the overall transmission time, the algorithm allocates 60% of the entire user data to SF = 7 and the remaining 40% to SF = 8. The pseudocode of the proposed algorithm is shown in Algorithm 1.

Algorithm 1. Pseudocode for LRA algorithm.

```
//Synchronized Resource Allocation Algorithm
//For a logical channel that contains 2 physical channels with spreading //factors SF1 and SF2
and SF1 < SF2
//Assumptions:
//All parameters (packet sizes, SFs, BW, CR, etc.) are provided by
//the user
//Variables
m = size(input_byte_string);
p = packet_size;
N = floor(m/p) + 1;    //number of all packets
Delay;                 //delay time

//Initialize:
Set parameters for the transmitters
Based on the measured ToAs (Figure 5) for SF1 and SF2, determine:
n1 = number of all packets for SF1
n2 = number of all packets for SF2 (n2 = N − n1)

//Loop until all packets are transmitted
For (i = 1:N, i++) {
Transmit using SF1;     //to complete n1 packets
Transmit using SF2;     //to complete n2 packets
//delay after each parallel transmission to allow packet processing
//on the receiver
Delay;}
}
```

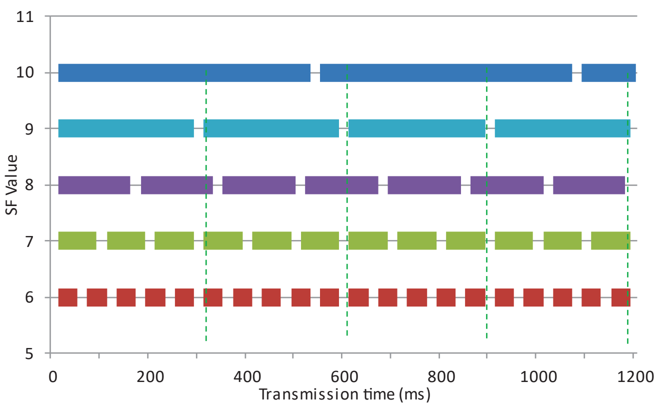

Figure 5. ToA of burst transmission of 240 B packets over different SF with the same RF channel and BW.

3.4. SF Selection

SF represents the number of chips per chirp or symbol; thus, as the SF grows, the symbol duration increases. In other words, higher SF leads to lower BR and higher ToA. Therefore, maximum BR depends on the ToA, which is calculated based on the BW and SF, as shown in (7) [24].

$$ToA = \left(20.25 + \left\lceil \frac{2PL - SF + 7}{SF} \right\rceil 5\right)\left(\frac{2^{SF}}{B}\right) \quad (7)$$

ToA will be the lowest for all the SFs where BW is the highest. Table 1 shows the ToA for BWs 250 kHz and 500 kHZ when SF is varied, and the relative BR improvement

($RBRI = 1 - BR_i/BR_{i+1}$) between two consecutive SFs for the same BW. It also indicates that the ToA with BW = 250 kHz and SF = 7 is only 20.4 ms (12%), less than the ToA with BW = 500 kHz and SF = 8. This differs more (55% to 57%) for the same BW with different SF. Therefore, parallel transmission using 250 kHz and 500 kHz BW can be used for two consecutive SF values. However, it is not used in the proposed LRA algorithm to avoid data loss due to inter-channel interference, as further explained in Section 4.

Table 1. ToA values of a 240-byte packet for different BWs and SFs.

SF	BW = 500 kHz		BW = 250 kHz		RBRI (%)
	ToA (ms)	BR (kbps)	ToA (ms)	BR (kbps)	
6	52.1	37.5	104.2	18.75	71
7	92.2	21.87	184.4	10.935	75
8	164.0	12.5	327.9	6.25	78
9	292.1	7.03	584.2	3.515	80
10	533.0	3.906	1066.0	1.953	82
11	963.6	2.148	1927.2	1.074	83
12	1804.3	1.172	3608.6	0.586	-

3.5. LRA Algorithm Data Rate

The actual data rate for the proposed LRA algorithm depends on the equivalent or total ToA for the parallel channels. Total ToA, which is the sum of the travel times of all packets using different SFs, can be represented by (8):

$$ToA_{tx} = \sum_{m=1}^{3}\sum_{n=0}^{6} ToA_{m,n} = \sum_{m=1}^{3}\sum_{n=1}^{6} ToA_{m,0}(\alpha^{-n}\beta^{-m}) \quad (8)$$

where m is the index of different BWs used in the range of 125 kHz to 500 kHz, and n is the index of different SF values used from 6 to 12. $ToA_{m,0}$ is the ToA at SF = 6 for a specific BW. Table 1 shows that the ToA is the lowest at SF = 6 for a specific BW.

The increment of the ToA for another SF is represented by α. The ToA increment for the same SF at a different BW is represented by β. Figure 6 shows the variation in ToA for different SFs and BWs, from which we can determine the values of α and β, which vary for different SFs and BWs. However, these variations are minimal, about 10%. Therefore, an approximation is used where α = 0.56 and β = 0.5.

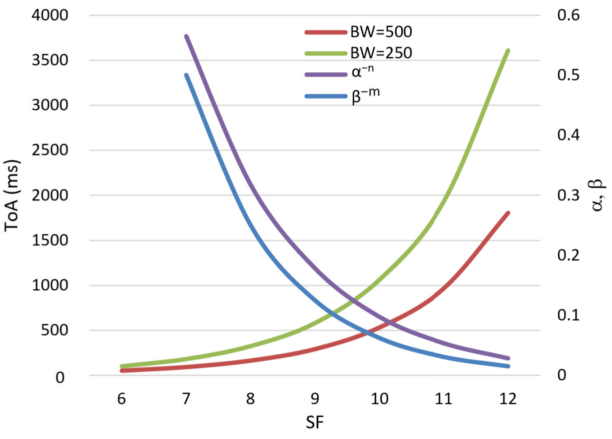

Figure 6. Impact of changing BW and SF on ToA.

Burst data transmission using the proposed algorithm requires multiple LoRa packets to be transmitted sequentially. This packet sequence can transmit a data stream in multiple time slots, as performed in TDMA, due to the different ToAs at different SFs. The number of packets for a burst transmission may also induce further underutilization. This utilization can be maximized using odd or even SF values for the stream of data packets, which corresponds to either SF = 7 and SF = 9, and SF = 8 and SF = 10 being paired together. However, it depends on the data processing and the SPI communication time, which are almost fixed for all SFs. Therefore, odd or even paired SFs may not be the best choice for maximum resource utilization.

For the burst transmission of multiple LoRa packets, the total burst transmission time T_{tx} includes the total ToA (ToA_{tx}) and the total processing time (T_u), as shown in (9). However, the number of packets (F) that need to be transferred will differ for different SFs in an LC. Considering the same processing time for all the SFs, ToA_{tx} and T_u can be rewritten as (10) and (11). From Figure 5, it can be shown that the synchronization loss will be the lowest when the ToA is the minimum time required for a packet, which is $ToA_n - t_u$, and that the transmission time utilization can be expressed by (12). The lowest ToA occurs for the lowest SF used, which is seven for n = 1. Therefore, the synchronization loss can be minimized by using the smallest SF possible and transmitting the largest data segment using that SF. The effective BR of the proposed algorithm can be calculated using (13), using PL as the payload size in bits and T_{tx} in seconds. t_u is the delay time required for packet processing and reception at the receiver.

$$T_{tx} = ToA_{tx} + T_u \tag{9}$$

$$ToA_{tx} = \sum_{m=1}^{3} \sum_{n=1}^{6} F_{m,n} ToA_{m,0} \left(\alpha^{-n} \beta^{-m}\right) \tag{10}$$

$$T_u = t_u \sum_{m=1}^{3} \sum_{n=1}^{6} F_{m,n} \tag{11}$$

$$\varphi = 1 - \frac{ToA_n - t_u}{T_{tx}} \approx 1 - \frac{ToA_1 - t_u}{T_{tx}} \tag{12}$$

$$BR_{LRA} = (1 - \varphi) \frac{PL}{T_{tx}} \tag{13}$$

3.6. Energy Consumption Model

The energy consumption of the LRA algorithm can be modeled by the total energy consumed by DEDs. This total energy can be determined by calculating the energy needed for transmitting on each radio (specific SF and BW), the energy spent in standby mode to allow packet reception and processing at the receiver, and the energy required for receiving and processing packets. Equation (14) shows the total energy dissipated across all nodes. As shown in Equations (15) and (16), E_{tx} is the energy required for burst data transmission, where P_{tx} and P_s are the LoRa transmit and standby power, respectively. T_u is the sum of packet processing times during which the nodes are in standby mode. Equations (17) and (18) present the energy required for packet reception and processing, E_{rx}. The power required for the LoRa transceiver (such as SX1276) to transmit and receive is the same for all BWs and SFs. Therefore, P_{tx} and P_{rx} can be replaced with P_0^{tx} and P_0^{rx}. These values are set as follows: $P_0^{tx} = 287.1$ mW, $P_0^{rx} = 37.95$ mW, and $P_s = 5.28$ mW [24]. The total energy consumed can be represented as (19).

$$E_{total} = E_{tx} + E_{rx} \tag{14}$$

$$E_{tx} = P_{tx} ToA_{tx} + P_s T_u \tag{15}$$

$$E_{tx} = P_0^{tx} \sum_{m=1}^{3} \sum_{n=1}^{6} F_{m,n} ToA_0 \left(\alpha^{-n} \beta^{-m}\right) + P_s t_u \sum_{m=1}^{3} \sum_{n=1}^{6} F_{m,n} \tag{16}$$

$$E_{rx} = P_{rx} ToA_{tx} + P_s T_u \tag{17}$$

$$E_{rx} = P_0^{rx} \sum_{m=1}^{3} \sum_{n=1}^{6} F_{m,n} ToA_0 \left(\alpha^{-n} \beta^{-m}\right) + P_s t_u \sum_{m=1}^{3} \sum_{n=1}^{6} F_{m,n} \tag{18}$$

$$E_{total} = \left(P_0^{tx} + P_0^{rx}\right) \sum_{m=1}^{3} \sum_{n=1}^{6} F_{m,n} ToA_0 \left(\alpha^{-n} \beta^{-m}\right) + 2P_s t_u \sum_{m=1}^{3} \sum_{n=1}^{6} F_{m,n} \tag{19}$$

4. Experimental Study and Results

At the time of the writing of this manuscript, no LoRa modules capable of parallel transmission were found. The experimental study is organized in two phases. In the first phase, the functionality of our DED and resource allocation algorithm is investigated by conducting three distinct experiments using some small bytes as pilot data. Once the optimal set of parameters is found, the second phase is performed by sending image data and reporting the T_{tx}, BR, BER, consumed energy, and received image quality.

4.1. Phase I

In these experiments we have investigated parallel transmission of the pilot data using:

1. Different radio channels with the same BW and SF;
2. Different BWs with the same radio channel and SF;
3. Different SFs with the same BW and radio channel.

Since the third experiment with different SFs has already been thoroughly investigated in the literature (such as [26,27]), we chose not to present the analysis results for it to avoid redundancy. While varying the experimental parameters as required during the experiment, the remaining LoRa parameters were kept constant. The radio spectrum is monitored via a Software Defined Radio (SDR) receiver. The received data quality, RSSI and SNR of the transmitted signal were monitored using another DED, identical to the one at the transmitter, configured for specific SF, BW, and radio channels. The experimental setup is shown in Figure 7.

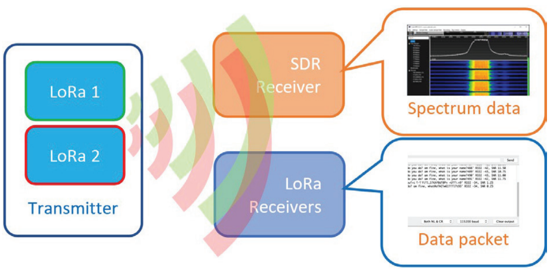

Figure 7. LoRa parallel data transfer experimental setup.

4.1.1. Different Radio Channels

Inter-radio channel interference was monitored to determine the best radio channels for parallel data transmission. In this experiment, the receiver was configured with SF = 7, BW = 250 kHz, and the radio channel frequency of 915 MHz. The transmitter was configured with different radio channel frequencies ranging from 900 MHz to 940 MHz; BWs of 125 kHz, 250 kHz and 500 kHz; and SF values from 7 to 12. The radio channel was monitored using the spectrum analyzer, which showed more than one reflected channel other than the transmitted channel. This caused interference with the configured radio channel. Figure 8 shows a reflected radio channel at 916 MHz for the transmitted signal using a 915 MHz radio channel with BW = 250 kHz and SF = 7. Although the reflected channel signal level was lower compared to the actual channel, the receiver configured for the reflected channel received 5–10% of the packets with 20% data-bit loss. Therefore, it was determined that multiple LCs with different radio frequencies could not be used for parallel transmission.

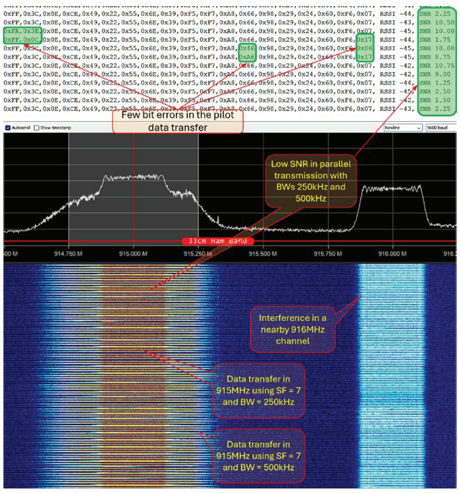

Pilot data: “0xFF, 0x3C, 0x0E, 0xCE, 0x49, 0x22, 0x55, 0x6E, 0x39, 0xF5, 0xF7, 0xA8, 0x66, 0x98, 0x29, 0x24, 0x60, 0xF6, 0x07”

Transmit power: 17 dBm

Data-bit errors:

31 bits for different radio channels (~20%)

29 bits for different bandwidths (~20%)

Figure 8. Different LoRa bandwidth and channel interference: The reflected radio channel (916 MHz) monitored for inter-channel interference. Data loss for LoRa parallel data transmission using two different BWs (BW 250 kHz and 500 kHz) with same SF = 7 and radio channel 915 MHz.

4.1.2. Different Bandwidths

In this experiment, one transmitter was configured to transmit 240 bytes of data using the 915 MHz radio channel with BW = 250 kHz and SF = 7. Another transmitter was configured to transfer a 240-byte packet using the same radio channel with SF = 7 and the BWs 125 kHz, 250 kHz, and 500 kHz. The receiver was configured using the 915 MHz radio channel with SF = 7. Figure 8 shows the parallel transmission of different BWs with the same SF and radio channel. The receiver received the data from the transmitter of a similar configuration (915 MHz, BW = 250 kHz, and SF = 7). However, the transmitted data with a BW of 500 kHz causes noise that affects the physical channel with a 250 kHz BW, resulting in an SNR decrease from 10 to 1.25. We also observed a few bits of data loss in 20% of the overlapped data packets, denoted by green boxes in Figure 8. Therefore, LCs of different BW could not be used for parallel transmission.

4.1.3. Different Spreading Factors

In this experiment, the two transmitters were configured with the same parameters, except for SFs transmitting 240 bytes over the 915 MHz radio channel. As expected, due to the quasi-orthogonality of the SFs, no significant data loss was observed during parallel transmission when using SF = 7 in conjunction with SFs ranging from 8 to 10. However, in small SF combinations with higher SF values such as 7 and 12, the SNR value experienced a meaningful decrease. As different SFs are not perfectly orthogonal, this issue stems from inter-SF interference caused by the extended overlapping duration of the two transmission chirps. To mitigate this, long-duration overlaps should be avoided during parallel transmission using different SFs.

4.2. Phase II

In this section, the parallel transmission of image data using different SFs is examined in terms of T_{tx}, BR, BER, energy consumption, and received image quality. To do this, small sized images (around 20 to 30 kB) are transformed into strings of bytes and stored in an SD RAM, connected to the processor. The communications were conducted in an open field spanning approximately 200 m, with both the transmitter and receiver positioned 3 m above the ground, ensuring a LoS link. On the transmitter and receiver, one LoRa radio is set to operate on SF = i and the other on SF = j, where i, j = {7, 8, 9, 10} and $i \neq j$, to maximize the utilization of the LC, as discussed earlier in Section 3.3. CR and BW are the other parameters that contribute to the ToA (transmission time of one packet) and thus T_{tx}. While a larger CR improves the robustness of the transmission against interference, it takes up packet capacity due to the added redundancy, thus diminishing the throughput of the LC and increasing the ToA. Therefore, CR in all experiments is fixed at 1 for all LoRa modules. We have repeated the experiment for every BW and measured the impact on T_{tx}. The payload size of all LoRa modules is set to the highest value, 255 bytes.

The image bytes are treated as a pool of information from which packets are formed and sent. To send an image over the LC, the LRA algorithm extracts the corresponding image bytes from the pool and segments them based on the SFs used by the LoRa modules at the transmitter (Section 3.3). In the first trial, the SFs on the transmitter and receiver are set to 7 and 8. According to Figure 5, to minimize synchronization loss in this parallel setup, a delay should be introduced to allow the reception of 2 packets over SF = 8 and 3 packets over SF = 7.

This results in a total of 5 packets being received in a single round of parallel transmission, with 2 of them delivered using SF = 8. Table 2 shows the results for the total parallel transmission time of a 24 kB image over the LC. The delay column represents the minimum time required to process received packets on both LoRa modules, ensuring no packets are missing. This delay time is determined through repeated transmissions using the same parameter set.

As shown in (6), a higher BW results in a higher BR, which in turn reduces the T_{tx}. The fastest image transfer was achieved with a BW of 500 kHz. This experiment was repeated for various combinations of SFs, with the corresponding T_{tx}s reported in Table 3. The LRA algorithm allocates data to ensure a balanced packet distribution between the two transmitters for various SF combinations. The proportions for each SF combination are as follows. For SFs 7 and 9, 75% of the image data is allocated to SF = 7, and 25% to SF = 9. For SFs 7 and 10, 85% is allocated to SF = 7, and 15% to SF = 10. For SFs 8 and 9, 67% of the data is assigned to SF = 8, and 33% to SF = 9. Lastly, for SFs 8 and 10, 75% is allocated to SF = 8, and 25% to SF = 10.

Table 2. T_{tx} results for parallel transmission of a 24 kB image over the LC on SFs 7 and 8.

BW (kHz)	SF	Delay (ms)	RSSI (dBm)	T_{tx} (s)	E_{tx} (J)	E_{rx} (J)	E_{total} (J)
125	7	700	−41	32.971	9.46	1.25	10.71
	8		−35				
250	7	400	−41	19.153	5.49	0.727	6.217
	8		−37				
500	7	250	−47	12.255	3.52	0.465	3.985
	8		−37				

Table 3. T_{tx} results for parallel transmission of a 24 kB image over the LC on other SF combinations.

BW (kHz)	SF	Delay (ms)	RSSI (dBm)	T_{tx} (s)	E_{tx} (J)	E_{rx} (J)	E_{total} (J)
125	7	950	−40	48.776	13.34	1.85	15.85
	9		−31				
	7	2000	−41	94.206	27.05	3.57	30.62
	10		−26				
	8	1450	−38	73.519	21.11	2.79	23.9
	9		−32				
	8	2500	−37	122.742	35.24	4.69	39.93
	10		−25				
250	7	600	−44	26.434	7.59	1.00	8.59
	9		−30				
	7	900	−44	42.126	12.09	1.60	13.69
	10		−22				
	8	870	−37	38.213	10.97	1.45	12.42
	9		−32				
	8	1150	−35	53.12	15.25	2.06	17.31
	10		−21				
500	7	350	−42	16.758	4.81	0.64	5.45
	9		−31				
	7	500	−44	23.675	6.80	0.89	7.69
	10		−25				
	8	460	−35	22.45	6.44	0.85	7.29
	9		−31				
	8	650	−37	29.971	8.60	1.14	9.74
	10		−25				

In the next trial, the total transmission times using our proposed algorithm is compared with a single transceiver setup. In this regard, the same experiment is repeated using a single LoRa module at the transmitter and receiver operating on SF = 7. This time, the whole string of bytes is formed into equal sized packets and fed into the buffer of the transmitter. Table 4 shows the T_{tx} for different BWs. In this case, the packet processing times are lower than the parallel transmission as no further delay is required for synchronizing a concurrently received packet. However, the overall transmission times are significantly longer compared to specific parallel SF combinations.

Table 4. T_{tx} results of the same image transmission over a single transceiver setup with different BWs.

BW (kHz)	SF	Delay (ms)	RSSI (dBm)	T_{tx} (s)	E_{tx} (J)	E_{rx} (J)	E_{total} (J)
125	7	550	−45	57.205	16.42	2.17	18.59
250	7	300	−40	29.138	8.37	1.10	9.47
500	7	200	−41	19.816	5.69	0.75	6.44

The underlying reason is the synchronization and distribution of data packets during parallel transmission. The proposed LRA algorithm assigns dedicated data segments to each LoRa radio in a synchronized manner, enabling simultaneous packet transmissions. This approach not only facilitates multiple transmissions at once but also reduces the total number of packets sent over each LoRa channel, ultimately leading to lower overall transmission times.

Figure 9 demonstrates the effect of different SF combinations on the T_{tx} compared to a single setup operating solely on SF = 7. In a single transceiver setup, the fastest transmission occurs with SF = 7, excluding SF = 6 due to its unavailability in some modules. As shown in Figure 9, the T_{tx} can be significantly improved using SF combinations of 7 and 8 or 7 and 9. Other SF combinations fail to enhance T_{tx}, as higher SFs lead to increased transmission times. The percentage of improvement for each parallel setup is detailed in Figure 10. The combination of SFs 7 and 8 improved the T_{tx} by 42.36%, 34.27%, and 38.16% for BWs of 125 kHz, 250 kHz, and 500 kHz, respectively. Meanwhile, the parallel setup with SFs 7 and 9 achieved improvements of 19.98%, 13.84%, and 15.43% for the same BWs.

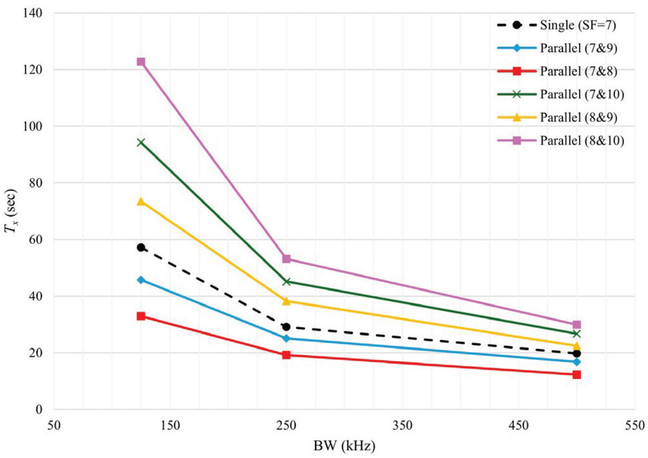

Figure 9. Transmission time for sending the same image over different parallel setups compared with a single transceiver setup.

The performance of SF combinations that enhance T_{tx} compared to a single transceiver setup is evaluated in terms of BR. Figure 11 presents the BR of a single LoRa channel operating on SF = 7, as well as LCs utilizing SF combinations of 7 and 8 and 7 and 9, while accounting for packet processing times. When SF = 7 and 8 are employed, the BR increases by 73.5%, 52.13%, and 61.7% for BWs of 125 kHz, 250 kHz, and 500 kHz, respectively. For the SF = 7 and 9 combination, the BR improvement is 24.97%, 16.06%, and 18.25% across the same BWs.

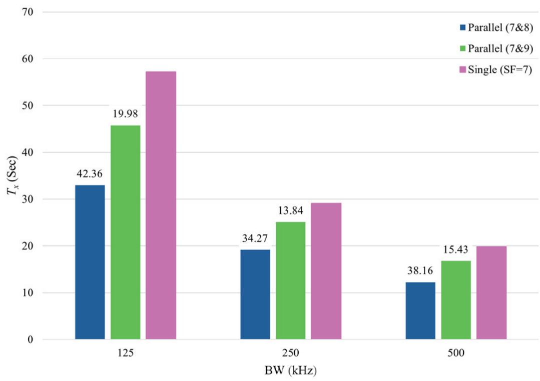

Figure 10. T_x improvement of parallel setup compared to single setup.

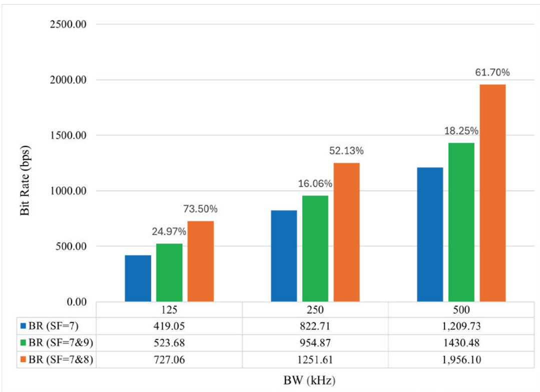

Figure 11. Bit rate improvement of parallel setup compared to single setup.

Figure 12 illustrates the energy consumption profile of our parallel setup using the proposed LRA algorithm, based on Equations (14)–(18). The transmitter amplifier and the receiver low noise amplifier consume the largest portion of the total energy. However, SF combinations 7 and 8, and 7 and 9 significantly reduce transmission time, allowing the amplifiers to remain active for shorter durations compared to a single transceiver setup. As a result, the LRA algorithm demonstrates better energy efficiency than the traditional single setup for SF combinations 7 and 8, and 7 and 9 across all BW values.

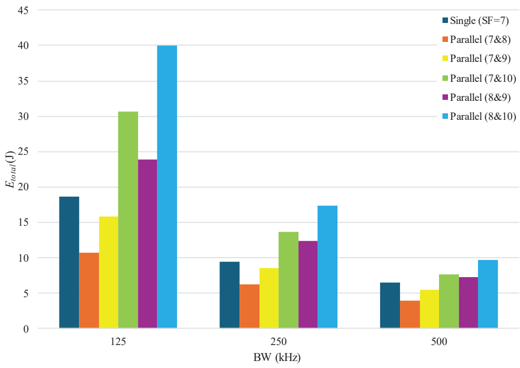

Figure 12. Comparison of total energy consumption of proposed LRA algorithm with single transceiver setup with SF = 7.

Next, we measured the ratio of errored bits to the total image bits to calculate the BER of the LC with a BW of 125 kHz and varying SFs. The experiments are carried out in the same location as earlier in this subsection, with the transmit power altered at the transmitter to have SNR values in the range of [−30, 0] dB. Figure 13 illustrates the BER of different parallel communication setups compared to the analytical BER of a single LoRa physical channel with a BW of 125 kHz and SFs of 7, 8, and 9, as reported in [25]. The solid lines represent the theoretical BER of single LoRa communication links in an LoS scenario with the presence of Additive White Gaussian Noise (AWGN).

It is evident that utilizing a lower SF increases the probability of error in LoRa communications. In our proposed parallel setup, higher SF combinations achieve better BER with SF = 8 and 9 lying just above single SF = 8, outperforming single SF = 7. LCs operating on SF = 7 and 9 and SF = 7 and 8, which improve the T_{tx}, perform worse than a single transceiver on SF = 7 in terms of probability of error. This is reasonable due to the inter-SF interference of a parallel communication link and the fact that our results are derived from experimental data rather than theoretical models. As shown in Figure 13, for SNR values greater than −5 dB, the BER remains within acceptable limits, demonstrating the viability of our parallel communication setup.

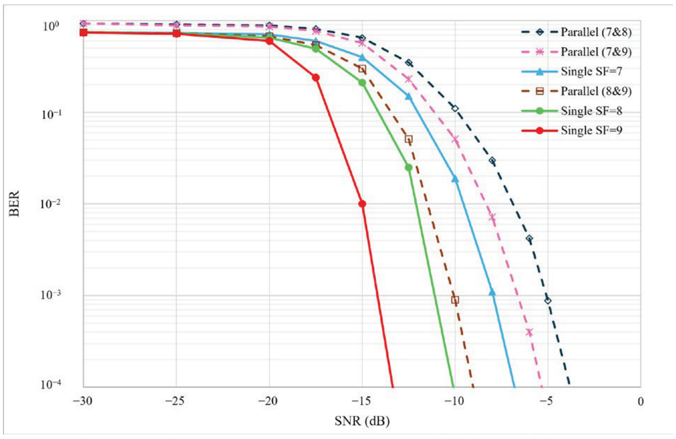

Figure 13. Comparison of BER of our LC (dashed lines) with single transceiver setup (solid lines) using SFs 7, 8, and 9.

Finally, the quality of the images received through the LC are investigated. Allowing sufficient delay time for packet processing at the receiver along with maintaining an adequate SNR value (higher than −5 dB for LoS communication link), results in high-quality images with BER of approximately 10^{-3} or less. However, reducing delay times to minimize the total T_{tx} or maintaining a lower signal power to reduce energy consumption will compromise image quality by increasing the probability of errors in the received data. Figure 14 illustrates the impact of utilizing delay times shorter than those derived from our experiments (left column) and the effect of SNR values below −5 dB (right column) on the quality of the received image for the parallel setup operating on SFs 7 and 8 and BW = 250 kHz. The quality of the received image is measured in terms of the ratio of bits received in error to the total number of bits (Error) and packet delivery rate (PDR). Additionally, the Structural Similarity Index Measure (SSIM) of the received image under different delay times and SNR values is calculated. Figure 15 presents the SSIM maps for those received images where lighter gray corresponds to higher similarity (SSIM values closer to 1) and darker gray indicates lower similarity (SSIM values closer to 0). The reference image for this metric is the transmitted image.

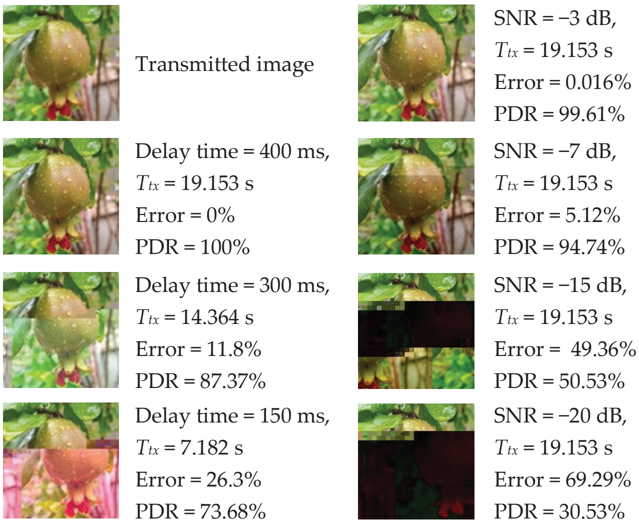

Figure 14. The impact of smaller delay times (left column) and lower SNR values (right column) on the quality of the received image over SF = 7 and 8 and BW = 250 kHz.

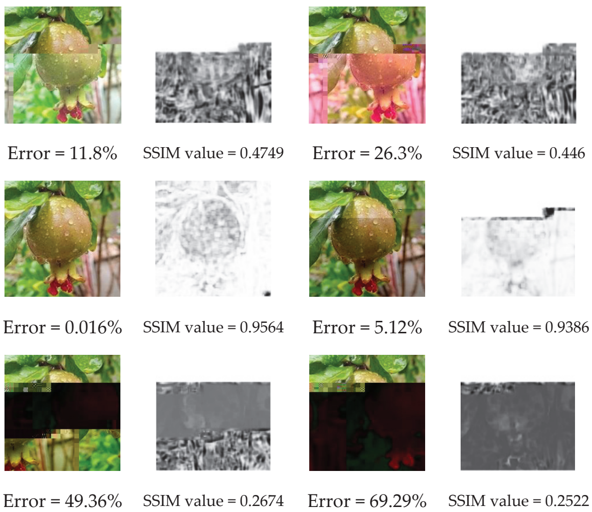

Figure 15. SSIM map and value of the received image with lower delay times and SNR values.

Figures 14 and 15 highlight the tradeoff between the quality of the image received and the T_{tx} or SNR. Depending on the application, if a certain amount of error can be tolerated, the transmission can take less time or less power can be spent on the transmitter amplifier.

In the end, we have compared our proposed algorithm with other LoRa capacity improvement schemes. This comparison is reported in Table 5. ICS-CSS and SSK-ICS improved LoRa capacity by changing the existing CSS modulation. Due to the change in modulation, these schemes may not be compatible with existing LoRa applications until chip-level implementations are available. Additionally, while these modulation changes can increase the BR by up to 42%, our proposed algorithm significantly outperforms them, achieving a 73.5% improvement in BR. TDM-LoRa [10] modulation doubled the data rate, increasing the BER at lower SF (SF = 7), whereas proposed algorithm improves the data rate up to 73.5% using the SF = 7 and 8. TDM-LoRa has modified the CSS modulation and is incompatible with the existing LoRa physical layer. The network access protocol proposed by [13] utilizes multiple SFs across different clusters to equalize transmission time.

Table 5. Comparison of our proposed LRA algorithm with the other LoRa capacity improvement schemes.

Scheme	**ICS-CSS [6]**	**SSK-ICS [7]**	**TDM-LoRa [10]**	**[13]**	**Cantor [14]**	**EWS [15]**	**MIMO-LoRa [16]**	**LRA Algorithm**
Technique	Modulation			Dynamic SF allocation	Optimization algorithm		Application layer	Physical and MAC layer
LoRa orthogonality	Similar to traditional CSS		Quasi-orthogonal on radio channel	Similar to traditional CSS		SF orthogonality		SF orthogonality
Compatibility	Incompatible to LoRa-PHY			Compatible with existing LoRaWAN-MAC			Incompatible with LoRaWAN	Hardware compatible with LoRa-PHY, incompatible with LoRaWAN MAC
Implementation	Need HW redesign			No HW redesign required, need SW implementation			May need HW redesign	No HW redesign needed. Simple SW implementation
Limitations	Incompatible with the existing LoRa technology due to change in modulation technique			Bottleneck for nodes closer to the GW for multi hop network due to use of higher SF	Calculation and control message overhead for the optimization algorithm	Require location data from GPS or derive from RSSI	Performs better at higher SFs (10, 11, 12)	Not suitable for combination of higher SF with lower (e.g., 7 and 12)
Advantages	May not impact the implementation of available LoRaWAN			Compatible with existing LoRaWAN	Compatible with existing LoRaWAN	Increase network size	Increased network coverage area	Easy implementation, suitable for image transmission
Performance Improvement	42% BR gain with 3.39% increase in BER	28.6% BR improvement for the same SF and BW	Doubled the BR, increased BER at lower SF (SF = 7)	62.8% BR improvement at SF = 7	70% BR improvement	18.2% to 55.25% BR improvement	10% to 50% BR improvement at SNR $\leq$ 10 dB	73.5% (at SF = 7 and 8), 24.9% (at SF = 7 and 9) BR improvement, 42.4% (at SF = 7 and 8), 19.98% (at SF = 7 and 9) ToA improvement

Cantor [14] and EWS [15] enhanced the existing LoRaWAN MAC by improving the Packet Reception Rate (PRR) or Packet Delivery Rate (PDR). Cantor introduced a parametric optimization algorithm, which, while increasing network goodput by up to 70%, may generate higher control traffic. EWS, on the other hand, can suffer from a higher collision rate due to inaccurate distance calculations at low RSSI levels. Unlike the CSMA (Carrier Sense Multiple Access) used in LoRaWAN, the proposed algorithm mitigates collisions by employing Listen Before Talk (LBT) and utilizing multiple SFs, instead of RF channels, for parallel transmissions. However, the implementation of Cantor and EWS might not require any hardware modifications, depending on the processing and energy demands. MIMO-LoRa [16] enables the reception of multiple signals with different SFs transmitted in parallel by the same EDs, utilizing SNR and transmit power optimization without needing synchronization. In contrast, the proposed algorithm requires synchronization within the same ED, which adds complexity to the algorithm. While MIMO-LoRa is not suitable for low SFs, the proposed LRA algorithm is optimized for these conditions. However, the proposed algorithm may face challenges with higher SFs, due to increased inter-SF interference. Additionally, as a non-LoRaWAN protocol, the LRA may lack compatibility with existing networks built on LoRaWAN.

5. Conclusions

In this study, we addressed the challenge of image transmission using LoRa technology, which is typically constrained by its low data rate. To overcome this limitation, we proposed a resource allocation algorithm for LoRa (LRA) that leverages the quasi-orthogonality of spreading factors (SFs) to enable parallel transmissions of larger data sizes using multiple LoRa modules. To achieve this, we developed a specially designed end device (DED) that incorporates two LoRa modules connected to a single controller unit, minimizing hardware complexity. The LRA algorithm is introduced to assign data packets to the transmitters based on their operating SF in a synchronized manner. Furthermore, we examined the transmission time (T_{tx}) across different SFs of our logical channel (LC) to optimize the number of packets transmitted per parallel transmission round. We performed a two-phase experimental study to demonstrate the feasibility of the parallel transmissions using different parameters and to examine the performance of our proposed algorithm in terms of T_{tx}, BER, data rate, energy consumption, and the quality of the received image. The results indicate that our parallel setup significantly improves data rate and T_{tx} within the existing LoRa technology.

Considering the LRA algorithm in densely deployed LoRa networks to assess scalability would be our next focus to further assess its performance. To achieve this, machine-learning-based approaches for selecting SFs for the DEDs could prove beneficial.

Furthermore, Since LoRa signals with identical SFs can significantly interfere with each other, a coding scheme may exist allowing the receiver to distinguish and successfully demodulate these signals. This could open the door to parallel transmissions on the same SF, greatly boosting throughput. Finding such a coding system would be the subject of future research in this area.

Author Contributions: Conceptualization, G.M.E.R. and H.K.; Methodology, G.M.E.R. and H.K.; Software, H.K.; Validation, G.M.E.R. and H.K.; Formal analysis, G.M.E.R. and H.K.; Investigation, G.M.E.R. and H.K.; Visualization, G.M.E.R. and H.K.; Supervision, K.A.W. All authors have read and agreed to the published version of the manuscript.

Funding: This research was funded by Natural Sciences and Engineering Research Council of Canada (NSERC), grant number RGPIN-2018-06274.

Institutional Review Board Statement: Not applicable.

Informed Consent Statement: Not applicable.

Data Availability Statement: Data are contained within the article.

Conflicts of Interest: The authors declare no conflict of interest.

References

1. Pham, C. Low-cost, low-power and long-range image sensor for visual surveillance. In Proceedings of the Annual International Conference on Mobile Computing and Networking, MOBICOM, Association for Computing Machinery, New York City, NY, USA, 3–7 October 2016; pp. 35–40. [CrossRef]
2. Wei, C.-C.; Chen, S.-T.; Su, P.-Y. Image Transmission Using LoRa Technology with Various Spreading Factors. In Proceedings of the 2019 2nd World Symposium on Communication Engineering (WSCE), Nagoya, Japan, 20–23 December 2019; pp. 48–52.
3. Chen, T.; Eager, D.; Makaroff, D. Efficient Image Transmission Using LoRa Technology in Agricultural Monitoring IoT Systems. In Proceedings of the 2019 International Conference on Internet of Things (iThings) and IEEE Green Computing and Communications (GreenCom) and IEEE Cyber, Physical and Social Computing (CPSCom) and IEEE Smart Data (SmartData), Atlanta, GA, USA, 14–17 July 2019; pp. 937–944.
4. Sornin, N.; Champion, L. Signal Concentrator Device. US 2016.0020932A1, 21 January 2016.
5. Chiani, M.; Elzanaty, A. On the LoRa Modulation for IoT: Waveform Properties and Spectral Analysis. *Internet Things J.* **2019**, *6*, 8463–8470. [CrossRef]
6. Edward, P.; El-Aasser, M.; Ashour, M.; Elshabrawy, T. Interleaved Chirp Spreading LoRa as a Parallel Network to Enhance LoRa Capacity. *IEEE Internet Things J.* **2021**, *8*, 3864–3874. [CrossRef]
7. Mondal, A.; Hanif, M.; Nguyen, H.H. SSK-ICS LoRa: A LoRa-Based Modulation Scheme with Constant Envelope and Enhanced Data Rate. *IEEE Commun. Lett.* **2022**, *26*, 1185–1189. [CrossRef]
8. Kang, J.M. A New Index Modulation for LoRa. *IEEE Internet Things J.* **2023**, *10*, 11938–11939. [CrossRef]
9. Hanif, M.; Nguyen, H.H. Frequency-Shift Chirp Spread Spectrum Communications with Index Modulation. *IEEE Internet Things J.* **2021**, *8*, 17611–17621. [CrossRef]
10. An, S.; Wang, H.; Sun, Y.; Lu, Z.; Yu, Q. Time Domain Multiplexed LoRa Modulation Waveform Design for IoT Communication. *IEEE Commun. Lett.* **2022**, *26*, 838–842. [CrossRef]
11. Jadhav, A.R.; Rajalakshmi, P. Enhanced LoRa Data Rate through PATCH. In Proceedings of the 2020 IEEE 6th World Forum on Internet of Things (WF-IoT), New Orleans, LA, USA, 2–16 June 2020; pp. 1–6.
12. Zorbas, D.; Nurbay, T.; Yeltay, A. Cooperative Transmission of Large Files Over LoRa in Multimedia IoT Networks. In Proceedings of the 2024 IEEE International Black Sea Conference on Communications and Networking (BlackSeaCom), Tbilisi, Georgia, 24–27 June 2024; pp. 153–158. Available online: https://www.researchgate.net/publication/380574178 (accessed on 1 January 2025).
13. Zhu, G.; Liao, C.H.; Sakdejayont, T.; Lai, I.W.; Narusue, Y.; Morikawa, H. Improving the Capacity of a Mesh LoRa Network by Spreading-Factor-Based Network Clustering. *IEEE Access* **2019**, *7*, 21584–21596. [CrossRef]
14. Xu, D.; Chen, X.; Zhang, N.; Ding, N.; Zhang, J.; Fang, D.; Gu, T. Cantor: Improving Goodput in LoRa Concurrent Transmission. *IEEE Internet Things J.* **2021**, *8*, 1519–1532. [CrossRef]
15. Saluja, D.; Singh, R.; Gautam, S.; Kumar, S. EWS: Exponential Windowing Scheme to Improve LoRa Scalability. *IEEE Trans. Ind. Inform.* **2022**, *18*, 252–265. [CrossRef]
16. Kang, J.M. MIMO-LoRa for High-Data-Rate IoT: Concept and Precoding Design. *IEEE Internet Things J.* **2022**, *9*, 10368–10369. [CrossRef]
17. Hou, Y.; Sun, D.; Liu, Z. A novel MAC protocol exploiting concurrent transmissions for massive LoRa connectivity. *J. Commun. Netw.* **2020**, *22*, 108–117. [CrossRef]
18. Guerra, K.; Casavilca, J.; Huamán, S.; López, L.; Sanchez, A.; Kemper, G. A low-rate encoder for image transmission using LoRa communication modules. *Int. J. Inf. Technol.* **2023**, *15*, 1069–1079. [CrossRef]
19. Dede, O.L.; Jalajamony, H.M.; Fernandez, R.E. Image Transmission over LoRa-Based Networks: A Performance Study Using Image Compression and Reconstruction Methods. In Proceedings of the 2024 IEEE 21st Consumer Communications & Networking Conference (CCNC), Las Vegas, NV, USA, 6–9 January 2024; Institute of Electrical and Electronics Engineers Inc.: Piscataway, NJ, USA; pp. 642–643. [CrossRef]
20. Scarvaglieri, A.; Palazzo, S.; Busacca, F. A lightweight, fully-distributed AI framework for energy-efficient resource allocation in LoRa networks. In Proceedings of the IEEE/ACM 16th International Conference on Utility and Cloud Computing, Taormina, Italy, 4–7 December 2023; Association for Computing Machinery, Inc.: New York, NY, USA; pp. 1–6. [CrossRef]

21. Ta, D.-T.; Khawam, K.; Lahoud, S.; Adjih, C.; Martin, S. LoRa-MAB: Toward an Intelligent Resource Allocation Approach for LoRaWAN. In Proceedings of the 2019 IEEE Global Communications Conference (GLOBECOM), Big Island, HI, USA, 9–13 December 2019.
22. Zhong, H.; Ning, L.; Wang, J.; Suo, S.; Chen, L. Optimization of LoRa SF Allocation Based on Deep Reinforcement Learning. *Wirel. Commun. Mob. Comput.* **2022**, *2022*, 1690667. [CrossRef]
23. Busacca, F.; Mangione, S.; Neglia, G.; Tinnirello, I.; Palazzo, S.; Restuccia, F. FedLoRa: IoT Spectrum Sensing Through Fast and Energy-Efficient Federated Learning in LoRa Networks. In Proceedings of the 2024 IEEE 21st International Conference on Mobile Ad-Hoc and Smart Systems, MASS, Seoul, Republic of Korea, 23–25 September 2024; Institute of Electrical and Electronics Engineers Inc.: Piscataway, NJ, USA; pp. 295–303. [CrossRef]
24. "SX1276/77/78/79". Semtech. Available online: https://semtech.my.salesforce.com/sfc/p/#E0000000JelG/a/2R0000001Rbr/6EfVZUorrpoKFfvaF_Fkpgp5kzjiNyiAbqcpqh9qSjE (accessed on 9 January 2022).
25. Mroue, H.; Nasser, A.; Parrein, B.; Hamrioui, S.; Mona-Cruz, E.; Rouyer, G. Analytical and Simulation study for LoRa Modulation. In Proceedings of the 2018 25th International Conference on Telecommunications, ICT, Saint-Malo, France, 26–28 June 2018; Institute of Electrical and Electronics Engineers Inc.: Piscataway, NJ, USA; pp. 655–659. [CrossRef]
26. Zhu, G.; Liao, C.-H.; Suzuki, M.; Narusue, Y.; Morikawa, H. Evaluation of LoRa Receiver Performance under Co-technology Interference. In Proceedings of the 2018 15th IEEE Annual Consumer Communications & Networking Conference, Las Vegas, NV, USA, 12–15 January 2018; p. 172.
27. Croce, D.; Gucciardo, M.; Mangione, S.; Santaromita, G.; Tinnirello, I. Impact of LoRa Imperfect Orthogonality: Analysis of Link-Level Performance. *IEEE Commun. Lett.* **2018**, *22*, 796–799. [CrossRef]

sensors

Article

A Self-Configurable BUS Network Topology Based on LoRa Nodes for the Transmission of Data and Alarm Messages in Power Line-Monitoring Systems

Bartomeu Alorda-Ladaria [1,2,3,*], Marta Pons [1] and Eugeni Isern [1,2]

1 Department of Industrial Engineering and Construction, University of Balearic Islands, Ctra. Valldemossa, km 7.5, Ed. Mateu Orfila, Illes Balears, 07122 Palma, Spain; martaponsnieto@gmail.com (M.P.); eugeni.isern@uib.es (E.I.)
2 Health Science and Technology Cross-Cutting Department, Balearic Islands Health Research Institute (IdISBa), 07120 Palma, Spain
3 Institute for Environmental Agro-Environmental Research and Water Economics (INAGEA), 07120 Palma, Spain
* Correspondence: tomeu.alorda@uib.es

Abstract: Power transmission lines transfer energy between power plants and substations by means of a linear chain of towers. These towers are often situated over extensive distances, sometimes in regions that are difficult to access. Wireless sensor networks present a viable solution for monitoring these long chains of towers due to their wide coverage, ease of installation and cost-effectiveness. The proposed LoRaBUS approach implements and analyses the benefits of a linear topology using a mixture of LoRa and LoRaWAN protocols. This approach is designed to enable automatic detection of nearby nodes, optimise energy consumption and provide a prioritised transmission mode in emergency situations. On remote, hard-to-reach towers, a prototype fire protection system was implemented and tested. The results demonstrate that LoRaBUS creates a self-configurable linear topology which proves advantageous for installation processes, node maintenance and troubleshooting node failures. The discovery process collects data from a neighbourhood to construct the network and to save energy. The network's autonomous configuration can be completed within approximately 2 min. In addition, energy consumption is effectively reduced 25% by dynamically adjusting the transmission power based on the detected channel quality and the distance to the nearest neighbour nodes.

Keywords: wireless sensor network; power line monitoring; LoRaWAN BUS topology; Internet of Things multiprotocol

1. Introduction

The power grid system is one of the most critical energy infrastructure items formed by power plants, transmissions lines, sub-stations with transformers and consumers. Infrastructure ageing, electricity demand and climate change impact are addressed to ensure smart grid management, high quality service and increasing reliability requirements. In this sense, efficient monitoring and controlling systems based on information and communication technologies are introduced in power line monitoring to enhance normal operation and infrastructure damages. The use of information and communication technologies ensures robust, cost-efficient and proactive power grid operation [1–3]. Sensor and camera-based remote monitoring have recently gained great attention. The advantages of wireless sensor networks (WSNs) such as adaptability and scalability lead to the ability to find solutions in a variety of engineering environments, including military and defence applications [4], environmental disaster-control applications [5], monitoring of biomedical parameters affecting health [6], household applications [7] and also in what is called "precision agriculture" [8].

The use of WSNs in power grid systems offers real-time information to improve high-voltage power network monitoring and controlling to face climate change scenarios and electricity sector demands in a collaborative, cost-effective and energy-constrained way [9]. Especially for a long chain of towers covering mountain areas, wireless sensor networks (WSNs) are gaining attention due to their easy installation and high adaptability with respect to connecting different types of sensors to work collaboratively, as insect nets, monitoring a great variety of physical variables [10].

Protocols like 3G and WiFi have achieved a wide coverage area around the world, although connectivity cannot be guaranteed in some remote or non-urban areas. The lack of coverage limits the effective smart grid deployment centred on an Internet of Things (IoT) solution. To overcome this coverage constraint and expand the monitoring and controlling capabilities in remote areas, raw-LoRa and LoRaWAN protocols are gaining attention by offering a wide range of coverage with efficient energy consumption and low-cost infrastructure [9,10]. In contrast to other IoT protocols, raw-LoRa defines only the physical layer which operates in unauthorised frequency bands, and allows self-organising of the network topology like WSNs [11,12]. The raw-LoRa protocol can be configured to deploy communication solutions with one of the three most common network topologies: star, mesh or cluster tree. As shown in Figure 1, the differences between these network topologies are based on the type of nodes they include and the connection between them. In short, the nodes can be classified as "*end nodes*" which are able to measure and communicate some variable of interest, the "*router nodes*" that are used to connect end nodes located outside the coverage area with the coordinator node and the "*coordinator or gateway node*" which is the link between an end-user and the sensor network. In addition, the LoRaWAN protocol introduces the definition of the link and network layers. This establishes different roles for nodes, the ability to address messages to specific nodes, the format of messages, the use of encryption to protect the content of messages and the definition of a typical topology based on the star topology, see Figure 1.

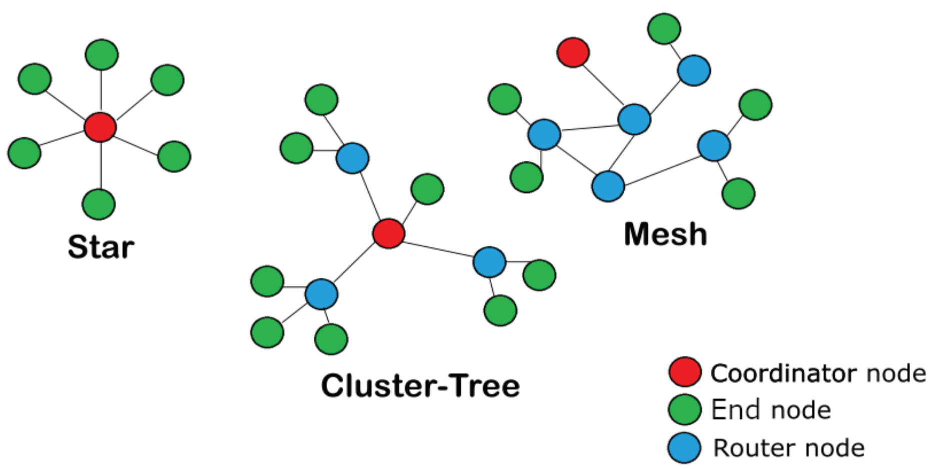

Figure 1. Typical topologies of WSN. Adapted from [13].

In the case of large power tower chains across remote or mountainous areas, raw-LoRa has been identified as the most suitable protocol compared to alternatives like Narrowband Internet of Things (NB-IoT), which is more dependent on cellular mobile coverage [10]. However, the low communication speed of raw-LoRa is the main constraint in meeting the real-time requirements of power line-monitoring systems. Therefore, the combination of network technologies is a promising alternative to achieve an optimal balance between network performance of enough quality and the increase in cost that they may entail.

Compared with ordinary infrastructure monitoring located near urban areas with easy access, the monitoring challenges in mountainous and remote areas presents differences in terms of maintenance, implementation and monitoring operation [10]. In this work, a linear topology-based WSN combining raw-LoRa and LoRaWAN nodes for non-urban power transmission line monitoring is proposed. LoRaBUS is able to transmit operational monitoring data in a regular mode or generate warning messages in emergency scenarios. The complete system-monitoring scheme in mountainous areas is based on the three-layer network structure presented in [10], where raw-LoRa is selected as the collecting protocol for sensor data. This protocol offers a balanced delay time and costs results when it is combined with a cellular mobile network at the second layer to transmit sensor data to the monitoring centre.

In summary, while existing literature discusses various WSN implementations, LoRaBUS introduces several novel aspects related to topology optimisation, hybrid raw-LoRa and LoRaWAN protocol design, Emergency Transmission Priority Mode and a specific prototype for Fire Protection applications. Most prior studies focus on general WSN deployment, but LoRaBUS specifically designs a linear topology tailored for power-transmission lines. This structure improves network reliability and data-collection efficiency along a chain of towers. The combination of LoRa and LoRaWAN in LoRaBUS enhances range and network coverage while maintaining low power consumption. LoRaBUS introduces a prioritised mode for emergencies, improving the responsiveness of power line-monitoring systems. LoRaBUS goes a step further by implementing and testing a fire-protection system for remote towers, providing a tangible application of its network capabilities.

The proposed LoRaBUS topology is shown in Figure 2, formed by three types of nodes: the coordinator, the end and the router. The coordinator node is responsible for connecting the nodes of the BUS topology with a wider pre-existing network based on WAN protocols, maintaining communication between the entire network of nodes and the data-processing centre. The router node is located as the first and last node of the LoRaBUS topology as shown in Figure 2, and is responsible for translating the raw-LoRa messages from end nodes forming the BUS to the coordinator node. Therefore, the LoRaBUS topology can be connected to a wider network using one of the router nodes. If one router node is configured to connect with the coordinator node, the other router node will act as a last BUS node. And finally, the end nodes are in charge of creating the communication BUS, sending the data from the sensors and maintaining the links between them.

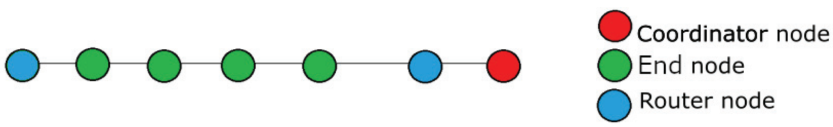

Figure 2. Linear topology of LoRaBUS.

The main contribution of LoRaBUS is the concept and practical implementation of a robust and self-configurable tower chain communication system, which transmits sensor values during normal operation or warning messages in emergency mode. LoRaBUS uses long-range wireless communication, creating a self-configuration protocol to recognise closed nodes for easy management and fail-node recovery.

The main contributions of this paper are summarised as follows:

- The concept of a BUS topology in WSN with two final nodes acting as routers to improve connectivity with upper system layers.
- The self-configuring algorithm which detects nearby nodes and adjusts power consumption during transmission to avoid channel interference between adjacent nodes.
- The algorithm to transmit data between nodes avoiding data duplication and reducing power consumption.
- The communication architecture based on a combination of LoRa and LoraWAN for worldwide connection with controlling centre.
- The proposed network topology is implemented in a real prototype to test power consumption and quality coverage in a campus and non-urban scenarios.

The remaining sections of this paper are presented as follows. Section 2 discusses the network architecture by defining the different elements and connections between them. Section 3 defines the designed communication protocol and the self-configuration algorithm. Section 4 presents the experimental results obtained with the prototype in a campus and non-urban scenarios. Section 5 concludes the paper and outlines directions for future work.

2. System Architecture

The designed system architecture consists of three main parts: the nodes forming the BUS topology, the LoRa Network Server and the display platform where the data are represented. In this work, the LoRaBUS topology requires four different nodes: the main node (this connects the LoRaBUS topology to a coordinator node using the LoRaWAN network as shown Figure 2), the sensor nodes (represented as "end nodes" in Figure 2), the final node (special "router node" in Figure 2) and the gateway (represented as "coordinator node" in Figure 2).

- The ***gateway* node** maintains the connection between the LoRaWAN network with the network server. The data received from the BUS nodes are re-transmitted to the TTN (the global LoRaWAN community named The Thinks Network, [14]) via TCP/IP connections, such as WiFi or 3G.
- The ***main node*** is represented as the router node in Figure 2 and is the node placed nearest to the *gateway*. Its main function is to convert the messages from the sensor nodes (via raw-LoRa) to a LoRaWAN message that could be sent to the gateway. Furthermore, this node decides which sensor node in the BUS topology will take control of the BUS to transmit the information at each transmission cycle.
- The ***sensor nodes*** are able to measure the environmental conditions near their position and then send this information through the LoRaBUS implemented by themselves. Each of these nodes is therefore capable of measuring sensor data and processing an alarm message, as well as maintaining the connection between nodes to create the BUS network topology. Therefore, it is not only a node with *end node* capabilities, but is also a typical *router node* using the usual nomenclature in a WSN network. The designed LoRaBUS protocol has no restriction on the maximum number of nodes, so the total distance that could be covered by the proposed LoRaBUS topology has no theoretical limitations.

- The ***final sensor*** is a particular node similar to the sensor nodes which is located at the last position of the BUS; i.e., at this node the sequence of nodes in the BUS topology ends. Because the BUS communication finishes on this node, it has a different firmware although the hardware is the same as the sensors nodes. The complete functionality of this special node and other advantages are explained in Section 3.

The proposed overall system architecture described as LoRaBUS is illustrated in Figure 3, which mainly includes the different elements and the proposed connections between them.

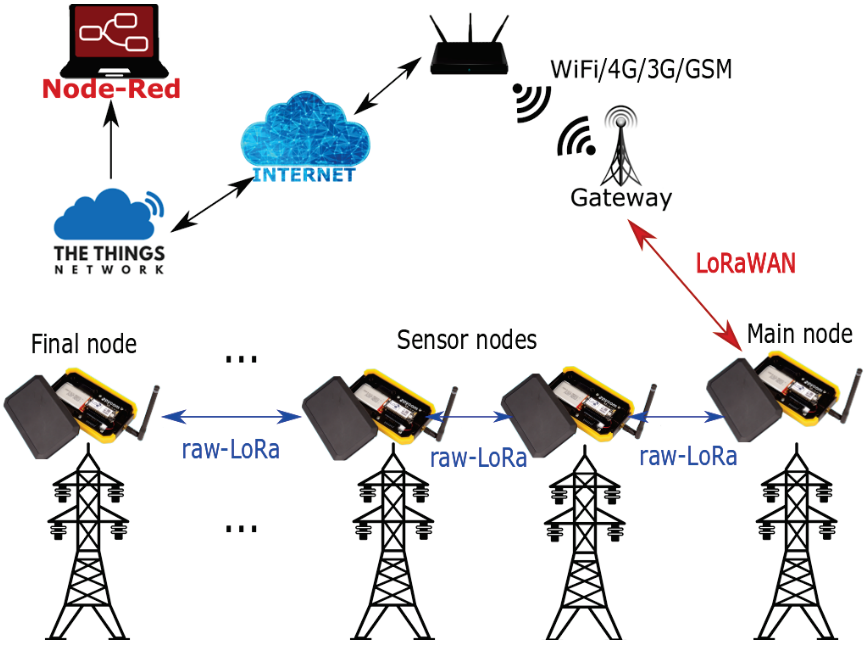

Figure 3. Elements of the proposed LoRaBUS system and their connections.

The LoRaBUS system proposal makes use of the LoRaWAN and raw-LoRa protocols to implement the different links of the proposed topology. The LoRaWAN protocol is used to communicate between the main node and the gateway. Consequently, using the LoraWAN protocol to communicate the main node with the gateway node allows the integration of several LoRaBUS topologies into a larger LoRaWAN network. That is, the gateway node could communicate with different LoRaBUS sections through the link to the main node of each section. By contrast, the raw-LoRa protocol is used to create the BUS topology between the main node, the sensor nodes and the final node. The raw-LoRa protocol is used to build the LoRaBUS protocol described in this work, benefiting from the long-range features of the LoRa modulation. Therefore, the node accesses the radio hardware directly and messages are transmitted using LoRa modulation on the selected frequency, without message format or encryption. The next section will describe the benefits of both protocols on the LoRaBUS topology approach.

The rest of the parts of the system architecture were selected using freeware options. In this way, an open-source platform called *The Things Network* (TTN) was selected as the LoRaWAN Network Server. This platform provides easy-to-use functions to manage messages received using LoRaWAN protocols. Thus, the information from the sensors is transmitted to the gateway, which uploads it to a user-friendly display platform with a web-based GUI called Node-Red. These software solutions are used to validate the LoRaBUS topology configuration in real experiments summarised in Section 4.

Raw-LoRa and LoRaWAN

LoRa is a wireless communication technology that was patented by *Smetech* [15] and uses a radio frequency modulation to transmit data through the ISM bands (in Europe it represents frequencies between 867 and 869 MHz). LoRa is part of the *Low-Power Wide-Area Networks* (LPWAN) and represents one of the most popular technologies in IoT projects together with Bluetooth, Zigbee or SigFox. LoRa specifications state that its coverage is up to 15 km in rural areas, and uses very low transmission rates, from 250 bps to a maximum of 5.5 kbps. In addition, this technology aims to ensure high power efficiency, which is an important feature when remote deployments are considered.

Communication through LoRa is defined in two different ways: raw-LoRa and LoRaWAN. The difference between them is related to the OSI layers that they use. For example, in a raw-LoRa mode, the communication is set point-to-point only by using the physical layer. Instead, the LoRaWAN connection defines both MAC and NET layers. Another difference is that in a LoRaWAN connection, any node needs to be in the coverage area of the coordinator or router nodes, which is unusual in remote scenarios such as forests. For that reason, we designed a prototype of communication protocols, and different types of nodes. Figure 4 represents the different types of nodes, showing the OSI layers stack used to implement each of them in the LoRaBUS.

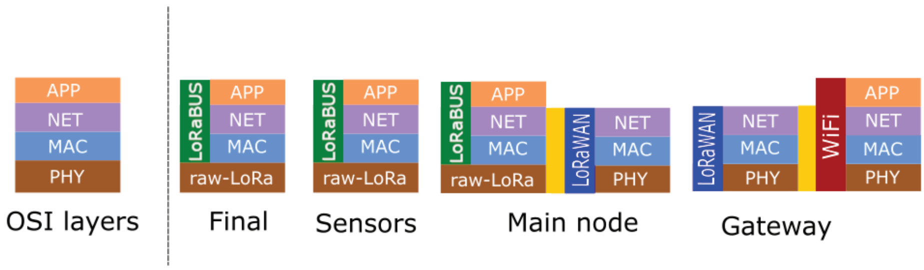

Figure 4. OSI layers defined in each node type.

The proposed LoRaBUS is implemented in the nodes forming the BUS topology and it uses the raw-LoRa as a physical layer as Figure 4 shows. The main node is the first node of the BUS topology and it is responsible for making the translation between data to and from the BUS nodes, from and to the LoRaWAN Gateway. While the LoRaWAN Gateway is capable of sending and receiving data from the TTN platform using Wifi connection to the Internet. The data received from the TTN platform is visualised using the Node-Red web-based GUI.

3. LoRaBUS Communication Protocol

In this section, the LoRaBUS communication protocol is described and explained in detail. The proposed approach tries to implement a BUS topology using LoRa-based nodes, improving the autonomy of the network. The LoRaBUS protocol is based on the implementation of a precise management of the transmission power used for sending messages between neighbouring nodes. Thus, two neighbouring nodes may be at a distance that will require a certain level of transmission power. This power must be discovered because it will depend on the distance, but also on link quality factors. Although the LoRa protocol allows management of the spreading factor which adjusts the transmission rate, receiver sensitivity and chirp rate to improve the range of the nodes, this option was not used in the proposed system because of its negative effects: increasing the time of flight of the messages and increasing battery consumption. It has been considered that a network intended for emergency alerting should not use spreading factors that reduce the data rate, increase the message flight time or reduce the battery life. Therefore, the nodes will have a spreading factor value that will not be modified by the protocol defined in this work.

The self-configuration protocol is important for the deployment of nodes in remote environments, where it is necessary to resolve situations such as the inclusion of nodes for maintenance, the addition of new nodes to the BUS or the tolerance to node failure. In cases of one node failure, the *Discovering Neighbours* process provides enough information to recover the LoRaBUS connection. The next sections will describe the protocol implemented by the LoRaBUS to create a robust and efficient approach.

3.1. Discovering Neighbours

When the nodes are initialised after powering on, or due to a reconfiguration process of the topology, the first stage involves self-definition and self-configuration of the linear communication BUS. This process, referred to as "Discovering Neighbours", is based on a methodology in which each node identifies its closest neighbouring nodes on the BUS, and also the correct direction for information flow to reach the *main node* and, consequently, the user's application.

The purpose of the "Discovering Neighbours" methodology is to construct the *nodelist* and the neighbours' table, as depicted in Figure 5. The *nodelist* is an array containing the identifiers of all *sensor nodes* comprising the BUS, sorted sequentially from the main node to the final node. The information stored in the *neighbours' table* of each node will be used both to establish communications between them and to prevent network cuts due to failures in nearby nodes. As can be seen in Figure 5, the table stores not only the nearest neighbour nodes, but also the following ones, so that each node has up to two nodes to maintain communication in the appropriate direction: towards the *main node* or towards the *end node*. This duplicity of neighbours introduces a certain degree of tolerance to node failures, which in outdoor environments can be due to a large number of situations. Figure 5 illustrates an example of a BUS with six nodes, where the *main node* is identified as "ID1" and the *final node* is labeled "ID6". In this network, if node "ID2" fails then node "ID3" could attempt communication with node "ID1" based on its neighbour table. If the node that fails is ID5 then node ID3 could communicate with node ID4 and it would be "ID4" that would be in charge of reaching node "ID6" as the *final node* of the BUS topology. Thus, in order to cut off the communication, two consecutive nodes would have to fail to function correctly and then the network would be cut off at that point without the capacity to continue sending messages. The detailed procedure for obtaining the *nodelist* is described in Section 3.1.1.

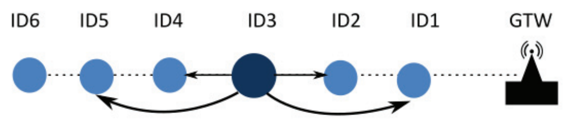

Node 3 neighbours' table:

ID	Tx_Power
2	Min power
4	Min power
1	Max power
5	Max power

Nodelist = ID1 ID2 ID3 ID4 ID5 ID6

Figure 5. Schematic example of the results obtained with the *Discovering Neighbours* process on a 6-node BUS network: *nodelist*, *neighbour's table* of node 3 and initial transmission power level.

On the other hand, each node in the BUS must discover and construct its neighbour's table. This table contains the identifiers of the four nearest nodes. For example, in Figure 5, the sensor node "ID3" will identify that its closest nodes are "ID2" and "ID4", while the next closest nodes are "ID1" and "ID5". In addition, the Discovering Neighbours methodology is designed to define the minimum power required to transmit data between each node, i.e., to determine the lowest possible energy needed for communication. Initially, the required transmission power will be set to the minimum capable by the transmitter for the closest nodes, and to the maximum power available for the next closest nodes. This initial configuration, as shown in the table in Figure 5, will be evaluated and adjusted during the normal operation of the BUS network to determine the optimal minimal transmission power requirements for each neighbouring node. The procedure designed to obtain the *final power requirements*, the *neighbour's table* and the *nodelist* will be explained in subsequent sections.

3.1.1. Obtaining the "Nodelist"

The process to obtain the *nodelist* in a certain LoRaBUS topology can be initiated every time the end user decides, for example, in cases in which new *sensor nodes* have been introduced, or due to a network-maintenance event (battery replacement, sensor repair or other actions). The methodology to obtain a new *nodelist* is initiated by the *main node* transmitting a CONFIG message. The payload of the CONFIG message is detailed in Table 1. It contains the level of the power transmission used to send this message (*tx_power*, the list of node identifiers of the current *nodelist* that the message has passed through and a checksum based on CRC16.

Table 1. Payloads of messages used in the *Discovering Neighbours* process.

Message Type	Payload
CONFIG	CONFIG + power_tx + id1 + id2 +. . . + idFinal + checksum
STOP	STOP + power_tx + *nodelist* + idSend + checksum

The first node that sends the CONFIG message is the *main node*. The message is transmitted using just the transmission power required to reach to the next node in the topology. After that, whenever the next node receives a CONFIG message, it will check if its identifier (idx) is already included in the payload of the message. If not, it will add its identifier *idx* at the end of the list, recalculate the checksum and resend the message using the lowest transmitting power available at the transmitter. On the other hand, if a node receives a CONFIG message with its *idx* included, the node should consider the message as a confirmation that a previous sent message has been received correctly by the next node so, when it happens, the node stops retransmitting the message again. With this procedure, we reduce the duplicity of the messages in both directions of the BUS because we suppose that there will be a minimum level of power transmission which allows a node to communicate with its nearest neighbour without reaching the next closest neighbour in the BUS due to the increment in the distance between consecutive nodes. When the CONFIG message is received by the *final node*, this node will determine the complete *nodelist* by selecting the message that contains the largest number of identifiers in the *nodelist*.

Finally, with the final *nodelist* at the *final node*, a STOP message (see Table 1) is sent from the *final node* to the *main node*. In this case, the information about who is sending this message is appended at the end of the message (*idSend* in Table 1). When a *sensor node* receives an STOP message, firstly, it stores the final *nodelist*. Next, it checks who is the sender to determine if the message originated from the previous node in the *nodelist*. If so, the message must be forwarded to the next nearest *sensor node* in the direction of the *main node*. Otherwise, the message retransmission is not necessary, and it should be considered as the confirmation reception of a previous STOP message which comes from a *sensor node* nearest to the *main node*. In this case, the *sensor node* completes its configuration process and remains listening to the BUS.

Finally, when the STOP message arrives at the *main node*, all the *sensor nodes* in the BUS will continue listening the BUS, and the *nodelist* is completed and fully propagated to all nodes.

3.1.2. Obtaining the Neighbour's Table

Afterwards the *nodelist* is known for all nodes, the *Discovering Neighbours* process continues at each *sensor node* with the extraction of their nearest neighbours. Each *sensor node* creates the *neighbour's table* with the closest and next closest nodes (four nodes at each *sensor node*). Up to four neighbours instead of just the two nearest neighbours were included to serve as a backup to automatically resolve communication conflicts, or BUS topology outages (e.g., in cases of failures of the nearest nodes). Therefore, each *sensor node* will be able to communicate with two neighbours in each direction of the BUS topology, see Figure 5. Only the two *sensor nodes* nearest to the BUS ends reduce the number of nodes included in the *neighbour's table*.

The *neighbour's table* is completed, initially, with the minimum transmission power observed during transmissions in the *Discovering Neighbours process*. This minimum transmission power is obtained from the payload of CONFIG and STOP messages, see details in Table 1. With the objective of improving the energy efficiency of the LoRaBUS network, the transmission power is optimised at each node to the minimum necessary to send messages to all nodes included in the *neighbour's table*. This process is performed by one *sensor node* at a time while the rest of the nodes are only listening to the medium. The access to the medium to transmit is self-arbitrated by *sensor* nodes to reduce the interferences and retransmissions between nodes sharing the BUS.

The power of each node in the *neighbour's table* is estimated using the procedure shown in Figure 6. The channel between nodes is tested using the specific *DISCOVERY* message (see Table 2). If the node receives a *HELLO* message with the correct *neighbour node* ID value then the level of transmission power used to send the *DISCOVERY* message is stored in the *neighbour's table* confirming that messages reach the neighbour node using this minimum power level. At the end of this process, the final transmission power for each node in the table will be between the minimum transmission power used during the *"nodelist process"* and the maximum transmission power available at the *sensor node*. If after a timeout period, any correct *HELLO* message is received, then the *sensor node* will increase the transmission power level used in the previous *DISCOVERY* message and it will repeat the evaluation for all nodes in the *neighbour's table* with still no response. The process finishes when the table is completed and the minimum transmission power is established for all nodes. The first node that will start the neighbour's table will always be the *final node* after receiving the response message from the next node to the *STOP* message. This is because the *final node* is the first node which will send the *STOP* message to the rest of the nodes in the BUS, highlighting that *nodelist* is completed. The process (detailed in Figure 6) uses the *DISCOVER* messages to send from the *sensor node* that is discovering its table, while *HELLO* messages are the answers from its neighbour nodes. In both message types, the nodes include the power-transmission level used to send the message and, therefore, the receiver can store the level used by the other node.

When the node that is searching for neighbouring nodes and the minimum power requirements, has finished and completed the table, it must then send a final transmission using the *DISCOVER_NEXT* message. This special message defines the next node in the BUS that will start the process to complete its own *neighbour's table*. The next node is defined following the *nodelist* from the *final node* to the *main node*. Therefore, the last node in completing the *neighbour's table* will be the *main node*. If the next *sensor node* does not send its *DISCOVER* message after a timeout, the *DISCOVER_NEXT* message is resent to the next node. If the resend fails again, the *DISCOVER_NEXT* message is sent to the second nearest node, considering that the closest neighbour node is not working properly. This fail condition is reported to the *main node* for maintenance purposes. Finally, when all nodes have defined their own *neighbour's table* the *main node* will send the *DISCOVER_END* message which will be re-transmitted to all nodes in the BUS, finishing the *Discovering Neighbours* process with the LoRaBUS configured for data communications between *sensor* nodes.

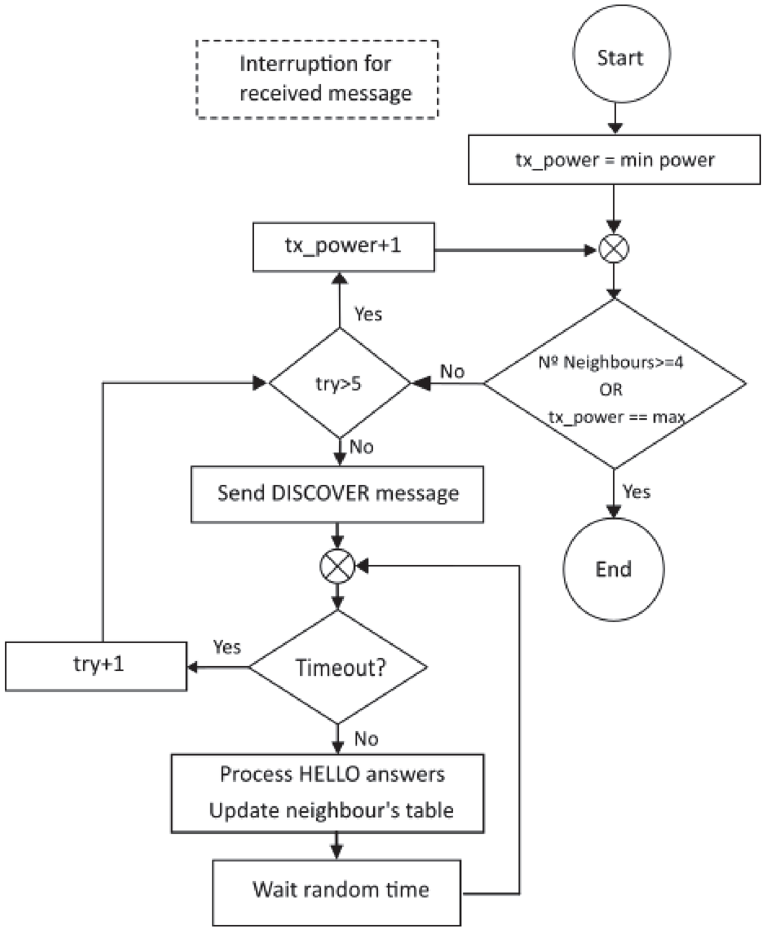

Figure 6. Procedure followed to complete the neighbour's table with minimum transmission power for each node.

Table 2. Payloads of messages used in the *neighbour's table* process.

Message Type	Payload
DISCOVER	DISCOVER + tx_power + *id* + checksum
DISCOVER_NEXT	DISCOVER_NEXT + tx_power + *id_next* + checksum
DISCOVER_END	DISCOVER_END + tx_power + *id* + checksum
HELLO	HELLO + tx_power + *id* + checksum

3.2. LoRaBUS Data Communication

The LoRaBUS configuration is proposed to create a hybrid communication protocol combining features from BUS and mesh topologies to be used in remote serial communication applications without the use of specific intermediate routers, coordinators or nodes along the line. As has been mentioned previously, the LoRaBUS is primarily proposed as an alternative for implementing a remote monitoring system near the high-voltage power lines along long distances without communication coverage. For this reason, the proposed communication protocol includes different transmission modes (stable or alarm) depending on the data value and the situation context. Therefore, the LoRaBUS approach can communicate using either of the two possible modes. In fact, LoRaBUS could be considered as a mesh network during alarm mode, and a BUS topology with arbitration during stable mode.

In stable mode, the information will be sent by each node in the network like a remote monitoring system. The stable mode is a proactive mode in which messages are sent by nodes at regular intervals. BUS access and management, in this case, is performed by the *main node* through individual requests for BUS access. The arbitration methodology used to access to the BUS is based on a combination of the well-known *master–slave* organisation, and the *token–ring* arbitration. LoRaBUS defines the *main node* as the *master* of the BUS. This means that the main node has to decide which node is going to send its information during the stable period at regular intervals. This decision is managed using a *TOKEN* message described in Table 3 where *id_token* refers to the identifier of the node that has to receive the *token*, *id_from* is the node identifier of the sender of this message and *id_to* is the identifier of the addressed node. Each node receives the *TOKEN* message at regular internals depending on the availability of the network. The use of token arbitration reduces the number of messages to be retransmitted and reduces the energy consumption due to collisions between retransmitted messages.

On the other hand, in alarm mode, the *sensor node* will start sending *ALARM* messages which includes sensor-measurement data and node identifiers (see Table 3). This mode is a reactive mode in which the nodes analyse the sensor values and decide to create and send the message in reaction to an event in process. In this case, any alarm message received by a node will be retransmitted automatically stopping any individual request for BUS usage. When this kind of message is received by any other node in the network, it will put the receiver node into alarm mode, and the message will be retransmitted to ensure it reaches the *main node*. When the *ALARM* message arrives at the end user, it must then evaluate the situation and decide whether to ignore the alert or notify emergency services. This person can also deactivate the alarm mode, allowing all nodes to return to stable operation. In *ALARM* mode, the LoRaBUS approach could be considered a mesh topology with reduced number of operations in the nodes. The message is not transmitted to all nodes in the line and is only transmitted to the nodes that allow one to reach the *main node*.

In order to achieve maximum power efficiency, the first node that will send its monitored information will be the furthest one from the gateway. This means that the final node will be the first one in sending its data to the server so it will be the first one that will receive the *TOKEN*. Following this strategy, each node in the BUS can be in a low power-consumption mode, with the function called *Deep Sleep*, a time proportional to the number of nodes which are in front of it. This provides a reliable guarantee for the long-term operation of the system.

Table 3. Payloads of messages used in the *LoRaBUS* for data transmission.

Message Type	Payload
TOKEN	TOKEN + *id_token* + *id_from* + *id_to* + checksum
ALARM	ALARM + *id_from* + *sensor_data* + checksum
INFO	INFO + *id_from* + *id_to* + *sensor_data* + checksum

After the reception of the *TOKEN*, the monitored data will be transmitted by the sensor node with a message of type *INFO* which includes the identifiers of the owner of those data, and the addressed node obtained from the *nodelist*. Usually the destination node will be the *main node*, but the proposal is able to allow transmissions between nodes too. The total length of the data field is considered in this work to be equal to 20 bytes, enough to include the data collected from the sensors connected to the node. The power-transmission level that will use any node would be, initially, the value saved in the neighbour's table. Even so, if the transmitter does not detect the *INFO* message from the next node, the node will try a new transmission, increasing the transmission power level. After three failed transmissions, the node which has the token will send its information to the next neighbour available in the *neighbour's table*, considering that the previous node was out of service.

4. System Test and Analysis

A proof of concept implementation was developed using one *gateway*, one *main node* and three *sensor* nodes. The last node in the BUS will work as the *final node*. All nodes and elements of the LoRaBUS network were implemented with the same transmitter equipment consisting of a Pycom LoPy 4 [16] (Pycom Ltd., Eindhoven, The Netherlands). This device is equipped with the ESP32 dual-core processor, and incorporates connectivity circuitry for WiFi, BLE and LoRa/Sigfox technology. The LoRa transmitter is built on Semtech's SX1276 circuitry incorporating the full LoRaWAN protocol stack and capabilities to create both Class A and Class C devices. It has a 4 MB RAM capacity and is programmed using the MicroPython language.

The sensor nodes are the most critical part of the system in terms of power requirements because they are supposed to be distributed in a remote and non-controlled area so that they would have to be powered with batteries and/or solar panels. This implies assuring an efficient management of the power consumption. In addition, the *Sensor* nodes were designed to calculate some fire indexes such as the Fire Weather Index (FWI) [17]. Therefore, the sensors considered include the SEN0114 (soil moisture) (LONG WHALE FASHION UK Ltd., Kington, UK), the HPMA115S0 (particle sensor) (Honeywell International Inc., Charlotte, NC, USA), the AMG8833 (tiny thermal camera) (Adafruit Industries, LLC, New York, NY, USA), the HTU21D (temperature and humidity) (TE Connectivity Corporation, Carlsbad, CA, USA) the and BMP085 (pressure and temperature) (Adafruit Industries, LLC, New York, NY, USA). Of course, other sensors could be considered depending on the final application.

The rest of the system approach was implemented to validate not only the BUS topology, but also the connection with the end user is a realistic context. Therefore, the *main node* connects to the *gateway* using the LoRaWAN protocol. Finally, the *gateway* is registered in the Network Server TTN platform and all messages sent and received from the BUS nodes are transmitted to the Node_Red App as the final application, where the sensor data can be displayed in the user-friendly platform. The measurements can be represented in graphs, levels and warning pop-up indicators so an end user can easily interpret the data efficiently. The sensor data are visualised using the app implemented using TTN and Node_Red tools and presented in Figure 7.

Figure 7. Data screen implemented on Node_Red where *sensor* node information can be reviewed.

This complete approach was used to analyse and evaluate the LoRaBUS approach considering its power requirements, the link quality and its performance in different scenarios.

4.1. Sensor Node Power-Consumption Requirements

The power consumption of a *sensor* node was measured during different stages of its workflow. The experimental results show that the highest current consumption corresponds to the LoRa transmission with a value of 160 mA. The transmission was performed with frequency = 868 MHz, tx-power = 2 dBm, bandwidth = 125 KHz, spread factor (SF) = 7 and coding rate (CR) = 4/5. In contrast, when the LoRa transceiver was turned off and CPU was in Deep Sleep mode, the consumption dropped to 7 mA. Due to a couple of issues with the LoPy design, reported by the manufacturer in [16], the CPU module draws more current than it should while in Deep Sleep. In any case, as was expected, consumption results presented in Table 4 demonstrate that the transmission task is one of the most energy-wasting processes in the entire workflow of a *sensor* node.

In contrast, when analysing the total time allocated to each task, it becomes evident that the sensor node spends most of its time idle in Deep Sleep mode (refer to the *Time* column in Table 4). Consequently, the energy consumption over a complete node cycle must consider the time dedicated to each task. Although the LoRa transmission task exhibits the highest energy consumption per unit time, the duration of this task is very short. As a result, the *Consumption* column in Table 4 shows that the energy consumption attributed to transmission is negligible compared to the energy consumed during the node's standby periods.

These results highlight the importance of optimising both the choice of sensor devices and the CPU, particularly concerning their idle (particularly, the Deep Sleep mode) power consumption. Reducing idle power consumption is critical to significantly lowering the overall energy requirements, especially given the operational cycle anticipated for these remote monitoring systems.

An important parameter to adjust when sending a message is the transmission power level. In order to evaluate its impact on power consumption, two sensor nodes were placed 5 m apart, and the same message was transmitted while gradually increasing the transmission power level from 2 dBm (minimum) to 14 dBm (maximum). The results, shown in Figure 8, indicate that reducing the transmission power level to the minimum can decrease power consumption by 50 mA (a reduction of 25%). This behaviour is aligned with the reported work in [18], where similar IoT transmitters were evaluated reporting exponential dependence between the power consumption and the transmission power level used to send messages.

Table 4. Summary of energy consumption of a node during transmission operation.

Mode	Current (mA)	Time (s)	Consumption (mAh)
raw-LoRa Transmitt	160	0.1150	0.0051
Idle	140	5	0.194
To read sensors	140	5.3	0.21
Deep Sleep	7	300	0.58
Cycle	-	310.415	0.9891

Deep Sleep mode was evaluated and tested in the proposed implementation, although the hardware used is not suitable for long periods of sleep. As for the synchronisation process between nodes, the implementation described is designed to establish long periods of communication inactivity. Therefore, it is expected that the Deep Sleep mode will be useful to maintain battery life as long as possible. The nodes in Deep Sleep mode will be synchronised by defining a similar Deep Sleep period for all nodes, and when they regain activity, a full cycle of *stable mode* will be required for success; thus, the nodes will be online until the *end node* sends its *INFO* message. After the last *INFO* message and if no *ALARM* message is received, all sensor nodes will return to Deep Sleep mode until the next period of activity. This methodology synchronises all nodes with the transmission of the last *INFO* message from *final node*.

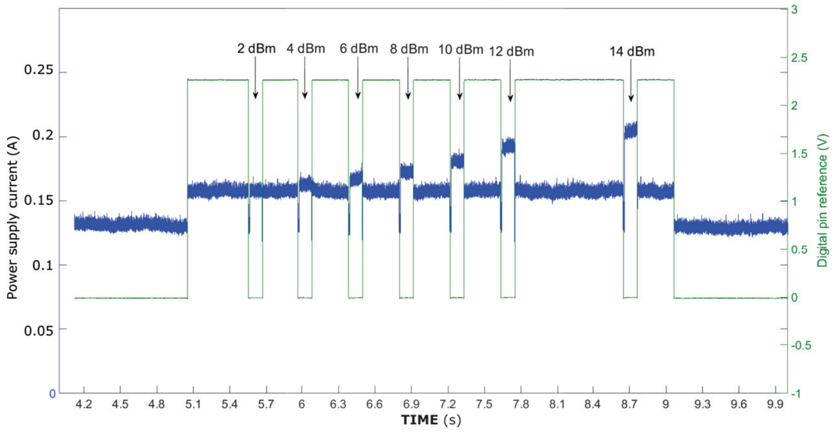

Figure 8. Consumption of a node with different LoRa power transmission levels.

Taking into account that the hardware used was not specifically selected for low power consumption, as the data show in Table 4, the length of time that the node will be operational will depend on the time it takes for the battery to be consumed based on its nominal level of available charge. Therefore, the node lifetime is estimated considering a battery with a capacity of 2000 mAh. The lifetime would be 2022 cycles = 7.27 days, assuming one transmission with x_power of 2 dBm every 5 min. It must be noted that the hardware used to prototype the nodes was not specifically designed for long periods of Deep Sleep function. In the current implementation, the use of renewable power sources such as solar panels is mandatory.

4.2. Node Communication Quality

The quality and reliability of the LoRa-based communications were also evaluated using the implemented prototype. Because the communication links use two types of

LoRa-based protocols, firstly, the LoRaWAN communication between the *main node* and the *gateway* is tested and afterwards the coverage between *sensor nodes* using LoRaBUS, followed by a performance test of the proposed protocol.

The main goal of the LoRaWAN test was to evaluate three characteristic parameters of the communications, observing the influence of physical and electromagnetic interference on the communication link between the *main node* and the *gateway*. The metrics used in this test are as follows: Packet Delivery Ratio (PDR), Signal-to-Noise Ratio (SNR) and Received Signal Strength Indication (RSSI). The obstacles of this test were implemented by increasing the distance and building elements between the nodes that were continuously trying to communicate up to 300 messages every 5 min with a *payload* of 22 bytes (frequency = 868 MHZ, bandwidth = 125 kHz, SF = 7, CR = 4/5). With this configuration, the receiver has a typical sensitivity of −123 dBm. Overall, three different scenarios were evaluated:

- Scenario 5 m: This represents direct communication over a 5 m distance with no obstacles. The test was carried out in a laboratory on the first floor of the University of the Balearic Islands.
- Scenario 7 m: In this scenario, the two nodes were placed in separate rooms with a single wall between them.
- Scenario 20 m: This was the most complex scenario, where one node was placed 20 m away, separated by three walls and an aisle.

The RSSI results are presented in Figure 9 considering all scenarios. The x-axis is the number of messages sent from the transmitter, while the y-axis is the RSSI value expressed in dBm.

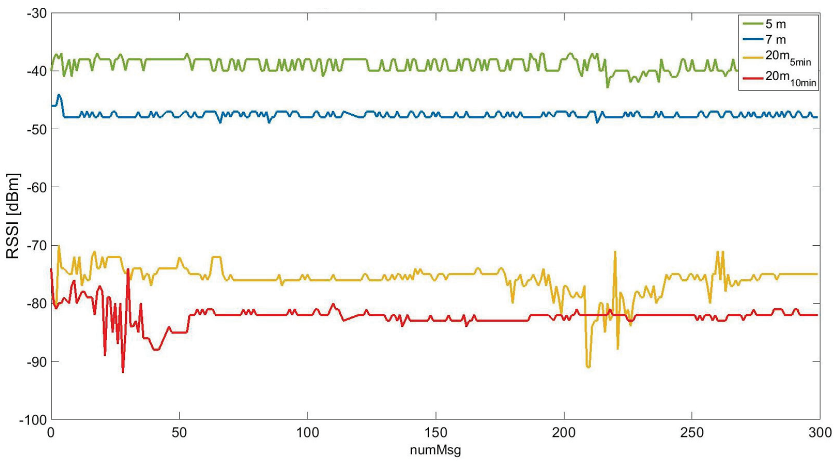

Figure 9. Received Signal Strength Indication (RSSI) with different distances between nodes. RSSI axis range is [−30, −100] dBm.

These results are coherent because when the signal propagation and received signal parameters in scenario 5 m are stronger, the RSSI is greatest (around −37 dBm). In contrast, when some obstacles are added between the nodes, the RSSI goes down to lower values below −75 dBm. Additionally to the three scenarios considered, for the scenario 20 m the time between message transmission was increased, from 5 min to 10 min. This change had as its aim exploring the impact of TTN servers on the message-processing cue. In Figure 9, the increase in time between messages during the test is observed in the RSSI values as a light reduction, explainable by a reduction in the transmission power level used by the transmitter node due to the presence of less noise in the wireless channel.

The LoRaWAN protocol automatically adjusts the power transmission needed to ensure a stable value for the SNR parameter. Again, this behaviour is the main reason explaining the low differences between scenarios reported in Figure 10 in line with the RSSI results. Most messages were received with an SNR of 6 dB, which is considered acceptable for LoRa-based communications [19].

The methodology then analyses the PDR values using the gateway to send all the messages received from the *main node* to the network server (based on the TTN platform), and then the network server sends them to the NodeRed environment, which stores all the received data. As can be seen in Table 5, the PDR value computed by sending messages every 5 min was not as high as expected, but this values cannot be explained only due to the poor quality of the communication channel because the other parameters reported satisfactory behaviour. In order to understand these results, a review of the temporary uses of the communications space was carried out to verify compliance with the recommendations for the use of the LoRa channel. In this sense, the experiment was designed to achieve a Time on Air (ToA) of 0.0566 s per message, and the transmissions were carried out at a frequency of 868 MHz every 5 min so the duty cycle was 0.02%. This means that the experiment complies with the ETSI duty cycle (<1%) [20], and the TTN Fair Use Policy (maximum uplink airtime of 30 s per day) [14]. Even so, the scenario 20 m was repeated with an interval time between messages of 10 min; as a result, the PDR obtained was 97%. Clearly, the total message received is directly related to the TTN workload.

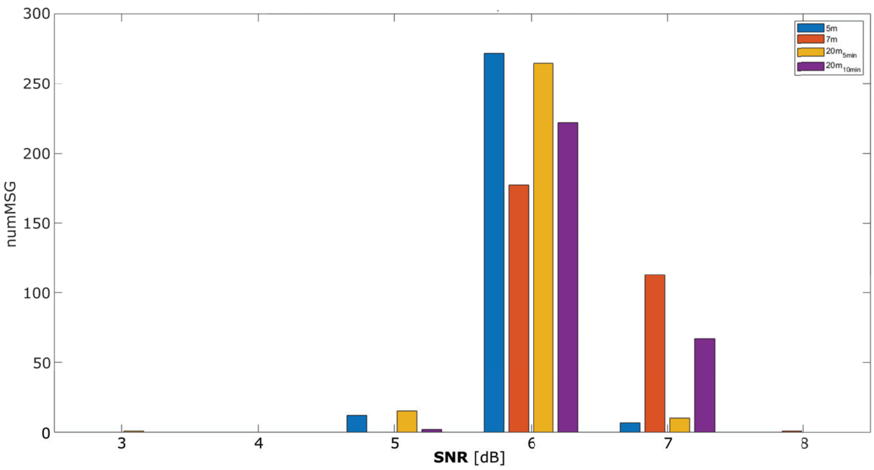

Figure 10. SNR for the different test scenarios. On the x-axis, we find the SNR values within the range [+3, +8] dB. On the y-axis, we find the number of messages received with each corresponding SNR value.

Table 5. Packet delivery ratio in indoor environment.

Distance (m)	Messages Sent	Messages Received	PDR (%)
5	300	231	77
7	300	230	76.67
20	300	239	79.6
20 (10 min)	300	291	97

The obtained results can be compared with the study in [21], which involved indoor experiments conducted in a nine-story building at the National Research University. According to this study, for a one-floor distance (@868 MHz, SF = 7), the average RSSI was −77.83 dBm, the SNR was 9.55 dB and the PDR was 99.8%.

4.3. Point-to-Point Communication

In order to evaluate the feasibility of the raw-LoRa connection in a non-controlled scenario, a *sensor node* (station) was placed in an urban area near Binissalem, a village of Mallorca (Spain), while another *sensor node* (rover) was located at different places and distances. The station node was activated to constantly transmit messages every 5 min at 14 dBm using raw-LoRa. The payload of the message was formed by an increasing counter to measure how many consecutive messages could be received at the rover node location. Figure 11 shows the position of the station node (blue point) and the different places for the rover node. The initial rover position was in another city (Inca), 7 km away from the station node.

The rover node moved from the initial point to places closer to the station node. In each location, the rover node was left 30 min to receive messages from the station node. Considering the number of consecutive messages received, the different positions were classified into three types: good quality (green), limited coverage (yellow) and out of coverage (red). From results reported in Figure 11, the distance raw_LoRa communication between nodes can be considered acceptable in the range of 1 and 2.5 km, considering urban environments and the specific hardware selected. This result aligns closely with the analysis presented in [12] by X. Zhang et al., where the authors concluded that the point-to-point communication range of LoRa is around 1km under complex environmental conditions.

Figure 11. Experimental coverage test in an urban area, performed between Inca and Binissalem (Mallorca, Spain).

4.4. LoRaBUS Performance Analysis

Finally, the LoRaBUS proposal was tested by means of a performance analysis that included the evaluation of the duration of node-management periods, the auto-configuration of node discovery and transmission power management, as well as the sending of messages from one end to the other of the created BUS topology network. In this performance test, three nodes were deployed on the rooftops of various buildings at the University of the Balearic Islands. The spatial distribution of these nodes is shown in Figure 12.

Once all nodes were installed in the designed location, the self-configuration stage was initialised assuming stable (no alarm) state. This process involves the Neighbour's Discovering stage described in Section 3, after which the main node queried the monitored data from the other nodes. Table 6 summarises the time increments, following the HH:MM:SS format, required by all nodes considering the initial time as the instant of time where the *main node* sends the first *CONFIG* message. These temporal references were extracted from all transmitted and received messages, stored on SD cards at each node.

Table 6. Most relevant timestamps of the workflow (timestamp format HH:MM:SS).

Instant Description	Main Node Node	Sensor Node	Final Node
Installing and placing the node	00:00:00	00:00:00	00:00:00
Sending the first CONFIG msg	00:02:01	00:02:13	00:02:15
Receiving the first CONFIG msg	00:02:14	00:02:07	00:02:13
Obtaining the *nodelist*	00:03:12	00:03:11	00:03:10
Sending DISCOVER for the 1st time	00:05:56	00:05:31	00:05:17
Obtaining its neighbour's table	00:06:09	00:05:39	00:05:36

The main findings of the performance test are as follows:

- The *nodelist* was correctly generated in various configurations and locations. All BUS nodes successfully recognised which node identifier corresponds to the main, and final node, and also which nodes are its neighbours. Furthermore, in some locations, the *final node* directly received the *CONFIG* message from the *main node*. While this message could have been interpreted as the *nodelist*, the *final node* correctly waited for an alternative version and ultimately determined that the version forwarded by the *sensor node* was the correct one.
- The total time that elapsed from the moment the *main node* sent the initial *CONFIG* message to the point where all three nodes had established the *nodelist* was approximately 1 min and 10 s (from 00:02:01 to 00:03:12).
- The *neighbours' table* of the *main node* and the *sensor node* included the identifiers of the other two nodes. Additionally, the *final node* correctly registered the identifier of the *sensor node*.
- The time required to construct the *neighbours' table* was approximately 8 s per node, resulting in a total process duration of approximately 14 s.
- Following the configuration phase, the *main node* initiated a request for monitored data from the *final node* by sending a *TOKEN* message. The *sensor node* received this message and forwarded it to the *final node*. In response, the *final node* transmitted the monitored sensor data back to the *main node*, completing the process in 46 s. All communications during this phase were conducted using the minimum transmission power level.
- Finally, the *main node* sent a *TOKEN* to the *sensor node*, and the response was received in 17 s. The total time required to collect data from both nodes was approximately 64 s.

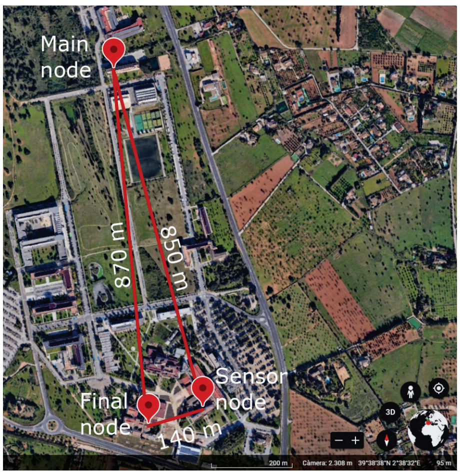

Figure 12. Map example of different locations used for the network operation test in the campus.

5. Conclusions

In this work, we presented a linear, LoRa-based Wireless Sensor Network approach (LoRaBUS) designed for monitoring transmission power lines. This network aims to provide a reliable communication system for electrical companies to monitor variables of interest, such as weather conditions and early forest fire detection.

Related works in the literature include the study cited in [9], where the authors propose a sensor network for monitoring overhead transmission line sag and temperature. However, their approach utilises a LoRa-Mesh topology, requiring a gateway with GSM/LTE connectivity every 4 km. The proposed LoRaBUS approach requires only one gateway on one side of the BUS, while the last node acts as a BUS termination. In the same sense, the proposed LoRaBUS system was focused on overhead transmission lines which often follow linear paths in remote areas where conventional communication technologies may not be reliable. Additionally, these infrastructures are often difficult to access, necessitating a system that is autonomous in terms of operation, maintenance and power supply. Experimental evaluations of the LoRa communication demonstrated that, with the selected hardware, sensor nodes can be spaced up to 2.5 km apart in suburban areas. However, this distance is highly dependent on the presence of obstacles between nodes. Furthermore, the network prototype was used to assess the performance of the communication protocol.

The results show that LoRaBUS creates a self-configurable linear topology that is advantageous for node-installation processes, node maintenance and node fault location. The discovery process collects data from the neighbourhood to build the network and save energy. Each node has enough information to be fault tolerant to nearby nodes and can reconfigure the BUS topology by introducing changes in transmission parameters (increasing transmission powers). The autonomous network configuration can be completed in approximately 2 min. In addition, energy consumption is effectively reduced by 25% by dynamically adjusting the transmission power based on the detected channel quality and the distance to the nearest neighbour nodes.

Future work will involve studying the impact of distribution power lines on LoRa communication, exploring other relevant low-power hardware prototypes to enhance LoRaBUS autonomy, and evaluating the benefits of small solar panels with respect to sustaining the system's energy requirements.

Author Contributions: Conceptualisation, M.P. and B.A.-L.; methodology, M.P. and B.A.-L.; software, M.P.; validation, M.P. and B.A.-L.; formal analysis, B.A.-L. and E.I.; investigation, M.P.; resources, B.A.-L.; data curation, M.P. and B.A.-L.; writing—original draft preparation, B.A.-L.; writing—review and editing, B.A.-L. and E.I.; visualisation, M.P. and B.A.-L.; supervision, B.A.-L. and E.I.; funding acquisition, E.I. All authors have read and agreed to the published version of the manuscript.

Funding: This research was partially funded by the *Cátedra Endesa Red de Innovación Energética de la UIB*.

Data Availability Statement: The original contributions presented in this study are included in the article. Further inquiries can be directed to the corresponding author(s).

Acknowledgments: The authors would like to thank to the University of the Balearic Island and the IOTIB Laboratory for supporting this work.

Conflicts of Interest: The authors declare no conflicts of interest. The funders had no role in the design of the study; in the collection, analyses or interpretation of data; in the writing of the manuscript; or in the decision to publish the results.

References

1. Dong, Z.; Cao, F.; Xiong, N.; Dong, P. EE-MPTCP: An Energy-Efficient Multipath TCP Scheduler for IoT-Based Power Grid Monitoring Systems. *Electronics* **2022**, *11*, 3104. [CrossRef]
2. Petrariu, A.I.; Coca, E.; Lavric, A. Large-Scale Internet of Things Multi-Sensor Measurement Node for Smart Grid Enhancement. *Sensors* **2021**, *21*, 8093. [CrossRef] [PubMed]
3. Yilmaz, S.; Dener, M. Security with Wireless Sensor Networks in Smart Grids: A Review. *Symmetry* **2024**, *16*, 1295. [CrossRef]
4. Jain, U.; Hussain, M. Securing Wireless Sensors in Military Applications through Resilient Authentication Mechanism. *Procedia Comput. Sci.* **2020**, *171*, 719–728. [CrossRef]
5. Arshad, B.; Ogie, R.; Barthelemy, J.; Pradhan, B.; Verstaevel, N.; Perez, P. Computer Vision and IoT-Based Sensors in Flood Monitoring and Mapping: A Systematic Review. *Sensors* **2019**, *19*, 5012. [CrossRef] [PubMed]
6. Vo, D.-K.; Trinh, K.T.L. Advances in Wearable Biosensors for Healthcare: Current Trends, Applications, and Future Perspectives. *Biosensors* **2024**, *14*, 560. [CrossRef] [PubMed]
7. Barsocchi, P.; Calabrò, A.; Ferro, E.; Gennaro, C.; Marchetti, E.; Vairo, C. Boosting a Low-Cost Smart Home Environment with Usage and Access Control Rules. *Sensors* **2018**, *18*, 1886. [CrossRef] [PubMed]
8. Popescu, D.; Stoican, F.; Stamatescu, G.; Ichim, L.; Dragana, C. Advanced UAV–WSN System for Intelligent Monitoring in Precision Agriculture. *Sensors* **2020**, *20*, 817. [CrossRef] [PubMed]
9. Wydra, M.; Kubaczynski, P.; Mazur, K.; Ksiezopolski, B. Time-Aware Monitoring of Overhead Transmission Line Sag and Temperature with LoRa Communication. *Energies* **2019**, *12*, 505. [CrossRef]
10. Zeng, H.; Zuo, P.; Deng, F.; Zhang, P. Monitoring System of Transmission Line in Mountainous Area Based on LPWAN. *Energies* **2020**, *13*, 4898. [CrossRef]
11. Sundaraman, J.; Du, W.; Zhao, Z. A Survey on LoRa Networking: Research Problems, Current Solutions, and Open Issues. *IEEE Commun. Surv. Tutorials* **2020**, *22*, 371–387. [CrossRef]
12. Zhang, X.; Zhang, M.; Meng, F.; Qiao, Y.; Xu, S.; Hour, S. A Low-Power Wide-Area Network Information Monitoring System by Combining NB-IoT and LoRa. *IEEE Internet Things J.* **2019**, *6*, 590–598. [CrossRef]
13. Ergen, S.C. *ZigBee/IEEE 802.15. 4 Summary*; UC Berkeley: Berkeley, CA, USA, 2004; Volume 10, p. 11.
14. The Things Industries. *TTN Documentation: Maximum Duty Cycle;* The Things Industries: Amsterdam, The Netherlands, 2024.
15. Alliance, L. *Lorawan Specification*; LoRa Alliance: Fremont, CA, USA, 2015; pp. 1–82.
16. Pycom Product Info & Datasheets. LoPy4 Datasheet. Available online: https://docs.pycom.io/gitbook/assets/specsheets/Pycom_002_Specsheets_LoPy4_v2.pdf (accessed on 23 February 2025).
17. Novo, A.; Fariñas-Álvarez, N.; Martínez-Sánchez, J.; González-Jorge, H.; Fernáández-Alonso, J.M.; Lorenzo, H. Mapping Forest Fire Risk—A Case Study in Galicia (Spain). *Remote Sens.* **2020**, *12*, 3705. [CrossRef]
18. Rodriguez-Navas, G.; Ribot, M.A.; Alorda, B. Understanding the Role of Transmission Power in Component-Based Architectures for Adaptive WSN. In Proceedings of the 2012 IEEE 36th Annual Computer Software and Applications Conference Workshops, Izmir, Turkey, 16–20 July 2012; pp. 520–525. [CrossRef]
19. Mobilefish. *LoRa/LoRaWAN Tutorial 10: RSSI and SNR*; Mobilefish: Zaandam, The Netherlands, 2023.
20. European Telecommunications Standard Institute. *Final Draft ETSI EN 300 220-2 V3.2.1. 33*; ETSI: Sophia Antipolis, France, 2018.
21. Bobkov, I.; Rolich, A.; Denisova, M.; Voskov, L. Study of LoRa Performance at 433 MHz and 868 MHz Bands Inside a Multistory Building. In Proceedings of the 2020 Moscow Workshop on Electronic and Networking Technologies (MWENT), Moscow, Russia, 11–13 March 2020; pp. 1–6. [CrossRef]

sensors

MDPI

Article

Performance Evaluation of a Mesh-Topology LoRa Network

Thomas Gerhardus Durand [1,†] and Marthinus Johannes Booysen [1,2,*,†]

[1] Department of Electrical and Electronic Engineering, Stellenbosch University, Stellenbosch 7600, South Africa; 17554497@sun.ac.za
[2] Department of Industrial Engineering, Stellenbosch University, Stellenbosch 7600, South Africa
* Correspondence: mjbooysen@sun.ac.za
† These authors contributed equally to this work.

Abstract: Research into, and the usage of, Low-Power Wide-Area Networks (LPWANs) has increased significantly to support the ever-expanding requirements set by IoT applications. Specifically, the usage of Long-Range Wide-Area Networks (LoRaWANs) has increased, due to the LPWAN's robust physical layer, Long-Range (LoRa), modulation scheme, which enables scalable, low-power consumption, long-range communication to IoT devices. The LoRaWAN Medium Access Control (MAC) protocol is currently limited to only support single-hop communication. This limits the coverage of a single gateway and increases the power consumption of devices which are located at the edge of a gateway's coverage range. There is currently no standardised and commercialised multi-hop LoRa-based network, and the field is experiencing ongoing research. In this work, we propose a complementary network to LoRaWAN, which integrates mesh networking. An ns-3 simulation model has been developed, and the proposed LoRaMesh network is simulated for a varying number of scenarios. This research focuses on the design decisions needed to design a LoRa-based mesh network which maintains the low-power consumption advantages that LoRaWAN offers while ensuring that data packets are routed successfully to the gateway. The results highlighted a significant increase in the packet delivery ratio in nodes located far from a centralised gateway in a dense network. Nodes located further than 5.8 km from a gateway's packet delivery ratio were increased from an average of 40.2% to 73.78%. The findings in this article validate the concept of a mesh-type LPWAN network based on the LoRa physical layer and highlight the potential for future optimisation.

Keywords: LoRa; LoRaWAN; IoT; network; mesh; multi-hop; sensor networks; LPWAN; ns-3

1. Introduction

There is a worldwide industry trend towards Industry 4.0, smart-cities, smart- agriculture, and a connected future. The main goals are to reduce operational costs by optimising resource consumption, reducing waste, and automating processes through the use of a network of intelligent sensors and actuators in the Internet of Things (IoT) and Machine to Machine (M2M) networks. To achieve this vision, Low Power Wide-Area Networks (LPWANs) have allowed nodes that require ultra-low power consumption, low data throughput, low-cost, and deep coverage to be deployed in a variety of applications.

Amongst the various types of IoT-network, the IoT industry worldwide has taken a keen interest in Long-Range Wide-Area Networks (LoRaWANs) due to the LPWAN's robust physical layer LoRa modulation scheme. LoRaWAN [1] appears particularly suitable for research applications due to (i) the open protocol, (ii) the availability and low cost of hardware components, and (iii) the possibility of establishing small, stand-alone private networks on unlicensed Industrial, Scientific, and Medical (ISM) frequency bands (US: 902–928 MHz, EU: 863–870 MHz). LoRaWAN is a protocol that defines the data-link and network layer in the Open System Interconnection (OSI) model. The main advantages of LoRa are the low cost of transceivers and gateways, the low power consumption and high link budget of transceivers, and the ease of deployment attributable to the licence-free sub-GHz ISM frequency bands usage of LoRa.

In a typical LoRaWAN, specified in [2], nodes transmit messages based on a pure-Aloha Medium Access Control (MAC) protocol, followed by opening two reception slots to receive acknowledge messages from the gateway (if an acknowledgement was requested by the node), or possibly down-link messages. In this up-link-centric network, with no collision avoidance, the network suffers from significant packet loss (or re-transmissions in the case of packet acknowledgement) in high-node-density networks.

In this paper, we propose a novel mesh-network based on the LoRa physical layer and compare it to a traditional LoRaWAN implementation. We have developed a simulation model in ns-3 that simulates the behaviour of the proposed mesh-network based on LoRa in an accurate way and use it to simulate comparable results to LoRaWAN.

2. Contributions

The primary contributions of the work in this publication are as follows:

- A novel rule-based LoRaWAN-derived LoRa mesh networking protocol to serve as a complimentary network technology to the industry standard LoRaWAN. This includes a proposal for a beacon frame flooding approach to integrate time synchronisation in the multi-hop network.
- An ns-3 model to simulate and compare a multi-hop LoRa network vs. a single-hop LoRaWAN.
- Improvements have been made to the standard LoRaWAN NS3 simulation model to improve the power consumption simulation model to support the modelling of various transmission power strengths.

3. LoRaWAN Overview

This section briefly introduces LoRaWAN and covers the LoRa physical layer, LoRa Channel Activity Detection, the LoRaWAN MAC layer, and adaptive data rate mechanisms implemented in LoRaWAN.

3.1. LoRa Physical Layer

LoRa modulation is Semtech's (Camarillo, CA, USA) proprietary Chirp Spread Spectrum (CSS) technology. Since the operational principles of LoRa modulation have been covered extensively in the literature [3–5], we will only focus on the influence of the transmission parameters on the effective bit rate of the modulation, its resistance to interference noise, power consumption, and its link-budget. The key transmission parameters that nodes can control are the transmission frequency channel (F_c), the bandwidth (BW), the spreading factor (SF), the coding rate (CR), and the transmission power (P_{Tx}).

LoRa transmissions can be modulated by selecting an SF between $SF7$ and $SF12$. An increment in the selected SF increments the receiver's sensitivity, thereby increasing the link-budget. However, this also increases the time-on-air (ToA) of a packet, which increases power consumption and collision probability and decreases the data rate and throughput of a node. LoRa transmissions using different SF's are semi-orthogonal to each other; thus, networks can utilise SF variation to increase its capacity.

The centre frequency (F_c) is the carrier frequency used to modulate LoRa packets. Packets sent between nodes and gateways can be spread out on different centre frequencies/frequency channels. Nodes need to adhere to the maximum transmit duty cycle relative to the sub-band used and local regulations. In [2], the LoRa Alliance, the non-profit association responsible for the LoRaWAN standard, specifies that LoRaWAN devices should select a frequency channel pseudo-randomly, increasing frequency diversity and thereby increasing the interference robustness.

BW specifies the range of frequencies around the F_c used for transmitting, thereby indirectly specifying the rate of change in the frequency of the chirp. A higher BW translates to a higher data rate and a lower receiver sensitivity (i.e., a lower link budget). LoRaWAN messages are typically transmitted with a BW of either 125 kHz or 250 kHz, depending on the selected datarate. Lastly, LoRa packets are transmitted at a specific CR, which specifies the Forward Error Correction (FEC) rate. Increasing the CR increases the packet size, and consequently increases the ToA. However, it also decreases the packet's susceptibility to burst noise, which decreased the Packet Error Ratio (PER) (percentage of transmitted messages incorrectly received by the receiver).

Selecting the correct transmission parameters is important, as the ToA impacts the node's throughput due to the duty cycle limitations implemented in the ISM band. In Europe, duty cycles are regulated by Section 4.3.3 of the ETSI EN300.220 standard [6]. This standard defines the following sub-bands and their prescribed duty cycles:

- 863.0–868.0 MHz: 1%
- 868.0–868.6 MHz: 1%
- 868.7–869.2 MHz: 0.1%
- 869.4–869.65 MHz: 10%
- 869.7–870.0 MHz: 1%

3.2. LoRa Channel Activity Detector

LoRa Channel Activity Detection (CAD) is a mechanism implemented in the LoRa transceiver to detect activity on the channel before transmission. LoRa CAD does not use the traditional Received Signal Strength Indicator (RSSI) approach of channel activity detection implemented in other transceivers, as LoRa transceivers can demodulate transmissions below the noise floor.

The LoRa CAD mechanism requests the transceiver to attempt to capture preamble symbols on a specified frequency and with specific SF/BW settings. The LoRA radio post-processes the received signal and checks for a correlation between the transceiver's captured data and an ideal preamble waveform [7]. This CAD method allows LoRa CAD to differentiate between random noise and a LoRa signal. If a preamble is detected, the transceiver will switch to Rx mode and receive the payload. The time (Rx_{time}), in seconds, that the LoRa radio receiver should be active can be calculated according to Equation (1) [8], with the SF, BW, and CR settings corresponding to the settings used to setup the CAD mechanism. It is also possible for the transceiver to detect the RSSI of the detected preamble message. LoRa CAD relies on detecting whether or not a preamble is currently being transmitted, and cannot detect channel activity when the payload of a message is being transmitted.

$$Rx_{time} = \frac{2^{SF} + 32}{BW} \tag{1}$$

The LoRa CAD mechanism is used as a key mechanism in the proposed LoRaWAN relay specification [9], which allows a relay node to periodically scan whether or not a child node requires a packet to be forwarded to a gateway. The proposed multi-hop network protocol in this research relies on Real-Time Clock (RTC) synchronisation in the network to ensure that relay nodes are in receive mode when a child node requires a packet to be forwarded.

3.3. LoRa and LoRaWAN MAC

The LoRaWAN topology consists of nodes, gateways, and a network server configured in a star-of-star network. Gateways have both a multi-channel LoRa transceiver, as well as some form of traditional IP-based (e.g., Fibre, LTE, 5G, etc.) interface. Figure 1 provides an overview of a LoRaWAN. Nodes utilise the LoRa physical layer to relay packets, while the gateways utilise a traditional IP-based back-end network to connect to the network server. The LoRaWAN gateways are designed to receive LoRa packets from a large number of nodes as they offer eight parallel demodulation paths for LoRa messages on different SFs and frequency channels.

Messages are relayed from the nodes, through the gateways to the network server. The network server is responsible for decoding packets sent by the nodes, generating the packets that should be sent back to the devices, and serving as an interface to the application and join server.

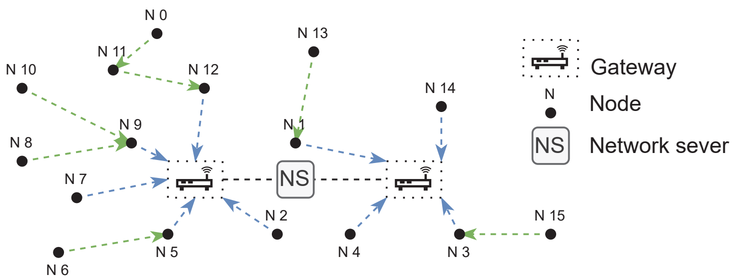

Figure 1. LoRaWAN topology.

Devices in a LoRaWAN adhere to a contention-based MAC protocol similar to a pure-Aloha MAC protocol. In [10], an up-link-only LoRaWAN is compared to the performance of a pure-Aloha network. The authors found that through the capture effect, the LoRaWAN outperformed a pure-Aloha network. The capture effect is a radio-level feature whereby, when two concurrently transmitting nodes are utilising the same medium, the node with the stronger received signal strength at the receiver's packet will be decoded successfully, and the lower signal strength packet will be detected as noise. The difference in received signal strength can be relatively small; however, when the difference is too small, the receiver will keep switching between the two signals. This translates in the receiver not being able to decode either transmission. As LoRa is a form of frequency modulation, it exhibits the capture effect. This effect allows the effective throughput of a network to be increased substantially, as not all packet collisions will result in packet loss.

Three classes of nodes are specified in the LoRaWAN standard [2]. Class A devices are typically implemented in most power-constraint up-link-focused nodes. This class offers bi-directional communication, where each up-link transmission by a node is followed by two short down-link receive windows. Class B nodes extend the functionality of Class A devices, with scheduled reception slots. Class C devices are continuously in reception mode, except when transmitting. Both Class B and C sacrifice power consumption for improved down-link latency.

To extend the above-mentioned Class A device type, various research articles [11–13] have proposed a slotted ALOHA MAC protocol to improve the performance of the network. The additional complication of time-slotted coordination provides additional challenges in LoRa nodes and renders the implementation impractical in some use cases where precision timekeeping is not possible. However, in most cases, nodes follow a periodic cycle, where nodes stay in Ultra-Low Power (ULP) mode until measurements are required, upon which a node samples a sensor and reports the data. In these types of applications, a Real-Time Clock (RTC) is typically available for precise time keeping, which would allow the use of slotted ALOHA. LoRaWAN gateways can receive accurate timings via an IP-based network; however, gateways embedded with a GPS module will provide the most accurate timing for slotted ALOHA. In a typical slotted ALOHA MAC protocol, the nodes rely on beacon frames sent by the gateway to synchronise the start of the current frame period, with n being the number of slots following the frame start [12].

The authors in [11] proposed a slotted ALOHA protocol, with periodic time- synchronisation based on the ACK message received in the down-link slot of an acknowledged up-link message. The proposed solution was implemented in the application layer, with no modification on either the node's gateway's, or network server's LoRaWAN stack. The maximum timing uncertainty measured for the unmodified LoRaWAN stack was 15 ms.

3.4. LoRaWAN Adaptive Data Rate

The LoRaWAN protocol offers an Adaptive Data Rate (ADR) mechanism, which allows optimisation of the power consumption, throughput, and performance of nodes in the network by adapting the transmission parameters of the devices. Several studies have been conducted that aim to improve the standard LoRaWAN ADR mechanism proposed by Semtech in [14].

The power consumption of a LoRa transmission is indirectly proportional to its BW and CR, and directly proportional to its selected SF, packet size, and transmission power. In a typical homogeneous network, the CR, BW, and packet size are kept fixed, similar to what is specified by LoRaWAN [2]. The energy required to transmit a packet will depend on the time-on-air (ToA) and the transmission power. Based on Equation (2), increasing the SF by one halves the data rate of a transmission (thereby doubling the ToA). Based on the information provided in [7], increasing the SF only increases the RF sensitivity of the receiver by between one and two dBm. The transmission power can be adapted between 0 and 14 dBm, which only increases the power consumption by a factor of 1.88. Therefore, due to the quadratic nature of the SF's effect on a packet's ToA, it is always preferred to adjust the transmission power up to the legally allowed limit, before considering increasing the SF.

$$DataRate = \frac{BW}{2^{SF}} \times CR \tag{2}$$

A LoRaWAN node can set the ADR bit in an up-link transmission, indicating to the network server that it is in a stable radio channel attenuation environment and is open to adapting its transmission parameters. The LoRaWAN will respond in a down-link message whether it is able to send ADR commands or not. The network server is now able to send ADR requests through MAC commands which form part of the LoRaWAN frame, to which nodes will respond to in future up-link-frames with MAC commands which contain link-adaptive data-rate answers. Nodes are free to disable ADR control at any time if they detect or anticipate unstable/worse radio channel attenuation conditions.

Research in the field of ADR mechanisms is extensive and includes topics such as enhanced ADR for LoRaWANs with mobility [15] and extending the performance of LoRa by suitable spreading factor allocation [16]. Implementing an optimised ADR mechanism is beyond the scope of this research article; thus, we used the industry standard rule-based LoRaWAN ADR mechanism proposed in [14].

4. Current Research

Several recent research publications have suggested LoRa-based multi-hop routing topologies for LPWAN applications to further extend the capabilities of these networks. They typically focus on improving aspects such as power consumption, coverage, and scalability. This section only covers a small overview of the current research in the field of multi-hop LoRa; however, a more comprehensive overview of the current research can be found in [17]. Furthermore, the authors in [18] provide an overview of the latest studies, based on four main categories: energy-awareness, concurrent access and duty-cycle regulations, routing protocol, and security.

"LoRa for the Internet of Things" [12] was the first published research paper to propose a multi-hop LoRa network. The authors proposed LoRaBlink, which was designed for reliable and energy-efficient multi-hop LPWAN communication. In this study, devices transmitted up-link packets in a staggered, slotted pattern to minimise power consumption and packet collisions. A flooding approach was used to organise the network routing. Six nodes and a gateway were deployed in an urban environment, and a packet delivery ratio of 80% was measured throughout the test. This was an improvement over a standard LoRaWAN, as some of the nodes were not able to reach the gateway through a single-hop up-link transmission.

In [19], the authors proposed a novel low-cost, peer-to-peer, multi-hop, and gateway-free LoRa-based mesh LPWAN. The research article proposed moving away from gateways as the central role as concentrators and rather relying on a peer-to-peer-based network. The advantages of such a network are the improved security, as no information needs to be relayed through a network server, and improved performance, as no fixed central gateway is required (for example, in the case of first responders in a remote location).

The authors in [20] proposed a novel gateway-centric mesh routing topology and simulated the performance in an OMNET++ simulation model. The research specifically focused on the packet delivery latency and packet delivery ratio. Nodes are assumed to be in Rx mode continuously and transmit in a pure ALOHA fashion. All devices in the network are assumed to be using the same spreading factor, and the routing model is optimised to minimise path loss between nodes. The simulation model showed a >98% packet delivery ratio for a network containing 40 nodes with a single gateway.

The authors of [21] assessed a Distance-Ring Exponential Stations Generator (DRESG) where nodes in a multi-hop network are assigned to a ring, based on the distance to the central gateway. The study considers three routing topologies and evaluates each topology based on the complete network's energy efficiency and the node load balance amongst all the nodes in the network. The three topologies considered were a single-hop, where nodes transmit directly to the gateway, a next-ring hop, where nodes transmit directly to their parent node in the adjacent ring closer to the gateway, and an optimal-hop routing, where nodes transmit relay messages to a ring to minimise bottleneck nodes.

The authors created a Matlab-based simulation model of the proposed routing schemes, with a layer of abstraction where various low-power sub-GHz transceiver models can be used, including LoRa. Each node in the network generates a data payload with a fixed size and fixed packet header. Static routing and negligible idle, sleeping, and microprocessor currents are assumed. A basic Time-Division Multiple Access (TDMA) MAC protocol was used to enable slotted communications between children nodes and parent nodes. The simulation model used an 802.11 ah pic/hot zone deployment path loss model, as defined in [22]. Data aggregation was used per ring, where data received from the children nodes were combined with the routing node's own data.

The routing results highlight the high power consumption of nodes furthest from a gateway in a single-hop network, due to the high transmission power required. As expected, the nodes in a next-ring hop network topology closest to the gateway showed the highest power consumption due to payload aggregation. Optimal-hop routing showed the best distribution of power consumption among the nodes, minimising bottlenecks in the network. A 96% reduction in power consumption was observed in nodes far from the gateway.

Meshtastic [23,24] is a LoRa-based mesh ad hoc networking standard aimed at peer-to-peer communication for long-range off-grid communication without a centralised gateway. Meshtastic adopts Carrier-Sense Multiple Access with Collision Avoidance (CSMA/CA) and uses flooding for multi-hop messaging. The focus of the Meshtastic research is more aimed at ad hoc P2P mesh networks, compared to the gateway-centric approach in this research. However, the Meshtastic research is ongoing and supports the argument for the research and development of a mesh-based LoRa network.

The LoRa Alliance proposed a multi-hop strategy which could be used to enable add-hoc multi-hop networking, based on the existing LoRaWAN protocol, which is outlined in [9]. The proposed solution relies on Wake On Radio (WOR) frames to keep relay nodes in a low-power state for the majority of the time and only scan the channel periodically to detect any nodes which need to relay packets. This mechanism relies on the LoRa channel activity detector discussed in Section 3.2. The efficacy of the proposed solution has not yet been proven through simulations or empirical testing for large-scale deployments.

Similar to [9], the research in [25] also proposes a multi-hop LoRa network, which is based on extended LoRa preambles and LoRa CAD. The authors provided a discrete-event cross-layer simulator based on LoRaEnergySim [26] and validated the results with a real-world test bench. The focus of the proposed multi-hop LoRa protocol is energy efficiency in a small-scale deployment. Based on the described low-node-count and low-throughput use case, the asynchronous protocol is perfect, as no overhead is needed for the synchronization mechanisms.

The authors of [27] investigated the Optimizing Link-State Routing Based on Load Balancing (LB-OLSR) protocol as an approach for constructing LoRa distributed two-hop networks. The network relies on Multipoint Relay (MPR) nodes to forward messages from end-nodes to the central gateway. The study relies on a simulation model to validate the proposed mechanism. Although the work focuses on optimizing the construction of a LoRa distributed two-hop network, limited details are provided on the implementation of such a network in an LPWAN context.

Another load balancing routing optimisation algorithm is proposed in [28]. The researchers used a UCB1 multi-armed bandit reinforcement-learning-based routing mechanism for multi-hop networks. The authors set up a reward function to balance fairness (evenly spread energy consumption among relay nodes), reliability (prioritize choosing paths with the smallest path-loss), and route length (minimize latency). The network was simulated in LoRaEnergySim, and the results showed an improvement, compared to a random route selection approach, in energy consumption, package delivery ratio, latency, and the number of hops. The research is promising; however, the model is currently limited to a single data rate, and there is no discussion regarding packet scheduling to reduce power consumption.

5. Proposed Approach: LoRaMesh

For the purpose of this research article, we developed LoRaMesh, a novel LoRa-based multi-hop network protocol. The proposed network protocol is based upon LoRaWAN with changes and additions made to the packet headers and transmission scheduling, and additional reception windows. The right-hand side of Figure 2 provides an overview of the proposed mesh network. Nodes in the network can either act as up-link-only nodes (as illustrated by nodes 3, 5, and 6 in the figure), or have the additional functionality of being a relay node (as illustrated by nodes 1, 2, and 4 in the figure). Relay nodes receive LoRa packets from their assigned child nodes, queue the data in a buffer, and re-transmit the collected data, forwarding it to the next relay node or the gateway, if within reach. Relay nodes, as opposed to gateways, are single-channel devices and are mostly power-constraint. This research article will focus only on the up-link performance of the network; however, down-link messages could potentially be implemented in future work.

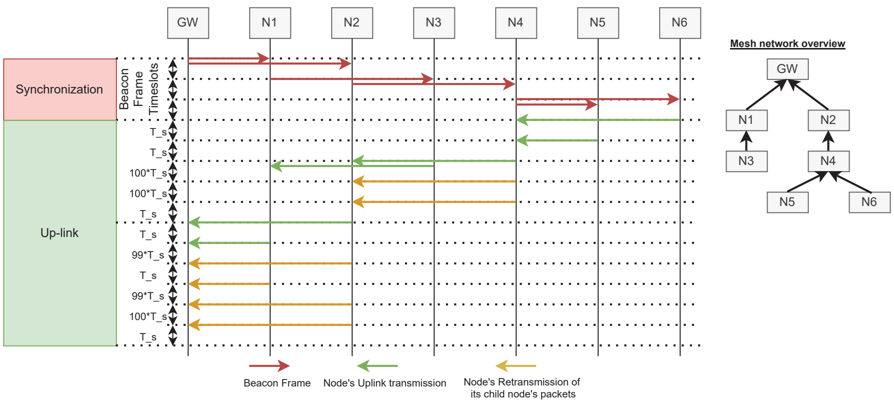

Figure 2. Real-Time Clock (RTC) synchronisation and up-link messages overview.

5.1. *LoRa-Mesh MAC*

Nodes in the LoRaMesh topology will follow a TDMA protocol. Figure 2 provides an overview of the Real-Time Clock (RTC) synchronisation and up-link procedures followed in the network. The network in Figure 2 consists of six nodes with a maximum of three hops, the overview of which can be seen on the right-hand side of the figure. The following two sections will provide an overview of the RTC synchronisation and the up-link transmissions.

5.1.1. Real-Time Clock (RTC) Synchronisation in the Network

The LoRa mesh network topology requires strict transmission and reception scheduling to minimise the guard time required before each reception window is opened. This minimises the time each repeating node spends in standby mode, waiting for a child node to transmit, and minimises packet collisions due to timing issues. To achieve these stringent timing requirements, a network synchronisation method is proposed.

Out-of-band time synchronisation is a technique where timing information is disseminated on a channel other than what is used for data traffic. Common technologies employed in IoT technologies include using a Global Navigation Satellite System (GNSS) (e.g., GPS, BDS, Galileo, ect.), radio-controlled clocks (e.g., DCF77), or an FM radio data broadcasting systems (e.g., FM-RDS) [29]. Each of these technologies comes with its drawbacks, such as coverage and availability, and most importantly, requires specialised electronic components to be added to the bill of material.

Power consumption is also a major factor to consider when using GNSS as a synchronisation system, as most applications keep the receiver off until a position/timing update is required to minimise idle power consumption. When attempting to acquire and lock onto the satellite signal, the navigation message data rate is low (50 bits/s), hence the receiver must be powered on for several seconds to receive the broadcast data (typically 28 s or longer), which can have a significant impact on power-constrained LPWAN devices. Due to the above-mentioned drawbacks, we propose the use of an in-band time synchronisation technique in this study. The LoRa Alliance have also proposed an in-band timing synchronisation method for single-hop nodes in [30], where timing information is requested by nodes from the gateway in a periodic method.

We propose the use of a simple, periodic, flooding-based, beacon frame timing dissemination. The gateway is responsible for the initialisation of the beacon frame flooding; therefore, it requires access to accurate timing information. Possible sources include an IP-based network or a GNSS radio receiver. The gateway should capture the current time-stamp immediately before transmitting the timing beacon frame. Emphasis should be placed on the gateway's firmware to minimise the processing delay between the time capture and the beacon transmission.

A new timing synchronisation update is initialised by a gateway transmitting a single beacon timing frame. This single beacon frame, transmitted by the gateway, is received by all the nodes in the network which are assigned to the first hop. These nodes then re-transmit the beacon frame based on whether or not they have any child nodes assigned to them (it is assumed that the routing structure of the network is known at this point, and this topic will be discussed further in Section 5.2). This prevents unnecessary re-transmission of the beacon frame if no child nodes are assigned to the node, thereby reducing the power consumption of the timing synchronisation update and minimising the risk of collisions between re-transmitted beacon frames. Nodes in the next hop then re-transmit the beacon frame based on the same criteria. The re-transmission of the beacon frame by the routing nodes is continued until all the nodes have re-transmitted the packet to their assigned child nodes, or the network's max number of hops (a network configuration parameter) has been reached.

In networks with a high node density, the re-transmission of these beacon frames can potentially lead to packet collisions, which could lead to nodes not receiving the beacon frames. To minimise the possible packet collisions, we propose the following three techniques to minimise the beacon-frame packet collision, and evaluate the efficacy with a simulation model:

- Re-transmissions: Beacon frames are re-transmitted three times sequentially by each relay node to improve the probability that child nodes receive the beacon frame successfully. The gateway only transmits a beacon frame once, as the probability of a packet collision is low since no nodes are scheduled to transmit during this time slot.
- Frequency diversity: Re-transmissions of the beacon frames occur on a randomly assigned frequency channel. With the increase in the number of channels available for transmissions, the probability of a packet collision is reduced. Nodes in the first hop are set to receive beacon frames on 868.1 MHz, and the gateways only transmit the beacon frame on this specific frequency. The nodes in the first hop then re-transmit the beacon frame once on each of the standard LoRa channels (868.1 MHz, 868.3 MHz, 868.5 MHz) and each of the child nodes are set to only receive a beacon frame on a specific frequency channel.
- Time diversity: Re-transmitted beacon frames are re-transmitted with a randomly selected time-offset. This time-offset is transmitted as part of the beacon frame header,

to allow the nodes to successfully calculate the beacon frame start time. Including this time diversity minimises the probability of packet collisions.

We performed a simulation using a varying number of nodes to determine the effectiveness of different beacon frame dissemination methods. The nodes were distributed uniformly within a 5 km radius from a single gateway, and all nodes were within 2 hops from the gateway. The simulations were conducted for ten different randomly generated node location distributions and ten beacon frame dissemination routines were performed per distribution. The configured simulation setup is deemed sufficient to converge reliably to an accurate result. The results of the simulation can be seen in Figure 3. From the simulation results, it is clear that time diversity in the re-transmission of the beacon frame messages increased the beacon frame distribution to greater than 99%. The results also showed a minimal increase in the beacon frame distribution when all the beacon frames were re-transmitted three times. The minimal advantage of re-transmission of the beacon frames will need to be considered against the additional time required for a single beacon-frame distribution routine and the additional power consumption requirements. For the remainder of this research article, the reader can assume that a beacon frame dissemination method, with time diversity and re-transmissions and without frequency diversity, has been used to ensure the best possible packet delivery ratio.

Nodes recalculate the start of a new beacon frame dissemination process, Beacon Frame start time (BF_{start}) according to Equation (1), where the Beacon Frame packet duration (BF_{time}) represents the total time required to transmit a beacon frame (a network configuration parameter), $TotalDelay$ is the total amount of time delay added by the multiple time delays (this information is transmitted the message content of the beacon frame), which were added to add time diversity, and $CurrentTime$ is the node's RTC.

$$BF_{start} = CurrentTime - BF_{time} \times HopNo - TotalDelay \tag{3}$$

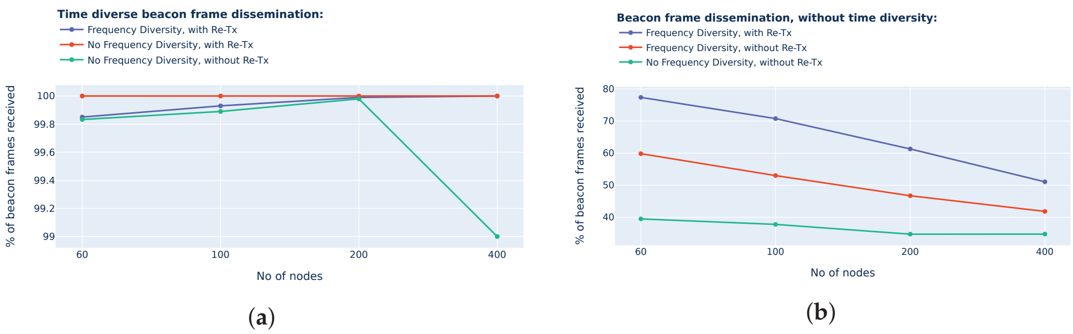

Figure 3. Beacon frame dissemination proposed methods performance. (**a**) Time diverse beacon frame dissemination performance. (**b**) Beacon frame dissemination without time diversity performance.

5.1.2. Up-Link Scheduling Procedure

The up-link procedure in the research is a rule-based approach, with a fixed up-link schedule. The up-link schedule is determined at the network start. In this approach, we assume the routing mechanism as a global view of the path loss between all nodes in the network. The routing mechanism and proposed routing information distribution mechanism will be discussed in Sections 5.2 and 5.3, accordingly.

All child nodes are assigned an up-link time slot, with the aim of decreasing the packet collision probability. The duration of the up-link time slot is based on the slowest DR and maximum packet size transmitted in the network. This time slot duration is kept fixed. The total up-link time will be determined by the network server and will depend on the max allowed child-nodes per parent routing node, the transmission slot duration, and the maximum number of hops in the network. The total up-link time will limit the throughput and up-link latency of the network. Minimising the total up-link time should be one of the major priorities of the routing and transmission parameter selection mechanisms.

Two children nodes from two different parent nodes will be allowed to transmit simultaneously, as we rely on spatial diversity, frequency diversity, semi-orthogonal spreading factors, and the capture effect to minimise the packet loss probability.

The up-link time slot assignment mechanism first assigns a transmission time slot to edge nodes, which are assigned to the furthest transmission hop in the network. Nodes are assigned time slots to allow sequential transmissions to their respective parent node. See the pseudo code Algorithm 1 for an overview of the procedure. The parent node schedules a reception window at the selected up-link time, with the predetermined SF and centre frequency.

Algorithm 1 Algorithm for assigning up-link slots for edge nodes

```
nodes[]= index(of all nodes in the network)
for i = 0 to nodes.length do
    if (nodes[i].HopNumber == MaxHopNo) then
        nodes[i].TxSlotTime = SlotDuration * nodes[i].parent.NoRxSlots
        nodes[i].parent.appendRxSlot(nodes[i].TxSlotTime)
    end if
end for
```

Nodes that are assigned to any number of transmission hops, other than the maximum amount, follow Algorithm 2's up-link time-slot assignment mechanism. This is similar to Algorithm 1, with the addition of adding a mechanism to re-transmit the received packets. It is important to note that an additional delay is required between the transmission of packets to adhere to the duty-cycle limitations of the ISM band.

Algorithm 2 Algorithm for assigning up-link slots for relay nodes

```
nodes[]= index(of all nodes in the network)
for i = 0 to nodes.length do
    if (nodes[i].HopNumber == CurrentHopNo) then
        nodes[i].TxSlotTime = SlotDuration * nodes[i].parent.NoRxSlots
        nodes[i].parent.appendRxSlot(nodes[i].TxSlotTime)
        for i = 0 to nodes.childNodes.length do
            nodes[i].ReTxSlotTime = nodes[i].TxSlotTime + SlotDuration * 100 * (i + 1)
            nodes[i].parent.appendRxSlot(nodes[i].ReTxSlotTime)
        end for
    end if
end for
```

In addition to the up-link time-slot algorithms defined above, the up-link frequency, up-link slot time and duration, up-link DR, transmitter location, and receiver location are logged per transmission in the network. This information is used in the in multi-hop parameter selection mechanism, described in Section 5.4, to optimise the performance of the network.

5.2. Routing Method

The current routing method implemented in the NS3 simulation model assumes a global overview of the node locations. The objective of the routing helper is to minimise the number of hops in the network, minimise bottleneck nodes, and minimise the path loss between the child and the parent node.

To achieve this, the path loss between the GW and all nodes are calculated. All nodes that are able to reach the GW with a single transmission hop are assigned to the hop number 0. Thereafter, the path loss between all nodes without a parent node and the nodes in hop number 0 is calculated. All nodes that are able to reach these relay nodes with a single transmission hop are assigned to hop number one. This routine is continued until all nodes have been covered, or until the maximum number of hops has been reached. The criteria for whether a node or a GW can be considered is based on the path-loss Equation (4). In Equation (4), P_{Tx} refers to the node's transmission (kept at maximum when attempting to set up node routing), PL_{dB} represents the path losses between the node and possible parent node, $RxSensitivity_{dB}$ is the receiver sensitivity at the selected SF, and $LinkBudgetMargin_{dB}$ is a user-defined option, which will ensure that there is some margin for the transmissions between the node and possible parent node.

$$P_{Tx} - PL_{dB} > RxSensitivity_{dB} + LinkBudgetMargin_{dB} \tag{4}$$

Figure 4a,b present a visualisation of two different routing topologies in which a network with identical node locations can be configured. The difference in the two networks is down to the $LinkBudgetMargin_{dB}$ selected. An increment in the $LinkBudgetMargin_{dB}$ increases the number of hops, as it decreases the transmission range of a node.

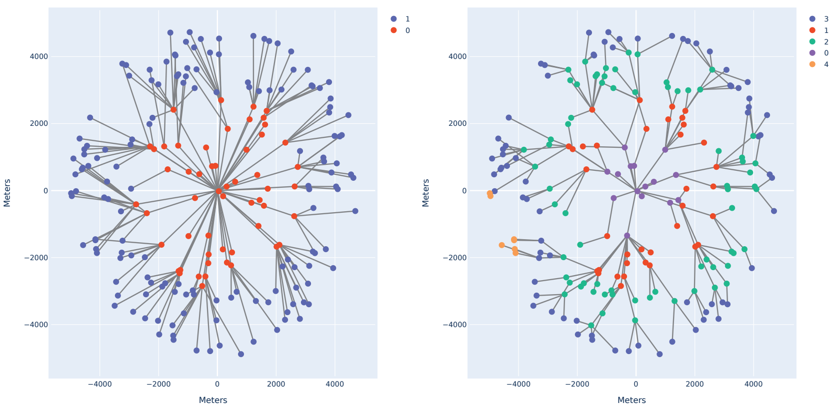

(**a**) Two-hop network (**b**) Five-hop network

Figure 4. Simulation of two different layout networks.

To minimise the bottlenecks at relay nodes and the path loss between the child and the parent nodes, the child node's parent choice is based on the routine shown in Figure 5. Since this is a sequential routing assignment algorithm, it can lead to non-optimal routing solutions. This is a complex optimisation problem which should be addressed through continuous research.

The following are three variations of the proposed parent node selection routines discussed in Figure 5, which could possibly be implemented as rule-based solutions:

- Nodes attempt to select the closest parent node to them while attempting to minimise bottlenecks at parent nodes.
- Nodes attempt to select the parent node which is the closest to the gateway while attempting to minimise bottlenecks at parent nodes.
- Nodes randomly select a parent node within their allowed link-budget to them, while attempting to minimise bottlenecks at parent nodes.

To determine the optimal parent node selection to be used in the multi-hop network, we simulated the three different approaches in the ns-3 simulation model. The varying number of nodes have been evenly distributed in a 6.5 km radius around a gateway. Nodes transmit 10-byte messages every 600 s for a total of 10 transmissions. The simulation results shown in Figure 6 demonstrated no drastic changes in the power consumption of nodes in the network due to the parent node selection method. Selecting the closest parent node, while attempting to minimise bottlenecks at parent nodes, showed the lowest median power consumption; hence, throughout the rest of the simulations, this method will be used.

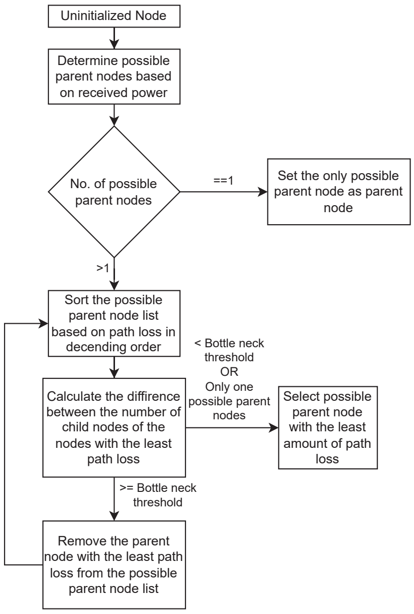

Figure 5. Parent node selection.

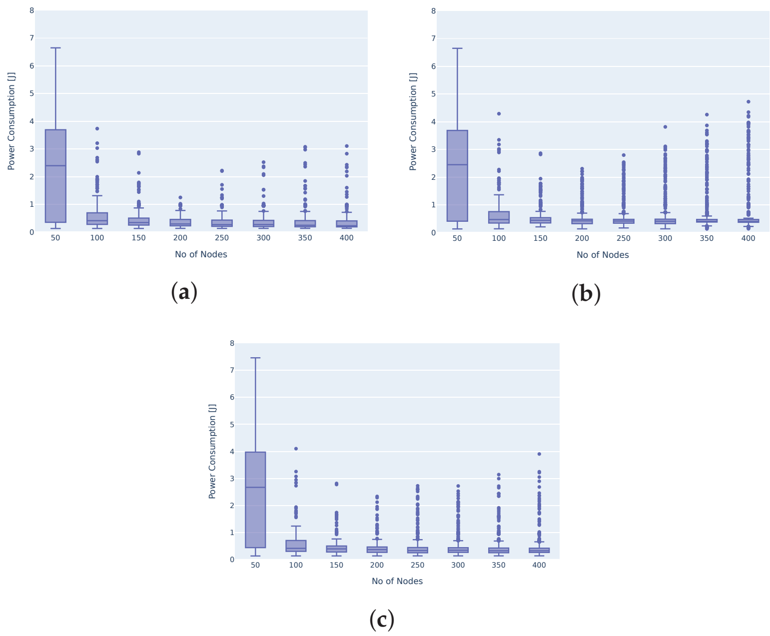

Figure 6. LoRaMesh parent node selection's impact on power consumption. (**a**) Closest parent node selected (with bottleneck prevention). (**b**) Furthest parent node selected (with bottleneck prevention). (**c**) Random parent node selection (with bottleneck prevention).

5.3. Routing Information Dissemination

In this research article, we only evaluated a basic routing topology, with limited optimisation regarding the routing of nodes in the network. Nodes are assumed to have a fixed routing at the network start time, based on the routing method discussed in Section 5.2. The following theoretical network routing process is proposed, which could potentially be deployed in a realistic scenario to set up the network's routing and transmission schedule:

- All new nodes in the network shall start in reception mode, waiting for a beacon frame.
- The gateways in the network transmit a beacon frame (with maximum transmission power and SF to reach as many devices in a single hop as possible).
- All nodes within the reception range of the gateway range receive the beacon frame and log the Received Signal Strength Indication (RSSI) of the beacon frame.
- The nodes that received the beacon frame are assigned as single-hop nodes, with the possibility of serving as a routing node as well. All other nodes in the network will need to follow a multi-hop up-link route.
- Multi-hop nodes transmit their device address three times, with random offset times.
- All single-hop nodes receive these messages and compile a list of child nodes and their respective RSSIs between the child–parent node.
- Single-hop nodes transmit these compiled lists to the gateways in the network.
- The gateways forward the information to a network server, which assigns child nodes to parent nodes to evenly distribute the load on parent nodes to prevent bottleneck nodes (a more optimised solution is possible, but is beyond the scope of the current research).
- The gateways transmit the multi-hop device's parent nodes to them, along with their upload slot assignments, via the routing nodes.
- The process where multi-hop nodes without parent nodes transmit their device address, transmit the path-loss between each child/parent node to the network server, and distribute the routing information is repeated for a fixed number of cycles, depending on the network's maximum number of hops.

Once all nodes have been assigned either to a gateway or a parent routing node, devices can start to upload data in their assigned upload slot.

This proposed network routing setup procedure requires significant transmission overhead as routing cannot be solved on a child–parent node level, resulting in additional network congestion and power consumption. Furthermore, mobile sensor networks require a self-adaptive multi-hop structure rather than a fixed, precomputed network layout. Future work should focus on adaptive routing mechanisms to handle dynamic topologies with a solution that could resolve routing at the node level.

5.4. Multi-Hop Parameter Selection

Quality of Service (QoS) remains the highest priority in the LoRaMesh network. To achieve this goal, in a multi-hop network the priority of a Multi-Hop Parameter Selection (MHPS) mechanism should be to limit packet collisions, while maximising throughput and minimising power consumption. In the proposed multi-hop network, this mechanism optimises the following transmission parameters: the spreading factor, bandwidth, code rate, and carrier frequency. The MHPS does not qualify as an ADR mechanism, as it does not adapt dynamically based on network conditions.

As all nodes in the network need to adhere to the duty cycle limitations of the 868 MHz ISM band, we limit the SF selection in the network to 7, 8, and 9, as this will keep the max transmission time slot to 500 ms and allow transmissions with a max packet size of 76 bytes.

The centre frequency choice for the LoRaMesh model in this study is limited to only 868.1 MHz, 868.3 MHz, and 868.5 MHz, as these are the centre frequencies which are required by all LoRaWAN devices, thereby ensuring compatibility with existing hardware.

The MHPS mechanism suggested in this paper is a static rule-based approach and is only implemented to improve the performance of the network as a proof of concept.

During the network setup phase, the information related to all scheduled transmissions of a single up-link transmission window is logged. The MHPS mechanism iterates through all the transmissions and investigates possible packet collisions. The MHPS flags a possible packet as a collision whenever the following occur:

- The timing of the two transmissions overlaps;
- The same centre frequency is used by both transmissions;
- The same SF is used by both transmissions;
- The two receiver locations are within $D_{collision}$ km proximity to another.

Whenever a packet collision is detected, the MHPS mechanism will attempt to alter the centre frequency and restart the packet collision detection until all listed centre frequencies have been tested. If a packet collision is unavoidable by a centre frequency change, the MHPS mechanism will postpone the transmission by one time slot length and restart the packet collision detection. If a packet collision is still present, the MHPS mechanism will postpone the transmission until no transmission collision is detected or the transmission has been postponed by a max of five time slots. If a collision is unavoidable, the MHPS mechanism will randomly assign a time slot delay and centre frequency.

LoRa CAD is a solution, described in Section 3.2, that could possibly allow devices to automatically adjust their respective transmission slots (after updating their respective parent Rx time slot). This solution is recommended for a setup where the TDMA scheduler does not have an overview of the network (which is assumed in our simulation model) and reinforcement learning is used to optimise the network performance.

5.5. Power Consumption

In a Class A LoRaWAN, the power consumption of a node can easily be calculated by $E_{Tot} = E_{stby} + E_{Tx} + E_{Rx}$, where E_{Tx} is the energy required for the transmission of a packet, E_{Rx} is the energy required to open two receive windows, and E_{stby} is the energy consumed during standby. In a multi-hop mesh network, it is important to determine the additional power consumption required by mesh nodes. The total energy (E_{Tot}) in Joules per up-link transmission cycle is calculated by Equation (5). Where:

- E_{stby}: energy consumed during standby;
- E_{beacon}: energy required for the reception and possible re-transmission of the beacon frame;
- E_{frwd}: energy required for the possible reception and forwarding of child node packets;
- E_{Tx}: energy required for the transmission of a node's own packet.

$$E_{Tot} = E_{stby} + E_{beacon} + E_{frwd} + E_{Tx} \tag{5}$$

Based on the research done in [31] and the datasheet of the Semtech SX1272 [7], Table 1 lists the power consumption values which are used within the ns-3 simulation model. We assume that the PA0 output is on the RFO pin, since no boost power amplifiers will be needed as we are limited to 14 dBm in the 868.1 MHz ISM band.

Table 1. Power consumption of the SX1272 LoRa transceiver.

Mode	Current Consumption	Notes
Transmit (Tx)	38 mA @ +14 dBm	Reduced currents @ lower Tx power
Receive (Rx)	11 mA	Continuous receive mode
Sleep	1.5 uA	Register retention mode

Given the information in Table 1, we can calculate the theoretical energy consumption of a Class A LoRaWAN device which is transmitting a 10-byte data packet at a transmission power of 14 dBm once every 600 s at a DR 1 (selected at random). Only the energy consumption of the LoRaWAN radio is taken into account.

The ToA for the transmission of the 10-byte LoRaWAN packet at the given datarate is 741.4 ms. The transceiver operates at 3.3 V. Hence, the E_{Tx} is calculated at 0.09297 J per transmission. The Rx duration is calculated, based on Equation (1) at the given datarate, as 16.64 ms. Since two reception windows are required in Class A LoRaWAN devices, the Rx duration will be 33.28 ms per up-link, resulting in $E_{Rx} = 0.0012$ J. Given that the transceiver is in sleep mode and the remaining time of the 600 s up-link cycle, the standby energy power consumption is $E_{stby} = 0.002966$ J. The total power consumption then results in $E_{Tot} = 0.097136$ J per up-link cycle.

Calculating a theoretical power consumption value for an LoRaMesh device will not reflect the actual power consumption, as the reception time of waiting for beacon frames or the SF of received packets to the relay varies. To approximate the power consumption, Section 7.2 simulates the energy consumption of such relay nodes to model the effect of beacon frames and relayed packets on relay nodes.

6. The ns-3 Simulation Model

6.1. Overview

The ns-3 [32] simulation model in this study is based on a modified version of the LoRaWAN ns-3 simulation model proposed in [33], for which the source code can be found in [34]. The simulation model has been improved to support multi-hop packet routing, TDMA scheduling, RTC synchronisation, and multiple supporting performance monitors.

The simulation model currently only supports a single gateway, unconfirmed up-link messages for data traffic, and unconfirmed down-link messages for RTC synchronisation. Furthermore, the model is currently limited to a single bandwidth and spreading factor. Support for dynamically adjusting these transmission parameters is beyond the scope of the current research.

A static mobility model is used by all nodes and gateways. The gateway is placed at position (0,0), with the nodes distributed randomly in an area around the gateway with a defined max radius of R_{max}; see Figure 4a for an example.

In this simulation model, we base our performance measurements on the SX1272 IC [7], developed by Semtech, as this is the industry standard single-channel LoRa transceiver for the 800–1000 MHz frequency band.

The model is a representation of an ideal real-world scenario, where node positions are static and the attenuation between nodes is constant. These assumptions are required to reduce the complexity of the simulation model and allow a comparison between a single-hop network and a multi-hop network for a static LPWAN network. The performance of the multi-hop model will be significantly different in a dynamic environment.

6.2. Path-Loss Model

The work in [35] conducted a large-scale measurement study to quantify the path loss of LoRa networks in urban areas. The study concluded that a log-distance propagation loss model provides good estimations in an urban environment; therefore, it will be the model used in the simulations. The path loss model for the log-distance model is represented by Equation (6):

$$L = L_0 + 10nlog_{10}(\frac{d}{d_0}) \tag{6}$$

where n is the path loss distance, d_0 is the reference distance (m), L_0 is the path loss at reference distance (dB), d is the distance (m), and L is the path loss (dB).

In all of the simulations performed in this study, a path loss exponent (n) of 3.76 is used to simulate a dense urban environment. The complex signal propagation characteristics are influenced by buildings, vehicles, and other obstacles that can significantly attenuate signals. The dense urban path loss model accurately accounts for these factors, providing more realistic simulation results and enhancing the reliability of network performance predictions. This assumption is based on the ns-3 model setup in [33], and the same path loss model is used in all simulations of LoRaWAN and LoRaMesh networks. The path-loss model can easily be altered in the simulation model; thus, the results should not be limited to the above proposed model.

6.3. Join Procedure

The joining procedure is beyond the scope of this current study. The following settings are assigned to nodes during the join procedure:

- Transmission parameter; default SF, BW, and transmission power values are assigned to all nodes at the start.
- Routing tables; the current study assumes a global view of the gateway and the nodes. Using the default setup information (SF, BW, Node locations, and transmission power) available, the simulation model assigns the nodes parent/child nodes where applicable.
- Channel assignment; based on the LoRaWAN Regional parameter specifications, we only consider the three network channels that are required to be implemented in all EU863–870 nodes, namely, 868.10 MHz, 868.30 MHz, and 868.50 MHz. During the joining procedure, a network channel is assigned to each parent-node. All child-nodes are required to use this network channel, as this will minimise packet collisions.

6.4. Up-Link Outage Probability

The full explanation of packet destruction detection is omitted in this publication. The LoRa physical layer's packet collision model is based on the work done in [33], which can be referred to for a complete overview. The model assumes that RF interference only comes from other LoRa transmissions, and we assume the partial orthogonality property of different SF to simulate packet collisions. The model also takes the capture effect into account.

7. Results

The simulation results in this section rely on the following definitions: the packet delivery rate (PDR) is the ratio of the number of packets received per node successfully by the GW to the number of packets transmitted by each node during the simulation runtime. The results in this section assume the LoRaWAN operates based on the specifications listed in [2] and the multi-hop network is set up based on the proposed network in Section 5, with the simulation conducted according to the setup described in Section 6.

7.1. Node Density and Number of Hops in a Network

To investigate the effect of node density in a network, a varying number of nodes are placed within a 3.927 km, 5 km, and 7.071 km radius of the GW. The simulations are performed with ten randomly generated node location maps, and ten complete up-link cycles are simulated per setup. The results of the simulations can be seen in Figure 7.

From the simulations, three conclusions can be drawn. Firstly, a higher node density negatively affects the performance, which can directly be attributed to the higher probability of packet collision due to the reduced spatial diversity of concurrent transmissions. The second important note from the results relates to the number of devices in a network. As the number of devices in a network increase, so does the interference in the network. Although nodes attempt not to transmit simultaneously in the network, the additional transmissions on other SFs and the accumulated RF interference, caused by other nodes beyond the reception range, of the receiving node can lead to substantial packet loss.

Lastly, in the simulation, the number of hops in the network increases as the network radius increases. Due to the inherent nature of a multi-hop network, the number of packets transmitted in the network increases with the number of hops in the network, thereby increasing the collision probability.

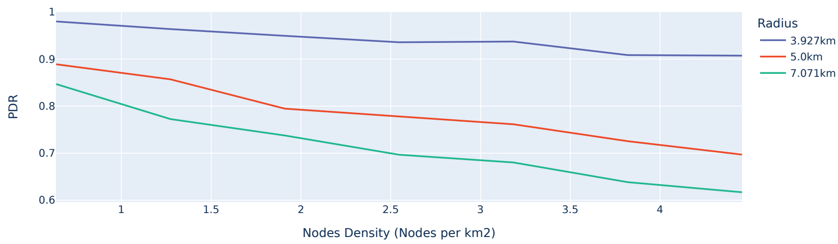

Figure 7. PDR of a multi-hop network with different numbers of nodes placed within a 3.927 km, 5 km, and 7.071 km radius of the GW, normalised to node density.

7.2. Power Consumption Comparison

To compare the power consumption of LoRaMesh directly to LoRaWAN, a single example scenario has been set up to demonstrate the differences. The example parameters have been chosen to specifically highlight the advantages of LoRaMesh; however, this does represent typical network deployments. In the example scenario, 260 devices are randomly distributed around a single gateway within a radius of 6.5 km, and 10-byte up-link data transmissions are scheduled every 600 s. We have chosen a 10-byte data packet as it is representative of the typical requirements of an IoT sensor such as an air quality sensor, soil moisture sensor, or latitude and longitude GPS location. The network radius is chosen to force the use of all the different *SFs* available to the LoRaWAN devices. The power consumption includes the transmission, receive, standby, and relay (in the case of the LoRa mesh network).

Figure 8 highlights the inherent problem of multi-hop networks. The nodes located in the first hop from the GW exhibit the highest energy consumption due to the node's increased time spent in reception mode to aggregate child packages and re-transmitting the packages. When comparing the results of Figure 8 vs. the results in Figure 9, the advantages and disadvantages of a mesh-based network become apparent. Nodes located further than 5 km from the GW will, on average, have a reduction in power consumption in a mesh-based network compared to a LoRaWAN-based network. This is an advantage for energy constraint devices, which have a high attenuation to a centralised gateway. This higher attenuation is typically due to devices being placed in adverse locations where maintenance on the devices is difficult. However, relay nodes which are closer to the central GW have significantly higher power consumption. The results and advantages of such a network will be highly dependent on the targeted application.

In Section 5.5, the E_{Tot} per up-link cycle was calculated as 0.097136 J, which was calculated for an identical test case to that which is represented in Figure 9. The E_{Tot} can be calculated as 0.097136 J for 10 consecutive up-link cycles, which matches the simulated results in Figure 9 for devices transmitting with SF11.

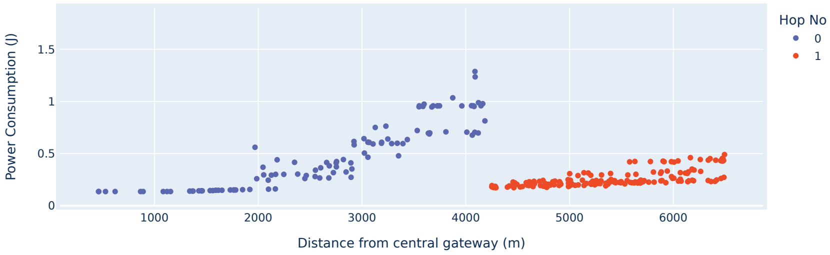

Figure 8. Energy consumption of a multi-hop network vs. distance from the GW.

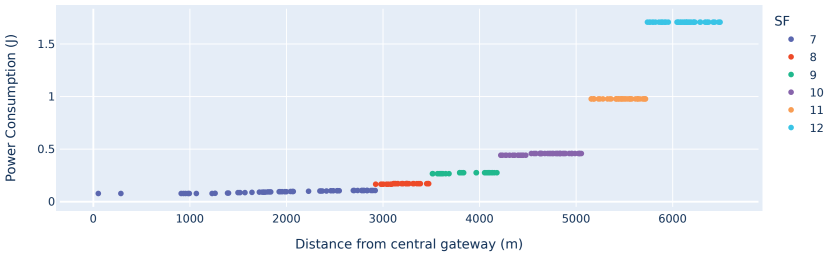

Figure 9. Power consumption of a LoRaWAN with ADR vs. distance from the GW.

Table 2 summarises the energy consumption measurements of the relay nodes in the simulation results depicted in Figure 8. The percentage difference in power consumption of nodes utilising the same spreading factor with varying number of child nodes highlights the additional energy consumption of these relay nodes. Although the relay nodes need to relay the data packets, the energy consumption is not increased linearly, as the energy used in standby and during synchronisation is not scaled. The large delta increase in power consumption between SF7 nodes not relaying any packet and SF7 nodes relaying a single packet is due to the average power consumption of nodes close to the gateway being extraordinarily low due to a high data rate and low transmission power.

To provide a more comprehensive average power consumption comparison of a single-hop network vs. multi-hop network, we simulated a varying amount of nodes in both single-hop and multi-hop networks. The nodes are randomly distributed around a single gateway, within a 6.5 km radius; 10-byte data transmissions are scheduled every 600 s for a total of 10 transmissions. The network radius is once again chosen to force the use of all the different *SFs* available to the LoRaWAN devices.

Table 2. Analysis of the impact of additional child nodes on the energy consumption by nodes designated as relays.

SF	No of Child Nodes	Average Power Consumption (J)	Increased % Due to Additional Child Node
7	0	0.143111	
7	1	0.287213	100.6922
7	2	0.398114	38.61287
7	3	0.534921	34.36384
8	0	0.491797	
8	1	0.623426	26.76483
8	2	0.826416	32.56048
9	0	0.710039	
9	1	0.97174	36.85714
9	2	1.236393	27.23506

Figure 10 summarises the average power consumption of the devices for three different distances from the gateway. The displayed power consumption of devices located between 1 and 2 km represent nodes which all transmit directly to the gateway, while nodes located between 3 and 4 km from the gateway represent nodes which need to relay packets in the multi-hop network. Lastly, nodes located between 5 and 6 km from the gateway represent nodes that are in the first hop of the multi-hop network, or nodes which use a higher SF (10–12 SF) in the single-hop network.

In Figure 10, it is clear that the number of nodes in an evenly distributed network does not have a statistically significant impact on the average power consumption of the nodes in the network. An increase in nodes which need packets that need to be relayed is met with an increase in relay nodes. Furthermore, it is clear that although there is a significant increase (315%) in the average power consumption of nodes which need to relay packets in the multi-hop network, the nodes located 5–6 km sees a dramatic decrease (477%) in power consumption, as their ToA is reduced due to the lower transmission SF.

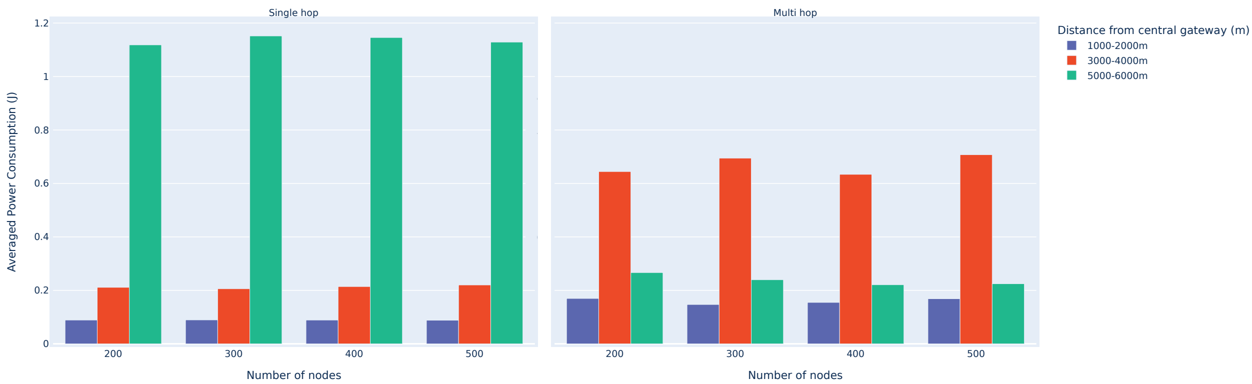

Figure 10. Average power consumption comparison of a single-hop network vs. multi-hop network.

7.3. A QoS Comparison

In this subsection, we compare the PDR of LoRaWAN vs. a multi-hop network. To that aim, the results shown in Figures 11 and 12 show the PDR vs. the distance of a LoRaWAN vs. a multi-hop network, respectively. In this comparison, 1000 devices are uniformly randomly placed in an 8.5 km radius around a single gateway. Ten messages are transmitted to the gateway.

The results showed a 96.9% PDR for nodes located in the first hop, 57.87% for nodes in the second hop, and 73.78% for nodes located in the last hop. This highlights the high rate of collisions in a dense network. However, it also highlights how nodes located further from the gateway can still achieve a high PDR, compared to LoRaWAN. The nodes located beyond 5.8 km in the LoRaWAN had a PDR of 40.2% (nodes using DR0), which is significantly lower than the performance of any hop in the LoRaMesh network.

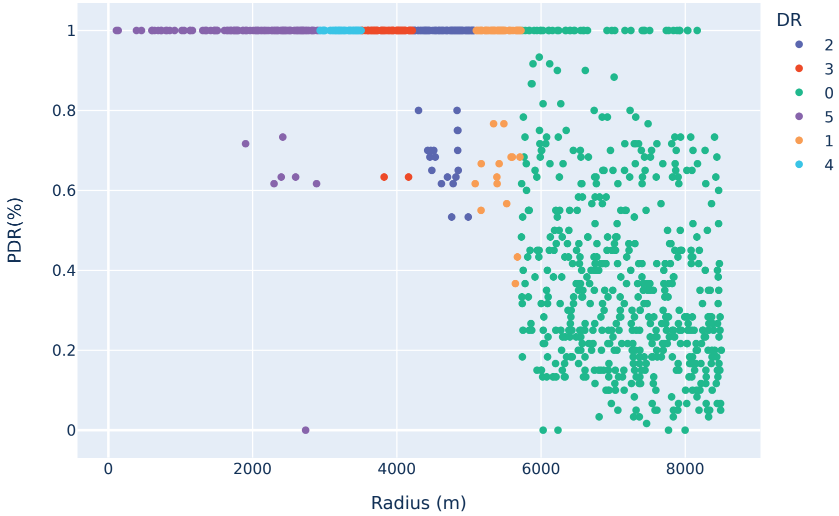

Figure 11. Packet delivery ratio of LoRaWAN vs. distance from the GW.

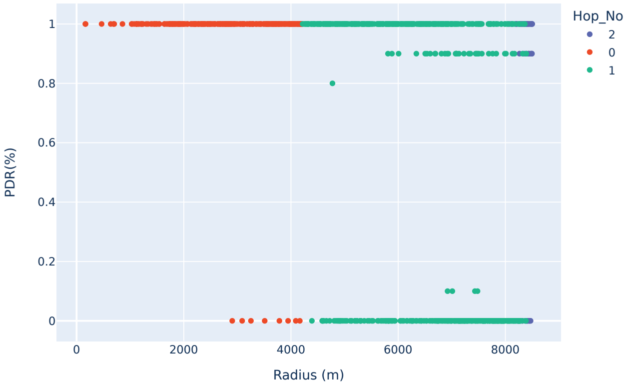

Figure 12. Packet delivery ratio of LoRaMesh vs. distance from the GW.

In the LoRaMesh PDR analysis, shown in Figure 12, it is clear that the nodes typically either have a successful up-link or not. This can be attributed to the static nature of the network configuration. Nodes are set to always transmit on a specific SF, time, and channel; therefore, this results in certain packet collisions being repeated for every transmission cycle. This highlights the need for a reinforcement-learning-based approach, which should assist nodes in adapting their transmission parameters dynamically to optimise the network QoS.

8. Typical Use Cases of LoRaMesh

IoT applications vary drastically, as do their requirements regarding power consumption, throughput, latency, coverage, cost, and QoS. In this section, we will only briefly highlight two examples of LPWAN IoT applications that could utilise the advantages of LoRaMesh vs. LoRaWAN.

LPWAN technology assists the agriculture sector by providing improved monitoring and precise control, in sectors such as water management, irrigation management, livestock monitoring, and precision agriculture. A study in [36] identified reliability, QoS, and scalability as the top requirements in smart-agriculture IoT transceivers. Another area where LPWAN networks have become quite prevalent is in smart cities in sectors such as parking, waste management, lighting, infrastructure monitoring, and smart grids. The requirements for these applications overlap significantly with those of smart agriculture.

LoRaMesh offers two main advantages above LoRaWAN to exceed in both power consumption, coverage, and QoS:

- Extended coverage, through multi-hop networks. Devices further away from a gateway or with significant attenuation can receive network coverage. This not only improves coverage in extreme use-cases, but also reduces the number of GW's needed to cover an area, thereby reducing the cost of network deployment.
- Improved power consumption for nodes in extreme environments. Nodes located further from the GW do not need to default to a higher SF to reach a GW, thereby increasing ToA and power consumption. This is a significant advantage as nodes with attenuation are typically located in inhospitable environments. An increased battery lifetime can thereby reduce maintenance requirements.

9. Conclusions

The current LoRaWAN standard performs well as an LPWAN standard for IoT applications; however, nodes located far from a GW are prone to increased transmission power and data-rate requirements to provide coverage for these nodes. This negatively affects the power consumption of these nodes.

The proposed LoRaMesh network offers a network topology that can address this shortcoming. The simulation results shown in Section 7 highlight how the proposed network could potentially reduce the power consumption requirements of devices located further from a GW. Furthermore, it highlights the capabilities of such a network to provide adequate network performance in terms of PDR to nodes located further away from a gateway.

LoRaMesh proved to be a promising alternative to the current industry standard, LoRaWAN, specifically in the smart agriculture and smart city industries.

The proposed network protocol is not fully optimised and could potentially be improved by implementing a more advanced rule-based approach or reinforcement learning.

The future challenges that remain are to explore energy-efficient methods to implement routing information dissemination, especially to implement local routing tables to reduce the overhead required by transmitting routing tables to the gateway, and to address dynamic networks, where new nodes can join networks, failed nodes can be detected, and nodes could potentially have a non-static mobility model.

Author Contributions: Methodology, T.G.D.; Investigation, T.G.D.; Writing— original draft, T.G.D.; Writing—review and editing, M.J.B.; Supervision, M.J.B. All authors have read and agreed to the published version of the manuscript.

Funding: This research received no external funding.

Institutional Review Board Statement: Not applicable.

Informed Consent Statement: Not applicable.

Data Availability Statement: The original contributions presented in the study are included in the article; further inquiries can be directed to the corresponding author.

Conflicts of Interest: The authors declare no conflicts of interest.

References

1. LoRa Alliance. LoRa Alliance: Wide Area Networks for IoT. Available online: https://lora-alliance.org/ (accessed on 2 March 2025).
2. LoRa Alliance Technical Commitee. *LoRaWAN 1.1 Specification*; LoRaWAN Alliance Inc.: Beaverton, OR, USA, 2017; p. 101.
3. Augustin, A.; Yi, J.; Clausen, T.H.; Townsley, W. A Study of LoRa: Long Range & Low Power Networks for the Internet of Things. *Sensors* **2016**, *16*, 1466. [CrossRef] [PubMed]
4. Marquet, A.; Montavont, N.; Papadopoulos, G.Z. Towards an SDR implementation of LoRa: Reverse-engineering, demodulation strategies and assessment over Rayleigh channel. *Comput. Commun.* **2020**, *153*, 595–605. [CrossRef]
5. Durand, T.; Visagie, L.; Booysen, M.T. Evaluation of next-generation low-power communication technology to replace GSM in IoT-applications. *IET Commun.* **2019**, 13, 2533–2540. [CrossRef]
6. *EN 300 220-2 V3.2.1*; Short Range Devices (SRD) Operating in the Frequency Range 25 MHz to 1000 MHz; Part 2: Harmonised Standard for Access to Radio Spectrum for Non Specific Radio Equipment. European Telecommunications Standards Institute (ETSI): Sophia-Antipolis, France, 2018. Available online: https://www.etsi.org/deliver/etsi_en/300200_300299/30022002/03.02.01_60/en_30022002v030201p.pdf (accessed on 5 December 2024).
7. Semtech. SX1272-LoRa® Transceiver Datasheet. Semtech Datasheet. 2019; pp. 1–129. Available online: https://www.semtech.com/products/wireless-rf/lora-connect/sx1272 (accessed on 2 March 2025).
8. Semtech. Introduction to Channel Activity Detection. Semtech Datasheet (AN1200.85). 2024. Available online: https://www.semtech.com/uploads/technology/LoRa/cad-ensuring-lora-packets.pdf (accessed on 2 March 2025) .
9. LoRa Alliance Technical Commitee. *LoRaWAN Relay Specifications TS011-1.0.0*; LoRa Alliance: Beaverton, OR, USA, 2022.
10. Bor, M.; Roedig, U.; Voigt, T.; Alonso, J. Do LoRa Low-Power Wide-Area Networks Scale? In Proceedings of the MSWiM '16—19th ACM International Conference on Modeling, Analysis and Simulation of Wireless and Mobile Systems, Floriana, Malta, 13–17 November 2016; ACM Press: New York, NY, USA, 2016; pp. 59–67. [CrossRef]
11. Polonelli, T.; Brunelli, D.; Benini, L. Slotted ALOHA Overlay on LoRaWAN: A Distributed Synchronization Approach. In Proceedings of the 2018 IEEE 16th International Conference on Embedded and Ubiquitous Computing (EUC), Bucharest, Romania, 29–31 October 2018.
12. Bor, M.; Vidler, J.; Roedig, U. LoRa for the Internet of Things. In Proceedings of the International Conference on Embedded Wireless Systems and Networks (EWSN), Graz, Austria, 15–17 February 2016; pp. 361–366.
13. Zorbas, D.; Abdelfadeel, K.; Kotzanikolaou, P.; Pesch, D. TS-LoRa: Time-slotted LoRaWAN for the Industrial Internet of Things. *Comput. Commun.* **2020**, *153*, 1–10. [CrossRef]
14. Semtech Corporation. *LoRaWAN—Simple Rate Adaptation Recommended Algorithm Class A/B Specification*; Semtech: Camarillo, CA, USA, 2016; pp. 1–8.
15. Benkahla, N.; Tounsi, H.; Song, Y.Q.; Frikha, M. Enhanced ADR for LoRaWAN networks with mobility. In Proceedings of the 2019 15th International Wireless Communications Mobile Computing Conference (IWCMC), Tangier, Morocco, 24–28 June 2019; pp. 1–6. [CrossRef]
16. Cuomo, F.; Campo, M.; Caponi, A.; Bianchi, G.; Rossini, G.; Pisani, P. EXPLoRa: Extending the performance of LoRa by suitable spreading factor allocations. In Proceedings of the 2017 IEEE 13th International Conference on Wireless and Mobile Computing, Networking and Communications (WiMob), Rome, Italy, 9–11 October 2017; pp. 1–8. [CrossRef]
17. Rodrigues Cotrim, J.; Kleinschmidt, J. LoRaWAN Mesh Networks: A Review and Classification of Multihop Communication. *Sensors* **2020**, *20*, 4273. [CrossRef] [PubMed]
18. Wong, A.; Goh, S.L.; Hasan, M.K.; Fattah, S. Multi-Hop and Mesh for LoRa Networks: Recent Advancements, Issues, and Recommended Applications. *ACM Comput. Surv.* **2023**, *56*, 1–43. [CrossRef]
19. Berto, R.; Napoletano, P.; Savi, M. A LoRa-Based Mesh Network for Peer-to-Peer Long-Range Communication. *Sensors* **2021**, *21*, 4314. [CrossRef] [PubMed]
20. Pham, V.D.; Kisel, V.; Kirichek, R.; Koucheryavy, A.; Shestakov, A. Evaluation of A Mesh Network based on LoRa Technology. In Proceedings of the 2021 23rd International Conference on Advanced Communication Technology (ICACT), PyeongChang, Republic of Korea, 7–10 February 2021; pp. 1–6. [CrossRef]
21. Barrachina-Muñoz, S.; Bellalta, B.; Adame, T.; Bel, A. Multi-hop Communication in the Uplink for LPWANs. *Comput. Netw.* **2016**, *123*, 153–168. [CrossRef]
22. Hazmi, A.; Rinne, J.; Valkama, M. Feasibility study of IEEE 802.11ah radio technology for IoT and M2M use cases. In Proceedings of the 2012 IEEE Globecom Workshops, Anaheim, CA, USA, 3–7 December 2012; pp. 1687–1692. [CrossRef]
23. Cass, S. It's Meshtastic! > LoRa-based Tech Brings Mesh Radio to Makers. *IEEE Spectr.* **2024**, *61*, 16–18. [CrossRef]

24. Suryadevara, N.K.; Dutta, A. Meshtastic Infrastructure-less Networks for Reliable Data Transmission to Augment Internet of Things Applications. In Proceedings of the Wireless and Satellite Systems, Virtual Event, China, 31 July–2 August 2021; Guo, Q., Meng, W., Jia, M., Wang, X., Eds.; Springer: Cham, Switzerland, 2022; pp. 622–640.
25. Leenders, G.; Callebaut, G.; Ottoy, G.; van der perre, L.; De Strycker, L. An Energy-Efficient LoRa Multi-Hop Protocol through Preamble Sampling for Remote Sensing. *Sensors* **2023**, *23*, 4994. [CrossRef] [PubMed]
26. DRAMCO, "LoRa Multihop Simulator", GitHub Repository. Available online: https://github.com/DRAMCO/LoRa-multihop-simulator (accessed on 4 March 2025).
27. Pang, S.; Lu, J.; Pan, R.; Wang, H.; Wang, X.; Ye, Z.; Feng, J. Optimizing Routing Protocol Design for Long-Range Distributed Multi-Hop Networks. *Electronics* **2024**, *13*, 3957. [CrossRef]
28. Scarvaglieri, A.; Panebianco, A.; Busacca, F. MAGELLAN: A distributed MAB-based algorithm for Energy-Fair and Reliable Routing in Multi-Hop LoRa networks. In Proceedings of the [PREPRINT] GLOBECOM 2024—2024 IEEE Global Communications Conference, Cape Town, South Africa, 8–12 December 2024; pp. 1–6.
29. Beltramelli, L.; Mahmood, A.; Ferrari, P.; Österberg, P.; Gidlund, M.; Sisinni, E. Synchronous LoRa Communication by Exploiting Large-Area Out-of-Band Synchronization. *IEEE Internet Things J.* **2021**, *8*, 7912–7924. [CrossRef]
30. LoRa Alliance Technical Commitee. *LoRaWAN ® Application Layer Clock Synchronization Specification TS003-2.0.0*; LoRa Alliance Technical Committee: Beaverton, OR, USA, 2022; p. 101.
31. Finnegan, J.; Brown, S.; Farrell, R. Modeling the Energy Consumption of LoRaWAN in ns-3 Based on Real World Measurements. In Proceedings of the 2018 Global Information Infrastructure and Networking Symposium (GIIS), Thessaloniki, Greece, 23–25 October 2018; pp. 1–4. [CrossRef]
32. Henderson, T.R.; Lacage, M.; Riley, G.F.; Dowell, C.; Kopena, J. Network simulations with the ns-3 simulator. *SIGCOMM Demonstr.* **2008**, *14*, 527.
33. Magrin, D.; Centenaro, M.; Vangelista, L. Performance evaluation of LoRa networks in a smart city scenario. In Proceedings of the 2017 IEEE International Conference on Communications (ICC), Paris, France, 21–25 May 2017; pp. 1–7.
34. Magrin, D.; Capuzzo, M.; Romagnolo, S.; Luvisotto, M. LoRaWAN ns-3 Module. 2020. Available online: https://github.com/signetlabdei/lorawan (accessed on 2 March 2025).
35. Petajajarvi, J.; Pettissalo, M.; Mikhaylov, K.; Roivainen, A.; Hänninen, T. On the Coverage of LPWANs: Range Evaluation and Channel Attenuation Model for LoRa Technology. In Proceedings of the 2015 14th International Conference on Its Telecommunications (ITST), Copenhagen, Denmark, 2–4 December 2015. [CrossRef]
36. Sinha, B.B.; Dhanalakshmi, R. Recent advancements and challenges of Internet of Things in smart agriculture: A survey. *Future Gener. Comput. Syst.* **2022**, *126*, 169–184. [CrossRef]

sensors

Article

Nanosecond Time Synchronization over a 2.4 GHz Long-Range Wireless Link

Pascal Müller, Dominic Berger and Luciano Sarperi *

Institute of Signal Processing and Wireless Communications, ZHAW School of Engineering, 8401 Winterthur, Switzerland; pascal.mueller@zhaw.ch (P.M.); dominic.berger@zhaw.ch (D.B.)
* Correspondence: luciano.sarperi@zhaw.ch

Abstract: Time synchronization between geographically separated equipment, such as, for example, that required in sensor networks for radio localization, is often based on global navigation satellite systems (GNSSs). However, in environments that are GNSS-denied due to signal blockage or interference, alternative timing synchronization methods are necessary. In this work, an experimental wireless time synchronization system based on long-range (LoRa) modulation has been developed and tested in the field. LoRa modulation operating in the license-free 2.4 GHz industrial, scientific and medical (ISM) band was chosen due to the potentially large coverage area of several kilometers and the availability of a ranging engine in the SX1280 transceiver by Semtech, which facilitates the implementation of time synchronization. The prototype system was tested over 170 m, where it achieved a time deviation (TDEV) of 30 ps for an average time of 1 s and a maximum TDEV of 3 ns over one day of measurement, improving over existing work on time synchronization with LoRa modulation by around three orders of magnitude. The field tests showed that ns accuracy can be achieved using LoRa modulation, making it suitable for the synchronization of remote sites, for example, for radio localization.

Keywords: time synchronization; wireless synchronization; long-range (LoRa) modulation; nanosecond accuracy

1. Introduction

Time synchronization plays an important role in many systems and applications, such as in cellular networks for frequency and time synchronization between base stations, in distributed sensor networks for the timestamping of data or for radio localization using the time difference of arrival method [1].

A typical way of achieving time synchronization between two points is using global navigation satellite systems (GNSSs) [2]. The accuracy of a 1 Hz pulse per second (PPS) can reach 200 ps with additional signal conditioning [3]. However, when GNSS signals are not available due to blocked lines of sight from the receiver to the satellites or when external interference is present, other time synchronization methods are required.

When cables can be used, high-accuracy clock synchronization may be implemented with White Rabbit (WR) time synchronization technology, which is based on optical ethernet networks. WR is an extension of the Precision Time Protocol (PTP) and has been incorporated into the IEEE 1588 standard. It uses a PHY-layer frequency synchronization of the involved nodes and phase measurements, thereby achieving accuracies in the sub-ns level [4].

However, when synchronization between ad hoc nodes is required and GNSSs cannot be used, alternative, wireless methods for time synchronization are desirable. Time synchronization over optical free space links can achieve remarkably high accuracies, with reported values in the sub-ps level for a 113 km link [5]. However, optical free-space links require a line-of-sight path and are susceptible to adverse weather conditions such as precipitation, fog or turbulent air, with an additional link loss that may exceed 100 dB/km in case of fog [6], which can render the operation impossible.

Compared to optical free-space links, wireless time synchronization systems using radio frequency (RF) signals are less influenced by atmospheric conditions and can, in principle, also be employed without a direct line-of-sight link between the two terminals. There is a large amount of previous work on wireless time synchronization for sensor networks, with typical accuracies in the µs level, for example [7,8]. Other work on wireless time synchronization focuses on short-range wireless time synchronization, for example, using ultra-wideband (UWB) technology, with reported accuracies in the ns range [9]. In [10], a wireless system for positioning and time synchronization operating in the 2.4 GHz industrial, scientific and medical (ISM) band is evaluated, with a reported maximum time interval error (MTIE) of 3 ns averaged over multiple distances of up to 105 km.

In the area of wireless time synchronization with long-range (LoRa) modulation, existing work focuses either on the actual time synchronization of devices or on methods for timestamping events or data packets. In the following, previous work on the time synchronization of LoRa devices is reviewed, which is related to our work. In [11,12], an energy-efficient synchronization method with low-layer timestamping based on interrupt signals is proposed, which achieves an accuracy of 15 µs. However, since it uses a one-way exchange, the propagation delay cannot be compensated. In [13], a time synchronization method for LoRaWAN networks based on low-layer interrupt signals is proposed. It uses either one two-way exchange to adjust local clocks and perform a first-order compensation of clock drift rate or two two-way exchanges to additionally compensate the propagation delay. With one two-way exchange, an accuracy of 3 µs is achieved, while, with two two-way exchanges over distances of up to 4 km, an accuracy of 10 µs is achieved. The method in [14] presents a time synchronization method for LoRa devices with the aim of optimizing the channel access by introducing scheduling to increase the system capacity. The proposed time synchronization protocol, which does not use low-layer timestamps, has a time resolution of 10 ms. In [15], a synchronization method for LoRa devices using the ranging function of the SX1280 transceiver from Semtech is proposed, which is used to compensate the propagation delay. Few details about the measurement setup are provided, but an accuracy of about 1 µs for distances of 100 m is reported.

Recent work on the timestamping of events or data packets in LoRa networks includes [16,17]. In [16], a synchronization-free timestamping of uplink data at the LoRa gateway with ms accuracy is proposed, while, in [17], a posteriori time synchronization for LoRa devices is proposed, which can be used for the timestamping of events with ms accuracy. Since, in both works, no actual synchronization between devices is performed, these approaches are not directly applicable to time synchronization.

The aim of this work is the wireless time synchronization of a remote device over potential distances of several kilometers with ns accuracy using LoRa modulation. In [18], we investigated the use of LoRa modulation for outdoor ranging and positioning, which we extend here to time synchronization. LoRa modulation is popular for low-data-rate IoT applications due to its large coverage of several kilometers and low energy consumption [19]. Compared to previous work on LoRa time synchronization in [11–14], we employ the ranging engine of the SX1280 transceiver from Semtech, which is intended for distance measurements. The ranging engine uses a two-way exchange with dedicated ranging packets containing 15 ranging symbols. Although no implementation details of the ranging engine are provided in the data sheet [20], a best-case standard deviation for distance measurement with the Development Kit of 0.4 m is reported in the application note [21], corresponding to 1.3 ns. This makes the SX1280 a suitable platform for implementing an experimental wireless time synchronization system with the aim of ns accuracy. Although [15] also uses the ranging engine of the SX1280, the system is implemented with a lower clock resolution, resulting in significantly lower accuracy. Compared to the method in [10], which does not use LoRa modulation but obtains similar performance to our system, we measure and compensate the time of flight between the two terminals, making it more suitable for ad hoc applications. To the best of our knowledge, this work is the first application of LoRa modulation for time synchronization that achieves ns accuracy.

2. Time Synchronization with LoRa Modulation

2.1. LoRa Modulation

Long-range (LoRa) modulation is a chirp spread spectrum (CSS) modulation that was developed by the Semtech Corporation [22] and has become popular for IoT applications. Each symbol consists of a cyclically shifted frequency ramp with a bandwidth BW, as shown in Figure 1.

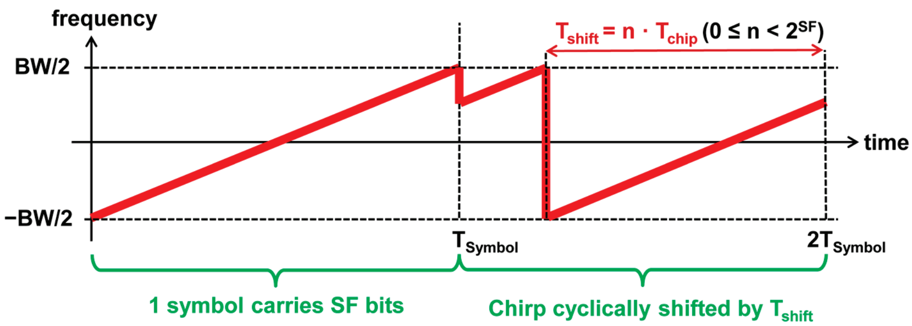

Figure 1. LoRa modulation.

The information to be transmitted is modulated on the symbol by 2^{SF} possible cyclic time shifts T_{shift} of the frequency ramp, whereby a symbol carries SF bits. The value SF is also termed spreading factor but does not play the same role as in code-division multiple-access (CDMA) systems, since the bandwidth can be configured independently of the spreading factor. The cyclic shift T_{shift} has a resolution of $T_{chip} = 1/BW$.

LoRa modulation is typically used in the license-free 863–870 MHz band in Europe and 902–928 MHz in North America. However, in Europe, the duty cycle is limited to 1 % and the effective radiated power (ERP) is limited to 14 dBm in most of the 863–870 MHz frequency range [23]. Since this duty cycle limitation would not allow for a regular packet exchange as required for time synchronization, in this work, the 2.4 GHz ISM frequency band was used for implementing the time synchronization system, where no duty cycle limitation is in place.

The SX1280 transceiver of Semtech was chosen, since it operates in the 2.4 GHz ISM frequency band and incorporates a ranging engine, which is primarily intended to measure the time of flight between two SX1280 transceivers [20]. The SX1280 supports bandwidths

$BW = 406,\ 812$ and 1625 kHz and spreading factors $SF = 5,\ 6,\ \ldots,\ 10$ for ranging. With the maximum bandwidth of 1625 kHz, a distance resolution of

$$d_R = \frac{c}{BW} = \frac{3 \cdot 10^8}{1625 \cdot 10^3} = 185 \text{ m} \tag{1}$$

can be achieved; see Section 2.1.3 in [24]. The distance resolution translates into a time-of-flight resolution of $t_{TOF} = d_R/c = 185/3 \cdot 10^8 = 617$ ns, which seems to be too large for a time synchronization system with a targeted accuracy in the ns range. However, since the time synchronization system must not resolve different multipaths but rather compensate the time of flight as seen by the system between the transmitter and receiver, it is possible to achieve a higher time synchronization accuracy than the limited temporal resolution provided by the relatively small signal bandwidth. This is shown by the time deviation of 3 ns obtained by the proposed system in Section 3.2, which is significantly lower than the time-of-flight resolution $t_{TOF} = 617$ ns. However, the accuracy will depend on the signal-to-noise ratio (SNR) [25].

Regarding the achievable range, the best RX sensitivity of -122 dBm is obtained with $BW = 406$ kHz and $SF = 10$, resulting in a maximum coupling loss of 134.5 dB for the maximum TX power of 12.5 dBm supported by the SX1280 ranging engine [20]. This corresponds to a range of several kilometers in a rural non-line-of-sight environment with omni-directional antennas.

2.2. Time Synchronization Protocol and Method

The time synchronization is based on the SX1280 PHY-layer ranging engine, which uses a two-way exchange for half-duplex systems according to Section 6.1 of [24] to determine the time of flight (TOF) between two SX1280 devices. With a two-way exchange, it is also possible to measure the clock offset between two terminals with unsynchronized clocks, which will be used here to align the clock of the secondary side to the reference clock on the primary side [26]. Figure 2 shows an overview of the developed time synchronization system. The external reference clock in the form of a 1 Hz PPS signal is input to the primary side, where it is used to synchronize the internal local clock to provide local timestamps. Using the subsequently described time synchronization protocol, the internal local clock on the secondary side is synchronized in frequency and phase to the primary side. The synchronized time is then provided as a 1 Hz PPS signal, with an additional 10 MHz reference frequency signal.

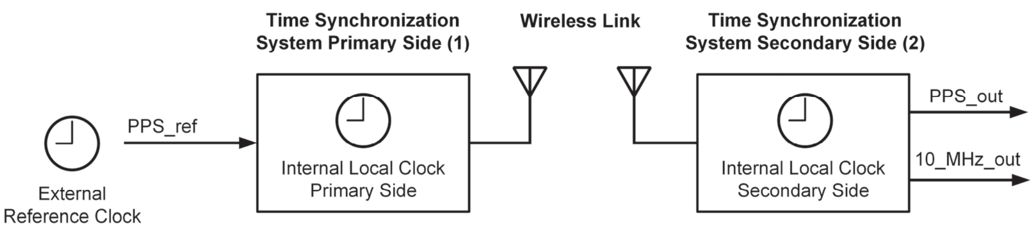

Figure 2. Experimental wireless time synchronization system.

In Figure 3, two sequential two-way exchanges between the primary and secondary side are shown, each consisting of a request, followed by a response after a fixed delay. The ranging engine of the SX1280 transceiver is primarily designed to measure the range between two devices based on the round-trip time of flight, which it determines using a single two-way exchange. To perform time synchronization with a single two-way exchange, both the transmit and receive interrupts (to determine a transmission and reception timestamp) of each of the two messages are required. However, the SX1280 ranging engine only provides transmit and receive interrupts for the response.

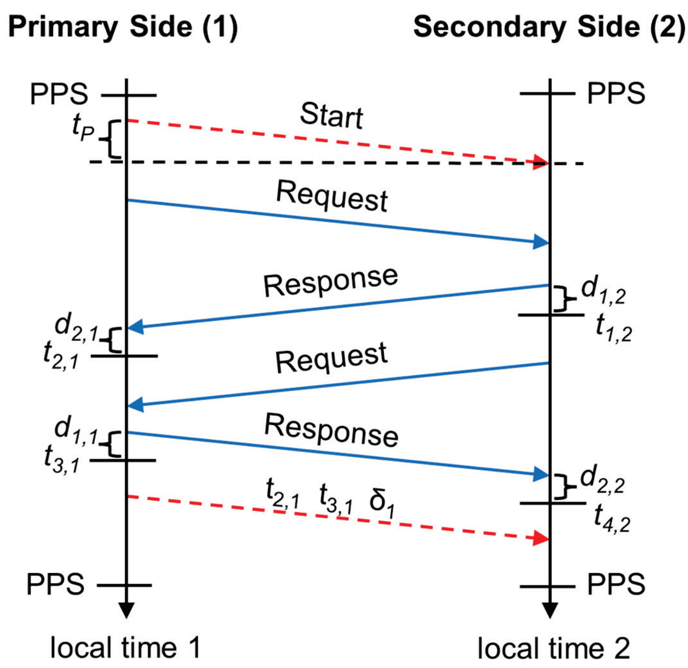

Figure 3. Ranging exchanges used for time synchronization.

Therefore, we use two sequential two-way ranging exchanges of the SX1280 to mimic a single two-way ranging exchange to provide the four required timestamps. By defining the timestamp $t_{a,b}$ in Figure 3 as the timestamp number a on side b, the transmit and receive interrupts are then used to obtain the corresponding four timestamps $t_{1,2}$, $t_{2,1}$, $t_{3,1}$ and $t_{4,2}$. To mark the beginning of the ranging exchanges, we use a start packet. Additionally, a packet with timestamps $t_{2,1}$, $t_{3,1}$ and the normalized local clock frequency δ_1 is sent from the primary to the secondary side at the end of the ranging exchanges, as described subsequently.

In the first ranging exchange, started from the primary side according to Figure 3, the timestamp number 1 at the secondary side (2) $t_{1,2}$ is measured, as well as the timestamp number 2 at the primary side (1) $t_{2,1}$. These two timestamps correspond to the transmission time of the response plus an internal delay $d_{1,2}$ and to the reception time of the response plus an internal delay $d_{2,1}$ on side 2 and side 1, respectively. In the second ranging exchange, started from the secondary side, the timestamps number 3 and 4 are measured, at the primary side (1) as $t_{3,1}$ and at the secondary side (2) as $t_{4,2}$. These timestamps also include their corresponding internal delays.

The timestamps are measured using local unsynchronized clocks (a free running timer on the primary and secondary side), as the controller only moves the position of the one-second period start to synchronize the local clock on both sides. The one-second period start corresponds to the positions of the PPS marker shown in Figure 3. This PPS marker corresponds on the secondary side to the synchronized time information. It should be noted that Figure 3 shows the synchronized state, where the PPS marker positions of the primary and secondary side have been aligned. Therefore, the local timestamps from the free running timers must be corrected to reflect the correction of the control algorithm on the local clock. For the local time on the primary side (1) as an example, this corrected time is

$$t_{2,1corr} = \frac{t_{2,1}}{\delta_1} \tag{2}$$

in which the locally measured unsynchronized timestamp 2 on the primary side 1, expressed as $t_{2,1}$, is translated into timestamp 2 with the correction of the control algorithm $t_{2,1corr}$. The correction value is the normalized frequency of the timer on the primary side,

$$\delta_1 = 1 + \frac{\Delta f_1}{f_{nominal}}, \tag{3}$$

where Δf_1 is the frequency error and $f_{nominal}$ is the nominal frequency of the local timer. The local time on the secondary side can be corrected in an analogous way. Equation (2) may also be rewritten to calculate local unsynchronized times from corrected times.

Time synchronization can be achieved by minimizing the time error Δt_2 between the timestamp $t_{1,2}$ in the local unsynchronized time of side 2 and the nominal timestamp $t_{1,2,nominal}$, which is also in the local unsynchronized time 2 but calculated from the reference time as shown subsequently. The same time offset can also be expressed using the timestamp $t_{4,2}$, resulting in

$$\Delta t_2 = t_{1,2} - t_{1,2,nominal} = t_{4,2} - t_{4,2,nominal}. \tag{4}$$

The measured value of Δt_2 is used as the control deviation by the controller of the local timer to adjust the position of the 1 s PPS marker. Using the correction in Equation (2) and by introducing the signal propagation time t_p between the two devices, the two nominal timestamps according to Figure 3 become

$$t_{1,2,nominal} = \left(\frac{t_{2,1}}{\delta_1} - \frac{d_{2,1}}{\delta_1} - t_p + \frac{d_{1,2}}{\delta_2} \right) \delta_2 \tag{5}$$

$$t_{4,2,nominal} = \left(\frac{t_{3,1}}{\delta_1} - \frac{d_{1,1}}{\delta_1} + t_p + \frac{d_{2,2}}{\delta_2} \right) \delta_2, \tag{6}$$

where t_p corresponds to the propagation delay plus any hardware delays (due to transmission lines, filters and the low-noise amplifier on the printed circuit board and RF cables). Since the channel is assumed to remain static during the two sequential two-way ranging exchanges, the delay t_p is constant. Additionally, t_p is assumed to be identical in both directions.

Combining Equations (4)–(6) produces

$$\Delta t_2 = \frac{1}{2}(t_{1,2} - t_{1,2,nominal}) + \frac{1}{2}(t_{4,2} - t_{4,2,nominal}) =$$

$$\frac{1}{2}\left[t_{1,2} - \left(\frac{t_{2,1}}{\delta_1} - \frac{d_{2,1}}{\delta_1} + \frac{d_{1,2}}{\delta_2} \right) \delta_2 + t_{4,2} - \left(\frac{t_{3,1}}{\delta_1} - \frac{d_{1,1}}{\delta_1} + \frac{d_{2,2}}{\delta_2} \right) \delta_2 \right]. \tag{7}$$

Although the datasheet of the SX1280 [20] does not specify the following values and they are not accessible to the user, based on our observations, we assume for the delays that $d_{1,1} = d_{1,2}$ and $d_{2,1} = d_{2,2}$ hold and that the values are < 20 µs. Furthermore, with the chosen local oscillator, the normalized frequency errors are guaranteed to fulfill

$\epsilon_1 = \Delta f_1 / f_{nominal} < \pm 1$ ppm and $\epsilon_2 = \Delta f_2 / f_{nominal} < \pm 1$ ppm. With these assumptions, we obtain

$$\left| \frac{d_{2,1}}{\delta_1} - \frac{d_{2,2}}{\delta_2} \right| < 40 \text{ ps}, \tag{8}$$

which is significantly smaller than the desired accuracy. An analogous statement can also be made for $d_{1,1}$ and $d_{1,2}$. With the above assumptions, the terms containing the delays $d_{2,1}$, $d_{2,2}$, $d_{1,1}$ and $d_{1,2}$ in Equation (7) are negligible. Consequently, the time offset in Equation (7) simplifies to

$$\Delta t_2 \approx \frac{1}{2} \left[t_{1,2} - \left(\frac{t_{2,1}}{\delta_1} \right) \delta_2 + t_{4,2} - \left(\frac{t_{3,1}}{\delta_1} \right) \delta_2 \right], \tag{9}$$

which expresses Δt_2 in terms of uncorrected local times on the secondary side 2. Equation (9) can be converted to the corrected local times on the secondary side 2 based on Equation (2) as

$$\Delta t_{2corr} = \frac{\Delta t_2}{\delta_2} \approx \frac{1}{2} \left(\frac{t_{1,2}}{\delta_2} - \frac{t_{2,1}}{\delta_1} + \frac{t_{4,2}}{\delta_2} - \frac{t_{3,1}}{\delta_1} \right). \tag{10}$$

Since the goal of the time synchronization is to minimize the time offset between the secondary and primary side, either Equation (9) or (10) may be used as a control input for adjusting the position of the 1 s PPS marker.

Equation (10) corresponds to a standard two-way ranging procedure [24], which is started from the secondary side, except for the addition of the time corrections. The correction values δ_1 and δ_2 are determined from the integral components of the employed proportional–integral (PI) controllers on the primary side 1 and secondary side 2, respectively, as described in Section 2.3.2. The value δ_1 is transmitted at the end of the ranging exchanges together with the stamps $t_{2,1}$ and $t_{3,1}$ from the primary to the secondary side, as shown in Figure 3. The initial values of δ_1 and δ_2 are set to zero.

2.3. Time Synchronization System Design

The following subsections describe the design and implementation of the wireless time synchronization system. This section is structured as follows. The first subsection provides an overview of a time synchronization device configured for primary-side and for secondary-side operation. The second subsection explains the measurement of the timestamp values $t_{1,2}$, $t_{2,1}$, $t_{3,1}$ and $t_{4,2}$, as well as the 1 Hz PPS signal generation. Next, the phase offset and cable delay compensation are described. The last subsection gives an overview of the implemented LoRa communication protocol and timing.

2.3.1. Overview

Figure 4 shows the block diagram of our wireless time synchronization system based on the LoRa transceiver SX1280. Starting at the antenna, an SAW filter and low-noise amplifier are used in the receive direction to improve the immunity against out-of-band interference and to reduce the total noise figure. The necessary RF switches to change between the receive and transmit direction are controlled by the MCU.

The STM32F474 microcontroller unit (MCU) contains the application that covers the tasks for communication protocol handling, including timestamp measurement, the PPS controller and the low-level hardware drivers, as well as the visualization of the network and time synchronization status on a display. National Marine Electronics Association (NMEA) compliant time and date information can be exchanged with the help of the RS232 and USB interfaces.

The internal and external clock signals are generated within an Analog Devices AD9545 "1 PPS synchronizer and jitter cleaner" using an Abracon AOCJY3A 100 MHz oven-controlled crystal oscillator (OCXO) with a rated frequency stability of 10 ppb. The 52 MHz clock for the LoRa transceiver and the 20 MHz clock for the MCU are generated from a primary analogue phase-locked voltage-controlled oscillator (VCO) that is linked to the OCXO, while the 1 Hz PPS and 10 MHz output signals are derived from a secondary phase-locked loop (PLL) with a VCO running at 2.46 GHz. This secondary PLL digitally compares the divided 1 Hz PPS output with a 1 Hz reference input and disciplines the underlying analogue PLL, which is also linked to the OCXO. This secondary PLL contains a 10 mHz loop filter used to clean up the signal by reducing the jitter and quantization noise of the output 1 Hz PPS signal. The OCXO and AD9545 are the main energy consumers, having a total steady state power consumption of 3 W.

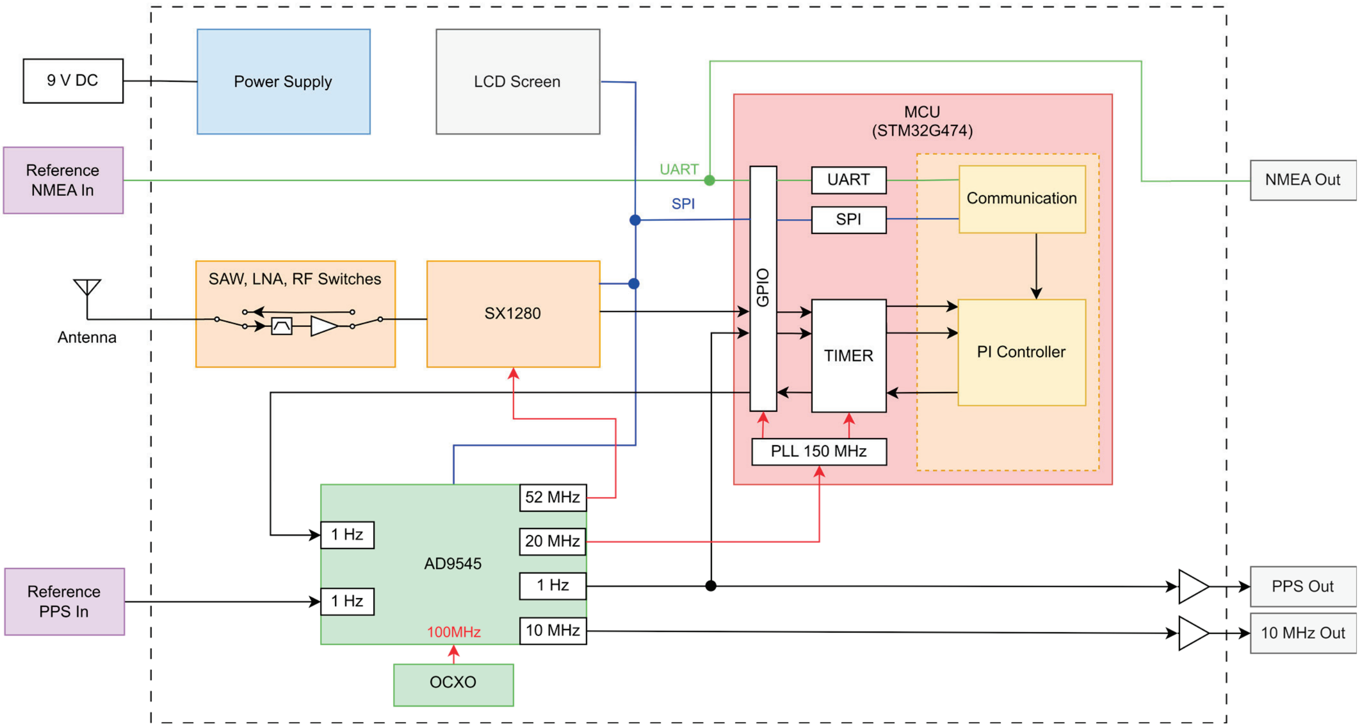

Figure 4. Wireless time synchronization system block diagram (primary-side and secondary-side operation shown).

The secondary PLL configuration depends on the device operating mode. For the primary side, the frequency and phase synchronization are based on the external 1 Hz PPS signal of the reference clock. The cleaned-up internal 1 Hz PPS signal output of the DPLL is then synchronous to the external reference clock and is measured by an internal 32-bit hardware timer of the MCU. This measurement is used to synchronize the internal local clock of the MCU, which serves as the time base for the application. Due to the limited counting frequency of 150 MHz for the timer, a time quantization error of up to ± 3.33 ns arises. This is also valid for the timestamp measurement of the interrupt signals $t_{1,2}$, $t_{2,1}$, $t_{3,1}$ and $t_{4,2}$ generated by the LoRa transceiver.

The secondary side uses the same timer to generate the 1 Hz PPS signal of the local clock based on the timestamps of the ranging exchanges using a PI controller. The secondary PLL uses this 1 Hz PPS signal as reference and reduces its quantization error to the sub-ns range in the 1 Hz PPS output signal.

2.3.2. Timer-Based Timestamp Measurement and 1 Hz PPS Generation

An internal 32-bit hardware timer of the MCU running at 150 MHz is used to measure the timestamps of the interrupt signals and to generate the output 1 Hz PPS signal of the MCU on the secondary side. The timer clock signal is derived from the OCXO without frequency offset correction. It is configured to count from 0 to $P - 1$ and restarts again from 0, where P is the overflow or 1 Hz period value. P is initially set to $P_N = 150 \cdot 10^6$, which corresponds to the nominal duration of one period of the 1 Hz PPS signal.

The frequency and phase offset measurement between the 1 Hz PPS signal of the external reference clock cleaned up by the DPLL and the internal local clock on the primary side is performed with one input capture/compare channel. The first 1 Hz PPS timestamp measurement is used to correct the coarse phase offset by adapting the overflow value P for one period and then switches back to $P = P_N$. The following measurements are then expected to be within some microseconds before or after an overflow (corresponding to the positions of the PPS marker shown in Figure 3) and are fed as time error values Δt_{ref} to the PI controller. Small positive values are measured when an overflow event occurs before receiving the reference 1 Hz PPS signal, which indicates a too-high local oscillator frequency and vice versa.

The PI controller is responsible for adapting the overflow value P to align the phase of the PPS Out signal to the phase of the reference signal and increases P in case of a too-high local oscillator frequency to compensate the deviation. This is implemented according to

$$P = P_N + K_P \Delta t_2 + K_I \int_0^t \Delta t_{ref}, \tag{11}$$

where $K_P = 0.05$ and $K_I = 0.005$ are heuristically determined constants.

The normalized local clock frequency error can be determined by

$$\epsilon = \frac{P}{P_N} - 1 = \frac{\Delta f}{f_{nominal}} \tag{12}$$

and the correction value required for the time synchronization method in Section 2.2 corresponds to

$$\delta = \epsilon + 1 = \frac{P}{P_N} \tag{13}$$

where δ can stand for δ_1 or δ_2 depending on the device operation mode.

The secondary side uses the calculated time error $\Delta t_{ref} = \Delta t_2$ from (9) as input to the PI controller, which adapts the timer overflow period in the same way as for the primary side. The interrupt timestamp measurements are also made using capture/compare channels.

2.3.3. Phase Offset and Cable Delays

Internal delays between the connectors and the integrated circuits, such as transmission lines on the printed circuit board, level-shifters, filters and the low-noise amplifier, have been measured and are compensated in the firmware.

However, external delays, for example, due to cables carrying PPS signals, can vary between setups. To remove setup-dependent external delays, the system was calibrated using an RF transmission over a coaxial cable of 75 m electrical length with one node placed in an RF shielding box to avoid coupling over the air between the two nodes. The PPS Out of the two devices can be measured with an oscilloscope at the cable ends to determine the time difference. This difference can be configured and compensated in one of the two devices.

2.3.4. Communication Protocol

The devices of the wireless time synchronization system use a simple protocol to identify and to help to set up the required wireless links. They randomly transmit beacon messages every 3 to 5 s containing a unique device address. These beacon messages combined with a received signal power measurement within the LoRa transceiver can be used to check the antenna setup and wireless link quality. The communication and ranging/synchronization exchanges are performed in the 2.4 GHz ISM frequency band at a bandwidth $BW = 812$ kHz and the LoRa spreading factor SF10, which is a compromise between time-of-flight resolution and range based on the specified sensitivity of the SX1280 [20]. Using $BW = 812$ kHz obtains only half the distance resolution compared to $BW = 1625$ kHz, but has a 6 dB higher sensitivity, which leads to a higher SNR and improved accuracy for timestamp measurements.

The primary device first sends a start packet as shown in Figure 3, which contains the target address, and it then switches to the ranging mode to perform the two sequential two-way ranging exchanges. It finally switches back to the data transmission mode and sends the timestamp values $t_{2,1}$ and $t_{3,1}$ together with the normalized clock frequency δ_1 to the secondary side if the exchange could successfully be finalized. Additionally, not shown in Figure 3, a UNIX timestamp in seconds is sent to the secondary side. This procedure is performed every second, 700 ms after the timer overflow event, and takes about 200 ms.

3. Results

3.1. Setup

The performance of the time synchronization system was assessed with a GPS-disciplined atomic clock and a WR link for transfer of the reference time as illustrated in Figure 5. The reference time in the form of a 1 Hz PPS signal (PPS_ref) is transferred to the primary synchronization device over a WR optical fiber link having a maximal time deviation (TDEV) of 30 ps over the measurement interval. Compared to a setup with two separate atomic clocks (one at either side of the time synchronization system), this setup does not suffer from phase drifts of the atomic clocks due to temperature changes. The reference time signal PPS_ref′ is then transferred by the time synchronization system over the LoRa RF link back to the secondary synchronization device, where the synchronized 1 Hz PPS time signal PPS_out is compared to the atomic clock time pulse on an oscilloscope. The time differences are then recorded on the oscilloscope to calculate the TDEV.

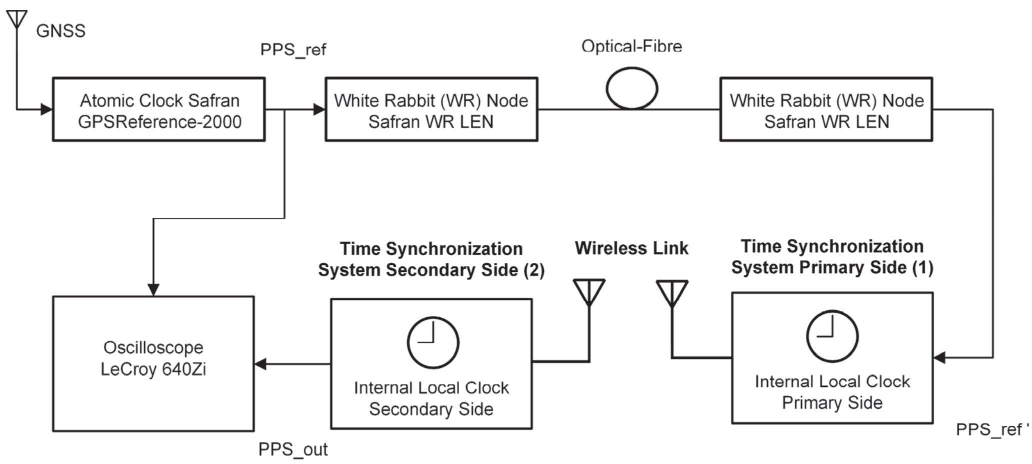

Figure 5. Field test setup.

The time synchronization system is set up with a line-of-sight link distance of about 170 m between the roofs of the two buildings shown in Figure 6. There was additionally several meters of coaxial RF cable between the antennas and time synchronization system devices. In the first setup, two 10 dBi directional patch antennas were used on both sides of the wireless link. In the second setup, the primary side used the same 10 dBi directional patch antenna while the secondary side used an omni-directional rod antenna with a gain of 2 dBi. Even though no channel measurements were conducted, in the second setup, a more pronounced multipath propagation is expected compared to the first setup. The equipment was set up in a weather-protected environment at both ends (container room at the secondary side and a metal box at the primary side), but without temperature control.

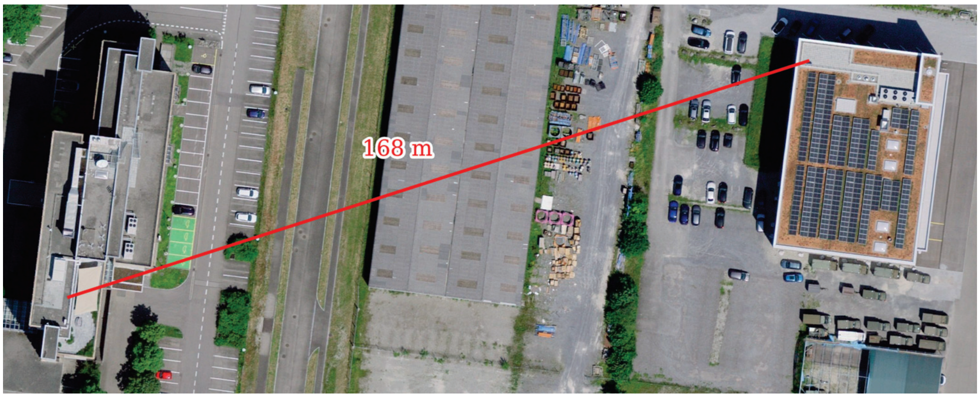

Figure 6. Field test with wireless link setup between two buildings (source: Federal Office of Topography swisstopo).

3.2. Results Time Synchronization Performance

Figure 7 shows the measured time differences between the 1 Hz PPS signals PPS_ref and PPS_out after a few minutes of operation to allow for the stabilization of the control algorithm. The measurement was started without the compensation of external cable delays, leading to a considerable time difference of about 90 ns until nearly 9000 s. At this point, the external PPS cable delays were manually configured, which compensates the time difference.

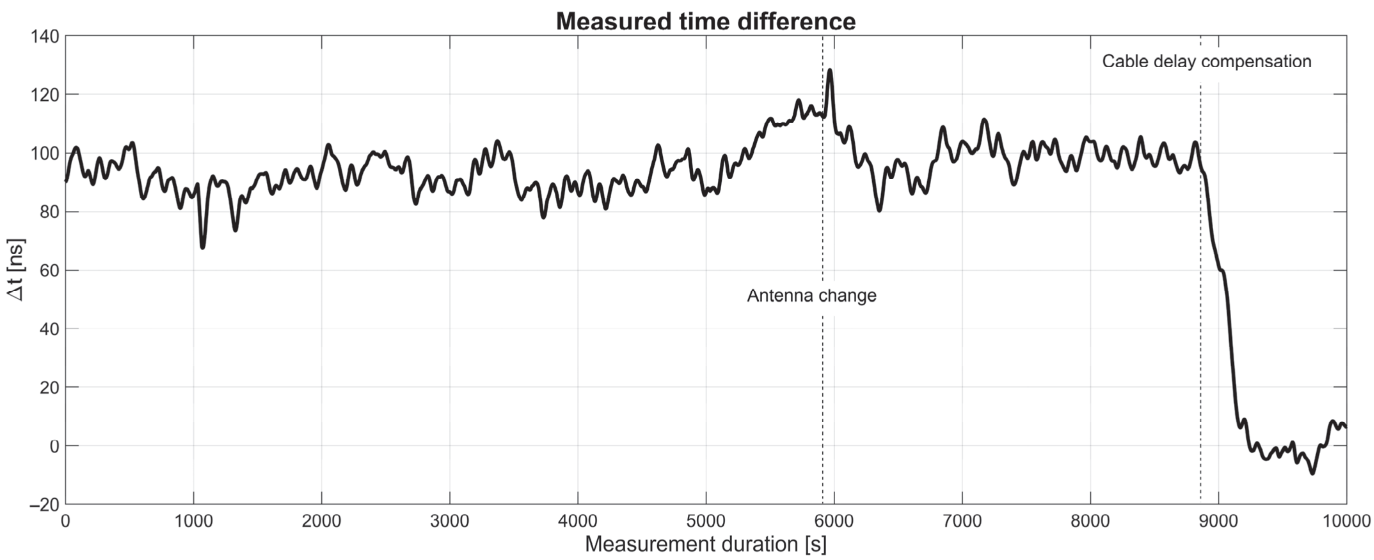

Figure 7. Measured time differences.

The first 5900 s was recorded with the first setup using patch antennas at both sides of the wireless link, at which point the antenna on the secondary side was swapped for an omni-directional rod antenna. This second setup was active starting at 6000 s. It can be observed from Figure 7 that there is no obvious change in the behavior of the time difference when using the second setup with an omni-directional antenna on one side.

Figure 8 shows the TDEV for setup 1 (patch antennas) and setup 2 (patch and omni-directional rod antenna), which was calculated using Stable32 [27] according to the National Instggitute of Technology's Handbook of Frequency Stability Analysis [28]. The deviations for 1 s intervals are 30 ps and increase to 3 ns in the average time interval from 2 s to 60 s. The deviations for both setups reach a plateau at around 3 ns for longer average times. Both setups obtain comparable performance, even though a stronger multipath propagation is expected with setup 2 compared to setup 1. This suggests that the system has a certain robustness against multipath propagation, which could be explained by the fact that the time synchronization system only needs to compensate the time of flight as measured by the system, while it is not required to resolve the individual propagation paths. The small TDEV difference between the two setups may partially be also due to the lack of a temperature-controlled environment for the equipment.

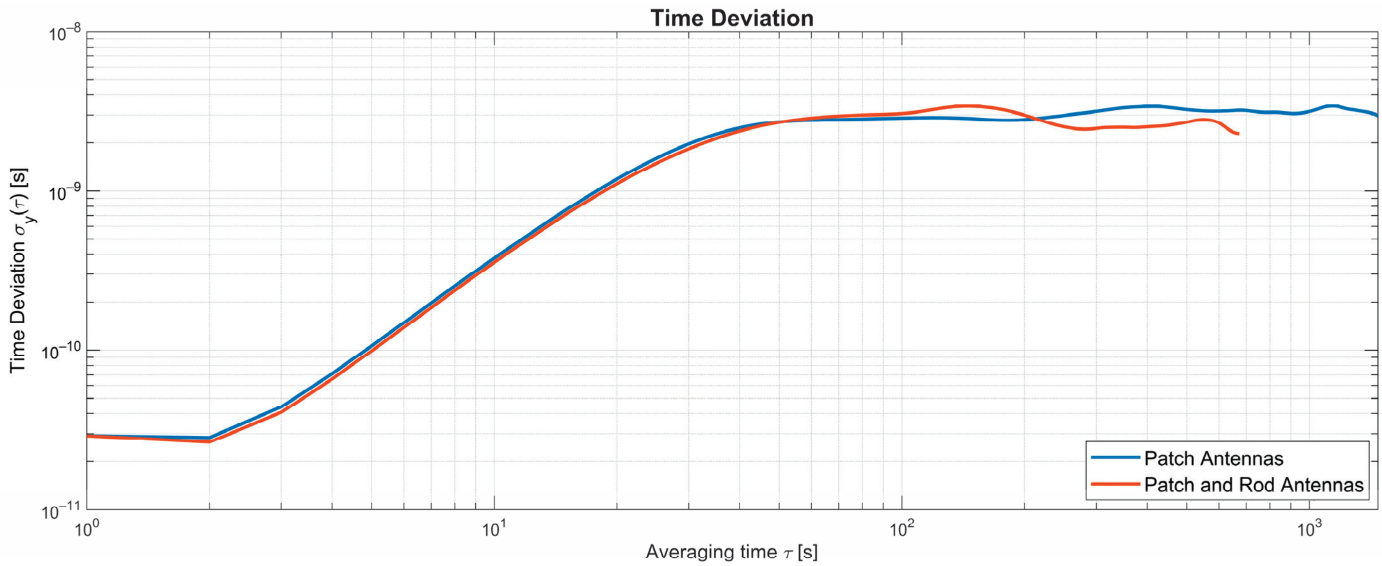

Figure 8. Measured time deviation (TDEV).

A separate measurement of one-day duration showed that the TDEV remains constant at a plateau of around 3 ns.

3.3. Operation over Large Distances

An early version of the time synchronization system has been operated with reliable ranging exchanges over a wireless link distance of 14 km with a line of sight between the primary and secondary side and using directional antennas with a gain of 24 dBi. By reducing the transmit power, it is possible to operate the link within the 10 dBm effective isotropic radiated power (EIRP) limit for devices without spectrum-sharing mechanisms operating in the 2.4 GHz ISM frequency band in Europe [23]. However, since the Analog Devices AD9545 jitter cleaner had not been implemented yet and no WR link for accurate transfer of the reference time was available, comparable time synchronization performance measurements were not possible. Nevertheless, this test indicates that time synchronization over distances of several kilometers is feasible.

3.4. Conclusions

The measured time deviations between the two synchronization devices were below 3 ns for a 170 m free-space link operating for one day. The time deviation for short intervals reduced to 30 ps for one-second intervals, which is mainly due to the frequency stability of the OCXO combined with the Analog Devices AD9545 jitter cleaner. The combination of a LoRa-based time synchronization and an adequate PLL loop circuit enabled the distribution of time information in the ns range. This is a significantly higher accuracy compared to previous work on time synchronization with LoRa modulation, which has reported accuracies in the µs range.

The channel occupancy amounts to about 20% and allows for more frequent synchronization exchanges, which would be beneficial for applications with mobile devices, and enables a multi-node network with up to five secondary devices in a star topology network without incurring accuracy losses due to time synchronization over multiple hops.

4. Discussion

This work demonstrates the usage of the low-power LoRa communication protocol to synchronize two devices with ns accuracy. The experimental wireless time synchronization system could be used in sensor networks for the synchronization of nodes and additionally for the transfer of small data volumes. The wireless approach is particularly suited to mobile applications or in terrain where cables are difficult to lay. The measured time deviation of 3 ns equals a range error of less than 1 m of wireless propagation, which makes it suitable for radio localization.

Table 1 provides a benchmark comparison between different time synchronization methods. GNSS-based synchronization obtains a TDEV of 1.5 ns ($\tau = 100$ s), using post-processing to remove the effect of the limited time quantization of the PPS pulse provided by the u-blox ZED-F9T module used in [3]. The optical-cable-network-based WR technology achieves the lowest TDEV, with 3 ps in the setup in [29] for $\tau = 100$ s. For the UWB system in [9], a standard deviation of 840 ps is reported, but no TDEV values. Our proposed system obtains an accuracy of 3 ns for $\tau = 100$ s, which is twice the value for GNSS-based synchronization. Compared to the simple deployment of GNSS synchronization, our system also has a higher deployment complexity and energy consumption, but the advantage is that it can be operated independently from other systems, as is the case with WR and UWB synchronization. However, UWB systems have a range of only a few tens of meters, while WR requires an optical cable network.

Table 1. Benchmark comparison of different time synchronization methods based on TDEV with average durations τ = 1 s and 100 s.

Technology	TDEV	Power Consumption (One Node)	Deployment Complexity
GNSS [3]	200 ps ($\tau = 1$ s) 1.5 ns ($\tau = 100$ s)	0.26 W	low
WR [1] [29]	30 ps ($\tau = 1$ s) 3 ps ($\tau = 100$ s)	7.5 W	high
UWB [9]	No TDEV reported (standard deviation $\sigma = 840$ ps)	0.7 W	medium
Proposed LoRa system	30 ps ($\tau = 1$ s) 3 ns ($\tau = 100$ s)	3.0 W	medium-high

[1] A 50 km fiber connection between two WR nodes.

The deployment complexity for GNSS time synchronization is low since only the installation of an outdoor GNSS antenna is required. For WR, the deployment requires a Synchronous Ethernet (SyncE) network and an external reference clock for the primary side, while, for UWB, the deployment requires an external reference clock for the primary side. Finally, for our proposed system, an outdoor antenna and an external reference clock at the primary side is required.

Considering the obtained TDEV of 3 ns for $\tau = 100$ s for our system, we assume that a large contributor is the ranging engine in the SX1280 transceiver, which has a reported best-case standard deviation equivalent to 1.3 ns, as described in Section 1.

The implementation of encryption and authentication protocols, which are well established in LoRaWAN links [30], may be used for secured operation. This is in contrast with GNSS-based systems, which often rely on the unencrypted GPS and Galileo L1 signals.

The presented system uses power-intensive PLL chips and oven-controlled oscillators to create a frequency-stable reference clock. However, this is not suitable for low-power devices. To reduce the power consumption, unheated oscillators and a simpler clock filter are needed, which could lead to higher time deviations. This may partially be compensated with improved oscillator drift and noise modeling. Oscillator modeling can also be used to minimize the number of synchronization exchanges and adapt to predicted timestamp uncertainty.

Considering other applications, mesh networks could benefit from accurate time to optimize the channel access and active/sleep timing slots. Additionally, the security of wireless networks could be improved by tightening timing restrictions against replay attacks.

The presented time synchronization system was optimized for static line-of-sight links without time-varying multipath fading. The extension of the system to mobile time synchronization would have practical applications, such as the time synchronization of equipment in vehicles. However, in such applications, the channel would be time varying, and the coherence time may be below the duration of one time synchronization exchange. Future work could therefore optimize the physical layer modulation and protocol for applications in mobile time synchronization.

Author Contributions: Hardware development, D.B.; hardware and software development, P.M.; investigation, P.M.; methodology and supervision, L.S.; writing—original draft, P.M. and L.S., writing—review and editing, D.B. All authors have read and agreed to the published version of the manuscript.

Funding: This research was funded by armasuisse W+T, contract number 8003536460.

Institutional Review Board Statement: Not applicable.

Informed Consent Statement: Not applicable.

Data Availability Statement: The original contributions presented in this study are included in the article material. Further inquiries can be directed to the corresponding author.

Acknowledgments: The authors would like to thank armasuisse W+T for providing the atomic clocks and access to a suitable test site with a WR link.

Conflicts of Interest: The funders have agreed to the publication of the results and provided access to a suitable test site.

References

1. Chowdhury, D.D. *NextGen Network Synchronization*, 1st ed.; Springer: Cham, Switzerland, 2021; ISBN 978-3-030-71178-8.
2. Kaplan, E.D.; Hegarty, C.J. *Understanding GPS/GNSS Principles and Applications*, 3rd ed.; Artech House: London, UK, 2017; pp. 144–148, ISBN 978-163-081-058-0.

3. Aanen, M.; Lavrenko, A.; Woodward, G. Evaluation of GNSS-based Time Synchronisation for ToF Localisation with Software-Defined Radio. In Proceedings of the 2023 IEEE 98th Vehicular Technology Conference (VTC2023-Fall), Hong Kong, China, 10–13 October 2023. [CrossRef]
4. Dierikx, E.F.; Wallin, A.E.; Fordell, T.; Myyry, J.; Koponen, P.; Merimaa, M.; Pinkert, T.J.; Koelemeij, J.C.J.; Peek, H.Z.; Sments, R. White Rabbit Precision Time Protocol on Long-Distance Fiber Links. *IEEE Trans. Ultrason. Ferroelectr. Freq. Control* **2016**, *63*, 945–952. [CrossRef] [PubMed]
5. Shen, Q.; Guan, J.-Y.; Ren, J.-G.; Zeng, T.; Hou, L.; Li, M.; Cao, Y.; Han, J.-J.; Lian, M.-Z.; Chen, Y.-W.; et al. Free-space dissemination of time and frequency with 10^{-19} instability over 113 km. *Nature* **2022**, *610*, 661–666. [CrossRef] [PubMed]
6. Kaushal, H.; Jain, V.K.; Kar, S. *Free Space Optical Communication*; Springer: New Delhi, India, 2017; pp. 50–52, ISBN 978-81-322-3691-7.
7. Masood, W.; Schmidt, J.F.; Brandner, G.; Bettstetter, C. DISTY: Dynamic Stochastic Time Synchronization for Wireless Sensor Networks. *IEEE Trans. Ind. Inform.* **2017**, *13*, 1421–1429. [CrossRef]
8. Djenouri, D.; Bagaa, M. Synchronization Protocols and Implementation Issues in Wireless Sensor Networks: A Review. *IEEE Syst. J.* **2016**, *10*, 617–627. [CrossRef]
9. Dongare, A.; Lazik, P.; Rajagopal, N.; Rowe, A. Pulsar: A Wireless Propagation-Aware Clock Synchronization Platform. In Proceedings of the 2017 IEEE Real-Time and Embedded Technology and Applications Symposium (RTAS), Pittsburgh, PA, USA, 18–21 April 2017. [CrossRef]
10. Locata Corporation. Locata Technology Demonstration for the European Commission Technical Report v1.5, 2022. Available online: https://www.locata.com/s/7-JRC-DEFIS-Appendix-Report_Locata.pdf (accessed on 24 January 2025).
11. Huan, X.; Chen, W.; Wang, T.; Hu, H. A Microsecond Energy-Efficient LoRa Time Synchronization Based on Low-Layer Timestamping and Asymmetric Time Translation. *IEEE Trans. Veh. Technol.* **2024**, *73*, 7328–7332. [CrossRef]
12. Huan, X.; Chen, W.; Wang, T.; Hu, H.; Zheng, Y. A One-Way Time Synchronization Scheme for Practical Energy-Efficient LoRa Network Based on Reverse Asymmetric Framework. *IEEE Trans. Commun.* **2023**, *71*, 6468–6481. [CrossRef]
13. Ramirez, C.G.; Sergeyev, A.; Dyussenova, A.; Iannucci, B. LongShoT: Long-Range Synchronization of Time. In Proceedings of the 18th ACM/IEEE International Conference on Information Processing in Sensor Networks (IPSN), Montreal, QC, Canada, 16–18 April 2019; pp. 289–300.
14. Singh, R.K.; Berkvens, R.; Weyn, M. Time Synchronization with Channel Hopping Scheme for LoRa Networks. In *Advances on P2P, Parallel, Grid, Cloud and Internet Computing*; Barolli, L., Hellinckx, P., Natwichai, J., Eds.; Springer: Cham, Switzerland, 2020; Volume 96, pp. 786–797. ISBN 978-3-030-33508-3.
15. Zhendong, R.; Zhou, Y.; Wang, H.; Sun, X. Clock synchronization method for micro-power wireless networks based on LoRa ranging. In Proceedings of the International Conference on Smart Grid and Green Energy (ICSGGE 2022), Hangzhou, China, 20–22 May 2022.
16. Gu, C.; Jiang, L.; Tan, R.; Li, M.; Huang, J. Attack-aware data timestamping in low-power synchronization-free LoRaWAN. In Proceedings of the 2020 IEEE 40th International Conference on Distributed Computing Systems (ICDCS), Singapore, Singapore, 29 November–1 December 2020. [CrossRef]
17. Rizzi, M.; Depari, A.; Ferrari, P.; Flammini, A.; Rinaldi, S.; Sisinni, E. Synchronization uncertainty versus power efficiency in LoRaWAN networks. *IEEE Trans. Instrum. Meas.* **2019**, *68*, 1101–1111. [CrossRef]
18. Müller, P.; Stoll, H.; Sarperi, L.; Schüpbach, C. Outdoor Ranging and Positioning based on LoRa Modulation. In Proceedings of the 2021 International Conference on Localization and GNSS (ICL-GNSS), Tampere, Finland, 1–3 June 2021.
19. Gkotsiopoulos, P.; Zorbas, D.; Douligeris, C. Performance Determinants in LoRa Networks: A Literature Review. *IEEE Commun. Surv. Tutor.* **2021**, *23/3*, 1721–1758. [CrossRef]
20. SX1280 LoRa Connect™ Long Range Low Power LoRa® 2.4GHz RF Transceiver with Ranging. Available online: https://www.semtech.com/products/wireless-rf/lora-connect/sx1280 (accessed on 24 January 2025).
21. Application Note: An Introduction to Ranging with the SX1280 Transceiver. Available online: https://www.semtech.com/products/wireless-rf/lora-connect/sx1280 (accessed on 20 February 2025).
22. LoRa® and LoRaWAN®. Available online: https://www.semtech.com/uploads/technology/LoRa/lora-and-lorawan.pdf (accessed on 24 January 2025).
23. ERC Recommendation 70-03. Available online: https://docdb.cept.org/download/25c41779-cd6e/Rec7003e.pdf (accessed on 24 January 2025).
24. Bensky, A. *Wireless Positioning Technologies and Applications*, 2nd ed.; Artech House: Norwood, MA, USA, 2016; ISBN 978-1-60807-951-3.
25. Stein, S. Algorithms for ambiguity function processing. *IEEE Trans. Acoust. Speech Signal Process.* **1981**, *29*, 588–599. [CrossRef]
26. Levine, J. A review of time and frequency transfer methods. *Metrologia* **2008**, *45*, 162–174. [CrossRef]

27. Welcome to the Stable32 Web Site. Available online: http://www.stable32.com (accessed on 24 February 2025).
28. Riley, W.J. *Handbook of Frequency Stability Analysis*; Special Publication (NIST SP), National Institute of Standards and Technology: Gaithersburg, MD, USA, 2008.
29. Smotlacha, V.; Vojtech, J. White Rabbit in the Czech Time and Frequency Transfer Infrastructure. In Proceedings of the 2020 Joint Conference of the IEEE International Frequency Control Symposium and International Symposium on Applications of Ferroelectrics (IFCS-ISAF), Keystone, CO, USA, 19–23 July. [CrossRef]
30. Tsai, K.-L.; Leu, F.-Y.; You, I.; Chang, S.-W.; Hu, S.-J.; Park, H. IEEE: Low-Power AES Data Encryption Architecture for a LoRaWAN. *IEEE Access* **2019**, *7*, 146348–146357. [CrossRef]

sensors

MDPI

Article

LoRa Communications Spectrum Sensing Based on Artificial Intelligence: IoT Sensing

Partemie-Marian Mutescu, Valentin Popa and Alexandru Lavric *

Faculty of Electrical Engineering and Computer Science, Ștefan Cel Mare University of Suceava, 720229 Suceava, Romania; marian.mutescu@usm.ro (P.-M.M.)
* Correspondence: lavric@usm.ro

Abstract: The backbone of the Internet of Things ecosystem relies heavily on wireless sensor networks and low-power wide area network technologies, such as LoRa modulation, to provide the long-range, energy-efficient communications essential for applications as diverse as smart homes, healthcare, agriculture, smart grids, and transportation. With the number of IoT devices expected to reach approximately 41 billion by 2034, managing radio spectrum resources becomes a critical issue. However, as these devices are deployed at an increasing rate, the limited spectral resources will result in increased interference, packet collisions, and degraded quality of service. Current methods for increasing network capacity have limitations and require advanced solutions. This paper proposes a novel hybrid spectrum sensing framework that combines traditional signal processing and artificial intelligence techniques specifically designed for LoRa spreading factor detection and communication channel analytics. Our proposed framework processes wideband signals directly from IQ samples to identify and classify multiple concurrent LoRa transmissions. The results show that the framework is highly effective, achieving a detection accuracy of 96.2%, a precision of 99.16%, and a recall of 95.4%. The proposed framework's flexible architecture separates the AI processing pipeline from the channel analytics pipeline, ensuring adaptability to various communication protocols beyond LoRa.

Keywords: artificial intelligence; internet of things; LoRa; LPWAN; spectrum sensing

1. Introduction

The Internet of Things (IoT) transformed many industries and daily life by connecting the physical world to the Internet through devices that can collect, interact, and send data to the Internet using sensors, actuators, and wireless communication protocols [1]. With this in mind, wireless sensor networks (WSNs) have become the key enablers of the IoT ecosystem, using low-power wide area network (LPWAN) technologies to send and receive data from gateways and sink nodes [2]. LPWAN technologies offer long-range and energy-efficient communication that makes them suitable for many IoT applications, such as smart homes [3], healthcare [4], agriculture [5], smart grids [6], and transportation [7]. The IoT market experienced significant growth due to the versatility of its applications. Research shows that the number of IoT devices is growing by approximately 2 billion each year. Projections show that there will be around 41 billion connected IoT devices by the year 2034 [8]. Most LPWAN technologies use unlicensed frequency bands, such as the 868 MHz short-range devices (SRD) band, the 915 MHz band, and the 2.4 GHz industrial, scientific, and medical (ISM) band [9–11]. Each of these bands has its own bandwidth limitations.

For example, the 868 MHz SRD band has only 10 MHz of available bandwidth, while the 915 MHz and 2.4 GHz bands have 28 MHz and 100 MHz of available bandwidth, respectively. Currently, one of the most widely adopted LPWAN communication technologies worldwide is LoRa [12], which accounts for approximately 40% of global IoT connectivity. The increasing use of LoRa in IoT networks with limited radio resources presents several challenges, including higher packet collision rates, interference, and reduced capacity, which can lead to lower quality of service (QoS). Current methods of increasing scalability, such as duty cycle regulations [13] and redundancy mechanisms [14], are not always effective in addressing these issues, especially in large-scale, high-density deployments. Recent research proposed alternative modulation techniques aimed at improving performance in LPWAN environments. One example is dual-mode chirp spread spectrum (DM-CSS) modulation [15], which enhances spectral efficiency by simultaneously multiplexing even and odd chirp signals with phase shifts, resulting in a significant increase in the number of transmitted bits per symbol. DM-CSS demonstrated higher spectral and energy efficiency compared to classical LoRa modulation, making it a promising candidate for future IoT networks operating in crowded unlicensed spectrum environments.

Another approach is represented by advanced solutions, such as spectrum sensing (SS) techniques. These techniques allow us to detect and identify different wireless protocols operating within shared frequency bands [16–19]. This allows the IoT network operators to dynamically allocate frequencies and reduce interference. This approach is critical to maintaining optimal performance, reliability, and scalability of LoRa-based IoT networks, ensuring their continued growth and integration into future IoT infrastructure.

In addition, advanced channel analytics provide network operators with insights to evaluate scalability issues within the LoRa network architecture. Optimal allocation of spreading factors (SF) is essential to mitigate the capture effect and enhance network capacity [20]. In large-scale, high-density LoRa networks, the capture effect occurs at the gateway when multiple LoRa transmissions simultaneously arrive on the same communication channel and use identical SFs. Under these conditions, the gateway successfully demodulates only the signal with the highest received power, while all other transmissions are discarded, increasing packet error rates. Nevertheless, due to LoRa's use of SFs that are theoretically orthogonal [21], a gateway can typically extract and demodulate multiple signals transmitted simultaneously on the same frequency channel, provided that different SFs are used. This orthogonality is a fundamental property that underpins the scalability of LoRa-based networks, allowing multiple devices to share limited spectrum resources efficiently. However, it is important to recognize that perfect orthogonality is difficult to achieve in practical applications. Real-world factors such as timing misalignments between transmitters, carrier frequency offsets, and differences in received signal power can introduce imperfections that reduce the degree of orthogonality. These impairments may lead to inter-SF interference, especially in dense network scenarios where simultaneous transmissions are more frequent. Several studies, such as [22], analyzed the impact, demonstrating that LoRa's performance under real-world conditions can deviate from the idealized assumptions often made in theoretical models. In this context, while LoRa SFs offer strong resilience to interference under many operating conditions, it is important for network designers and operators to consider potential cross-interference when planning large-scale IoT deployments. Proper SF allocation strategies, along with synchronization and power control mechanisms, can help mitigate the practical limitations of SF orthogonality and improve overall network performance.

Live network monitoring tools based on SS techniques can help operators track how SF is being allocated. These tools can identify edge cases where sensors excessively use either SF7, which is good for low-latency applications, or SF12, which supports long-range but uses more energy, has higher time-on-air (ToA), and higher collision risks. The SS techniques make LoRa networks more adaptable by allowing SF assignments based on the sensing results. This helps address network optimization from a latency, power, and range perspective according to the specific needs of IoT applications. It also provides deeper insight into network behavior, enabling proactive intervention and more accurate troubleshooting of devices that consistently use inefficient SFs schemes.

The importance of spectral constraints and SF allocation in LoRa networks has been studied previously. Lavic et al. [23] have shown that a maximum number of 8000 nodes can simultaneously transmit LoRa packets to a gateway with an imposed duty cycle of 1%. Farhad et al. [24] propose a DL-based LoRa ADR mechanism that increases the packet success rate by up to 15% with 600 transmitting LoRa nodes. Housem et al. [25] propose and evaluate an artificial intelligence (AI)-based LoRaWAN optimization method using auto-regressive algorithms, support vector machines (SVMs), and temporal fusion transformers (TFTs). The authors employ these algorithms for network behavior prediction. Based on these predictions, they propose an optimization mechanism that conserves a percentage of the available duty cycle for anticipated increase in LoRaWAN network traffic.

Aohan et al. [26] proposes and evaluates an RL-based resource allocation mechanism for LoRaWAN networks. In his approach, the learning agent is represented by a LoRaWAN node that can choose its communication channel and SF, transmits the data frame to the LoRaWAN gateway, and receives an ACK or NACK response. If the transmission receives an ACK, the LoRaWAN node is rewarded, otherwise it is penalized. According to Aohan et al. [26], the proposed methodology can maintain an FSR of 1 for up to six simultaneously transmitting LoRaWAN devices, with the FSR dropping to 0.5 when the number of devices increases to eight. This method is compared to the random channel and SF selection mechanism, which has an FSR of 0.4 at six LoRa nodes, dropping below 0.3 when increasing to eight LoRaWAN nodes.

The LoRaWAN network enhancement methods presented so far are based on metrics that can be obtained directly from the MAC layer via radio packet metadata. However, in order to obtain MAC layer metrics for these methods, the LoRa packets must first be received and demodulated. In addition, these methods do not take into account other communication protocols that may be operating in the same unlicensed frequency bands. With this in mind, network sensing must be performed at the physical link layer using SS techniques.

Shahid et al. [27] analyze the performance of convolutional neural networks (CNNs) for detecting and classifying LPWAN radio communication protocols, including Sigfox, LoRa, and IEEE 802.15.4g [28] based on IQ samples input. Their study achieved a classification accuracy of 95% at SNR levels above 10 dB. However, classification accuracy significantly decreases at lower SNR values, dropping below 70% at 0 dB and further declining to approximately 25% at -10 dB. Almohamad et al. [29] propose an enhancement to the methodology described in [27], focusing specifically on classifying LoRa radio transmissions according to their SFs, using cyclostationary features as input data for a CNN model. According to their results, the cyclostationary features signal representation achieves a classification accuracy of approximately 99% at an SNR of -10 dB.

In our previous work [30], we designed and evaluated DL-based spectrum sensing techniques for LoRa SF detection using spectrograms as the input. Using a proprietary dataset consisting of spectrograms of LoRa radio transmissions in the -20 to 30 dB SNR range, we trained and evaluated an image classification CNN for LoRa SF detection, obtaining a classification accuracy of 98%. However, this methodology can be applied when the spectrogram image contains only one LoRa transmission. In [31], we extend the capabilities of the approach in [30] to the simultaneous detection of multiple LoRa and Sigfox radio transmissions within a spectrogram. The developed DL spectrum sensing network was based on the second iteration of You Only Look Once (YOLO) [32].

Compared to our previous work [30,31], which primarily focused on deep learning-based LoRa SF detection using spectrogram inputs, in this paper, we propose and evaluate a hybrid SS framework specifically designed for SF detection in LoRa modulation and advanced channel analysis. Our proposed framework combines traditional signal processing techniques and advanced AI models to detect, classify, and extract detailed channel information such as center frequency, bandwidth, and occupancy level for multiple simultaneous LoRa transmissions within a wideband signal. It relies entirely on IQ sample processing to ensure accurate and efficient signal analysis. A key feature of our approach is the separation of the AI processing pipeline from the advanced analysis pipeline, making the framework more flexible.

This paper makes several important contributions: it develops a new hybrid framework that combines signal processing and AI for effective LoRa SF detection and classification, introduces robust methods for advanced channel analysis directly from IQ samples, designs a flexible architecture by separating the processing pipelines to support different communication standards, and presents a thorough evaluation of the effectiveness, and reliability of the framework in realistic scenarios.

The remainder of this paper is organized as follows: Section 2 provides an overview of the proposed SS framework. Section 3 details the transmission detection and clustering algorithm, which is specifically designed to detect and isolate individual radio transmissions within a wideband signal and prepare them for subsequent analysis. Section 4 outlines the methodology used to create the dataset used in the training and evaluation of the LoRa SF detection AI model. Section 5 describes the design, training procedures, and evaluation of this LoRa SF detection model. Section 6 provides a description of the channel analytics processing pipeline and a comprehensive evaluation of the overall framework through two live deployment scenarios involving software-defined radio (SDR) devices and dedicated LoRa transceivers. Finally, Section 7 summarizes the key findings and concludes the paper.

2. Spectrum Sensing Framework for LoRa Modulation Detection and Communication Channel Analytics

In this section, we present the system design of our proposed SS framework for LoRa modulation detection and communication channel analytics. We consider a wideband signal $x(n)$ subjected to typical wireless channel impairments, including Rayleigh fading and additive white Gaussian noise (AWGN), potentially containing multiple concurrent LoRa transmissions. The principal objective of this framework is the accurate detection and classification of each LoRa transmission within the received wideband signal, along with detailed channel analytics for every identified transmission.

In Figure 1, we provide a graphical representation of the framework. This hybrid SS approach integrates classical detection techniques, such as energy detection and signal processing, with AI-driven solutions based on CNNs. By combining these complementary methods, we enhance both the accuracy and robustness of LoRa detection and classification.

The SS algorithm Input comprises IQ sample streams produced by an SDR device, at the baseband frequency, that captures the wideband radio signal in the target frequency band. These IQ samples represent the real and imaginary components of the wideband signal, enabling the extraction of time domain features. The power of the received signal is normalized using (1) and (2), where P_t denotes the power of the wideband signal $x(n)$, N is the number of IQ samples of $x(n)$, and $x_n(n)$ is the resulting normalized signal. The normalization process reduces the computational overhead, enhances the processing capabilities of the CNN both during training and inference, and improves the model convergence.

$$P_t = \frac{1}{N}\sum_{n=1}^{N}|x(n)|^2. \quad (1)$$

$$x_n(n) = \frac{x(n)}{\sqrt{P_t}}. \quad (2)$$

Following normalization, the signal is passed through a transmission detection and clustering algorithm, which will be presented in the following section, that identifies and isolates individual radio transmissions within the wideband signal. Each identified transmission is then passed to two separate processing pipelines. The first pipeline is represented by the AI model for LoRa modulation detection. This processing pipeline identifies the LoRa SF using a time series CNN taking IQ samples as input. The second processing pipeline is represented by the communication channel analytics algorithm. The two processing pipelines can be individually used, making the SS framework more versatile. Finally, the SS algorithm outputs both the detection results and the corresponding channel analytics.

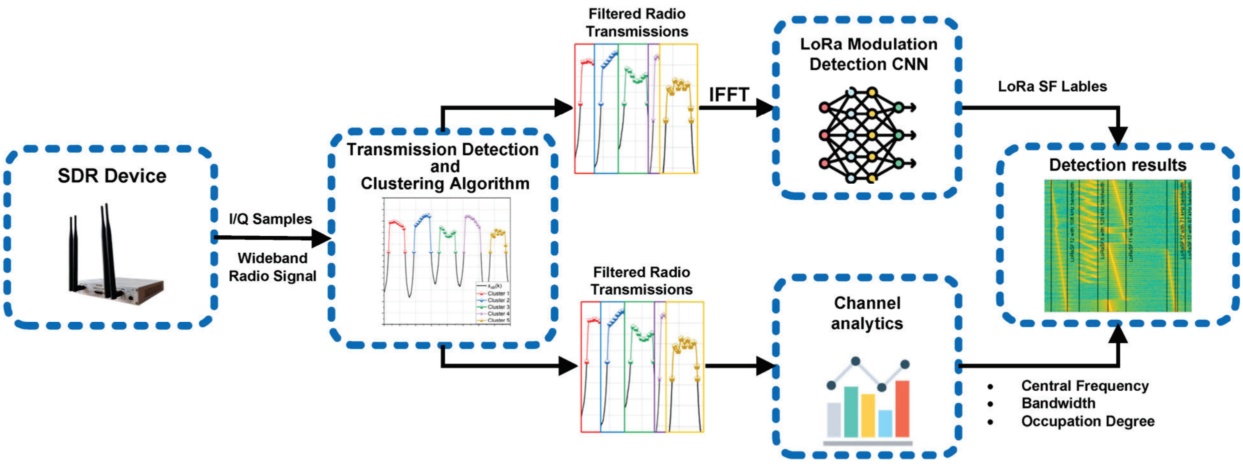

Figure 1. Spectrum sensing framework for LoRa modulation detection and communication channel analytics.

3. Transmission Detection and Clustering Algorithm

This section presents the design and implementation of the transmission detection and clustering algorithm (TDCA), which enables the SS framework to identify and separate individual radio transmissions within the received wideband signal and prepare them for further processing trough the two processing pipelines.

As presented in the introduction of this section, the SS framework input receives a wideband signal at the baseband frequency that can contain multiple radio transmissions. However, considering that a CNN can predict a single modulation class for the input signal, the individual radio transmissions within the wideband signal must be firstly separated in frequency and filtered individually.

For this, we implemented a transmission detection and clustering algorithm based on traditional SS approaches [33] and signal processing. Firstly, the TDCA uses the normalized $x_n(n)$ wideband signal, which is converted to the frequency domain by applying a discrete

Fourier transform using (3), where N is the number of IQ samples in $x_n(n)$, and $x(k)$ is the representation of $x_n(n)$ in the frequency domain.

$$x(k) = \sum_{n=0}^{N-1} x_n(n)\, e^{-j\dfrac{2\pi kn}{N}}. \tag{3}$$

After obtaining the frequency domain representation of the wideband signal, the 0 Hz component is shifted to the center of the spectrum, using (4). In this operation, the frequency associated with each discrete index k is mapped to a real frequency according to (5), where F_s is the sampling frequency and N is the number of samples. After shifting, the frequency axis spans from $-F_s/2$ to $F_s/2$, aligning the discrete bins with their corresponding physical frequencies. The magnitude is then represented as power spectral density (PSD) using (6).

$$x_{shifted}(k) = \begin{cases} x(k+N/2), 0 \le k < N/2 \\ x(k-N/2), N/2 \le k < N \end{cases}. \tag{4}$$

$$f(k) = \left(\frac{k}{N} - \frac{1}{2}\right)F_s. \tag{5}$$

$$x_{dB}(k) = 20\log_{10}\left(\frac{\left|x_{shifted}(k)\right|}{N}\right). \tag{6}$$

A noise suppression is performed using a moving average operation, as described in (7) and (8), where (7) defines the window size w as the floor of 1% of N and N represents the number of frequency bins in $x_{db}(k)$. Equation (8) then updates the $x_{db}(k)$ values by applying the moving average operation.

$$w = \left\lfloor \frac{N}{100} \right\rfloor. \tag{7}$$

$$x_{dB}{}'(k) = \frac{1}{w} \sum_{m=\max(1,k-\frac{w}{2})}^{\min(N,k+\frac{w}{2})} x_{dB}(m). \tag{8}$$

Each frequency bin in the $x_{db}{}'(k)$ is compared to a threshold determined by the mean value of $x_{db}{}'(k)$. Any frequency bin index that exceeds this threshold is stored in a vector. This approach is similar to the energy detection [33] method commonly used in spectrum sensing algorithms for identifying occupied and unoccupied frequency bands. However, in this work, this method is used specifically to identify frequency bins that may be part of clusters representing a distinct narrowband radio transmission in the $x(n)$ wideband signal.

After determining the relevant frequency bin indexes, the difference between adjacent indexes is calculated and compared against a predefined threshold. This comparison helps determine whether the adjacent indexes belong to the same cluster or to separate clusters. Through multiple tests and empirical studies, an index difference of 0.3% of the total number of frequency bins was found to generate optimal clustering results.

Once preliminary clusters are formed, an additional filtering step is applied. Clusters that exceed the imposed PSD threshold but do not contain a sufficient number of frequency bins to represent a radio transmission are discarded. Figure 2 presents an example of the TDCA applied on a wideband signal containing five distinct LoRa transmissions.

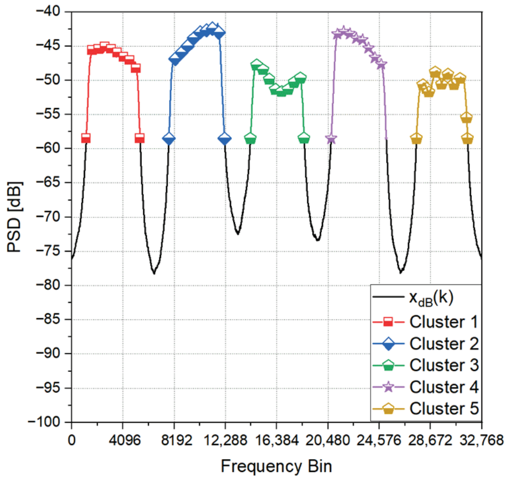

Figure 2. Transmission detection and clustering algorithm applied on a 1 MHz radio signal containing five LoRa transmissions.

After the clusters representing individual radio transmissions are identified, their frequency boundaries are mapped onto the overall wideband frequency range, extending from $-F_s/2$ to $F_s/2$, where F_s is the sampling frequency of $x(n)$. A passband filter with a transition band of 10 kHz is then designed for each cluster according to its frequency boundaries and applied in the frequency domain to suppress all other signal components. The resulting signals, each containing only one cluster, are transformed back into the time domain via an inverse discrete Fourier transform, as indicated in (9), where $x_f(k)$ is the filtered signal represented in the frequency domain, N is the number of frequency bins in $x_f(k)$, and $x_f(n)$, is the resulting filtered signal in the time domain. Finally, each single-transmission signal is shifted to the center of the baseband using (10). This is accomplished by multiplying the filtered signal $x_f(n)$ by a complex exponential of unit amplitude at a frequency equal to the negative of the cluster's center frequency. In (10), f_c is the central frequency of the signal cluster, n denotes the discrete time sample index and spans from 0 to $N-1$. The center frequency f_c is a real-valued offset within $[-F_s/2\ F_s/2]$.

$$x_f(n) = \frac{1}{N} \sum_{k=0}^{N-1} x_f(k)\, e^{j\frac{2\pi}{N}kn}. \tag{9}$$

$$x'_f(n) = x_f(n)\, e^{-j2\pi \frac{f_c}{F_s} n}. \tag{10}$$

At the end of this process, the TDCA produces multiple single-transmission signals corresponding to the number of detected signal clusters. These signals are then passed to the CNN processing pipeline for LoRa modulation detection, and to the channel analytics processing pipeline for central frequency, bandwidth, and occupation degree computing. Although the current implementation is optimized for LoRa signals, the TDCA is based on general spectrum sensing principles and can be adapted to alternative narrowband modulations such as FSK or NB-IoT. Adapting the framework would involve tuning the frequency resolution, adjusting thresholding criteria based on the new signal characteristics, modifying the passband filter parameters to match different bandwidths, and retraining the CNN classifier using features representative of the target modulation scheme. The modular structure of the framework facilitates such adaptations with minimal architectural changes.

4. Dataset Creation

The first step in designing, training, and evaluating the LoRa modulation detection CNN is creating a comprehensive dataset. This dataset encompasses six LoRa spreading factors (SF7 through SF12), each corresponding to the number of bits that can be encoded in a LoRa symbol. Using MATLAB 2023a and the library developed by Al Homsi et al. [34], we generated 26,000 signal samples for each spreading factor at a sampling rate of 1 MS/s. Each sample employed random byte sequences as the LoRa packet payload, a transmission power of 14 dB following European LoRa Regional parameters [35], and a bandwidth of 125 kHz.

Each signal sample was then passed through a channel model simulating various propagation impairments, including Rician multipath fading (for urban, suburban, and rural environments), Doppler shift, clock offset between the transmitter and receiver, and different SNR conditions imposed via additive white Gaussian noise (AWGN).

Because LoRa can operate below the noise floor, we considered 26 SNR values ranging from -20 dB to 30 dB with an increment of 2 dB, generating 1000 samples at each SNR level. The multipath fading model used path gains of 0 dB, -2 dB, and -10 dB, and the maximum Doppler shift was set to 4 Hz at a carrier frequency of 868 MHz. Additionally, the clock offset was randomly varied between -5 ppm and 5 ppm for both the carrier frequency and the sampling rate.

Each LoRa signal sample was truncated to 4096 consecutive IQ samples, which is the minimum amount of IQ samples required to capture an SF9 symbol at a 1 MS/s sampling rate, and provides a sufficient amount of samples to differentiate between SF10, SF11, and SF12 symbols. Since every LoRa transmission starts with eight consecutive upchirps, the 4096 samples were selected starting with a random offset to enhance dataset diversity with respect to symbol distribution. Figure 3 illustrates examples of the resulting dataset through time/amplitude (a) plots and spectrograms (b). In the time/amplitude plots, the I and Q channels are represented in blue and red, respectively, while the spectrogram images are plotted with a window size of 256. The complete dataset, containing 156,000 signal samples, is publicly available on GitHub [36].

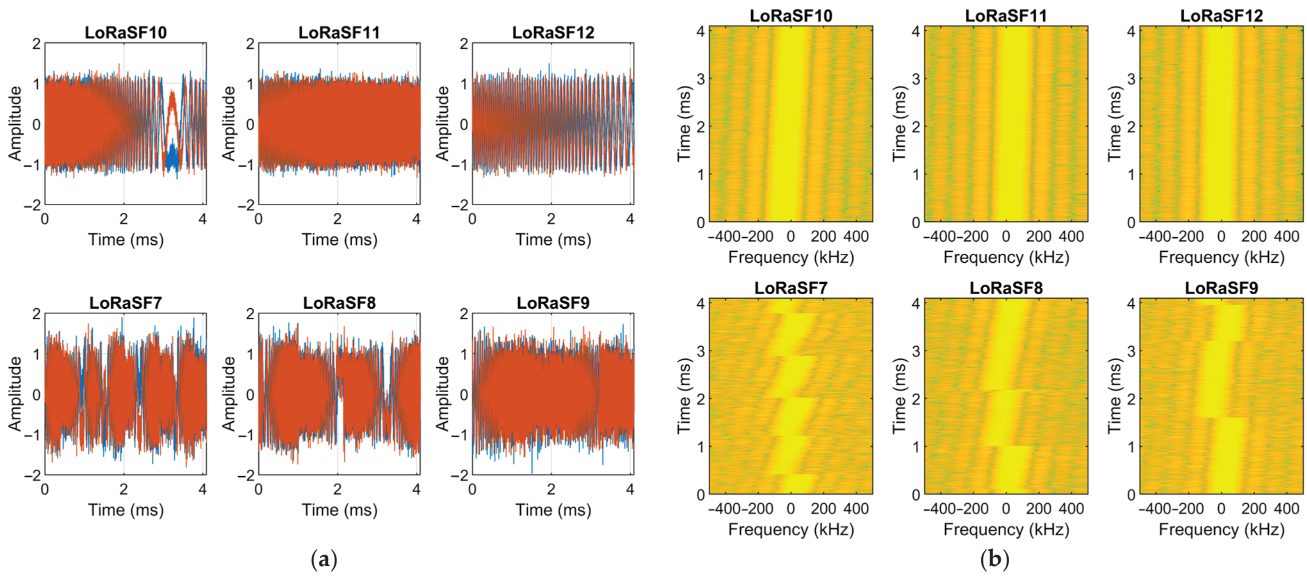

Figure 3. Samples of the generated dataset used for training and evaluating the LoRa SF detection CNN. (**a**) Amplitude/time plots (Blue—In Phase, Red—Quadrature); (**b**) spectrogram plots.

5. Design, Training, and Evaluation of the LoRa Modulation Detection Convolutional Neural Network

The proposed CNN architecture adopts a classical hierarchical structure, as shown in Figure 4. It begins with a sequence input layer configured to receive a minimum of 4096 samples, which is sufficient to capture a LoRa SF9 symbol at a 1 MS/s sampling rate, but can also receive signal frames with more than 4096 samples. Within this layer, z-score normalization is applied, and the complex input samples are split into real and imaginary components.

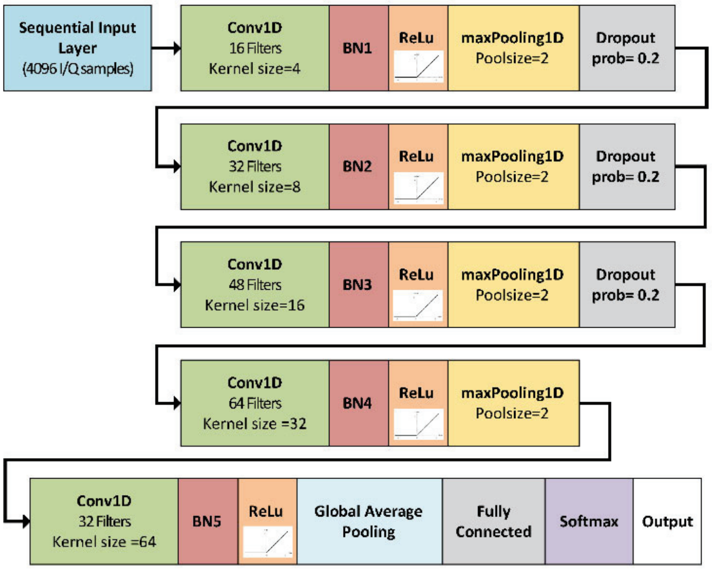

Figure 4. Designed LoRa SF detection convolutional neural network structure.

After the input layer, the network is organized into multiple hierarchical blocks. In the first block, there is a 1D convolutional layer (Conv1D) with a filter size of 4 and 16 filters. This block also includes a batch normalization layer, a ReLU activation layer, a max pooling layer, and a dropout layer. In subsequent blocks, the filter size doubles incrementally to 8, respectively, 16, and the number of filters increases by 16 in each block. Max pooling and dropout layers help mitigate overfitting.

In the fourth block, the Conv1D layer continues to increase filter size to 32 and filter count to 64, but the dropout layer is removed. In the fifth block, the Conv1D layer has a filter size of 64 and 32 filters, and the max pooling layer is replaced by a global average pooling layer. The global average pooling layer aggregates the extracted features into a single vector, which is then passed to a fully connected layer and a softmax layer to produce class probabilities for the different LoRa SF categories.

The selected filter sizes are derived from the number of IQ samples (1024) required to represent a LoRa SF7 symbol at a 1 MS/s sampling rate. By using smaller filter sizes in the initial layers, the CNN can capture localized features such as transient events or short-term patterns. In deeper layers, larger filter sizes enable the extraction of broader contextual information. The resulting network has a total of 26 layers with 258,950 trainable parameters.

For the training and evaluation of the CNN, the dataset was partitioned into 70% for training, 15% for validation during the training process, and 15% for testing. The CNN was trained over a total of 100 epochs. Considering that the network was initialized without pretraining, an initial learning rate of 0.3 was set, with a drop factor of 0.75 applied every six epochs. Training was conducted using the stochastic gradient descent with momentum (SGDM) optimizer. A batch size of 256 was employed, and validation was performed at the end of each training epoch. Additionally, to mitigate overfitting and enhance the CNN's generalization capabilities, the training dataset was shuffled at the beginning of each epoch. The training hardware platform included an Alienware Aurora R10 system (AMD Ryzen9 3950X, 64GB DDR4, and 2xGeForce RTX 3060 6GB). The training process was evaluated using accuracy and loss metrics, the progression of which is presented in Figures 5a and 5b, respectively. The CNN converged within the initial training epochs, achieving 98% accuracy after only four epochs.

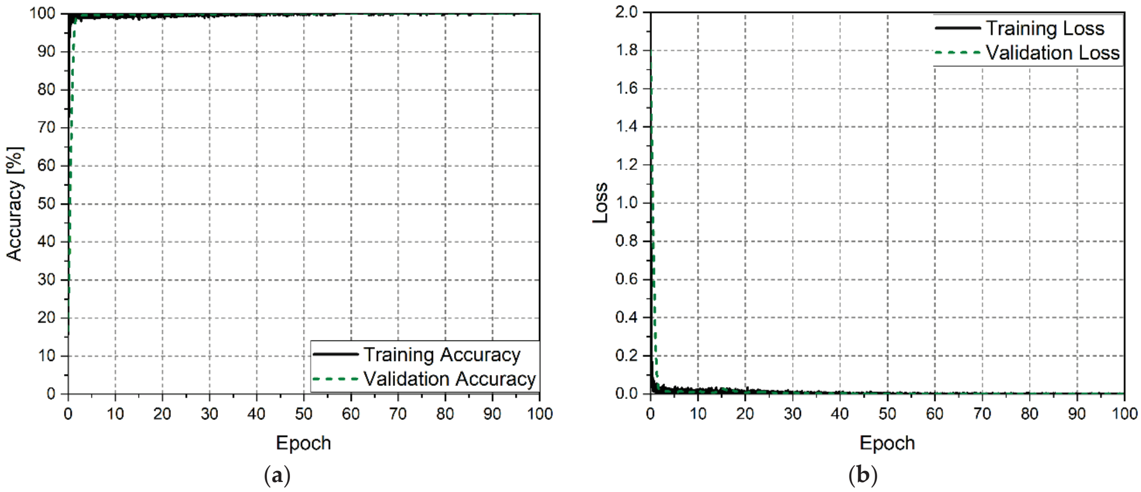

Figure 5. Performance parameters for the training process for the LoRa convolutional neural network algorithm. (**a**) Training and validation accuracy; (**b**) training and validation loss.

Following the training process, the CNN was evaluated under two distinct testing scenarios. In the first scenario (scenario A), it was tested on a partition of the original empirically generated dataset with emulated channel impairments, comprising 3900 signal samples per LoRa SF. In this scenario, the CNN achieved 100% accuracy. To eliminate the possibility of overfitting, a second testing dataset was generated. This secondary dataset contained 2600 samples for each LoRa SF, with 100 signal samples for each SNR value. On this dataset, the CNN achieved an accuracy of 99.69%.

From the confusion matrix shown in Figure 6, it can be seen that classification consistency among the LoRa SF classes is high, with the majority of signal samples correctly classified. This shows that the CNN successfully captured the features of different SFs and is capable of generalizing. Most misclassifications occurred between LoRa SF11 and LoRa SF12, and in every SF from 8 to 12, there was at least one misclassification as SF7. Nonetheless, the number of misclassified signals is minimal compared to the total number of analyzed LoRa signal samples.

In the second test scenario (scenario B), we conducted real-world testing using SDR devices positioned indoors at a distance of 10 m. An Adalm Pluto SDR [37] was configured on the transmitter side to continuously transmit 5000 LoRa packets for each spreading factor (SF). On the receiver side, an Ettus USRP N310 SDR [38] was set up to receive the LoRa signal samples in IQ format and pass them on to the CNN for classification. Both SDRs were set to a center frequency of 868.1 MHz with a sampling rate of 1 MS/s.

Under these conditions, the CNN achieved an accuracy of 99.97%. From the confusion matrix in Figure 7, we can see that each SF is correctly identified, even in a real-world testing scenario. Although the SF8-to-SF12 misclassification with SF7 observed earlier is also present here, the CNN maintains a high level of performance in this evaluation scenario.

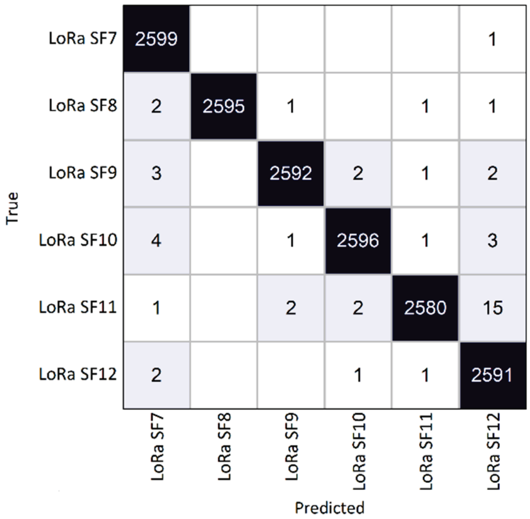

Figure 6. Confusion matrix for empirical data testing (test scenario A).

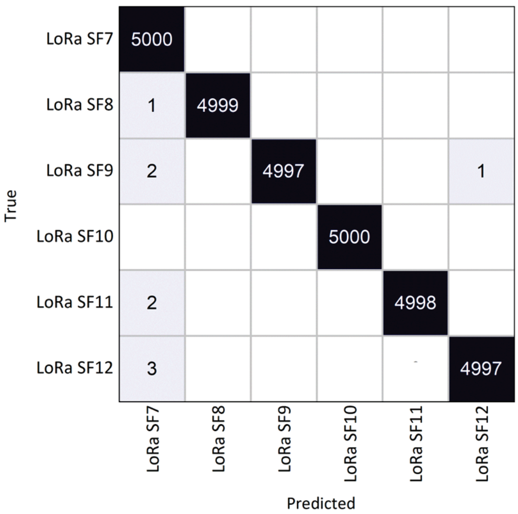

Figure 7. Confusion matrix for a real operating environment (test scenario B).

6. Radio Channel Analytics and Live Testing

In this section, we present the radio channel analytics processing pipeline along with the live testing and implementation of the proposed SS framework. As presented in Section 2, the second processing pipeline of the SS framework involves computing channel analytics for both the overall frequency band and each detected transmission. For each identified radio transmission, the SS framework reports the central frequency, bandwidth, and SF if the radio transmission uses LoRa modulation. The central frequency is determined during preprocessing of the wideband signal using the TDCA. Since each transmission is isolated by a passband filter with a 10 kHz transition band, the bandwidth is calculated using the 99% occupied bandwidth method. This approach identifies the lower (f_{lo}) and upper (f_{hi}) frequency boundaries that account for 99% of the total signal power, satisfying (11), where P_{total} is the total power of the signal from $-F_s/2$ to $F_s/2$, and $P(f)$ is the power of the signal at frequency f.

$$\int_{f_{lo}}^{f_{hi}} P(f)df = 0.99P_{total}. \tag{11}$$

Beyond the individual channel analytics for the detected LoRa transmissions, the overall occupancy degree of the analyzed frequency band is computed using (11). In this expression, M is the total number of detected transmissions, T_{BW} is the total bandwidth of the analyzed frequency band, and $BW(m)$ is a vector containing the bandwidth values of each detected LoRa transmission.

$$OD = \frac{100}{T_{BW}} \sum_{m=1}^{M} BW(m). \tag{12}$$

In Figure 8, three examples of the SS framework outputs are shown. The detected LoRa transmissions are bounded by the determined frequency limits. By measuring the symbol time for each detection, it can also be observed that the CNN correctly identified the LoRa spreading factors. In Figure 8c, due to the long symbol time of the LoRa SF12 transmission, it was identified as two separate LoRa SF12 transmissions with smaller bandwidths. Nonetheless, the overall occupancy degree of the analyzed frequency band remains accurate.

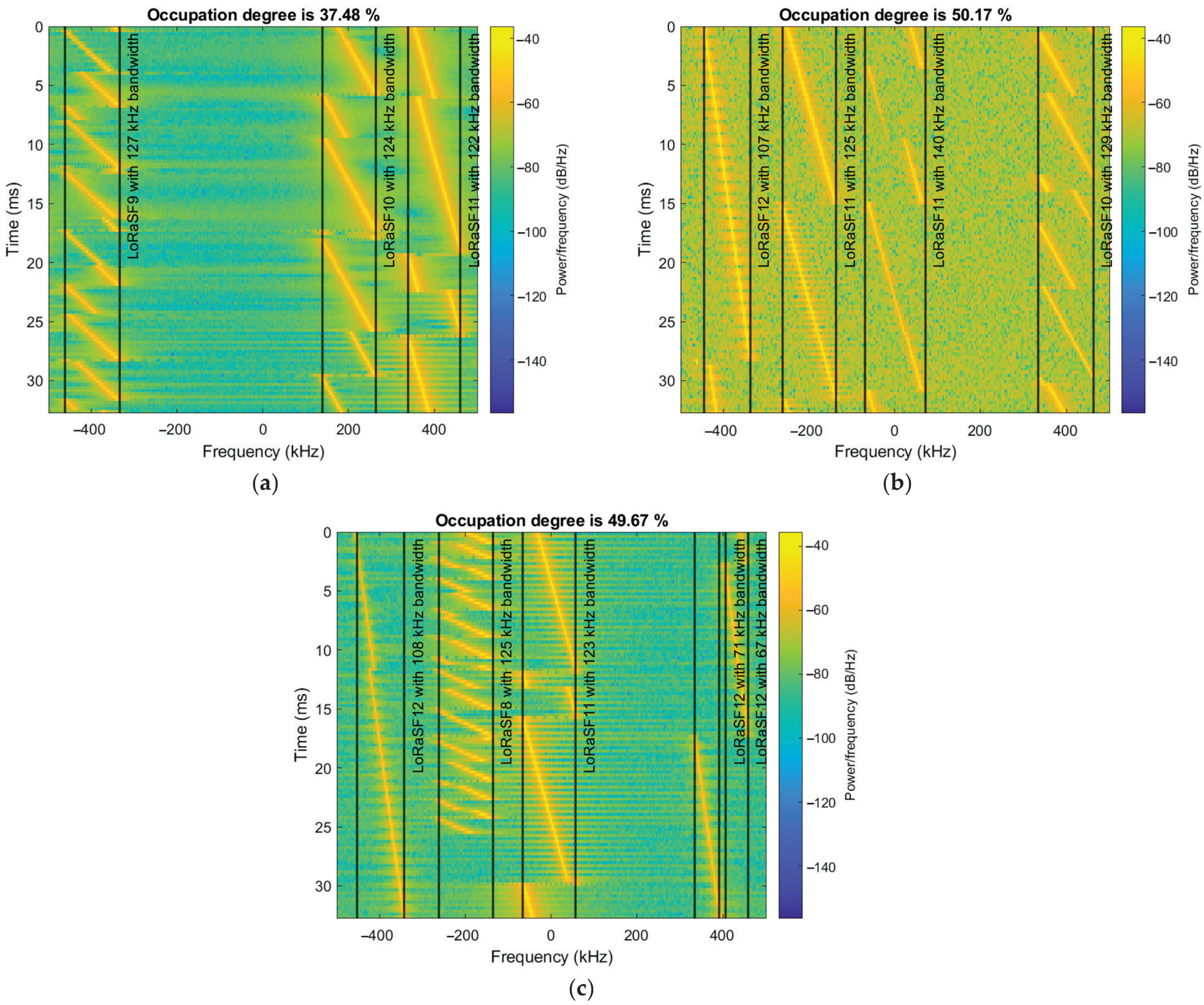

Figure 8. Spectrum sensing framework for LoRa modulation detection and communication channel analytics output examples. (**a**) Channel occupancy degree of 37.48%; (**b**) channel occupancy degree of 50.17%; and (**c**) channel occupancy degree of 49.67%.

The next step is to perform the live implementation and evaluation of the SS framework for LoRa SF detection. As described in the previous section, the developed CNN was trained and evaluated on a dataset of 156,000 empirically generated LoRa signal samples, which included simulated channel impairments with SNR values ranging from −20 dB to 30 dB. This resulted in a classification accuracy of 99.69%. A second evaluation scenario involved two SDR devices deployed in an indoor environment at a distance of 10 m, resulting in an accuracy of 99.97%. However, to fully assess the performance of the SS framework, a third evaluation scenario was conducted. In contrast to the previous test setups, this scenario uses IoT nodes equipped with LoRa radio transceivers.

From Figure 9, which illustrates the test setup (scenario C) for evaluating the SS framework in a real-world environment, we see that the setup consists of two main components:

- TX (transmitter): Five IoT nodes using LoRa transceivers, connected to a transmission orchestrator.
- RX (receiver): A host machine running the SS framework along with an SDR device for capturing signals.

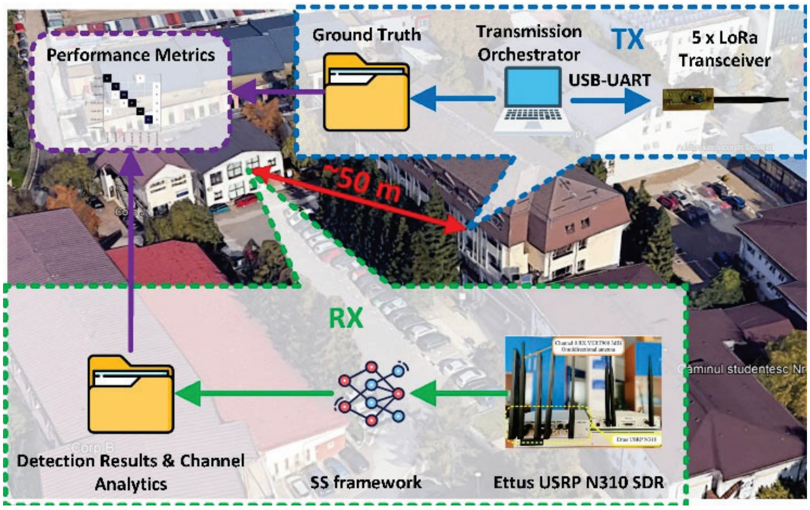

Figure 9. Spectrum sensing framework live implementation. Test setup for real-world evaluation using dedicated LoRa transceivers.

The transmitter and receiver were placed approximately 50 m apart, in separate buildings, indoors. In this setup, we evaluate the performance of the SS framework using several metrics that assess both the TDCA and the CNN:

- Detection accuracy: Represents the total number of detections made by the TDCA relative to the total number of LoRa transmissions. This metric reflects the TDCA algorithm's effectiveness in detecting and separating individual narrowband transmissions within the wideband signal, and it indicates the SS framework's capability to correctly report the occupancy status of a communication channel.
- Precision: the proportion of correctly classified LoRa transmissions among all detected LoRa transmissions.
- Recall: the proportion of correctly detected and classified LoRa transmissions out of the total transmissions sent by the IoT nodes and transmission orchestrator.
- Confusion matrix: shows instances of misclassification among the detected LoRa spreading factors.
- Mean absolute central frequency deviation (MACFD): measures the average deviation of the detected LoRa transmissions central frequencies from the known central frequencies.

- Mean absolute bandwidth deviation (MABD): measures the average deviation of the calculated bandwidths for the detected LoRa transmissions from their known bandwidth.

For these metrics, a LoRa transmission is considered correctly detected and classified if it has the same SF as specified in the ground truth and if its central frequency deviates by no more than 50 kHz from the specified ground truth. Only correctly detected and classified LoRa transmissions are included when calculating MACFD and MABD.

(1) Implementation of LoRa IoT nodes and transmission orchestrator

The transmitter part of the test setup consists of five IoT nodes based on LoRa transceivers. Each node includes an Atmega328p microcontroller [39] connected to an SX1276 LoRa transceiver [40] through the SPI interface. The transceivers use omnidirectional antennas with a 0.5 dB gain, which artificially increases the effective distance between the transmitter and receiver. Custom firmware on each microcontroller enables control of the communication channel and SF via the serial interface. Figure 10 shows the transmission orchestrator deployment setup.

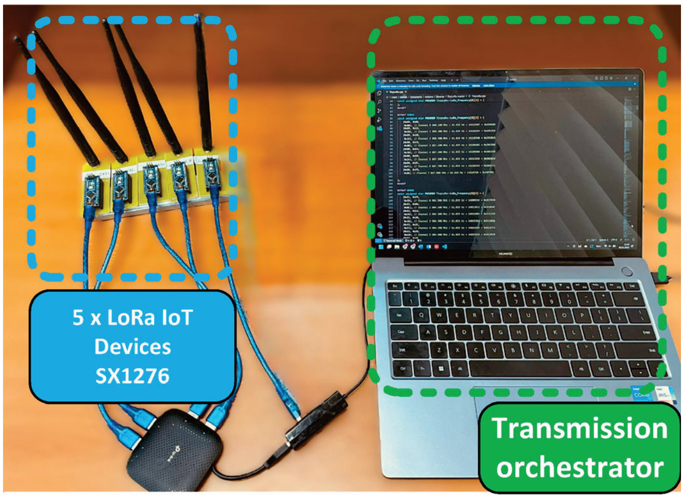

Figure 10. Transmission orchestrator deployment for live evaluation of SS framework.

For the LoRa packet payload, a random byte sequence of variable length (ranging from 1 to 51 bytes) is used, ensuring a broad distribution of transmitted LoRa symbols. There is no delay between consecutive LoRa transmissions; once configured by the transmission orchestrator, a node continuously transmits LoRa packets with random payloads using the assigned SF and channel until instructed otherwise. This approach ensures a controlled environment for assessing the detection performance of the SS framework, eliminating the need for signal capture synchronization between the transmitting side and the receiving side within a transmission frame.

The transmission orchestrator is connected to the five IoT LoRa nodes via USB-to-serial converters. At the transmission orchestrator level, a list of LoRa channels and SFs is defined. In this test setup, LoRa channels span from 867.7 MHz to 868.5 MHz, specifically CH6, CH7, CH0, CH1, and CH2, with central frequencies of 867.5 MHz, 867.9 MHz, 868.1 MHz, 868.3 MHz, and 868.5 MHz, respectively, and a bandwidth of 125 kHz. Each IoT node is assigned a unique channel and SF, forming a transmission frame. This configuration is recorded in a ground truth file for later comparison with detection results.

After the IoT nodes are configured, the transmission orchestrator signals the receiver via an IP connection that the SDR can begin capturing radio signal samples. The SDR forwards the recorded IQ samples and forwards them to the SS framework, which detects, classifies, and generates channel analytics for all LoRa transmissions within the current frame. Once the receiver confirms successful capture, the transmission orchestrator randomly reassigns LoRa channels and SFs to the IoT nodes, and the cycle repeats. This setup ensures a controlled environment for accurate performance evaluation of the SS framework.

(2) Implementation of SS framework for LoRa modulation detection

In this test setup, the receiver component consists of an Ettus USRP N310 SDR, connected via Ethernet to an Alienware Aurora R10 host machine (AMD Ryzen 9 3950X, 64GB DDR4, 2 x GeForce RTX 3060 6GB). The SDR is configured to a center frequency of 868.1 MHz and a sampling rate of 1 MS/s, ensuring coverage of the LoRa channels defined at the transmission orchestrator. The SDR uses a VERT900 antenna [41] with a gain of 3 dB.

On the host machine, the SS framework, encompassing the SDR interface, TDCA, CNN, and channel analytics algorithms, runs in a MATLAB [42] environment. Once the framework receives confirmation that the IoT nodes have been successfully configured, the SDR captures 32,768 IQ samples (32.76 ms of radio signal at a 1 MS/s sample rate) in burst mode to prevent data overflows or underflows. The captured signal is processed by the SS framework, and the detection results, which include the identified SF, central frequency, and bandwidth, are recorded in a file for performance evaluation against the ground truth. After processing the current transmission frame, the SS framework signals the transmission orchestrator via IP to update the IoT nodes configuration, repeating the cycle.

(3) Test setup methodology and performance metrics computation

As presented in the transmitter and receiver description, the test setup was designed to provide a controlled environment for accurately assessing the performance of the SS framework in a real-world operation context. To achieve this, LoRa transmission frames with known parameters were created, and both the transmitter and receiver were synchronized via an IP connection to ensure that the signal captured at the receiver matches the current configuration set by the transmission orchestrator.

In this test setup, 100 LoRa transmission frames were generated and processed by the SS framework, with each frame containing five LoRa transmissions on different channels and using different spreading factors. During each iteration, the transmission orchestrator first assigns a unique channel and SF to the IoT nodes, storing this information in a ground truth file. The receiver is then signaled to capture the signal and pass it to the SS framework, which records the detection results and channel metrics in a detection results file. After processing the current frame, the SS framework signals to the transmission orchestrator that it can configure the next frame. To simplify the performance metric calculations, a "new frame" separator is inserted in both the ground truth file and the detection results file, allowing clear demarcation of individual transmission frames.

After obtaining the ground truth and detection results file, the performance metrics are computed according to the following criteria:

- A radio transmission is considered correctly detected if its central frequency deviates by no more than 50 kHz from the specified ground truth. If the deviation exceeds 50 kHz or it is not detected and clustered by the TDCA, the transmission is labeled as undetected.
- A LoRa transmission is considered correctly detected and classified if its attributed label matches the ground truth label and its central frequency deviates by no more than 50 kHz from the ground truth.
- For the MACFD and MABD metrics, only LoRa transmissions that are both correctly detected and correctly classified are included.

From a total of 500 LoRa transmissions sent by the transmission orchestrator, the SS framework successfully detected 481, resulting in a detection accuracy of 96.2%. Upon closer inspection, most of the undetected transmissions occurred on LoRa CH6 and LoRa CH2, which are located at the edges of the analyzed frequency band. This issue may arise from the frequency response of the analog and digital filters in the SDR's RX path. In practical scenarios, it can be mitigated by sampling a wider frequency band than the specific band of interest.

The SS framework achieved a precision of 99.16%, aligning with the results obtained from the empirically generated dataset and indicating robust performance of the developed CNN in real-world inference scenarios. The obtained recall value was 95.4%. In the confusion matrix shown in Figure 11, where compared to previously presented confusion matrices, an "undetected" class was added, and we can see that there were only a few misclassifications (one SF7 as SF11, one SF9 as SF8, one SF10 as SF9, and one SF11 as SF7). Most of the undetected transmissions involved SF9 and SF12. Nevertheless, the well-defined diagonal in the confusion matrix confirms the framework's high level of accuracy in LoRa detection and classification.

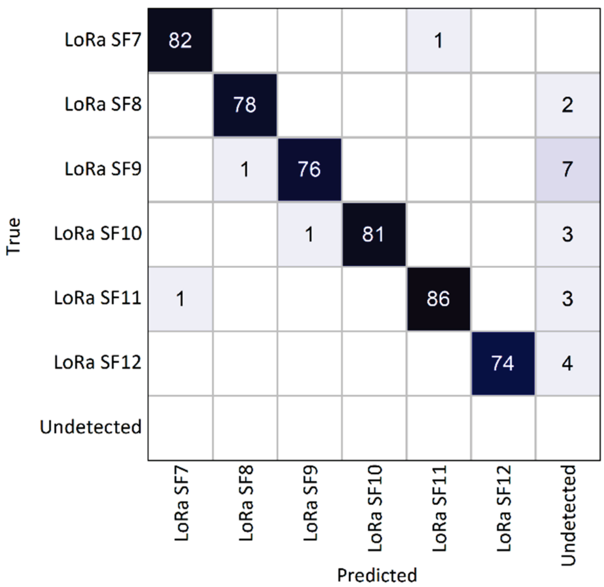

Figure 11. Confusion matrix for real operating environment (test scenario C).

When computing the MACFD metric, the mean deviation in the central frequency was 9.13 kHz, which is 7.3% of a LoRa transmission's total bandwidth. The MABD metric showed a mean bandwidth deviation of 10.2 kHz, corresponding to 8.16% of the total bandwidth.

7. Conclusions

This paper proposes and evaluates a novel hybrid SS framework for LoRa SF detection and communication channel analytics computation. By combining traditional signal processing methods with AI techniques, the developed framework is capable of detecting and classifying multiple simultaneous LoRa transmissions in a wideband signal based solely on the input IQ samples. The live inference evaluation demonstrated a high level of performance, achieving a detection accuracy of 96.2%, a precision of 99.16%, and a recall of 95.4%. In addition, the low mean frequency deviation (MACFD of 9.13 kHz) and reduced communication channel bandwidth deviation (MABD of 10.2 kHz) highlight the performance of the proposed SS framework.

The developed SS framework aims to address the increasing challenges of the ever-growing large-scale, high-density IoT wireless sensor networks based on LoRa communication in terms of packet collision, interference, and reduced channel capacity within the constrained spectral resources. The ability to dynamically allocate communication channels and accurately analyze channel conditions ensures the optimal performance, scalability, and reliability of IoT networks. In addition, the framework's flexible architecture, achieved by separating the LoRa SF detection processing pipeline from the communication channel analytics processing pipeline, allows it to adapt to being used for various communication standards beyond LoRa, enhancing its applicability in diverse IoT scenarios.

However, the framework revealed certain limitations, primarily related to the TDCA algorithm, which relies on classical energy detection and rule-based clustering methods. This can lead to missed transmissions, especially under noisy or difficult conditions. Future research should explore replacing TDCA with a more advanced 1D semantic segmentation neural network capable of learning and extracting radio transmissions based on clustering patterns even under challenging conditions.

Another limitation is the currently fixed 1 MHz sampling rate required for the CNN input. To address this, future iterations of the SS framework will include training datasets with varying sampling rates, thereby enhancing the ability of the CNN to process inputs directly without explicit resampling operations. Addressing these issues will significantly improve the framework's versatility, accuracy, and applicability in dynamic IoT environments, ensuring the continued growth and robustness of LoRa-based IoT networks.

Author Contributions: Conceptualization, P.-M.M. and A.L.; methodology, P.-M.M., A.L. and V.P.; software, P.-M.M. and A.L.; validation, P.-M.M., A.L. and V.P.; formal analysis, P.-M.M., A.L. and V.P.; investigation, P.-M.M., A.L. and V.P.; resources, A.L. and V.P.; data curation, P.-M.M. and A.L.; writing—original draft preparation, P.-M.M., A.L. and V.P.; writing—review and editing, P.-M.M., A.L. and V.P.; visualization, P.-M.M., A.L. and V.P.; supervision, A.L and V.P.; project administration, A.L.; funding acquisition, A.L. All authors have read and agreed to the published version of the manuscript.

Funding: This work was supported by a grant of the Ministry of Research, Innovation and Digitization, CNCS-UEFISCDI, project number PN-IV-P2-2.1-TE-2023-1476, within PNCDI IV.

Institutional Review Board Statement: Not applicable.

Informed Consent Statement: Not applicable.

Data Availability Statement: The original data presented in the study are openly available in spectrumHiveDatasets at https://github.com/WirelessLabUSV/spectrumHiveDatasets/blob/main/spectrumHive_LoRa.md or [33] reference of the paper.

Conflicts of Interest: The authors declare no conflicts of interest.

References

1. Rath, K.C.; Khang, A.; Roy, D. The Role of Internet of Things (IoT) Technology in Industry 4.0 Economy. In *Advanced IoT Technologies and Applications in the Industry 4.0 Digital Economy*; CRC Press: Boca Raton, FL, USA, 2024; pp. 1–28. [CrossRef]
2. Lazarescu, M.T. Wireless Sensor Networks for the Internet of Things: Barriers and Synergies. In *Components and Services for IoT Platforms: Paving the Way for IoT Standards*; Springer: Berlin/Heidelberg, Germany, 2017; pp. 155–186. [CrossRef]
3. Madhu, S.; Padunnavalappil, S.; Saajlal, P.P.; Vasudevan, V.A.; Mathew, J. Powering Up an IoT-Enabled Smart Home. *Int. J. Softw. Sci. Comput. Intell. (IJSSCI)* **2022**, *14*, 1–21. [CrossRef]
4. Guimaraes, M.A.; De Araujo Macedo, R.J. Energy-Efficient eHealth Monitoring with LPWAN. In Proceedings of the Brazilian Symposium on Computing System Engineering (SBESC), Recife, Brazil, 26–29 November 2024. [CrossRef]

5. García, L.; Parra, L.; Jimenez, J.M.; Parra, M.; Lloret, J.; Mauri, P.V.; Lorenz, P. Deployment Strategies of Soil Monitoring WSN for Precision Agriculture Irrigation Scheduling in Rural Areas. *Sensors* **2021**, *21*, 1693. [CrossRef] [PubMed]
6. Khan, F.; Siddiqui, M.A.B.; Rehman, A.U.; Khan, J.; Asad, M.T.S.A.; Asad, A. IoT Based Power Monitoring System for Smart Grid Applications. In Proceedings of the 2020 International Conference on Engineering and Emerging Technologies (ICEET 2020), Lahore, Pakistan, 22–23 February 2020. [CrossRef]
7. Zhu, F.; Lv, Y.; Chen, Y.; Wang, X.; Xiong, G.; Wang, F.Y. Parallel Transportation Systems: Toward IoT-Enabled Smart Urban Traffic Control and Management. *IEEE Trans. Intell. Transp. Syst.* **2020**, *21*, 4063–4071. [CrossRef]
8. Current IoT Forecast Highlights—Transforma Insights. Available online: https://transformainsights.com/research/forecast/highlights (accessed on 21 January 2025).
9. Queralta, J.P.; Gia, T.N.; Zou, Z.; Tenhunen, H.; Westerlund, T. Comparative Study of LPWAN Technologies on Unlicensed Bands for M2M Communication in the IoT: Beyond LoRa and LoRaWAN. *Procedia Comput. Sci.* **2019**, *155*, 343–350. [CrossRef]
10. Chaudhari, B.S.; Zennaro, M.; Borkar, S. LPWAN Technologies: Emerging Application Characteristics, Requirements, and Design Considerations. *Future Internet* **2020**, *12*, 46. [CrossRef]
11. Masek, P.; Younesian, E.; Bahna, M.; Mozny, R.; Mikulasek, M.; Stusek, M.; Ometov, A.; Hosek, J.; Fujdiak, R.; Mlynek, P. Performance Analysis of Different LoRaWAN Frequency Bands for mMTC Scenarios. In Proceedings of the 2022 45th International Conference on Telecommunications and Signal Processing (TSP 2022), Prague, Czech Republic, 13–15 July 2022; pp. 417–420. [CrossRef]
12. Lavric, A.; Petrariu, A.I. LoRaWAN communication protocol: The new era of IoT. In Proceedings of the 2018 14th International Conference on Development and Application Systems (DAS 2018—Proceedings), Suceava, Romania, 24–26 May 2018; pp. 74–77. [CrossRef]
13. Islam, M.; Jamil, H.M.M.; Pranto, S.A.; Das, R.K.; Amin, A.; Khan, A. Future Industrial Applications: Exploring LPWAN-Driven IoT Protocols. *Sensors* **2024**, *24*, 2509. [CrossRef] [PubMed]
14. Borkotoky, S.; Bettstetter, C.; Schilcher, U.; Raffelsberger, C. Allocation of repetition redundancy in LoRa. In Proceedings of the European Wireless 2019; 25th European Wireless Conference, Aarhus, Denmark, 2–4 May 2019. Available online: https://ieeexplore.ieee.org/abstract/document/8835940/ (accessed on 29 March 2025).
15. Azim, A.W.; Bazzi, A.; Shubair, R.; Chafii, M. Dual-Mode Chirp Spread Spectrum Modulation. *IEEE Wirel. Commun. Lett.* **2022**, *11*, 1995–1999. [CrossRef]
16. Mutescu, P.M.; Lavric, A.; Petrariu, A.I.; Popa, V. Evaluation of a new spectrum sensing technique for Internet of Things: An AI approach. In Proceedings of the 2022 International Conference on Development and Application Systems (DAS), Suceava, Romania, 26–28 May 2022; pp. 91–94. [CrossRef]
17. Zhang, L.; Liang, Y.C. Joint Spectrum Sensing and Packet Error Rate Optimization in Cognitive IoT. *IEEE Internet Things J.* **2019**, *6*, 7816–7827. [CrossRef]
18. Hou, C.; Liu, G.; Tian, Q.; Zhou, Z.; Hua, L.; Lin, Y. Multisignal Modulation Classification Using Sliding Window Detection and Complex Convolutional Network in Frequency Domain. *IEEE Internet Things J.* **2022**, *9*, 19438–19449. [CrossRef]
19. Lavric, A.; Patachia-Sultanoiu, C.; Mihai, R.M.; Mutescu, P.-M. AI-Powered Spectrum Sensing Capabilities for Future Networks Beyond 5G. In Proceedings of the 2024 15th International Conference on Information, Intelligence, Systems & Applications (IISA), Chania Crete, Greece, 17–19 July 2024; pp. 1–7. [CrossRef]
20. Pham, C.; Ehsan, M. Dense Deployment of LoRa Networks: Expectations and Limits of Channel Activity Detection and Capture Effect for Radio Channel Access. *Sensors* **2021**, *21*, 825. [CrossRef] [PubMed]
21. Lavric, A.; Petrariu, A.I.; Coca, E.; Popa, V. LoRa Traffic Generator Based on Software Defined Radio Technology for LoRa Modulation Orthogonality Analysis: Empirical and Experimental Evaluation. *Sensors* **2020**, *20*, 4123. [CrossRef] [PubMed]
22. Croce, D.; Gucciardo, M.; Mangione, S.; Santaromita, G.; Tinnirello, I. Impact of LoRa Imperfect Orthogonality: Analysis of Link-Level Performance. *IEEE Commun. Lett.* **2018**, *22*, 796–799. [CrossRef]
23. Lavric, A.; Popa, V. Performance Evaluation of LoRaWAN Communication Scalability in Large-Scale Wireless Sensor Networks. *Wirel Commun. Mob. Comput.* **2018**, *2018*, 6730719. [CrossRef]
24. Farhad, A.; Kim, D.H.; Yoon, J.S.; Pyun, J.Y. Deep Learning-Based Channel Adaptive Resource Allocation in LoRaWAN. In Proceedings of the 2022 International Conference on Electronics, Information, and Communication (ICEIC 2022), Jeju, Republic of Korea, 6–9 February 2022. [CrossRef]
25. Elbsir, H.E.; Kassab, M.; Bhiri, S.; Bedoui, M.H.; Castells-Rufas, D.; Carrabina, J. LoRaWAN Optimization using optimized Auto-Regressive algorithm, Support Vector Machine and Temporal Fusion Transformer for QoS ensuring. In Proceedings of the International Conference on Wireless and Mobile Computing, Networking and Communications, Thessaloniki, Greece, 10–12 October 2022; pp. 302–307. [CrossRef]

26. Li, A. Deep Reinforcement Learning Based Resource Allocation for LoRaWAN. In Proceedings of the IEEE 2022 IEEE 96th Vehicular Technology Conference (VTC2022-Fall), London, UK, 26–29 September 2022. [CrossRef]
27. Shahid, A.; Fontaine, J.; Camelo, M.; Haxhibeqiri, J.; Saelens, M.; Khan, Z.; Moerman, I.; De Poorter, E. A Convolutional Neural Network Approach for Classification of LPWAN Technologies: Sigfox, LoRA and IEEE 802.15.4g. In Proceedings of the Annual IEEE Communications Society Conference on Sensor, Mesh and Ad Hoc Communications and Networks Workshops, Boston, MA, USA, 10–13 June 2019. [CrossRef]
28. IEEE SA-IEEE 802.15.4g-2012. Available online: https://standards.ieee.org/ieee/802.15.4g/5053/ (accessed on 24 April 2025).
29. Almohamad, A.; Hasna, M.; Althunibat, S.; Tekbiyik, K.; Qaraqe, K. A Deep Learning Model for LoRa Signals Classification Using Cyclostationay Features. In Proceedings of the 2021 International Conference on Information and Communication Technology Convergence (ICTC), Jeju Island, Republic of Korea, 20–22 October 2021; pp. 76–81. [CrossRef]
30. Mutescu, P.M.; Lavric, A.; Petrariu, A.I.; Popa, V. Deep Learning Enhanced Spectrum Sensing for LoRa Spreading Factor Detection. In Proceedings of the 2023 13th International Symposium on Advanced Topics in Electrical Engineering (ATEE), Bucharest, Romania, 23–25 March 2023; pp. 1–5. [CrossRef]
31. Mutescu, P.M.; Lavric, A.; Petrariu, A.I.; Popa, V. A Hybrid Deep Learning Spectrum Sensing Architecture for IoT Technologies Classification. In Proceedings of the 2023 17th International Conference on Engineering of Modern Electric Systems (EMES 2023), Oradea, Romania, 9–10 June 2023. [CrossRef]
32. Redmon, J.; Farhadi, A. YOLO9000: Better, faster, stronger. In Proceedings of the 30th IEEE Conference on Computer Vision and Pattern Recognition (CVPR 2017), Honolulu, HI, USA, 21–26 July 2016; pp. 6517–6525. [CrossRef]
33. Atapattu, S.; Tellambura, C.; Jiang, H. *Energy Detection for Spectrum Sensing in Cognitive Radio*; Springer: New York, NY, USA, 2014. [CrossRef]
34. Al Homssi, B.; Dakic, K.; Maselli, S.; Wolf, H.; Kandeepan, S.; Al-Hourani, A. IoT Network Design Using Open-Source LoRa Coverage Emulator. *IEEE Access* **2021**, *9*, 53636–53646. [CrossRef]
35. LoRaWAN® Specification v1.0.3. Available online: https://resources.lora-alliance.org/technical-specifications/lorawan-specification-v1-0-3 (accessed on 6 June 2023).
36. WirelessLabUSV/spectrumHiveDatasets: Signal Datasets for AI-Based Spectrum Sensing Applications. Available online: https://github.com/WirelessLabUSV/spectrumHiveDatasets/tree/main (accessed on 20 March 2025).
37. ADALM-PLUTO Evaluation Board | Analog Devices. Available online: https://www.analog.com/en/resources/evaluation-hardware-and-software/evaluation-boards-kits/adalm-pluto.html#eb-overview (accessed on 23 September 2024).
38. USRP N310 | Ettus Research, a National Instruments Brand | The Leader in Software Defined Radio (SDR). Available online: https://www.ettus.com/all-products/usrp-n310/ (accessed on 16 July 2024).
39. ATMEGA328P | Microchip Technology. Available online: https://www.microchip.com/en-us/product/atmega328p (accessed on 28 January 2025).
40. LoRa Connect Transceiver, SX1276, 137 MHz to 1020 MHz | Semtech. Available online: https://www.semtech.com/products/wireless-rf/lora-connect/sx1276 (accessed on 24 April 2023).
41. VERT900 Antenna | Ettus Research, a National Instruments Brand | The leader in Software Defined Radio (SDR). Available online: https://www.ettus.com/all-products/vert900/ (accessed on 17 July 2024).
42. MATLAB—MathWorks—MATLAB & Simulink. Available online: https://www.mathworks.com/products/matlab.html (accessed on 24 March 2022).

sensors

MDPI

Article

Implementation of a Remote Monitoring Station for Measuring UV Radiation Levels from Solarimeters Using LoRaWAN Technology

Iván Sánchez [1,*], Cristian Guamialama [1], Alexis Padilla [1], Pablo Palacios Játiva [2] and Andre Nicolás Mosquera [1]

[1] Department of Networking and Telecommunication Engineering, Universidad de las Américas, Quito 170503, Ecuador; cris.guamialama@gmail.com (C.G.); alexoaps14@hotmail.com (A.P.); andre.mosquera@udla.edu.ec (A.N.M.)

[2] Escuela de Informática y Telecomunicaciones, Universidad Diego Portales, Santiago 8370190, Chile; pablo.palacios@mail.udp.cl

* Correspondence: ivan.sanchez.salazar@udla.edu.ec

Abstract: This work presents the development and implementation of a remote UV radiation monitoring station using LoRaWAN technology at the Universidad de las Américas. The main objective was to establish a system capable of measuring UV radiation levels through solarimeters, ensuring the remote transmission of data to protect the health and safety of students and staff exposed to solar radiation. To achieve this, several activities were conducted, including analyzing the architecture and communication components of LoRaWAN technology, designing a prototype based on this architecture, implementing the prototype based on the proposed design, and conducting functional tests to validate the system's operability. The system included the installation of a solarimeter and a receiver or gateway, configured to operate from 8 a.m. to 6 p.m. The data collected by the prototype were validated through comparisons with measurements from the environmental monitoring system of the Secretariat of Environment of the Metropolitan District of Quito, which allowed for the verification of the prototype's reliability. With this system, it was possible to identify patterns of high UV radiation and calculate error percentages in comparison with reference systems.

Keywords: Heltec ESP32; IoT; LoRaWAN; remote monitoring; Ubidots; UV radiation

1. Introduction

In Latin America, concerns about ultraviolet (UV) radiation are a significant issue for health and environmental preservation. The region is exposed to high levels of UV radiation due to its proximity to the equator and the varying climatic conditions characteristic of different areas. Specifically, Ecuador, located in the equatorial zone, experiences intense UV exposure throughout most of the year. Between 2007 and 2008, UV radiation levels ranged from 20% to 25% lower than those in 2009. In recent years, these levels have increased by up to 34% [1,2]. Ecuador's diverse geography, which includes the Pacific coast, the Amazon, and the Andes, presents specific challenges for UV radiation monitoring, emphasizing the importance of accurate records and measurements.

The private sector has also expressed concerns about this situation. Companies like Casabaca have shown interest in the high levels of UV radiation recorded in recent years in Quito, as they negatively impact the comfort of their clients and employees. This issue is particularly intensified in areas of prolonged exposure, such as outdoor vehicle displays and customer service zones, directly affecting potential buyers [3]. In the automotive sector, concerns include the effects of ultraviolet (UV) radiation on displayed vehicles, as it can lead to premature wear. Continuous exposure to high levels of UV radiation affects human health and the quality and lifespan of automobiles. Recent studies have shown that prolonged exposure to UV radiation causes damage to the paint, interiors, and plastic components of vehicles, accelerating depreciation and impacting customer satisfaction [4,5]. For example, ultraviolet radiation, particularly ultraviolet C (UVC), has been shown to deteriorate finishes, compromising both aesthetics and durability [4]. In addition, the application of high-quality waxes and sealants is recommended to protect the paint and minimize UV-induced damage [5].

As mentioned in [4], the effects of UV radiation on the paint and interior of vehicles represent a challenge that affects both car owners and automotive companies. Proper maintenance not only preserves the aesthetics and functionality of vehicles but also enhances the company's reputation by ensuring an immaculate presentation of the vehicles on display.

In the study by [6], the impact of UV radiation on human health was explored in depth, particularly its relationship with skin cancer. This knowledge is crucial for designing monitoring systems that not only measure radiation levels but also provide preventive recommendations.

In contrast, the research conducted by [7] on LoRaWAN not only addressed the limitations of the protocol but also offered a critical analysis of its performance under various operating conditions. By evaluating factors such as channel access, network capacity, and interference, this study has become an essential tool for optimizing communication networks.

Comparative analyses of similar projects have been crucial. The study by [**?**], titled "Ultraviolet Radiation Measurement Station Powered by Photovoltaic Systems", and the research conducted by [9], titled "Design and Implementation of a Sensor Network for Monitoring Solar Radiation Levels in the City of Loja", have proven particularly relevant. Both studies applied UV radiation monitoring technology; however, the approach proposed in this work is distinguished by the use of LoRaWAN and the integration of educational information regarding the risks associated with prolonged exposure to solar radiation. The implementation of pyranometers in the solution will enable the precise measurement of UV radiation, optimized for various contexts and geographical locations.

The relationship between UV radiation and skin cancer is well documented, highlighting the need for effective monitoring systems [10]. Furthermore, it is essential to explore the safety and efficiency aspects of LoRaWAN technology to ensure the reliability of UV monitoring networks [11]. Studies evaluating various technologies for UV radiation monitoring provide a comparative framework that can inform the selection of appropriate tools and methods [12]. Furthermore, insights into wireless sensor networks for environmental monitoring highlight how to effectively implement LoRaWAN in a UV monitoring context [13]. Lastly, understanding the broader impacts of solar radiation on human health can guide the development of informed preventive strategies within monitoring systems [14]. LoRaWAN, with its scalable and flexible infrastructure, ensures efficient long-distance data transmission with low energy consumption, making it ideal for various IoT applications, such as environmental monitoring and logistics management [15]. According to the information provided by [16], LoRaWAN operates in the 902–928 MHz frequency range in Latin America. This frequency band is regulated by the International Telecommunication Union (ITU), which allows low-power devices to operate without the need for licenses. This regulatory framework ensures that devices do not interfere with other telecommunication services or equipment, thereby guaranteeing proper operation within legal parameters.

Considering these challenges, the establishment of a real-time UV radiation monitoring station using solarimeters in conjunction with LoRaWAN technology presents a viable solution to the issue at hand. Accordingly, the proposed research encompasses the measurement of radiation as well as the benefits associated with the visualization and archival of climatic data. With LoRaWAN, a technology that facilitates long-range communication with low power consumption, effective implementation with UV radiation sensors is made possible, ensuring precise and continuous monitoring. Furthermore, the interoperability with various environmental monitoring sensors and the easy integration with existing infrastructures allow for the successful incorporation of such systems.

The integration of an effective solution for monitoring and recording ultraviolet (UV) radiation is a priority for health, environmental management, the preservation of automotive assets, and corporate reputation. The implementation of a monitoring station using LoRaWAN technology and solarimeters will not only address the challenges of radiation measurement but also promote the execution of preventive measures to safeguard human health.

Although LoRaWAN is a mature and widely adopted protocol, this work focuses on evaluating its performance in a highly constrained urban-ecological environment in the Andean region, where commercial solutions are often not optimized for terrain complexity, vegetation density, and infrastructure limitations. Rather than proposing novel protocol-level contributions, the development and deployment of custom hardware nodes allow for practical adaptation and empirical validation in suboptimal field conditions. This applied perspective provides valuable information for low-cost IoT deployments in similar regions, particularly in Latin America, where access to robust, commercial LoRaWAN infrastructure may be limited. It is important to note that for the evaluation of hostile scenarios where the performance of LoRaWAN technology was critically assessed Radio Mobile version 11.6.6 was employed as the simulation tool.

The outline of this paper is as follows. Section 2 provides a description of the problem and the methodology used. Subsequently, Section 3 details design and implementation system. Finally, the conclusions in Section 4 summarize the key aspects.

2. Problem Description and Methodology

The issue faced by the Universidad de las Américas lies in the need to protect its students and employees exposed to sunlight, ensuring their health and well-being. As the institution continues to grow and reports increases in enrollment and resources, it must also address the risks associated with UV radiation, which can affect both the quality of the educational environment and the health of its users.

To mitigate these risks, the Universidad de las Américas aims to implement a UV radiation monitoring station using LoRaWAN technology. This solution not only aligns with its commitment to the well-being of the university community but also promotes a safe and healthy environment. By accessing real-time data, the university will be able to make rapid adjustments to avoid exposure to dangerous levels of radiation, thus protecting the health of its students and employees and strengthening trust in the institution.

Selection and Identification of the Optimal Solution

In the implementation process of a real-time UV radiation monitoring station, various solutions were evaluated, considering the challenges and objectives of the project. One option explored was a nanosatellite for UV radiation monitoring [**?**]. However, it presented significant challenges, such as the need for precise sensors and the logistical complexity of its launch and operation, making it unviable.

Another alternative was the use of UV radiometers, based on the work of [18]. This option was rejected due to its high cost and the technical complexity required for maintenance, which would complicate its implementation.

Ultimately, it was determined that the implementation of a real-time monitoring station using solarimeters and LoRaWAN technology was the most suitable solution.

A qualitative SWOT (Strengths, Weaknesses, Opportunities, Threats) analysis was performed to assess the feasibility of each option, taking into account the technical, operational, and economic factors relevant to environmental monitoring in real-world conditions, as shown in Table 1.

Table 1. Qualitative SWOT analysis of the proposed monitoring solutions.

Proposal	Strengths	Weaknesses	Opportunities and Threats
Nanosatellite-based Monitoring	- High-precision data - Extensive coverage - Scientific value	- High cost and complexity - Launch and control limitations	*Opportunities:* International collaboration, high-impact research *Threats:* Launch failure, obsolescence, funding limitations
UV Radiometers with Traditional Telemetry	- Reliable and accurate data - Suitable for benchmark use	- Expensive equipment - Requires skilled maintenance	*Opportunities:* Use in industry or research labs *Threats:* Poor scalability, limited integration with LPWAN
Solarimeters with LoRaWAN (Selected)	- Cost-effective - Easy to deploy - Wireless long-range communication	- Lower precision than radiometers - Dependent on local gateways	*Opportunities:* Scalable for urban and rural networks, educational use *Threats:* Environmental interference, requires calibration

Three technological alternatives for real-time UV radiation monitoring were evaluated: nanosatellites, UV radiometers with traditional telemetry, and solarimeters integrated with LoRaWAN technology. Nanosatellites offer high-precision sensing and extensive coverage, with potential for international collaboration and advanced scientific research; however, they involve extremely high development costs, complex logistics, and dependence on orbital parameters, in addition to significant risks such as launch failure and rapid obsolescence. UV radiometers represent a proven and accurate technology, suitable for fixed-location scientific reference. However, their high cost, maintenance requirements, and lack of integration with modern low-power networks limit their scalability, particularly in remote areas. In contrast, the solarimeter-based solution using LoRaWAN stands out as cost-effective and simple to deploy with standard components. It supports low-power, long-range communication, enabling distributed monitoring; yet, its limitations include lower precision and dependence on local gateways. Despite these limitations, its scalability, compatibility with cloud platforms such as Ubidots, and resilience in urban and academic settings make it the most practical option, although it remains vulnerable to environmental noise and requires periodic calibration.

Considering the project's scope, which emphasizes cost-efficiency, real-time monitoring, and ease of deployment in an urban ecological setting, the solution with the solarimeter and LoRaWAN was deemed the most suitable. Although it is not the most precise solution, it strikes an optimal balance between performance, cost, and scalability.

Additionally, its integration with cloud platforms such as Ubidots facilitates rapid deployment, data visualization, and user-friendly alert configuration. These features are particularly valuable in university-led initiatives aimed at public health awareness and environmental education.

The selection prioritizes proven, low-risk technologies adaptable to local conditions, ensuring operational continuity and system scalability in the face of evolving monitoring needs.

The solution to be implemented was selected, and the methodology was clarified. The overall solution flowchart provides a sequential guide to the various stages and decisions involved in the implementation process, as illustrated in Figure 1. This flowchart encompasses everything from the acquisition of optimal resources, such as sensors and microcontrollers, to the final testing, offering a clear visual representation of the steps to be followed in the development of the solution prototype.

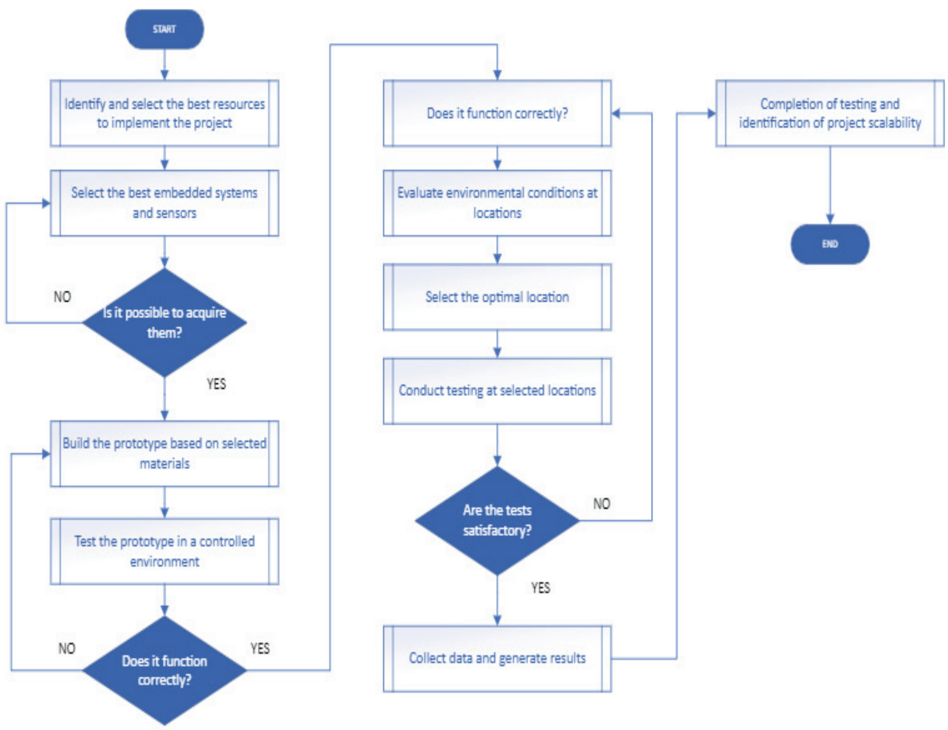

Figure 1. Flowchart of the solution development process.

3. Design and Implementation of the UV Monitoring Station

This section presents a comprehensive overview of the design and implementation of the proposed solution. A detailed account of the methodology and steps undertaken during the development and implementation phases is provided.

3.1. Design of the Solution

In the prototype, the data processed by the MAC layer are transmitted through the LoRa network to the gateways, which forward them to an external platform (Ubidots) for storage and analysis, facilitating decision-making. The LoRa Heltec ESP32 modules provide an efficient solution for LoRaWAN connectivity, and the UV UVM-30A sensor measures ultraviolet radiation and easily integrates into IoT systems. This architecture optimizes data transmission through access control and error correction techniques, ensuring reliability in noisy environments.

3.1.1. UV Sensor Characteristics and Power Requirements

The UV monitoring node is equipped with calibrated UV sensors that provide a sensitivity of ±1 μW/cm² and a measurement range from 0 to 15 mW/cm² [19]. These values are suitable for capturing variations in environmental UV radiation under different solar exposure conditions. The accuracy was validated in a laboratory setting by comparing the sensor outputs with a certified radiometer from the Environmental Monitoring Network of Quito, Ecuador. This allowed us to verify and correct sensor deviations, ensuring reliability in field measurements.

The power supply system consists of a 3.7 V 2500 mAh lithium-polymer (LiPo) battery regulated to 3.3 V to power the ESP32 microcontroller manufactured by Espressif Systems (Shanghai) Co., Ltd., headquartered in Shanghai, China. and peripheral components [20]. A 5 V–500 mA solar panel is integrated to support battery charging and ensure energy autonomy during prolonged outdoor deployment. This configuration enables continuous operation under variable sunlight conditions without an external power infrastructure.

3.1.2. UV Measurement Transmitter Circuit

The LoRa Heltec ESP32 microcontroller plays a crucial role in data acquisition and processing and is distinguished by its ability to handle long-range communication via the LoRa protocol. In addition, the ESP32 offers multiple analog and digital ports for input and output, making it suitable for connecting various types of sensors. For a better understanding of its capabilities, the specifications of the LoRa Heltec ESP32 are shown in Table 2.

Table 2. Specifications of the LoRa Heltec ESP32 microcontroller, taken from [21].

Parameter	Description
Master Chip	ESP32-S3FN8 (Xtensa®32-bit lx7 dual-core processor)
LoRa Chipset	SX1262
USB-to-Serial Chip	CP2102
Frequency	470~510 MHz, 863~928 MHz
Max. TX Power	21 ± 1 dBm
Max. Receiving sensitivity	-134 dBm
Wi-Fi	802.11 b/g/n, up to 150 Mbps
Bluetooth	Bluetooth LE: Bluetooth 5, Bluetooth mesh

ESP32 microcontroller manufactured by Espressif Systems (Shanghai) Co., Ltd., headquartered in Shanghai, China.

Regarding the microcontroller's pin layout, the most notable pins are the VCC pin, GND pin, and OUT pin, which are essential for connecting and integrating the UV sensor. In Proteus, a package was developed that accurately replicates the connection between the LoRa Heltec ESP32 microcontroller and the UVM-30A ultraviolet radiation sensor, (generic module commonly distributed without a specified manufacturer, for this project, it was sourced from DFRobot, Shanghai, China) generating virtual models that faithfully reproduce the physical layout of the pins and the electrical characteristics of both devices. The ESP32 was modeled with all relevant pins, including those for LoRa communication and input/output ports, ensuring a precise and consistent simulation with its physical version. The flowchart in Figure 2 details each stage of the process, from data transmission to error management in ESP32 communication.

Before undertaking the integration of the circuit, an analysis was conducted on three primary components: the UV radiation sensor, the LEDs, and the power supply, as illustrated in Figure 3. The following is a detailed description of each component:

- The UVM-30A sensor, known for its accuracy, provides an analog output connected to the ESP32's ADC, converting a 606 mV signal into a digital value of 752, corresponding to a level 6 solar radiation, using a 12-bit ADC (4096 levels).
- To enhance the visualization of UV radiation data, we integrated LEDs with differentiated colors to represent various levels of radiation, acting as a visual indicator similar to a traffic light. These LEDs, controlled by SONGLE SRD-05VDC-SL-C relays from the ESP32, provide a clear and visible representation, even in daylight conditions.
- To ensure a stable power supply, a 7805 voltage regulator was used, which converts a 12V input into a constant 5V output, complemented by capacitors and an indicator LED to guarantee the correct operation of the circuit.

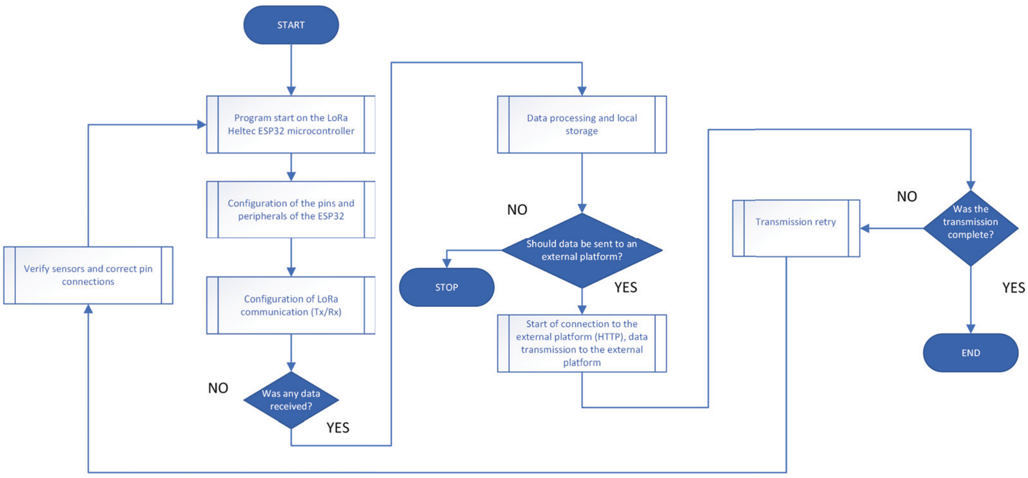

Figure 2. Flowchart of the LoRa Heltec ESP32 microcontroller operation.

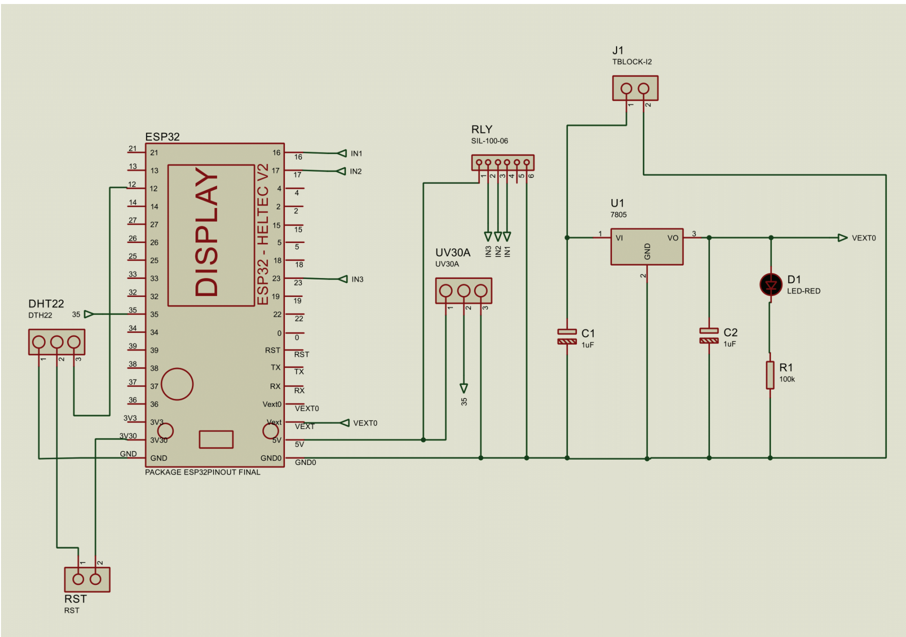

Figure 3. Structure of the voltage regulator alongside the LoRa Heltec ESP32 microcontroller and UVM-30A sensor on the Proteus platform.

3.1.3. UV Measurement Receiver Circuit

The receiver, or gateway, uses the LoRa Heltec ESP32 V2 module in receiver mode, with the same power supply configuration as the transmitter. The data received are transmitted to an external platform through HTTP communication. For direct visualization, 8 × 8 MAX7219 LED matrices were integrated to display UV radiation levels on a numerical scale from 1 to 11, allowing users to access this information without the need to connect to the Ubidots platform, as shown in Figure 4.

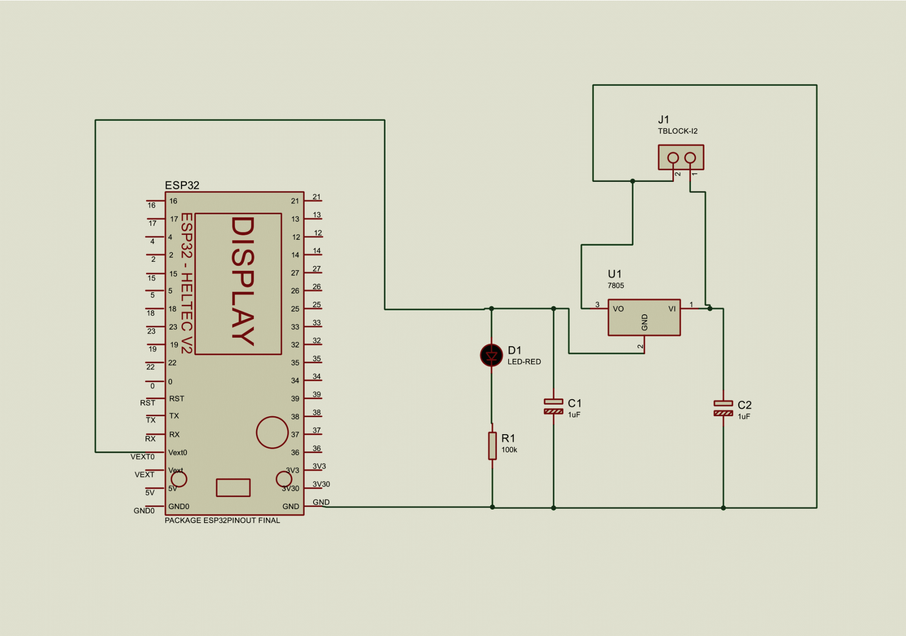

Figure 4. Design of the receiver circuit on the Proteus platform.

3.1.4. Calibration, Energy Management, and Node Deployment Strategy

Calibration of the UV sensors was performed by comparing the sensor readings with those obtained from certified professional radiometers used by the Quito Environmental Monitoring Network, Ecuador. The reference equipment is regularly calibrated to international standards. Discrepancies between the sensor data and the reference radiometers were recorded, and a correction function was implemented in the system's microcontroller firmware to ensure accurate and consistent measurements in the field. The measurement node operates with an average energy consumption of approximately 75 mA during active measurement and LoRa transmission [22], which lasts around 2–3 s per cycle. In deep sleep mode, when the node is not performing measurements, the current consumption drops to less than 10 µA, optimizing energy usage for extended periods of operation without constant recharging. The node is powered by a 3.7 V lithium-polymer (LiPo) rechargeable battery with a capacity of 2500 mAh. This battery is supported by a 5 V–500 mA solar panel, ensuring energy autonomy and continuous operation even in remote off-grid environments. To further reduce power consumption, the ESP32 microcontroller is set to enter deep sleep mode between measurements. The system performs measurements every 10 min, adhering to the 1% duty cycle limitation imposed by the LoRaWAN protocol. Each measurement cycle, including data transmission, lasts only 100 ms before the node returns to deep sleep mode, optimizing the energy efficiency of the system. The node locations were chosen based on key criteria: direct exposure to sunlight to ensure accurate UV measurements and effective solar panel charging; verified LoRaWAN network coverage, confirmed through preliminary field tests with a strategically placed gateway; and accessibility for regular maintenance and to ensure the physical security of the equipment.

Table 3 summarizes the technical specifications outlined in the preceding section.

Table 3. Technical specifications and implementation details of the UV monitoring system.

Aspect	Description
Sensor sensitivity	Calibrated UV sensors with a typical sensitivity of ±1 μW/cm²
Measurement range	0 to 15 mW/cm²
Accuracy	Validated in the laboratory by comparing against a certified professional radiometer from the Quito Environmental Monitoring Network
Power supply	A 3.7 V LiPo battery with a 2500 mAh capacity, combined with a 5 V–500 mA solar panel for energy autonomy
Average energy consumption	75 mA during active mode (lasting 2–3 s per cycle); below 10 μA in deep sleep mode
Energy-saving strategies	Deep sleep mode of the ESP32 microcontroller, cyclic measurement every 10 min, short LoRa transmission duration (100 ms)
Calibration process	Calibration was conducted by comparing the sensor's readings with certified equipment from the municipal UV monitoring network; a correction function was applied in the firmware
Node placement criteria	Nodes were placed along an ecological trail on the university campus, considering (a) direct sunlight exposure; (b) verified LoRaWAN coverage from a strategically located gateway; and (c) physical safety and accessibility for periodic maintenance

3.2. Implementation of the Solution

3.2.1. Development of Transmitters on Protoboards

To initiate the transmitter prototype, protoboards were chosen to facilitate easy modifications and functional tests. Components such as the Heltec ESP32 LoRa microcontroller, the UVM-30A ultraviolet radiation sensor, and an ESP32 LoRa antenna with a nominal gain of 2 dBi were assembled, as specified in [23]. The prototyped transmitter circuit shown in Figure 5 was programmed using the Arduino environment due to its library support and ease of use, which allows efficient implementation of UV radiation data transmission functions.

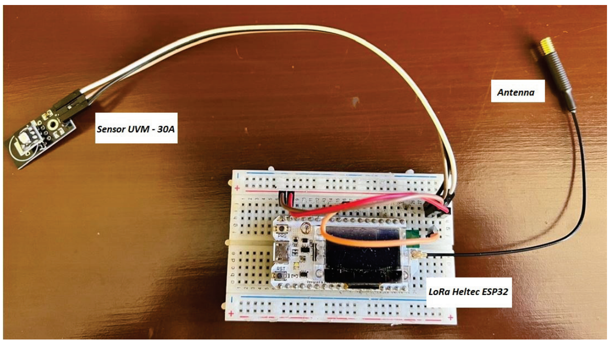

Figure 5. Transmitter circuit on a protoboard.

The transmitter prototype includes an OLED display integrated with the LoRa module, which displays real-time UV radiation values before transmitting them to the gateway. This design ensures reliable data visualization on the OLED and validates data reception by the gateway, as shown in Figure 6.

3.2.2. Development of the Receiver (Gateway)

Subsequently, a receiver or gateway was developed on a protoboard for initial testing and adjustments. Using components such as the LoRa Heltec ESP32, an ESP32 LoRa antenna, and a 12 V power supply, the prototype was assembled, as shown in Figure 6.

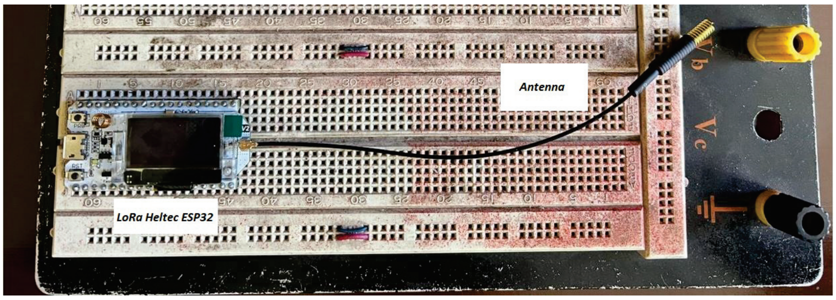

Figure 6. Receiver or gateway circuit in operation on a protoboard.

The gateway program enables the reception of UV radiation data from the transmitters, displays it on its OLED screen, and sends it to the Ubidots platform via HTTP communication. Within the module's programming, libraries such as 'SPI.h', 'LoRa.h', 'SSD1306.h', and 'UbidotsEsp32Mqtt.h' were used to enable LoRa protocol communication, SPI functionality, OLED management, and connectivity to Ubidots through MQTT.

3.2.3. Migration to PCBs

To enhance durability and performance stability, the circuits were migrated from the protoboards to printed circuit boards (PCBs) to provide efficient integration, a compact size, and improved reliability for data collection and transmission, as verified during testing and shown in Figure 7.

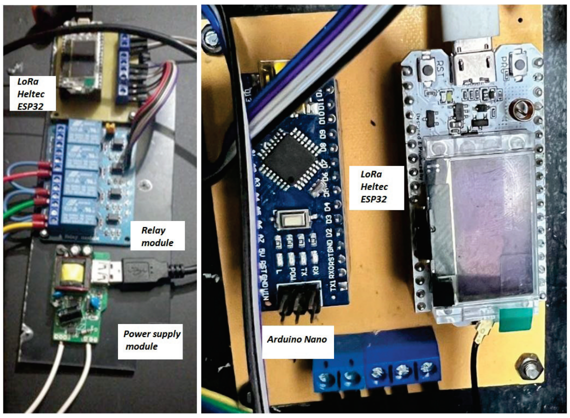

Figure 7. Prototypes on PCBs.

3.2.4. Additional Elements

In addition to transmitters and receivers, additional elements, such as protective structures and visual aids, were incorporated to enhance the reliability and durability of the system. The QPLITE EDMP-12 LED model, operating at 50/60 Hz with a controlled voltage input range of 85–265 V, was selected for its robustness and visual feedback. These LEDs, placed on the transmitters, use red, yellow, and green indicators to represent various radiation levels, while the 8 $\times$ 8 LED matrices on the gateway allow for quick indoor visualization of radiation levels, as shown in Figures 8–10.

Figure 8. LEDs to indicate radiation levels.

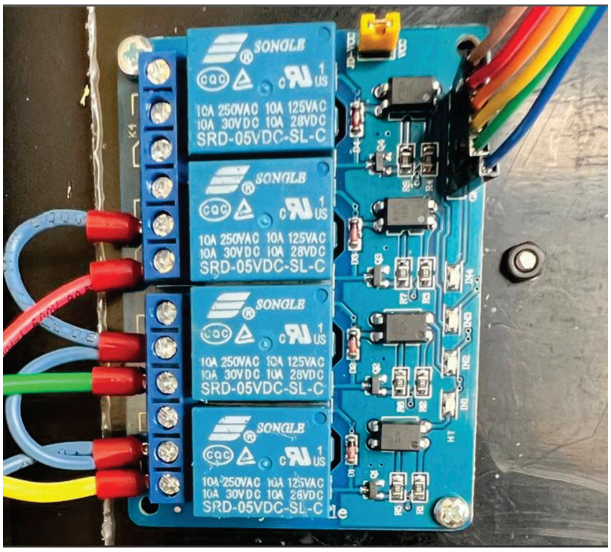

Figure 9. Connection of LED wires to the relays.

Figure 10. LED matrix on the receiver or gateway.

To protect electrical devices from adverse weather conditions, physical structures were implemented to house the transmitters, LEDs, and receivers with their LED matrices. Materials such as steel were used for the structures and vinyl for the visual elements, while a simpler plastic structure was used for the receiver or gateway, as shown in Figures 11 and 12.

Figure 11. Qualitative LED matrix on the receiver or gateway.

Figure 12. Quantitative matrix of the LEDs on the receiver or gateway.

As mentioned above, to display real-time UV radiation data, alert users for high levels, and store information, the system is connected to the Ubidots platform. To start, an account must be registered on their website, a new project created, and the ESP32 microcontroller selected, thus generating a unique ID and API token to facilitate communication.

In receiver programming, the connection to Ubidots is configured using its library, first entering the WiFi network credentials, followed by the ID and API token. This enables the ESP32 to connect to the network and send data, including two variables of UV radiation from the two solarimeters, as shown in Figure 13.

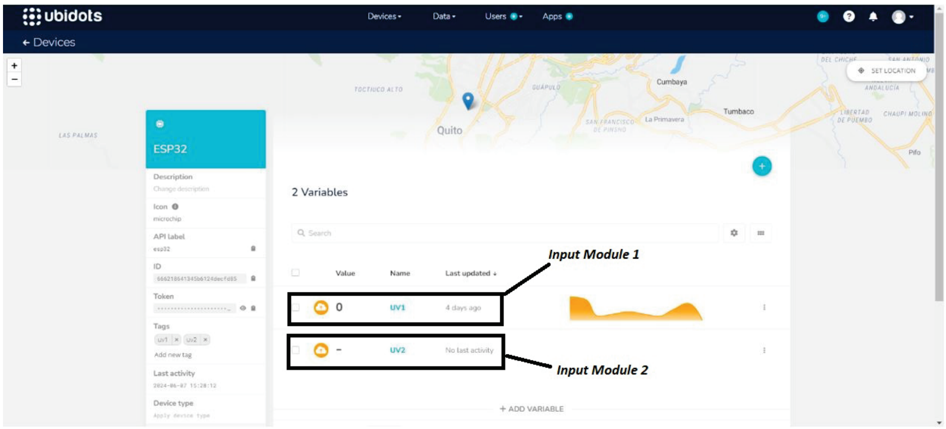

Figure 13. Selection of the number and type of variables in Ubidots.

Finally, on the main Ubidots dashboard, widgets are selected to visualize UV radiation levels, receive alerts if they exceed safe thresholds, and determine the type of data to be stored, as shown in Figures 14 and 15.

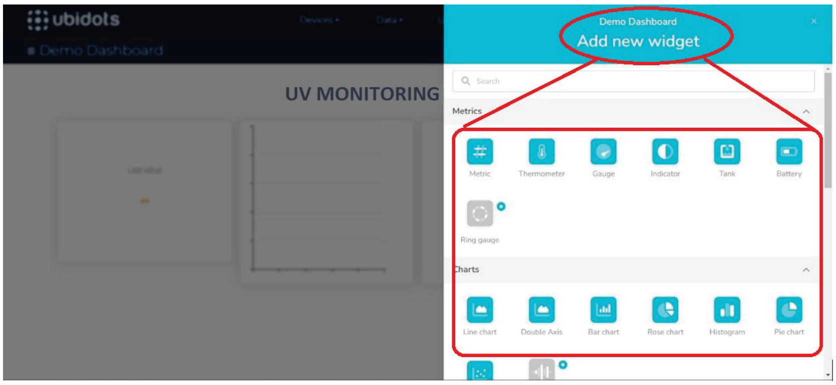

Figure 14. Selection of widgets.

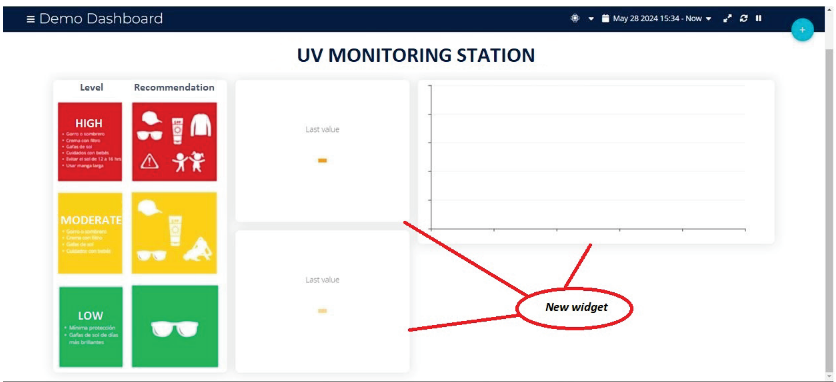

Figure 15. Selected widgets on the main dashboard of Ubidots.

3.3. Testing and Evaluation of the Prototype

At this stage, tests for measuring UV radiation were conducted using LoRa communication at a frequency of 433 MHz to ensure continuous range and transmission. The data were stored in the cloud and validated using the official environmental monitoring system of the Secretary of Environment of the Metropolitan District of Quito, which measures UV radiation as one of its parameters.

3.3.1. UV Radiation Tests

To validate the UV radiation levels of the UVM-30A sensor, tests were conducted under various climatic conditions, as shown in Figure 16. The initial tests, carried out on the protoboards, indicated that at 2:30 p.m. on 7 June 2024, a radiation level of 5 was recorded near the University of the Americas, confirming the UV data collection.

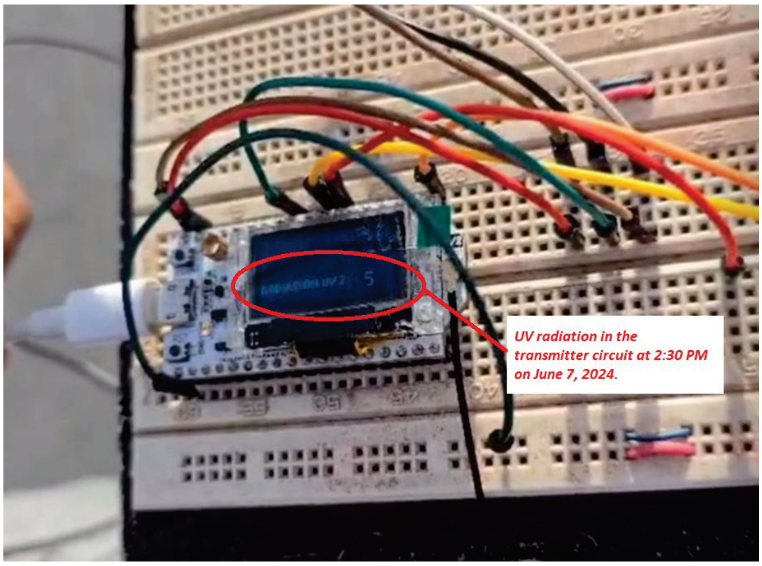

Figure 16. UV radiation in the transmitter circuit on a breadboard at 2:30 p.m. on 7 June 2024.

A UV radiometer (Biospherical Instruments GUV2511) from the Ministry of Environment was used as a reference, located in Jipijapa, Quito, less than 3 km from the testing sites, as shown in Figure 17. At the same date and time, this radiometer also recorded levels close to 5, which corresponded to the data from the prototype.

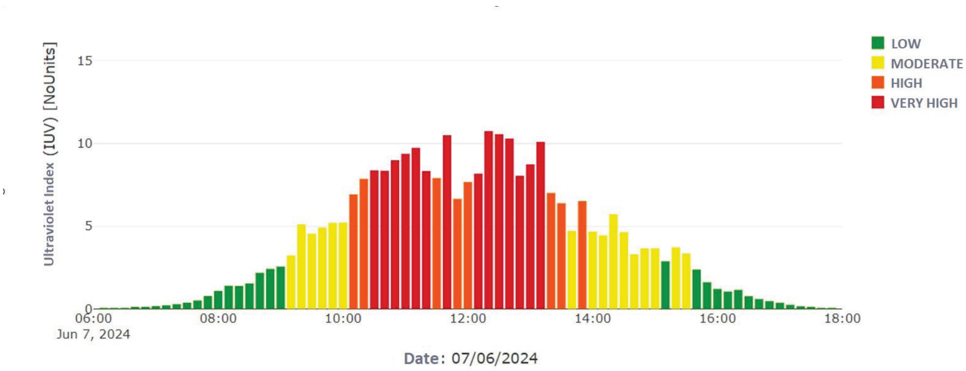

Figure 17. Bar graph showing UV radiation records provided by the Ministry of Environment's radiometer for 7 June 2024 [24].

Subsequently, the test was replicated with the circuit on a PCB, yielding similar results but showing a notable improvement in stability and accuracy compared to the protoboard tests, as shown in Figures 18 and 19. These results validated the effectiveness of the UV30 sensor compared to the official radiometer.

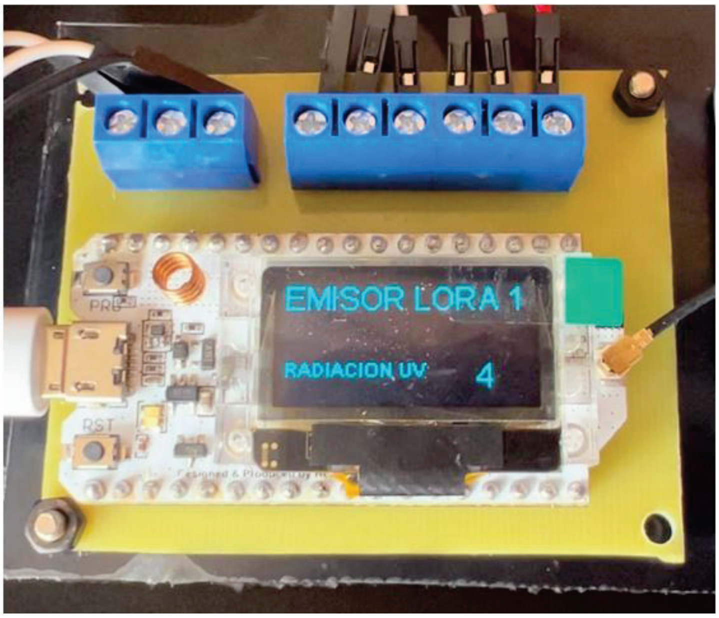

Figure 18. UV radiation in the transmitter circuit on a PCB at 3 p.m. on 12 June 2024.

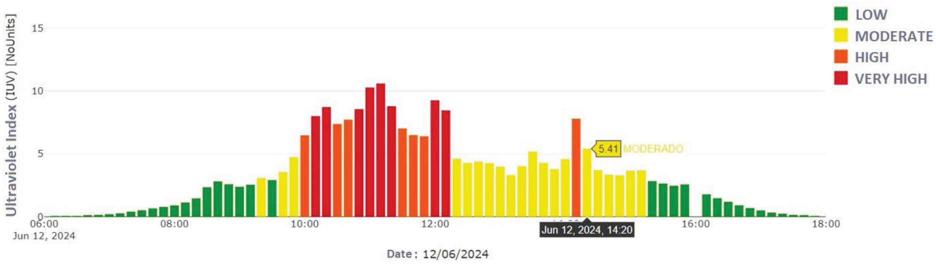

Figure 19. Bar graph of UV radiation records provided by the Ministry of Environment's radiometer for 12 June 2024 [24] .

3.3.2. Distance Tests with Heltec LoRa Modules

The next phase of the test focused on LoRa communication, assessing the range and continuous transmission. The trials were carried out in a controlled environment at the Universidad de las Américas, where effective communication between the transmitters and receivers on the protoboards was achieved, reaching up to 220 m, as shown in Figure 20. At this distance, the signal exhibited an attenuation of 88.07 dB.

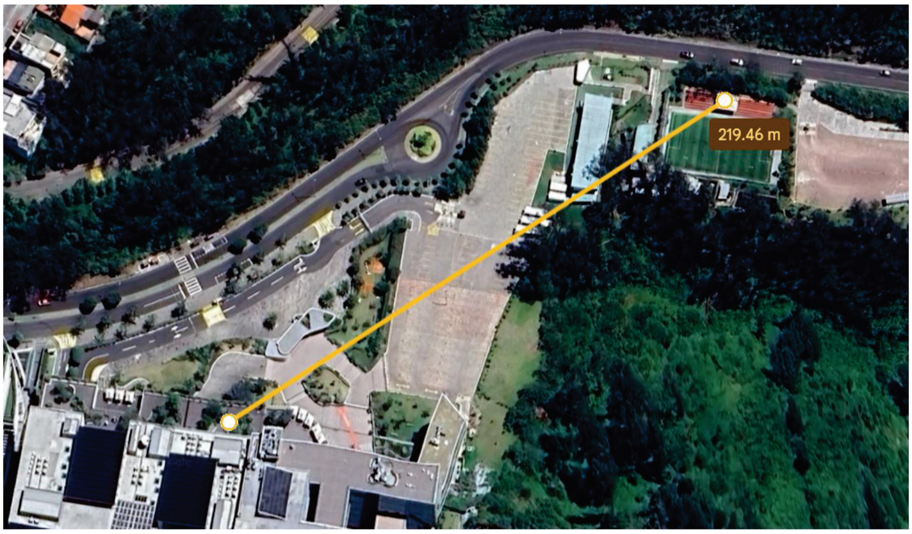

Figure 20. Maximum distance achieved with the prototypes on the protoboards.

With the circuit implemented on the PCBs, communication improved significantly, reaching 335 m with an attenuation of 91.59 dB, as shown in Figure 21. This increase is consistent with the expected behavior of electromagnetic waves, where signal loss increases with distance.

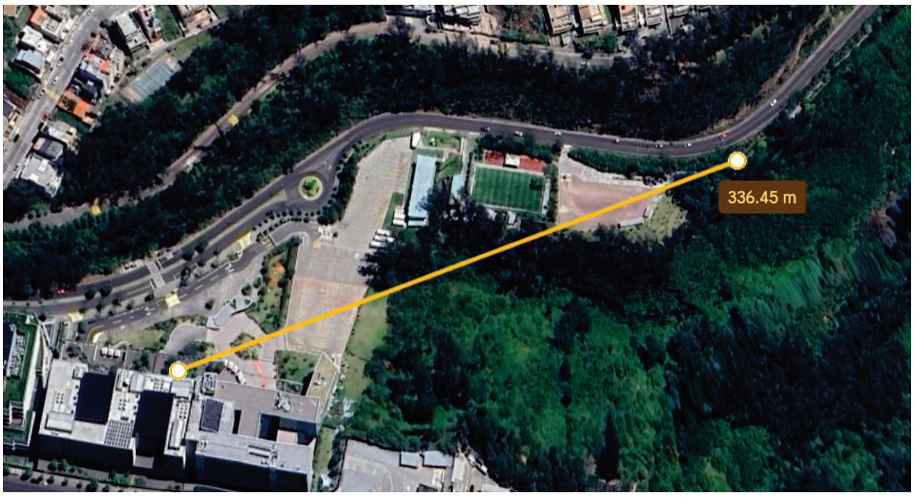

Figure 21. Maximum distance achieved with the prototypes on the PCBs.

3.3.3. Radio Propagation Modeling and Simulation

To complement the empirical measurements conducted in the field, a series of simulations were performed using the Radio Mobile tool, which is based on the Longley–Rice propagation model. This tool enables the prediction of terrain-aware radio coverage by incorporating elevation data (SRTM) and environmental conditions.

The simulations were conducted to replicate and analyze signal behavior under the real topographical and environmental conditions of the ecological trail. Each scenario was designed using georeferenced profiles and actual device parameters, such as frequency (433 MHz), antenna heights, and transmission power, to model the expected path loss and received power over various terrain configurations. The goal was to identify potential coverage limitations, assess line-of-sight (LoS) availability, and compare the simulated results with in situ measurements to determine the impact of vegetation, terrain irregularities, and elevation profiles on LoRaWAN signal performance.

This simulation approach provides a predictive baseline to contrast with real-world behavior, especially in conditions where dynamic losses (e.g., multipath or vegetation absorption) are difficult to fully capture using theoretical models alone. Scenarios were selected to represent both optimal and suboptimal propagation conditions, including clear terrain, forested sections, and elevation transitions near a ravine. Table 4 describes the simulated scenarios, and Table 5 provides the technical details of the simulation using Radio Mobile. For all simulation scenarios, the transmitter coordinates and parameters were the latitude (Tx): −0.162929; longitude (Tx): −78.45917; transmit power (dBm): 15; and receiver sensitivity (dBm): −124.

Table 4. Summary of Radio Mobile simulation scenarios.

Scenario	Brief Description	Distance (m)	Tx/Rx Height (m)	Environmental Characteristics
1	4° slope profile, LoS evaluation	336	2 / 1	Sloped terrain, no major obstructions
2	Real case with observed loss at 336 m	336	10 / 1	Moderate vegetation, link failure despite sufficient power
3	Communication across a ravine	370	10 / 1	Rx in lower areas, dense vegetation, vertical obstruction
4	Open area (control)	490	10 / 1	Clear terrain, good alignment with transmitter
5	Forested section	490	10 / 1	Dense vegetation, same profile as Scenario 4 for comparison
6	Extended path with vegetation	560	10 / 1	Similar elevation to Tx, light vegetation, most distant point

Table 5. Details of simulation scenarios.

S	Latitude (Rx)	Longitude (Rx)	TxH (m)	RxH (m)	D (m)	OD (m)	Path Loss (dB)	Rx Power (dBm)	Observation
1	−0.161931	−78.456219	2	1	336	90	102.6	−84.6	Simulated with identical Tx and Rx height.
2	−0.161931	−78.456219	10	1	336	320	91.8	−73.8	Real case, data loss observed at 91.58 dB.
3	−0.162470	−78.455889	10	1	370	90	106.2	−88.2	Receiver located deeper within the ecological trail near the ravine (Simulated).
4	−0.163669	−78.454818	10	1	490	480	88.7	−70.7	Receiver positioned above the trail, near Tx height, with vegetation (Simulated).
5	−0.163669	−78.454818	10	1	490	480	88.7	−70.7	Same location as scenario 4, without vegetation (Simulated).
6	−0.163611	−78.454160	10	1	560	570	93.3	−75.3	Farthest point, aligned with Tx height, with vegetation (Simulated).

Note: S—Scenario; TxH—Tx Height; RxH—Rx Height; D—Distance; OD—Obstruction Distance.

Scenario 1: A section of the ecological trail with a slope of 4° was simulated using SRTM elevation data in Radio Mobile. The transmitter and receiver antennas were set at 2 m and 1 m, respectively, over a distance of 336 m. The goal was to assess the LoS conditions and estimate the path loss. The results showed a path loss of 102.6 dB and a received power of −84.6 dBm, which is well above the sensitivity threshold (−124 dBm), indicating a functional link. However, significant signal degradation was evident due to the inclined terrain. This effect can be observed in Figure 22.

Scenario 2: A simulation was conducted in Radio Mobile to replicate the real conditions that caused a 92 dB signal at 336 m. The setup used a higher transmitter height (10 m) to analyze the impact of the terrain, antenna height, and 433 MHz frequency on link performance. Despite a theoretical received power of −73.8 dBm with a simulated path loss of 91.8 dB, the link failed in practice. This suggests the presence of additional unmodeled losses, such as vegetation absorption, destructive multipath, or environmental interference. Although the receiver sensitivity was −124 dBm, the actual sensitivity depends on the spread factor (SF) and bandwidth (BW); default settings prioritizing low latency or energy savings may reduce effective sensitivity, increasing demodulation errors, and contributing to communication loss. This effect can be observed in Figure 23.

Scenario 3: LoRaWAN communication was evaluated over a distance of 370 m in an environment characterized by natural vertical obstructions, where the receiver was located in a low-lying area near a ravine, at a negative relative elevation compared to the transmitter, and surrounded by dense vegetation. This configuration resulted in significant signal degradation, with a path loss of 106.2 dB and a received signal strength of −88.2 dBm. Although the signal remained above the sensitivity threshold, it approached a low link margin. Sloped terrain, ground humidity, and dense vegetation contributed significantly to signal attenuation, demonstrating how topographic and environmental factors can severely impair the propagation of 433 MHz signals, even over relatively short distances. This scenario can be observed in Figure 24.

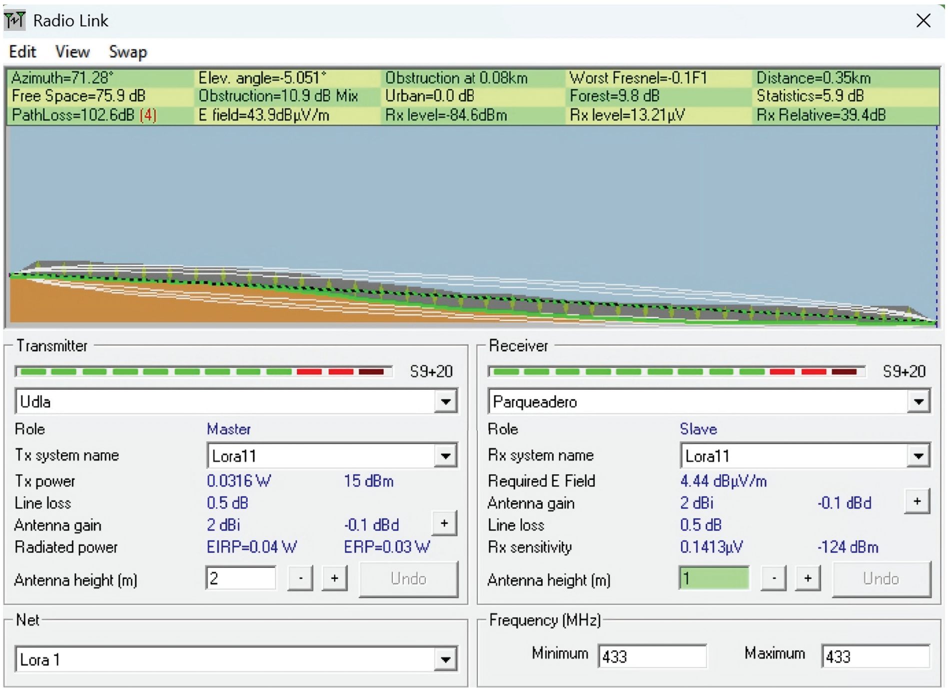

Figure 22. Simulation of Scenario 1: Line-of-sight conditions and path loss on a 4-degree slope section of the ecological trail using elevation data in Radio Mobile.

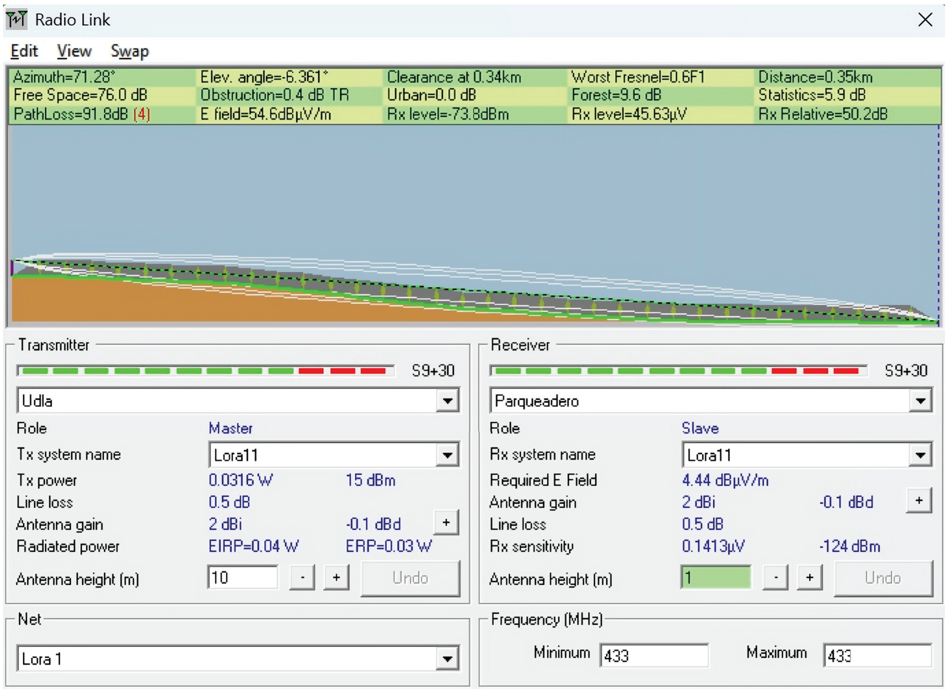

Figure 23. Simulation of Scenario 2: Terrain and antenna height effects on link performance at 433 MHz over 336 meters with observed signal loss.

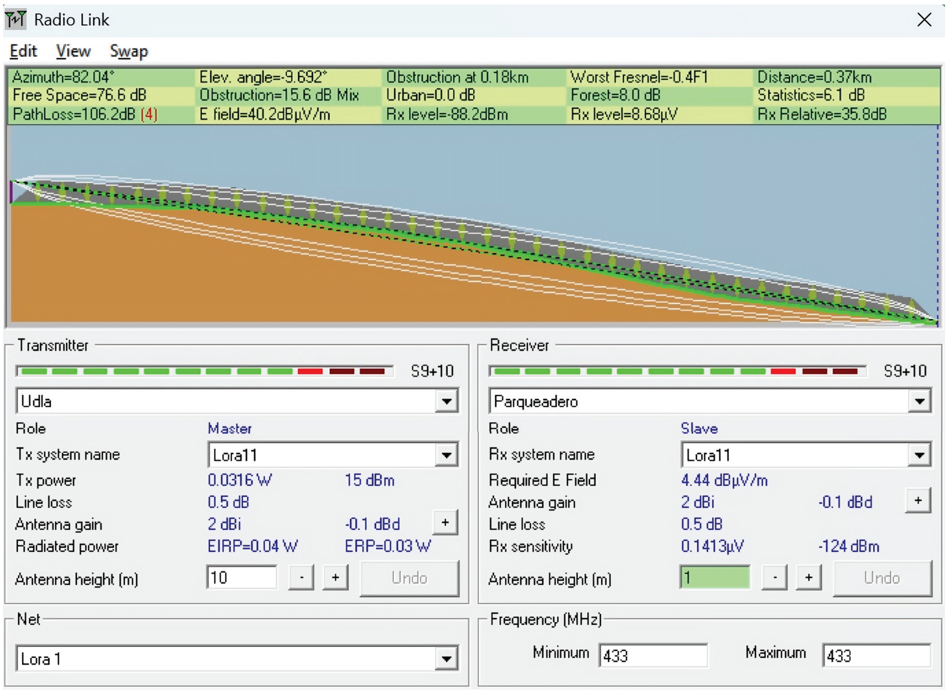

Figure 24. Simulation of Scenario 3: Evaluation of 433 MHz signal degradation over 370 meters due to terrain slope, dense vegetation, and negative receiver elevation.

Scenarios 4 and 5: These scenarios enabled a comparative analysis between an open area and a forested area, maintaining a constant transmission distance (490 m) and antenna heights (10 m at the transmitter and 2 m at the receiver). Two profiles were selected: one located on a clear terrain segment and another within a densely vegetated ecological trail. The objective was to demonstrate the direct impact of the surrounding environment on the propagation loss, highlighting how the presence of vegetation can increase the path loss and degrade link performance, despite identical geometric conditions. Both cases yielded identical simulation results, with a path loss of 88.7 dB and received power of −70.7 dBm, suggesting that vegetation had no significant effect under the simulated model. However, real-world deployments may differ. In particular, the elevation of the receiver, which was comparable to that of the transmitter, considerably reduced the propagation loss, indicating that favorable topography mitigates the impact of distance. These scenarios can be observed in Figures 25 and 26.

Scenario 6: This scenario focused on an open area adjacent to a forested area, using a link distance of 560 m and identical antenna heights enabled by the topographic profile. This setup aimed to evaluate how environmental characteristics, particularly dense vegetation, as found along the ecological trail, influence the propagation loss. By keeping the technical parameters constant, the effect of natural clutter was isolated, showing that even with equivalent geometric conditions, vegetated environments can increase the path loss and compromise link quality. The simulation yielded a path loss of 93.3 dB and a received power of −75.3 dBm. Although the signal remained within the link margin, the conditions were more demanding. This scenario confirms that, even at longer distances, favorable alignment and relative visibility can sustain the link despite environmental obstacles. These effects can be observed in Figure 27.

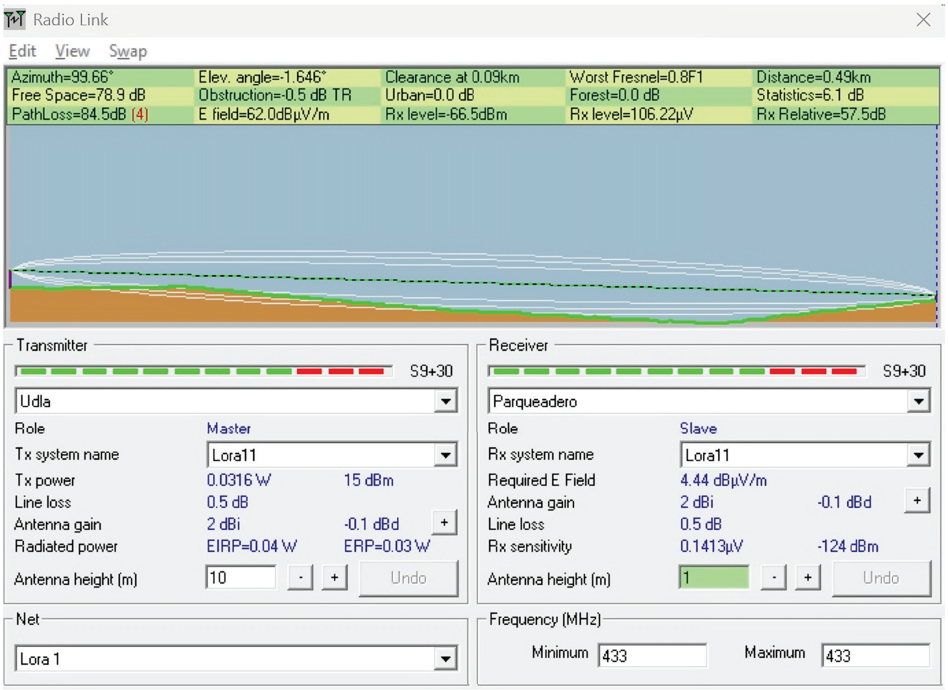

Figure 25. Simulation of Scenario 4: Simulated 433 MHz signal propagation over 490 meters in an open area with favorable topography.

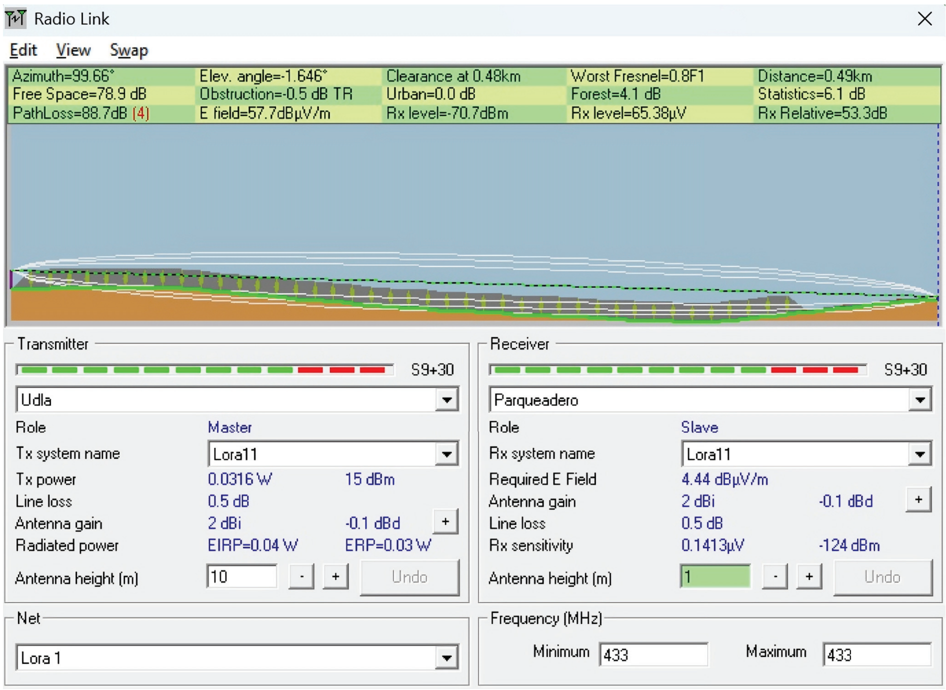

Figure 26. Simulation of Scenario 5: Simulated 433 MHz signal propagation over 490 meters in a densely vegetated area with comparable elevation.

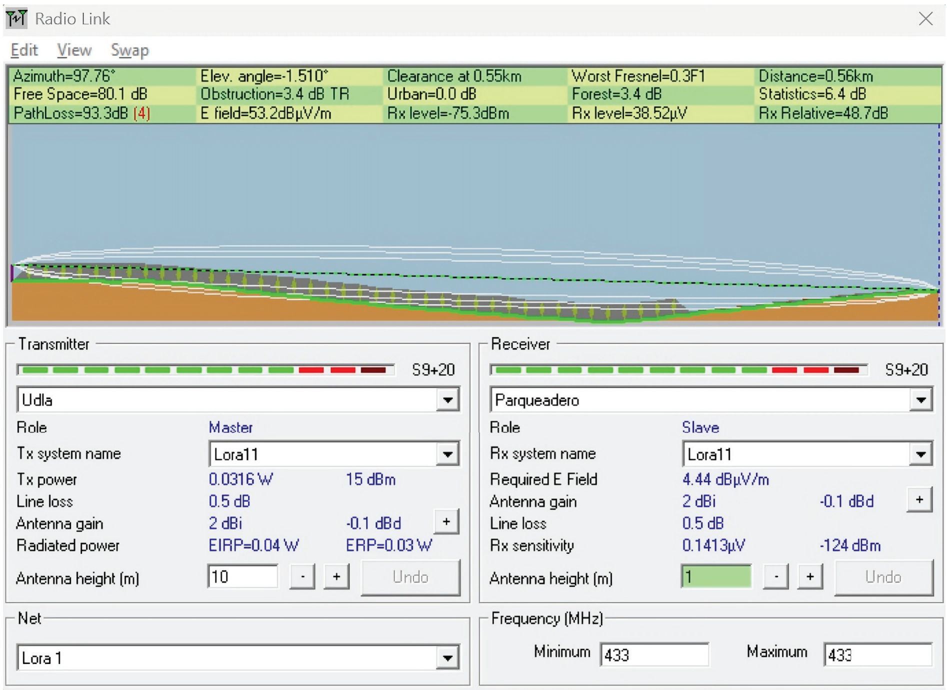

Figure 27. Simulation of Scenario 6: Simulation of 433 MHz signal propagation over 560 meters near a forested area to assess vegetation impact under aligned topographic conditions.

3.3.4. Tests with the Ubidots Platform

The proper functioning of the Ubidots platform is crucial for visualization, data storage, and notifications about elevated levels of UV radiation. To ensure its effectiveness, various tests were conducted.

First, it was verified that the radiation levels from each UV meter were displayed in real time in their respective dashboard widgets. As shown in Figure 28, the UV radiation level reached a value of 5 at 2:30 p.m. on 7 July 2024, which coincides with the readings taken on the protoboards and confirms the precision of the data reflected on the platform (see Figures 18 and 19). A minimum data update frequency was configured, and the bar chart widget was scheduled to update every 10 min, allowing the monitoring of radiation trends.

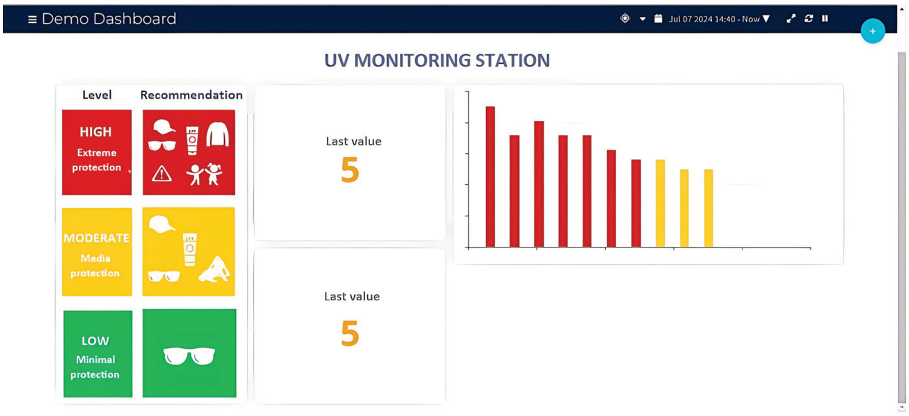

Figure 28. UV radiation at 2:30 p.m. on 7 June 2024, as shown on the Ubidots platform. UV radiation levels: green (low risk), orange (high risk), and red (very high risk).

Additionally, the capability of the platform to store historical data was evaluated. By activating the "timestamp" feature, the data were securely saved in the "Events" section, enabling comparisons with other UV radiation data sources. It was decided to record data twice per hour, in accordance with the limitations of the free version of Ubidots.

Finally, the system alerts, which notify users of dangerous levels of UV radiation, were tested. Maximum thresholds were established, and when these thresholds were exceeded, automatic alerts were generated, facilitating prompt decision-making.

3.3.5. Estimated Duty Cycle Calculation

To estimate the duty cycle, the following assumptions were made:

- Transmission frequency: **6 times per hour.**
- Approximate duration of each packet: **100 ms** (conservative estimate based on the initial LoRa configuration).

$$\text{Total transmission time per hour} = 6 \times 100\text{ ms} = 600\text{ ms}$$
$$\text{Total time in one hour} = 3600\text{ s} = 3,600,000\text{ ms}$$
$$\text{Duty cycle} = \frac{600\text{ ms}}{3,600,000\text{ ms}} \approx 0.0167\%$$

The results showed that the estimated duty cycle was approximately **0.0167%**, which is significantly below the maximum allowed limit of **1%** for ISM band operations, as specified by the ETSI EN 300 220-2 V3.2.1 (2018-06) standard [25].

3.4. Results and Discussion

A data collection period was established for testing purposes due to the limited storage available in the free version of Ubidots for meteorological data. In addition, the system was configured to operate from 8 a.m. to 6 p.m. and then enter 'deep sleep' mode to conserve energy and comply with ITU recommendations. This setup also aimed to replicate the monitoring system used by the Environmental Secretariat in Quito and ensure data accuracy. The results are presented below.

3.4.1. Comparison of UV Radiation Recorded by Each Individual Solarimeter

To evaluate the individual performance of each solarimeter, the data collected on Tuesday, 2 July, and Wednesday, 3 July, were analyzed. The results showed consistent radiation readings between both devices, except at 3:00 p.m. on Tuesday, when the first solarimeter recorded a level of 4 and the second a level of 1, reflecting a difference of 3 units, as shown in Figure 29. After monitoring the second solarimeter the following day, it was found that the shadow of a nearby column in the northeast courtyard of the Universidad de las Américas affected its readings. To correct this, the solarimeter was relocated out of the shadow's range, thus ensuring the reliability of the UV radiation data in the area.

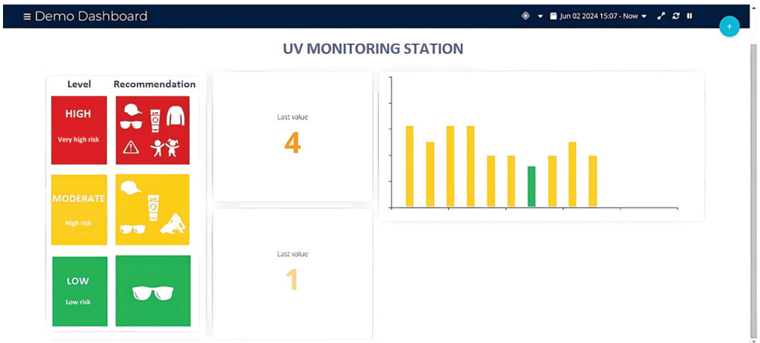

Figure 29. UV radiation at 3:00 p.m. on 2 July 2024, as shown on the Ubidots platform. UV radiation levels: green (low risk), orange (high risk), and red (very high risk).

3.4.2. Data Collection and Analysis

The first step was to validate these data by comparing them with those recorded by the Environmental Secretariat during the same period. The comparison revealed consistent results, as seen in Figure 30, taking into account operating hours and the equipment used, which supports the reliability of the measurements.

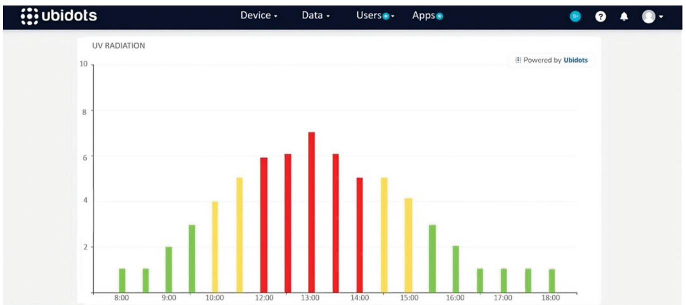

Figure 30. Bar chart showing the average UV radiation during the testing period.

The analysis indicated that UV radiation levels increased exponentially from 10:00 a.m., reaching their peak between 11:00 a.m. and 2:00 p.m., as illustrated in Figure 2, which presents the average UV radiation by hour. Although UV radiation followed a general pattern, significant variations were observed on specific days and hours, reaching health-threatening levels. Six alerts were issued, primarily between 11:00 a.m. and 2:00 p.m., as shown in Figures 31 and 32.

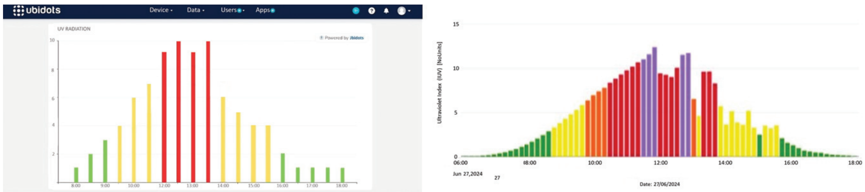

Figure 31. Variationsrecorded on 27 June 2024. Note: Data compared with the [24]. UV radiation levels (Left graph): green (low risk), orange (high risk), and red (very high risk). UV radiation levels (Right graph): green (low risk), yellow (moderate risk), orange (high risk), red (very high risk), and violet (extreme risk).

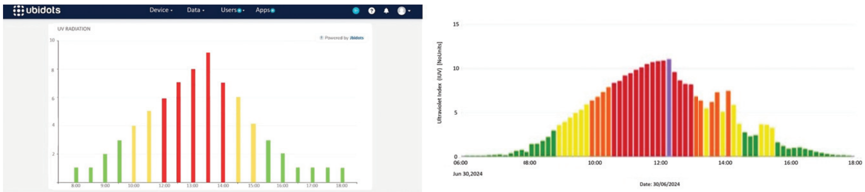

Figure 32. Variations recorded on 30 June 2024. Note: Data compared with the [24]. UV radiation levels (Left graph): green (low risk), orange (high risk), and red (very high risk). UV radiation levels (Right graph): green (low risk), yellow (moderate risk), orange (high risk), red (very high risk), and violet (extreme risk).

3.4.3. Prototype Accuracy Compared to Other Professional UV Radiation Meters

The data obtained from the solarimeters were compared with those collected by the receiver or gateway and the radiometers recorded by the Environmental Secretariat, aiming to assess the accuracy of the implemented prototype. This was achieved by computing the percentage error, as demonstrated in the calculation below. The percentage error is quantified using the following expression:

$$\%_{error} = \frac{Xprofessional - Xrecorded}{Xprofessional * 100}, \tag{1}$$

where $Xprofessional$ corresponds to the specific level measured by the radiometer from the Environmental Secretariat and $Xrecorded$ is the level registered by the prototype. For the calculation, the following values recorded on 4 July 2024 were used: the value recorded by the Environmental Secretariat at 10:40 a.m., which was 7.5, as shown in Figure 33.

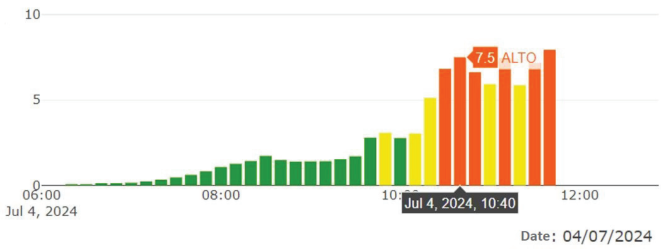

Figure 33. Value of radiation recorded by the Environmental Secretariat at 10:40 a.m. on 4 July 2024. Taken from the [24]. UV radiation levels: green (low risk), orange (high risk), and red (very high risk).

Figure 34 shows that the value recorded by the prototype at 10:40 a.m. was 7.3.

Applying these values within the context of Equation (1), the resulting expression is derived as follows:

$$\%_{error} = \frac{7.5 - 7.3}{7.5 * 100},$$

$$\%_{error} = 2.67 \quad (2)$$

The correlation between the data collected by the solarimeters and the radiometers showed a discordant value of 3%. Based on these data, it can be concluded that there is a strong relationship between the two UV radiation records, with a correlation coefficient of 0.97. This result demonstrates the precision of the prototype in measuring UV radiation, meeting the required levels of precision necessary for both health-related applications and environmental monitoring.

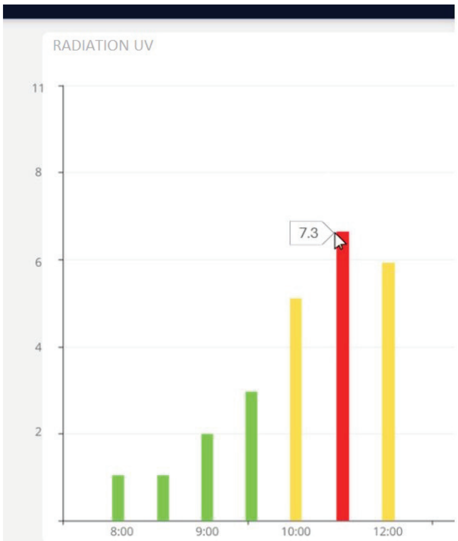

Figure 34. Value of radiation recorded by the prototype at 10:40 a.m. on 4 July 2024. UV radiation levels: green (low risk), orange (high risk), and red (very high risk).

4. Conclusions

An analysis of the architecture and components of LoRaWAN technology enabled the design of an effective solution for monitoring UV radiation, considering the operating frequencies recommended by the ITU and compatible devices. The prototype demonstrated its efficiency during validation on the protoboards and PCBs, as well as in its implementation at Universidad de las Américas, where the testing revealed only a 3% discrepancy compared to professional systems, demonstrating its reliability.

The collected data revealed significant patterns in UV radiation levels, showing an exponential increase between 11:00 a.m. and 2:00 p.m., a critical period for protecting the health of students and staff. Effective integration with the Ubidots platform facilitated data visualization and storage, allowing students to monitor elevated UV radiation levels. These results highlight the positive impact of the implemented solution at the Universidad de las Américas.

The precision of the prototype was validated against the records of the Environmental Secretariat, showing a correlation of 97% and a percentage error of only 2.67%. This shows that the prototype meets the required precision levels for health and environmental monitoring applications, offering a reliable and accessible alternative to professional systems.

During implementation, technical challenges were encountered in LoRa communication, particularly in terms of continuous transmission and signal range. In controlled tests within the Universidad de las Américas, effective communication between the transmitters and receivers on the protoboards was achieved up to 220 m, with an attenuation of 88.07 dB. However, with their implementation on the PCBs, the range improved significantly to

335 m, with an attenuation of 91.59 dB, confirming the expected relationship between distance and signal loss.

Although simulations in Radio Mobile provided a solid technical foundation, real-world environmental conditions, such as vegetation, humidity, multipath propagation, and irregular topography, could introduce significant additional losses that may not always be captured by the model, potentially leading to link failure even before reaching the theoretical sensitivity limit. It was confirmed that transmitter elevation significantly enhanced link performance, particularly in sloped terrain and vegetated environments. Furthermore, the area adjacent to the ravine represents a critical environment that requires experimental validation, while scenarios with favorable transmitter positioning demonstrated the potential to achieve greater distances, even in the presence of light vegetation.

With regard to scalability and sustainability, the findings suggest that the solution can be expanded to other areas or institutions. Future work should consider installing at least five additional devices in the Quito Metropolitan District, allowing data concentration on the Ubidots platform. This would facilitate public access to real-time UV radiation data via mobile devices or web-based applications.

Finally, there are significant opportunities for improvement and innovation based on the results obtained. A key next step would be to optimize the remote connectivity of modules in different locations within Quito, as well as develop a cloud-based platform that centralizes the data and presents them in a user-friendly format for web and mobile applications. These enhancements would not only expand the reach of the system but also strengthen its impact on education, research, and public health decision-making.

Author Contributions: Conceptualization, I.S., C.G., A.P., and A.N.M.; methodology, I.S., C.G., and A.P.; software, I.S., C.G., and A.P.; validation, P.P.J. and I.S.; formal analysis, I.S., C.G., A.P., and A.N.M.; investigation, I.S., C.G., A.P., and A.N.M.; resources, I.S., C.G., A.P., and A.N.M.; data curation, I.S., C.G., A.P., and A.N.M.; writing—original draft preparation, I.S. and P.P.J.; writing—review and editing, P.P.J.; supervision, P.P.J. and I.S.; project administration, P.P.J. and I.S.; funding acquisition, P.P.J. and I.S. All authors have read and agreed to the published version of the manuscript.

Funding: This research was funded by ANID/FONDECYT Iniciación No. 11240799, ANID FONDECYT Regular No. 1211132, ANID Vinculación Internacional FOVI240009, Universidad de Las Américas under project 563.B.XVI.25, SENESCYT "Convocatoria abierta 2014-primera fase, Acta CIBAE-023-2014", and the Department of Networking and Telecommunication Engineering, Universidad de las Américas.

Institutional Review Board Statement: Not applicable.

Informed Consent Statement: Not applicable.

Data Availability Statement: The dataset is available upon request from the authors.

Conflicts of Interest: The authors declare no conflicts of interest.

References

1. WHO. Ultraviolet Radiation and Health Risks. 2022. Available online: https://saudijournals.com/media/articles/SJEAT_710_533-541.pdf (accessed on 14 October 2024).
2. UN Environment Programm; World Meteorological Organization. *Environmental Effects of Ozone Depletion and Climate Change: 2018 Assessment*; UN Environment Programme: Nairobi, Kenya, 2018.
3. Bustamante, D.; Mercado, M. Radiación UV en Ecuador: Factores de Riesgo y Monitoreo. *Rev. Climatol.* **2016**, *12*, 45–57.
4. Figueroa, C.; Hanania, E.; Gámez Espinosa, E.J.; Deya, M.C. Estudio de la acción de la luz UVC sobre pinturas. *Rev. Cienc. Tecnol.* **2023**, *10*, 25–26.
5. Quest, A. Safeguarding Your Vehicle: Effective Strategies for Protecting Against UV Damage. 2023. Available online: https://automotivequest.com/protecting-against-uv-damage/ (accessed on 14 October 2024).

6. Curbelo, F.; Leonard, D.D.; Cruz, Y.B.; Rodríguez, A.E.S. Cáncer de piel no melanoma y radiaciones ultravioletas. *Rev. Cuba. Med. Gen. Integral* **2020**, *36*, 152–160.
7. Bankov, D.; Khorov, E.; Lyakhov, A. On the Limits of LoRaWAN Channel Access. *IEEE Wirel. Commun. Lett.* **2018**, *7*, 76–79. [CrossRef]
8. Marín-García, E.J.; Alzate-Plaza, S.L.; Serna-Ruiz, A.F. Estación de medición de rayos ultravioleta alimentada por sistemas fotovoltaicos. *Nr. J. Rev.* **2020**, *16*, 163–179.
9. Jaramillo, O.; Rodrigo, K.; Mendieta, O.; José, Á. Diseño e implementación de una red de sensores para el monitoreo de los niveles de radiación solar en la ciudad de Loja. *Nr. J. Rev.* **2019**, *10*, 44–55. [CrossRef]
10. Moan, J.; Grigalavicius, M.; Baturaite, Z.; Dahlback, A.; Juzeniene, A. The relationship between UV exposure and incidence of skin cancer. *J. Skin Health* **2015**, *31*, 26–35. [CrossRef] [PubMed]
11. Mehic, M.; Duliman, M.; Selimovic, N.; Voznak, M. LoRaWAN End Nodes: Security and Energy Efficiency Analysis *Alex. Eng. J.* **2022**, *61*, 8997–9009. [CrossRef]
12. Kanellis, V.G. Ultraviolet radiation sensors: A review. *Biophys. Rev.* **2019**, *11*, 895–899. [CrossRef] [PubMed]
13. Okpara, C.R.; Idigo, V.E.; Oguchienti, S.M. Wireless Sensor Networks for Environmental Monitoring: A Review. *IJETT J.* **2020**, *68*, 68–71. [CrossRef]
14. Seckmeyer, G.; Zittermann, A.; McKenzie, R.; Greinert, R. Solar Radiation and Human Health. In *Environmental Toxicology*; Springer: New York, NY, USA, 2013; pp. 529–564. [CrossRef]
15. Monfort, I.O. Estudio de la Arquitectura y el Nivel de Desarrollo de la Red LoRaWAN y de los Dispositivos LoRa. Master's Thesis, Universitat Politècnica de València, Valencia, Spain, 2017.
16. Frequency Plans by Country. The Things Network. 2024. Available online: https://www.thethingsnetwork.org/docs/lorawan/frequencies-by-country/ (accessed on 25 June 2024).
17. Bohórquez, L.; Alexander, J. Nano-satélite Recuperable Para Estudios de los Efectos de la Radiación Cósmica en una Carga Biológica Expuesta en la Estratósfera: Fase II. 2019. Available online: https://repositorio.unbosque.edu.co/items/deba3c65-1b3a-4007-b5e5-3d88911b6e4b (accessed on 28 Jun 2024).
18. Guerrero, C. Implementación de un Sistema de Control y Monitoreo para la Radiación Ultravioleta en la Universidad Técnica de Cotopaxi en el Periodo Marzo 2019—Agosto 2019. 2019. Available online: https://repositorio.utc.edu.ec/items/87f850c6-e59d-4b18-93a9-d0a0bd00d700 (accessed on 28 June 2024).
19. Industries, A. GUVA-S12SD Analog UV Light Sensor Breakout. 2011. Available online: https://cdn-shop.adafruit.com/datasheets/1918guva.pdf (accessed on 25 April 2025).
20. DNK Power Co., Ltd. DNK505573 3.7V 2500mAh LiPo Battery Pack with PCM–Specification Sheet. 2023. Available online: https://www.dnkpower.com/wp-content/uploads/2023/11/DNK505573-3.7V-2500mAh-Lipo-Battery-Specification.pdf (accessed on 25 April 2025).
21. LoRa Node Development Kit. Heltec Automation. 2022. Available online: https://heltec.org/project/lora-kit-151/ (accessed on 25 April 2025).
22. SEMTECH Corporation. SX1262 Long Range, Low Power, Sub-GHz RF Transceiver Datasheet. 2018. Available online: https://www.semtech.com/products/wireless-rf/lora-connect/sx1262 (accessed on 25 April 2025).
23. Heltec Automation. *LoRa Node Development Kit Datasheet*. 2022. Available online:https://heltec.org/project/lora-node-151/ (accessed on 25 October 2023).
24. Municipio de Quito. Estaciones de Índice Ultravioleta (IUV). 2024. Available online: https://iuv.quito.gob.ec/ (accessed on 4 June 2024).
25. *ETSI EN 300 220-2 V2.1.2*; Electromagnetic compatibility and Radio spectrum Matters (ERM); Short Range Devices (SRD); Radio Equipment to be Used in the 25 MHz to 1,000 MHz Frequency Range with Power Levels Ranging up to 500 mW; Part 2: Harmonized EN Covering the Essential Requirements of Article 3.2 of Directive 2014/53/EU. European Telecommunications Standards Institute: Sophia Antipolis, France, 2018.

MDPI AG
Grosspeteranlage 5
4052 Basel
Switzerland
Tel.: +41 61 683 77 34

Sensors Editorial Office
E-mail: sensors@mdpi.com
www.mdpi.com/journal/sensors

MDPI

Academic Open
Access Publishing

mdpi.com

ISBN 978-3-7258-4476-0